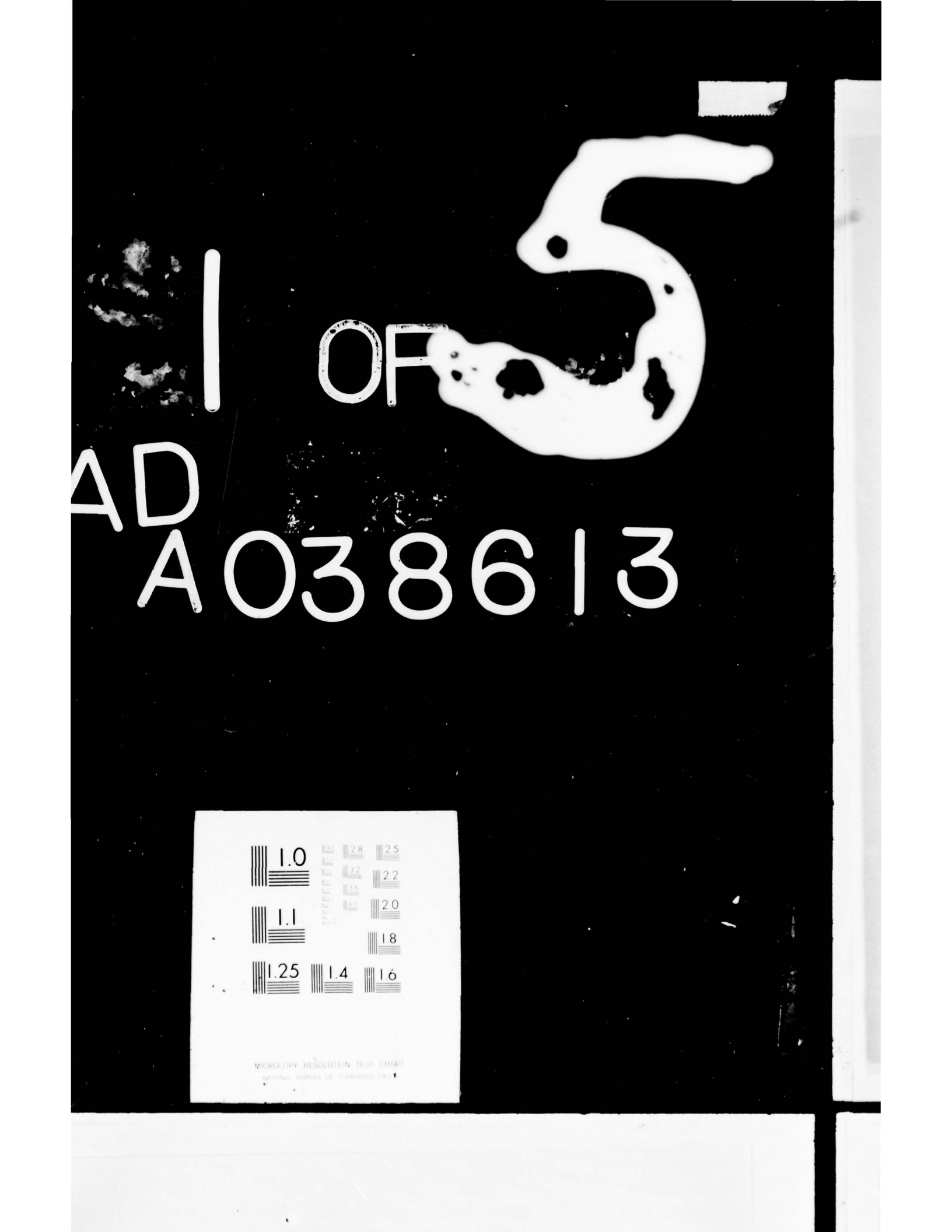
AD-A038 613 GENERAL ELECTRIC CO CINCINNATI OHIO AIRCRAFT ENGINE GROUP F/G 20/1
SUPERSONIC JET EXHAUST NOISE INVESTIGATION. VOLUME II. TECHNICA--ETC(U)
JUL 76 P R KNOTT, R MANI, C L MERKLE F33615-73-C-2031
UNCLASSIFIED R74AE6452-VOL-2 AFAPL-TR-76-68-VOL-2 NL

1 OF 5
AD A038613




1 OF 5
AD
A038613
1.0
1.1
1.25
1.4
1.6
2.8
2.5
3.2
2.2
3.6
2.0
4.0
1.8
MICROCOPY RESOLUTION TEST CHART
NATIONAL BUREAU OF STANDARDS-1963-A

AD A038613

AFAPL-TR-76-68

SUPERSONIC JET EXHAUST NOISE INVESTIGATION

Volume II
TECHNICAL REPORT

GENERAL ELECTRIC COMPANY
AIRCRAFT ENGINE GROUP
ADVANCED ENGRG. AND TECH. PROGRAMS DEPT.
CINCINNATI, OHIO 45215

JULY 1976

TECHNICAL REPORT AFAPL-TR-76-68
FINAL REPORT FOR THE PERIOD 1 DECEMBER 1972 - 23 SEPTEMBER 1975

Approved for public release; distribution unlimited

DDC
APR 26 1977
C

AIR FORCE AERO PROPULSION LABORATORY
AIR FORCE SYSTEMS COMMAND
WRIGHT-PATTERSON AIR FORCE BASE, OHIO 45433
and
DEPARTMENT OF TRANSPORTATION
OFFICE OF NOISE ABATEMENT
WASHINGTON, D.C.

AD No.
DDC FILE COPY

NOTICE

When Government drawings, specifications, or other data are used for any purpose other than in connection with a definitely related Government procurement operation, the United States Government thereby incurs no responsibility nor any obligation whatsoever; and the fact that the Government may have formulated, furnished, or in any way supplied the said drawings, specifications, or other data, is not to be regarded by implication or otherwise as in any manner licensing the holder or any other person or corporation, or conveying any rights or permission to manufacture, use or sell any patented invention that may in any way be related thereto.

This report has been reviewed by the Information Office, ASD/OIP, and is releasable to the National Technical Information Service (NTIS). At NTIS, it will be available to the general public, including foreign nations.

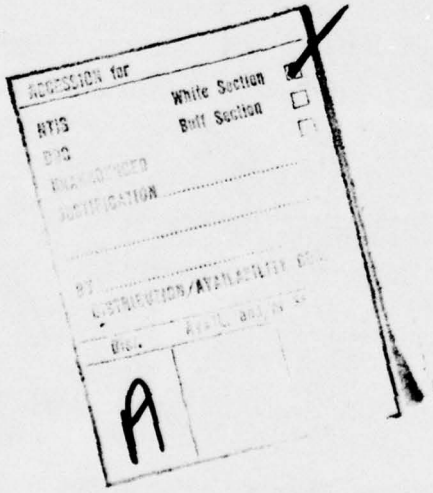
This technical report has been reviewed and is approved for publication.

Paul A. Shahady
PAUL A. SHAHADY
Project Engineer
USAF

G Banerian
DR. GORDON BANERIAN
Project Manager
Department of Transportation

FOR THE COMMANDER

Robert E. Henderson
ROBERT E. HENDERSON
Manager, Combustion Technical Area



Copies of this report should not be returned unless return is required by security considerations, contractual obligations, or notice on a specific document.

AIR FORCE - 5 MARCH 72 - 225

Unclassified

SECURITY CLASSIFICATION OF THIS PAGE (When Data Entered)

REPORT DOCUMENTATION PAGE

READ INSTRUCTIONS BEFORE COMPLETING FORM

1. REPORT NUMBER: AFAPL-TR-76-68, Vol-II
2. GOVT ACCESSION NO.
3. RECIPIENT'S CATALOG NUMBER

4. TITLE (and Subtitle): Supersonic Jet Exhaust Noise Investigation • Volume II - Technical Report.

5. TYPE OF REPORT & PERIOD COVERED: Technical Report (Final) 1 Dec 1972 - 23 Sept 1975

6. PERFORMING ORG. REPORT NUMBER: R74AEG452-Vol-2

7. AUTHOR(s): P.R. Knott, R. Mani, C.L. Merkle, H.S. Ribner, P. Scott, M.A. Smith, K.R. Bilwakesh

8. CONTRACT OR GRANT NUMBER(s): F33615-73-C-2031

9. PERFORMING ORGANIZATION NAME AND ADDRESS: General Electric Company, Advanced Engineering & Technology Programs Dept., Aircraft Engine Group, Cincinnati, Ohio 45215

10. PROGRAM ELEMENT, PROJECT, TASK AREA & WORK UNIT NUMBERS: P.E. 62203F, Project 3066, Task 306614, W.U. 30661407

11. CONTROLLING OFFICE NAME AND ADDRESS: Air Force Aero Propulsion Lab (TBC), Wright-Patterson Air Force Base, Ohio 45433

12. REPORT DATE: JULY 1976

13. NUMBER OF PAGES: 365

14. MONITORING AGENCY NAME & ADDRESS (if different from Controlling Office): Final Rept. 1 Dec 72-23 Sep 75

15. SECURITY CLASS. (of this report): Unclassified

15a. DECLASSIFICATION/DOWNGRADING SCHEDULE

16. DISTRIBUTION STATEMENT (of this Report): 3066 14

Approved for public release; Distribution Unlimited

396p.

17. DISTRIBUTION STATEMENT (of the abstract entered in Block 20, if different from Report)

18. SUPPLEMENTARY NOTES: This report is Volume II of a four-volume final Technical Report prepared by the Advanced Engineering and Technology Programs Department, Aircraft Engine Group, of the General Electric Company, under the joint sponsorship of the Air Force Aero Propulsion Laboratory, Wright-Patterson Air Force Base, Ohio, and the Department of Transportation, Washington, D.C.

19. KEY WORDS (Continue on reverse side if necessary and identify by block number): Supersonic Jet Exhaust Noise, Fluid Shielding, Turbulent Mixing Noise, Orderly Structure, Jet Refraction, Swirl Noise, Combustion Noise, Turbulence, Laser Velocimeter, Turbulence Spectra, Cross-Correlation, Aeroacoustics.

20. ABSTRACT (Continue on reverse side if necessary and identify by block number)

This report discusses detailed accounts of major theoretical and experimental investigations directed toward obtaining better understanding and mathematical specification of supersonic turbulent jets. Complete theoretical discussions are given describing the influence of a jet's mean flow shrouding on acoustic radiation of heated and unheated jets,

DD FORM 1 JAN 73 1473 EDITION OF 1 NOV 65 IS OBSOLETE

Unclassified

SECURITY CLASSIFICATION OF THIS PAGE (When Data Entered)

403468

20. ABSTRACT (continued)

approximate closed form acoustic expressions for turbulent mixing noise characterized by self-noise and shear-noise are given, and theoretical aeroacoustic formulations for the orderly structure of supersonic jets are reviewed. Extensive theory/data comparisons of developed acoustic models are given. Experimental investigations aimed at studying high velocity jet refraction, and the influence of jet swirl and upstream combustion roughness on jet noise is presented. Additionally, an extensive series of laser velocimeter measurements for high velocity and high temperature simple circular jets is discussed. Results include hot-film/laser velocimeter comparisons for ambient jets, mean velocity and turbulent velocity plume surveys of heated supersonic shock-free and shocked flow nozzles, and a demonstration experiment illustrating the capability of performing in-jet turbulence to far-field acoustic cross-correlation.

FOREWORD

This is Volume II of the final Technical Report prepared by the Advanced Engineering and Technology Programs Department, Aircraft Engine Group, of the General Electric Company, Evendale, Ohio under the joint sponsorship of the Air Force Aero-Propulsion Laboratory, Wright-Patterson Air Force Base, Ohio and the Department of Transportation, Washington, D.C., under contract F33615-73-C-2031. The inclusive dates for this work were December, 1972 through August, 1975. The work herein was accomplished under Project 3066, Task 14, Work Unit 07, with Mr. Paul A. Shahady (AFAPL/TBC) as Project Engineer. Dr. Paul R. Knott of the General Electric Company was technically responsible for the work. Other General Electric personnel were: Mr. F. Ahlgrin, Information Theory Specialist; Dr. K. R. Bilwakesh, Experimentalist; Mr. P. Mossey, Laser Velocimeter Specialist; Dr. R. Mani, Theoretican; Mr. P. Scott, Information Theory Specialist; and Mr. M. Smith, Acoustic Engineer. Other personnel were: Dr. C. Merkle, Consultant (Flow Research, Inc.); and Professor H. S. Ribner and Mr. N. S. M. Nosseir, Consultants (Institute for Aerospace Studies, University of Toronto).

TABLE OF CONTENTS

VOLUME II

Section		Page
	INTRODUCTION	107
	CHAPTER I - Theoretical Acoustic Developments for Turbulent Jets	109
1.0	THE INFLUENCE OF JET FLOW ON JET NOISE	110
	1.1 The Noise of Unheated Jets	110
	1.1.1 Background	110
	1.1.2 Formulation and Method of Solution	113
	1.1.3 Application of Theory to Experimental Results	130
	1.1.4 Concluding Remarks	139
	1.2 The Noise of Heated Jets	141
	1.2.1 Interpretation of Lilley's Equation for Heated Jets	141
	1.2.2 Method of Solution	147
	1.2.3 Physical Interpretation of the Solutions and Applications to Jet Noise Experiments	151
	1.2.4 Concluding Remarks	155
2.0	TESTS OF A THEORETICAL MODEL OF JET NOISE	165
	2.1 Background	165
	2.2 Basic Theoretical Analysis for Model Development	166
	2.3 Formalism for Tests of the Model	167
	2.4 Tests I: Invariance of β; Similarity of Self- and Shear-Noise Spectra	170
	2.5 Tests II: Model as a Framework for Jet Noise Prediction	176
	2.6 Discussion	185
	2.7 Conclusions	187
	APPENDIX 1 - Theoretical Considerations for Ribner's Self-Noise Model	189
3.0	ANALYTICAL MODELING FOR A JET'S ORDERLY STRUCTURE	193
	3.1 Background	193
	3.2 The Stability of Turbulent Axisymmetric Compressible Jets	193
	3.2.1 The Equations for the Mean Flow and the Wave	194
	3.2.2 The Eigenvalue Equation	197

PRECEDING PAGE BLANK-NOT FILMED

TABLE OF CONTENTS (Continued)

Section			Page
	3.3	Determination of the Spectral Characteristics of the "Orderly Structure"	200
		3.3.1 Tam's Single-Frequency Analysis	200
		3.3.2 Multiple Frequency approaches	206
		3.3.3 Effects of Finite Amplitude Waves	207
	3.4	Experimental Evidence of Orderly Structure in Jets	208
	3.5	Sound Radiation from the Orderly Structure in a Jet	209
	3.6	Orderly Structure Flow Field Calculations	212
		3.6.1 Integral Form of the Equations of Motion	212
		3.6.2 Fluid Dynamic Calculations	214
		3.6.3 Equations for the Acoustic Radiation	214
	3.7	Summary and Conclusions	220
		APPENDIX 2 - Solution of the Eigenvalue Equation in the Region Near the Singularity	223
		CHAPTER II - Aeroacoustic Investigations for High-Velocity, High-Temperature Jets	227
1.0		UPSTREAM DISTURBANCE INFLUENCES ON JET EXHAUST NOISE	228
	1.1	Background	228
	1.2	Influence of Upstream Swirl on Jet Noise Generation	229
		1.2.1 Analytical Aerodynamic Swirl Model	230
		1.2.1.1 Description of the Model	233
		1.2.1.2 Aeroacoustic Predictions	239
		1.2.2 Swirling Jet Aeroacoustic Experiment	241
		1.2.2.1 Experiment Apparatus, Test Setup and Conditions	246
		1.2.2.2 Aerodynamic Results	258
		1.2.2.3 Acoustic Results	277
	1.3	Influence of Upstream Turbulence on Jet Noise Generation	291
		1.3.1 Analytical Aerodynamic Model for Turbulent Production	291
		1.3.2 Combustion Roughness Aeroacoustic Experiment	292
		1.3.2.1 Experimental Apparatus, Test Setup, and Conditions	299
		1.3.2.2 Aerodynamic Results	301
		1.3.2.3 Acoustic Results	305
		1.3.3 Afterburner Flameholder/Spraybar Aeroacoustic Experiment	309
		1.3.3.1 Experimental Apparatus, Test Setup, and Conditions	309
		1.3.3.2 Aerodynamic Results	316
		1.3.3.3 Acoustic Results	316
	1.4	Summary and Conclusions	327

TABLE OF CONTENTS (Continued)

Section		Page
2.0	JET REFRACTION EXPERIMENTS	340
	2.1 Background	340
	2.2 Ribner's Refraction Concepts	340
	2.2.1 Method of Approach	341
	2.3 Test Facility and Apparatus	350
	2.3.1 Test Facility	350
	2.3.2 Description of Tone Source	351
	2.3.3 Instrumentation	356
	2.4 Test Matrix and Procedure	356
	2.5 Discussion of Results	359
	2.5.1 Influence of Tone Source Hardware on Jet Noise	359
	2.5.2 Methods of Data Reduction	362
	2.5.3 Influence of Velocity Variations on Jet Refraction	362
	2.5.4 Influence of Temperature Variations on Refraction	373
	2.6 Further Analysis of the Data	373
	CHAPTER III - Laser Velocimeter Investigations	389
1.0	PARAMETRIC LASER VELOCIMETER STUDIES OF HIGH-VELOCITY, HIGH-TEMPERATURE, TURBULENT JETS	390
	1.1 Background	390
	1.2 The Laser Velocimeter Arrangement	390
	1.2.1 Actuator and Seeding	394
	1.2.2 Signal Processing and Recording	397
	1.3 Laser Velocimeter Jet Plume Survey	397
	1.3.1 Cold Jet Laser Velocity Measurements	397
	1.3.2 Hot Supersonic Jet Laser Velocimeter Measurements	397
	1.3.2.1 Shock-Free Jet	397
	1.3.2.2 Conical Nozzle Shock Flow Profiles	401
	1.3.2.3 Exit Plane Parametric Studies	404
	1.4 Summary and Conclusions	414
2.0	IN-JET/FAR-FIELD CROSS-CORRELATION EXPERIMENTS	417
	2.1 Background	417
	2.2 Acoustic Theory and General Approach	417
	2.3 The Random Sample Correlation Estimator	419
	2.4 Simulation Experiments	426

TABLE OF CONTENTS (Concluded)

Section		Page
2.5	Cross-Correlation Experiments with General Electric's Laser Velocimeter	429
	2.5.1 Experimental Arrangement and Test Conditions	429
	2.5.2 Discussion of Results	433
2.6	Conclusions	441
APPENDIX 3 -	Tabular Listing of Hot-Film/LV Measurements on 4.3-inch Conic Nozzle	442
APPENDIX 4 -	Contour Plots of Mean Velocity, Turbulent Velocity for C/D Shock-Free Flow, M_j=1.55, $T_T \cong$ 1500°, 2500° R.	447
-	Contour Plots of Mean Velocity and Turbulent Velocity for a Conic Nozzle (Shocked-Flow) $M_j \sim 1.55$, $T_T \sim 1500°$ R	447
APPENDIX 5 -	Ground Reflection Correction for Cross-Correlation Measurements	455
REFERENCES		458

LIST OF ILLUSTRATIONS

VOLUME II

Figure		Page
46.	Cylindrical Coordinate System for Plug Flow Acoustic Model.	117
47.	Notation for a Moving Source.	121
48.	Schematic of Source Models.	125
49.	Phase Speed or Wave Number Differences Between Incident and Refracted Waves.	128
50.	Comparison with Data of Lush at $M_j = 0.366$ ($V_j = 125$ m/s).	133
51.	Comparison with Data of Lush at $M_j = 0.57$ ($V_j = 195$ m/s).	134
52.	Comparison with Data of Lush at $M_j = 0.878$ ($V_j = 300$ m/s).	135
53.	Comparison with Data of Ahuja and Bushell at $M_j = 0.363$ ($V_j = 400$ ft/s).	136
54.	Comparison with Data of Ahuja and Bushell at $M_j = 0.546$ ($V_j = 600$ ft/s).	137
55.	Comparison with Data of Ahuja and Bushell at $M_j = 0.909$ ($V_j = 1000$ ft/s).	138
56.	Coordinate System for the Heated Jet.	143
57.	Schematic for a Transverse Dipole Proportional to ρ (y).	145
58.	Coordinate System for the Plug-Flow Acoustic Model for a Heated Jet.	148
59.	Jet Density Exponent for Total Power as a Function of (V_j/c_o).	154
60.	Jet Density Exponent for $V_j/c_o = 0.447$ as a Function of Angle from the Jet Axis.	156
61.	Jet Density Exponent for $V_j/c_o = 0.589$ as a Function of Angle from the Jet Axis.	157
62.	Jet Density Exponent for $V_j/c_o = 0.741$ as a Function of Angle from the Jet Axis.	158

LIST OF ILLUSTRATIONS (Continued)

Figure		Page
63.	Jet Density Exponent for V_j/c_o = 0.891 as a Function of Angle from the Jet Axis.	159
64.	Jet Density Exponent for V_j/c_o = 1.023 as a Function of Angle from the Jet Axis.	160
65.	Jet Density Exponent for V_j/c_o = 1.175 as a Function of Angle from the Jet Axis.	161
66.	Index at 90° to the Jet Axis as a Function of V_j/c_o.	162
67.	Jet Density Exponent at 90° for Various Frequencies for Three Jet Mach Numbers.	163
68.	Convection and Refraction Modify "Basic" Noise Pattern.	168
69.	Tests of the Predicted Invariance of β with Frequency.	171
70.	Basic Self-Noise Spectrum a (CS) with Spectrum Measurements at θ = 45° and the Extracted Basic Shear-Noise Spectrum b (CS).	172
71.	Shear- and Self-Noise Spectra Derived from Cross Correlations Between Hot-Wire and Microphone Signals.	173
72.	Comparison of Normalized Self-Noise and Shear-Noise Spectra (the Self-Noise Has Been Downshifted One Octave).	175
73.	Variation of the Convective Amplification Exponent with (CS) and M.	177
74.	Variation of β with Jet Diameter D (from the Measurements of Reference 35).	178
75.	Empirical Universal Self-Noise Spectrum a $(CS)_e/a_{max.}$.	180
76.	Variation of Source Strouhal Number of Self-Noise Spectrum Peak $(CS)_p$ with Mach Number M.	181
77.	Directivity of 1/3-Octave Intensity; Comparison of Experimental Data of Lush, D=25 mm.	182
78.	Directivity of 1/3-Octave Intensity; Comparison with Experimental Data of Chu.	183

LIST OF ILLUSTRATIONS (Continued)

Figure		Page
79.	Directivity of 1/3-Octave Intensity; Comparison with Experimental Data of Ahuja.	184
80.	Directivity of 1/3-Octave Intensity; Experimental Data from Ahuja. Theory Based on Empirical β (2.82), on "Theoretical" β (2.0), and on Vanishing β (Complete Neglect of Shear Noise).	186
81.	Deformed Path for Integration Around Logarithmic Singularity in Eigenvalue Equation for Self-Excited and Damped Cases.	201
82.	"Preferred" Waves in Supersonic Jet, Based on Periodic Shock Cell Structure in Nearly Ideally Expanded Jet (from Tam, 1972).	204
83.	Schematic Diagram Showing Broad Band Amplification Which is Available in a Jet (According to Parallel Flow Stability Theory), as Compared with the Energy Distribution in the Orderly Structure Wave (According to Tam, 1972).	205
84.	Variation of Half-Thickness of Mixing Layer with Distance from Nozzle Exit Plane.	215
85.	Variation of Core Radius as a Function of Axial Distance from Nozzle Exit Plane.	216
86.	Wave Number of Large-Scale Oscillation as a Function of Half-Width of Shear Layer.	217
87.	Amplification Rate of Large-Scale Oscillation as a Function of Half-Width of Shear Layer.	218
88.	Real and Imaginary Parts of a Eigenfunction in Region of Numerical Integration.	219
89.	Directional Distribution of Acoustic Power.	221
90.	Axisymmetric Turbulent Jet Flow Field.	240
91.	Comparison of Predicted and Measured Centerline Decay of Mean Axial Velocity for Swirling Isothermal Subsonic Jets.	241
92.	Predicted Centerline Decay of Mean Axial Velocity for Swirling and Nonswirling Isothermal Subsonic Jets.	242

LIST OF ILLUSTRATIONS (Continued)

Figure		Page
93.	Predicted Variation of Turbulence Intensity Along the Centerline of Swirling and Nonswirling Isothermal Subsonic Jets.	243
94.	Predicted Variation of Overall Sound Pressure Level Around a 40-foot Arc for Swirling and Nonswirling Isothermal Subsonic Jets.	244
95.	Predicted 1/3-Octave-Band Sound Pressure Level Spectra at 30° from the Jet Axis on a 40-foot Arc for Swirling and Nonswirling Subsonic Isothermal Jets.	245
96.	Single-Flow Facility Burner System.	247
97.	JENOTS Single-Flow Facility.	248
98.	Swirl Test Setup with View of Swirl Vanes.	249
99.	Swirl Vane Section.	250
100.	Swirl Test Setup Schematic.	252
101.	Acoustic Far-Field Measuring Stations.	253
102.	Laser Velocimeter Optics Package.	254
103.	Laser Doppler Velocimeter Setup at JENOTS.	255
104.	Cobra Probe Sensing Head.	256
105.	Swirl Test Setup with Cobra Probe.	257
106.	Cobra Probe Measurements 0.5" Downstream of Nozzle Exit, Test Point 1.	259
107.	Cobra Probe Measurements 0.5" Downstream of Nozzle Exit, Test Point 2.	260
108.	Cobra Probe Measurements 0.5" Downstream of Nozzle Exit, Test Point 3.	261
109.	LDV Measurements 0.5" Downstream of Nozzle Exit, Test Point 1.	263
110.	LDV Measurements 0.5" Downstream of Nozzle Exit, Test Point 2.	264

LIST OF ILLUSTRATIONS (Continued)

Figure		Page
111.	LDV Measurements 0.5" Downstream of Nozzle Exit, Test Point 3.	265
112.	LDV Measurements on the Jet Centerline, Test Point 1.	266
113.	LDV Measurements on the Jet Centerline, Test Point 2.	267
114.	LDV Measurements on the Jet Centerline, Test Point 3.	268
115.	LDV Measurements of Radial Velocity Profiles, Baseline Test Point 1.	269
116.	LDV Measurements of Radial Velocity Profiles, Baseline Test Point 2.	270
117.	LDV Measurements of Radial Velocity Profiles, Baseline Test Point 3.	271
118.	LDV Measurements of Radial Velocity Profiles, Swirl Test Point 1.	272
119.	LDV Measurements of Radial Velocity Profiles, Swirl Test Point 2.	273
120.	LDV Measurements of Radial Velocity Profiles, Swirl Test Point 3.	274
121.	Calculated Profiles 0.5" Downstream of Nozzle Exit.	276
122.	Measured Overall Sound Pressure Levels, Test Point 1.	278
123.	Measured Overall Sound Pressure Levels, Test Point 2.	279
124.	Measured Overall Sound Pressure Levels, Test Point 3.	280
125.	Measured 1/3-Octave-Band Sound Pressure Level Spectra, Test Point 1, Microphone at 30° to Jet Axis.	282
126.	Measured 1/3-Octave-Band Sound Pressure Level Spectra, Test Point 2, Microphone at 30° to Jet Axis.	283
127.	Measured 1/3-Octave-Band Sound Pressure Level Spectra, Test Point 3, Microphone at 30° to Jet Axis.	284
128.	Measured 1/3-Octave-Band Sound Pressure Level, Test Point 1, Microphone at 90° to Jet Axis.	285

LIST OF ILLUSTRATIONS (Continued)

Figure		Page
129.	Measured 1/3-Octave-Band Sound Pressure Level, Test Point 2, Microphone at 90° to Jet Axis.	286
130.	Measured 1/3-Octave-Band Sound Pressure Level, Test Point 3, Microphone at 90° to Jet Axis.	287
131.	Perceived Noise Level Measurements, Test Point 1.	288
132.	Perceived Noise Level Measurements, Test Point 2.	289
133.	Perceived Noise Level Measurements, Test Point 3.	290
134.	Physical Configuration for Analytical Model.	293
135.	Turbulence Intensity at End of Mixing Chamber Versus Air Mach Number at Mixing Station (Plane 1).	294
136.	Turbulence Intensity at End of Mixing Chamber Versus Fuel/Air Ratio.	295
137.	Turbulence Intensity at End of Mixing Chamber Versus Fuel Jet Swirl Number at Mixing Station (Plane 1).	296
138.	Turbulence Intensity at End of Mixing Chamber Versus Fuel-to-Air Velocity Ratio at Mixing Station (Plane 1).	297
139.	Turbulence Intensity at Nozzle Exit Plane Versus Fuel-to-Air Velocity Ratio at Mixing Station (Plane 1).	298
140.	4.31" Throat Diameter Water-Cooled, Parallel-Flow, Converging/Diverging Nozzle.	300
141.	LV Measurements 0.5" Downstream of Nozzle Exit.	302
142.	LV Measurements at $x/D_8 = 3.98$.	303
143.	LV Measurements at $x/D_8 = 3.98$.	304
144.	Measured 1/3-Octave-Band Pressure Fluctuation Spectra, Preburner Static Pressure.	306
145.	Measured 1/3-Octave-Band Pressure Fluctuation Spectra, Afterburner Static Pressure.	307
146.	Measured 10-Hz-Narrowband Pressure Fluctuation Spectra.	308

LIST OF ILLUSTRATIONS (Continued)

Figure		Page
147.	Measured Overall Sound Pressure Levels.	310
148.	Measured 1/3-Octave-Band Sound Pressure Level Spectra, $\theta_{jet} = 40°$.	311
149.	Measured 1/3-Octave-Band Sound Pressure Level Spectra, $\theta_{jet} = 90°$.	312
150.	Measured Overall Sound Pressure Levels.	313
151.	Measured 10-Hz-Narrowband Sound Pressure Level Spectra, $\theta_{jet} = 30°$.	314
152.	Measured 10-Hz-Narrowband Sound Pressure Level Spectra, $\theta_{jet} = 90°$.	315
153.	Flameholder and Typical Spraybar from JENOTS Afterburner Section.	317
154.	LV Measurements 0.5" Downstream of Nozzle Exit, Test Point 1.	318
155.	LV Measurements 0.5" Downstream of Nozzle Exit, Test Point 2.	319
156.	LV Measurements 0.5" Downstream of Nozzle Exit, Test Point 3.	320
157.	LV Measurements on the Jet Centerline, Test Point 1.	321
158.	LV Measurements on the Jet Centerline, Test Point 2.	322
159.	LV Measurements on the Jet Centerline, Test Point 3.	323
160.	LV Measurements of Radial Velocity Profiles, Test Point 1.	324
161.	LV Measurements of Radial Velocity Profiles, Test Point 2.	325
162.	LV Measurements of Radial Velocity Profiles, Test Point 3.	326
163.	Overall Sound Pressure Levels, Test Point 1.	328
164.	Overall Sound Pressure Levels, Test Point 2.	329
165.	Overall Sound Pressure Levels, Test Point 3.	330

LIST OF ILLUSTRATIONS (Continued)

Figure		Page
166.	Measured 1/3-Octave-Band Sound Pressure Level Spectra, θ_{jet} = 30°, Test Point 1.	331
167.	Measured 1/3-Octave-Band Sound Pressure Level Spectra, θ_{jet} = 30°, Test Point 2.	332
168.	Measured 1/3-Octave-Band Sound Pressure Level Spectra, θ_{jet} = 30°, Test Point 3.	333
169.	Measured 1/3-Octave-Band Sound Pressure Level Spectra, θ_{jet} = 90°, Test Point 1.	334
170.	Measured 1/3-Octave-Band Sound Pressure Level Spectra, θ_{jet} = 90°, Test Point 2.	335
171.	Measured 1/3-Octave-Band Sound Pressure Level Spectra, θ_{jet} = 90°, Test Point 3.	336
172.	Measured 10-Hz-Narrowband Sound Pressure Level Spectra, Test Point 2.	337
173.	Measured 10-Hz-Narrowband Sound Pressure Level Spectra, Test Point 3.	338
174.	Ribner's Jet Acoustic Refraction Model.	342
175.	Effect of Jet Velocity on Directivity (Reference 13).	343
176.	Jet Noise Directivity for Air Jet (Reference 13).	344
177.	Effect of Jet Temperature on Directivity (Reference 15).	345
178.	Effect of Source Frequency on Directivity (Reference 15).	346
179.	Refraction Schematic for a Point Source Injected into a Jet Flow.	348
180.	Refraction Schematic for a Jet Flow.	349
181.	Schematic of Experimental Setup for Acoustic Far-Field Measuring Stations.	352
182.	Siren Used for Point Source.	353
183.	Directivities of Siren Output in the 500-5000-Hz Frequency Range on a 20-foot Arc with a 0.81" ID Output Port.	354

LIST OF ILLUSTRATIONS (Continued)

Figure		Page
184.	Comparison of Sound Source Output with Measured Jet Noise Data; Jet at 1670 ft/sec and T_T = 1500° R.	355
185.	Refraction Experimental Setup with Siren Uncovered.	357
186.	Refraction Experimental Setup with Siren Acoustically Isolated.	358
187.	Jet Acoustics with and without the Tone Source Hardware in the Nozzle.	361
188.	Typical 2-Hz and 10-Hz Bandwidth Data f_{tone} = 783 Hz, M_o = 1.3, $T_{T_{jet}}$ = 1500° R, and θ_{jet} = 20°.	363
189.	Typical 1-Hz and 5-Hz Bandwidth Analysis of Siren Tone Data Over the Entire Period of Recording (∿ 120 secs), f_{tone} = 783 Hz, No Jet.	364
190.	Typical 2-Hz Bandwidth Analysis of (Tone + Jet) Data Over the Entire Period of Recording (∿ 120 Seconds), f_{tone} = 783 Hz, M_o = 0.9, $T_{T_{jet}}$ = 2000° R.	365
191.	Effect of Jet Velocity on Tone Directivity, f_{tone} = 783 Hz, T_o = Ambient, M_o = 0.5, 0.7, 0.9.	367
192.	Effect of Jet Velocity on Tone Directivity, f_{tone} = 783 Hz, T_o Ambient, M_o = 0.9 and 1.3.	368
193.	Comparison of 2-Hz Narrowband Jet Noise Directivity with Siren Tone Directivity, M_o = 1.3, $T_{T_{jet}}$ = 1000° F.	369
194.	Effect of Jet Velocity on Tone Directivity, M_o = 0.9, 1.3, 1.5, $T_{T_{jet}}$ = 1500° R.	370
195.	Comparison of 2-Hz Narrowband Jet Noise Directivity with Siren Tone Directivity, M_o = 1.5, $T_{T_{jet}}$ = 1500° R.	371
196.	Effect of Jet Velocity on Tone Directivity, M_o = 1.5, $T_{T_{jet}}$ = 2000° R.	372
197.	Effect of Jet Temperature on Directivity.	374
198.	Effect of Jet Temperature on Tone Directivity, M_o = 0.9, f_{tone} = 783 Hz, $T_{T_{jet}}$ = 1000° and 1500° R.	375

LIST OF ILLUSTRATIONS (Continued)

Figure		Page
199.	Effect of Jet Temperature on Tone Directivity, M_o = 1.3, f_{tone} = 783 Hz, $T_{T_{jet}}$ = 1000°, 1500°, and 2000° R.	376
200.	Effect of Jet Temperature on Tone Directivity, M_o = 1.5, f_{tone} = 783 Hz, $T_{T_{jet}}$ = 1500° and 2000° R.	377
201.	Tone SPL Reduction Due to Flow, Experiment Versus Theory, M_o = 0.5, $T_{T_{jet}}$ = Ambient, f_{tone} = 783 Hz.	379
202.	Tone SPL Reduction Due to Flow, Experiment Versus Theory, M_o, = 0.7, $T_{T_{jet}}$ = Ambient, f_{tone} = 783 Hz.	380
203.	Tone SPL Reduction Due to Flow, Experiment Versus Theory, Including Convection Amplification Factor, M_o = 0.9, T_T = Ambient, f_{tone} = 783 Hz.	382
204.	Tone SPL Reduction Due to Flow, Experiment Versus Theory, Including Convection Amplification Factor, M_o = 1.3, f_{tone} = 783 Hz, $T_{T_{jet}}$ = 1000°, 1500°, and 2000° R.	383
205.	Tone SPL Reduction Due to Flow, Experiment Versus Theory, Including Convective Amplification Factor, M_o = 1.5, f_{tone} = 783 Hz, $T_{T_{jet}}$ = 1500° and 2000° R.	384
206.	Influence of Jet Temperature on Tone SPL Reduction Due to Flow, Experiment Versus Theory.	385
207.	Influence of Tone Frequency on Tone SPL Reduction Due to Flow, M_o = 1.5, T_T = 2000° R, f_{tone} = 783 and 3000 Hz.	386
208.	Influence of Tone Frequency on Tone SPL Reduction Due to Flow Theory, M_o = 1.5, T_T = 2000° R, f_{tone} = 783 and 3000 Hz.	387
209.	LV Hot-Film Mean Velocity Measurements.	391
210.	LV Hot-Film Turbulent Measurements.	391
211.	LV-Measured Mean Velocity and Turbulent Velocity Axial Decays for a Shock-Free, High-Velocity, High-Temperature Jet.	392
212.	LV-Measured Turbulent Spectrum for Ambient and Heated Jets.	393
213.	Laser Velocimeter Optics Package.	395

LIST OF ILLUSTRATIONS (Continued)

Figure		Page
214.	Laser Velocimeter Setup at JENOTS.	396
215.	Hot-Film Arrangement on Laser Velocimeter Cart.	398
216.	Mean Velocity Profile Comparison of LV with Hot-Film; $X/D = 2.0$, $M_j = 0.5$.	399
217.	LV-Measured Normalized Radial Mean Velocity Profiles for $M_j = 0.5$, T_T = Ambient (Conical Nozzle Data).	400
218.	LV-Measured Contour Plot of Mean Velocity in fps at $M_j = 0.5$, T_T = Ambient.	401
219.	LV-Measured Contour Plot of Turbulent Velocity in fps at $M_j = 0.5$, T_T = Ambient.	402
220.	LV-Measured Contour Plot of Turbulent Intensity at $M_j = 0.5$, T_T = Ambient.	403
221.	Laser-Velocimeter-Measured Mean Velocity and Turbulent Intensity Radial Profiles; $M_j = 1.55$, $T_T = 1500°$ R, $X/D = 9.6$ (C/D Shock-Free Data).	405
222.	LV-Measured Normalized Radial Mean Velocity Profiles for $M_j = 1.55$, $T_T = 1500°$ R (C/D Shock-Free Data).	406
223.	LV-Measured Normalized Radial Turbulence Velocity Profiles for $M_j = 1.55$, $T_T = 1500°$ R.	407
224.	LV-Measured Normalized Radial Mean Velocity Profiles for $M_j = 1.55$, $T_T = 1500°$ R (Conical Nozzle Shocked Data).	408
225.	LV Measuring Positions for Shock Turbulence Study.	409
226.	Mean Velocity and Turbulence Velocity on Centerline.	410
227.	LV-Measured Turbulence Properties for Shocked Nozzle Flow (Series 2).	411
228.	LV-Measured Turbulence Properties for Shocked Nozzle Flow (Series 3).	412
229.	Influence of Jet Velocity on Exit-Plane Turbulence.	413
230.	Influence of Upstream Temperature on Jet Exit-Plane Temperature.	415

LIST OF ILLUSTRATIONS (Concluded)

Figure		Page
231.	Influence of Upstream Temperature on Jet Exit-Plane Turbulence Intensity.	416
232.	Schematic of Sampling Scheme.	420
233.	Bias Error in Derivative Estimate as a Function of Cut-Off Frequency.	424
234.	Influence of Window Function to Improve Stability of Second Derivative.	425
235.	Schematic of System Used to Generate Simulated Data.	427
236.	Simulation Specifications.	428
237.	Analysis of Simulated Data, N = 20,000 Samples.	430
238.	Analysis of Simulated Data, N = 100,000 Samples.	431
239.	Analysis of Simulated Data, N = 500,000 Samples.	432
240.	General Arrangement for LV to Far-Field Acoustic Cross-Correlation Experiments.	434
241.	Test Arrangement Showing Microphone Slightly out of Plane for LV Far-Field Acoustic Cross-Correlation Experiments.	435
242.	LV-Measured Normalized Cross Correlation of In-Jet Velocity to Far-Field Acoustic (180,000 Samples).	436
243.	LV-Measured Cross-Power Spectrum.	438
244.	Expected Shape of Cross Correlation and Cross-Power Spectrum without Ground Reflection.	439
245.	Cross Spectra of Final Correlation Files.	440

LIST OF TABLES

VOLUME II

Table		Page
2.	Experimental Data for Determining the Ratio of Self-Noise to Shear-Noise.	174
3.	Test Matrix.	360
4.	Hot-Film Turbulence Measurements.	443
5.	LV Turbulence Measurements.	444
6.	M_j = 0.5 LV Measurements.	445

INTRODUCTION

Over the past two decades, a considerable amount of research has been directed toward understanding the aerodynamic and acoustic nature of heated supersonic exhaust jets. The advent of larger and more powerful military and commercial aircraft propulsion systems made it apparent that to improve the general community environment greater efforts should be taken to reduce jet engine noise. Because of a lack of clear understanding and detailed mathematical specification of the dominant noise-producing sources, only partial success was met in reducing jet noise with acceptable jet nozzle performance.

During 1971, the Air Force Aero Propulsion Laboratory initiated exploratory programs to develop the technology to significantly reduce supersonic aircraft propulsion system noise. In 1973 a joint program was sponsored by the Department of Transportation and the Air Force Aero Propulsion Laboratory to extend these initial efforts. The primary emphasis of the resulting work was on developing the theoretical and experimental technology for understanding simple circular exhaust jets over a range of velocities and temperatures typical of present and future military and commercial supersonic aircraft propulsion systems. References 1, 8, and 10 represent General Electric's work summarizing these findings to date.

This volume is Volume II of the final report performed at General Electric on the joint DOT/AF program. The report summarizes the major theoretical and experimental tasks accomplished during the second year of the joint program and extends the findings presented in the first-year interim report[8].

Chapter I of this report deals with recent theoretical acoustic modeling for turbulent jets. A major portion of the work described discusses a new concept of jet acoustic radiation for unheated and heated jets. The new work emphasizes the influence of a jet's mean flow shrouding on acoustic radiation. This work extends the classical Lighthill/Ribner/Ffowcs-Williams turbulent mixing point of view by abandoning the usual stationary acoustic analogy but yet maintains the notion of convected, compact eddy sources of a quadrupole character. New insights are discussed regarding scaling, low frequency convective amplification, convective/refractive coupling, and the acoustic influence of jet temperature,on jet noise. A section of this chapter also deals with an approximate turbulent mixing theory which offers closed form expressions for testing the existence of the aerodynamic source strength terms of self noise and shear noise. In addition, a section of work is dedicated to reviewing theoretical aeroacoustic formulations of the jet as an orderly structure. Although the latter work offers insight regarding the aerodynamic structure of turbulent jets, no new insights could be gained as to key acoustic characteristics of turbulent jets. Of the acoustic models considered during this program the model selected for further development and use in predictive procedures is the slug-flow fluid shielding model by R. Mani, and discussed in detail in Section 1 of Chapter I.

Chapter II reports on a series of high-velocity and high-temperature aeroacoustic analytical and experimental investigations.

The prime concerns in this chapter are studying the influences of upstream disturbances on jet exhaust noise and a series of jet refraction experiments. Results are presented which illustrate the influence of upstream swirl, combustion roughness, and an afterburner section on noise generation and reduction. The series of refraction experiments suggested that injected pure tone experiments may not be as useful as was first expected for gaining further insights into turbulent mixing noise at high subsonic and supersonic jet Mach numbers. However, it was found that the jet can act as an amplifier of injected or perhaps internally generated low frequency noise.

Chapter III is devoted to an extensive series of laser velocimeter measurements and to developing General Electric's laser velocimeter for performing in-jet noise source location measurements. The results of a parametric series of laser velocimeter rms mean velocity and turbulent velocity measurements are presented for high-temperature and high-velocity supersonic shock-free and shocked jets. Additionally, Chapter III discusses the theory and error analysis necessary for performing in-jet turbulence to far-field acoustic cross correlations for noise source location. A demonstration experiment, illustrating the capability of General Electric's laser velocimeter for performing in-jet noise source location, also is presented.

CHAPTER I

THEORETICAL ACOUSTIC DEVELOPMENTS FOR TURBULENT JETS

The work described below represents three areas of investigation related to developing a greater insight in understanding the mechanisms of jet noise generation and methods for modeling and predicting their characteristics. The three areas considered are: 1) the influence of jet flow on jet acoustics, 2) the test of a theoretical model for jet noise, and 3) analytical modeling for a jet's orderly structure.

The first section discusses an approach to jet noise which incorporates the influence of a jet's mean flow shrouding on the radiation of convected quadrupoles for unheated and heated jets. Although the notion of convected, compact eddies of quadrupole character is maintained, this work extends the classical Lighthill/Ribner/Ffowcs-Williams turbulent mixing point of view in that it abandons the usual stationary acoustic analogy approach. This new approach yields significant insight into concepts of scaling, low frequency convective amplification, convective/refractive coupling, and the acoustic influences of jet temperature on jet noise.

Section 2.0 of this chapter illustrates an approximate turbulent mixing theory which yields a closed-form expression for narrow band directivity of jet noise for angles where refraction is negligible. The work presented also offers a method for testing the existence of the aerodynamic source strengths of self noise and shear noise with relative ease. Both Section 1.0 and Section 2.0 illustrate their formulations with extensive theory/data comparisons.

Section 3.0 reviews some of the leading contenders for formulating the jet model as an orderly structure. Particular care is given to the formulation of the problem and its theoretical basis for applicability to high velocity jets. Recommendations are also made for extending current orderly structure models for broadband noise spectra (as opposed to the usual discrete frequency methods) and how such an analysis could be incorporated into an eigensolution for local acoustic sources at each point in the jet in a manner analogous to General Electric's turbulence acoustic models. Although this work has lead to greater appreciation of concepts concerning orderly structure and the validity of the theoretical framework of such analysis, it has not given any further insights into explaining key features of jet noise. On the contrary, the formulations which model a jet as a compact source have yielded more fruitful results toward explaining many of the heretofore unexplained characteristics of jet noise, such as those discussed in Sections 1.0 and 2.0.

SECTION 1.0

THE INFLUENCE OF JET FLOW ON JET NOISE

R. Mani

1.1 THE NOISE OF UNHEATED JETS

The present section is a study of the sound field produced by a convected-point quadrupole embedded in and moving along the axis of a round, plug-flow jet. Only subsonic eddy convection velocities are considered. We examine both cold and hot jets (in Subsections 1.1 and 1.2). A principal feature of the study is extensive comparison with jet noise data. It appears that this simple model problem succeeds in explaining all the major interesting features of jet noise data, of both hot and cold jets, and for jet exit velocities into the low supersonic regime. Particular success is achieved in explaining aspects of the data not explainable by the Lighthill acoustic analogy approach. The picture of jet noise generation that emerges (at least for jet velocities into the low supersonic regime) is in many respects a striking reaffirmation of the Lighthill point of view. It appears that there is an intrinsic or universal distribution of compact quadrupoles responsible for jet noise generation, whose strength and frequency distribution scales with jet velocity and nozzle diameter as would be expected from simple dimensional reasoning. These quadrupoles, of course, are convected by the mean flow, and satisfactory agreement with the data is obtained by assuming that they are devoid of any intrinsic directionality. There appears to be no significant jet Mach number (compressibility) or jet temperature effect on the scaling of this intrinsic distribution. The essential improvement over the Lighthill analysis is the incorporation of mean flow shrouding effects on the radiation of the convected quadrupoles. It is perhaps no exaggeration to claim that, with the incorporation of such a shrouding effect, the scaling problem of jet noise with regard to jet velocity, jet temperature, jet size, and angle from jet axis appears to be completely resolved. (The "scaling" principle, of course, is not very simply expressed and, in fact, needs calculations of the sort contained in this present study to implement it.)

1.1.1 Background

The generation of aerodynamic noise by free turbulence received its first quantitative formulation in the papers of Lighthill[44,45]. The principal quantitative step achieved by Lighthill was his rearrangement of the continuity and momentum equations to yield an equation:

$$\frac{\partial^2 \rho}{\partial t^2} - a_o^2 \nabla^2 \rho = \frac{\partial^2 T_{ij}}{\partial x_i \partial x_j} \quad . \; . \; . \tag{18}$$

where $T_{ij} = \rho\, u_i\, u_j + p_{ij} - a_o^2\, \rho\, \delta_{ij}$. ρ denotes the density, a_o a reference speed of sound, p_{ij} the compressive stress tensor, and u_i a velocity component. δ_{ij} is the Kronecker delta function. Even if we assume that p_{ij} can be approximated by $p\, \delta_{ij}$, where p is the pressure, there are two major problems in the use of equation (18). Firstly, even in cases where the pressure and density are related in an isentropic fashion, for a thermally stratified flow such as a hot jet, the relation $dp = a^2\, d\rho$ would require employing different values of a^2 in the different regions of the flow [i.e., no one value of a_o^2 can be used to eliminate the source term $(p_{ij} - a_o^2\, \rho\, \delta_{ij})$]. Secondly, even if the part of T_{ij} that is $(p_{ij} - a_o^2\, \rho\, \delta_{ij})$ is ignored (as is reasonable for cold jets), the equation:

$$\left(\frac{\partial^2 \rho}{\partial t^2} - a_o^2\, \nabla^2 \rho\right) = \frac{\partial^2}{\partial x_i \partial x_j}\, (\rho\, u_i\, u_j) \quad . \quad . \quad . \qquad (19)$$

can be used only to derive an integral equation for ρ (assuming that u_i, u_j is known). This difficulty is circumvented by Lighthill (1952, 1954) by his approximation of $(\rho\, u_i\, u_j)$ on the right-hand side of equation (19) by $(\rho_j\, u_i\, u_j)$ where ρ_j is the mean jet density.

Based on equation (19) (with $\rho\, u_i\, u_j$ approximated by $\rho_j\, u_i\, u_j$), Lighthill[46] produced his famous intensity law, to wit, that the far-field intensity would vary as:

$$I \sim \frac{\rho_j^2\, V_j^8\, D^2}{\rho_o\, a_o^5\, R^2\, (1 - M_c \cos\theta)^5} \quad . \quad . \quad . \qquad (20)$$

In equation (20), V_j denotes the jet exit velocity, D the nozzle diameter, R the radius of measurement, ρ_o the ambient density, a_o the ambient speed of sound, M_c the eddy convection Mach number usually taken as about $(0.65\, V_j/a_o)$, and θ the angle from the jet axis where the intensity is measured. The theory, of course, is valid only for $M_c < 1$ (subsonic eddy convection speeds). As Ahuja-Bushell[47] have pointed out, for cold jets (when $\rho_j \sim \rho_o$), equation (20) actually yields potentially an extremely valuable scaling principle. It suggests that if the far-field sound pressure level (SPL) at a particular frequency f and angle from the jet axis θ is analyzed by plotting the quantity Q given by:

$$SPL - 10 \log(V_j/V_{ref})^8 - 10 \log(D/R)^2 - 10 \log[(1 - M_c \cos\theta)^{-5}]$$

(where V_{ref} denotes a reference velocity) against a frequency parameter P given by:

$$\left[\frac{fD}{V_j}\, (1 - M_c \cos\theta)\right]$$

(this factor denoting a source Strouhal number allowing for a Doppler shift of the source frequency), then one should, as per the Lighthill analysis, obtain a universal curve of Q versus P regardless of jet velocity, frequency, angle of observation, nozzle size, or radius of measurement. To account for heating effects, the parameter Q should be modified to:

$$\left[Q - 10 \log(\rho_j^2/\rho_{ref}^2)\right]$$

(where ρ_{ref} denotes a reference density).

Recent experimental studies by Lush[18], Ahuja-Bushell[47], and Hoch[48], have shown that such a scaling principle is not able to collapse the data into one universal curve. For cold jets it is found that, for low values of P, an expression of type $(1 - M_c \cos\theta)^{-5}$ contained in equation (20) underestimates the variation of noise with angle. Conversely at high values of P, a factor of the type $(1 - M_c \cos\theta)^{-5}$ overestimates the variation with angle. For hot jets, the data of Hoch[48] appear best correlated by changing the dependence ρ_j in equation (20) to ρ_j^ω, where ω itself is dependent on (V_j/a_o), θ, and P. It is only for values of (V_j/a_o) in excess of about 1.3 that ω approaches 2. Also, the effects of heating generally cause the relative spectrum of the far-field pressure to be progressively biased toward the lower frequencies.

The principle contention of this part of the present study is that, for the noise of unheated jets, most of these discrepancies can be resolved if, while retaining the Lighthill notion of ascribing jet noise to convected quadrupoles, we account for the fact that the eddies do not communicate directly with the ambient atmosphere but are subject to a shrouding effect of the jet mean flow. Mathematically this entails further manipulations of equation (18) to explicitly extract out the influence of the mean flow and arrive at an equation which is clearly in the form of an inhomogeneous wave equation driven by convected, solenoidal, turbulent velocity fluctuations. Such a development was originated by Phillips[21] and has been developed more fully by Lilley[28] and Goldstein[29]. Historically, the Lilley-Goldstein development appears to have been first anticipated by White in an appendix to Eldred, et al[49]. The present study may be regarded as a simplified attempt to solve equations of the type derived by Lilley and Goldstein where, in the interest of obtaining closed-form solutions and motivated by the desire to avoid obscuring the physics by complicated numerical approaches, the jet flow is modeled as a simple, round, plug-flow jet. The reader's attention also is drawn to the work of Tester[50] and Berman[51] who have expounded ideas very similar to those contained in the present study. The papers of Ribner[52,53], Powell[25], and Csanady[26] also deserve mention as having drawn attention to mean flow shrouding effects.

In concluding the background, it is perhaps worth noting that Lighthill (Reference 45, p. 11-12) himself was somewhat concerned with how well the reader would accept the idea of quadrupole convection without inclusion of the effect of the jet flow itself on the radiation by the quadrupoles. He discusses the problem at some length in the cited reference and concludes by

conceding that in his model, "the quadrupoles can move but not the fluid." Since the convection of the quadrupoles is in itself an effect arising from the jet flow, it appears somewhat artificial to neglect the jet fluid flow and yet retain eddy convection. Lighthill probably regarded his work as a valid low frequency theory (at which condition the jet flow was presumed by him to be acoustically compact and, hence, ignorable). However, one of the most interesting conclusions of the present study is that the presence of the jet flow affects both low and high frequency radiation. Thus, the Lighthill analysis leading to equation (20) is not a valid low frequency limit. To describe the Lighthill analysis leading to equation (20) as a valid low jet Mach number limit appears somewhat gratuitous as it was precisely the motivation to extend his results to high jet Mach numbers that led Lighthill to develop the result of equation (20). In any case, when hot jet flows are considered, it emerges that equation (20) is not a valid low Mach number result either. In fact, in the case of the noise of heated jets at low jet velocities, some fairly profound differences from the Lighthill point of view arise upon the inclusion of the effect of jet flow. Crudely speaking, there is now a need to significantly revise one's ideas about both the right-hand and left-hand sides of equation (18). Lilley's[28] elegant formulation reveals both mean flow shrouding and additional source terms due to the gradients of the mean density or temperature. For the reason that the noise of heated jets exhibits so many unusual features, it was decided to deal with that problem separately in Subsection 1.2 of the current study.

1.1.2 Formulation and Method of Solution

Both Lilley[18] and Goldstein[29] have developed equations in which, under certain restrictions, a more explicit relationship than equation (18) can be obtained insofar as the generation of aerodynamic noise is concerned. Lilley's development is very briefly sketched below so as to clearly indicate the assumptions. Consider an inviscid, nonheat-conducting gas. The continuity, momentum, and energy equations (in the absence of heat, mass, and momentum sources) can be written as:

$$\frac{1}{\rho}\frac{D\rho}{Dt} + \frac{\partial u_i}{\partial x_i} = 0 \quad . \quad . \quad . \tag{21}$$

$$\frac{1}{\gamma}\frac{Du_i}{Dt} + \frac{a^2}{p}\frac{\partial p}{\partial x_i} = 0 \quad . \quad . \quad . \tag{22}$$

$$\frac{1}{p}\frac{Dp}{Dt} - \frac{\gamma}{\rho}\frac{D\rho}{Dt} = 0 \quad . \quad . \quad . \tag{23}$$

where $\frac{D}{Dt}$ denotes differentiation following the fluid. Also let $r = \log(p/p_o)$ where p_o is a reference pressure. Then eliminating ρ from equation (21), equations (21) and (23) may deal with equations (24) and (25) as under:

$$\frac{Dr}{Dt} + \gamma \frac{\partial u_i}{\partial x_i} = 0 \ . \ . \ . \tag{24}$$

$$\gamma \frac{Du_i}{Dt} + a^2 \frac{\partial r}{\partial x_i} = 0 \ . \ . \ . \tag{25}$$

Lilley[28] next decomposes all field variables u_i, r, and a^2 into a steady part and a fluctuating part (i.e., as $u_i = \bar{u}_i + u_i'$, etc). The mean values of equations (24) and (25) are next subtracted from equations (24) and (25) themselves. Lilley's equation follows from manipulations of equations (24) and (25) and three additional assumptions, namely that:

(a) the mean flow is at constant static pressure.

(b) whenever second-order products of fluctuating quantities such as $(r' u_i')$, $(r')^2$, $(a^2)' u_i'$, $(a^2)' r'$, and $[(a^2)']^2$ appear, they are neglected. However, second-order velocity products of type $u_i' u_j'$ are retained.

(c) the mean flow is undirectional (say $\bar{u}_i = V_1 \delta_{1i}$) and varies only in one direction normal to the direction x_1 (say along the x_2 direction). Also $\overline{a^2}$ is only a function of x_2. This leads to Lilley's equation which is:

$$\frac{\bar{D}^3 r'}{\bar{D}t^3} + 2 \frac{dV_1}{dx_2} \frac{\partial}{\partial x_1} \left(\frac{1}{a^2} \frac{\partial r'}{\partial x_2} \right) - \frac{\bar{D}}{Dt} \frac{\partial}{\partial x_i} \left(\frac{1}{a^2} \frac{\partial r'}{\partial x_i} \right)$$

$$= -2\gamma \frac{dV_1}{dx_2} \frac{\partial^2}{\partial x_i \partial x_k} \left(u'_2 u'_k \right)$$

$$+ \gamma \frac{\bar{D}}{Dt} \frac{\partial^2 \left(u_i' u_j' \right)}{\partial x_i \partial x_j} \ . \ . \ . \tag{26}$$

From this point on, Lilley's equation needs an interpretation similar to that by Lighthill of equation (19). The quantity r', for small values of p' compared to the ambient pressure p_A, may be shown to be equal to (p'/p_A). The u_i' on the right-hand side of equation (26) are regarded as the known,

solenoidal, turbulent velocity fluctuations and equation (26) then provides the required correct inhomogeneous wave equation for (p'/p_A) driven by the turbulent velocity field. The improvement of equation (26) over equation (18) or even Phillips'[21] equation is that the source term is clearly in the form of a quadratic function of the fluctuating velocities. The operator $\bar{D}/\bar{D}_t$ in equation (26) stands for $(\delta/\delta_t + V_1\ \delta/\delta x_1)$. We will deal in the present study primarily with the noise produced by the source term:

$$\gamma \frac{\bar{D}}{\bar{D}t} \frac{\partial^2}{\partial x_i \partial x_j} \left(u_i' u_j'\right)$$

Both Lilley's equation (26) and Lighthill's equation (18) exhibit "self-noise" and "shear-noise" source terms. However, the relationship of the self-noise term in Lilley's equation namely $\bar{D}/\bar{D}_t\ \partial^2/\partial x_i\ \delta x_j\ (u_i' u_j')$ to the shear-noise term in Lilley's equation, i.e.,

$$\frac{dV_1}{dx_2} \frac{\partial^2}{\partial x_1 \partial x_k} \left(u_2' u_k'\right)$$

is quite different from that for Lighthill's equation where the analogous terms would be as $\partial^2/\partial x_i\ \partial x_j\ (u_i' u_j')$ and $d\ V_1/dx_2\ \partial u'_2/\partial x_1$. Lighthill's equation (18) suggests the following three notions concerning "shear" and "self" noise. Firstly, it appears that shear noise might be much more important than self noise since shear noise is only linear in the turbulent velocities, while self noise is quadratic in the turbulent velocities. This is what Lighthill[44,45] had in mind when he referred to the "amplifying" effect of mean flow gradients on jet noise. Secondly, it appears that the shear noise may be responsible for the low frequency sound with the self-noise accounting for the high frequency sound. Related to this is the observation by Jones[30] that shear noise should have a convection factor of $(1 - M_c \cos\theta)^{-3}$ as opposed to the $(1 - M_c \cos\theta)^{-5}$ factor for self noise. Finally, unlike self noise which has an isotropic or omnidirectional character, the shear-noise term appears to a preferred axial directionality. In Lilley's formulation, neither of the first two notions are true, while the third notion still carries over (in a somewhat weaker form). Since the shear noise term of Lilley's equation is quadratic in the fluctuating velocities, as is the self noise term, it is neither more important than the self-noise term nor is it responsible for lower frequency radiation as compared to the self-noise term. In fact, the two terms in Lilley's equation are qualitatively very similar since the operator $\bar{D}/\bar{D}_t$ operating on the self-noise term $\partial^2/\partial x_i\ \partial x_j\ (u_i' u_j')$ essentially effects a multiplication of it by ω_o, where ω_o is a frequency of the self-noise eddy in its own (convected) frame of reference. The experimental study of Davies, Fisher, and Barrat[27] has shown that $\omega_o \sim (d\ V_1/dx_2)$; and, thus, there exists a considerable qualitative similarity between the self-noise and shear-noise terms of Lilley's

equation. It is true, of course, that the scalar function $\partial^2/x_1\ \partial x_k\ (u_2'\ u_k')$ associated with the shear-noise term in Lilley's equation has a mildly preferred axial orientation as compared to the isotropic function $\partial^2/\partial x_i\ \partial x_j$ $(u_i'\ u_j')$ associated with the self-noise term. This aspect is ignored in the present study. We will deal only with solutions to equation (26) with a source term of type $\overline{D/D_t}\ \partial^2/\partial x_i\ \partial x_i\ (u_i'\ u_j')$ to be abbreviated as $\overline{D/D_t}\ \partial^2/\partial x_i\ \partial x_j\ (Q_{ij})$ where $Q_{ij} = (u_i'\ u_j')$. One further point with regard to equation (26) worth nothing is that, since the jet flow is at constant static pressure, a^2 can be written as $\gamma\ p_A/\overline{\rho(x_2)}$. Then, for r' depending on (x_1, t) as $\exp[j(\alpha\ x_1 - \omega t)]$ and for small r', the homogeneous portion of equation (26), i.e. equation (26) with the right-hand side set equal to zero, yields that across a thin shear layer the quantity:

$$\frac{1}{\overline{\rho(x_2)}\ \ \omega - \alpha\ V_1(x_2)^2}\ \left(\frac{\partial p'}{\partial x_2}\right)$$

must be continuous. This, of course, is equivalent to the usual kinematic condition that the transverse acoustic particle displacement across the shear layer be continuous. The reason for pointing out this feature of the homogeneous form of Lilley's equation (26) is that the homogeneous form of Phillips'[21] equation fails to yield the correct kinematic condition when examined in the limit for a vanishingly thin shear layer.

As indicated earlier, in what follows we will deal with equation (26) in a cylindrical coordinate system (see Figure 46), where V_1 = a constant for $0 \leq r < a$ and V_1 = zero otherwise. The source term is associated with solenoidal turbulent velocity fluctuations; hence, a suitable choice of a fundamental form for Q_{ij} would be $Q_{ij}^0\ \delta(y)\ \delta(z)\ \delta(x - V_c t)e^{j\omega_o t}$ (where Q_{ij}^0 is a constant), which would represent an eddy embedded in the jet convecting along its centerline at V_c. Centerline eddy convection would be representative of an average result for eddies distributed across the jet cross section [see Mani[54] in this context]. In this subsection, the speed of sound in the jet and its density are assumed to have the same value c_o, ρ_o as the ambient. ω_o would represent the oscillation frequency of the eddy in its own frame of reference. The mathematical problem then involves solving for:

$$\frac{D}{Dt}\ (\nabla^2 p') - \frac{1}{c_o^2}\ \frac{\bar{D}^3 p'}{Dt^3}$$

$$= -\rho_o\ Q_{ij}^0\ \frac{\bar{D}}{Dt}\ \frac{\partial^2}{\partial x_i \partial x_j}\ \left[\delta(y)\ \delta(z)e^{j\omega_o t}\ \delta(x - V_c t)\right]$$

$$\text{(inside the jet } 0 \leq r < a) \ . \ . \ . \qquad (27)$$

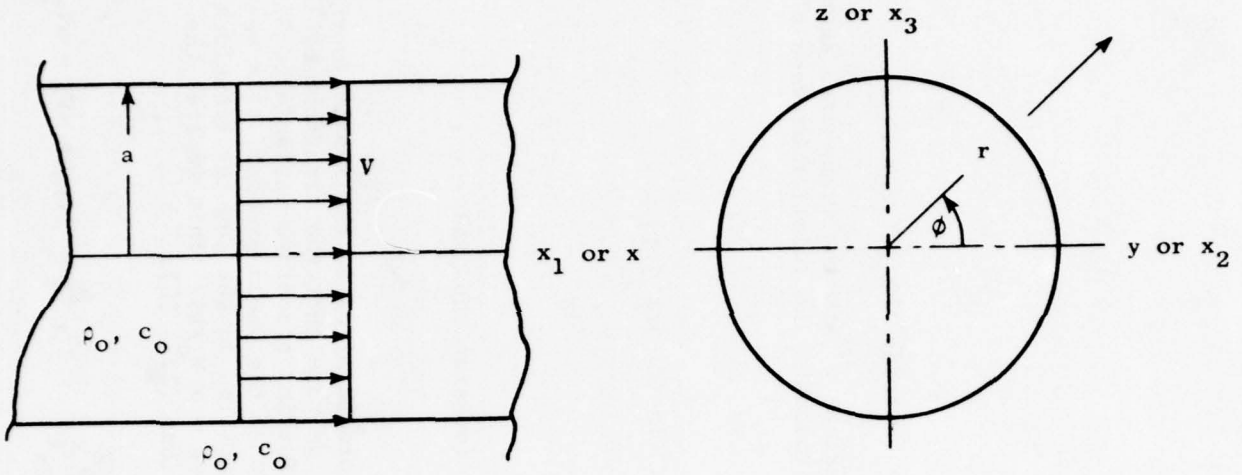


Figure 46. Cylindrical Coordinate System for Plug Flow Acoustic Model.

where:

$$\frac{\bar{D}}{Dt} = \left(\frac{\partial}{\partial t} + V_1 \frac{\partial}{\partial x}\right)$$

and:

$$\nabla^2 p' - \frac{1}{C_o^2} \frac{\partial^2 p'}{\partial t^2} = 0 \qquad (28)$$

(outside the jet for r> a)

Across the jet still-air interface p' and the transverse acoustic particle displacement η should be continuous. The relation between p' and η is:

$$\frac{D^2\eta}{Dt^2} = -\frac{1}{\rho_o} \frac{\partial p'}{\partial r} \qquad \text{(inside the jet) . . .} \qquad (29)$$

and:

$$\frac{\partial^2\eta}{\partial t^2} = -\frac{1}{\rho_o} \frac{\partial p'}{\partial r} \qquad \text{(outside the jet) . . .} \qquad (30)$$

We now apply a Fourier transform parallel to the x-axis to equations (27), (28), and (29). In doing so, we note that the transform of $\delta(x - V_c t)$ is $\exp(j \alpha V_c t)$ (where α is the Fourier transform variable). Since $e^{j\omega_o t}$ $\delta(x - V_c t)$ is the driving term of the whole problem, this means that the $(x - t)$ dependence of all quantities in the Fourier transform formulation will be as $\exp(-j \alpha x) \exp[j(\omega_o + \alpha V_c)t]$. This implies the following operator equivalence in equations (27 - 30):

$$\frac{\partial}{\partial t} \sim j(\omega_o + \alpha V_c), \quad \frac{\partial^2}{\partial x^2} \sim -\alpha^2, \quad \frac{D}{Dt} \sim j(\omega_o + \alpha V_c - \alpha V_1)$$

In what follows, it is convenient to assume that $V_1 - V_c = V$. Such an assumption is consistent with a plug flow model for the jet flow. The assumption is not necessary, but it does help to simplify the algebra. Also, one can identify that four types of basic quadrupole solutions to

equations (27) - (30) need to be worked out corresponding to the x-x, x-y, y-y, and y-z type quadrupoles.

Consider first the x-x case. We may rewrite equations (27) - (30) in the form of a problem in the transverse (y-z) coordinates as under:

$$\nabla^2_{y,z}\, p' + \left(k_o^2 - \alpha^2\right) P' = \rho_o\, Q^0_{xx}\, \alpha^2\, \delta(y)\, \delta(z)$$

$$\text{for } 0 \leq r < a, \ldots \text{(note that } \nabla^2_{y,z} \text{ stands for } \left(\frac{\partial^2}{\partial y^2} + \frac{\partial^2}{\partial z^2}\right) \tag{31}$$

$$\nabla^2_{y,z}\, P' + \left[\left(k_o + \alpha M\right)^2 - \alpha^2\right] P' = 0 \text{ for } r > a \tag{32}$$

$$N = \frac{1}{\rho_o \omega_o^2} \frac{\partial P'}{\partial r} \text{ for } 0 \leq r < a \tag{33}$$

and,

$$N = \frac{1}{\rho_o \omega_o^2 \left(1 + \frac{\alpha M}{k_o}\right)^2} \frac{\partial P'}{\partial r} \text{ , for } r > a \tag{34}$$

Note that $k_o = \omega_o/c_o$, $M = V/c_o$, and P', N are the axial Fourier transforms of p', η. Since we are interested only in propagating solutions in the far field, the range of α interest is $-k_o/(1 + M) \leq \alpha \leq k_o/(1 - M)$. We are primarily interested in the solution for P' for $r > a$, and this works out in the case of equations (31) - (34) as under:

For $-\frac{k_o}{1+M} \leq \alpha \leq k_o$:

$$P'(\alpha) = \frac{-\rho_o\, Q^0_{xx}\, \alpha^2\, H_o^{(2)}(\alpha^+ r)}{2\pi \left[H_o^{(2)}(\alpha^+ a) J_o'(\alpha^+ a)(\alpha^+ a) - \frac{J_o(\alpha^+ a) H_o^{(2)'}(\alpha^+ a)}{\left(1 + \frac{\alpha M}{k_o}\right)^2}\right]} \tag{35}$$

and for $k_o \leq \alpha \leq \left(\frac{k_o}{1-M}\right)$ as:

$$P'(\alpha) = \frac{-\rho_o Q^0_{xx}}{2\pi \left[(\underline{\alpha}^+ a) I_o'(\underline{\alpha}^+ a) H_o^{(2)}(\alpha^+ a) - \frac{(\alpha^+ a) H_o^{(2)'}(\alpha^+ a) I_o(\underline{\alpha}^+ a)}{\left(1 + \frac{\partial M}{k_o}\right)^2} \right]} \tag{36}$$

where α^+ is the positive square root $\sqrt{(k_o + \alpha M)^2 - \alpha^2}$, $\underline{\alpha}^+$ is the positive square root $\sqrt{k_o^2 - \alpha^2}$, and $\underline{\alpha}^+$ is the positive square root $\sqrt{\alpha^2 - k_o^2}$. Thus, the expression for p' can be written as:

$$p' = \frac{1}{2\pi} \int_{-\infty}^{\infty} P'(\alpha) e^{-j\alpha(x-Vt)} e^{j\omega_o t} \, d\alpha \tag{37}$$

In terms of Figure 47, with $(x - Vt) = R' \cos(\theta')$ and $r = R' \sin(\theta')$, we may examine equation (37) by the method of stationary phase for large R'. The details are omitted, but we may show that, with retarded coordinates R, θ defined as in Figure 47, and with $P'(\alpha)$ written as $F(\alpha) H_o^{(2)}(\alpha^+ r)$, the far-field expression for p' is:

$$p' \sim \frac{j F(\alpha_o) e^{j\omega_o t} e^{-jk_o R}}{\pi R (1 - M \cos\theta)} \tag{38}$$

where:

$$\alpha_o = \frac{k_o \cos\theta}{(1 - M \cos\theta)} \tag{39}$$

It is worth noting that $\alpha^+(\alpha_o) = k_o \sin\theta/(1 - M \cos\theta)$. The result of equation (38) does ignore the Kelvin-Helmholtz instability associated with the jet still interface. In a recent study,[54] the reason why such a step is permissible was discussed in some detail. Basically, the argument is that such instabilities have, in fact, created the jet turbulence and, hence, should not be included again when analyzing the radiation due to this turbulence (in which calculation we are assuming the turbulent source terms to be known). The real jet flow represents a statistically stable system, and the plug flow model is merely an artifice employed in the analysis to conveniently assess the mean flow shrouding effects.

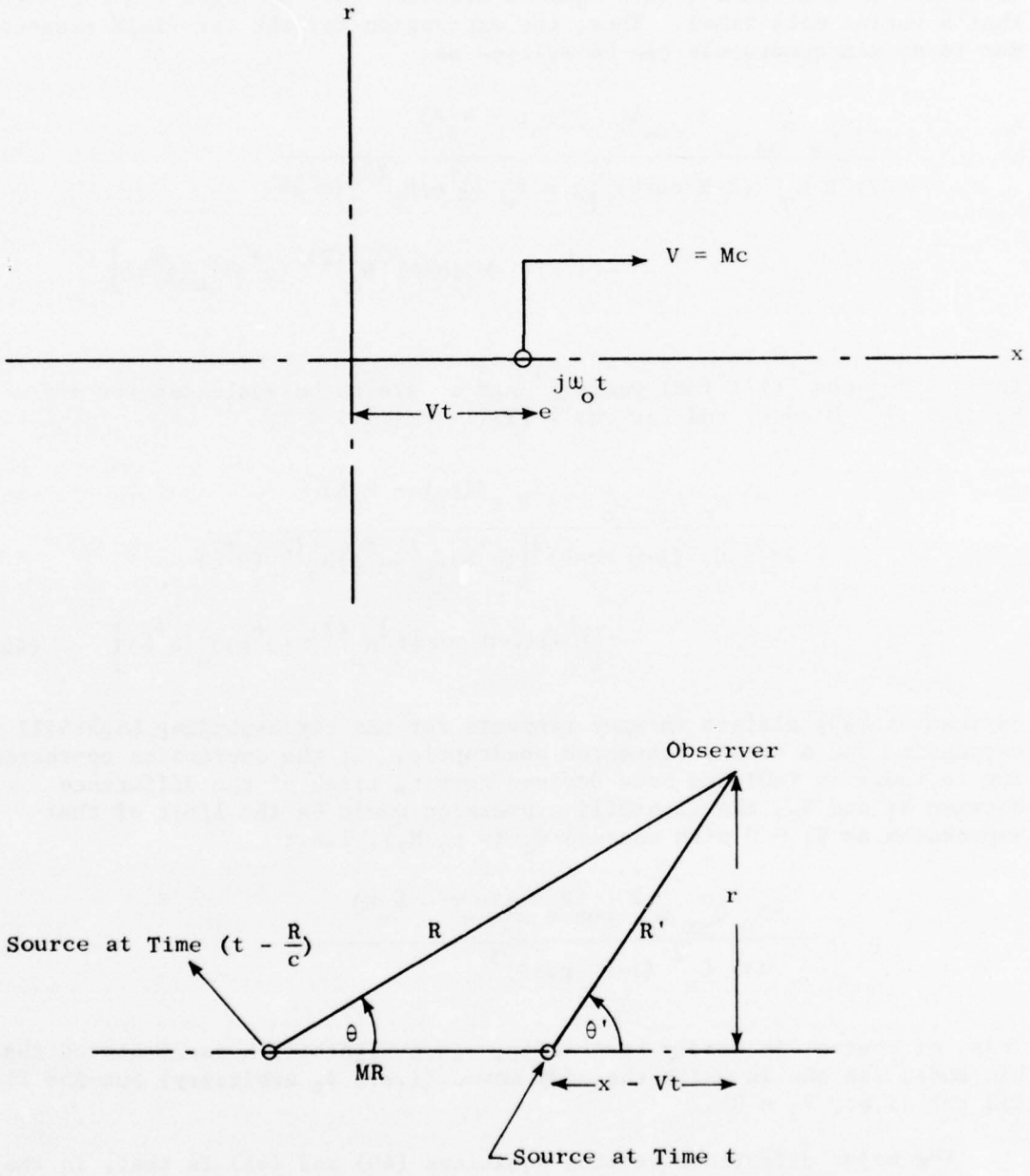


Figure 47. Notation for a Moving Source.

The Doppler shift formula is obtained by noting that the time rate of variation of the phase $(\omega_o t - k_o R)$ in equation (38) is $(\omega_o/1 - M\cos\theta)$ (note that R varies with time). Thus, the expression for the far-field pressure due to an x-x quadrupole can be written as:

$$\frac{-j\,\rho_o\,Q^0_{xx}\,\omega_o^2\cos^2\theta\,e^{j(\omega_o t - k_o R)}}{2\pi^2 R\,C_o^2\,(1-M\cos\theta)^3\left[\underline{\underline{\alpha}}^+ a\,I_o'(\underline{\underline{\alpha}}^+ a)H_o^{(2)}(\alpha^+ a) - (\alpha^+ a)(1-M\cos\theta)^2 H_o^{(2)\prime}(\alpha^+ a)I_o(\underline{\underline{\alpha}}^+ a)\right]}$$

for $0 \leq \theta \leq \cos^{-1}(1/1+M)$ where $\underline{\underline{\alpha}}^+$ and α^+ are to be evaluated for $\alpha = k_o\cos\theta/(1 - M\cos\theta)$ and for $\cos^{-1}[1/(1+M)] \leq \theta \leq \pi$,

$$p' = \frac{-j\,\rho_o\,Q^0_{xx}\,\omega_o^2\cos^2\theta\,e^{j(\omega_o t - k_o R)}}{2\pi^2 R\,C_o^2(1-M\cos\theta)^3\left[(\underline{\underline{\alpha}}^+ a)J_o'(\underline{\underline{\alpha}}^+ a)H_o^{(2)}(\alpha^+ a) - (\alpha^+ a)(1-M\cos\theta)^2 H_o^{(2)\prime}(\alpha^+ a)J_o(\alpha^+ a)\right]} \qquad (40)$$

Expression (40) differs in many respects for the corresponding Lighthill expression for a freely convected quadrupole. If the expression corresponding to equation (40) had been derived keeping track of the difference between V_1 and V_c, the Lighthill expression would be the limit of that expression as $V_1 \to 0$ with nonzero V_c $(= c_o M_c)$, i.e.:

$$p' \sim \frac{-\rho_o\,Q^o_{xx}\,\omega_o^2\cos^2\theta\,e^{j(\omega_o t - k_o R)}}{4\pi R\,C_o^2\,(1-M_c\cos\theta)^3} \qquad (41)$$

This, of course, is hardly surprising, since Lighthill himself stated that his model was one in which the eddy moved (i.e., V_c arbitrary) but the fluid did not (i.e., $V_1 = 0$).

The major difference between equations (40) and (41) is that, in the case of equation (40), the far-field directivity is now completely frequency-dependent. The relevant nondimensional parameters governing the directivity are now M and $(k_c a)$. For $0 \leq \theta \leq \cos^{-1}(1/1+M)$ (the so-called "zone of silence") and high $(k_o a)$ the exponential nature of the I functions is a manifestation of refraction of the sound by the jet. Also, for nonzero $(k_o a)$, $p' \to 0$ logarithmically as $\theta \to 0$ or $\theta \to \pi$. [Gottlieb[31] refers to this as

the "Lloyd's mirror" effect.] A most interesting result is obtained by examining equation (40) as $(k_o a) \to 0$ (low frequency result) we find that:

$$p' \sim \frac{-\rho_o Q^o_{xx} \omega_o^2 \cos^2\theta \, e^{j(\omega_o t - k_o R)}}{4\pi C_o^2 R (1-M\cos\theta)^5} \tag{42}$$

[If the problem had been worked with $V_1 \neq V_c$, the expression $(1 - M\cos\theta)^5$ in the denominator of equation (42) would be modified to $(1 - M_c \cos\theta)^3 (1 - M_1 \cos\theta)^2$, where $M_c = V_c/c_o$ and $M_1 = V_1/c_o$]. In other words equation (41) is not a valid low frequency limit. Such a feature of low frequency noise emission was first noticed experimentally by Mollo-Christenson and Narasimha[32] and qualitatively ascribed by them to the influence of the jet flow. Berman[51] has also drawn attention to it, pointing out that it is not an instability effect but rather that "the noise generation process is enhanced by a fully stable resonance phenomenon."

Equations (42) and (40), to some extent, explain why an expression of the type found in equation (41) due to Lighthill has seemingly worked well in the past at least for the noise of cold jets. It turns out, roughly speaking, that equation (41) underestimates the variation of p' with respect to θ at low frequencies [when compared to equation (40)] as indicated by equation (42), while overestimating it at high frequencies. The overestimation arises essentially because [as pointed by Ribner[52,53], Powell[25], and Csanady[26] at high frequencies], the radiation of the eddy is primarily governed by its own immediate environment (namely the jet flow) with respect to which it is not convecting at all. Regardless of how high $(k_o a)$ may be, both $(\alpha^+ a)$ and $(\underline{\underline{\alpha}}^+ a)$ or $(\underline{\alpha}^+ a)$ approach zero as $\theta \to 0$ or π and $\theta \to \cos^{-1}(1/1 + M)$. Because of this, it was not possible to extract a high frequency limit of equation (40). Besides, a plug flow model of the jet flow is obviously a poor model at high frequencies. In any event, this feature of underestimation of noise generation at low frequencies by equation (41) and overestimation at high frequencies is apparently the reason why expressions of the type found in equation (41) essentially succeeded in explaining jet noise directivity in the past, when such directivities were measured for the overall sound pressure (i.e., the integral of the pressure spectrum over all frequencies). Jet noise research owes a great deal to the selective plotting of directivities at constant source frequencies [i.e., at constant $(k_o a)$] in the manner done by Lush[18], Ahuja-Bushell[47], and others. It is such displays that have revealed clearly the shortcomings of expressions of the type found in equation (41). We should like to conclude this discussion of equation (40) by emphasizing that it is an expression that exhibits simultaneously the combined convection-refraction effect which is so crucial to the determination of jet noise directivity. It also emphasizes the need to plot all jet noise directivity data at constant source frequencies, as this is the only directivity plot that can be checked directly against an acoustic theory. It is the only manner in which we can bypass our current inability to predict the turbulence source spectrum in detail.

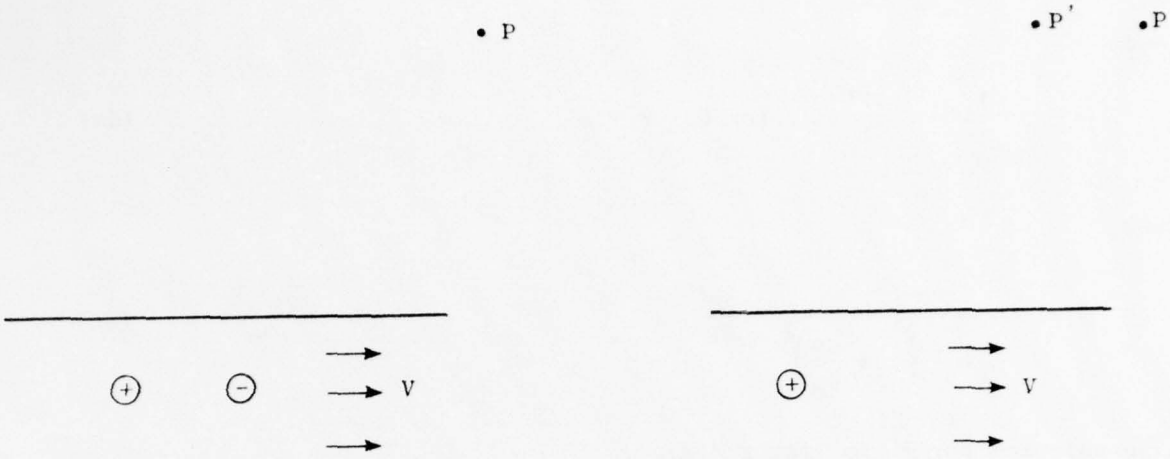
Turning now to the sound field of the x-y type quadrupole, the transverse nature of this singularity turns out to impose a basic difference between the way these sound fields were deduced by Lighthill and the manner in which they must be deduced for equations (27) - (30). The left-hand side of Lighthill's equation consists only of constant coefficient operators [namely $(\partial^2/\partial_t{}^2 - a_o^2 \nabla^2)$]. Also, the only boundary condition associated with equation (18) is a "radiation" condition. This means that having solved equation (18) with a right-hand side of type say $\delta(x)\ \delta(y)\ \delta(z)$, one may differentiate this solution in the far field with respect to x_i, x_j to obtain the results for the higher-order singularities. In other words, the well-known reciprocity of the solutions to equation (18) with respect to observer and source positions enables one to derive the higher-order singular solutions in the far field with relative ease. Equations (27) - (30) or Lilley's equations, however, are homogeneous only in time and in the axial direction (assuming a nonspreading jet); thus, only singularities involving derivatives of a source term with respect to time or the axial coordinate (as is the case for the x-x quadrupole) admit to such a simple solution procedure. Equations (27) - (30) are inhomogeneous with regard to the transverse coordinates y and z; hence, special procedures must be adopted to derive the sound fields of the transverse singularities. Figure 48 is an attempt to illustrate this difference between Lighthill's and Lilley's formulations.

Two approaches may be employed to deal with this situation. The first, more general approach, is to derive the fundamental solutions for an arbitrary, transverse source position in the jet. This means solving for a fundamental form $\delta(x - Vt)e^{j\omega_o t}\ \delta(y - y_o)\ \delta(z - z_o)$. It is now perfectly admissible to differentiate the far-field form of this solution with regard to the source coordinates y_o, z_o (and then, if so desired, set y_o, $z_o = 0$) to derive the higher-order singular solutions. This is because the coefficients and boundary conditions associated with equations (27) - (30) are independent of source position, i.e., y_o, z_o. The only problem with this approach is that, for arbitrary y_o, z_o, even the first fundamental solution will be nonaxially symmetric (due to the nonsymmetric source location in the transverse plane). For this reason, a second more restricted approach will be adopted in the following. Specializing to the case of an x-y quadrupole, the problem in the y-z plane for the transforms P' and N for equations (27) - (30) is:

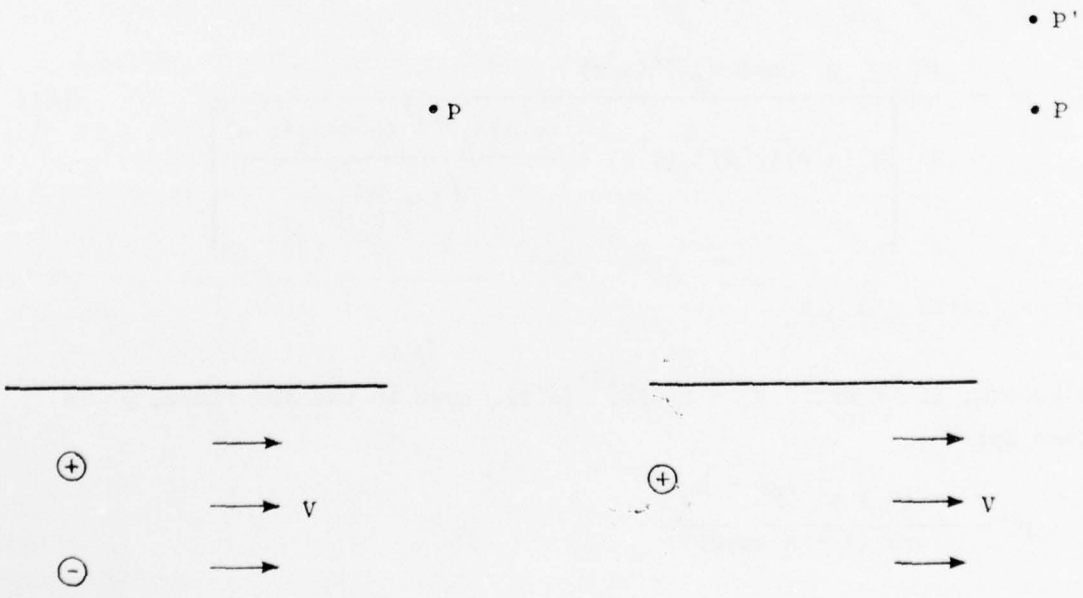
$$\nabla^2_{y,z} P' - \alpha^2 P' + k_o^2 P' = j\alpha\rho_o Q^o_{xy} \frac{\partial}{\partial y}[\delta(y)\delta(z)] \tag{43}$$

for $0 \leq r < a$,

$$\nabla^2_{y,z} P' + [(k_o + \alpha M)^2 - \alpha^2]P' = 0 \tag{44}$$



(a) To derive the solution at P due to the sources at the left, we may take the difference between the solutions at P and P' due to one source as shown on the right.



(b) A similar equivalence does not hold for the case above.

Figure 48. Schematic of Source Models.

and:

$$N = \frac{1}{\rho_o \omega_o^2} \quad \frac{\partial P'}{\partial r} \quad , \text{ for } 0 \leq r < a \tag{45}$$

and,

$$N = \frac{1}{\rho_o \omega_o^2 \left(1 + \frac{\alpha M}{k_o}\right)^2} \quad \frac{\partial P'}{\partial r} \tag{46}$$

The solution for P' is (for r > a):

$$P' = \frac{j\alpha\rho_o \, Q^o_{xy} \, \underline{\alpha}^+ \cos\phi \, H_1^{(2)}(\alpha^+ r)}{2\pi \left[H_1^{(2)}(\alpha^+ a)(\underline{\alpha}^+ a) I_1'(\underline{\alpha}^+ a) - \frac{(\underline{\alpha}^+ a) H_1^{(2)}(\alpha^+ a) I_1(\underline{\alpha}^+ a)}{\left(1 + \frac{\alpha M}{k_o}\right)^2}\right]}$$

for $k_o \leq \alpha \leq \left(\frac{k_o}{1-M}\right)$ and,

$$P' = \frac{j\alpha \, Q^o_{xy} \, \underline{\alpha}^+ \cos\phi \, H_1^{(2)}(\alpha^+ r)}{2\pi \left[H_1(\alpha^+ a)(\underline{\alpha}^+ a) J_1'(\underline{\alpha}^+ a) - \frac{(\alpha^+ a) H_1^{(2)'}(\alpha^+ a) J_1(\underline{\alpha}^+ a)}{\left(1 + \frac{\alpha M}{k_o}\right)^2}\right]} \tag{47}$$

for $-k_o/(1+M) \leq \alpha \leq k_o$

As before, if we write $P' = F(\alpha) H_1^{(2)}(\alpha^+ r)$, then in the far field, p' is given by:

$$p' \sim \frac{-F(\alpha_o) \, e^{j(\omega_o t - k_o R)}}{\pi R \, (1 - M \cos\theta)}$$

with $\alpha_o = k_o \cos\theta/(1 - M \cos\theta)$.

Explicity then, for the x-y quadrupole:

$$p' \sim \frac{-j\,\rho_o\,\omega_o^2\left(\frac{\alpha^+}{k_o}\right)\cos\theta\,\cos\phi\; e^{j(\omega_o t - k_o R)} Q_{xy}^o}{2\pi^2 R\, C_o^2 (1 - M\cos\theta)^2 \left[(\underline{\alpha}^+ a) I_1'(\alpha^+ a) H_1^{(2)}(\alpha^+ a) - (\alpha^+ a)(1 - M\cos\theta)^2 H_1^{(2)'}(\alpha^+ a) I_1(\underline{\alpha}^+ a)\right]}$$

for $0 \leq \theta \leq \cos^{-1}(1/1+M)$ where $\alpha^+ = k_o \sin\theta/(1-M\cos)$ and $\underline{\alpha}^+ = \sqrt{\alpha^2 - k_o^2}$ is to be evaluated for $\alpha = k_o \cos\theta/(1-M\cos\theta)$. For $\cos^{-1}(1/1+M) \leq \theta \leq \pi$, p' is given by:

$$p' \sim \frac{-j\,\rho_o\,\omega_o^2\left(\frac{\alpha^+}{k_o}\right)\cos\theta\,\cos\phi\; e^{j(\omega_o t - k_o R)} Q_{xy}^o}{2\pi^2 R\, C_o^2 (1 - M\cos\theta)^2 \left[(\underline{\alpha}^+ a) J_1'(\underline{\alpha}^+ a) H_1^{(2)}(\alpha^+ a) - (\alpha^+ a)(1 - M\cos\theta)^2 H_1^{(2)'}(\alpha^+ a) J_1(\underline{\alpha}^+ a)\right]} \qquad (48)$$

Equation (48), in addition to the frequency dependence of equation (40), exhibits another significant difference from the Lighthill result for an x-y quadrupole. This is the fact that the explicit convection amplification factor appearing in equation (48) is only $(1 - M\cos\theta)^{-2}$ and not $(1 - M\cos\theta)^{-3}$. An additional (frequency-independent) convection factor is contained in $(\underline{\alpha}/k_o)$ or $(\underline{\alpha}^+/k_o)$ which works out to:

$$\frac{\sqrt{|1-2M\cos\theta - \cos^2\theta(1 - M^2)|}}{(1 - M\cos\theta)}$$

The above expression, in general (especially for $0 \leq \theta \leq \pi_2$), is less than $(1 - M\cos\theta)^{-1}$. This is due to the fact that the enhancement of the phase cancellation (which is responsible for the convective amplification) for the transverse component of the singularity is now related inversely to the transverse phase speed of the sound wave within the flow. As shown in Figure 49 for a plane wave, this phase speed is (for $0 \leq \theta \leq \pi/2$) greater than that of the refracted wave outside the flow. Such a feature need not be considered for the axial quadrupole, because the axial phase speeds are matched inside and outside the flow in Figure 49.

The theory for the y-y and y-z quadrupoles can be worked out analogously, and we give only the final results.

For $0 \leq \theta \leq \cos^{-1}(1/1 + M)$, with the usual definitions of α^+, $\underline{\alpha}^+$, for the y-y quadrupole:

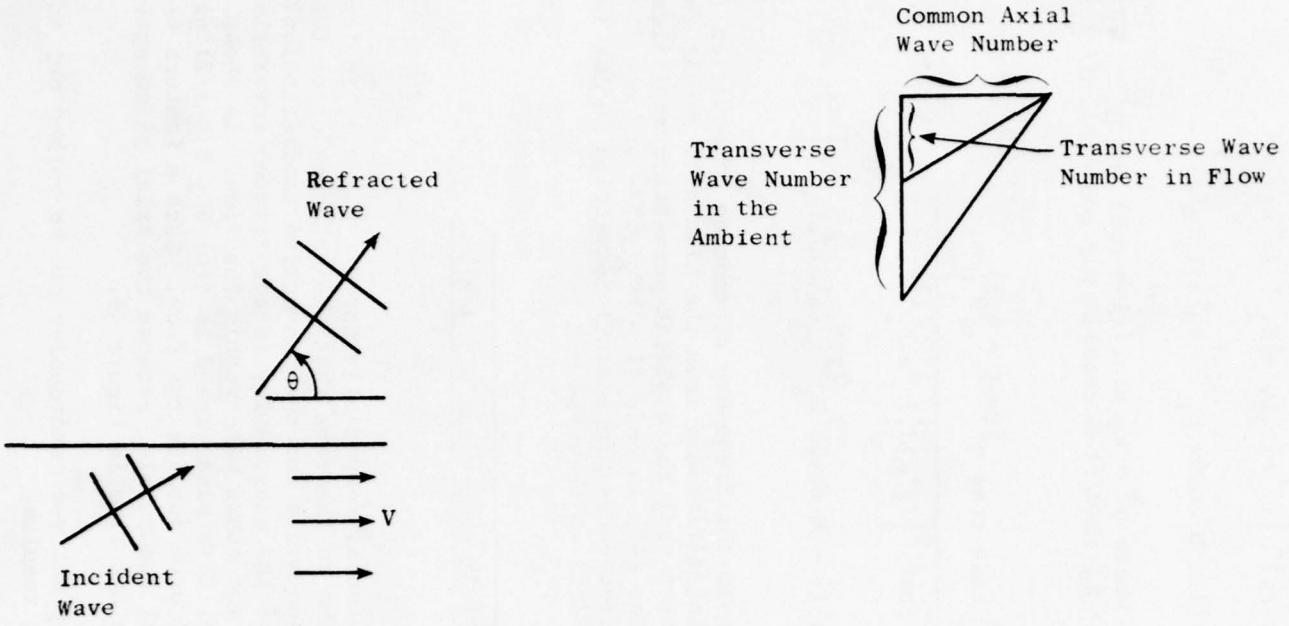


Figure 49. Phase Speed or Wave Number Differences Between Incident and Refracted Waves.

$$p' \sim \frac{j\,\rho_o\,Q^o_{yy}\,e^{j(\omega_o t - k_o R)}\,\omega_o^2\left(\frac{\underline{\underline{\alpha}}^+}{k_o}\right)^2}{4\pi^2 R\,(1 - M\cos\theta)\,C_o^2} \times$$

$$\left\{ \frac{-\cos(2\phi)}{\left[(\underline{\underline{\alpha}}^+ a)I_2'(\underline{\underline{\alpha}}^+ a)H_2^{(2)}(\alpha^+ a) - (\alpha^+ a)(1 - M\cos\theta)^2 H_2^{(2)'}(\alpha^+ a)I_2(\underline{\underline{\alpha}}^+ a)\right]} \right.$$

$$\left. + \frac{1}{\left[(\underline{\underline{\alpha}}^+ a)I_o'(\underline{\underline{\alpha}}^+ a)H_o^{(2)}(\alpha^+ a) - (\alpha^+ a)(1 - M\cos\theta)^2 H_o^{(2)'}(\alpha^+ a)I_o(\underline{\underline{\alpha}}^+ a)\right]} \right\}$$

(49)

For $\cos^{-1}(1/1 + M) \leq \theta \leq \pi$, the same expression applies except that $\underline{\underline{\alpha}}^+$ should be replaced by α^+ and the I functions by the J functions. For the y-z quadrupole, for $0 \leq \theta \leq \cos^{-1}(1/1 + M)$:

$$p' \sim \frac{-j\,\rho_o\,Q^o_{yz}\,\omega_o^2\left(\frac{\underline{\underline{\alpha}}^+}{k_o}\right)^2 e^{j(\omega_o t - k_o R)}\sin(2\phi)}{4\pi^2\,C_o^2 R\,(1 - M\cos\theta)} \times$$

$$\frac{1}{(\underline{\underline{\alpha}}^+ a)I_2'(\underline{\underline{\alpha}}^+ a)H_2^{(2)}(\alpha^+ a) - (1 - M\cos\theta)^2(\alpha^+ a)H_2^{(2)'}(\alpha^+ a)I_2(\alpha^+ a)}$$

(50)

For $\cos^{-1}(1/1 + M) \leq \theta \leq \pi$, a similar expression applies with $(\underline{\underline{\alpha}}^+)$ replaced by $\underline{\alpha}^+$ and the I functions by the J functions.

From equations (49) and (50), we see that the only explicit convection factor that appears is now $(1 - M\cos\theta)^{-1}$. In fact, this term appears from the stationary phase method of evaluation of integrals of the type found in equation (37) and represents the purely volumetric dilatation effect due to singularity convection identified by Lighthill[44,45]. When evaluating the intensity, i.e., $\langle p'^2 \rangle$, this term will be corrected from $(1 - M\cos\theta)^{-2}$ to $(1 - M\cos\theta)^{-1}$ to allow for the reduced number of quadrupoles emitting simultaneously [Ffowcs-Williams[38]]. There are additional convection effects

associated with the term $(\underline{\alpha}^+/k_o)^2$ or $(\underline{\alpha}^+/k_o)^2$; but, as with the x-y quadrupole, these terms are now less than the factor $(1 - M\cos\theta)^{-2}$ for $0 \leq \theta \leq \pi/2$.

We should like to conclude this section by pointing out two implications of these results particularly for experimental work. Lighthill's equation (1) has tremendous simplicity and, being essentially devoid of any boundary conditions (except the radiation condition), has the simple consequence that the directionality of the sound field for any convected quadrupole can be written in the far field as $D(\theta, \phi)(1 - M_c\cos\theta)^{-3}$, where $D(\theta, \phi)$ is the intrinsic directionality of the stationary quadrupole which is just $(x_i x_j/R^2)$ for the i-j quadrupole. As we have shown in this section, such a simple result is invalid when one considers mean flow shrouding effects. One consequence of Lighthill's result (for his equation) was that, so far as the far field was concerned, the source term $\rho_o\, \partial^2/\partial x_i\, \partial x_j\, (u_i\, u_j)$ could be replaced by $\rho_o/c_o^2\, \partial^2/\partial t^2\, (v_r^2)$ where v_r was the component of u_i or u_j between the source point and the observer. This result is sometimes referred to as the Lighthill-Proudman form of the source term [Ribner(55)]. It has recently gained some popularity in the area of source location in jets by cross correlation of an in-jet measurement taken such as by an optical or hot wire anemometer (used to measure v_r^2) with a far-field microphone [Lee and Ribner(55)]. Such an identification of $\rho_o\, \partial^2/\partial_t{}^2\, (v_r^2)$ as a source term is only valid to the extent that Lighthill's equation is valid. It is not a valid source location procedure if we admit the importance of mean flow shrouding effects and, hence, of the need to pose the noise generation problem in terms of convected-wave equations.

Secondly, the term $[(\underline{\alpha}^+a)J_n'(\underline{\alpha}^+a)H_n^{(2)}(\alpha^+a) - (1 - M\cos\theta)^2\, (\alpha^+a)J_n(\underline{\alpha}^+a)H_n^{(2)'}(\alpha^+a)]$ which appears in the denominator of equations (40), (48), (49), and (50) with n = 0, 1, or 2 for $\cos^{-1}(1/1 + M) \leq \theta \leq \pi$, degenerates to a simple constant $(2j/\pi)$ when $\theta = \pi/2$ (when $\alpha = 0$, $\underline{\alpha}^+ = \alpha^+$). This is related to the obvious result that, for cold jets, one does not expect any mean flow shrouding effects at the 90° location (there being no component of flow along this direction). Thus, Lilley's equation (for cold jets) yields results at $\theta = 90°$ identical to those of Lighthill's equation. Experimentally then, at $\theta = 90°$, one does expect (for cold jets) the scaling principle deduced from Lighthill's equation to work. This means that, at $\theta = 90°$, one should get good 8th-power-law scaling of the intensity and good Strouhal scaling with regard to jet velocity, nozzle size, etc. This is, in fact, what recent experiments on cold jets by Lush(18) and Ahuja-Bushel(47) do confirm, namely that the Lighthill theory does work well at $\theta = 90°$.

1.1.3 Application of Theory to Experimental Results

In a recent study, Ribner(34) has explained how the fundamental solutions associated with the various quadrupoles can be employed to derive the axially symmetric sound field of a round jet. His results for the contribution due to "self noise" in his study [which uses Lighthill's equation (18) and the associated Lighthill-Proudman form of the source function as a basis] are particularly relevant here. Ribner studies the

expression for the mean square pressure and, employing a model of homogeneous, isotropic turbulence in its own frame of reference for the eddies and by examining the directional average in the ϕ-coordinate of the sound field, he is able to ascribe "weights" to the various quadrupole contributions. By and large, the six basic quadrupoles (x-x, x-y, x-z, y-z, y-y, and z-z) contribute independently though there are weak cross-quadrupole contributions (i.e., of the type xx-yy, xx-zz, yy-zz, etc.). With some slight liberties, we may derive from Ribner's study the conclusion that the self-noise contribution may be elevated by the formula:

(far-field intensity) ~

(mean square pressure of x-x quadrupole) +

4 × (circumferential average of mean square pressure of x-y or x-z quadrupoles)

+ 2 × (circumferential average of mean square pressure of yy-y or z-z quadrupoles) + 2 × (circumferential average of mean square pressure of y-z quadrupole) . . . (51)

The only difference from the above formula and that of Ribner is in the neglect of the weak cross-quadrupole contributions (i.e., of the xx-yy, xx-zz, and yy-zz types). Both the above formula and Ribner's more exact result yield a basic omnidirectional pattern for the self-noise for Lighthill's equation excepting for the $(1 - M_c \cos\theta)^{-5}$ convection effect. The other assumptions used in the comparison with the data are:

(a) To allow for jet spread, etc., the comparisons are all carried out assuming eddies moving at 65% of the nominal, ideal jet exit velocity in a plug flow which is also assumed to be at 65% of the nominal, ideal jet exit velocity. As noted earlier, with a plug-flow jet model, it seemed inconsistent to allow "slip" of velocity between the eddy convection velocity and the jet velocity, and this assumption seemed to be the best compromise. It should be noted that the assumption of eddies convecting at 65% of the nominal, ideal jet exit velocity is one that is commonly used by experimentalists. We also assume centerline eddy convection as representative of an average result for eddies distributed across the cross section.

(b) The predictions in this section are carried out by assuming that ρ_j, $c_j = \rho_o$, c_o (jet density and speed of sound equal to those of the ambient). The principal prediction carried out is that of the directional distribution of the sound pressure intensity for fixed values of nominal jet exit velocity and source frequency parameter ($k_o a$). This involves combining the results for the various quadrupoles according to the formula indicated earlier. As in all jet noise work, we assume that the angle θ of Figure 47 (angle measured from the position of the eddy at the time of emission of the acoustical signal reaching the observer at current time)

can be identified with the angle of measurement from the jet axis quoted by the experimentalists. This assumes that the radius of measurement is large compared to a length parallel to the jet axis over which the eddies may be assumed to have coherent existence.

(c) As noted in the previous section, the theory of the present paper is basically an acoustic theory; hence, no attempt is made to predict the turbulence source function spectrum. Thus, only relative directional distribution predictions are carried out. In comparison with the data of Lush[18] and Ahuja-Bushell[49], one vertical level adjustment of the directional distribution to "best fit" the data has been carried out. For this reason, in Figures 50 - 55, no absolute levels are shown though the 10-dB increment is clearly indicated. Sometimes it is suggested that such comparisons ought to be carried out by anchoring the theory and data at the 90° point. This suggestion seems to have at least two deficiencies. Firstly (especially at high velocities and low frequencies), the pressure levels at the 90° point are as much as 20 dB below the peak value. It seems unwise to anchor the prediction to a location where the pressure levels are orders of magnitude weaker than at the location of peak intensity. Secondly, most theories of jet noise deal with doubly infinite jet columns, thereby failing to account for the presence or influence of the tailpipe on the directivity of the noise. Inclusion of tailpipe effects would give rise to mixed boundary value problems. Thus we would not expect such theories to yield very accurate predictions for $\pi/2 \leq \theta \leq \pi$ (in this angular sector one would expect some influence of the tailpipe).

(d) Finally, as in Lighthill's theory, we assume the convected sources to be compact.

With these assumptions, in Figures 50 - 55 are shown comparisons of computed directivity patterns at constant source frequencies for jet Mach numbers ranging from about 0.35 to 0.91. The comparison is with the data of Lush[18] and Ahuja-Bushell[47]. Source Strouhal numbers ranging from 0.03 to 1.0 were covered in these two sets of experiments and are compared with the current theory.

In general, the agreement appears to be very good between the theory and the experiment. The two sets of experiments give data at very comparable conditions, and it is very difficult to pinpoint instances where the theory fails systematically with both sets of data. The reduced convective amplification of the transverse quadrupoles (see, for instance, Figure 54 between $\theta = 60°$ and $\theta = 90°$ where the radiation is dominated by the transverse quadrupoles), the reduced amplification at the high frequencies, the balance between convection and refraction are all correctly predicted and apparent in the data. The reader may refer to both these papers (of Lush and Ahuja-Bushell) to see how well the Lighthill theory leading to a frequency-independent directivity factor $(1 - M_c \cos\theta)^{-5}$ was able to correlate the data. A systematic underestimation of the variation with θ at low frequencies and a systematic overestimation at the high frequencies by the Lighthill expression is evident. The refractive effect, of course, is not included in the Lighthill theory at all.

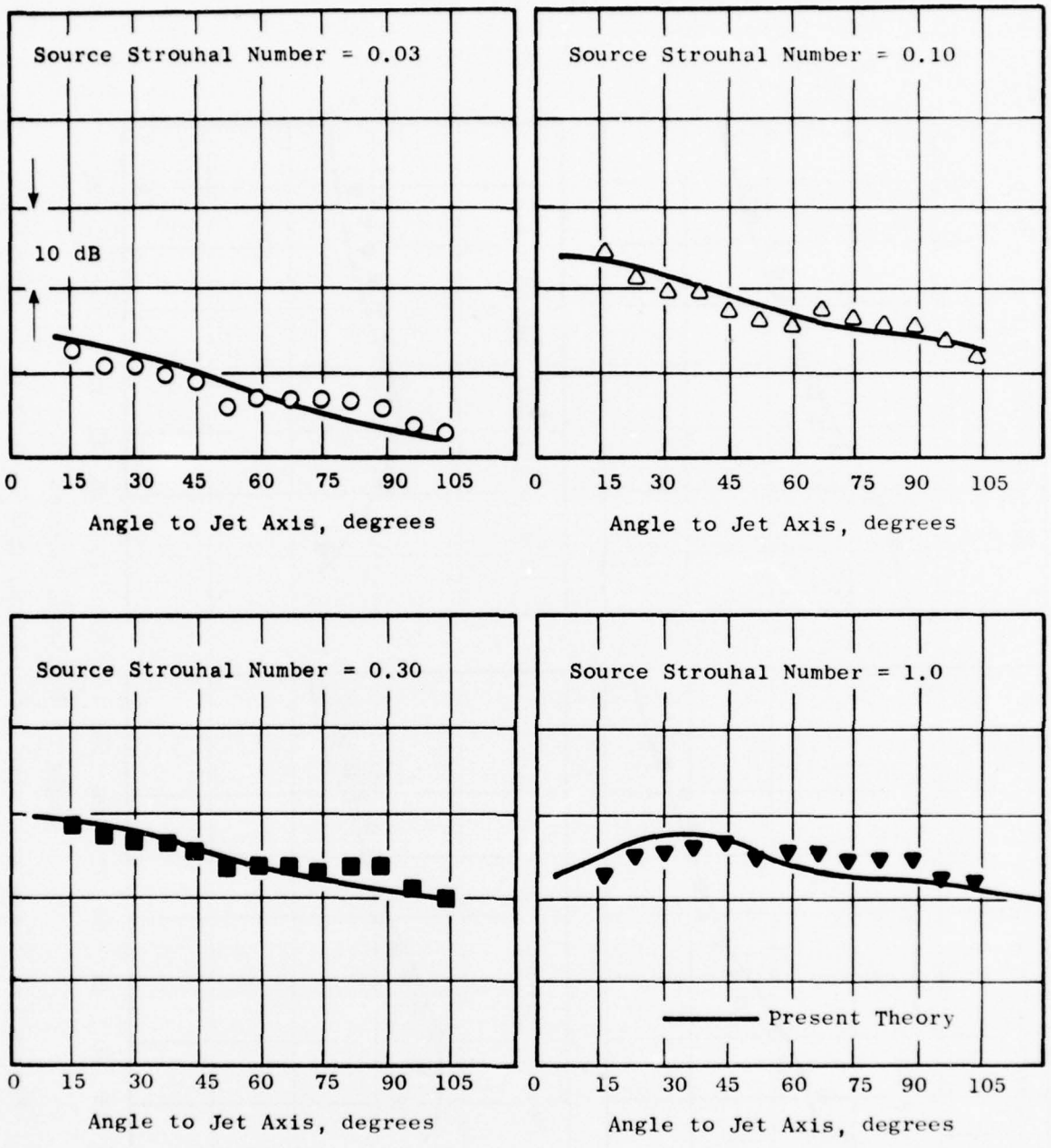


Figure 50. Comparison with Data of Lush at $M_j = 0.366$ (V_j = 125 m/s).

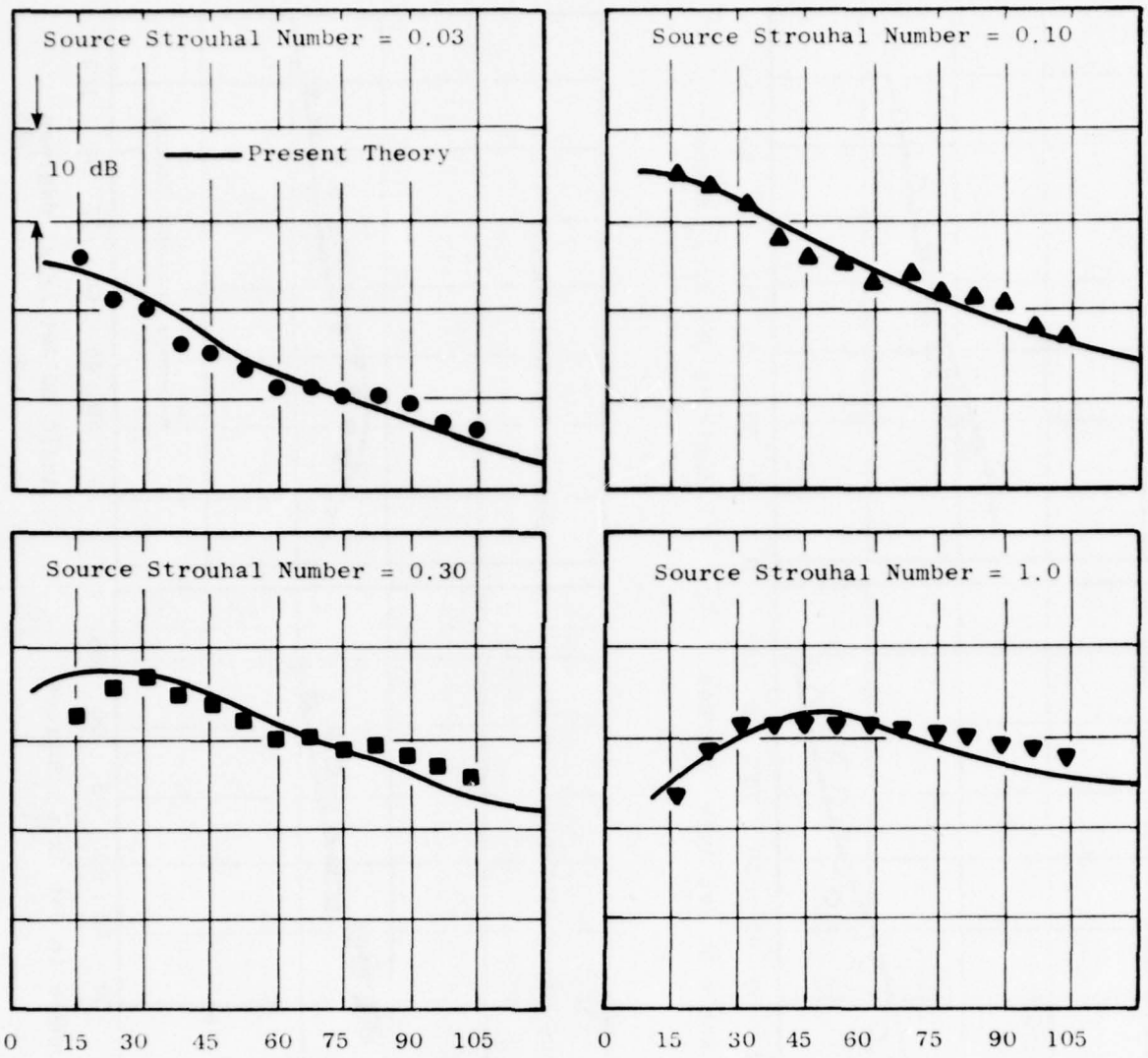


Figure 51. Comparison with Data of Lush at $M_j = 0.57$ ($V_j = 192$ m/s)

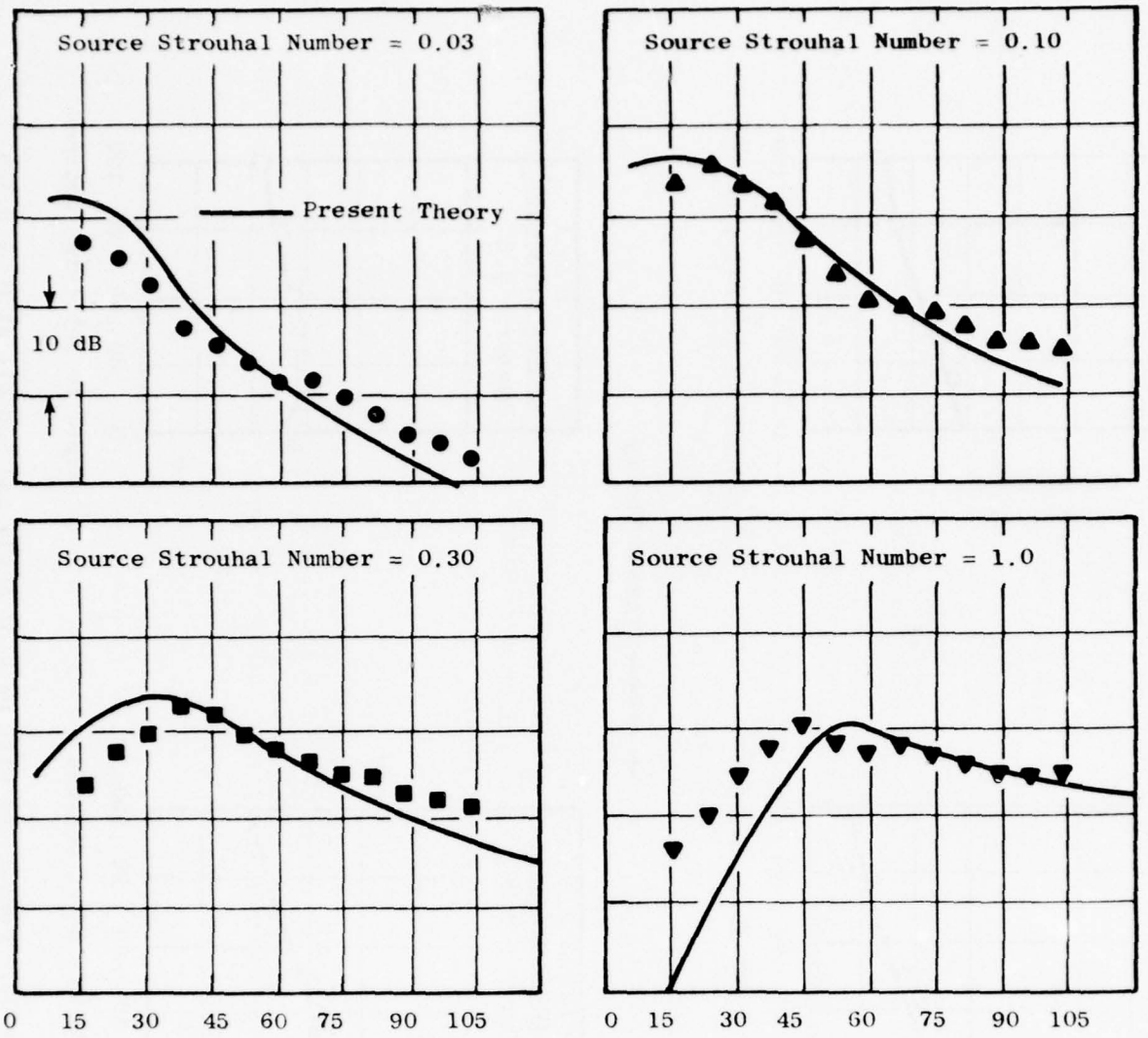


Figure 52. Comparison with Data of Lush at $M_j = 0.878$ ($V_j = 300$ m/s).

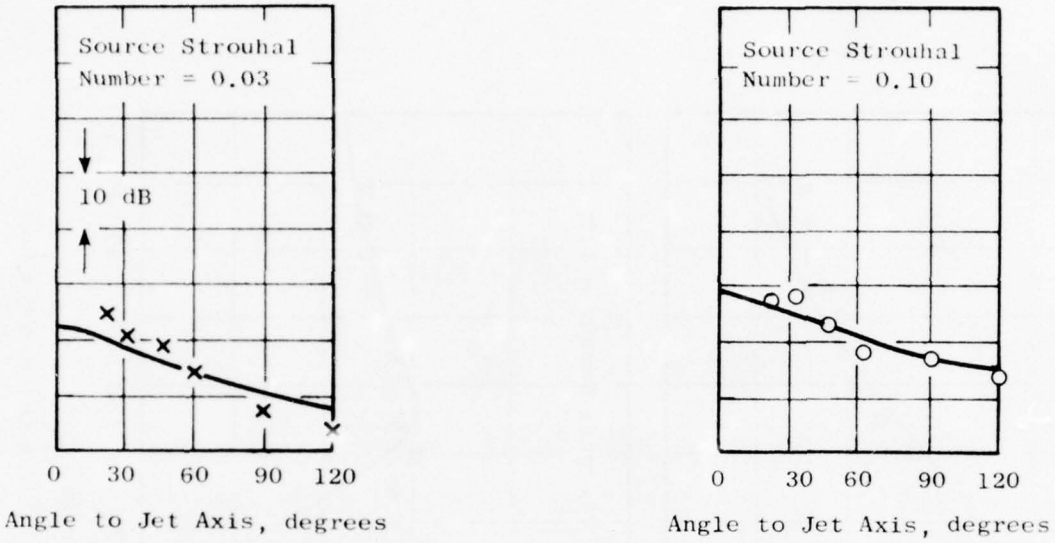


Figure 53. Comparison with Data of Ahuja and Bushell at $M_j = 0.303$ ($V_j = 400$ ft/s).

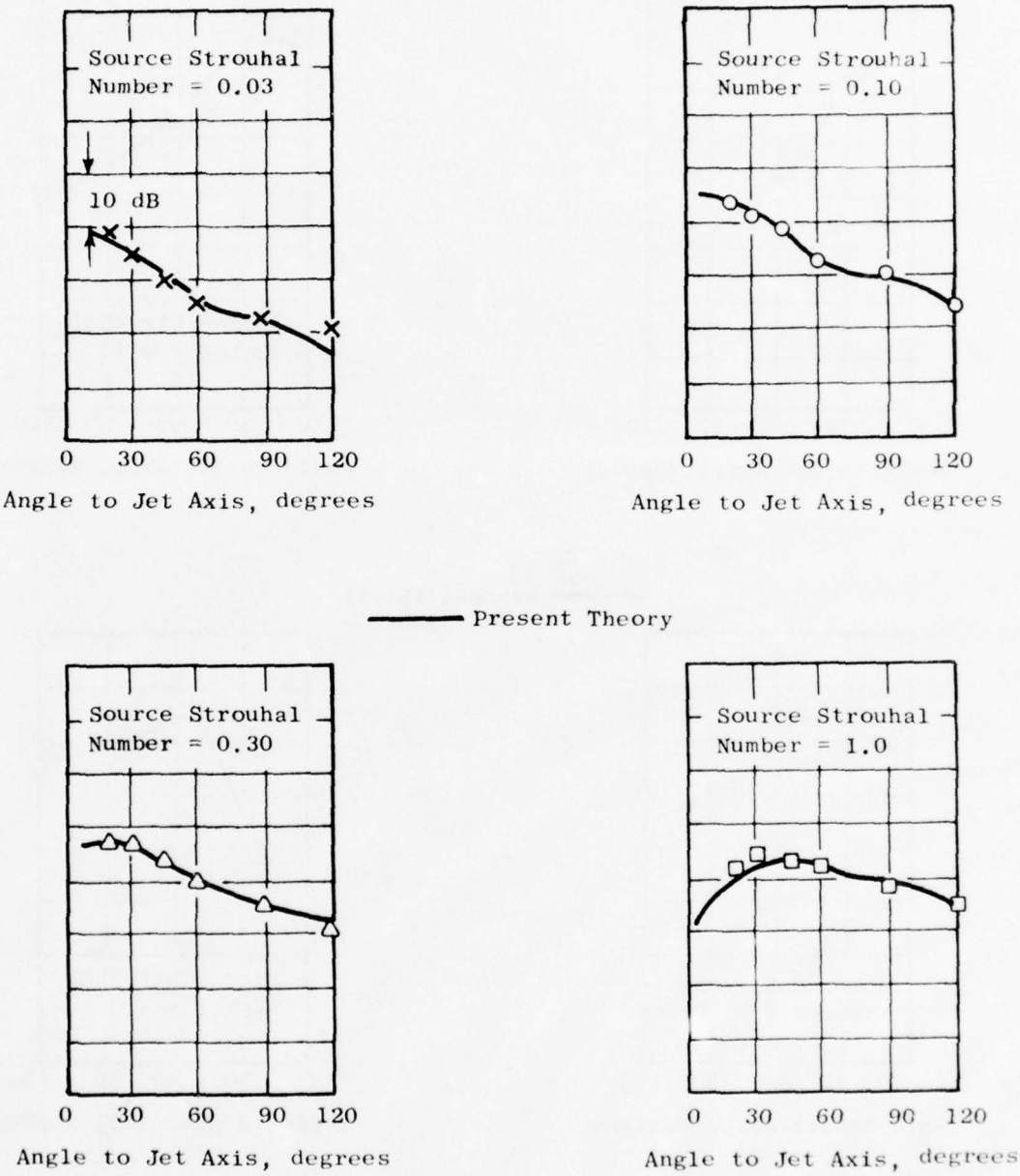


Figure 54. Comparison with Data of Ahuja and Bushell at $M_j = 0.546$ ($V_j = 600$ ft/s).

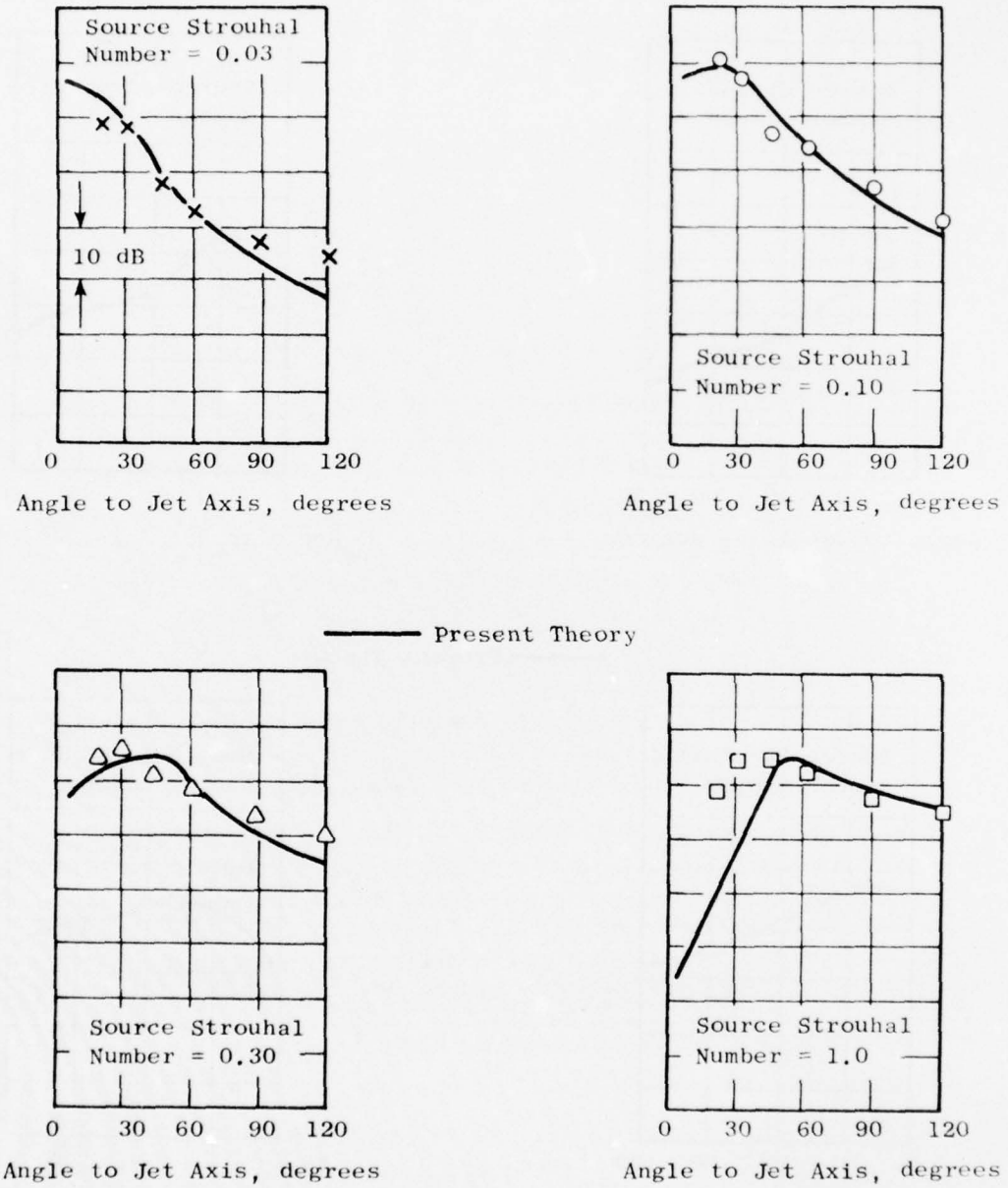


Figure 55. Comparison with Data of Ahuja and Bushell at $M_j = 0.909$ ($V_j = 1000$ ft/s).

The only systematic deficiency found is (in Figures 52, 55) in the overestimation of the refractive dip at the highest velocity (300 m/s and 1000 fps) and the highest source Strouhal number (1.0) covered in these experiments. This is obviously a deficiency of the plug-flow model. Even in this one instance, the radiation aft of the peak is quite reasonably predicted by the current model.

As mentioned earlier, the studies of Lush and Ahuja-Bushell, along with other studies, have confirmed that good Strouhal scaling with respect to velocity and nozzle size and a good eighth-power law for intensity versus jet velocity are obtained at $\theta = 90°$ for cold jets. This means (since we know both analytically and physically that mean flow shrouding effects for cold jets are absent at $\theta = 90°$) that the intrinsic distribution of quadrupoles generating jet noise does follow simple dimensional scaling. That is, the u_i^j, u_j^j scales with V_j, the ω_o varies as (V_j/D), and there does exist a universal strength distribution of (Q^0/V_j^2) against $(\omega_o D/V_j)$. Most importantly, the success of the Lighthill theory at $\theta = 90°$ indicates very little (if any) compressibility effect on this distribution at least up to sonic jet velocities. The calculations of the present paper then give procedures to compute the directional distribution of the sound (say in decibels re: the 90° point) for various source frequency parameters [which can then be translated to observed frequencies by the Doppler shift formula $(1 - M_c \cos\theta)^{-1}$]. Unfortunately, these distributions are not simply expressible as a frequency-independent function $(1 - M_c \cos\theta)^{-5}$. With the aid of a digital computer, however, calculations of the type leading to Figures 50 - 55 can be executed with extreme rapidity. Except for this need to program the results, it is true to say that this section of this study has essentially shown that there is a frequency-dependent procedure to scale cold jet noise with respect to angle from jet axis, nozzle size, and jet velocity. The calculations (with the assumptions outlined earlier) can be formally carried out up to nominal jet velocities of $(1/0.65)\ c_o$ (corresponding to subsonic eddy convection velocities). Comparison with data has so far been shown to be good up to around sonic velocity jets. It is likely that the plug-flow model will not be directly usable at nominal jet velocities higher than about $(1/0.65)\ c_o$. In addition, procedures to deal with the singularity at $M_c \cos\theta = 1$ will need to be devised [Ffowcs Williams(22)].

1.1.4 Concluding Remarks

In the present section, we have attempted to systematically account for the effect of the mean flow on the radiation from subsonically convected quadrupoles oscillating at some frequency in their own frame of reference. Lilley's(28) equation is used to make the application to the problem of cold jet noise. In the interest of deriving closed-form analytical solutions and illuminating the physics, a plug-flow model of the jet is adopted. Within this framework, one can obtain an exact representation of the balance between convective and refractive effects in jet noise. Several novel aspects of the jet noise problem, not at all descernible from the Lighthill acoustic analogy approach, have emerged from the current study:

(1) The Lighthill result for the directivity, namely the expression $(1 - M_c \cos\theta)^{-5}$, emerges only as the limit of zero jet flow Mach number and nonzero (arbitrary) eddy convection Mach number. It is not a good low frequency approximation. Indeed the results herein show that, fortuitously, it is some sort of approximation for the variation with angle of the overall sound pressure level. This is because of its tendency to underestimate the variation with angle of the low frequency sound while overestimating it for the high frequency sound.

(2) When mean flow shrouding effects are included, the technique employed by Lighthill to derive solutions for the higher-order singularities is useful only for the purely axial singularities, and even that application is possible only if the jet flow is assumed to be homogeneous in the axial coordinate (nonspreading jet). The inhomogeneity of the flow in the transverse coordinate necessitates special procedures for the development of solutions to the transverse singularities. A refracted wave emerging from the jet flow into the ambient is characterized in the forward arc by a higher phase speed in the transverse direction within the flow than outside it. This results in reduced convective amplification for the transverse singularities as compared to the predictions of the Lighthill theory. Also, the often-employed equivalence of source terms $\partial^2/\partial x_i\, \partial x_j\, (u_i\, u_j)$ and $1/c_o^2\, \partial^2/\partial t^2\, (v_r^2)$ (Lighthill-Proudman form) is no longer valid.

(3) Extensive comparisons of the theory (with clearly stated assumptions) have been carried out with experiments of Lush[18] and Ahuja-Bushell[47]. The comparisons are for the published directivity plots at constant source frequencies for jet velocities from about 100 m/s to nearly sonic velocities. The agreement in general is very good, especially concerning the new insights provided by the current analysis. We refer here to the tendency of the variation with angle of the low frequency sound to exceed that predicted by the $(1 - M_c \cos\theta)^{-5}$ formula and vice versa for the high frequency sound. We also refer to the tendency of the data to exhibit reduced convective amplification between $\theta = 60°$ to $\theta = 90°$, as compared to that between $\theta = 15°$ and $\theta = 60°$. This is related to the reduced convective amplification associated with the transverse quadrupoles.

(4) The data of Lush and Ahuja-Bushell, at $\theta = 90°$, scale very well on an eighth-power-law basis for the intensity and on an (fD/V_j) basis for the frequency (Strouhal scaling). This suggests very little Mach number (or compressibility) effect with regard to the turbulence source spectrum or "intrinsic quadrupole distribution" (at least up to sonic jet velocities). Together with the ability of the present calculations to predict the variation with angle of the intensity (at various source frequencies), it can be concluded that the scaling problem of cold jet noise with respect to angle from the jet axis, jet velocity, and jet nozzle size is essentially solved (within the limitation of subsonic eddy convection velocities).

(5) Finally, it should be reiterated that several ideas first advanced by Lighthill[44,45] have, in fact, been retained. The notion of convected, compact eddies of quadrupole character, radiating noise due to oscillations

of quadrupole strength in their own frame of reference, is adopted in its entirety from Lighthill's work. Analytically, Phillips, Lilley, et al., have pursued Lighthill's goal of deriving an inhomogeneous wave equation for the fluctuating pressure driven by spatial gradients of the solenoidal turbulent velocity fluctuations. The principal difference from Lighthill's point of view is in the accounting for the effect of the jet flow on the radiation by the eddies and the associated abandonment of the attempt to cast the problem in terms of an analogy to stationary media acoustics.

1.2 THE NOISE OF HEATED JETS

This section continues the study into the area of the noise of heated jets. The first part of the study discusses how a convected wave equation approach based on Lilley's equation leads to additional dipole and simple source-like terms associated with the velocity fluctuations due to transverse gradients of the mean density of the flow. Once these source terms have been identified and roughly estimated, we revert to a plug flow model of the jet flow (where now the jet temperature and jet density differ from the ambient) to estimate the radiation of these singularities. Several novel physical aspects of the hot jet noise problem are uncovered by the analysis. Indeed, the hot jet noise problem is the one where the greatest deviations from Lighthill's ideas on jet noise generation are evident. The results are applied to available data, and a very satisfactory measure of agreement is obtained with respect to the various predictions of the theory. "Excess" pure jet noise mechanisms scaling as M^6 and M^4 are found to result from the density gradients of the mean flow. The satisfactory agreement with the data suggests solution of the scaling program of jet noise with regard to jet temperature effects. The ability to correctly predict the data also suggests very little jet temperature effect on the turbulence source spectrum generating jet noise at least for jet exit velocities up to about 1.5 times the atmospheric speed of sound.

1.2.1 Interpretation of Lilley's Equation For Heated Jets

Lilley's equation can be written in terms of the fluctuating pressure:

$$\frac{1}{\bar{a}^2}\frac{\bar{D}^3 p'}{\bar{D}t^3} - \frac{\bar{D}}{\bar{D}t}(\nabla^2 p') - \frac{d}{dr}\log(\bar{a}^2) + \frac{\bar{D}}{\bar{D}t}\left(\frac{\partial p'}{\partial r}\right) + 2\frac{\partial V_1}{\partial r}\frac{\partial^2 p'}{\partial r}$$

$$= \bar{\rho}(r)\left[\frac{\bar{D}}{Dt}\frac{\partial^2}{\partial x_i\,\partial x_j}(u_i' u_j')\right] \qquad (52)$$

where, for simplicity, the shear-noise term of Lilley's equation has been dropped. Consider the source term $\overline{\rho(\mathbf{r})}\ \partial^2/\partial x_i\ \partial x_j\ (Q_{ij})$, where $Q_{ij} = u_i' u_j'$. As before, let $Q_{ij} = Q_{ij}^o\ \delta(x - Vt)\ \delta(y - y_o)\ \delta(z - z_o)$. The assertion now is that a quadrupole source term of type $\overline{\rho(\mathbf{r})}\ \partial^2/\partial x_i\ \partial x_j\ [\partial(y - y_o)\ \delta(z - z_o)\ \delta(x - Vt)]$ for either (or both of) i or j = 2, 3 contains additional source-like or dipole-like terms. Consider for example the term:

$$\overline{\rho(r)}\ \frac{\partial^2}{\partial y\ \partial x}\ [\delta(y - y_o)\ \delta(z - z_o)\ \delta(x - Vt)] \tag{53}$$

We first remind the reader of some results in generalized functions [see Lighthill[56] such as:

$$f(x)\ \delta(x) = f(o)\ \delta(x) \ . \ . \ . \tag{54a}$$

$$f(x)\ \delta'(x) = f(o)\ \delta'(x) - f'(o)\ \delta(x) \ . \ . \ . \tag{54b}$$

$$f(x)\ \delta''(x) = f(o)\ \delta''(x) - 2f'(o)\ \delta'(x) + f''(o)\ \delta(x) \ . \ . \ . \tag{54c}$$

Using a result such as (54b), we may show that:

$$\begin{aligned}\overline{\rho(r)}\ \frac{\partial^2}{\partial y\ \partial x}\ &[\delta(x - Vt)\ \delta(z - z_o)\ \delta(y - y_o)] \\ &= \overline{\rho(r_o)}\ \frac{\partial^2}{\partial y\ \partial x}\ [\delta(x - Vt)\ \delta(z - z_o)\ \delta(y - y_o)] \\ &\quad - \frac{\partial \rho}{\partial y}\ (r = r_o)\ \frac{\partial}{\partial x}\ [\delta(x - Vt)\ \delta(z - z_o)\ \delta(y - y_o)]\end{aligned} \tag{55}$$

Equation (55) shows that the quadrupole term associated with equation (53) is, in fact, a combination of a traditional x-y quadrupole term proportional to the mean density at $y = y_o$, $z = z_o$ and an axial dipole term proportional to the mean density gradient at $y = y_o$, $z = z_o$. Note that (with the definition skectch of Figure 56) $\partial\rho/\partial y = \cos\phi\ \overline{d\rho/dr\ (r = r_o)}$.

The result, equation (55), is of such importance to the heated jet noise problem that it is worth explaining it at least two other alternative ways. Firstly, consider any differential equation of type say:

$$Lp' = h\ (y,z)\ \frac{\partial^2 f}{\partial y\ \partial z} \tag{56}$$

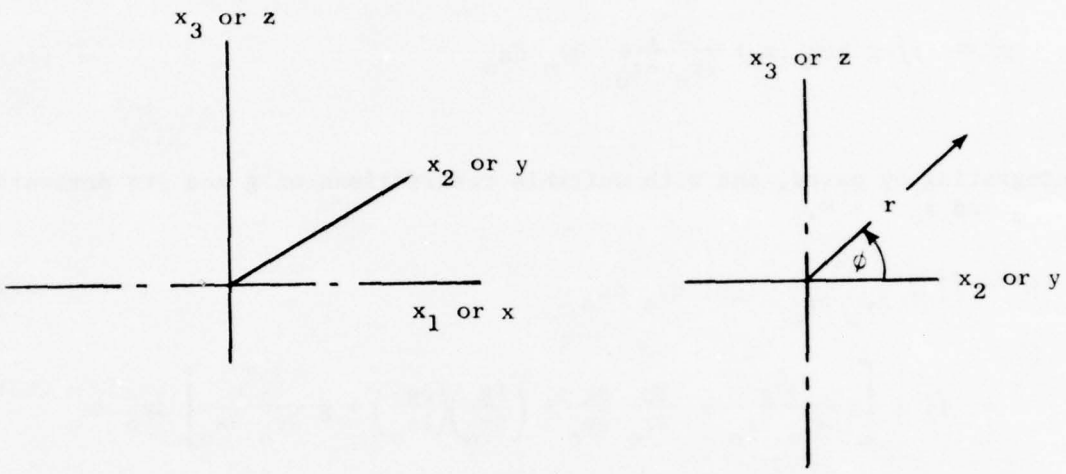


Figure 56. Coordinate System for the Heated Jet.

To solve the above (where, for convenience, assume L to be a linear operator involving only y and z), one could construct the Green's function $g(y - y_o, z - z_o)$ satisfying:

$$Lg = \delta(z - z_o)\ \delta(y - y_o) \tag{57}$$

so that

$$p' = \iint g\ h(y_o, z_o)\ \frac{\partial^2 f}{\partial y_o\ \partial z_o}\ dy_o\ dz_o \tag{58}$$

Integrating by parts, and with suitable restrictions on g and its derivatives at y_o and $z_o = \pm \infty$,

$$p' = \iint f\ \frac{\partial^2}{\partial y_o\ \partial z_o}\ (gh)\ dy_o\ dz_o \tag{59}$$

$$= \iint f \left[h\ \frac{\partial^2 g}{\partial y_o\ \partial z_o} + \frac{\partial h}{\partial z_o}\ \frac{\partial g}{\partial y_o} + \left(\frac{\partial g}{\partial y_o}\right)\left(\frac{\partial g}{\partial z_o}\right) + g\ \frac{\partial^2 h}{\partial y_o\ \partial z_o} \right] dy_o\ dz_o \tag{60}$$

Such a procedure is, in fact, the basis for deriving results such as equations (54a), (54b), (54c), or (55). Expression (60) clearly shows the generation of lower-order singular solutions (proportional to $\partial g/\partial y_o$ due to the gradients $\partial h/\partial z_o$, $\partial h/\partial y_o$, and $\partial^2 h/\partial y_o\ \partial z_o$.

Looking at it another way, whether one considers Lilley's equation or Phillips' equation which is:

$$\frac{\bar{D}^2 r'}{\gamma p_A \bar{D} t^2} - \frac{\partial}{\partial x_i}\left(\frac{1}{\bar{\rho}}\ \frac{\partial r'}{\partial x_i}\right) = \frac{1}{p_A}\left[2\ \frac{\partial \bar{u}_k}{\partial x_j}\ \frac{\partial u'_j}{\partial x_k} + \frac{\partial}{\partial x_i}\ v'_j\ \frac{\partial v'_i}{\partial x_j} \right] , \tag{61}$$

the fundamental solution to the above [i.e., with a $\delta(y - y_o)\ \delta(z - z_o)$ type term on the right-hand side] is proportional to $\bar{\rho}(r_o)$, due to the appearance of the term $(1/\bar{\rho})$ associated with the highest transverse derivative term $\nabla^2 r'$ on the left-hand side of equation (61). This characteristic leads to the generation of lower-order singularities when density gradients are considered.

In Figure 57, it is illustrated how a transverse dipole term proportional to $\rho(y)$ will produce both a dipole term proportional to $\rho(y_o)$ and a simple source-like term proportional to $-\rho'(y_o)$.

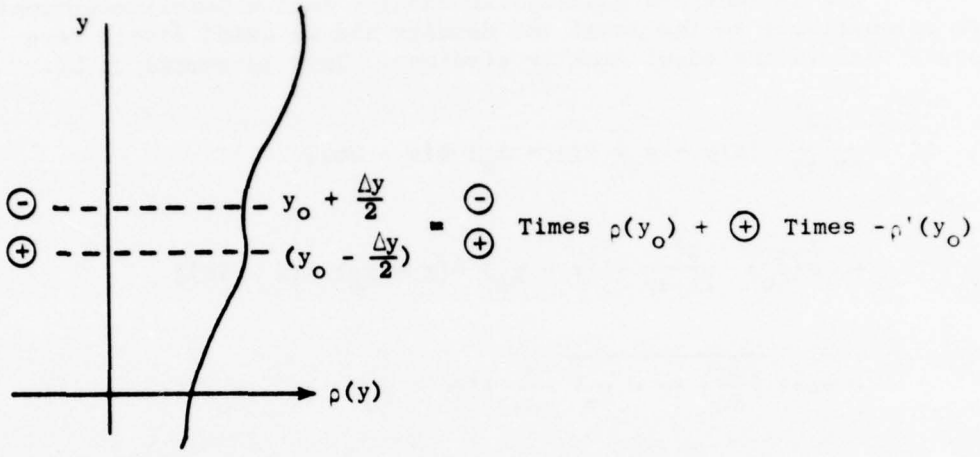


Figure 57. Schematic for a Transverse Dipole Proportional to ρ (y).

Enough has now been said concerning the role of mean density gradients in Lilley's equation to make the following observations [using Lilley's equation in the form of equation (51)]:

(a) The purely axial quadrupole x-x generates no lower-order singularities (since the mean density gradients are assumed to be purely transverse).

(b) The x-y and x-z quadrupoles resolve into a purely quadrupole term proportional to the local jet density and an axial dipole term proportional to the local density gradient. This is summed up by:

$$\overline{\rho(r)}\ \frac{\partial^2}{\partial x\ \partial y}\ [\delta(y - y_o)\ \delta(z - z_o)\ \delta(x - Vt)]$$

$$= \overline{\rho(r_o)}\ \frac{\partial^2}{\partial x\ \partial y}\ [\delta(y - y_o)\ \delta(z - z_o)\ \delta(x - Vt)]$$

$$- \cos\phi \left(\overline{\frac{d\rho}{dr}}\right)(r = r_o)\ \frac{\partial}{\partial x}\ [\delta(y - y_o)\ \delta(z - z_o)\ \delta(x - Vt)] \qquad (62)$$

and similarly for the x-z quadrupole.

(c) The y-y, y-z, and z-z quadrupoles generate both transverse dipoles (proportional to $\overline{d\rho}/dr$) and simple sources (proportional to $\overline{d^2\rho}/dr^2$ and $1/r\ \overline{d\rho}/dr$) in addition to the quadrupoles [proportional to $\overline{\rho(r)}$]. These aspects can be summed up as:

$$\overline{\rho(r)}\ \frac{\partial^2}{\partial y^2}\ \delta(x - Vt)\ \delta(z - z_o)\ \delta(y - y_o)$$

$$= \overline{\rho(r_o)}\ \frac{\partial^2}{\partial y^2}\ [\delta(x - Vt)\ \delta(z - z_o)\ \delta(y - y_o)]$$

$$- 2\cos\phi \left(\frac{\partial\rho}{\partial r}\right)(r = r_o)\ \frac{\partial}{\partial y}\ [\delta(x - Vt)\ \delta(z - z_o)\ \delta(y - y_o)]$$

$$+ \left[\cos^2\phi\ \frac{d^2\rho}{dr^2}(r = r_o) + \frac{\sin^2\phi}{r_o}\ \overline{\frac{d\rho}{dr}}(r = r_o)\right]$$

$$\delta(x - Vt)\ \delta(z - z_o)\ \delta(y - y_o) \ldots . \qquad (63)$$

and an analogous result for the z-z quadrupole:

$$\rho(r)\,\frac{\partial^2}{\partial y\,\partial z}\,[\delta(x - Vt)\,\delta(z - z_o)\,\delta(y - y_o)]$$

$$= \overline{\rho(r_o)}\;\frac{\partial^2}{\partial y\,\partial z}\,[\delta(x - Vt)\,\delta(z - z_o)\,\delta(y - y_o)]$$

$$- \frac{d\rho}{dr}\,(r = r_o)\,\Big\{\sin\phi\,\frac{\partial}{\partial y}\,[\delta(x - Vt)\,\delta(z - z_o)\,\delta(y - y_o)]$$

$$+ \cos\phi\,\frac{\partial}{\partial z}\,[\delta(x - Vt)\,\delta(z - z_o)\,\delta(y - y_o)]\Big\}$$

$$+ \frac{\sin(2\phi)}{2}\,\left[\frac{d^2\rho}{dr^2}\,(r = r_o) - \frac{1}{r_o}\,\overline{\frac{d\rho}{dr}}\,(r = r_o)\right]$$

$$\delta(x - Vt)\,\delta(z - z_o)\,\delta(y - y_o) \qquad (64)$$

1.2.2 Method of Solution

Once the additional singularities generated by the presence of mean density gradients have been identified, we may now use equation (52) with a plug-flow model of the jet flow as shown in Figure 58. We note that $\rho_1\,c_1^2$ must be equal to $\rho_o\,c_o^2$ due to the constancy of the mean static pressure. Equation (52) appears to be a preferred form of Lilley's equation in that in equation (52) the coefficient of the highest transverse derivative term involving p' (namely $\nabla^2 r'$) is unity. As in Section 1.1, we will deal with centerline eddy convection and with V_1 assumed equal to V_c. One important qualifier, however, is that it would not be meaningful to estimate $\overline{\rho(r)}$, $\overline{d\rho/dr}$, $d^2\rho/dr^2$ and $1/r\;\overline{d\rho/dr}$ by their values at the jet centerline ($r_o = 0$). Consistent with a plug-flow model, we must use some average representative estimates of $\overline{\rho}$, $\overline{d\rho/dr}$, etc. Some physical judgment is involved in this process, and we will discuss this matter in the next section.

The quadrupole singular solutions themselves can be derived in a manner very similar to those derived in Section 1.1, and the procedure is briefly illustrated for the x-x quadrupole. With a plug-flow model, we have to solve for:

$$\frac{1}{c_1^2}\,\frac{\bar{D}^2 p'}{\bar{D}t^2} - \nabla^2 p' = \rho_1\,Q^o_{xx}\,\frac{\partial^2}{\partial x^2}\,e^{j\omega_o t}\,[\delta(x - Vt)\,\delta(y)\,\delta(z)]$$

$$\text{for } 0 \le r < a \qquad (65)$$

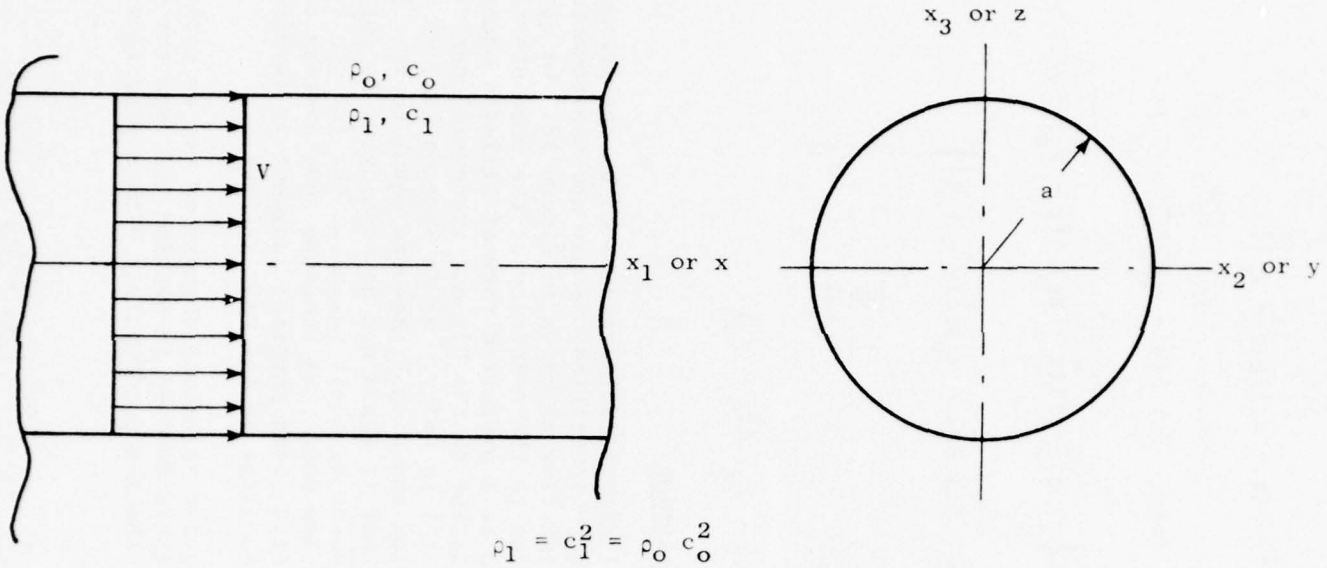


Figure 58. Coordinate System for the Plug-Flow Acoustic Model for a Heated Jet.

and for:

$$\frac{1}{c_o^2}\frac{\partial^2 p'}{\partial t^2} - \nabla^2 p' = 0 \qquad \text{for } r > a \tag{66}$$

where, at $r = a$, both p' and η are continuous where:

$$\frac{\bar{D}^2\eta}{\bar{D}t^2} = -\frac{1}{\rho_1}\frac{\partial p'}{\partial r} \tag{67}$$

for $0 \leq r < a$ and:

$$\frac{\partial^2\eta}{\partial t^2} = -\frac{1}{\rho_o}\frac{\partial p'}{\partial r} \qquad \text{for } r > a \tag{68}$$

The problem for the axial Fourier transforms P', N then is:

$$\nabla^2_{y,z} P' + \left(k_1^2 - \alpha^2\right) P' = \rho_1 Q^o_{xx} \alpha^2 \delta(y)\,\delta(z) \tag{69}$$

where $k_1 = \omega_o/c_1$ for $0 \leq r < a$,

and:

$$\nabla^2_{y,z} P' + \left[\left(k_o + \alpha M_o\right)^2 - \alpha^2\right] P' = 0 \tag{70}$$

for $r > a$, where $k_o = \omega_o/c_o$, $M_o = V/c_o$.

At $r = a$, P' should be continous, as should N (the transform of η'), where:

$$N = \frac{1}{\rho_1 \omega_o^2}\frac{\partial P'}{\partial r} \qquad \text{for } 0 \leq r < a \tag{71}$$

and:

$$N = \frac{1}{\rho_o\,\omega_o^2\left(1 + \frac{\alpha M_o}{k_o}\right)^2}\frac{\partial P'}{\partial r} \tag{72}$$

for $r > a$. The solution to P' can then be written down and p' deduced (in the far field) by the method of stationary phase. We give the expression for p' as:

$$p' \sim \frac{-j\,\rho_o\,Q^o_{xx}\,\omega_o^2\,e^{j(\omega_o t - k_o R)}\cos^2\theta}{2\pi^2 R(1-M_o\cos\theta)^3\,C_o^2\left[H_o^{(2)}(\alpha^+ a)I_o'(\underline{\alpha}^+ a)(\underline{\alpha}^+ a)\,\rho_o/\rho_1 - (\alpha^+ a)\,H_o^{(2)'}(\alpha^+ a)I_o(\underline{\alpha}^+ a)(1-M_o\cos\theta)\right]^2} \tag{73}$$

for $0 \leq \theta \leq \cos^{-1} 1/(c_1/c_o + M_o)$, where $\alpha^+ = k_o \sin\theta/(1 - M_o \cos\theta)$ and $\underline{\alpha}^+$ is the positive square root $\sqrt{k_1^2 - \alpha^2}$ with $\alpha = k_o \cos\theta/(1 - M_{o+} \theta)$. For $\cos^{-1}$ $[1/(c_1/c_o + M_o)] \leq \theta \pi$, the same expression applies with $\underline{\alpha}^+$ replaced by $\underline{\underline{\alpha}}^+$ which is the positive square root $\sqrt{\alpha^2 - k_1^2}$ and the I functions replaced by the J functions. The procedures for deriving the solutions for the x-y, y-z, and y-y quadrupoles carry over more or less mechanically from Section 1.1, with the only differences being that $\underline{\alpha}^+$ or $\underline{\underline{\alpha}}^+$ are now to be computed by $\sqrt{|k_1^2 - \alpha^2|}$; the zone of silence now ranges over $0 \leq \theta \leq \cos^{-1}$ $[(1/(c_1/c_o + M_o)]$, and a factor (ρ_o/ρ_1) multiplies the term involving I' or J' in the denominator of expressions such as equation (39).

The additional solutions that need to be worked out correspond to:

(a) An axial dipole solution, i.e., with a source term of type:

$$\frac{\partial}{\partial x}\left[\delta(x - Vt)\,\delta(y)\,\delta(z)\right]$$

(b) A radial dipole term of type:

$$\frac{\partial}{\partial r}\left[\delta(x - Vt)\,\delta(y)\,\delta(z)\right]$$

and (c) A pressure source term of type:

$$\delta(x - Vt)\,\delta(y)\,\delta(z).$$

These solutions are just as easy to derive as the quadrupole solution and, hence, only the broad outlines will be sketched. The solution to (a) is very similar to equation (73) with the multiplier $\omega_o^2/[c_o^2(1 - M\cos\theta)^2]$ (or α^2) replaced by just $\omega_o \cos\theta/[c_o(1 - M\cos\theta)]$ (or α). The solution to (b) is similar to that for (a) with α replaced by $\underline{\alpha}^+$ or $\underline{\underline{\alpha}}^+$ in the numerator and the Bessel functions of order zero replaced by those of order 1. Finally, the solution to (c) is identical to that of (a) except that no term α appears in the numerator.

1.2.3 Physical Interpretation of the Solutions and Applications To Jet Noise Experiments

At least three distinct mechanisms affecting jet noise can be identified as influencing the radiation by quadrupoles in a hot jet. Firstly, for the transverse quadrupoles (as in Section 1.1), the phase concellation or Stokes'-effect mechanisms are now governed by the flow properties within the jet. Since the speed of sound is higher within the jet than outside it, the Stokes' effect tends to diminish the radiative efficiency of the transverse quadrupoles as the jet temperature is increased. Secondly, especially at low frequencies, there is a transmission or dynamic density effect tending to enhance the radiation by a factor (ρ_o/ρ_1). Ribner[11] alludes to this by considering the problem of a monopole source of strength $Q_o\, e^{j\omega_o t}$ embedded in a sphere of gas of density ρ_1, c_1 (and of radius a) with the ambient at a density and speed of sound of ρ_o, c_o. In the limit of $(\omega_o a/c_o) \to 0$, the source appears to the ambient as if it were of strength $(Q_o\, \rho_o/\rho_1)$. Equation (73) manifests this same result because, in the limit of $(k_o a \to 0)$, p' is proportional to ρ_o even though the strength of the x-x quadrupole was taken as proportional to ρ_1 [see equation (65)]. Finally, Lilley's equation shows that, while the strength of the quadrupoles themselves varies as ρ_1 (and, hence, diminishes as the jet temperature increases), there are associated with the transverse singularities additional dipole- and source-like mechanisms related to the density gradients of the mean flow which increases with increasing jet temperature.

It is worthy of note that the Lighthill expression [equation (20) of Section 1.1] is not now identifiable as any valid limit whether at low Mach numbers or low frequencies or even at $\theta = 90°$. At the 90° point, jet flow shrouding effects are present for hot jets simply because a temperature inhomogeneity is a scalar inhomogeneity unlike a velocity inhomogeneity so that there is no question of there not being a component at $\theta = 90°$. Besides, the 90° radiation is dominated by the transverse singularities which generate the additional source-like and dipole-like terms not accounted for by Lighthill's expression. Indeed, of the various agencies identified as governing the radiation by quadrupoles in a hot jet, the Lighthill expression picks up only one effect, namely the variation of the quadrupole strength as ρ_j. Perhaps it can now be appreciated why it was mentioned earlier that the area of hot jet noise is one in which equations such as Lilley's equation yield insights which are far removed from that provided by Lighthill's theory.

We now turn to the problem of the application of the above to jet noise data. The x-y and x-z quadrupole each generate an additional dipole, while the y-y, y-z and z-z quadrupoles generate two additional terms. This gives rise to 14 primary solutions [unlike the 6 with which Ribner[34] dealt]. On constructing an expression for the mean square pressure, 196 types of interaction terms arise, though several of these will undoubtedly vanish upon averaging circumferentially. To avoid too complicated a solution procedure, the same formula employed for cold jets [equation (51)] was used in the current study with one additional simplification. Since representative average estimates were made of $\overline{d\rho}/dr$, $\overline{d^2\rho}/dr^2$ etc., whenever a quadrupole

singularity generates additional dipole-like and source-like terms, interference between different order multipole singularities is also neglected. In other words, each order of multipole singularity was assumed to contribute independently to the mean square pressure due to that quadrupole. Circumferential averaging in the ϕ direction was also carried out as usual.

In accordance with the assumption of the velocity of the plug-flow jet used to compare the predictions of the theory against the experiment used in Section 1.1, the temperature T_1 of the plug-flow jet was taken as [(0.65 × ideal jet exit temperature + (0.35) × ambient temperature]. The density ρ_1 was calculated correspondingly from $\rho_1 T_1 = \rho_o T_o$.

One last assumption was used, in connection with the estimation of density gradients, which needs some discussion. The relative contributions of the quadrupole, dipole, and simple source contributions appear (for given velocity fluctuation levels) to scale as:

$$\bar{\rho} k_o^2 \quad , \quad \left(\frac{\partial \bar{\rho}}{\partial r}\right) k_o \quad \text{and} \quad \frac{d^2 \bar{\rho}}{dr^2} \tag{74}$$

This then suggests that density gradients primarily influence the low frequency sound at a given jet velocity. It might even appear to explain the experimentally observed progressive biasing toward the lower frequencies of the pressure spectra when the temperature of a constant-velocity jet is raised. We believe that such an inference is erroneous for the following reasons. It must be recognized that the low-frequency sound is likely to be emitted from a region where the density gradients are likely to be small and, conversely, the high-frequency sound from the regions of the flow where the gradients are large. This notion can be empirically stated as:

$$\frac{d\bar{\rho}}{dr} = \frac{(\rho_o - \rho_1)}{a} \quad (\text{source Strouhal No.})\ C_1 \tag{75}$$

and

$$\frac{d^2 \bar{\rho}}{dr^2} \approx \frac{(\rho_o - \rho_1)}{a^2} \quad (\text{source Strouhal No.})^2\ C_2 \tag{76}$$

(C_1 and C_2 are nondimensional constants to be specified shortly). Equations (75) and (76) attempt to recognize that the low-Strouhal-number emission occurs further downstream in a jet and, conversely, high-Strouhal-number emission occurs close to the nozzle exit. With the aid of equations (75), (76) and reinstating the velocity fluctuation dependence in (74), for a given source Strouhal number, the quadrupole, dipole, and source terms should scale as:

$$(\text{jet velocity})^4 \left[\rho_1 , \frac{(\rho_o - \rho_1)}{M_o} , \frac{(\rho_o - \rho_1)}{M_o^2} \right] \qquad (77)$$

Equation (77) reveals [as does (74)] that there are "excess" noise mechanisms formally scaling as M_o^6 and M_o^4 (for the intensity) when density gradients are allowed for. This, of course, is merely a reflection of the dipole- and source-like nature of the additional singularities introduced by the density gradients. The situation with regard to a power law for the velocity, of course, is not very clear cut since often both density gradients and velocities are changed simultaneously in experiments. Equation (77) does show, however, that, if the velocity of a hot jet is changed at constant jet temperature, there will be M_o^6 and M_o^4 type noise contributions due to the coupling of the velocity fluctuations and density gradients. Interestingly enough, Bushell[57] in an effort to correlate high-bypass-ratio fan engine noise has found that the cold outer fan jet noise follows an eighth-power law down to much lower velocities than the hot core jet noise. Equation (77) also confirms that, at constant M_o, changing jet temperature does not affect the mix of the source terms proportional to ρ_j and $(\rho_o - \rho_j)$ differently for the different Strouhal numbers. Thus, it cannot explain the biasing of the power spectra progressively toward the lower frequencies due to heating. This appears to be a propagation effect. With regard to equations (75) and (76), one data point at $M_o = 0.4$ at $\theta = 90°$ from Tanna[58] was used to establish that $C_1 = C_2 = 1$ appear to suffice to explain that data. These values have subsequently been used in all the comparisons with all the data of Tanna[58] Hoch[59] and Hoch[60].

Two comparisons have been carried out with available data. As in Section 1.1, the theory is restricted to jet velocities such that only subsonic eddy convection velocities are involved (i.e., for jet velocities less than 1/0.65 the atmospheric speed of sound). In Figure 59, we compute the variation of the total power of the directivity pattern at constant jet velocity for various source Strouhal numbers (from 0.03 to 1.0) as a function of (ρ_j/ρ_o) and exhibit the answer as a jet density exponent ω, i.e., the acoustic power varies as ρ_j^ω for a constant jet velocity. Hoch[59], et al., have given such data for the overall power level and, as Figure 59 shows, the current theory brackets the data quite well when one considers the theoretical predictions for source Strouhal numbers of 0.03 and 1.0 (which should bracket the dominant eddy frequency range quite well). Especially at the lower jet velocities, the theory also predicts a progressive biasing of the power spectrum towards the lower frequencies due to heating (the index at a source Strouhal number of 0.03 is less than that at 1.0) which is also in accord with Hoch's study. The available data in the area of hot jet noise are rather sparse and are not yet available in the form of directivity plots at constant -source Strouhal numbers which is the sort of information that one can directly compare against the predictions of an acoustic theory.

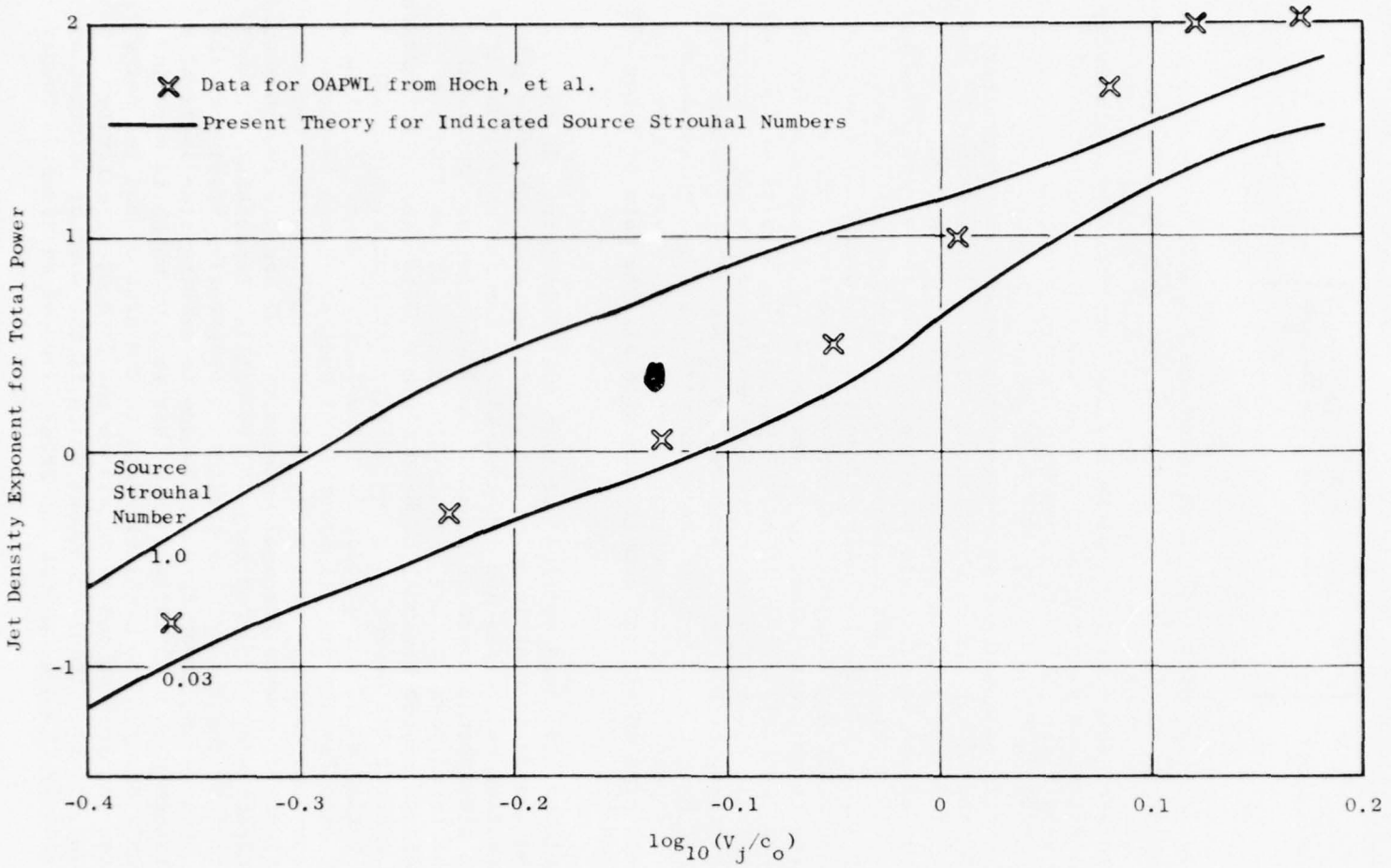


Figure 59. Jet Density Exponent for Total Power as a Function of (V_j/c_o).

Computed components are shown in Figures 60 - 65 at various angles from the jet axis for various jet velocities. Since we are dealing with a fixed angle now, the data can be exhibited in terms of observed Strouhal numbers - a more recognizable quantity than a source Strouhal number. The indices are computed for observed Strouhal numbers ranging from 0.1 to 1.0. Such index calculations are always carried out by fitting a straight line by the least-squares method to a plot of $\log\langle p^2\rangle$ against $\log(\rho_j/\rho_o)$. The calculations are carried out for (ρ_j/ρ_o) ranging from 0.2 to 1.0. Shown by crosses are the data for the index for the OASPL as measured by Hoch[60]. The broad agreement again is most encouraging. Note that, at shallow angles to the jet axis, the dominant observed Strouhal numbers for the pressure spectrum of a cold jet lie between 0.1 and 0.3 with values between 0.6 and 1.0 being more typical of the spectra at the larger angles ("reverse" Doppler shift). Thus, it is quite appropriate that the experimental data for the OASPL should agree better with the lower-frequency curves at the shallow angles and with the higher-frequency curves at the larger angles. The high, positive indices at the shallow angles for the high frequencies are a manifestation of the rapid diminution of sound pressure at these angles and frequencies due to heating because of the refractive sweepback of the pattern upon heating the jet. {Recall the enlargement of the zone of "silence" from $0 \leq \theta \leq \cos^{-1}(1/1 + M)$ to $0 \leq \theta \leq \cos^{-1}[1/(c_1/c_o) + M_o]$ due to heating}. Figure 66 is essentially a replot of the 90° data of Figures 60 - 65 since experimentalists often concentrate on this measurement station. With hot jets, however, we have shown that the 90° location is by no means a clear indicator of the turbulence source strength and spectrum variation and, thus, there seems little that is unique about such a location (except that convection effects are always absent at this location). Figure 66 indicates an apparent overprediction at the high-velocity end of the exponent by the theory. In Figure 67, however, we show comparisons with computed indices from the data of Tanna[58] for three different jet velocities and for several frequencies. The data-theory comparison at $M_o = 0.4$ should be discounted as the choice of c_1 and c_2 in equation (75) was based on these data. The theory predicts the data at $M_o = 0.8$ quite well, but now underpredicts the data at $M_o = 1.47$. Thus, considering the three sets of data of Hoch[59], Hoch[60] and Tanna[58], it is difficult to detect systematic failure of the theory.

As with the results of Section 1.1, this ability to predict the data suggests both the solution of the scaling problem of the effects of jet temperature on jet noise and the conclusion that there is very little temperature effect on the turbulence source spectrum so long as jet velocity is held fixed.

1.2.4 Concluding Remarks

The problem of noise generation by a heated jet has been systematically studied with the aid of Lilley's equation. Only the velocity fluctuations have been considered as the source of the sound, but mean density gradients act to generate dipole- and simple source-like terms which produce jet noise, scaling with jet velocity as M^6 and M^4 for constant values of (jet temperature - ambient temperature). Such additional singular source-like terms arise only for the transverse quadrupoles.

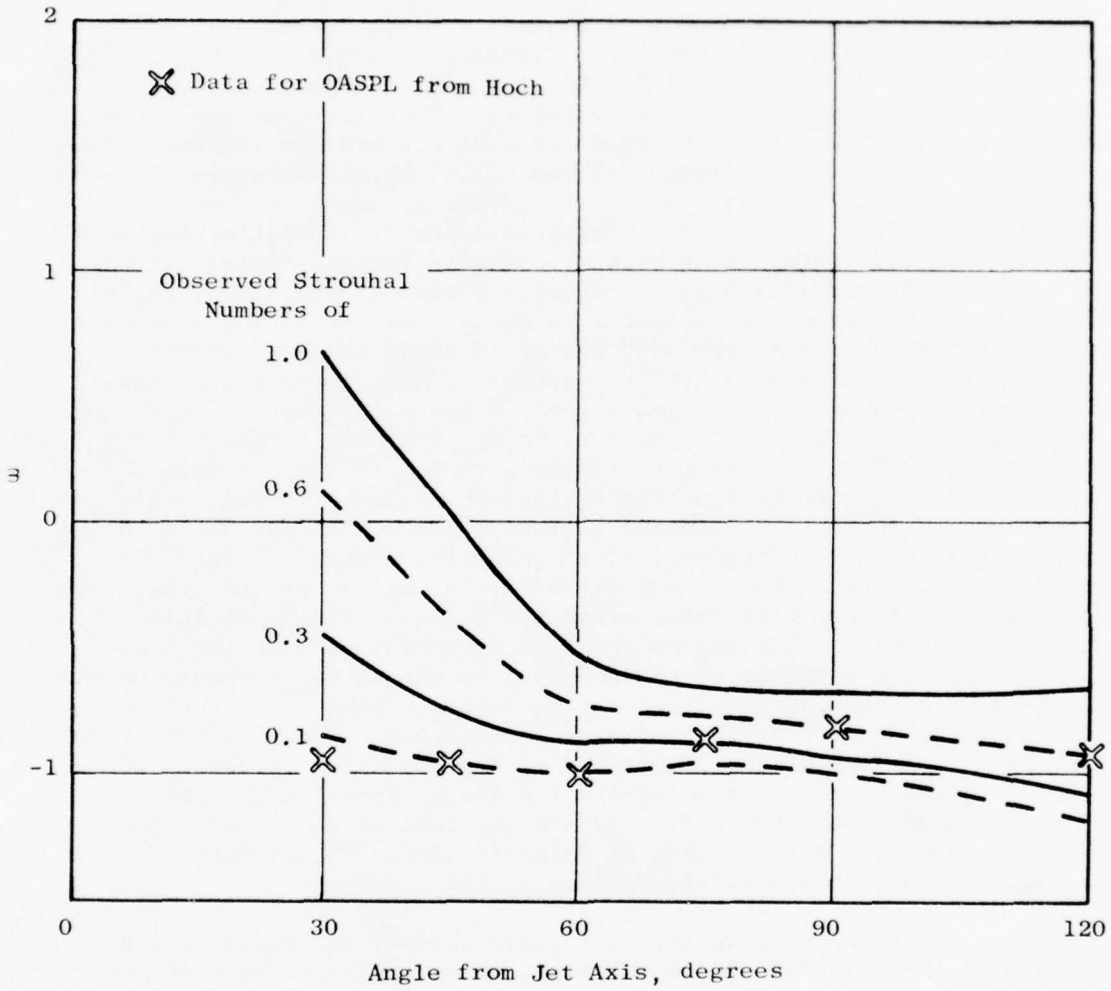


Figure 60. Jet Density Exponent for $V_j/c_o = 0.447$ as a Function of Angle from the Jet Axis.

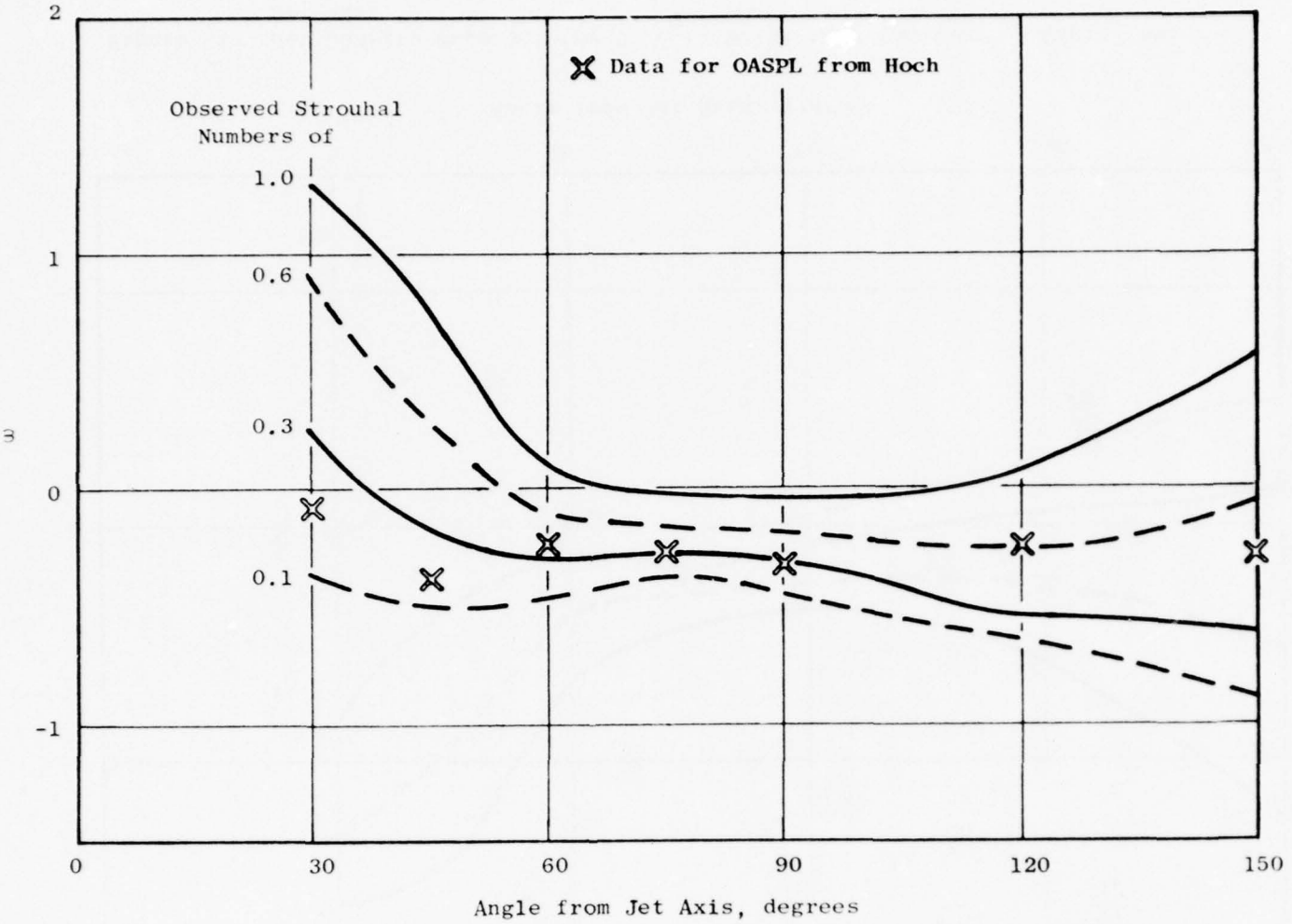


Figure 61. Jet Density Exponent for $V_j/c_o = 0.589$ as a Function of Angle from the Jet Axis.

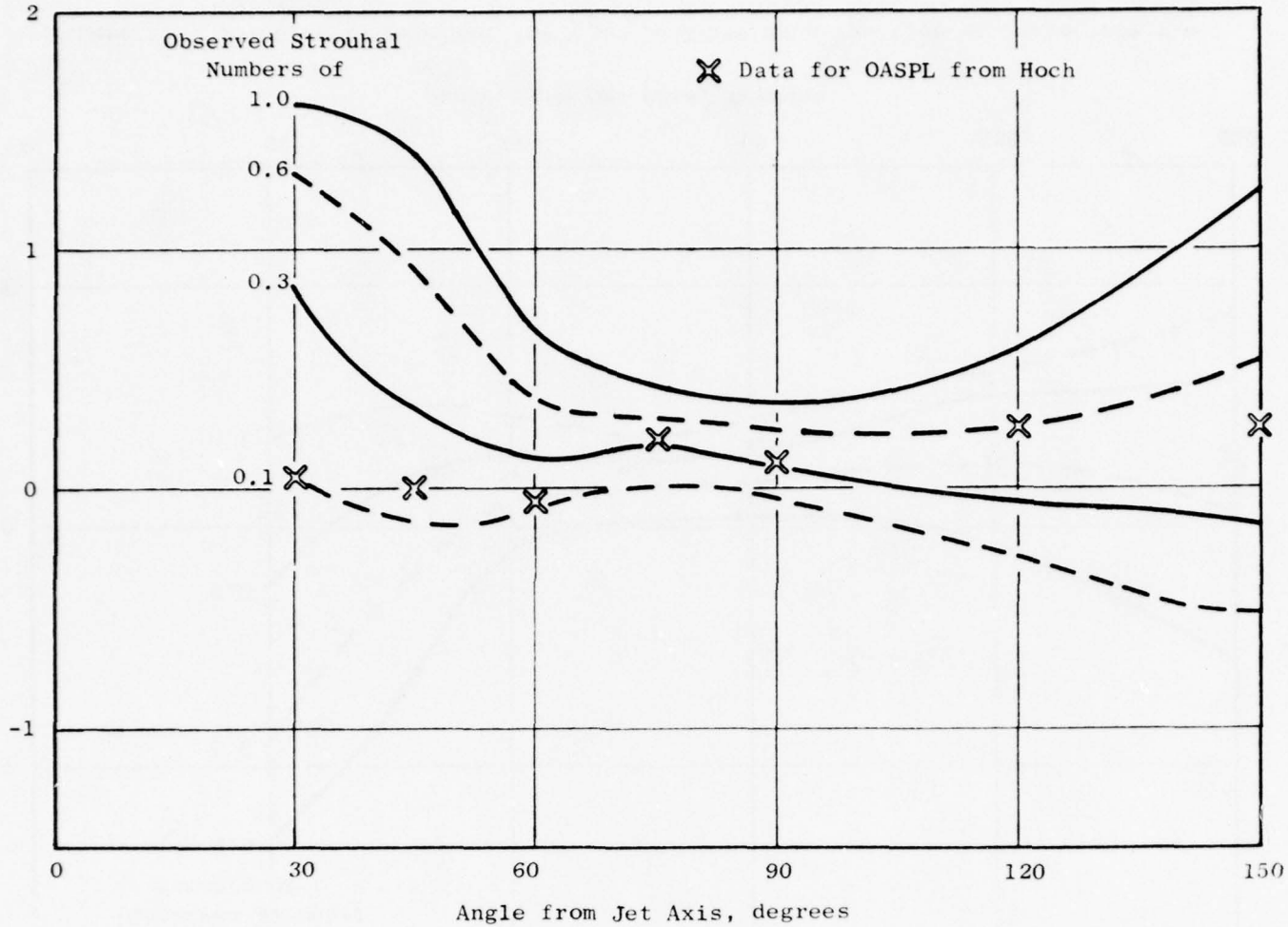


Figure 62. Jet Density Exponent for $V_j/c_o = 0.741$ as a Function of Angle from the Jet Axis.

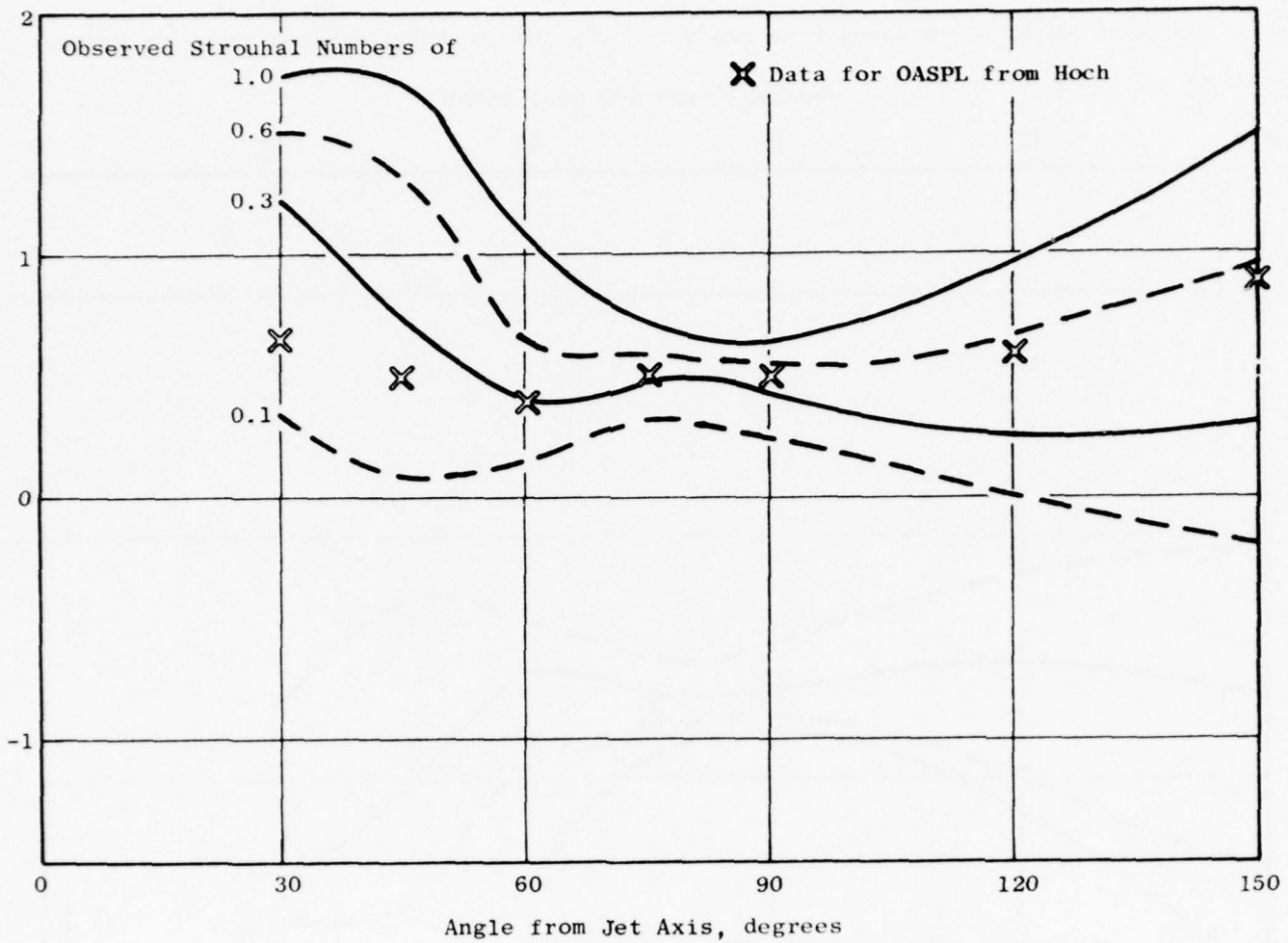


Figure 63. Jet Density Exponent for $V_j/c_o = 0.891$ as a Function of Angle from the Jet Axis.

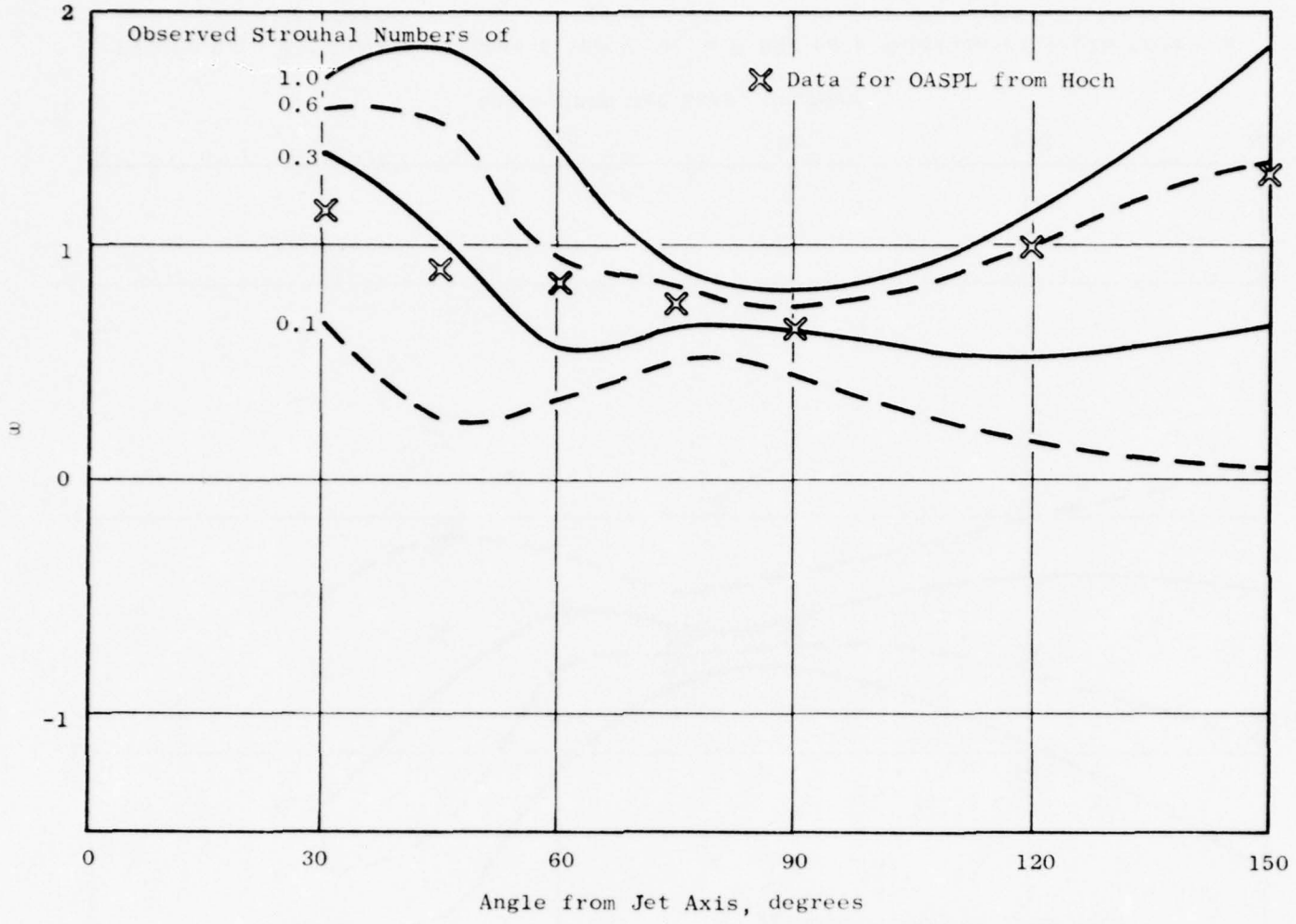


Figure 64. Jet Density Exponent for V_j/c_o = 1.023 as a Function of Angle from the Jet Axis.

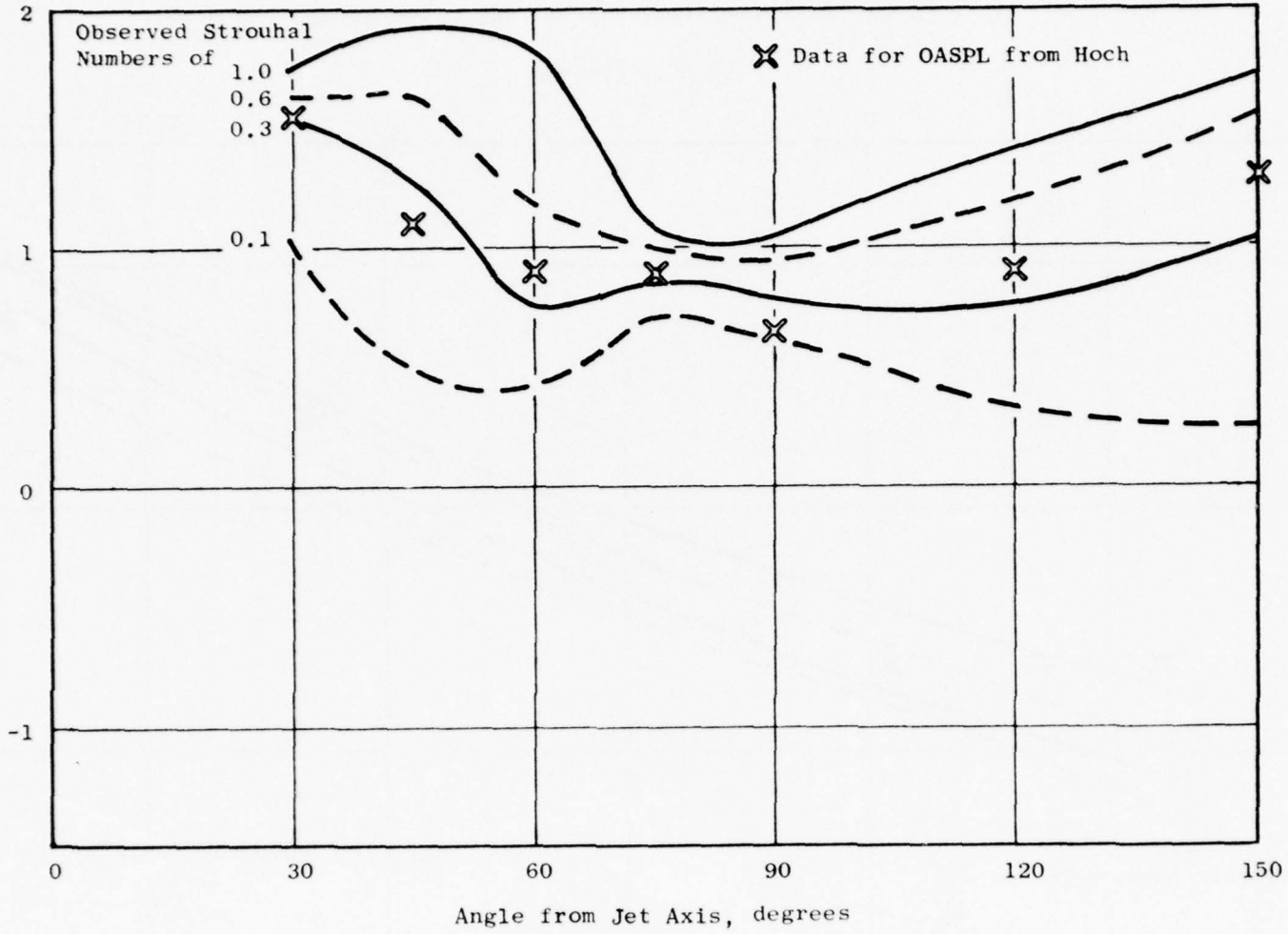


Figure 65. Jet Density Exponent for $V_j/c_o = 1.175$ as a Function of Angle from the Jet Axis.

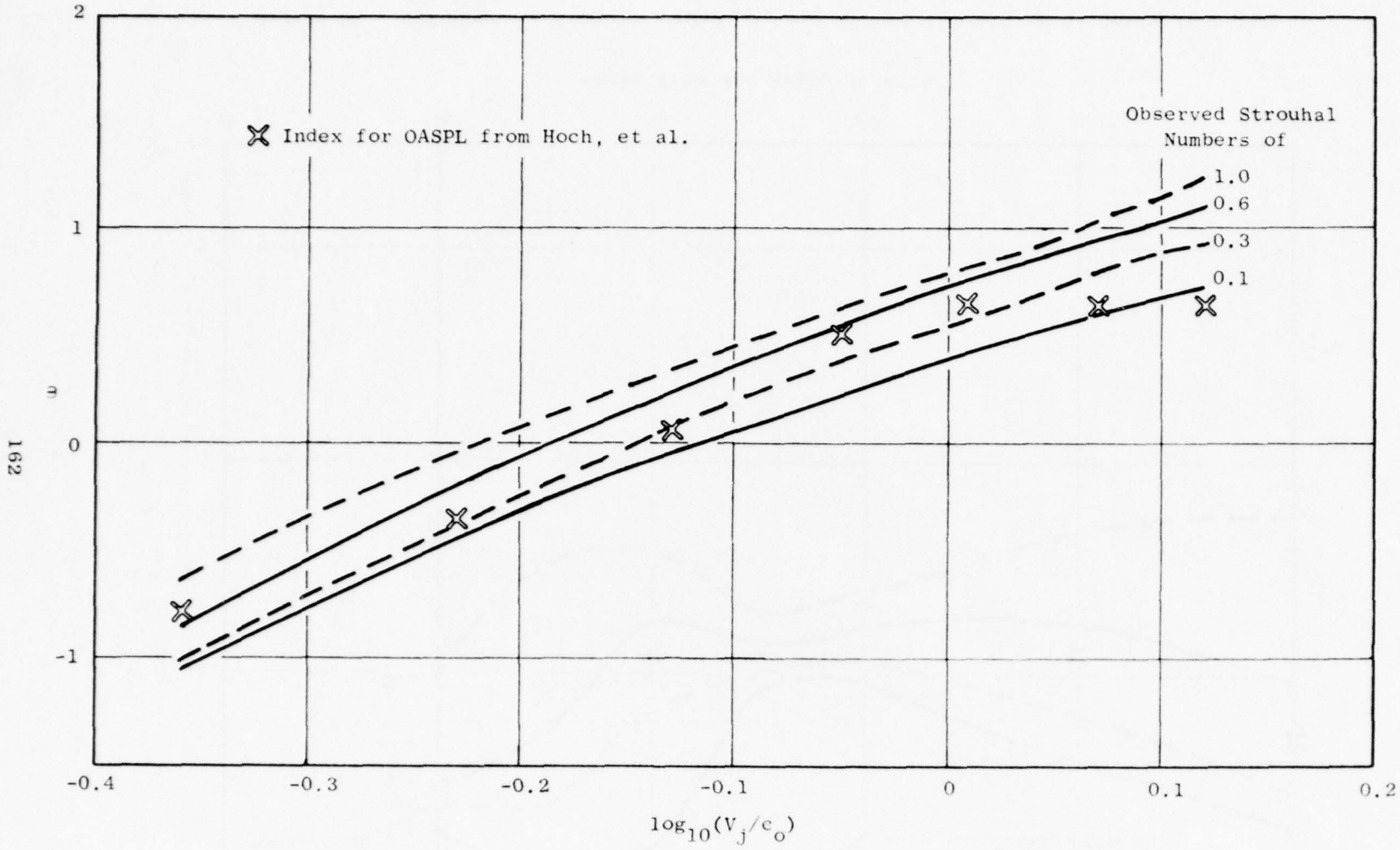


Figure 66. Index at 90° to the Jet Axis as a Function of V_j/c_o.

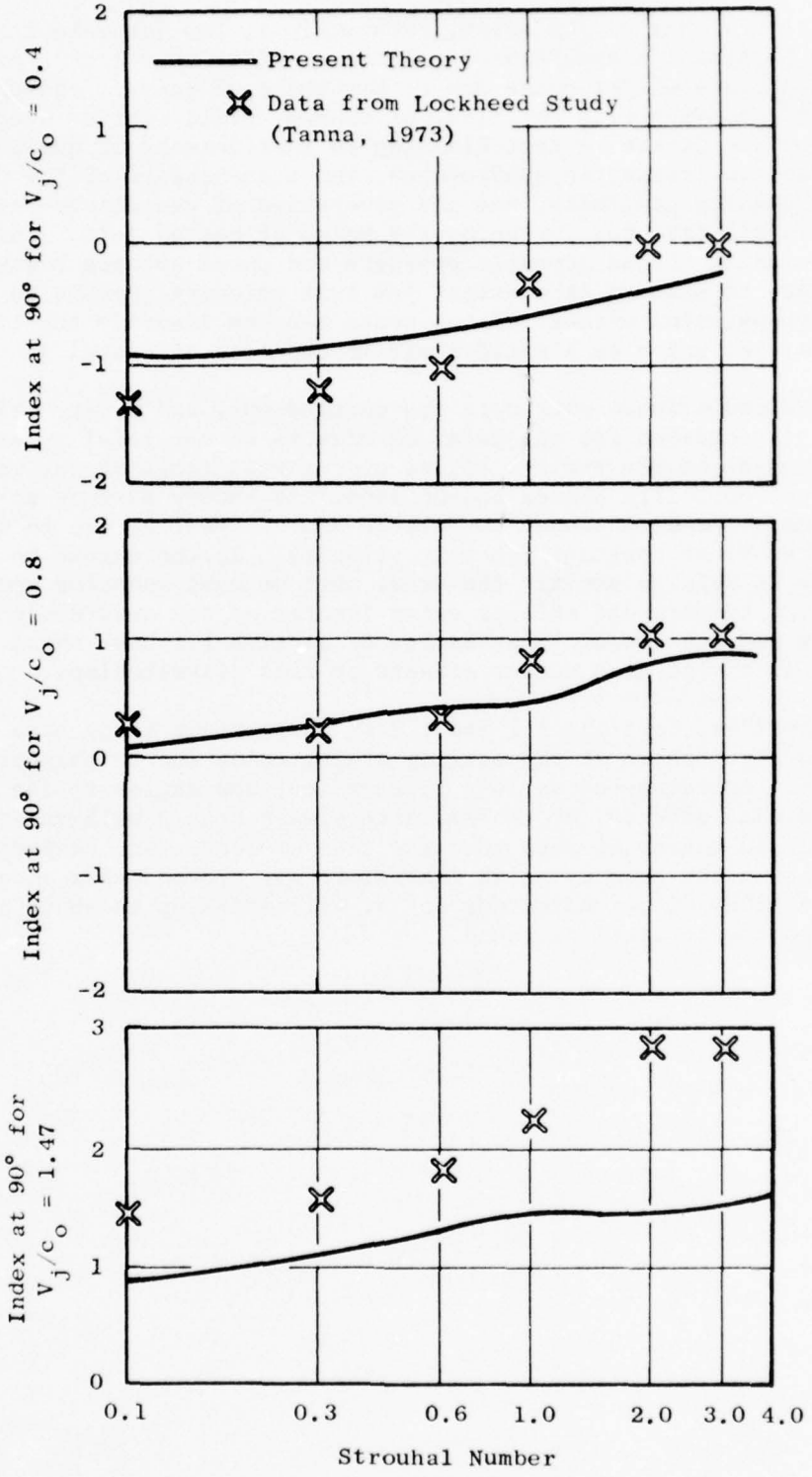


Figure 67. Jet Density Exponent at 90° for Various Frequencies for Three Jet Mach Numbers.

The problem of heated jet noise, especially at low jet velocities, is one in which Lighthill's analysis of jet noise offers very little guidance. The physical picture of jet noise due to Lighthill of compact eddies convecting and decaying with the flow, of course, still carries over. The enhancement of the Stokes' effect (leading to inefficiency of quadrupole radiation) for the transverse quadrupoles, the transmission of low frequency sound across density gradients, and the generation of new dipole- and source-like terms are all features governing the noise of heated jets. The progressive biasing of the acoustic pressure and power spectra towards lower frequencies due to heating at constant jet exit velocity appears to be primarily a propagation effect. In no sense can one identify the Lighthill expression for jet noise as a valid limit in the area of heated jet noise.

Extensive comparisons with data are carried out, and a very wide measure of agreement is achieved for the detailed effects on the total power and on the sound pressure at the various angles over a wide range of jet velocities. Apart from some explicity stated assumptions, the theory assumes no change of the intrinsic, nondimensional turbulence source spectrum due to variations of jet temperature at constant jet exit velocity. To the extent to which such a theory is able to explain the data, then we must question whether any significant jet temperature effects exist insofar as the quadrupole source distributions are concerned. The results of Section 1.1 have shown a comparable absence of jet Mach number effects on this distribution.

Taken together, Sections 1.1 and 1.2 of the current study have essentially solved the problem of the scaling of jet noise due to changes of jet velocity, jet temperature at various frequencies, and angles to the jet axis. Nozzle size effects, of course, have always been a well-understood phenomena. It is worthy of note that the idea of convected, compact quadrupoles being the primary noise generators has proved quite adequate in this whole study of jet noise due to jet velocities up to about 1.5 times the atmospheric speed of sound.

SECTION 2.0

TESTS OF A THEORETICAL MODEL OF JET NOISE

(N.S.M. Nosseir and H.S. Ribner)

2.1 BACKGROUND

The governing equation of jet noise can be posed in two equivalent ways; (1) as a wave equation for a medium at rest driven by source terms containing all of the effects of the jet flow (44-46, 61), or (2) as a convected wave equation with somewhat different source terms (e.g., References 18, 21, and 63). Formats of type (2) can be obtained from type (1) by transforming the source terms and shifting some of the parts to the left-hand side. The shifted terms are, quite properly, interpreted as propagation terms rather than true source terms.

The format (1), developed in the classical papers of Lighthill, is formally exact in the sense that it can, in principle, predict the sound field if the source terms are known. But those source terms that express propagation effects are not known a priori - they are, in effect, neglected in the Lighthill approach by the practical requirement to ignore the unknown density gradients: to hold the density constant in the source terms. This has the result that refraction of the sound by the mean flow (and, less importantly, scattering of the sound by the turbulence) is entirely suppressed in the predictions. Also, "shrouding effects" of the mean flow (20, 64-65) (Section 1.0 of the Chapter) are accounted for imperfectly. Chief among these seems to be an apparent change in the impedance seen by the sources: this can modify the predicted efficiency of sound generation and (what amounts in part to the same thing) the downstream amplifying effect of source motion: the "convection factor."

The cost of the greater potential accuracy of the convected wave equation approaches is an enormous increase in the analytical complexity: for the most part numerical solutions must be sought. In comparison, simple closed-form solutions of the Lighthill equation - on the basis of suitable assumptions concerning the flow - have been obtained (11, 34, 66 67). We are concerned here with the form specified by Ribner[34]: the others are essentially equivalent. In addition to the formal simplicity of the expression for sound intensity, it has another appeal: the source terms for the sound generation have a simple physical interpretation that we owe to Lighthill[44,45]. Indeed, as it is used in Reference (34), the source term becomes especially simple: it is merely the momentum flux ρv_x^2 in the direction of the observer, doubly time differentiated, (an even simpler interpretation in terms of fluid dilatations can be made by means of a momentum balance[12,53]. The particular form ρv_x^2 has experimental support from the work of Lee and Ribner[55], Morris[68], and Reethof and Seiner[69]: they identified ρv_x^2 as an apparent source term by cross-correlating a hot-wire signal with a microphone signal. (In fact, References 68 and 69 went further and decomposed ρv_x^2 into its self-noise and shear-noise components.)

Thus, there is strong motivation to see how well the analytically simple model of Reference 34, with source term $\sim \rho v_x^2$, fits measured jet noise data. To this end, relations derived from the model are tested herein against a large body of jet noise data taken from the work of four investigators: Mollo-Christensen[70], Ajuja[71], Lush[18], and Chu[72]. The procedure involves both marked similarities and differences from earlier exercises by Grande[13] and MacGregor, et al[14] employing versions of the model. Unlike the earlier work, the present study bypasses the role of refraction (13-15) by excluding from attention the refraction-dominated range of angles $0 \leq \theta \leq 45°$. (Opportunity is taken herein to correct a major error concerning the refraction correction in MacGregor, et al[14] (see Appendix 1, immediately following Chapter I, Section 2.0).

In passing, we suggest that it may be possible to retain the best of both worlds: to combine the simplicity of the Lighthill-Ribner model with the improvements afforded by a convected-wave-equation approach. This possibility is explored in Reference 17 in terms of a Green's function solution of the convected-wave equation.

2.2 BASIC THEORETICAL ANALYSIS FOR MODEL DEVELOPMENT

In the Lighthill theory of jet noise, as restated by Proudman[73], the radiated sound pressure is given by:

$$p(\underline{x},t) = \frac{1}{4\pi c_o^2 x} \int_V \frac{\partial^2}{\partial t^2} \rho_o \, v_x^2 \, dV \tag{78}$$

in terms of the momentum flux $\rho \, v_x^2$, where v_x is the velocity component directed toward the observer at $\underline{x}$. The instantaneous velocity v_x is compounded of turbulence u_x plus mean flow U_x (= Ucos θ) so that:

$$v_x^2 = \underbrace{u_x^2}_{\substack{\text{Self-}\\\text{Noise}}} + \underbrace{2u_x U_x}_{\substack{\text{Shear-}\\\text{Noise}}} + \underbrace{U_x^2}_{\substack{\text{nothing}\\\text{(D.C.)}}} \tag{79}$$

These relations were central to a comprehensive theory of the noise of a round jet developed by Ribner[11,34]; the labels "self-noise" and "shear-noise" with respective source terms as defined in equation (79) are a part of the development.

The theory postulates that $\underline{u}$ obeys the statistics of isotropic turbulence and the mean flow U possesses a shear defined by a prescribed two-point correlation function; in addition, the assumption of self-simularity of turbulent and mean velocity profiles in appropriate regions of the jet is exploited. The far-field mean square sound pressure $\overline{p^2}$ and its spectral and directional

properties are worked out, first as emitted by unit volume of the jet, and then as emitted by the entire jet.

For a unit frequency band centered at f, and direction θ with the jet axis, the mean square sound pressure emitted (spectral density) by the entire jet takes the form:

$$\tilde{p}^2_\theta\,(CS) = [a(CS) + b(CS)\,\frac{\cos^4\theta + \cos^2\theta}{2}].C^{-4} \qquad (80)$$

where, $C \equiv [(1-M_c\,\cos\theta)^2 + \alpha^2\,M_c^{\,2}]^{\frac{1}{2}}$

$S \equiv fD/U_j$ observed Strouhal number
$CS =$ effective source Strouhal number.

$$M_c = \frac{\text{effective average source convection speed, } U_c}{\text{ambient speed of sound, } C_o}$$

(taken herein as $0.5\ U_j/C_o$)

α = nondimensional parameter (taken herein as 0.55)

and a (CS) and b(CS) are related by the theory (see next section). The rationale for the choices for M_c and α is given in Reference 14 (Appendix 1) immediately following Chapter 1 Section 2.0 of this volume).

Note the breakdown into a "basic directivity" multiplied by a "convection factor" representing a powerful effect of source motion. This formalism, based as it is on a nonconvected-wave equation*, fails to account for the refraction of the sound as it passes through the jet velocity and temperature gradients; the refraction is powerful at small angles with the jet axis and becomes negligible beyond a certain angle (e.g., $\theta \geq 45°$) (13-15). The contributions of the basic directivity, convection, and refraction-diffraction to the jet noise directivity are illustrated in Figure 68.

2.3 FORMALISM FOR TESTS OF THE MODEL

At $\theta = 90°$ to the jet axis, the theoretical model equation (80) reduces to the self-noise alone:

$$C^4_{90}\,\tilde{p}^2_{90}\,(CS) = a(CS), \text{ self noise} \qquad (81)$$

Equations (80) and (81) can be combined to yield**

*Although refraction effects are implicit in the full Lighthill source term, the form leading to Equation (78) suppresses the density gradients that provide the convection terms in the wave equation.

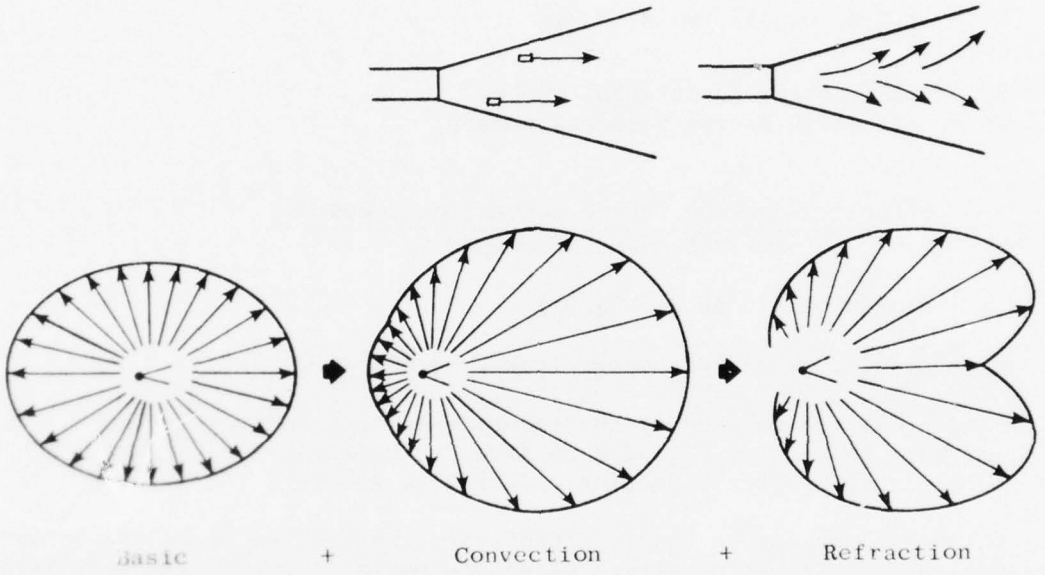


Figure 68. Convection and Refraction Modify "Basic" Noise Pattern.

Equations (80) and (81) can be combined to yield*

$$\frac{C^4_\theta \, \tilde{p^2}_\theta \, (CS) \; - \; C^4_{90} \, \tilde{p^2}_{90} \, (CS)}{(\cos^4_\theta \; + \; \cos^2\theta)/2} \; = \; b\,(CS), \text{ shear-noise} \qquad (82)$$

Thus, measurements of the spectral density $\tilde{p^2}_{90}$ and $\tilde{p^2}_\theta$ (for any θ above the refractive limit of $\sim 45°$) can separate out the shear noise b(CS) and the self noise a(CS).

We now incorporate the theoretical prediction that the shear-noise and self-noise spectra have similar shapes, and that the self-noise spectrum is shifted along the frequency scale relative to the shear-noise spectrum. We take the shift to be one octave to correspond to one form of the theory**:

$$b(CS) \; = \; \beta \;\; a(2CS) \qquad (83)$$

which states that the b spectrum and a spectrum have the same shape <u>after</u> the octave shift, but with a vertical scale factor β.

Upon dividing (82) by (81) evaluated at 2CS and using (83), the spectral amplitude ratio is obtained as:

$$\beta \; = \; \frac{b(CS)}{a(2CS)} \; = \; \frac{C^4_\theta \, \tilde{p^2}_\theta \, (CS) \; - \; C^4_{90} \, \tilde{p^2} \, (CS)}{C^4_{90} \, \tilde{p^2}_{90} \, (2CS) \; [(\cos^4\theta \; + \cos^2\theta)/2]} \qquad (84)$$

This parameter β can alternatively be regarded as a construct formed of three experimentally measured filtered m.s. sound pressures $\tilde{p^2}_\theta$ (CS), $\tilde{p^2}_{90}$ (CS), and $\tilde{p^2}_{90}$ (2CS), involving a defined parameter C. According to the theory (the spectral similarity relation (83), β should be an invariant at a given Mach number and jet diameter. Thus, plotted values of β (derived from experimental data) should be constant as CS (or θ)*** varies; this can be taken as a test of the theory.

---

*In this equation, $\tilde{p^2}_\theta$ and $\tilde{p^2}_{90}$ are evaluated at the same effective source Strouhal number CS. Since C is a function of θ, the equality might be written $C_\theta S_\theta = C_{90} S_{90}$; thus, the Strouhal numbers of the respective <u>field</u> measurements, S_θ, S_{90} are different. In the equation the subscripts are dropped in the respective arguments of $\tilde{p^2}_\theta$ and $\tilde{p^2}_{90}$ to make their equality apparent.

**A simple argument is that a spectral component $e^{i\omega t}$ in the shear noise appears as $e^{i2\omega t}$ in the self noise, owing to the squaring of u_x. More formal treatment[34,74] gives shifts varying from $\sqrt{2}$ to 2 depending on the form of the time autocorrelation.

***Equation (84) however, is not well suited to variations of θ: the RHS approaches 0/0 as $\theta \to 90°$, thus making the result very sensitive to scatter in the experimental values of $\tilde{p^2}_\theta$.

2.4 TESTS I: INVARIANCE OF β; SIMILARITY OF SELF- AND SHEAR-NOISE SPECTRA

In Figure 69, Equation (84) has been used (with $\theta = 45°$) to evaluate 10 log β as derived from the experimental data of several investigators[18,70-72]; the results are plotted versus source Strouhal number CS. The predicted constancy of β is largely confirmed: over much of the CS range the variation does not exceed 1 dB in most cases.

The constancy of β implies the similarity of the shear-noise and self-noise spectral shapes: cf., the inset diagram of Figure 69. A more detailed comparison of these shapes may be made in the context of deriving the separate spectra from the experimental data. Figure 70 shows an example case from data of Ahuja[71]. The self-noise curve (bottom) is the left-hand side of Equation (81) and the middle curve is C^4 times the left-hand side of Equation (80), applied to measurements at $\theta = 45°$. The shear-noise curve (top) is derived from the other two by means of equation (82).

The self-noise spectrum obtained in Figure 70 has roughly half the amplitude of the shear-noise spectrum and peaks approximately an octave higher: these are both features predicted by the theory[11,34]. Support for this kind of breakdown of the jet noise is also provided by experimental data of a totally different kind. In Figure 71, we have plotted self-noise and shear-noise spectra derived from cross correlations of a microphone signal with hot-wire signals; the hot-wire signals correspond on the one hand to the self-noise source term and on the other hand to the shear-noise source term of Equation (79). The spectral curves are generally similar to those of Figure 70, although with somewhat more than an octave displacement. (These curves were obtained by Dr. Philip Morris[68] in the laboratory during a short series of experiments that had to be truncated; thus the data must be regarded as rather tentative).

The displacement between the self-noise and shear-noise spectral peaks is tabulated in Table 2 for some 17 cases. The average ratio $[CS_{se}/CS_{sh}]_p$ of the self-noise peak frequency to shear-noise peak frequency is 1.92, just a bit short of one octave; the individual values range from 1.66 to 2.25.

The self-noise and shear-noise spectra derived in the manner of Figure 70 can be normalized to unity peak value; then, with the self-noise downshifted one octave, they can be superposed. Figure 72 shows examples of such superposition, using data from three respective sources: the match of the self-noise and shear-noise spectra varies from reasonably good to excellent, especially around the center.

A closer look at Figure 72 shows small, progressive deviations between a (2CS) and the derived b(CS) at low values of CS(<.2) and high values of CS (>.4). These may be attributed to the failure of the basic theory to allow properly for mean-flow "shrouding" effects on the effective convection factor: the convection factor herein is taken to be a constant C^{-4}, whereas recent work, especially that of Mani[20,64-65], suggests the factor should vary with CS. To determine the variation, we in effect can recompute b(CS)

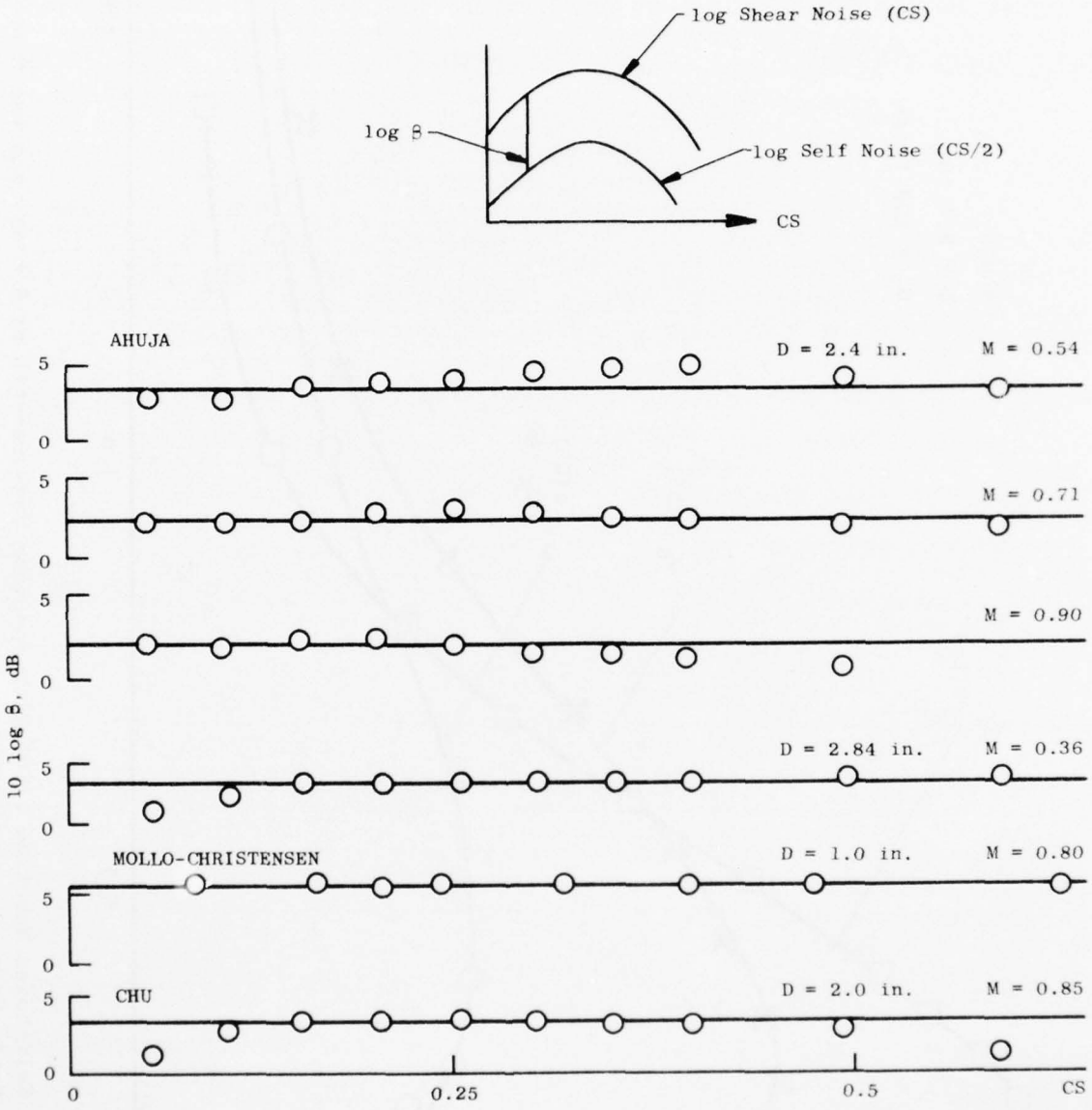


Figure 69. Tests of the Predicted Invariance of β with Frequency.

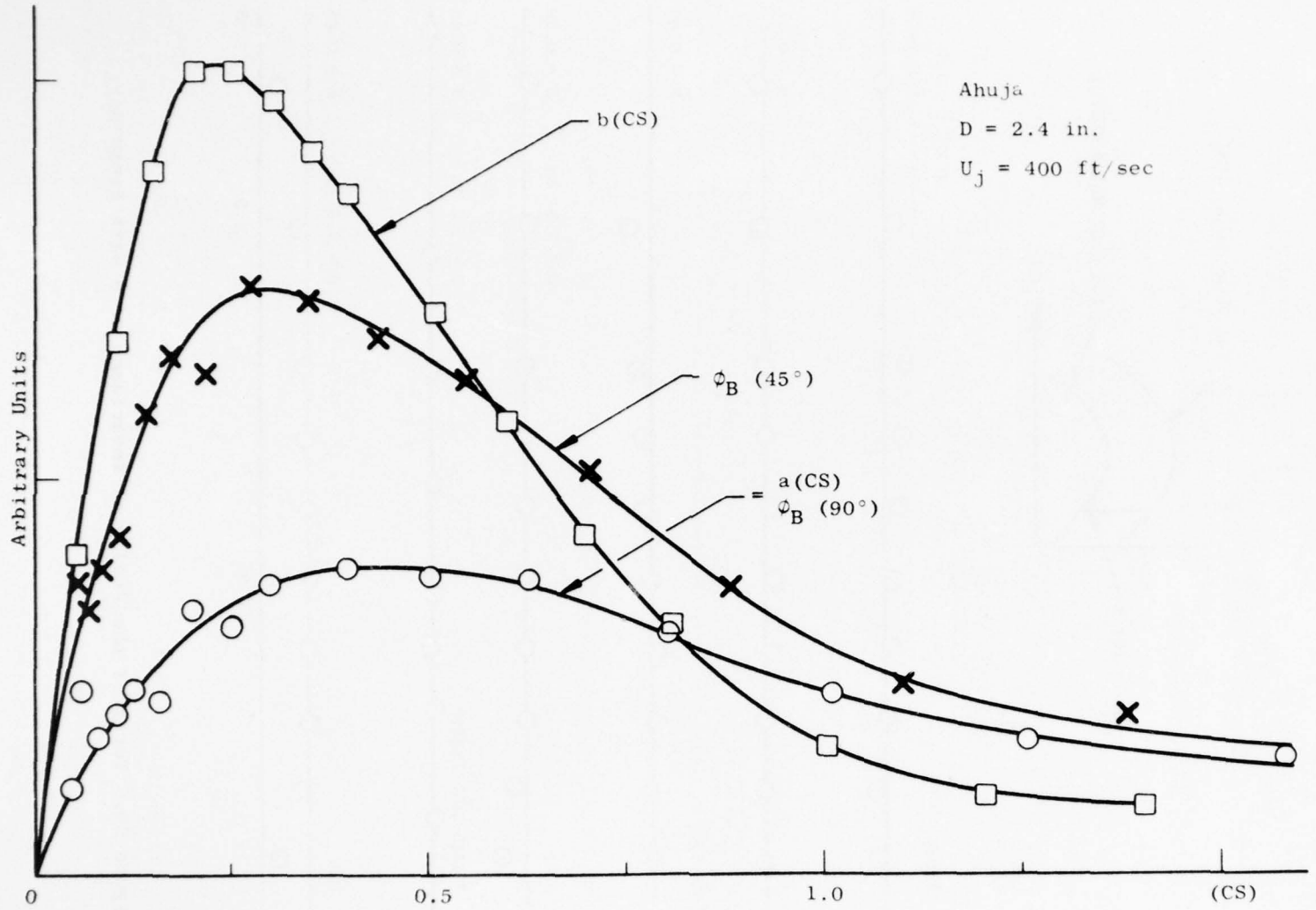


Figure 70. Basic Self-Noise Spectrum a(CS) with Spectrum Measurements at θ = 45° and the Extracted Basic Shear Noise Spectrum b(CS).

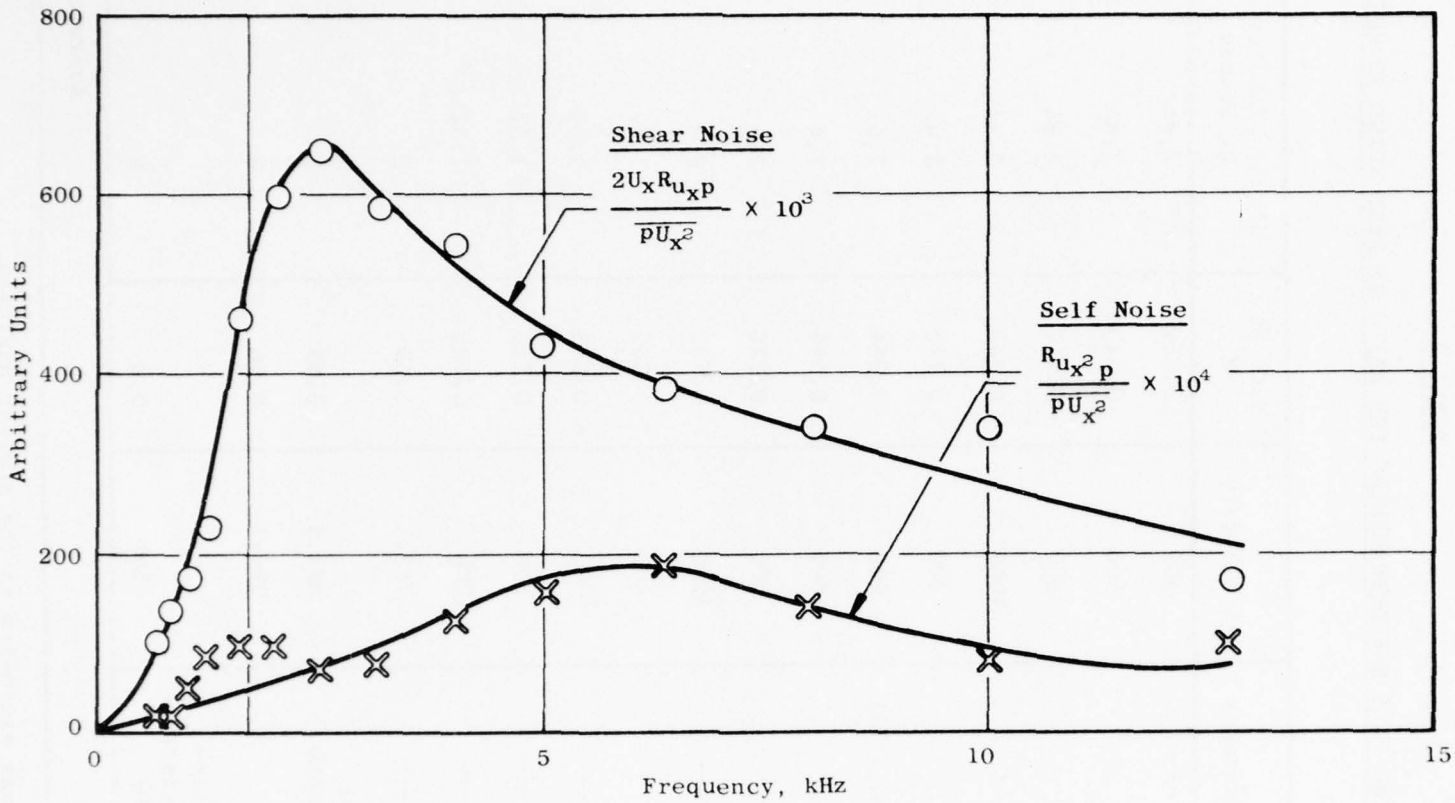


Figure 71. Shear- and Self-Noise Spectra Derived from Cross Correlations Between Hot-Wire and Microphone Signals.

TABLE 2

EXPERIMENTAL DATA FOR DETERMINING THE RATIO OF SELF NOISE TO SHEAR NOISE

Figure	Reference	Jet Velocity	Mach No. M	Nozzle Diameter, D, inches	$\left[\frac{(CS)se}{(CS)sh}\right]_p$
79	---	400	0.362	2.84	2.00
		600	0.543	2.84	2.25
78	---	800	0.714	2.84	1.70
		1000	0.543	2.84	2.25
		300	0.273	2.4	2.00
70, 72	Ahuja(71)	400	0.364	2.4	2.00
		600	0.546	2.4	1.84
		800	0.728	2.4	2.00
78	---	1000	0.901	2.4	1.92
		400	0.362	1.52	1.78
78	---	600	0.543	1.52	1.82
78	---	800	0.718	1.52	1.73
78	---	1000	0.905	1.52	2.0
74,75	---	743.1	0.69	2	1.66
72	Chu (unpub.)	887.5	0.85	2	1.80
		999.1	0.96	2	2.00
69	Mollo-Christensen (70)	650*	0.8	1	2.20
				Average	1.92

*This value was estimated in the present analysis.

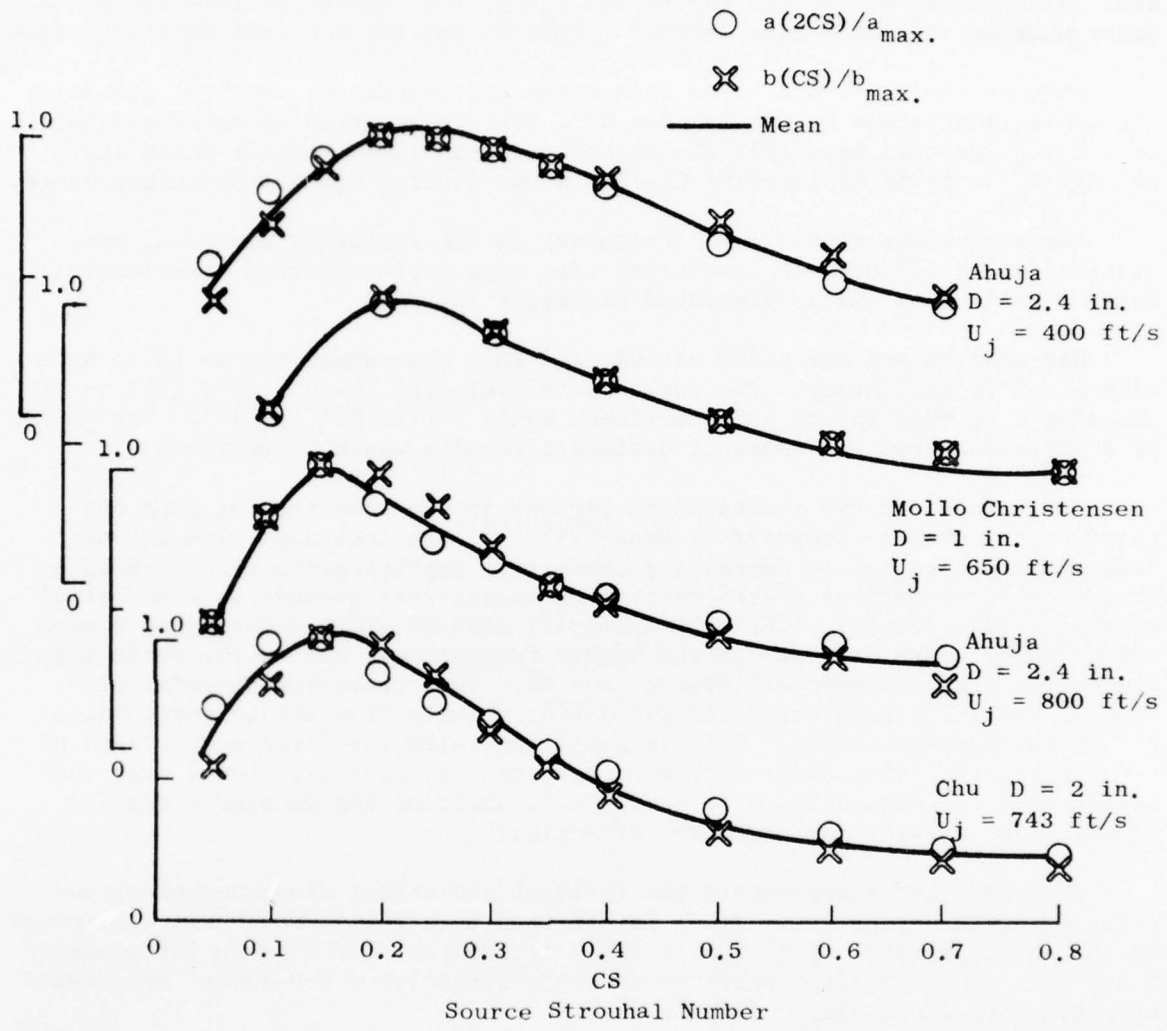


Figure 72. Comparison of Normalized Self-Noise and Shear-Noise Spectra (the Self-Noise has been Downshifted One Octave).

so as to agree with a(2CS) (both normalized to unity peak) at all values of CS by replacing C^{-4} by C^{-n} in the spectral density equations. The fitting process then determines n(CS). More specifically, in the predictive equation (85A) below, we replace the ratio C_{90}^4/C_θ^4, then solve for this ratio and hence n after inserting experimental values of the two spectral density ratios.

When we deal with one-third octave spectra instead of spectral densities the convection factor herein becomes C^{-5}: (see below: this is fully equivalent to C^{-4} for spectral density); the appropriate equation is (85C) below and now C_{90}^5/C_θ^5 is to be replaced by C_{90}^n/C_θ^n in the fitting process described above.

The equivalent n(CS) in the frequency in the frequency dependent convection factor C^{-n} has been evaluated from some representative experimental data of Ahuja (71) and is presented in Figure 73.

His spectra are one-third octave, and thus the comparison is to be made with n = 5 in our theory. The curves were evaluated for $\theta \approx 45°$, that is by choosing n so that theory and experiment would fit at 90° and 45°. For values of θ differing from 45° somewhat different results would be expected.

For comparison two curves n(CS) derived in the same fashion from one third octave spectra computed by Mani[20,64-65] are included. The curves indicate a monotonically decreasing convective amplification with increasing frequency - a behaviour argued earlier on theoretical grounds by a number of workers (e.g., 75, 76). The experimentally derived n(CS) curves show a much milder progressive decrease at the higher frequencies, but on the whole they are fairly flat and even dip down at low CS. Thus these experimental convective amplification factors do not differ greatly from the constant value C^{-5} of the present theory. This is consistent with the later comparisons of the theory with experiment: very good agreement is generally found over the broad range of frequencies $0.03 \leq CS \leq 1.0$, omitting the angular range $0 \leq |\theta| < 30°$ usually dominated by refraction.

The parameter β represents the ratio of the actual shear-noise/self-noise spectral values [with a(CS) downshifted to a(2CS)], which was eliminated by the normalization. Although 10 log β is constant for a given jet diameter D and Mach number M, it appears to increase linearly with D and to decrease slightly with increasing M (Figure 74).

2.5 TESTS II: MODEL AS A FRAMEWORK FOR JET NOISE PREDICTION

Equation (84) may be rearranged and divided by $C_{90}^4\ \bar{P}_{90}^2$ (CS) to give:

$$\frac{\tilde{P}_\theta^2\ (CS)}{\tilde{P}_{90}^2(CS)} = \frac{C_{90}^4}{C_\theta^4}\left[1 + \beta\ \frac{\tilde{P}_{90}^2\ (2CS)}{\tilde{P}_{90}^2\ (CS)} \cdot \frac{\cos^4\theta + \cos^2\theta}{2}\right] \qquad (85A)$$

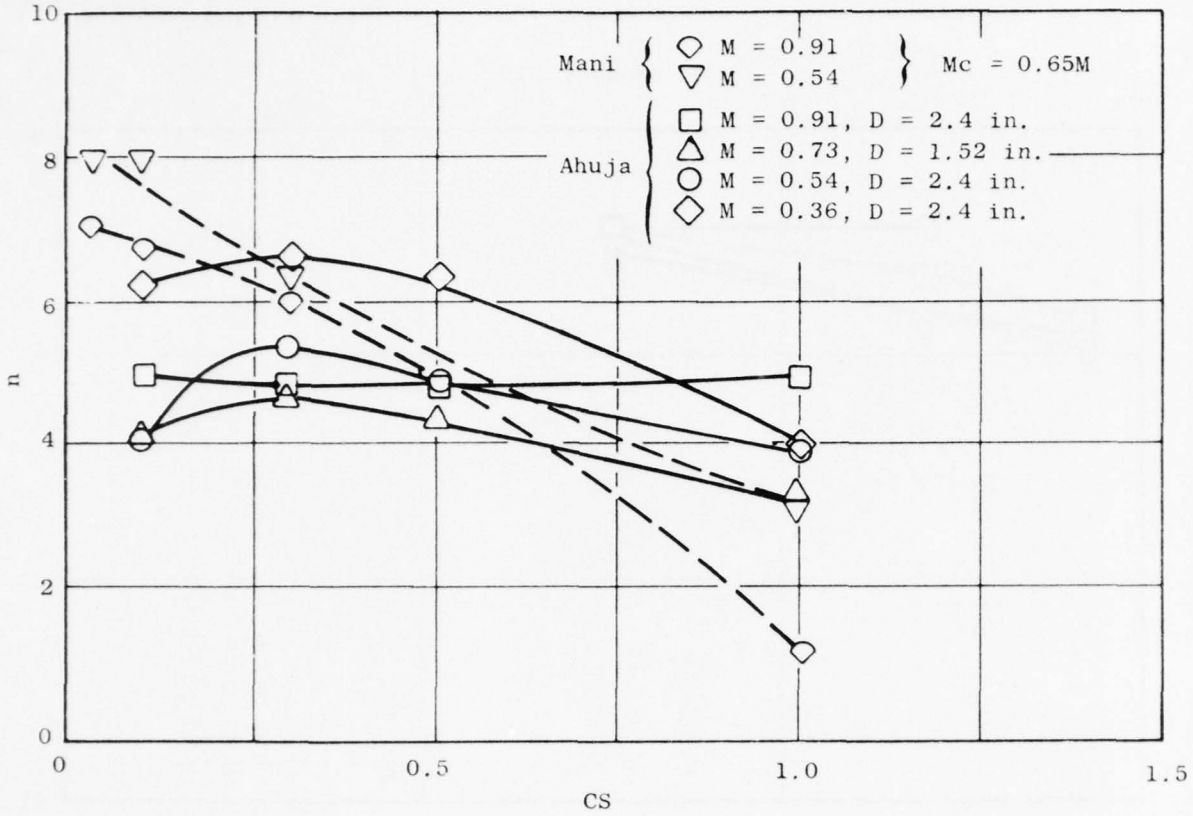


Figure 73. Exponent n Versus CS in Variable Convection Factor C^{-n} to Replace C^{-5} of Present Theory (1/3 octave bands). n Obtained by Fitting b(CS) to a(2CS) at All CS.

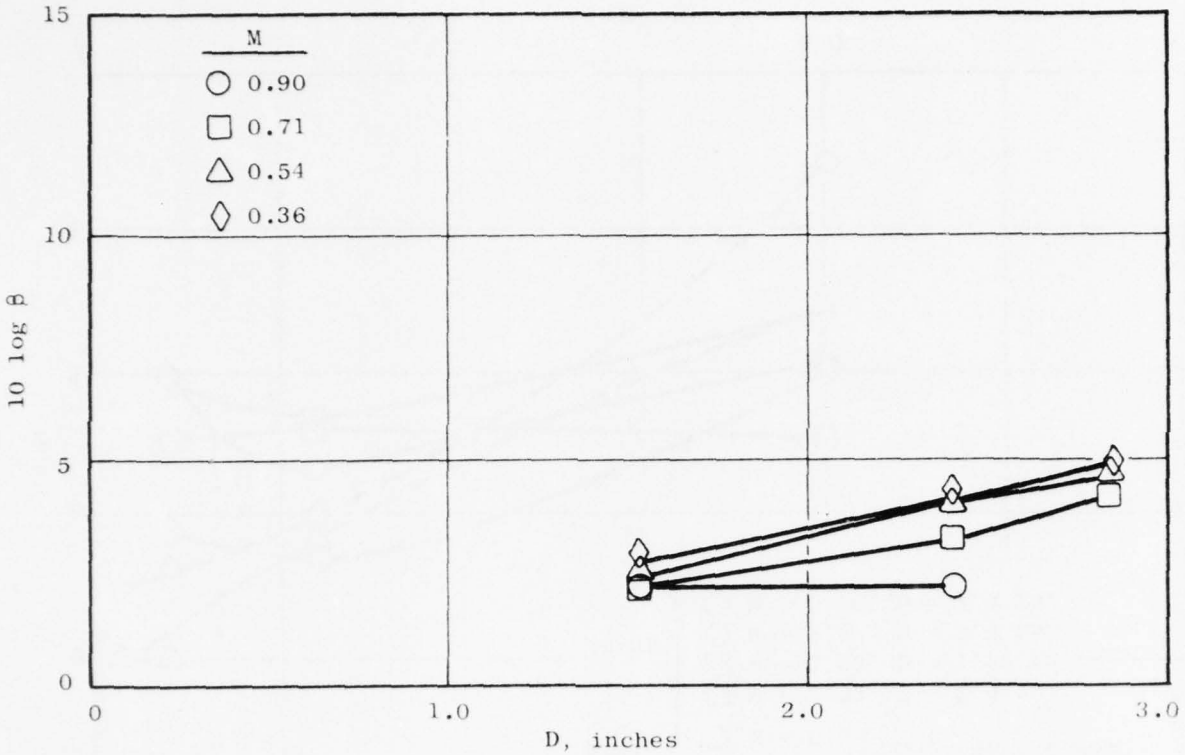


Figure 74. Variation of β with Jet Diameter D (from the Measurements of Reference 35).

where $\tilde{p}^2_\theta$, $\tilde{p}^2_{90}$, may be interpreted either as referring to unit band width (power spectral density) or to a fixed narrow bandwidth.

This is a prediction of m.s. sound pressure $\tilde{p}^2_\theta$ in direction θ, given three quantities: the filtered m.s. sound pressure in direction 90° at two frequencies f ($\sim$CS) and 2f ($\sim$2CS) and the parameter β. β may be taken (for fixed jet diameter and Mach number) as an empirical constant* (cf. Figure 74), or, less accurately, may be taken as $\simeq$2.0 from a formula of the theory with experimental jet aerodynamic data incorporated (Appendix 1, immediately following Chapter 1 Section 2.0 of this report).

For constant percentage bandwidth m.s. pressure spectra, designated Φ_θ, Φ_{90}, respectively, the equation must be altered; restricting $\tilde{p}^2$ to unit bandwidth, we observe that:

$$\Phi = \tilde{p}^2 \, \Delta f; \quad \Delta f \sim f \sim S \tag{85B}$$

so that $\tilde{p}^2 \sim \Phi/S = C\Phi/CS$

Insertion of (85B) into (85A) yields

$$\frac{\Phi_\theta(CS)}{\Phi_{90}(CS)} = \frac{C_{90}^5}{C_\theta^5}\left[1 + \frac{\beta}{2}\,\frac{\Phi_{90}(2CS)}{\Phi_{90}(CS)}\,\frac{\cos^4\theta + \cos^2\theta}{2}\right] \tag{85C}$$

since the fixed parameter CS cancels out. Much of what follows refers to one-third octave spectra, designated $\Phi_{1/3}$, for which equation (85C) replaces (85A) as the predictive equation.

The data for $C_{90}^4 \, \tilde{P}^2_{90}$ (the self-noise spectrum) when normalized to unity peak tend to collapse into a universal curve (Figure 75, developed with the aid of Figure 76) in terms of a modified abscissa parameter. Employment of this universal self-noise spectrum allows prediction of $\Phi_\theta(CS)$ at any θ (above 45°) and any value of CS, given a single measurement of $\Phi_{90}(CS)_{peak}$ evaluated at the spectral peak Strouhal number.

In Figures 77 to 79 a number of experimental one-third octave jet noise directivity curves[18,70-72] are compared with the predicted curves. Those predictions utilizing the universal self-noise curve are so labelled: the others, which are based on the measured self-noise curve (viz., the measured narrow band intensity at $\theta = 90°$), are labelled "1st method." The agreement above the main refractive dip ($0 \leq |\theta| < 30°$) is generally within 1 to 2 dB. At very low frequency the refractive valley contracts (e.g. $0 \leq |\theta| < 20°$ at CS = 0.03) and it should be appropriate to apply theory down to $\theta = 20°$. For this range at high subsonic Mach numbers there is disagreement, the theory underestimating the convective amplication.

*By this we mean the average value of β defined by one of the plots of Figure 69. Of course, if individual values βCS) were used, equation (85) would merely be recovering the value of $\tilde{P}^2_{45}$ used to compute the β's; then (85) would be an interpolation equation.

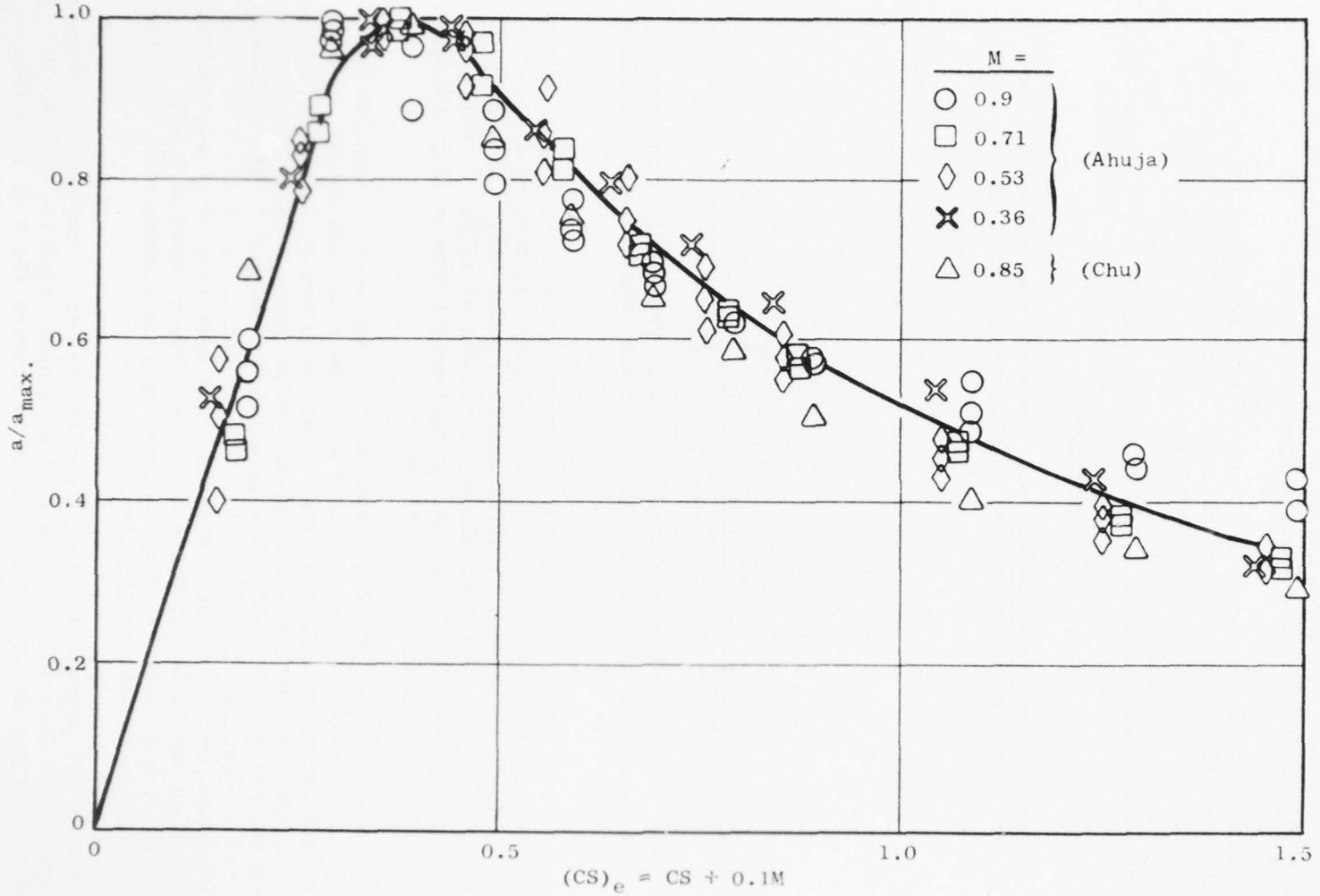
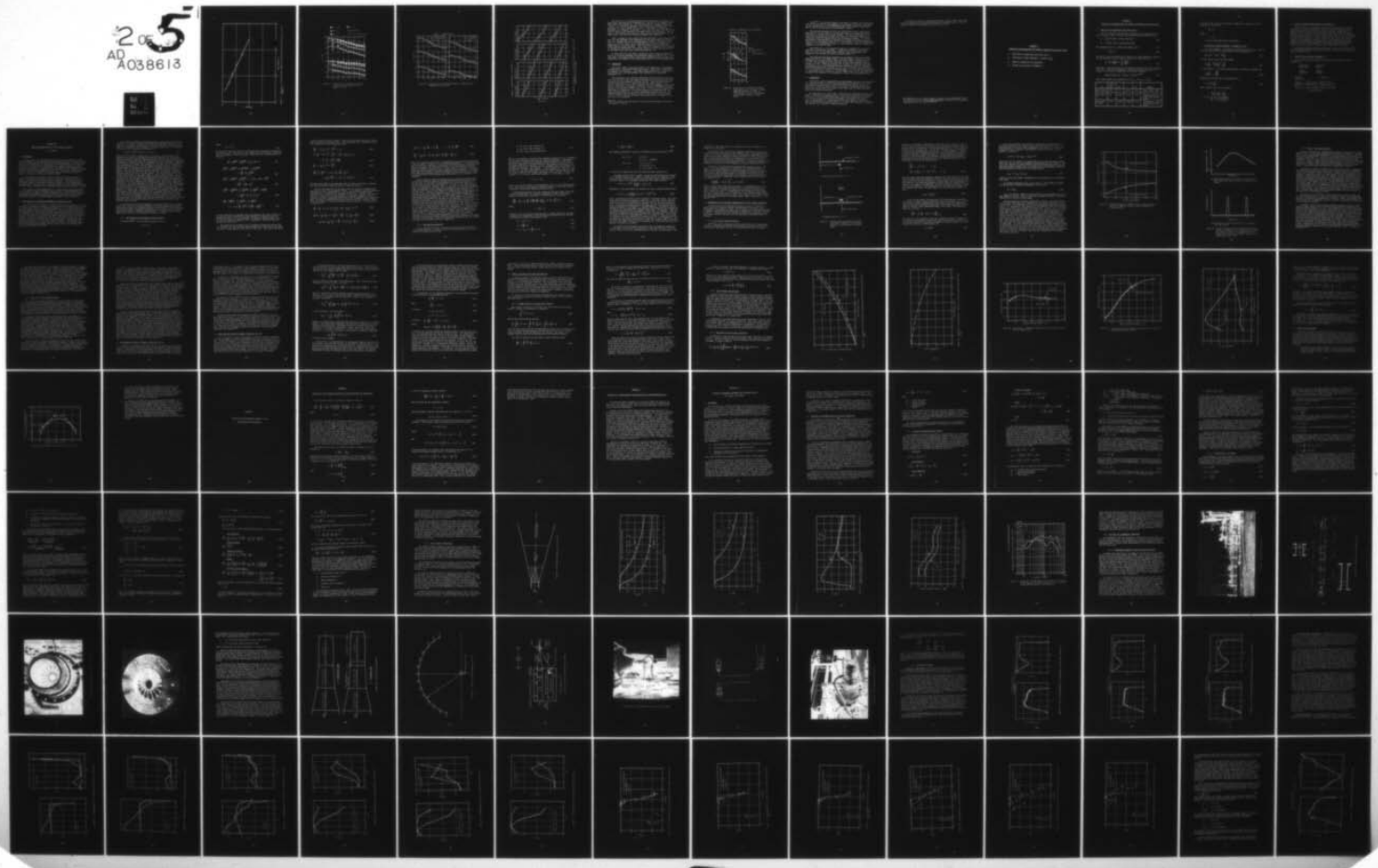
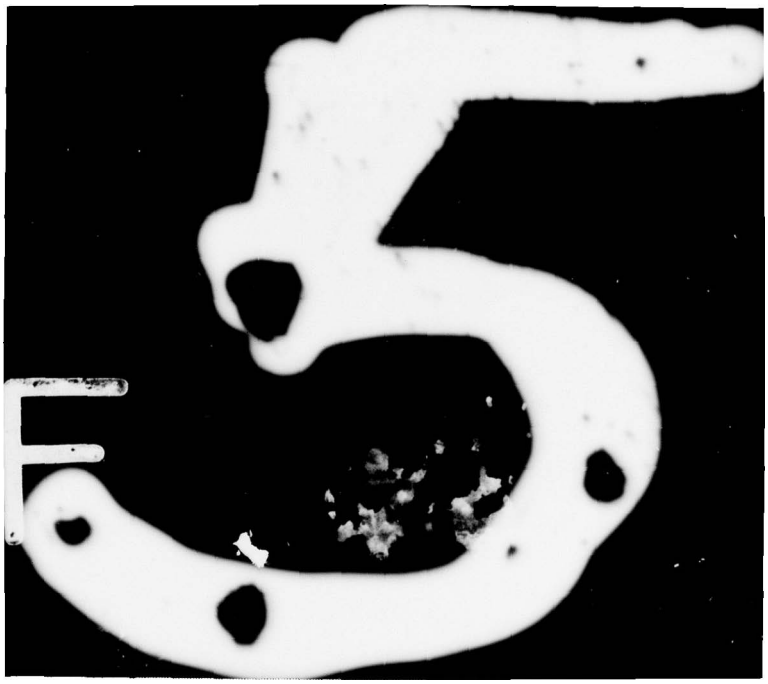


Figure 75. Empirical Universal Self-Noise Spectrum $a\,(CS)_e/a_{max.}$

AD-A038 613 GENERAL ELECTRIC CO CINCINNATI OHIO AIRCRAFT ENGINE GROUP F/G 20/1
SUPERSONIC JET EXHAUST NOISE INVESTIGATION. VOLUME II. TECHNICA--ETC(U)
JUL 76 P R KNOTT, R MANI, C L MERKLE F33615-73-C-2031
UNCLASSIFIED R74AEG452-VOL-2 AFAPL-TR-76-68-VOL-2 NL





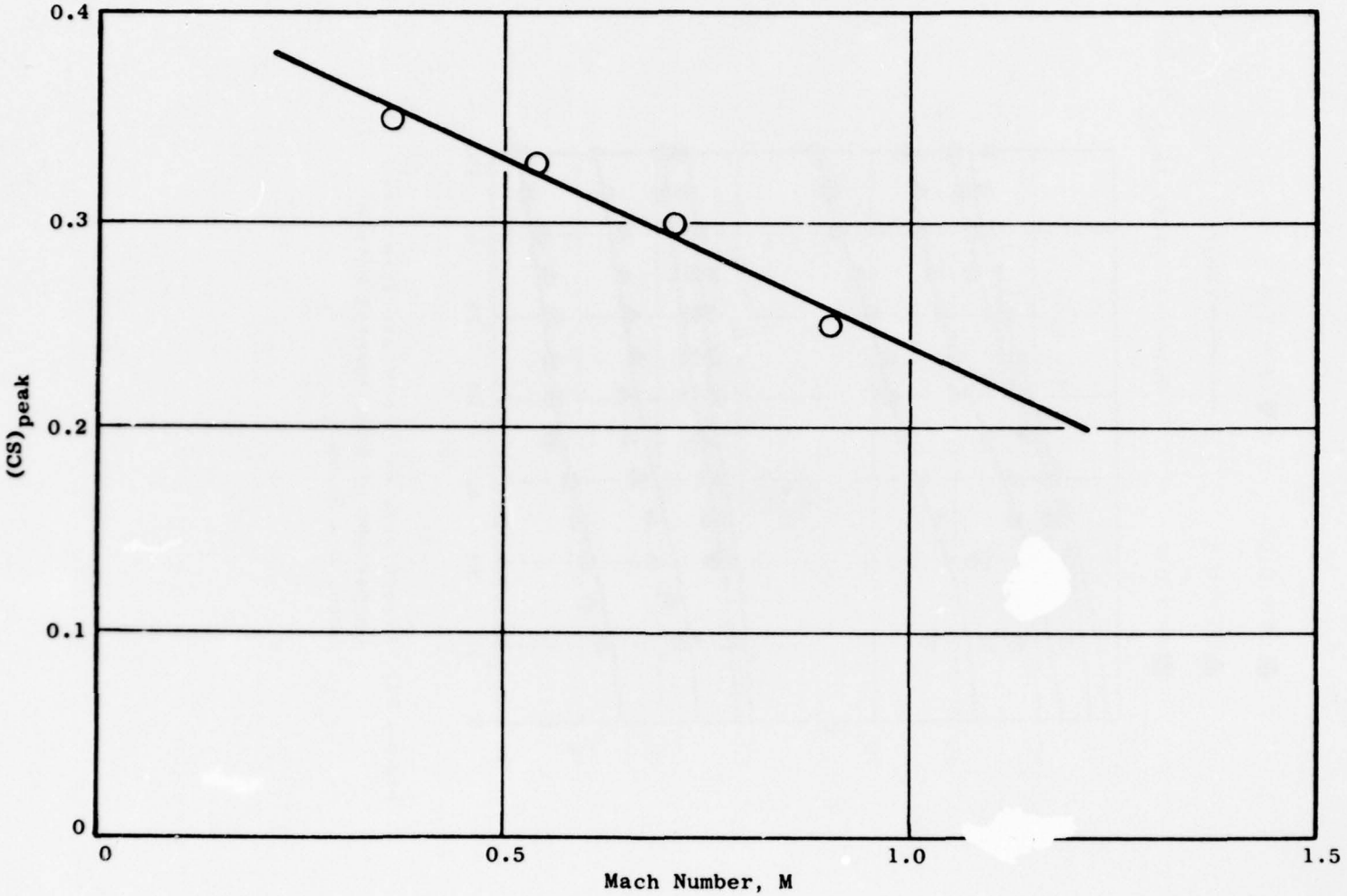


Figure 76. Variation of Source Strouhal Number of Self-Noise Spectrum Peak $(CS)_p$ with Mach Number M.

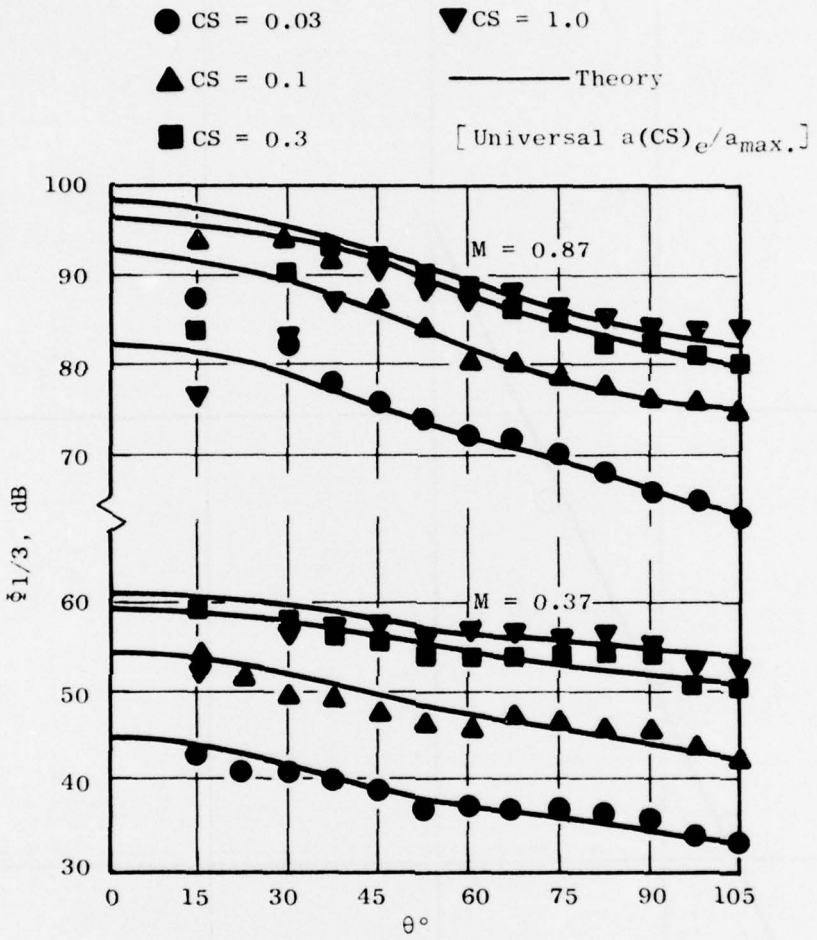


Figure 77. Directivity of 1/3-Octave Intensity; Comparison of Experimental Data of Lush, D = 25 mm.

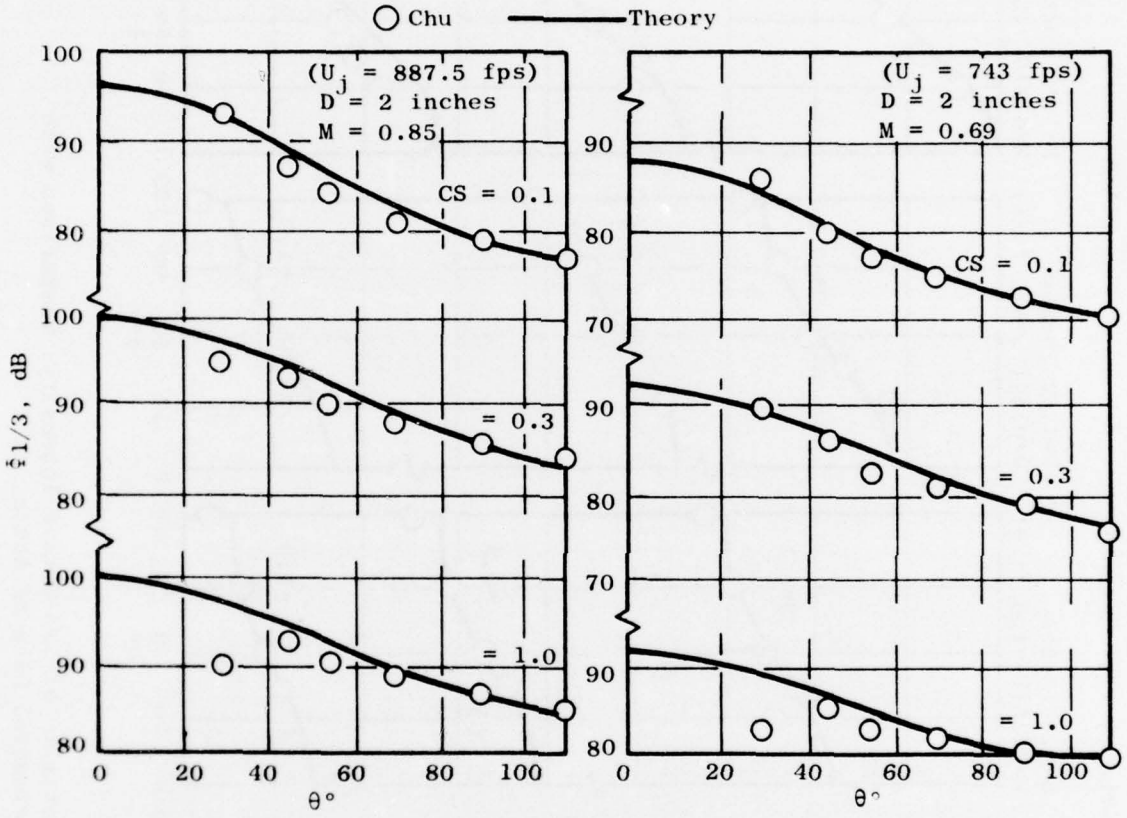


Figure 78. Directivity of 1/3-Octave Intensity; Comparison with Experimental Data of Chu.

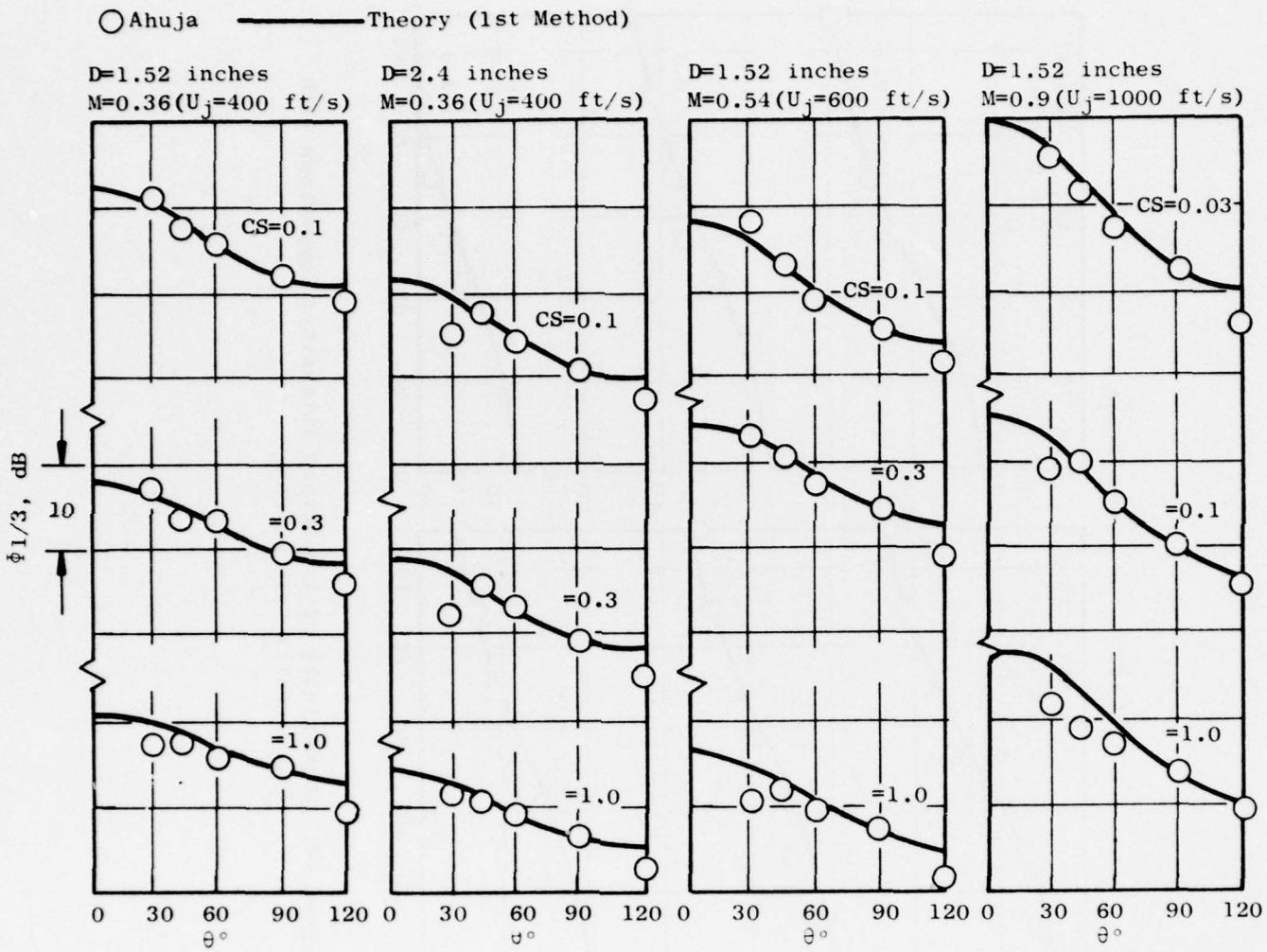


Figure 79. Directivity of 1/3-Octave Intensity; Comparison with Experimental Data of Ahuja.

The value of β , the shear-noise/self-noise amplitude ratio used in the predictions, was empirically determined as a function of jet diameter D and Mach number M from Figure 74. The empiricism may be removed by using the value $\beta \approx 2.0$ derived in Appendix 1 from theoretical considerations. Thus, in Figure 79, we may compare curves with $\beta = 2.84$ (shown in Figure 80, empirical) 2.0 (theoretic 1) and zero. It is seen that use of the theoretical value in place of the empirical value makes very little difference. But, if we go to the extreme of setting $\beta = 0$ (which implies complete neglect of the shear noise), the prediction disagrees markedly with experiment.

Thus, it seems at first rather surprising that Mani in his recent work[65] gets very good agreement with experiment with the specification (in effect) of $\beta = 0$. Perhaps this can be rationalized as follows. The effect of the $(\cos^4 \theta + \cos^2 \theta)/2$ factor of the shear-noise is to yield a downstream enhancement of the overall noise. But the convection factor [taken as $C^{-4}(\theta)$ herein] behaves rather similarly. Thus, there is a possibility of a tradeoff in theoretical formulations: an enhanced convection factor can play the role of the shear noise, which can then be discarded ($\beta = 0$).

It does seem clear that Mani's convection factor, which is enhanced at low CS, is in better agreement with experiment than the constant C^{-4}. On the other hand, the evidence herein (particularly Figures 69 and 72) seems conclusive as to the reality of the shear noise and its fit to the present model.

2.6 DISCUSSION

The subject model of jet noise leads to the formulation of a parameter β (essentially a shear-noise/self-noise spectral ratio) that is predicted to be invariant with frequency. The present study, directed to a large body of experimental jet noise measurements, has established the approximate invariance of β.

More physically, the study has established the near match of the shear-noise and self-noise spectral shapes (according to a certain definition) and an approximate one-octave shift between the two. These properties are predicted in the Ribner[11,34] theory, but are not unique thereto*. Any rational theoretical format that postulates self-noise quadratic in turbulent velocity and shear-noise linear in turbulent velocity, along with extensive regions of self-similar flow in a jet {e.g., $u'/U_o = f[(r-r_o)/x]$} would predict these same two properties. But for the theory to be compatible with the observed near-constancy of β, further constraints would be entailed: the postulated shear noise would have to have a basic directivity not unlike $(\cos^4\theta + \cos^2\theta)/2$, and the convection factor would have to resemble $C^{-4}(\theta)$ over much of the spectrum.

*There is, however, the more direct cross-correlation evidence of Reference 68 (Figure 77 herein).

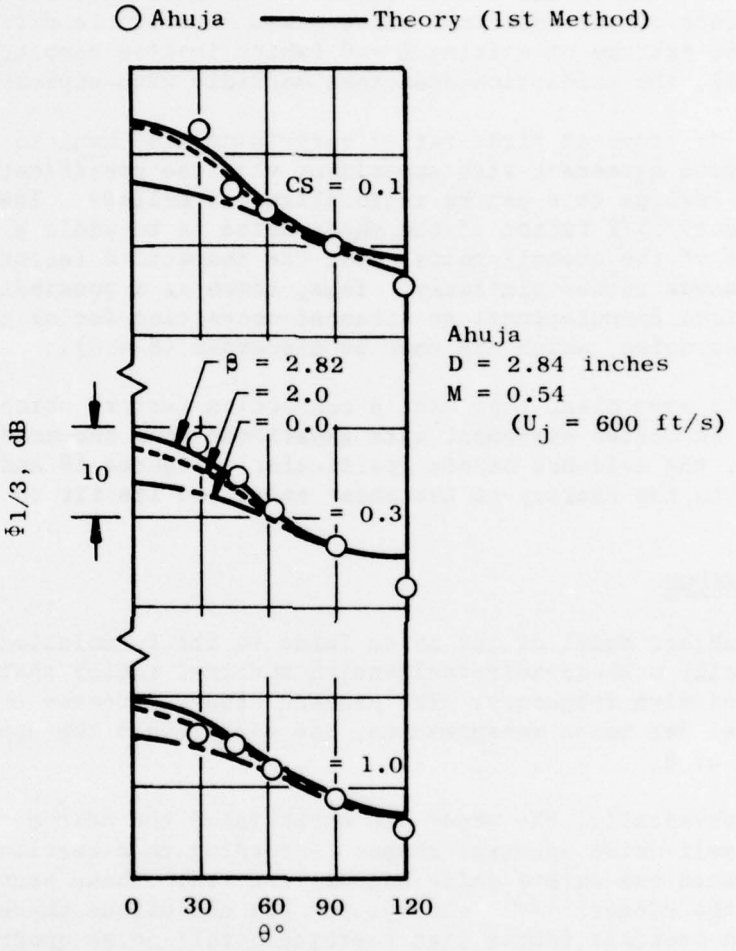


Figure 80. Directivity of 1/3-Octave Intensity; Experimental Data from Ahuja. Theory Based on Empirical β (2.82), on "Theoretical" β (2.0), and on Vanishing β (Complete Neglect of Shear Noise).

Lilley[63], in his recent model of jet noise, is rather firm in insisting that the source terms all be quadratic in the turbulent velocity. This rules out any approximate one-octave self-noise/shear-noise spectral displacement and is thus at variance with the experimental evidence.

The near match between the self- and shear-noise spectra found herein falls short of an exact match: in many cases these are progressive opposite deviations at low and high Strouhal numbers. This can be attributed to an inaccurate accounting in the theory for mean-flow "shrouding" effects that reduces the convective amplification with increasing frequency. It can be accounted for quantitatively by replacing the frequency invariant convection factor C^{-4} of the present theory by C^{-n}. The exponent n as derived empirically (Figure 73) is a decreasing function of source Strouhal number CS, somewhat as suggested by the work of Mani.

The attempt to use the theoretical model as a framework for jet noise prediction is reasonably successful. Progressive deviations (not large) show up at very low and high Strouhal numbers, again reflecting the inadequacy of the frequency-invariant convection factor C^{-4}.

The predicted directional patterns fit the general trend of the experimental data well in the middle range of Strouhal numbers. However, in comparisons with the data of Ahuja, there are often sizeable discrepancies at $\theta = 120°$, and in comparisons with the data of Lush, less prominent discrepancies at $\theta = 60°$. These can probably be accounted for (drawing on the work of subsection 1.0) by attributing different convection factors to different source term quadrupoles; in effect the n in the "corrected" convection factor C^{-n} is a function of θ as well as Strouhal number. It is noted that subsection 1.0 calculations show a better fit in this regard (they fail on the other hand, to exhibit the constancy of the parameter β found in the experimental data).

2.7 CONCLUSIONS

The present study has established the approximate invariance with frequency of a certain parameter β formed from experimental measurements of jet noise. The parameter β (essentially a shear-noise/self-noise spectral ratio) is a construct of Ribner's theory, and this invariance is predicted by the theory. But it must be one test of any theory of jet noise that it should correctly predict the observed invariance.

The invariance of β is not exact, reflecting the approximate nature of the theory. Mean-flow "shrouding" effects of the flow are imperfectly accounted for by use of the Ffowcs-Williams/Ribner narrow band convection factor C^{-4} (C^{-5} for broad band) which shows no dependence on frequency nor type of source term quadrupole. An improvement can be made (guided by the work of Mani) by writing the convection factor as C^{-n} with n as a function of frequency and (weakly) as a function of observer direction.

The theoretical model as used herein provides a simple closed-form framework for prediction of jet noise, excluding the refraction valley. The main empirical input is the spectrum at 90° to the jet axis.*

*The empiricism can be largely removed by going to more fundamental form of the theory tied to the fluid dynamic parameters of the jet: to the spatial distribution of u', U, and L[77,78,79].

APPENDIX 1

THEORETICAL CONSIDERATIONS FOR RIBNER's SHEAR-NOISE/SELF-NOISE MODEL

A. PREDICTION OF SHEAR-NOISE/SELF-NOISE RATIO β

B. EVALUATION OF SHEAR PARAMETER σ IN TERMS OF $\frac{\partial u}{\partial r_2}$

C. ERROR IN CORRELATION FOR REFRACTION

D. OMITTED FINAL EQUATION, REFERENCE 17

APPENDIX 1

THEORETICAL CONSIDERATIONS for RIBNER's SHEAR-NOISE/SELF-NOISE MODEL

A. PREDICTION OF SHEAR-NOISE/SELF-NOISE RATIO β

The basic spectra a(CS) and b(CS) and d(CS) may be integrated over a source Strouhal number to obtain the corresponding broad-band emissions:

$$A = \int_o^\infty a(CS)\, d(CS);\ \text{overall self-noise}$$
$$B = \int_o^\infty b(CS)\, d(CS):\ \text{overall shear-noise} \qquad (86)$$

The assumption $b(CS) = \beta\, a(2CS)$ then implies that: (87)

$$\frac{B}{A} = \beta/2 \qquad (88)$$

The value of B/A was worked out in terms of jet flow parameters in Reference 34 (see Reference 11 for an earlier version); it takes the form:

$$\frac{\beta}{2} = \frac{B}{A} = \frac{4\sqrt{2}\sigma}{(1+\sigma)^{3/2}} \frac{U^2}{u_1^{-2}} \frac{(g)^{iv}}{(g^2)^{iv}} \qquad (89)$$

where $g(\tau)$ is the time factor in the two-point turbulent velocity correlation and $(g)^{iv} \sim \partial^4 g/\partial\tau^4$; the parameter σ quantifies the mean-flow shear at y in terms of the two-point correlation in the radial direction,

$$U(\underline{y}+r_2/2)U^1(\underline{y}-r_2/2) \equiv UU^1(r) = U^2(\underline{y})e^{-\sigma\pi r_2^2/L^2} \qquad (90)$$

Three cases worked out in Reference 34 for $y_1 \simeq 4D$, $y_2 = D/2$ are:

$g(\tau)$	$(g^{iv}/)(g^2)^{iv}$	L/Y_1	σ	B/A	Remarks
$\exp(-\omega_f/\tau 1)$	1/16	---	0.45	1.16	Ribner (1963, 1964)
$\exp(-\omega_f^2\,\tau^2)$	1/4	0.075	0.070	1.15	Gaussian correlation; scale from Laurence (1956)
$\exp(-a_2\tau^2 - a_4\tau^4)$	1/2.4	0.048	0.0284	0.84	Experimental correlation and scale (Chu 1966)

Discounting the first case for reasons brought out in Reference 34, the average is, very nearly:

$$\frac{B}{A} \simeq 1.0$$

where,

$$\beta \simeq 2.0$$

A further development may be found below.

B. EVALUATION OF SHEAR PARAMETER σ IN TERMS OF $\partial U/\partial r_2$

The shear parameter σ is effectively defined by equation (90). The two factors on the LHS may be approximated by Taylor expansion as:

$$U(\underline{y} \pm r_2/2) \simeq U(\underline{y}) \pm \frac{r_2}{2} \frac{\partial U}{\partial r_2} \tag{91}$$

to first order, so that the LHS becomes:

$$U^2(\underline{y}) \left[1 - \frac{r_2^2}{4} \left(\frac{\partial U}{\partial r_2} \right)^2 \frac{1}{U^2} \right] \tag{92}$$

to second order. To a similar approximation, the RHS may be expanded as:

$$U^2(\underline{y}) \left[1 - \sigma\pi \frac{r_2^2}{L^2} \right] \tag{92a}$$

Equations 92 and 92a yield an expression for σ:

$$\sigma \simeq \frac{1}{4\pi} \left(\frac{L}{U} \frac{\partial U}{\partial r_2} \right)^2 \tag{93}$$

Thus, equation (89) may be rewritten:

$$\frac{\beta}{2} = \frac{B}{A} = \frac{\frac{\sqrt{2}}{\pi} \frac{L^2}{\bar{U}_1^2} \left(\frac{\partial U}{\partial r_2} \right)^2 \frac{g^{iv}}{(g^2)^{iv}}}{\left[1 + \frac{1}{4\pi} \left(\frac{L}{U} \frac{\partial U}{\partial r_2} \right)^2 \right]^{3/2}}$$

C. ERROR IN CORRECTION FOR REFRACTION, REFERENCE 14

Figures 3 and 4 of Reference 14 give the measured reduction of sound pressure level owing to refraction, relative to the 90° direction, when a certain pure tone "point" source is placed in the jet. Based thereon, Figures 5 and 6 (of Reference 14) give the calculated reduction of sound pressure level relative to the 90° direction (the "correction for refraction") for narrow-band jet noise. In both sets of figures, the curves are labelled with the source frequency Cf; this is where the error lies: the curves of Figures 3 and 4 should be labeled f, not Cf. Unfortunately, all of the quantitative developments of the paper are based on the interpretation of Figures 3 and 4 as being labeled Cf. These later results are, therefore, incorrect insofar as they are affected by the refraction correction.

Although relabelling the curves of Figures 3 and 4 with f instead of Cf will render them correct, such relabelling will not fully correct the derived curves, Figures 5 and 6.

D. OMITTED FINAL EQUATION, REFERENCE 17

The following equation should be inserted below the sketch on page 92 Reference 17:

Narrow Band Directivity: $\dfrac{\Phi_c(\theta,\omega)}{\Phi_c(90°,\omega')}$

Convection Factor: $\dfrac{C^{-4}(\theta)}{C^{-4}(90°)}$

Monopole Directivity: $\dfrac{F^2(\theta,\ \omega)}{F^2(90°,\ \omega')}$

Correction: $\dfrac{C^4(\theta)\int \Phi_q(\omega)\ \cdot\ (\text{phase @ }\theta)_c\, d^3\xi}{C^4(90°)\int \Phi_q(\omega)\ \cdot\ (\text{phase @ }90°)_c\, d^3\xi}$

Refraction Factor

SECTION 3.0

ANALYTICAL MODELING FOR A JET'S ORDERLY STRUCTURE

C.L. Merkle

3.1 BACKGROUND

For many years, the unsteady fluctuations in the flow field of a high-Reynolds-number jet have been assumed to be random in nature. However, recent advances in experimental techniques have allowed measurements to be made which indicate that there may be a large degree of "ordered" structure in the jet flow field. Although such information is most readily obtained from low-Reynolds-number jets, the companion theory suggests that this ordered structure persists in high-Reynolds-number flows as well. The extent to which the turbulence in the jet is ordered, and to what degree it affects the emitted acoustic radiation by the jet, are basic concerns.

In this section an attempt is made to review the salient features of a number of theoretical models that have been proposed to describe a jet's orderly structure and associated acoustic radiation. The discussion of the theoretical models is centered on stability arguments. The various models are discussed by comparing their similarities with, and their differences from, Tam's[80] theory (perhaps the most complete orderly structure analysis to date).

This section provides suggestions for incorporating a multiple-frequency acoustic model for orderly structure work, as well as providing methods for investigating the orderly structure aerodynamic and acoustic problem using the usual stability eigenfunction analysis in conjunction with existing finite difference aeroacoustic computer programs developed by General Electric.

3.2 THE STABILITY OF TURBULENT AXISYMMETRIC COMPRESSIBLE JETS

It is well known that laminar, incompressible jets are unstable to a broad spectrum of disturbances and that, if a perturbation is introduced into the jet, its amplitude will grow in an exponential fashion as it is swept downstream [see, for example, Betchov and Criminale[81]]. The experimental work of Crow and Champagne[82] further indicated that disturbances were likewise unstable in a turbulent jet, except that the appropriate Reynolds number of the jet was the one corresponding to the effective (rather than the molecular) viscosity. Stability analyses of compressible jets have likewise shown that small disturbances are amplified [Berman and Ffowcs-Williams[83]] although the amplification rate decreases as the jet Mach number increases. The equations describing the stability of a perturbation in a turbulent, compressible axisymmetric jet have been obtained by several authors, and in the following we follow the development by Tam[80].

The stability equations are obtained from the compressible Navier-Stokes equations. In order to include both instability waves and turbulent fluctuations in the analysis, we divide each of the flow variables into three parts. Thus, for a particular flow variable, q, we have a mean value, $\bar{q}$, an instability wave, $\tilde{q}$, and a turbulent fluctuation, q':

$$q(x_i,t) = \bar{q}(x_i) + \tilde{q}(x_i,t) + q'(x_i,t) \ , \tag{94}$$

where x_i is the spatial variable and t is the time. In the analysis, the instability wave will be distinguished from the turbulence not only by its orderly, wave-like variation with time and space, but also by a characteristic time which is much longer than that associated with the turbulence. Under this approximation, separate systems of equations for each of these three components can be obtained as follows: The equations for the mean flow are obtained by substituting equation (94) into the complete unsteady equations of motion and time-averaging (it being assumed that the time average of both $\tilde{q}$ and q' vanishes). This time-averaging, of course, introduces the familiar turbulent Reynolds stresses into the mean-flow equations but, in addition, introduces Reynolds stress terms due to the wave motion. The fluctuations $\tilde{q}$ and q' are assumed uncorrelated, so the time average of their product vanishes. Equations for the wave motion are obtained by again introducing equation (94) into the equations of motion and again time-averaging; but, this time, the averaging is performed over a time which is long compared to the characteristic time of the turbulence, and short compared to the characteristic time of the large-scale oscillation. The resulting equations retain time-dependent terms. Subtracting the mean-flow equations from this set yields the equations for the wave motion. Since correlations of the turbulence quantities appear in the mean-flow equations, a similar set of equations is required to determine their magnitude. However, as is well known, the equations for the turbulence correlations introduce higher (third-order) correlations and, eventually, some sort of turbulence model must be introduced in order to obtain a "closed" system of equations. Since we are primarily interested in the ordered waves, and not the turbulence itself, we introduce the turbulence modeling at the earliest possible stage and relate the Reynolds stresses to the rate of strain tensor by an isotropic eddy viscosity.

It should be noted that the equations for the wave motion can be obtained without the necessity of assuming different time scales for the wave and the turbulence by using phase-averaging [Hussain and Reynolds[84]] rather than the second time-average. A complete description of this derivation for incompressible flows is given by Reynolds and Hussain[85]. A partial account of the compressible version of this derivation is given by Liu[86]:

3.2.1 The Equations for the Mean Flow and the Wave

Following Tam[80], we first rewrite equation (94) as:

$$q = q^* + q', \tag{95}$$

where,

$$q^* = \bar{q} + \tilde{q}. \tag{96}$$

We then insert Equation (95) into the Navier-Stokes equations and obtain its time average over a time which is long compared to the turbulent fluctuations and short compared to the oscillation. This yields the following system of equations:

$$\frac{\partial \rho^*}{\partial t} + \frac{\partial \rho^* u^*}{\partial x} + \frac{1}{r}\frac{\partial \rho^* v^* r}{\partial r} + \frac{1}{r}\frac{\partial}{\partial \phi}\rho^* w^* = 0 \tag{97}$$

$$\frac{\partial \rho^* u^*}{\partial t} + \frac{\partial \rho^* u^{*2}}{\partial x} + \frac{1}{r}\frac{\partial \rho^* u^* v^* r}{\partial r} + \frac{1}{r}\frac{\partial \rho^* u^* w^*}{\partial \phi} = -\frac{\partial p^*}{\partial x} + \frac{1}{r}\frac{\partial \sigma_{rx}^*}{\partial r} \tag{98}$$

$$\frac{\partial \rho^* v^*}{\partial t} + \frac{\partial \rho^* u^* v^*}{\partial x} + \frac{1}{r}\frac{\partial \rho^* v^{*2}}{\partial r} + \frac{1}{r}\frac{\partial}{\partial \phi}\rho^* v^* w^* - \frac{\rho^* w^{*2}}{r} = -\frac{\partial p^*}{\partial r} + \frac{1}{r}\frac{\partial}{\partial r} r\sigma_{rr}^* \tag{99}$$

$$\frac{\partial \rho^* w^*}{\partial t} + \frac{\partial \rho^* u^* w^*}{\partial x} + \frac{1}{r}\frac{\partial \rho^* v^* w^*}{\partial r} + \frac{1}{r}\frac{\partial \rho^* w^{*2}}{\partial \phi} + \frac{\rho^* v^* w^*}{r} = -\frac{1}{r}\frac{\partial p^*}{\partial \phi} + \frac{1}{r^2}\frac{\partial}{\partial r}(r^2 \sigma_{r\phi}^*) \tag{100}$$

$$\frac{\partial p^*}{\partial t} + \frac{\partial p^* u^*}{\partial x} + \frac{1}{r}\frac{\partial p^* v^*}{\partial r} + \frac{1}{r}\frac{\partial p^* w^*}{\partial \phi} + (\gamma - 1)\, p^* \left[\frac{1}{r}\frac{\partial v^* r}{\partial r} + \frac{1}{r}\frac{\partial w^*}{\partial \phi} + \frac{\partial u^*}{\partial x}\right] = 0 \tag{101}$$

In these equations, the boundary-layer approximations have been invoked and the molecular shear stresses have been neglected in comparison with the turbulent stresses, σ^*_{rr}, σ^*_{rx}, and $\sigma^*_{r\phi}$. In addition, turbulent heat transfer has been ignored in Equation (101); consequently, these equations are restricted to cold jets.

The equations for the mean flow are obtained by inserting equation (96) into equations (97-101) and again time averaging, this time over a time interval which is long compared to the period of the wave. This process introduces

a second "Reynolds stress," namely, a term which describes the energy transfer between the wave and the mean flow. After performing the averaging, we obtain (for axisymmetric, nonswirling mean flow):

$$\frac{\partial \bar{\rho}\bar{u}}{\partial x} + \frac{1}{r}\frac{\partial}{\partial r}\left(\bar{\rho}\,\bar{v} + \overline{\tilde{\rho}\tilde{v}}\right) r = 0 \tag{102}$$

$$\bar{\rho}\bar{u}\frac{\partial \bar{u}}{\partial x} + \left(\bar{\rho}\bar{v} + \overline{\tilde{\rho}\tilde{v}}\right)\frac{\partial \bar{u}}{\partial r} = -\frac{\partial \bar{p}}{\partial x} + \frac{1}{r}\frac{\partial}{\partial r}\left(r\sigma_{rx}^{*}\right)$$

$$-\frac{1}{r}\frac{\partial}{\partial r}\left(\bar{\rho}\,\overline{\tilde{u}\tilde{v}} + \overline{\tilde{\rho}\tilde{u}\tilde{v}}\right) \tag{103}$$

$$\frac{\partial \bar{p}}{\partial y} = -\frac{\partial}{\partial y}\left(\tilde{0}\,\bar{\tilde{v}}^{2} + \overline{\tilde{\rho}\tilde{v}^{2}}\right) \tag{104}$$

$$\frac{\partial \bar{p}\bar{u}}{\partial x} + \frac{1}{r}\frac{\partial}{\partial r}\bar{p}\bar{v}r + (\gamma-1)\,\bar{p}\left[\frac{1}{r}\frac{\partial \bar{v}r}{\partial r} + \frac{\partial}{\partial x}\bar{u}\right]$$

$$= -\frac{1}{r}\frac{\partial}{\partial r}\left(\overline{\tilde{p}\tilde{v}}\,r\right) - (\gamma-1)\,\frac{1}{r}\left[\tilde{p}\frac{\partial}{\partial r}\tilde{v}r\right] \tag{105}$$

The additional terms on the right-hand side of equations (103-105)) represent the enhanced momentum transport which is caused by the wave.

Finally, the equations for the wave itself are obtained by substracting equations (102-105) from equations (97-101). As is common in stability analyses, the parallel flow approximations are used, along with the boundary-layer approximations, to simplify the equations for the wave. Parallel flow implies that the v-component of the mean velocity is negligible compared to the u-component, and that stream-wise derivatives of the u-component can be neglected. Thus, the stability equations hold only locally in the flow. Finally, terms which are quadratic in the wave variables are also dropped. The resulting set of equations is:

$$\frac{\partial \tilde{\rho}}{\partial t} + \frac{\partial}{\partial x}\left(\bar{\rho}\,\tilde{u} + \tilde{\rho}\,\bar{u}\right) + \frac{1}{r}\frac{\partial}{\partial r}\left(r\bar{\rho}\tilde{v}\right) + \frac{1}{r}\frac{\partial}{\partial \phi}\,\bar{\rho}\,\tilde{w} = 0 \tag{106}$$

$$\frac{\partial}{\partial t}\bar{\rho}\tilde{u} + \frac{\partial}{\partial x}\bar{\rho}\bar{u}\tilde{u} + \bar{\rho}\frac{\partial \bar{u}}{\partial r}\tilde{v} + \frac{\partial \tilde{p}}{\partial x} = \mu_t \frac{1}{r}\frac{\partial}{\partial r}\left(r\frac{\partial \tilde{u}}{\partial r}\right) \tag{107}$$

$$\frac{\partial}{\partial t}\bar{\rho}\tilde{v} + \frac{\partial}{\partial x}\bar{\rho}\bar{u}\tilde{v} + \frac{\partial \tilde{p}}{\partial r} = \mu_t \frac{1}{r}\frac{\partial}{\partial r}\left(r\frac{\partial \tilde{v}}{\partial r}\right) \tag{108}$$

$$\frac{\partial}{\partial t}\ \overline{\rho}\tilde{w} + \frac{\partial}{\partial x}\ \overline{\overline{\rho u}}\tilde{w} + \frac{1}{r}\ \frac{\partial \tilde{p}}{\partial \phi} = \mu_t\ \frac{1}{r}\ \frac{\partial}{\partial r}\left(r\frac{\partial \tilde{w}}{\partial r}\right) \tag{109}$$

$$\frac{\partial \tilde{p}}{\partial t} + \frac{\partial}{\partial x}\ \tilde{\overline{p}}\tilde{u} + \gamma\overline{p}\ \left(\frac{1}{r}\ \frac{\partial}{\partial r}\ r\tilde{v} + \frac{1}{r}\ \frac{\partial \tilde{w}}{\partial \phi} + \frac{\partial \tilde{u}}{\partial x}\right) = 0 \tag{110}$$

This set of equations can be used to determine the rate at which a disturbance in the jet grows (or decays) as it is convected downstream. It should be noted that this system of equations is identical to the system which is obtained for laminar flow except for two factors. First of all, the mean-flow profiles appear as variable coefficients in the linear system of equations. Of course, these mean-flow profiles are strongly affected by the turbulence. The second place where the turbulence enters is through the effective viscosity; however, as discussed below, this alteration has little effect on the solution of the equations.

It was originally proven by Rayleigh that the inviscid, incompressible, parallel flow stability equations possessed solutions which grew with time (or distance) if, and only if, the mean velocity profile possessed an inflection point [Betchov and Criminale[81]]. In such a case, the profile is said to be dynamically unstable. Thus, in the case of a flat-plate boundary layer, disturbances of all frequencies are damped if the inviscid form of the stability equations is used, because the Blasius profile possesses no inflection point. However, the presence of viscosity serves to destabilize the solution so that, at finite Reynolds numbers, the Blasius boundary-layer profile admits unstable solutions. If the boundary layer is subjected to an unfavorable pressure gradient, an inflection point appears in the profile and moves farther and farther from the wall as the magnitude of the pressure gradient is increased. As the inflection point moves away from the wall, the profile becomes more and more dynamically unstable, and the effects of viscosity have less and less influence on the solution. The velocity profile in a jet must of necessity have a "strong" inflection point, similar to that in a strongly retarded boundary layer; and, consequently, to a good approximation, the viscous terms in the stability equations can be neglected. A similar approximation has been used by Ko, Kubota, and Lees[88] and Ko[88] in their analyses of transition in a wake. As noted later, the neglect of viscosity in the stability equations generates a critical point in the equations which must be handled carefully by the proper insertion of a branch cut which, in some cases, crosses the prescribed integration path and requires that the path be deformed around the singularity.

3.2.2 The Eigenvalue Equation

We now proceed to solve the stability equations (equations 106-110). Since these equations are linear, we look for solutions which are periodic in ϕ and t, and which have the form:

$$\tilde{\rho} = \mathrm{Re}\,\{C\hat{\rho}(r)\ \exp\ [i(\alpha x+n\phi-\omega t)]\}$$
$$\tilde{p} = \mathrm{Re}\,\{C\hat{p}(r)\ \exp\ [i(\alpha x+n\phi-\omega t)]\} \qquad (111)$$
$$\tilde{u}_i = \mathrm{Re}\,\{C\hat{U}_i(r)\ \exp\ [i(\alpha x+n\phi-\omega t)]\}$$

where C is a constant. As can be seen, Equations (106-110) are all homogeneous, and the imposed boundary conditions are likewise homogeneous. Consequently, the solution of the stability equations vanishes identically unless some particular combination of the parameters in the system is specified so that an eigensolution can be obtained. If such an eigensolution is obtained, its amplitude is arbitrary. The constant, C, represents this arbitrariness. In our analysis, we regard the parameter, α, as the eigenvalue. Thus, for each frequency, ω, and each spiral mode, n, we will look for an appropriate value of α which allows all the boundary conditions to be satisfied. We take the frequency, ω, to be real, and the wave number, α, to be complex. Thus,

$$\alpha = \alpha_r + i\alpha_i \qquad (112)$$

where α_r is the wave number of the disturbance, and α_i is its spatial growth rate. Note that by the convention adopted, values of α_i which are negative correspond to waves whose amplitude increases with x.

Substituting equation (111) into equations (106-110) leads, after some algebraic manipulation, to a single, second-order ordinary differential equation for the radial variation of the amplitude of the pressure:

$$\frac{d^2\hat{p}}{dr^2} + \left(\frac{1}{r} - \frac{1}{\bar{\rho}}\frac{d\rho}{dr} - \frac{2\alpha}{\lambda}\frac{d\bar{u}}{dr}\right)\frac{d\hat{p}}{dr} + \left[\left(\frac{\bar{\rho}}{\gamma\bar{p}}\lambda^2-\alpha^2\right) - \frac{n^2}{r^2}\right]\hat{p} = 0 \qquad (113)$$

where,

$$\lambda = (\alpha\bar{u} - \omega) \qquad (114)$$

Equation (113) can be used to determine $\hat{p}(r)$. Having obtained $\hat{p}$, the other variables follow immediately from the additional relations (also obtained from equations (106-110) and Equation (111),

$$\hat{w} = -\,n\hat{p} \,/\, \bar{\rho}\, r\, \lambda \qquad (115)$$

$$\hat{v} = i\,\frac{d\hat{p}}{dr} \,/\, \bar{\rho}\lambda \qquad (116)$$

$$\hat{u} = -\,(\alpha\hat{p} - i\,\bar{\rho}\,\frac{d\bar{u}}{dr}\,\hat{v}) \,/\bar{\rho}\lambda \qquad (117)$$

$$\hat{\rho} = \frac{\bar{\rho}}{\gamma \bar{p}} \hat{p} + \frac{i}{\lambda} \frac{d\rho}{dr} \hat{v} \tag{118}$$

The boundary conditions on this set of equations have been given by Ko[87].

for n = 0, $\hat{u} = \hat{w} = 0$

$\hat{p}, \hat{v}, \hat{p}$, bounded,

for n ≠ 0, $\hat{u} = \hat{p} = \hat{\rho} = 0$,

$\hat{v} = -\hat{w}$, For n = 1,

$\hat{v} = \hat{w} = 0$ for n > 1.

At infinity, we require that all five quantities must approach zero.

Although equation (113) is linear, it must be solved numerically because of the variable coefficients. However, outside the jet the gradients of the mean quantities vanish, and equation (113) becomes a Bessel equation whose solution, subject to the boundary conditions, is a Hankel function:

$$\hat{p}\,(r) = C_1 \; H_n^{(0)} \left[\left(\frac{\rho_o \omega^2}{\gamma p_o} - \alpha^2 \right)^{1/2} r \right] \tag{119}$$

Similarly, in the core region, the solution can also be obtained analytically:

$$\hat{p}\,(r) = C_2 \; J_n \left\{ \left[\frac{\rho_j}{\gamma p_J} \left(u_J \, \alpha - \omega \right)^2 - \alpha^2 \right]^{1/2} r \right\} \tag{120}$$

Thus, the numerical solution is only necessary in the shear layer. The eigenvalue search proceeds by guessing a value for α. Both the solution and its derivative can then be determined at the outer edge of the jet from equation (119). Note that in doing this, the constant, C_1, can be chosen arbitrarily, since it represents the amplitude of the eigenfunction. The equation can be integrated numerically by means of a standard differential equation integration technique (such as a Runge-Kutta method) except that allowance must be made for the complex coefficients in the equation (recall that α is complex). When the numerical integration reaches the potential core, the solution and its derivative must be matched to the analytical function, equation (120). This allows the constant, C_2, to be determined (in terms of C_1) but, in addition, specifies an additional relation which can only be satisfied if α is an eigenvalue. To determine the appropriate characteristic value, the procedure again is repeated from the outer edge of the jet with a new guess for α until such time that the desired convergence is achieved.

For axial stations beyond the potential core, the numerical integration is continued all the way to the centerline so that equation (120) is not required. Thus, in the fully developed region of the jet, various values of the

eigenvalue, α, are tried until one is found which allows the pressure, p, to vanish at the centerline.

One difficulty which occurs in the numerical integration of equation (113) is that the solution must pass through a singular point of the equation where λ goes to zero. This singularity, which is introduced by neglecting the viscous terms in the stability equations, causes no difficulty for the case where the wave is being amplified; however, for damped waves, a branch cut must be inserted and the integration path must be deformed (in the complex r-plane) to allow the integration to proceed beyond this point, as shown in Figure 81. The mathematical significance of this singularity has been discussed by Lin[89].

In the jet, the mean-flow profile depends upon the axial location. Because of this, the eigensolution to equation (113) likewise depends upon x. Thus, if a particular frequency is chosen, the axial variation of its wave number and its amplification rate can be determined by solving equation (113) at a series of axial stations, using the local mean-flow profiles at each station to evaluate the coefficients in the equation. The resulting curve of α_1 versus x can then be integrated to give the amplification of the wave, A, as a function of x:

$$\frac{A(\omega,x)}{A_o(\omega,x_o)} = \exp\left[-\int_{x_o}^{x} \alpha_i(\omega,x)\,dx\right] \qquad (121)$$

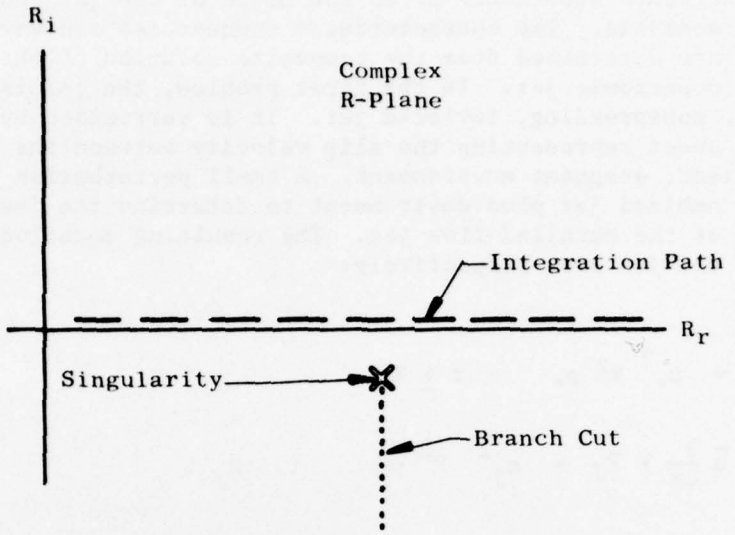
where A_o is the initial amplitude of the wave. It is emphasized that α_1 and, hence, A, depends on frequency and that the total energy involved in the orderly structure is obtained by integrating over the entire frequency spectrum. Finally note that, if the amplitude of the disturbance is specified at the initial axial location, x_o, the amplitude at each succeeding axial station can then be obtained from equation (121). Thus, equation (121) serves to define the remaining arbitrariness in the eigensolution, namely the constant, C_1, in equation (119).

3.3 DETERMINATION OF THE SPECTRAL CHARACTERISTICS OF THE "ORDERLY STRUCTURE"

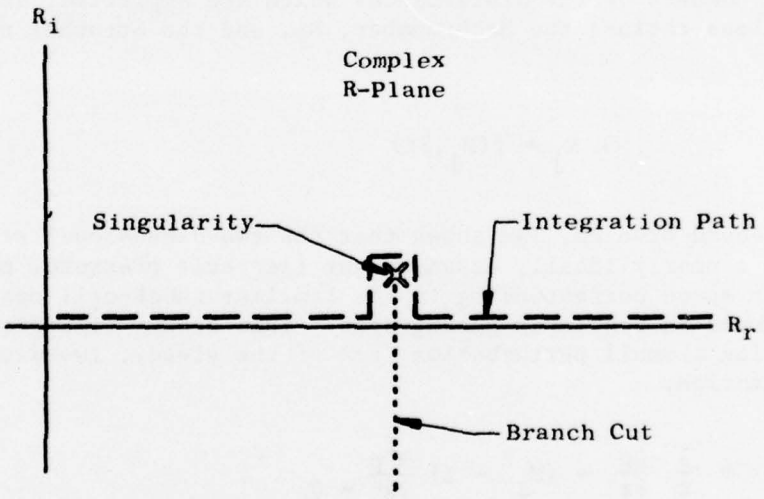
The previous Subsection describes the manner by which the eigenvalue, α (which gives both the growth rate and the wave number of the wave), can be determined if the frequency is known. This subsection first describes the manner in which the (single-frequency) disturbance is determined in the model developed by Tam[80]. Following this, some alternative methods for determining a wide-band orderly structure spectrum, using the same basic fluid dynamic model, are discussed.

3.3.1 Tam's Single Frequency Analysis

Tam[80] has used the spatially periodic characteristics of a steady supersonic jet to determine two characteristic "resonant" frequencies which will be preferentially amplified by the jet. Of these two waves, one is too high in



(a) Self-Excited Solution; $\alpha_i > 0$



(b) Damped Solution; $\alpha_i > 0$

Figure 81. Deformed Path for Integration Around Logarithmic Singularity in Eigenvalue Equation for Self-Excited and Damped Cases.

frequency to contribute substantially to the noise of the jet and is ignored in his acoustic analysis. The characteristic frequencies and wave numbers of these two waves are determined from the composite solution of three simplified pictures of the supersonic jet. In the first problem, the jet is assumed to be a supersonic, nonspreading, inviscid jet. It is surrounded by a constant-strength vortex sheet representing the slip velocity between the supersonic jet and the ambient, stagnant environment. A small perturbation problem is solved for the combined jet plus environment to determine the instability characteristics of the parallel-flow jet. The resulting equations for the environment and the jet are, respectively:

$$\frac{\partial^2 p_o}{\partial t^2} = a_o^2 \nabla^2 p_o \qquad r \geq R_J$$

$$\left(\frac{\partial}{\partial t} + \bar{u} \frac{\partial}{\partial x}\right) P_J = a_J^2 \nabla^2 p_J \qquad r < R_J \tag{122}$$

Note that these equations represent a special case of the previously obtained linear stability equations (equations 106-110), in which the shear layer (mean velocity profile) has been replaced by a vortex sheet (velocity discontinuity). The solution of the resulting eigenvalue problem shows that disturbances of a band of wave numbers are amplified. By curve fitting the results, Tam shows that the wave numbers of the disturbances which are amplified, depend on the two dimensionless ratios: the Mach number, M_j, and the Strouhal number, St. Thus,

$$k R_j = f(M_j, St) \tag{123}$$

In the second problem, Tam shows that the two-dimensional steady-state flow field of a nearly ideally expanded jet (jet exit pressure, $p_j = P_o + p$) is periodic in space corresponding to the familiar shock-cell periodicity which is observed in Schlieren photographs. This steady flow field is determined by solving a small perturbation form of the steady, two-dimensional equations of motion,

$$\frac{\partial^2 p}{\partial r^2} + \frac{1}{r} \frac{\partial p}{\partial r} - (M_J^2 - 1) \frac{\partial^2 p}{\partial x^2} = 0 \tag{124}$$

The solution of this equation, which was originally obtained by Prandtl, is an infinite Fourier-Bessel series which, near the nozzle exit, shows the jet to be nearly periodic in the axial coordinate at some wave number, k_o, which depends only upon the jet Mach number, M_j:

$$k_o = g(M_j) \tag{125}$$

As the third problem, Tam solves for the discrete frequencies which are resonantly amplified by the above (nearly) periodic steady flow field. In this analysis, he drops the radial dependence of the solution of the second problem and uses an unsteady, one-dimensional analysis with the acoustic pressure, p, given by:

$$p = \bar{p} + \epsilon \quad \text{Cos } (k_o \chi) \quad + \hat{p}(x)\ e^{-i\omega t} \tag{126}$$

where the first two terms on the right-hand side represent the known, steady flow field, and the last term represents the unknown, unsteady solution. The result is a system of equations which resembles the Mathieu equation and has the characteristic property that two discrete waves are resonantly amplified. These two waves can be written in functional form as

$$k_{1,2} = h_{1,2}\ (M_J, k_o) \tag{127}$$

where k_o is the wave number corresponding to the periodicity of the unsteady flow field.

By combining equations (123), (125), and (127), Tam obtains a relation which gives the two preferred frequencies of the jet as

$$St = F(M_j) \tag{128}$$

Thus, the Strouhal number of the unsteady oscillation depends only on the Mach number of the jet. A plot of these two resonant frequencies is given in Figure 82 as a function of Mach number.

Having obtained the resonant frequencies of the jet, their amplification rate and their amplitude can be obtained from the stability analysis, as described above. For comparison with the other approaches, which are described below, it is important to look carefully at the method by which this preferred frequency is chosen and to examine its growth rate. First of all, as equation (121) suggests, the amplification ratio, A/A_o, at a particular value of x, depends upon the frequency in a continuous manner, as shown schematically in Figure 83a. However, the actual magnitude of the waves at some downstream station depends on the initial spectral distribution of A_o as well as the variation of A/A_o. In Tam's analysis, the spectral distribution of A is a delta function centered at ω_1 (with a second spike at ω_2), as shown in Figure 83b. This requires that the disturbance level in the region of the nozzle exit plane must also have a distribution qualitatively similar to that shown in Figure 83b. It can be expected that there will be a broad band distribution of disturbances in the jet at the exit plane; but, Tam's model assumes that the periodic (shock-cell) structure of the jet resonantly amplifies the initial level of two specific frequencies so that, after passing through the broad-band amplifier of the jet flow field, these discrete frequencies still dominate the orderly structure.

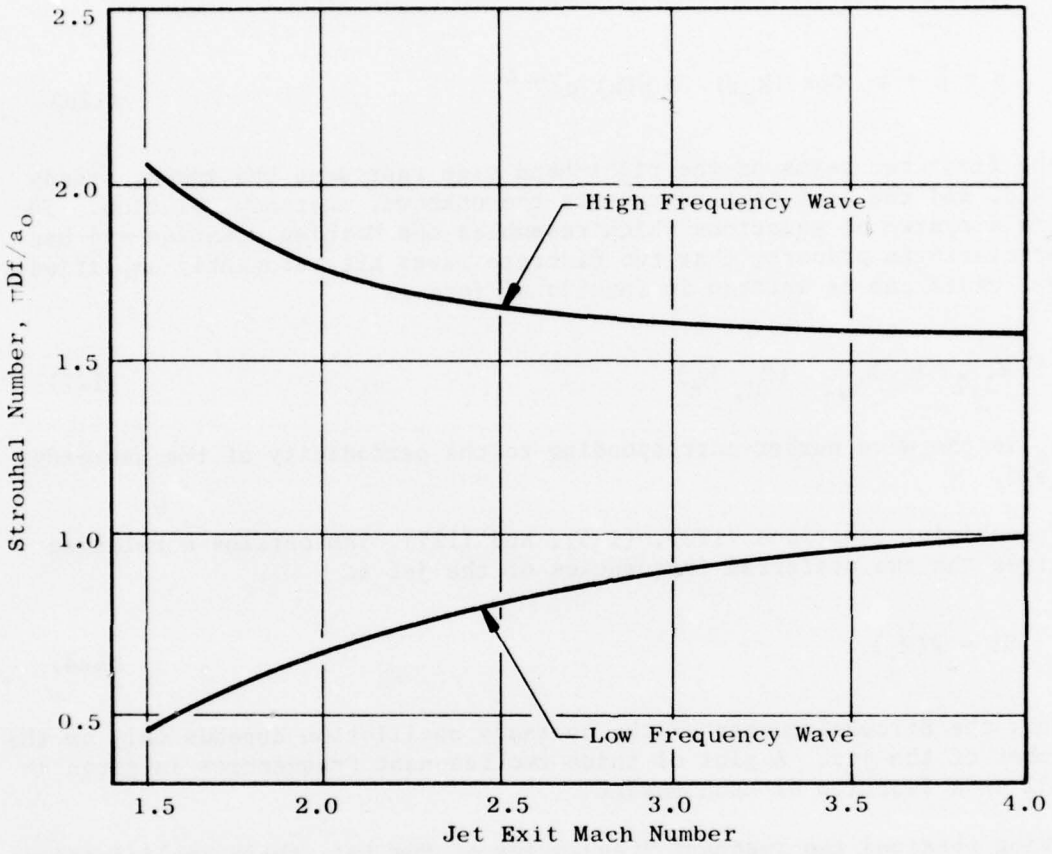
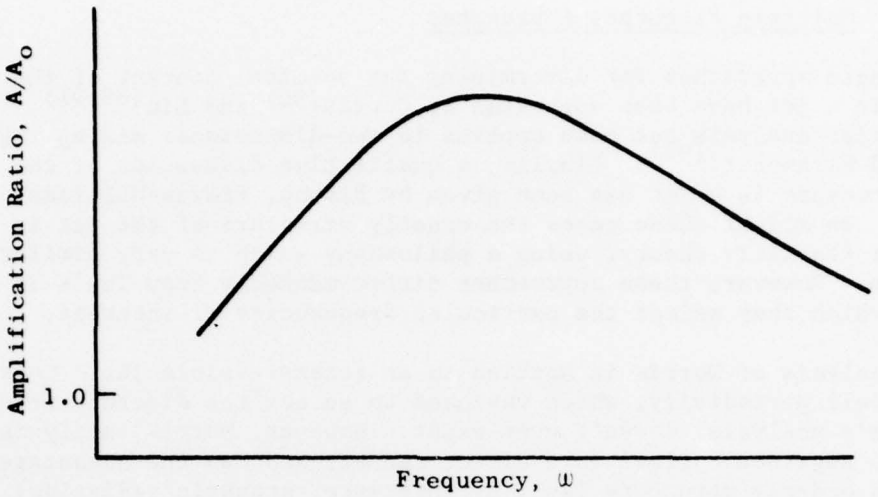
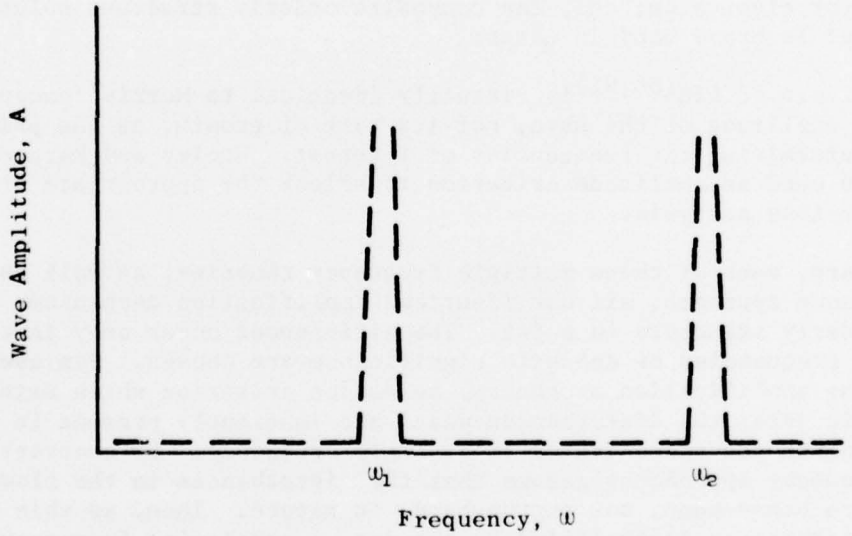


Figure 82. "Preferred" Waves in Supersonic Jet, Based on Periodic Shock Cell Structure in Nearly Ideally Expanded Jet (from Tam, 1972).



(a) Amplification ratio as a function of frequency at a particular axial station; inviscid linear stability theory.



(b) Amplitude of orderly structure wave in supersonic jet; Tam's model.

Figure 83. Schematic Diagram Showing Broadband Amplification Which is Available in a Jet (According to Parallel Flow Stability Theory), as Compared with the Energy Distribution in the Orderly Structure Wave (According to Tam, 1972).

3.3.2 Multiple Frequency Approaches

Alternate approaches for determining the spectral content of the orderly structure in a jet have been suggested by Morris[90] and Liu[86,91]. In addition a similar analysis has been applied to two-dimensional mixing regions by Woolley and Karamcheti[92]. Finally, a qualitative discussion of the expected orderly structure in a jet has been given by Bishop, Ffowcs-Williams, and Smith[93]. In all of these cases the orderly structure of the jet is described by means of stability theory, using a philosophy which is very similar to that used by Tam. However, these approaches differ markedly from Tam's in the manner in which they select the particular frequencies of interest.

The analysis of Morris is applied to an incompressible jet. Consequently, the shock-cell periodicity, which was used to select the discrete frequency wave in Tam's analysis, doesn't even exist. However, Morris' analysis can be extended to supersonic flows in a direct manner, and has the advantage that it predicts an orderly structure (and, by inference, acoustic radiation) at both subsonic and supersonic jet velocities. Morris uses the same stability equations as were used by Tam (except in their incompressible form) to determine the growth of a disturbance in a jet. A minor difference is that he retains the viscous terms. Thus, at each axial location in the jet, an eigenvalue, α, is determined; and, it is assumed that the single frequency which characterizes a given "slice" of the jet is that value of ω for which the amplification rate is the highest. Thus, because of the spreading of the jet, each slice has a different eigenvalue; and, the composite orderly structure solution for the entire jet is broad band in nature.

The analysis of Liu[86,91] is virtually identical to Morris' except that Liu uses the amplitude of the wave, not its rate of growth, as the prime criterion for determining the frequencies of interest. Wooley and Karamcheti[92] have likewise used an amplitude criterion to select the appropriate frequencies in their edge-tone analysis.

In summary, each of these multiple frequency theories, as well as Tam's single-frequency approach, all use identical amplification mechanisms to explain the orderly structure in a jet. The differences occur only in the manner in which the frequencies of acoustic significance are chosen. Tam uses an external (to the amplification mechanism) selection criterion which exists only for supersonic jets; the disturbances which are inherently present in the flow at the exit plane are concentrated at a single frequency. By contrast, the multiple-frequency approaches assume that the disturbances in the flow at the exit plane are broad-band, not narrow-band, in nature. Then, as this initially broad-band disturbance is amplified by the jet, a particular frequency (or group of frequencies) is selected as being "most important" at each axial location, depending on which frequency is growing most rapidly (Morris[90]), or depending on which frequency has the largest amplitude [Liu[91]. Woolley and Karamcheti[92]].

One final item of interest is to consider the relative merits of using the amplitude of the wave, A, as the frequency selection criteria, as compared to using the growth rate of the wave, α_1, for the same purpose. Morris[90] states that it is α_1 and not A which controls the growth of the turbulence. However, his mean-flow equations are coupled to his wave equations only through the wave correlation term, $< \tilde{u}\tilde{v} >$, which is clearly dependent on the amplitude, A, rather than the amplification rate, α_1. In fact, the amplification rate α_i doesn't appear anywhere in the equations for the mean flow, the orderly structure, or the turbulence, as shown in the analysis by Reynolds and Hussain[85]. However, before completely ruling out the importance of the most rapidly growing wave, we must first consider the acoustic arguments. It is well known that acoustic radiation cannot be emitted by constant amplitude waves unless their phase velocity is supersonic. However, this same statement is not true for waves whose amplitude changes with x; consequently, the growth rate is of extreme significance in the acoustic analysis. This phenomenon is discussed further in Subsection 3.5.

3.3.3 Effects of Finite Amplitude Waves

All of the above discussion implicitly refers to waves of small amplitude. Because of the rapid amplification which takes place in a supersonic jet, the wave amplitudes can become large enough to require the retention of the nonlinear terms. This is particularly true in a single-frequency analysis such as Tam's, in which all the energy in the wave motion is concentrated in one mode. For example, Tam's acoustic model visualizes a wave which contains enough energy to cause the entire mass in the jet to oscillate with the wave and, therefore, certainly requires a significant amount of energy in the wave.

In general, the nonlinearities can be grouped into two categories: energy transfer between the mean flow and the wave, and energy transfer from one spectral component to another. The first of these two categories is typified by noting that, when the energy of the overall wave system increases, it must increase at the expense of the energy in the mean flow (or perhaps the turbulence). Consequently, for waves whose amplitude is sufficiently large, the energy transfer from the mean flow to the wave must be included in the analysis by retaining terms such as the $< \tilde{u}\tilde{v} >$ correlation in the mean-flow momentum equation (as shown in equation 103). Inclusion of this energy transfer term introduces a mutual coupling between the mean flow and the oscillatory flow and requires that the two flow fields be computed simultaneously. The reward for this additional complexity is that the calculation remains valid for larger values of the wave amplitude.

The second effect concerns nonlinearities within the wave system itself. This effect could be included by retaining the quadratic terms in the stability equations (equations 102-105). The inclusion of this nonlinearity would introduce even greater complexities into the analysis. Because the stability equations would become nonlinear, the Fourier decomposition technique would lose much of its usefulness; that is to say, wave solutions of the form

$u = \hat{u}e^{i(\alpha x-\omega t)}$ would no longer be appropriate. Fortunately, experimental evidence has suggested that, at least for flows in which disturbances of only moderate amplitude are present, the coupling between the mean flow and the waves is more important than the energy cascade between frequencies (see discussion by Ko, Kubota, and Lees[87]). Because of this, inclusion of only the wave-mean-flow interaction substantially increases the maximum amplitude for which the analysis remains valid without incurring the undue complexity associated with solving the complete nonlinear equations.

This mean-flow-wave coupling was first included by Ko, Kubota, and Lees[87] and Ko[88], who were interested in the prediction of transition from laminar to turbulent flow in a wake. It was later included in the analyses of both Tam[80] and Morris[90] in an identical manner. However, in all of these analyses, the integral equations of motion were used for the mean flow, rather than the differential equations. When the integral equations are used, the shape of the cross-stream velocity profile is prespecified; the wave-mean-flow coupling affects only the spreading rate of the jet (or wake); in particular, the coupling appears as a modification to the eddy viscosity. This offers the advantage that, if the details of the jet spreading are not of interest (but only the effects of the orderly structure on the jet acoustics), the mean-flow field can be computed from an existing eddy viscosity formulation; and, the large amplitude wave calculation can then be uncoupled from the mean-flow calculation. Alternately, mean-flow profiles which have been measured in an experiment can be used to obtain the orderly structure solution.

It also is interesting to speculate on the possibilities of combining the orderly structure calculations with a differential equation solution procedure (such as the JETMIX computer program which was developed under this contract. See Volume III of this report). For the uncoupled case, only small quantitative differences would be expected between the differential and the integral approaches. However, for the coupled wave-mean-flow case, the use of the complete differential equations (which would allow the inclusion of the radial variation of the $< \tilde{u}\tilde{v} >$ correlation as obtained from the wave solution), means that the mean velocity profile shapes would be affected by the orderly structure. Observations of the development of the large-scale oscillations, and their interaction with and influence upon the mean-flow profiles, could give added insight into the physical reality of the model and the wave motion. For example, if the profile became severly distorted from typical experimentally measured shapes, it would indicate a shortcoming in the wave model. Such a shape verification is not possible in the integral approach, since the shape is a prespecified parameter in that analysis.

3.4 EXPERIMENTAL EVIDENCE OF ORDERLY STRUCTURE IN JETS

A number of experimenters have measured various properties of the flow field in a jet which indicate that there is some degree of orderly structure present. Although most of these experiments have been conducted at low Reynolds numbers, and at low Mach numbers, they lend strong support to the contention that supersonic, high-Reynolds-number jets possess orderly structure

characteristics also. For example, these low-speed experimental results are in agreement with the predictions of linear stability theory; and, the theory, in turn, indicates that there is no basic difference between low-speed and high-speed jets. The limited measurements which are available for supersonic jets also support the existence of large-scale oscillations in high-speed jets.

Low-speed jet measurements reported by Crow and Champagne[82] first showed that a turbulent jet would amplify disturbances in a manner similar to that observed for laminar jets. In these experiments, an artificial single-frequency disturbance was introduced into the jet, and its growth (or decay) rate was observed as it traveled downstream. Michalke[94] later obtained linear stability results which agreed reasonably well with these measurements. His calculations were based on the assumption that the wave-like disturbances were not directly affected by the turbulence but were indirectly affected through the influence of the turbulence on the mean profile. More recently, additional experimental results and corresponding calculations have been reported by Chan[95] which further substantiate this conclusion.

McLaughlin and McColgan[96] also have reported experimental hot-wire measurements of the fluctuations in a laminar, supersonic jet. (The flow was maintained laminar by exhausting the jet into a vacuum chamber.) Their spectral measurements show a very strong pure tone at a Strouhal number of 0.2 at very low Reynolds numbers and several pure tones at somewhat higher Reynolds numbers. These results seem to indicate that an instability mechanism is present in this supersonic jet, although the phase velocities and growth rates have not been measured experimentally, nor have the observed discrete tones been compared with the predictions of stability theory.

Perhaps the most conclusive evidence of orderly structure in jets has been reported by Fuchs[97]. Fuchs obtained narrow-band spatial correlations of the pressure fluctuations along the axis of symmetry of a low-speed jet. These correlations showed unmistakably wave-like behavior at wavelengths which were of the order of the width of the jet. This organized structure was observed to persist for more than five diameters and shows, without doubt, that there is an important ordered motion present inside the jet. Additional measurements also been been reported by Scharton and White[98], Ko and Davies[99], and Hussain and Reynolds[84].

3.5 SOUND RADIATION FROM THE ORDERLY STRUCTURE IN A JET

Once the orderly structure fluid dynamic flow field has been calculated, there still remains the task of determining the acoustic radiation from the jet. In Tam's[80] analysis, this was done by obtaining two unsteady velocities representing the unsteady flow entrainment by the jet and the unsteady vibration of the jet as a solid body. These two velocities were evaluated on the surface of a cylinder extending downstream from the nozzle exit plane and having the same diameter as the nozzle. The acoustic radiation of the jet was calculated by using these unsteady velocities as a boundary condition (and source term) for the acoustic equations in an ambient environment.

The methods whereby the unsteady entrainment and the unsteady vibration were determined are rather vague and somewhat questionable. The entrainment velocity was calculated by integrating the continuity equation describing the wave motion (our equation 106) to obtain:

$$\bar{\tilde{\rho}}\tilde{u}r\Big|_0^{r_e} = -\int_0^{r_e}\left[\frac{\partial\tilde{\rho}}{\partial t} + \frac{1}{r}\frac{\partial\bar{\tilde{\rho}}\tilde{w}}{\partial\phi} + \frac{\partial}{\partial x}(\bar{\tilde{\rho}}\tilde{u}+\tilde{\rho}\bar{u})\right] r\,dr \qquad (129)$$

where R_e represents the edge of the mixing layer. Then, inserting the wave decomposition, equation (111), we obtain:

$$\bar{\hat{\rho}}\hat{u}r\Big|_0^{r_e} = -\int_0^{r_e}\left[-i\omega\hat{\rho} + \frac{in\bar{\hat{\rho}}\hat{w}}{r} + i\alpha(\bar{\hat{\rho}}\hat{u}+\hat{\rho}\bar{u}) + \frac{d}{dx}(\bar{\hat{\rho}}\hat{u}+\hat{\rho}\bar{u})\right] r\,dr \qquad (130)$$

where the exponential function has been cancelled from both sides of the equation. Now, by again using equation (106), combined with equation (111), to simplify the integrand, and by changing the limits on the integrand to infinity, Tam obtains

$$\bar{\tilde{\rho}}\tilde{u}r\Big|_0^{r_e} = \int_0^{\infty}\frac{d\bar{\hat{\rho}}\hat{v}r}{dr}\,dr - \frac{d}{dx}\int_0^{\infty}(\bar{\hat{\rho}}\hat{u} + \hat{\rho}\bar{u})\,r\,dr \qquad (131)$$

so the entrainment velocity becomes:

$$\hat{u}_{ent} = -\frac{1}{\bar{\rho}_o r_o}\frac{d}{dx}\int_0^{\infty}(\bar{\hat{\rho}}\hat{u} + \hat{\rho}\bar{u})\,r\,dr \qquad (132)$$

However, the combination of equations (106) and (111) is identical to Equation (130), so the steps between equations (130) and (131) should give the trivial identity, zero equals zero. The reason they don't is because the limits of integration were changed inconsistently. (Also, recall that $\hat{u}$ and $\hat{\rho}$ are functions of r and that the variation of $\bar{u}$ and $\bar{\rho}$ with x have been neglected heretofore, so consistent evaluation of the limits of integration would give

$$\frac{\partial}{\partial x}\int_0^{\infty}(\bar{\hat{\rho}}\hat{u} + \hat{\rho}\bar{u})\,r\,dr = 0 \qquad (133)$$

as was previously assumed.

The details of the determination of the unsteady vibration velocity will not be given. The vibration velocity was obtained by starting from an F = ma equation and integrating once to obtain a velocity, assuming that the jet was a series of unconnected rigid discs subjected to an unbalanced pressure force. Having obtained this vibration velocity, it was then added to the unsteady entrainment to obtain the boundary condition for the acoustic calculation.

An alternate method for obtaining the acoustic radiation from the large-scale oscillation would be to simply take the value of $\hat{v}$, which is obtained from the eigenvalue equation, as the boundary condition on the $r/R_j = 1.0$ line. This appears to be both more self-consistent and easier than the method described above. For example, in the region outside the jet where the mean-flow gradients vanish, the stability equations become identical to the classical acoustic equations. However, the parallel-flow approximation implies that the far-field acoustic radiation, which is obtained from the stability equations, is the radiation due to a doubly-infinite jet whose width remained everywhere fixed. Thus, to include the first-order effects of the jet spreading, the value of the eigenfunction, $\hat{v}$, could be specified for each local value of the jet width. The ensuing calculation of the far-field noise for the "spreading" jet would be identical to the Fourier technique used by Tam, except that the boundary condition $\hat{v},(r=1,x)$ would be somewhat different than Tam's and, hence, the calculated acoustic radiation would be changed.

An improvement on this suggested alternative can be outlined by starting from the continuity and momentum equations:

$$\frac{1}{\gamma p}\frac{Dp}{Dt} + \nabla \cdot \underset{\sim}{u} = 0 \tag{134}$$

and:

$$\rho \frac{D\underset{\sim}{u}}{Dt} + \nabla p = 0 \tag{135}$$

If we let:

$$\underset{\sim}{u} = [\bar{u}(r) + \tilde{u}, \tilde{v}] \tag{136}$$

$$p = \bar{p} + \tilde{p} \; ; \; \rho = \bar{\rho} + \tilde{\rho}$$

We obtain:

$$\frac{1}{a^2}\frac{\partial^2 \tilde{p}}{\partial t^2} - \nabla^2 \tilde{p} = S'(x,y,t) \tag{137}$$

where,

$$S(x,y,t) = 2\bar{\rho}\frac{d\bar{u}}{dy}\frac{\partial \tilde{u}}{\partial x} + \frac{d\bar{\rho}}{dy}\left(\frac{\partial \tilde{u}}{\partial t} + \bar{U}\frac{\partial \tilde{u}}{\partial x}\right)$$

In equation 137, we have dropped the mean-flow terms on the left-hand side (i.e., we have neglected the velocity inside the jet). The terms due to the mean-flow gradients have been written as source terms. The perturbation velocities in the source term, S, are to be evaluated from the stability results and used as forcing functions for the acoustic equation. Two observations can be made regarding this second approach. First of all, this approach is philosophically similar to the approach of Lilley, Morris, and Tester[100], although it is a considerably simplified version. Second, the mathematical analysis required to obtain the acoustic radiation from the orderly structure fluid dynamics is the same as is used in the classical turbulence-generated noise approach. In particular, the same computer program (NOISE; see Volume III), which has been used for our Lighthill-type acoustic

predictions, could also be used to evaluate this orderly structure acoustic model. The only difference would be that the source terms would be evaluated from the orderly structure results, rather than from the turbulent kinetic energy.

3.6 ORDERLY STRUCTURE FLOW FIELD CALCULATIONS

A computer program to describe the orderly structure flow field in a turbulent jet has been written, and some initial results are described in this section. In the program, the mean-flow field is computed from an integral formulation of the equations of motion. (For completeness, the exact form of these equations is given below.) The large-scale wave motion is determined from the eigenvalue analysis which was given in a previous section. The energy transfer between the wave and the mean flow has been included in the results which are presented here; however, the program also is capable of performing calculations in which this coupling is neglected.

In addition to these fluid dynamic calculations, some acoustic predictions also have been obtained using Tam's acoustic model. These results are also given below.

3.6.1 Integral Form of the Equations of Motion

The integral equations for the mean flow, which have been obtained by Tam[80], include the conservation of momentum:,

$$\int_o^\infty \bar{\rho}\,\bar{u}^2\,r\,dr = M \tag{138}$$

and the mean kinetic energy equation:

$$\frac{d}{dx}\int_o^\infty \frac{1}{2}\bar{\rho}\,\bar{u}^3\,r\,dr = \int_o^\infty \bar{\rho}\,\overline{\tilde{u}\tilde{v}}\,\frac{\partial \bar{u}}{\partial r}\,r\,dr - \int_o^\infty \bar{\rho}\bar{\epsilon}\left(\frac{\partial \bar{u}^2}{\partial \gamma}\right) r\,dr \tag{139}$$

Equation (138) states that the net momentum flux in the jet is the same at all axial locations, whereas equation (139) indicates that the flux of kinetic energy decreases (increases) because of two factors: the energy lost to (gained from) the wave and the dissipation by the turbulent stresses.

The kinetic energy in the wave obeys a similar energy balance,

$$\frac{dE_t}{dx} = \int_o^\infty \rho\,\overline{\tilde{u}\tilde{v}}\,\frac{\partial \bar{u}}{\partial r}\,r\,dr - \phi \tag{140}$$

where ϕ is the dissipation associated with the wave motion and the integral is the source (or sink) of energy from the mean flow. The energy in the wave is defined as

$$Et = \int_0^\infty \left[\bar{\rho}\bar{u} \; \overline{\tilde{u}_i \tilde{u}_i} + \frac{\bar{u}}{2rpo} \; \overline{\tilde{p}^2} + \overline{\tilde{p}\tilde{u}} \right] r dr \tag{141}$$

and using the amplification rate, α_1, as defined by equation (111), we have

$$\frac{dEt}{dx} = -2 \; \alpha_i \; Et \tag{142}$$

The system of equations is completed by specifying that the total temperature is constant throughout the entire jet. This restricts the analysis to cold jets. In order to extend the analysis to hot jets, an equation for the variation of total temperature across the jet would have to be included. An integral form of the energy equation, such as the one derived by Ko[88], could be coupled with the above equations to determine the variation of the total temperature.

The success of an integral approach rests upon describing the cross-stream variation of the profiles in terms of a family of shapes which depend upon a minimum number of parameters. For the jet, the velocity profile is specified as:

$$u = u_j \; \exp\left[-C_B \left(\frac{r-h}{b}\right)^2\right], \quad \text{for } x < x_c, \tag{143}$$

and:

$$u = u_{\text{C}_L} \; \exp\left[-C_B \left(r/b\right)^2\right], \quad \text{for } x > x_c \tag{144}$$

where x_c represents the end of the potential core, h is the width of the potential core, and b is the radial distance from the inner edge of the shear layer to the location at which the velocity is one-half of its centerline value. From this definition, the constant, C_B, can be evaluated to be $C_B = 0.606742$. Having specified the velocity, the density profiles can be determined by combining the constant total temperature assumption, the perfect gas law, and the velocity profiles [Equations (143) and (144)] to give:

$$\rho = \rho_o \left[1 - \frac{\gamma-1}{2} \; (\bar{u}/a_o)^2\right]^{-1} \tag{145}$$

When the energy in the wave is ignored, equations (138) and (139) reduce to two equations in the two unknowns, b and h, or b and u. Then, after determining the cross-stream profiles, the variable coefficients in equation (123) can be evaluated, and equation (113) can be solved for the eigenvalue, α. If the energy loss to the wave is included in the mean flow, the calculation of the mean flow and the wave must be done iteratively. In practice, it has generally proven sufficient to first estimate the wave amplitude at a new axial location, $X + \Delta X$, and then to compute the mean flow based on this estimate. The mean-flow profile can then be used to determine the final estimate of the wave shape and energy.

In order to complete the problem definition, the eddy viscosity, ε, which appears in equation (139), has to be specified. Following Tam, we take

$$\varepsilon = \frac{1}{2} K\, b\, u_{\tilde{\ell}} \tag{146}$$

where u_{ℓ} is the velocity on the centerline (in either the potential core region or the fully developed region). The empirical coefficient, K, which was used to obtain the results which are presented herein, was allowed to vary with the half-height of the jet as

$$K = 0.045 \left[1 - \frac{0.85\, r_o}{b + h}\right] \tag{147}$$

3.6.2 Fluid Dynamic Calculations

Figures 84 through 87 show some flow-field calculations which have been made with our orderly structure computer program. Where possible, these results have been compared with the calculations which were reported by Tam[80]. Figure 84 shows the variation in the half-width of the shear layer, b/r_o, with distance from the jet exit plane. Figure 85 shows a similar plot of the half-height of the core, h/r_o, as a function of the distance from the nozzle exit, while Figures 86 and 87 show the variation of the wave number, α_r, and the amplification rate, α_i, as the half-height of the mixing layer increases. As can be seen from the figures, all of these solutions are qualitatively similar to the results obtained by Tam, but the comparisons are not identical. The specific source of these small differences is unknown, but they are presumed to arise from minor variations in the computational methods which were used, and are not considered to be significant.

In addition to the axial variations of the properties of the jet, some cross-stream variations are shown in Figure 88. This figure shows the real and imaginary parts of the eigensolution at one particular axial location ($x/r_o = 17$). This particular eigenfunction corresponds to an eigenvalue for an amplifying wave. Thus, for this case, as discussed in Appendix 2, no discontinuity is observed as the solution passes near the singular point.

3.6.3 Equations for the Acoustic Radiation

As indicated in the previous section, Tam's model visualizes two separate sources of acoustic radiation which are caused by the large-scale oscillation in a jet. The sum of these two sources (unsteady vibration and unsteady entrainment) is given by Tam as

$$\tilde{u}_s = -\frac{C}{\rho_o r_o} \frac{d}{dx} \left\{ \int_o^\infty \left[(\bar{\rho}\hat{u} + \hat{\rho}\bar{u}) + \frac{i\bar{\rho}\bar{u}}{\omega r_o} (\hat{V} - i\hat{w}) \right] r\, de \right\} e^{i(\alpha x + \phi - \omega t)} \tag{148}$$

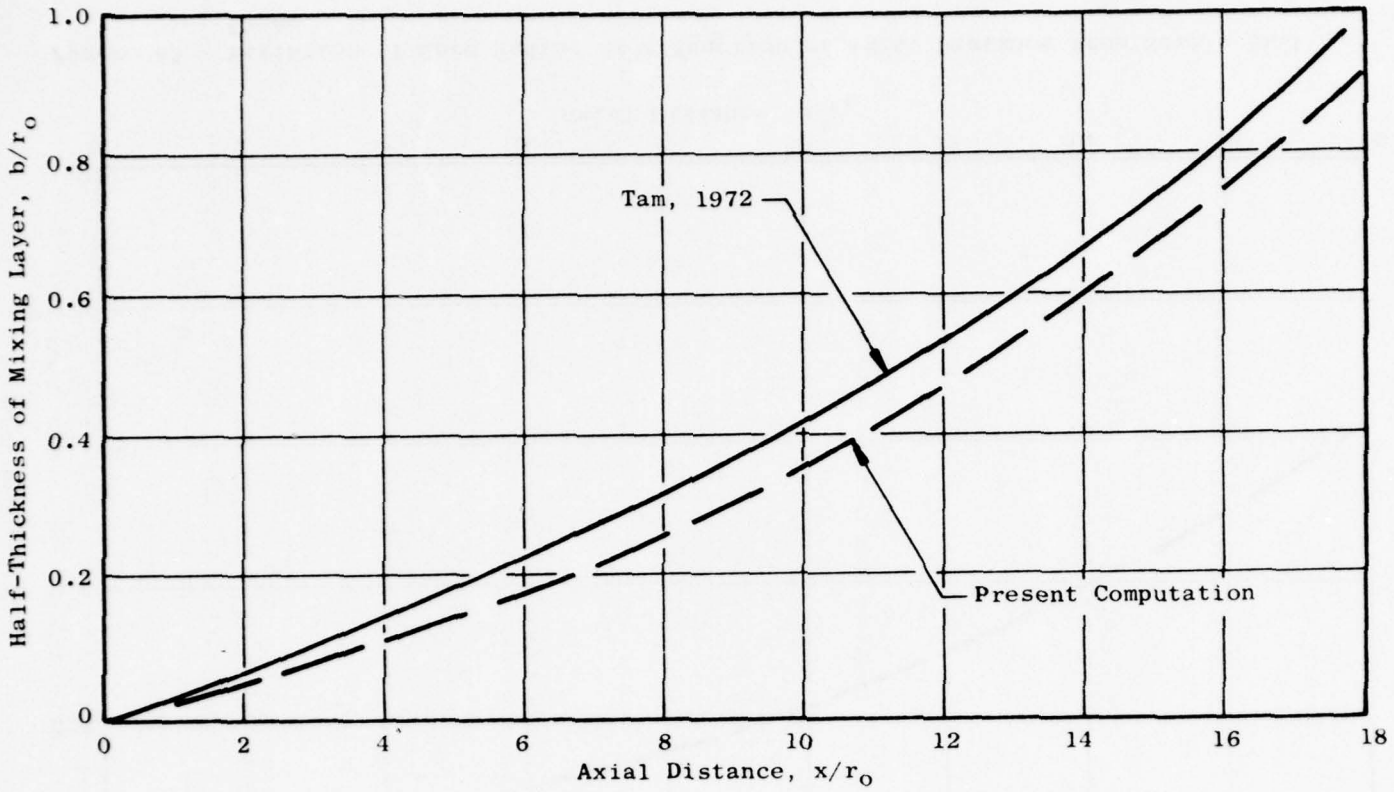


Figure 84. Variation of Half-Thickness of Mixing Layer with Distance from Nozzle Exit Plane.

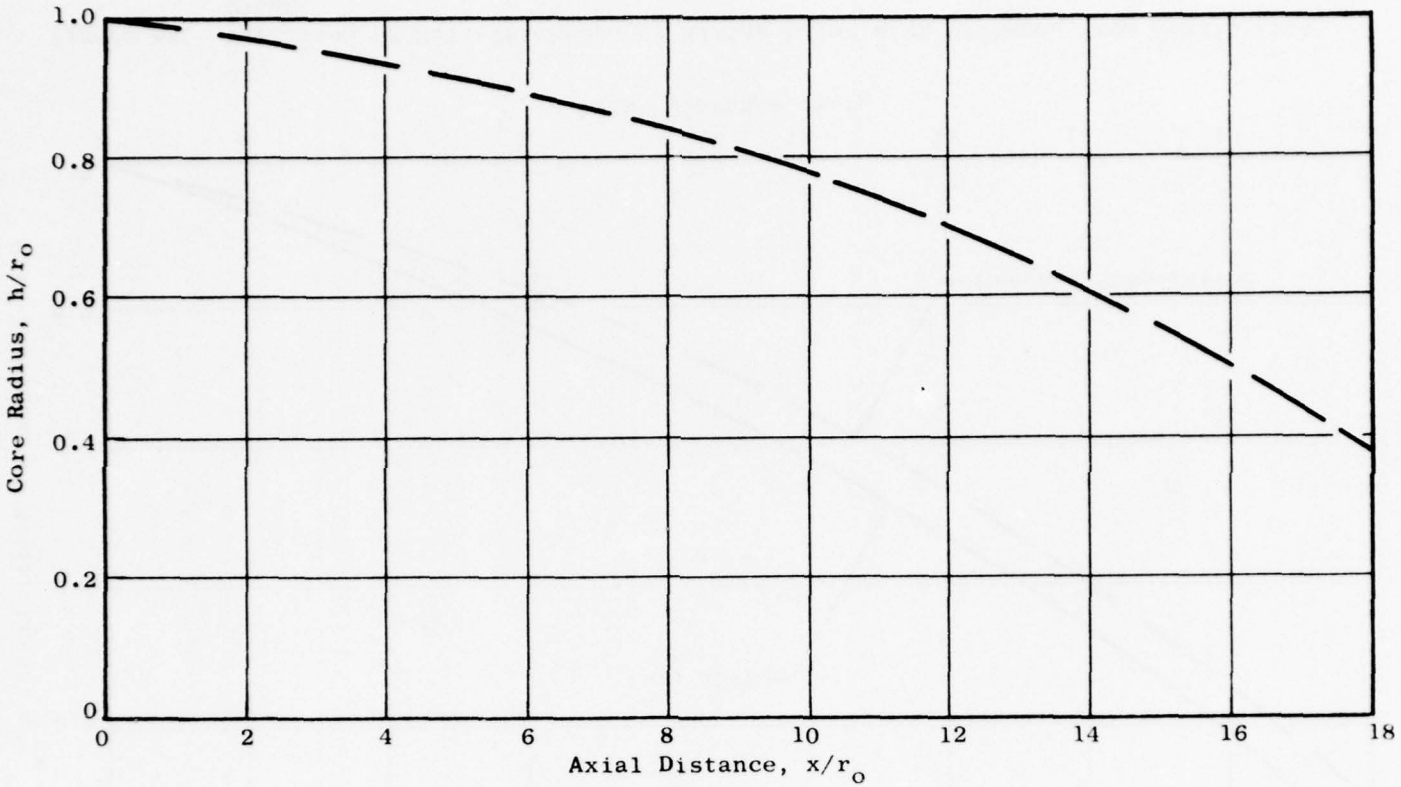


Figure 85. Variation of Core Radius as a Function of Axial Distance from Nozzle Exit Plane.

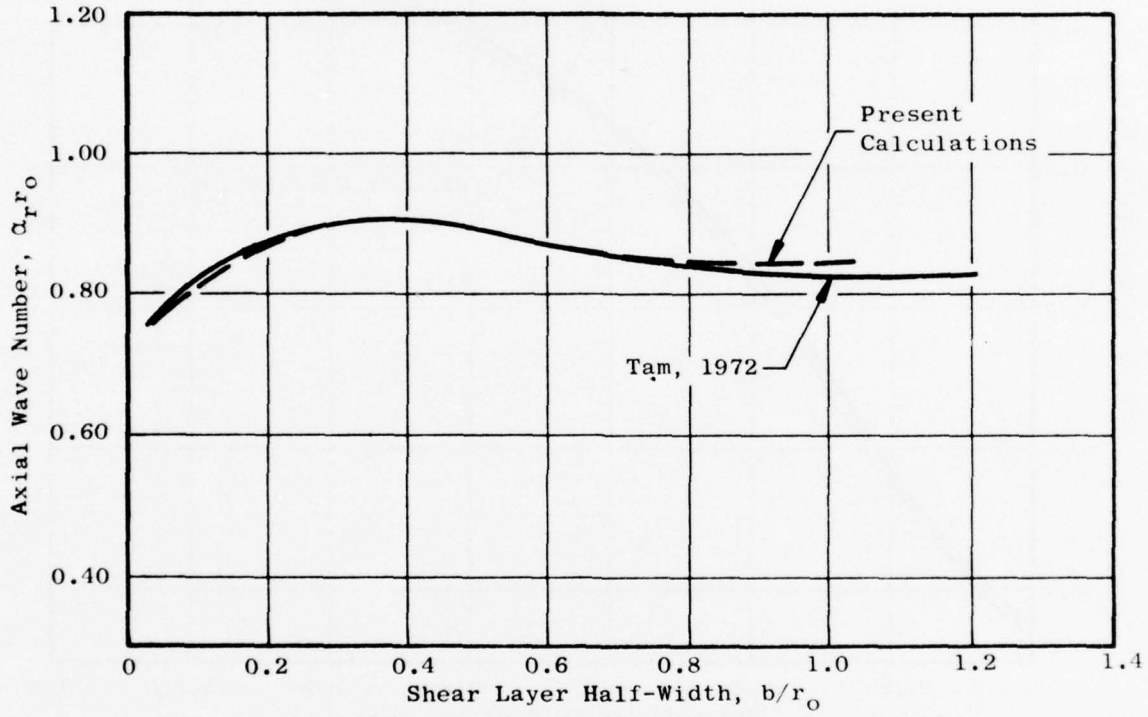


Figure 86. Wave Number of Large-Scale Oscillation as a Function of Half-Width of Shear Layer.

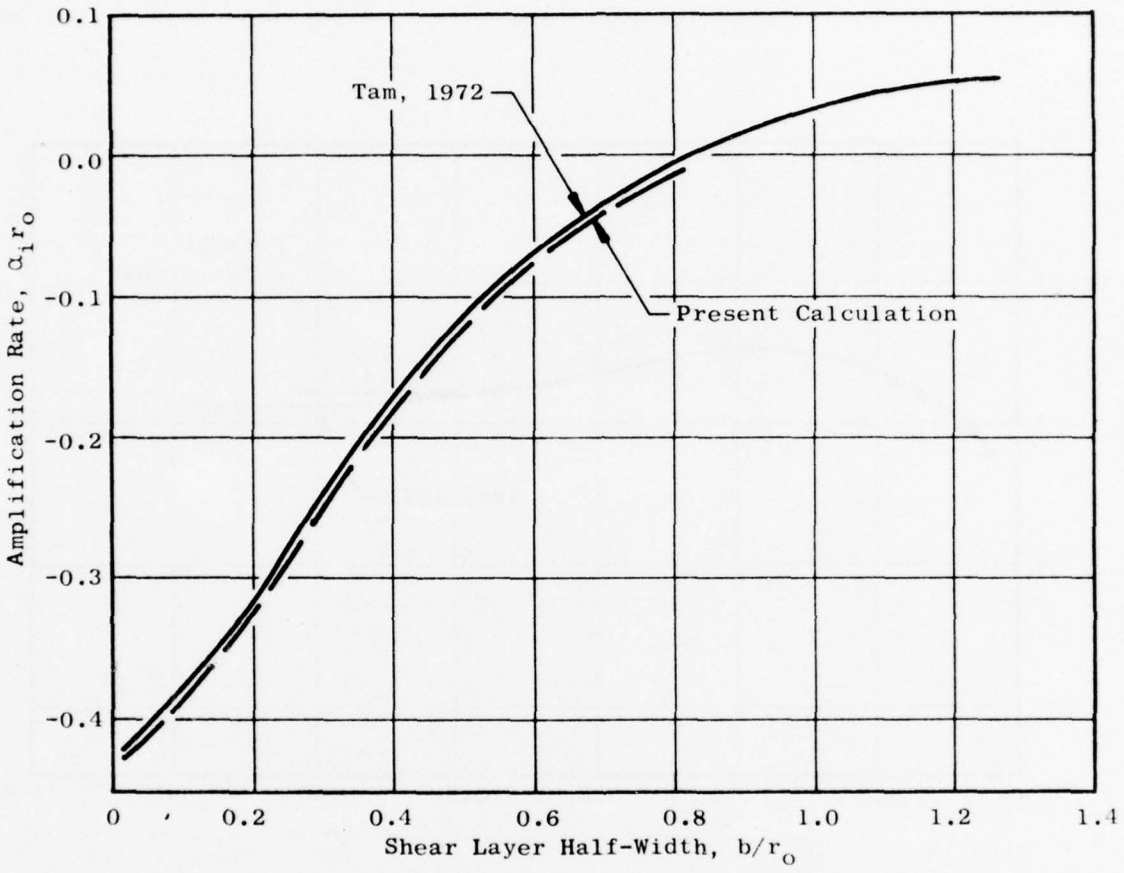


Figure 87. Amplification Rate of Large-Scale Oscillation as a Function of Half-Width of Shear Layer.

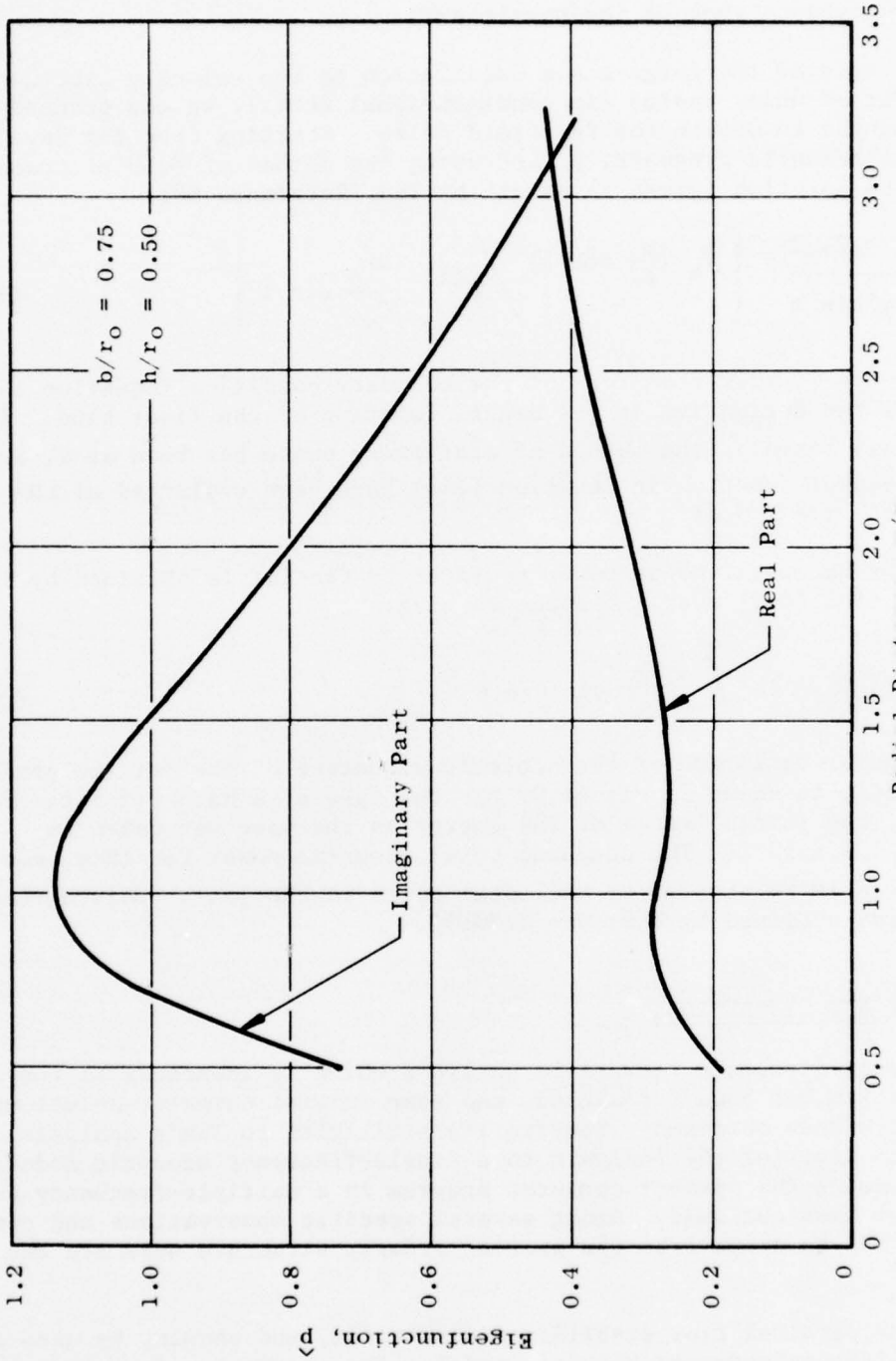


Figure 88. Real and Imaginary Parts of Eigenfunction in Region of Numerical Integration.

where C is the constant defined in Equation (111). This acoustic source term, v_s, represents the fluctuating v-component of velocity along a cylinder whose diameter is equal to that of the nozzle exit.

Having related the large-scale oscillation to the velocity fluctuation on a cylinder of unity radius (in nondimensional terms), we can proceed by standard methods to obtain the far-field noise. Starting from the wave equation for the acoustic pressure, p, and using the method of Fourier transforms, we obtain the solution (given in detail by Tam, Reference 80):

$$\langle p^2 \rangle = \frac{2\rho_o^2 a_o^2}{\gamma^2 \sin^2\phi} \left| \hat{V}_s \left(\frac{\omega}{a_o} \cos\phi\right) \Big/ H_1^{(1)} \frac{\omega r_o}{a_o} \sin\theta \right|^2 \qquad (149)$$

where $\hat{V}_s$ is the Fourier transform of the boundary condition (Equation 148), and $H_1^{(1)}$, is the derivative of the Hankel function of the first kind. In obtaining this formula, the method of stationary phase has been used, and both $\hat{V}_s$ and the Hankel function in Equation (149) have been evaluated at the stationary point, $z = \frac{\omega}{a_o} \cos\theta$.

Finally, the total noise power radiated by the jet is obtained by integrating Equation (149) over all space to give:

$$W = 2\pi \int_o^\pi \langle p^2 \rangle \sin\theta \, d\theta \qquad (150)$$

The angular variation of the acoustic signature of the jet, as predicted by Tam's model, is shown in Figure 89 for the case of a Mach 2.2 jet. For this calculation, the initial level of the energy in the wave was taken as $E_j/\rho_o u_j^3 r_j^2 = 2.0 \times 10^{-6}$. The computed total acoustic power for this case is W = 0.00160 (W is referenced to the total power in the jet). This agrees well with the value obtained by Tam: W = 0.00156.

3.7 SUMMARY AND CONCLUSIONS

An orderly structure flow field analysis which is identical to the one developed by Tam has been formulated, and some initial computer solutions of the model have been obtained. Despite its similarity to Tam's analysis, there is no need to restrict the analysis to a single-frequency acoustic model; methods for using the present computer program in a multiple-frequency acoustic analysis have been outlined. Among several specific observations and conclusions which may be drawn from the present orderly structure work are the following:

1. The parallel flow stability analysis can, and should, be used in a multiple-frequency acoustic model. The particular frequencies of interest should be chosen from those of maximum amplitude at each axial location.

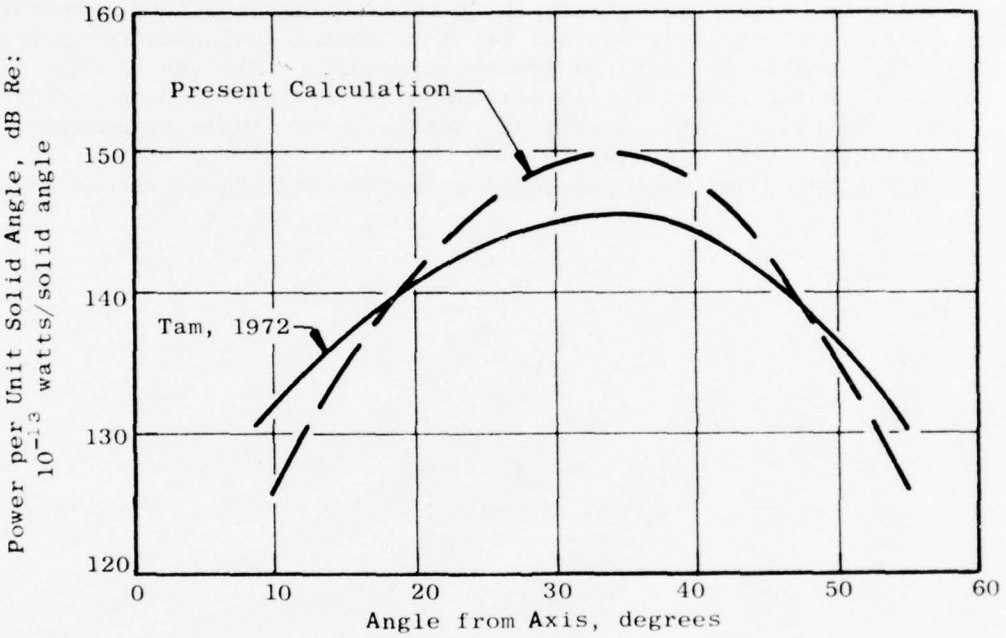


Figure 89. Directional Distribution of Acoustic Power.

2. It would be preferable to use the eigenfunction analysis in conjunction with an existing finite difference, mean-flow computer program, such as JETMIX, rather than using the integral model described herein. This would eliminate the necessity of optimizing the "constants" in the turbulence model for the integral method, and would also immediately provide a mean-flow field which is applicable to hot as well as cold jets.

3. In addition to coupling with an existing mean flow program, it is also recommended that the eigenfunction analysis be used in conjunction with the existing NOISE computer program. In this arrangement, the eigensolutions would be used to generate local acoustic sources at each point in the jet in a manner analogous to that presently used in our turbulence-acoustic model. The use of this existing computer program would allow a more accurate mathematical solution of the acoustic equations than the approximate technique outlined herein and, in addition, would be based on a simpler, more direct, and more palatable acoustic model than the one described by Tam.

APPENDIX 2

SOLUTION OF THE EIGENVALUE EQUATION IN THE REGION NEAR THE SINGULARITY

APPENDIX 2

SOLUTION OF THE EIGENVALUE EQUATION IN THE REGION NEAR THE SINGULARITY

The eigenvalue equation, as given in equation (113), is:

$$\frac{d^2\hat{p}}{dr^2} + \left[\frac{1}{r} - \frac{1}{\bar{\rho}}\frac{d\bar{p}}{dr} - \frac{2\alpha}{2}\frac{d\bar{u}}{dr}\right]\frac{d\hat{p}}{dr} + \left[\alpha^2\left(\frac{2\bar{p}}{\alpha\bar{p}\alpha^2} - 1\right) - \frac{1}{r^2}\right]\hat{p} = 0 \qquad (151)$$

where,

$$\lambda = \alpha\bar{u} - \omega \qquad (152)$$

As can be seen, equation (151) possesses a singularity at the location where the velocity, u, becomes equal to the ratio, ω/α. In addition, it can be shown that the ratio, ω/α, is always less than u , and greater than zero, so that this singularity occurs somewhere inside the jet (i.e., the singularity occurs within the region of interest). Further examination shows that so long as our integration path is real, the function λ (as defined by equation 152) does not vanish identically unless the wave number, α, is also purely real. Thus, at first glance, it appears that this singularity is of concern only in the isolated case for which the growth rate of the wave passes through zero. However, our analysis of the solution in the neighborhood of the singularity shows that a branch cut must be inserted at the singularity and that, as a result, considerable care must be taken when integrating past the singularity, even when it lies off the real axis. An analysis of the solution to equation (151) in the region near the critical point is given below.

Near the critical point, the coefficient which is singular can be expressed as:

$$\frac{2}{\lambda}\frac{du}{dz} = -\frac{2}{z-z_c} \qquad (153)$$

where we have replaced the radial coordinate, r, by the complex variable, z, and where z_c is the location of the critical point in the complex plane (at $z = z_c$, $u = \omega/\alpha$). We can also approximate the remaining variable coefficients in equation (1) by the constants:

$$A = \left[\frac{1}{z} - \frac{1}{\bar{\rho}}\frac{d\bar{p}}{dz}\right]\Bigg|_{z=z_c} \qquad (154)$$

and,

$$B = -\left(\alpha^2 + \frac{1}{z^2}\right)\Bigg|_{z=z_c} \qquad (155)$$

so that the eigenvalue equation becomes:

$$\frac{d^2\hat{p}}{dz^2} + \left(A - \frac{2}{z-z_c}\right) \frac{d\hat{p}}{dz} + B\hat{p} = 0 \tag{156}$$

Then, defining the new independent variable,

$$\zeta = z - z_c, \tag{157}$$

and using primes to denote differentiation with respect to ζ, we have:

$$\hat{p}'' + \left(A - \frac{z}{\zeta}\right) \hat{p}' + B\hat{p} = 0 \tag{158}$$

The solution of this equation can be readily obtained by the method of Frobenius. The procedure starts by assuming a solution of the form:

$$p = C_1 y_1 + C_2 y_2, \tag{159}$$

where,

$$y_1 = C_1 \zeta^3 \left[1 + a_1 \zeta + a_2 \zeta^2 + \ldots\right] \tag{160}$$

and,

$$y_2 = C_2 y_1, \ln \zeta + C_3 \left[1 + b_1 \zeta + b_2 \zeta^2 + \ldots\right] \tag{161}$$

Inserting equation into equation (158) and equating like powers of x to evaluate the unknown constants gives, to third order in ζ,

$$\hat{p} = C_1 \zeta^3 + C_2 \left[\zeta^3 \ln \zeta + \frac{3}{AB} \zeta - \frac{3}{2A} \zeta^2\right] \tag{162}$$

It is the presence of the logarithm in equation (162) which introduces the branch point in the solution. The decision as to which branch of the multiple-valued function, $\ln \zeta$, should be chosen can only be determined by considering the complete viscous stability theory. Lin[80] has shown that the proper choice for the branch cut is the one which allows a regular solution throughout the domain of integration in the amplified-wave case ($\alpha_i < 0$), but which requires the integration path to be deformed off the real axis and into the complex plane for the damped-wave case. This is shown schematically in Figure 80.

The practical implications of this are that the solution, p, must be required to be continuous if the wave is an amplified wave, but that it must be required to be discontinuous at the critical point for the damped-wave case. As stated in the main body of this Section (3.0), this was ensured in the numerical solutions by deforming the integration contour into the complex plane for the damped-wave cases.

CHAPTER II

AEROACOUSTIC INVESTIGATIONS FOR HIGH-VELOCITY, HIGH-TEMPERATURE JETS

The work described in Chapter II is directed toward two areas of concern. The first area of concern deals with the influence of upstream disturbances in jet exhaust noise, while the second area deals with a series of jet refraction experiments.

Section 1.0 of this chapter deals with disturbances which are of an aerodynamic nature (jet swirl, combustion roughness, and turbulence) produced by the physical obstruction of an afterburner section. The study treats the problem of swirl both analytically and experimentally. An outline of an analytical aerodynamic swirl model is given. Examples of an approximate aeroacoustic model are also given. The bulk of the work, however, concentrates on a series of experiments aimed at better understanding the influences of upstream aerodynamic disturbances on high-velocity and low-velocity heated jets. The investigation shows that upstream swirl does have a potential for reducing jet noise through the usual turbulent mixing process (however, at the expense of considerable aerodynamic performance losses). The results of a series of combustion roughness experiments indicated that combustion roughness by itself is not sufficient to raise the overall turbulent mixing noise. However, it was observed that for supersonic jet exhaust flows, there was an indication of low frequency noise amplification (perhaps combustion noise) due to the influence of the jet flow on the noise. This is somewhat supported by a series of findings in Section 2.0.

Section 2.0 discusses a series of refraction experiments aimed at experimentally defining the refractive properties of heated jets. The experiments are formulated around Ribner's concept of jet refraction. It is shown that, although at Mach numbers around 0.7, injected sound sources yield straightforward refraction patterns which are in agreement with classical acoustic predictions, at Mach numbers above or around 0.9, the jet can act as an amplifier of injected or internally generated low frequency noise. The mechanism appears to be the development of a columnar traveling instability wave. These results suggest that injected pure tone experiments may not be able to be used to gain an understanding of classical turbulent mixing noise in the high-Mach-number regime as was first thought.

SECTION 1.0

UPSTREAM DISTURBANCE INFLUENCES ON JET EXHAUST NOISE

M.A. Smith - P.R. Knott

1.1 BACKGROUND

One item which has received relatively little attention in jet noise studies is the influence on acoustic radiation of flow disturbances generated upstream of the nozzle exit. The disturbances considered here are those of an aerodynamic nature, in contrast to upstream-generated noise. In particular, the present study is directed toward understanding the influence of upstream-generated turbulence fluctuations and swirl on classical turbulent mixing jet noise.

During the first phase of the AF/DOT Supersonic Jet Exhaust Noise Program, an aeroacoustic model was developed at General Electric which linked a detailed turbulent mixing analysis with a jet aerodynamic noise generation model. Predictions showed that, by increasing the nozzle exit plane turbulence levels, higher levels of jet noise would result. These findings led to a series of tests performed during the FAA/DOT Core Engine Noise Program in which upstream turbulence was increased through the use of physical obstructions. These tests essentially corroborated the analytical predictions. Further exploration into the influence of upstream disturbances was carried out in the present program. This time, however, the emphasis was placed on flow disturbances which are most representative of those likely to occur in the operation of a gas turbine engine. Specifically, the following phenomena were considered:

- Swirl produced by rotating turbomachinery or stationary swirl vanes
- Turbulence produced by rough combustion process
- Turbulence produced by the physical obstructions (flameholders, spraybars) in an afterburner

This study included both experimentation and turbulent mixing analysis.

As was expected, the jet noise radiation pattern was significantly altered in the presence of swirl. There were reductions in overall sound pressure levels, due to low frequency suppression, near the jet axis. However, the reductions in perceived noise levels (PNdB) were not as large since the low frequency suppression is coupled with some increases in high frequency noise. It was also shown that substantial thrust losses would be incurred by a swirling jet. The results of the combustion roughness and afterburner flameholder/spraybar experiments were not as clear. The major reason for this was that neither increasing combustion roughness nor removing the test facility afterburner hardware changed the level of nozzle exit plane turbulence to a

significant degree. However, increases in low frequency noise were observed, even at the elevated temperatures and velocities of a supersonic jet. This low frequency noise is thought to be combustion noise which is amplified while propagating through the exhaust plume.

In addition to a series of detailed experiments, an analytical study of the aeroacoustic properties of swirling jets is also described below. The results of an analytical study of turbulence production in mixing processes are also presented in Section 1.3.1. The combustion roughness and afterburner flameholder/spraybar experiments are described in Sections 1.3.2 and 1.3.3, respectively. The overall results of this study are then summarized briefly in Section 1.4.

1.2 INFLUENCE OF UPSTREAM SWIRL ON JET NOISE GENERATION

An axisymmetric swirling jet is characterized by a helical flow pattern, resulting from a nonzero distribution of tangential velocity components in addition to the axial and radial components present in nonswirling jets. The swirling motion is created upstream of the nozzle exit by the action of rotating turbomachinery, swirl vanes, or tangential fluid injection. Experimental studies (101-105) have shown that the introduction of swirl has a considerable effect on the mixing processes in a turbulent jet. Increases in jet width, rate of mass entrainment, and rate of velocity decay are seen to accompany increases in the degree of swirl. Additionally, the presence of tangential velocity components results in the establishment of radial and axial pressure gradients which, for the case of strong swirl, can cause reverse flow in the central region of the jet.

It is to be expected that phenomena such as chemical reaction (combustion) and aerodynamic noise generation, which are strongly dependent on the structure of the jet flow field, will be significantly affected by the presence of swirl. Experimental studies of jet diffusion flames (106,107) and premixed flames (108) have shown that the introduction of swirl to the flow results in shorter, wider flames with increased combustion intensity and improved stability. Thus, swirling flows have found wide application in combustion chambers and burners as a means of flow stabilization and control. Based on his experimental observations, that swirling-flow burning results in less intense fluctuations and pulsations in the flow and a lower noise level than "straight-flow" burning, Schwartz (108) proposed the use of swirl as a means of suppressing jet noise. In Reference (109), he reported the results of an experiment in which stationary swirl vanes were installed in the primary exhaust nozzle of a small turbofan engine (JT15D-1). A 2- to 3-dB reduction in overall sound power level was obtained by swirling the primary jet, as compared to the nonswirling jet exhaust.

Reductions in jet noise that are obtained through the use of a particular suppression concept must be carefully balanced against any associated performance penalties. In the case of swirl, there is some question as to how it is possible to avoid severe thrust losses with any significant degree of swirl in the exhaust flow. Recall that gross thrust is given by:

$$F_G = \int_{A_e} (\rho u^2 + P - P_\infty)\, dA \qquad (163)$$

where:

A_e = nozzle exit area
P = static pressure
P_∞ = ambient pressure
u = axial velocity
ρ = density

It is obvious from equation (163) that the low static pressure found in the center of a swirling jet (due to the radial momentum balance) is one source of thrust loss. Another loss is associated with the existence of a tangential component of momentum, since only axial momentum contributes to thrust. Experiments have shown that mass flow (110) and thrust (111) are both reduced substantially in swirling flows.

The present investigation included both analytical and experimental studies of the aeroacoustic properties of swirling jets, as described in the following sections.

1.2.1 Analytical Aerodynamic Swirl Model

An axisymmetric swirling jet possesses a circumferential, or rotational, component of velocity, but is symmetric with respect to the axis of rotation. Thus, although the flow is three-dimensional, analysis can be accomplished using existing two-dimensional computational methods. In the case of low to moderate swirl, where adverse axial pressure gradients are not severe enough to cause reverse (recirculating) flow, the boundary layer approximations are valid and can be used to simplify the mean-flow equations of motion. For the steady, axisymmetric, compressible, turbulent flow of a perfect gas with constant specific heat, the mean-flow equations reduce to:

Continuity

$$\frac{\partial}{\partial x}(\rho u r) + \frac{\partial}{\partial r}(\rho v r) = 0 \qquad (164)$$

Axial Momentum

$$\rho u \frac{\partial u}{\partial x} + \rho v \frac{\partial u}{\partial r} = \frac{1}{r}\frac{\partial}{\partial r}(r \tau_{rx}) - \frac{\partial p}{\partial x} \qquad (165)$$

Radial Momentum

$$-\rho r \left(\frac{w}{r}\right)^2 = -\frac{\partial p}{\partial r} \qquad (166)$$

Tangential Momentum

$$\rho u r \frac{\partial}{\partial x}\left(\frac{w}{r}\right) + \rho v r \frac{\partial}{\partial r}\left(\frac{w}{r}\right) = \frac{1}{r^2} \frac{\partial}{\partial r}\left(r^2 \tau_{r\phi}\right) - 2\rho v \left(\frac{w}{r}\right) \tag{167}$$

Energy

$$\rho u c_p \frac{\partial T}{\partial x} + \rho v c_p \frac{\partial T}{\partial r} = -\frac{1}{r}\frac{\partial}{\partial r}\left(r q_r\right) + \tau_{rx}\left(\frac{\partial u}{\partial r}\right) + \tau_{r\phi} r \frac{\partial}{\partial r}\left(\frac{w}{r}\right) + u \frac{\partial p}{\partial x} + v \frac{\partial p}{\partial x} \tag{168}$$

State

$$p = \rho R_G T \tag{169}$$

Note that application of the boundary layer approximations does not eliminate the radial and tangential momentum equations as in the case of nonswirling flow. The radial momentum equation (166) represents the balance of centrifugal force against the radial pressure gradient. The tangential momentum equation (167) represents the balance of convection of tangential momentum by the mean flow and of diffusion by the action of shear stresses. Also, the energy equation (168) includes additional terms to reflect the presence of the shear stress $\tau_{r\phi}$ and the radial pressure gradient. The shear stress (momentum flux) and heat flux terms in equations (165) through (168) represent the effects of both laminar (molecular) diffusion and turbulent transport processes, although molecular diffusion generally can be neglected in free turbulent flows. Thus:

$$\tau_{rx} = \mu \frac{\partial u}{\partial r} - \rho\overline{u'v'} \approx -\rho\overline{u'v'} \tag{170}$$

$$\tau_{r\phi} = \mu r \frac{\partial}{\partial r}\left(\frac{w}{r}\right) - \rho\overline{w'v'} \approx -\rho\overline{w'v'} \tag{171}$$

$$q_r = -k \frac{\partial t}{\partial r} + \rho c_p \overline{T'v'} \approx \rho c_p \overline{T'v'} \tag{172}$$

The nomenclature used in equations (164) through (172) is defined by:

c_p = specific heat at constant pressure
k = thermal conductivity
P = mean static pressure
R_G = gas constant

T = mean static temperature
T' = fluctuating static temperature
x,r,ϕ = axial, radial, and tangential coordinates
u,v,w = axial, radial, and tangential components of mean velocity
u',v',w' = axial, radial, and tangential components of fluctuating velocity
μ = viscosity
ρ = mean density

Equations (164) through (169), in combination with the definitions given by equations (170) through (172), form a system of six equations with nine unknowns:

- mean flow variables (u,v,w,P,T,ρ)
- statistical correlations of turbulent fluctuations $(\overline{u'v'},\overline{w'v'},\overline{T'v'})$

In order to close the system of equations, it is necessary to formulate models of the turbulence correlations in terms of the mean flow variables and other quantities which can be readily determined.

Historically, the development of "turbulence models" can be traced to Boussinesq (Reference 112), who suggested, in 1877, that the turbulent (Reynolds) stress in two-dimensional nonswirling flow could be represented in the same form as the laminar shear stress:

$$-\rho\overline{u'v'} = \mu_t \frac{\partial u}{\partial y} \tag{173}$$

with an "eddy" or "turbulent" viscosity (μ_t) determined at each point in the flow field as a function of the local structure of turbulence. This approach is convenient in that it allows turbulent flows to be calculated using analytical techniques already established for laminar flows. However, if it is to yield meaningful results, a reliable model must be established for the eddy viscosity. One of the earliest attempts to formulate such a model was the mixing length concept introduced by Prandtl (113). He proposed that the eddy viscosity be expressed as:

$$\mu_t = \rho\, \ell_m^2 \left|\frac{\partial u}{\partial y}\right| \tag{174}$$

where the mixing length (ℓ_m) is a characteristic length scale of the local turbulent motion, to be prescribed algebraically. A further development was Prandtl's (114) proposal of a differential model in which the eddy viscosity is represented as:

$$\mu_t = c_\mu \rho \sqrt{e}\, \ell \tag{175}$$

where c_μ is a constant, ℓ is the turbulent length scale, and (e) is the mean kinetic energy per unit mass of the motion in the turbulent eddies:

$$e = \frac{1}{2}\left(\overline{u'^2} + \overline{v'^2} + \overline{w'^2}\right) \tag{176}$$

In this model, the length scale is prescribed algebraically, but the turbulent kinetic energy is determined from the solution of a differential conservation equation. A similar formulation was adopted by Kolmogorov (115), except that he determined two turbulence properties (e and $\sqrt{e}/\ell$) from differential equations. The differential turbulence models are more representative of real flow processes than algebraic models, since the turbulent shear stress at a point depends on the upstream history of the flow as well as the local mean-flow properties. Over a period of several years, many different turbulence models have been proposed. These range from the simple algebraic models to complex, multiequation differential models. A systematic review of existing turbulence models (as of 1972) is given in Reference 116, and the predictions of several models are compared against a standard set of test data in Reference 117.

At General Electric, an analysis of nonswirling compressible turbulent jets has been developed based on Prandtl's one-equation differential model as utilized by Glushko [4] and Spalding [118]. This analysis (Reference 6), which is incorporated in the JETMIX computer program, is used to predict jet plume aerodynamic properties required for the calculation of jet noise (References 10 and 119) and infrared radiation characteristics.

Turbulence models for swirling jets parallel those for nonswirling jets, although there is an additional shear stress ($-\rho\overline{w'v'}$) to be considered. However, it is only within the past five years that turbulence models for swirling flows have appeared in the literature. These include algebraic models [107,120,121], as well as two-equation [122] and multiequation [123] differential models. At General Electric, the JETMIX analysis, with its one-equation turbulence model, was "expanded" to accommodate swirling flows as part of an Army-sponsored investigation of the suppression of infrared radiation in turboshaft engine exhaust plumes (DAAJ02-73-C-0048, to be published). The analysis is described in the following section.

1.2.1.1 Description of the Model

The axisymmetric, swirling, turbulent jet is analyzed using the boundary layer form of the mean-flow conservation equations, as expressed in equations (164) through (169). Following Boussinesq, each momentum and heat flux term is expressed as the product of a turbulent transport coefficient and the relevant mean-flow property gradient:

$$\tau_{rx} = \mu_{rx} \frac{\partial u}{\partial r} \tag{177}$$

$$\tau_{r\phi} = \mu_{r\phi}\, r \frac{\partial}{\partial r}\left(\frac{w}{r}\right) \tag{178}$$

$$q_r = -\, k_r \frac{\partial T}{\partial r} \tag{179}$$

The quantities μ_{rx} and $\mu_{r\phi}$ are eddy viscosities, and k_r is an eddy conductivity. In an analysis of the data reported in Reference 104, Lilley and Chigier [124] showed that the turbulent shear stress distribution in a swirling jet is nonisotropic. Thus, two distinct eddy viscosities are defined, one corresponding to each shear stress component.

The eddy viscosity (μ_{rx}) is determined from the same basic relationship as is used for a nonswirling jet:

$$\mu_{rx} = c_\mu \rho \sqrt{e}\, \ell \tag{180}$$

The eddy conductivity (k_r) is also determined from the same relationship as in a nonswirling jet:

$$k_r = \frac{\mu_{rx} c_p}{Pr_t} \tag{181}$$

where the turbulent Prandtl number (Pr_t) is assumed to be a constant. It is also assumed, for the purposes of this analysis, that the two eddy viscosities can be related algebraically as:

$$\mu_{r\phi} = \mu_{rx}/\sigma_{r\phi} \tag{182}$$

where the quantity $\sigma_{r\phi}$ is an empirical function of the swirl number (S):

$$S = G_\phi/G_x R_e \tag{183}$$

The nondimensional swirl number is a convenient expression for characterizing the degree, or strength, of swirl. It is a function of the axial flux of linear momentum (G_x), the axial flux of angular momentum (G_ϕ), and the nozzle exit radius (R_e). For a jet emerging into undisturbed (stagnant) surroundings:

$$G_x = 2\pi \int_0^\infty (\rho u^2 + P - P_\infty)\, r\, dr \tag{184}$$

$$G_\phi = 2\pi \int_0^\infty \rho u w r^2\, dr \tag{185}$$

The final step in establishing the "framework" of the turbulence model is the formulation of equations for the determination of turbulent kinetic energy (e) and turbulent length scale (ℓ). As in the case of the nonswirling jet, the turbulent length scale is prescribed algebraically. However, the formulation has been revised to include an empirical dependence on swirl number. Turbulent kinetic energy (TKE) is determined from a semiempirical conservation equation. The exact form of the equation can be derived from the complete Navier-Stokes equations by multiplying each component of the momentum equation by the corresponding fluctuating velocity component, time- be grouped into four categories, depending on the nature of their contributions:

- Convection of TKE by the mean flow
- Diffusion of TKE by the action of turbulent fluctuations
- Conversion of mechanical energy to TKE (or, production of TKE) by the action of turbulent stresses working against the mean velocity gradients
- Conversion of TKE to thermal energy (or, dissipation of TKE) by the action of viscosity

The diffusion and dissipation terms contain additional unknown turbulence properties (statistical correlations involving velocity and pressure fluctuations) which must be approximated in terms of quantities that are known or can be determined. The final form of the equation is:

$$\underbrace{\rho u \frac{\partial e}{\partial x} + \rho v \frac{\partial e}{\partial r}}_{\text{convection}} = \underbrace{\frac{1}{r}\frac{\partial}{\partial r}\left(r \frac{\mu_{rx}}{\sigma_e}\frac{\partial e}{\partial r}\right)}_{\text{diffusion}}$$

$$\underbrace{+ \mu_{rx}\left(\frac{\partial u}{\partial r}\right)^2 + \mu_{r\phi}\, r^2 \left[\frac{\partial}{\partial r}\left(\frac{w}{r}\right)\right]^2}_{\text{production}} \underbrace{- C_D \rho \frac{e}{\ell}^{3/2}}_{\text{dissipation}} \qquad (186)$$

where σ_e and C_D (as well as $\sigma_{r\phi}$ and ℓ) are empirically determined functions of swirl number (From an Army sponsored Contract DAAJ02-73-C-0048, to be published). The effects of swirl are seen in the presence of a production term involving radial gradients of the tangential velocity, and in the functional dependence of σ_e and C_D, which are constants in the case of non-swirling flow. One probable reason for the enhanced mixing in swirling flows is an increased level of turbulence, as reflected by the additional production term in equation (186).

It should be noted that the thermal energy equation (168) is not consistent with equation (186) in the treatment of turbulent kinetic energy. This is because the TKE, being a relatively small quantity, is generally neglected in the definition of total energy (e_t):

$$de_t = c_v dT + d\left(\frac{u^2}{2} + \frac{v^2}{2} + \frac{w^2}{2}\right) + de \qquad (187)$$

Thus, the thermal-energy equation, formed by subtracting the mechanical-energy equation from the total-energy equation, has TKE "buried" in it. This is satisfactory for algebraic turbulence models, since TKE does not enter into these analyses. However, differential turbulence models treat TKE as a distinct quantity, and to be strictly accurate, the thermal energy equation must reflect this. Physically speaking, we can say that equation (168) assumes the direct conversion of mechanical energy to thermal energy in the

process of dissipation, while equation (186) reflects the concept of TKE as an intermediate state. Using this line of reasoning, the thermal energy equation would be "corrected" by replacing the mechanical dissipation term (or terms) with the turbulence dissipation term ($C_D \rho e^{3/2}/\ell$) to reflect the lag in energy conversion due to energy storage in the motion of the turbulent eddies. Analysis of the detailed revisions that must be made to the energy equation confirms that this is the net result. Thus, the thermal energy equation is properly expressed as:

$$\rho u c_p \frac{\partial T}{\partial x} + \rho v c_p \frac{\partial T}{\partial r} = -\frac{1}{r}\frac{\partial}{\partial r}(r\, q_r) + u\frac{\partial p}{\partial x} + v\frac{\partial p}{\partial r} + C_D\, \rho \frac{e^{3/2}}{\ell} \tag{188}$$

Equations (164) through (167), (186), and (188) can be expressed in more convenient form by introducing the following dimensionless variables:

$$X = \frac{x}{d_j}\,, \quad R = \frac{2r}{d_j}$$
$$U = \frac{u}{u_j}\,, \quad V = \frac{v}{u_j}\,, \quad W = \frac{w}{u_j} \tag{189}$$
$$E = \frac{e}{e_j}\,, \quad \Theta = \frac{T}{T_j}$$

where d_j is the initial jet diameter, and u_j, e_j, and T_j are the initial values of axial velocity, turbulence energy, and static temperature, respectively.

In terms of the new variables, the continuity equation (164) is expressed as:

$$\frac{\partial}{\partial x}(\rho UR) + 2\frac{\partial}{\partial R}(\rho VR) = 0 \tag{190}$$

This equation is identically satisfied by the stream function (Ψ), defined as:

$$\frac{\partial \Psi}{\partial R} = \frac{1}{2}\rho UR$$
$$\frac{\partial \Psi}{\partial x} = -\rho VR \tag{191}$$

Thus, the continuity equation is eliminated from the system of equations by use of the Von Mises transformation, which introduces the new independent variables ξ and Ψ:

$$\xi = X, \quad \Psi = \Psi\ (X,R) \tag{192}$$

Using the chain rule, the differential operators are defined:

$$\frac{\partial}{\partial x} = \frac{\partial}{\partial \xi} - \rho VR \frac{\partial}{\partial \Psi}$$
$$\frac{\partial}{\partial R} = \frac{1}{2} \rho UR \frac{\partial}{\partial \Psi} \tag{193}$$

The final set of partial differential equations is then expressed as:

Axial Momentum

$$\frac{\partial U}{\partial X} = \frac{1}{u_j d_j} \frac{\partial}{\partial \Psi} \left(\mu_{rx} \rho UR^2 \frac{\partial U}{\partial \Psi} \right) - \frac{1}{\rho u_j{}^2 U} \frac{\partial P}{\partial X} + \frac{RV}{u_j{}^2 U} \frac{\partial P}{\partial \Psi} \tag{194}$$

Radial Momentum

$$\frac{\partial P}{\partial \Psi} = \frac{2 u_j{}^2 \Omega^2}{U} \tag{195}$$

Tangential Momentum

$$\frac{\partial \Omega}{\partial X} = \frac{1}{u_j d_j R^2} \frac{\partial}{\partial \Psi} \left(\mu_{r\phi} \rho UR^4 \frac{\partial \Omega}{\partial \Psi} \right) - \frac{4V}{RU} \Omega \tag{196}$$

Energy

$$\frac{\partial \Theta}{\partial X} = \frac{1}{u_j d_j} \frac{\partial}{\partial \Psi} \left(\frac{\mu_{rx}}{Pr_t} \rho UR^2 \frac{\partial \Theta}{\partial \Psi} \right) + \frac{1}{\rho c_p T_j} \frac{\partial P}{\partial X} + \frac{C_D d_j e_j \mu_{rx} E}{C_\mu \rho c_p T_j u_j U \ell^2} \tag{197}$$

Turbulent Kinetic Energy

$$\frac{\partial E}{\partial X} = \frac{1}{u_j d_j} \frac{\partial}{\partial \Psi} \left(\frac{\mu_{rx}}{\sigma_e} \rho UR^2 \frac{\partial E}{\partial \Psi} \right) - \frac{C_D d_j \mu_{rx}}{C_\mu \rho u_j U \ell^2} (E) + \frac{u_j \mu_{rx}}{d_j e_j} \rho UR^2 \left(\frac{\partial U}{\partial \Psi} \right)^2 + \frac{u_j \mu_{r\phi}}{d_j e_j} \rho UR^4 \left(\frac{\partial \Omega}{\partial \Psi} \right)^2 \tag{198}$$

where the variable ξ has been designated as X, and the dimensionless angular velocity (Ω):

$$\Omega = \frac{W}{R} \tag{199}$$

has been introduced. The physical coordinate R can be recovered by integration of the first of equations (191). Assuming that $\Psi = 0$ at $R = 0$, it is given by:

$$R^2 = 4 \int_o^{\Psi} \frac{d\Psi}{\rho U} \tag{200}$$

The velocity ratio (V/U) can be determined from equations (193) as:

$$\frac{V}{U} = \frac{1}{2} \frac{\partial R}{\partial X} \Big|_{\Psi = \text{constant}} \tag{201}$$

The initial and boundary conditions for the solution of equations (194) through (198) are:

$$\begin{aligned} &X = 0: \quad U = \Theta = E = 1, \ \Omega = \Omega_j(\Psi) \\ &\Psi = 0: \quad \frac{\partial U}{\partial \Psi} = \frac{\partial \Theta}{\partial \Psi} = \frac{\partial E}{\partial \Psi} = \frac{\partial \Omega}{\partial \Psi} = 0 \\ &\Psi = \Psi_{edge}: \quad U = U_{ex}, \ \Theta = \Theta_{ex}, \ E = E_{ex}, \ \Omega = \Omega_{ex}, \ P = P_{ex} \end{aligned} \tag{202}$$

where the subscript (ex) denotes values in the external stream.

The partial differential equations (194) through (198) are all of the general diffusion equation form:

$$\frac{\partial F}{\partial X} = \alpha \frac{\partial}{\partial \Psi} \left(\beta \frac{\partial F}{\partial \Psi} \right) + \gamma + \delta F + \eta \frac{\partial F}{\partial \Psi} \tag{203}$$

where the coefficients $\alpha, \beta, \gamma, \delta$, and η may be functions of the independent variables X and Ψ, and of the dependent variable F. Since this equation is mathematically parabolic, a solution can be obtained numerically by the use of a "marching" procedure in which the solution propagates downstream step-by-step through a series of "computation planes" stretching across the jet flow field. The individual equations are solved numerically, in sequential order, at each successive computation plane. The order of solution, based on considerations of the coupling between equations, is:

- Axial momentum (solved for U)
- Tangential momentum (Ω)
- Radial momentum (P)
- Turbulent kinetic energy (E)
- Energy (θ)

The second-order equations (194), (196), (197), and (198) are expressed in finite difference form at discrete grid points (X,Ψ) on each computation plane. An implicit formulation is used, so that each partial differential equation is represented on a given plane as a set of simultaneous linear

algebraic equations for the values of the dependent variable at the cross-stream grid points. The system is characterized by a tri-diagonal coefficient matrix and can be solved efficiently by direct elimination techniques. The radial momentum equation (195) is solved directly by numerical integration across the computation plane (X = constant).

The mean flow equations of motion, as simplified by application of the boundary layer approximations, describe the flow in the thin annular mixing layer (Figure 90) formed at the boundary between the emerging jet and the surrounding fluid. The width of this region increases downstream of the nozzle exit until it encompasses the entire jet. The region "inside" the mixing layer, referred to as the potential core, is composed entirely of fluid discharged from the nozzle. While this is not a boundary layer flow regime, it can be represented as such, within a close approximation, in the case of an ideally expanded jet since all gradients are small and the flow remains essentially uniform. This allows a consistent formulation to be used throughout the jet flow field.

1.2.1.2 Aero Acoustic Predictions

The JETSWRL computer program was developed by modification of JETMIX to incorporate the swirl analysis described in the preceding section. The empirical algebraic models of turbulent length scale (ℓ) and the quantities $\sigma_{r\phi}$, σ_e, and C_D, as functions of swirl number, were developed from comparisons of analytical predictions with the test data reported in Reference 104. These data include measurements of mean axial swirl velocities, static pressure, and jet width for low Mach number, isothermal turbulent jets at swirl numbers ranging from 0 to 0.64.

The aerodynamic analysis has been found to give good agreement with data for moderate swirl (S ~ 0.4) and for nonswirling jets. This is illustrated by Figure 91, which shows the predicted centerline decay of mean axial velocity for these two cases compared with the corresponding data from Reference 104.

In order to predict the effect of swirl on jet noise, JETSWRL was coupled with the General Electric jet aerodynamic noise analysis (References 110 and 119), which is incorporated in the NOISE computer program. In this analysis, the jet flow field is divided into a series of small circular ring volume elements. Each volume is considered to be an independent sound generator which emits an amount of acoustic power at a certain frequency. The acoustic characteristics associated with each element are determined from the local mean flow and turbulence properties (ρ,u,u',ℓ). The overall jet acoustic characteristics are then determined by a combination of the individual source terms.

Figures 92 through 95 show the predicted effects of swirl on the aerodynamic and acoustic properties of an isothermal subsonic (M_j = 0.8) jet with 2% initial turbulence intensity. Figure 92 shows the mean axial velocity

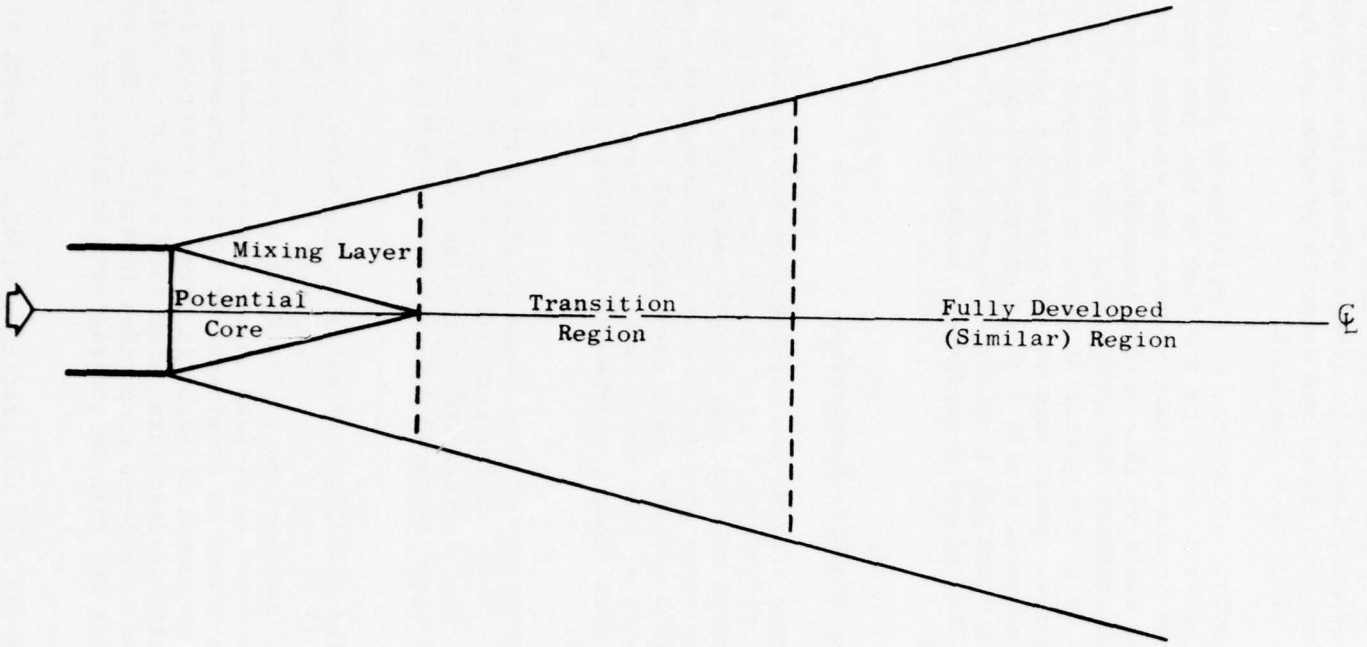


Figure 90. Axisymmetric Turbulent Jet Flow Field.

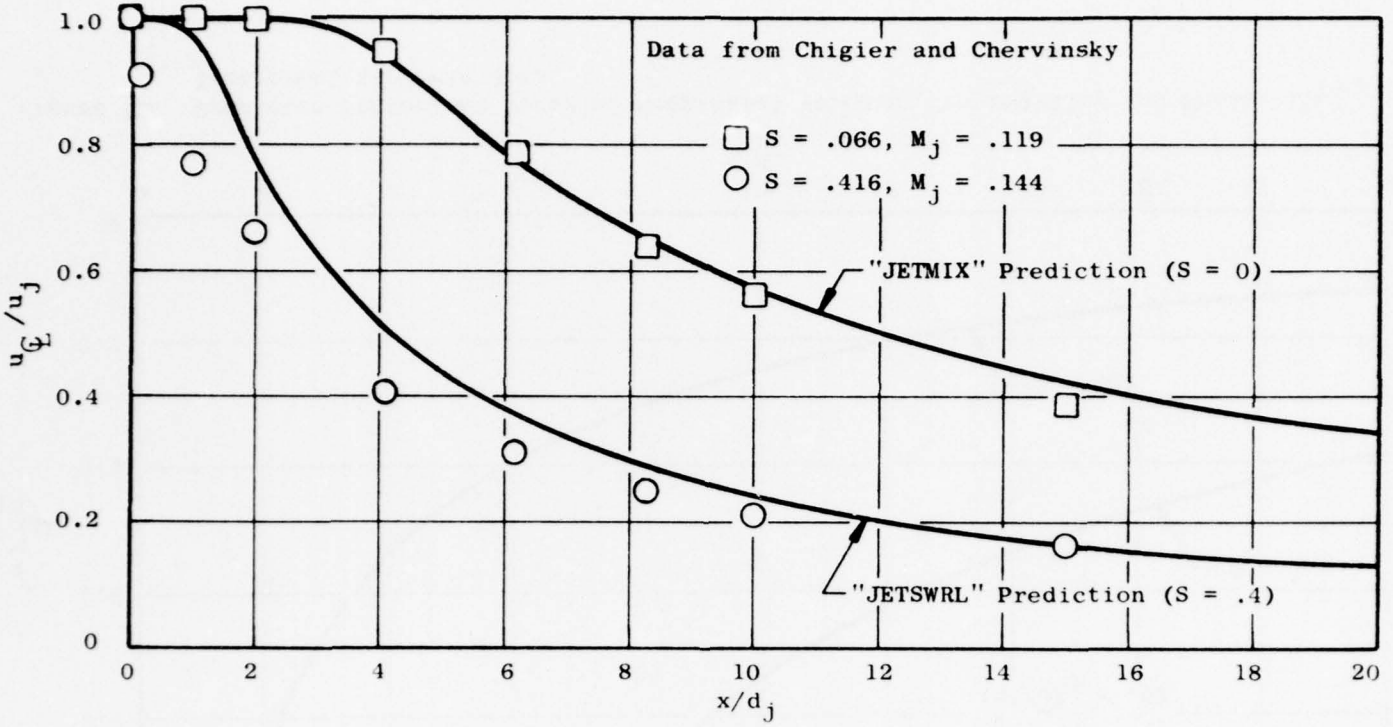


Figure 91. Comparison of Predicted and Measured Centerline Decay of Mean Axial Velocity for Swirling Isothermal Subsonic Jets.

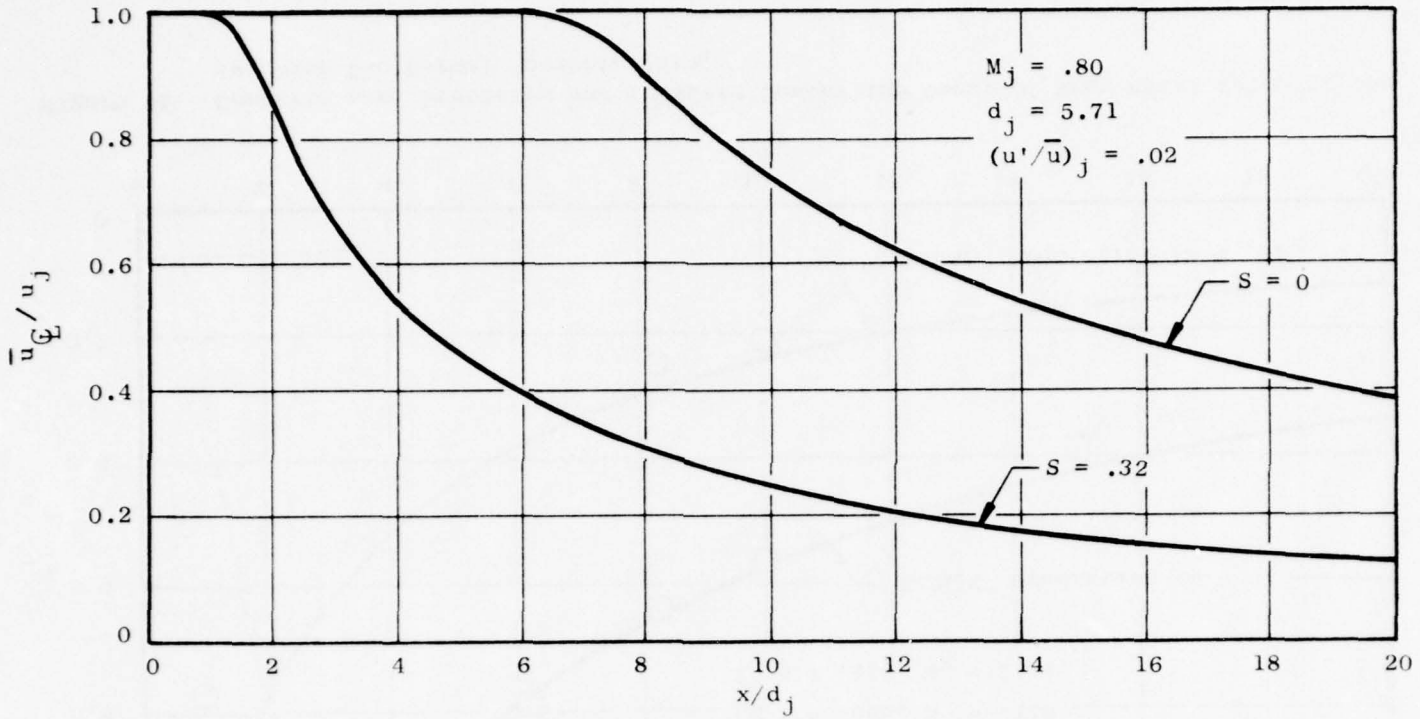


Figure 92. Predicted Centerline Decay of Mean Axial Velcoity for Swirling and Nonswirling Isothermal Subsonic Jets.

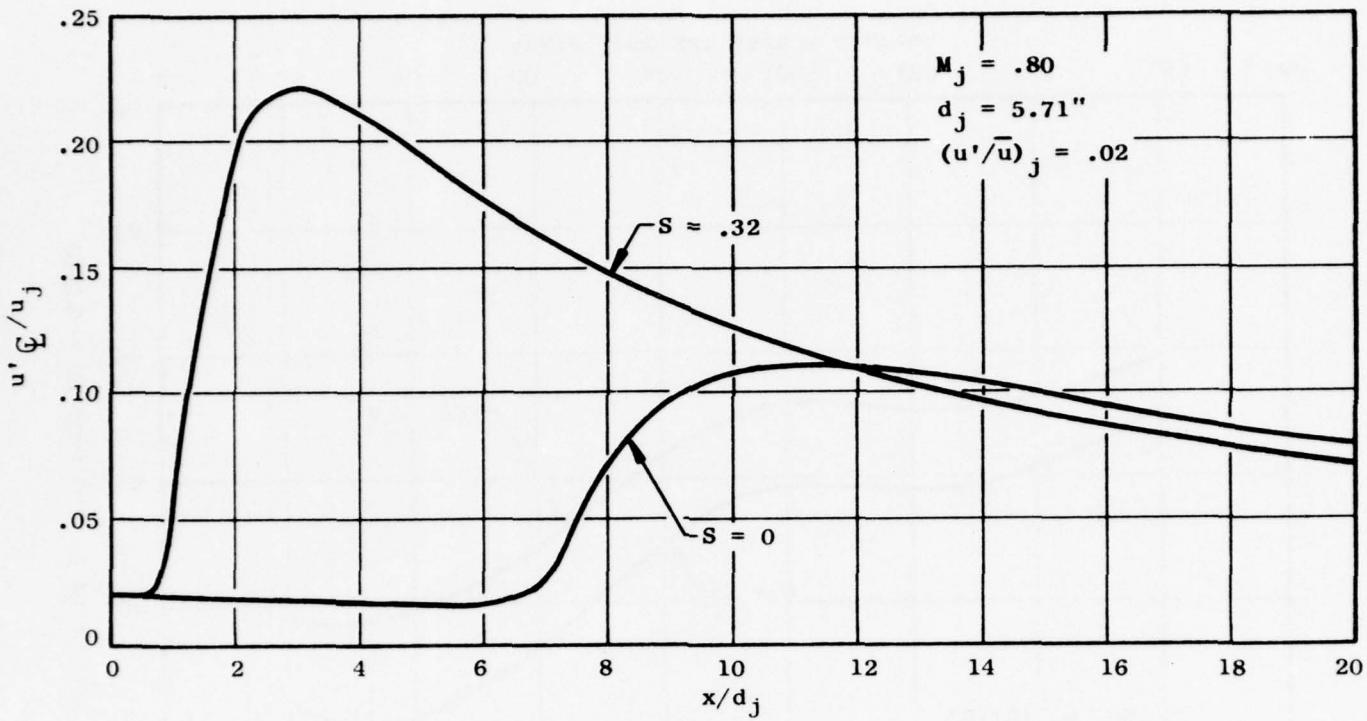


Figure 93. Predicted Variation of Turbulence Intensity Along the Centerline of Swirling and Nonswirling Isothermal Subsonic Jets.

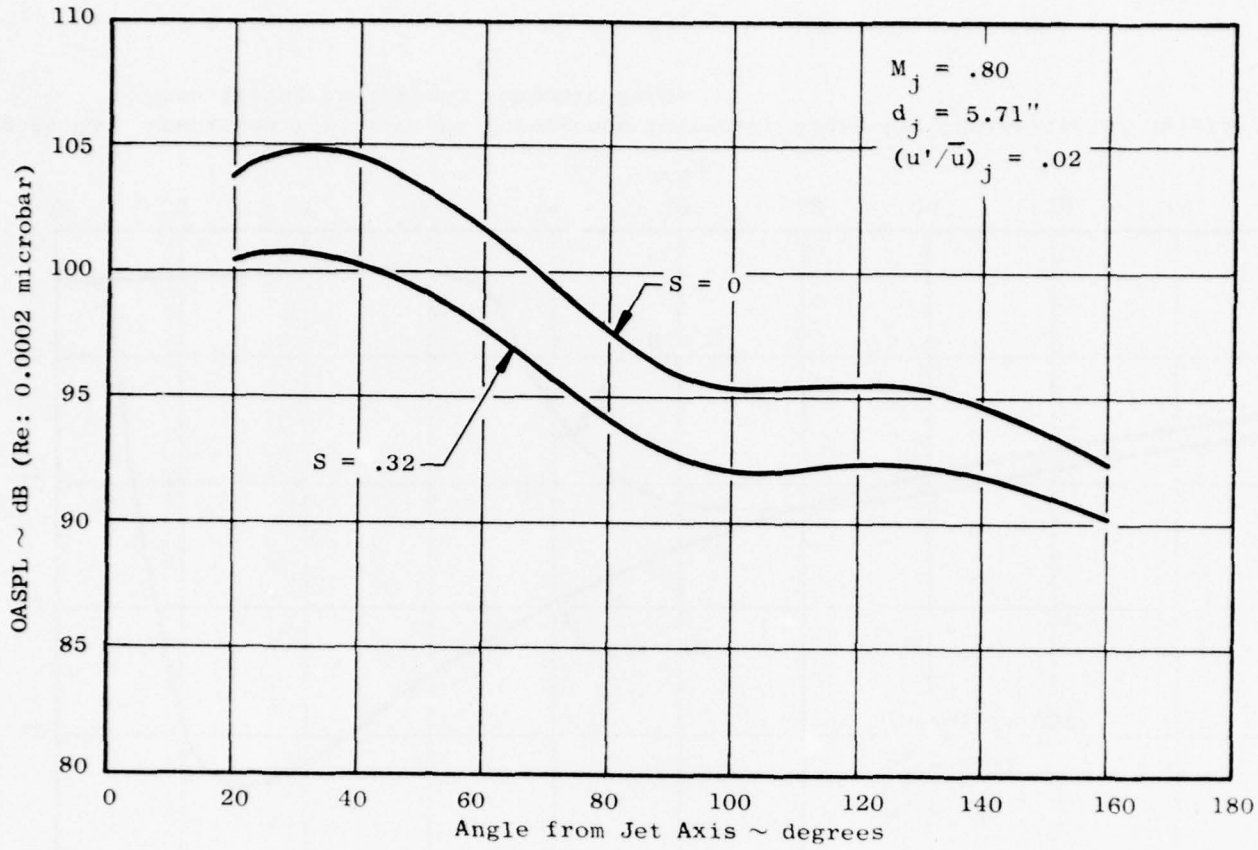


Figure 94. Predicted Variation of Overall Sound Pressure Level Around a 40-foot Arc for Swirling and Nonswirling Isothermal Subsonic Jets.

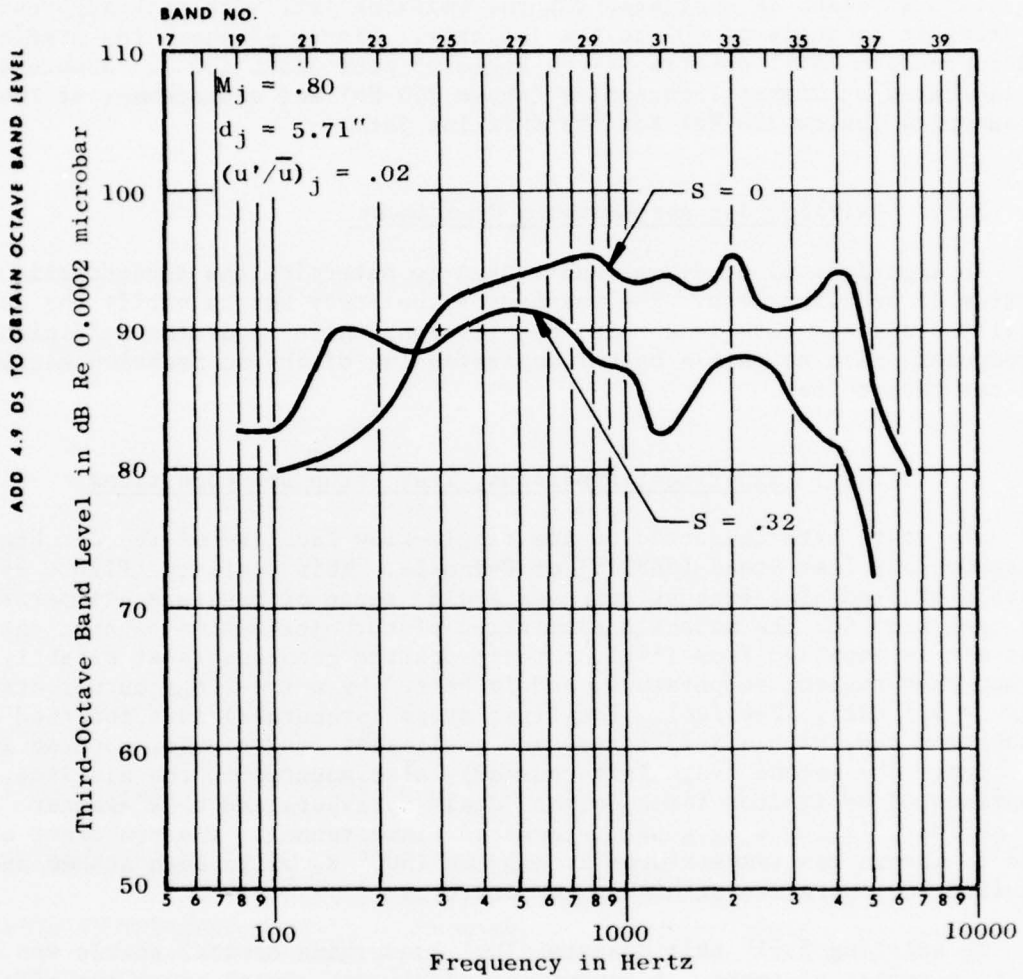


Figure 95. Predicted 1/3-Octave-Band Sound Pressure Level Spectra at 30° from the Jet Axis on a 40-foot Arc for Swirling and Nonswirling Subsonic Isothermal Jets.

decay along the centerline of both swirling (S = 0.32) and nonswirling jets. Figure 93 shows the variations in turbulence intensity along the jet centerline. A higher level of turbulence is indicated in the initial development of the swirling jet, accounting for the more rapid mean velocity decay seen in Figure 92. The predicted overall sound pressure levels around a 40' arc (for a 5.71" nozzle exit diameter) are shown in Figure 94. A 2.0- to 4.5-dB reduction in OASPL is indicated for the swirling jet, with peak suppression occuring at an angle of 40° to the jet axis. Figure 95 shows the predicted sound pressure level spectra at the angle of peak OASPL (30°). Suppression is indicated at higher frequencies (above 250 Hz) and enhancement at lower frequencies (below 250 Hz) for the swirling jet.

1.2.2 Swirling Jet Aeroacoustic Experiment

An experimental study was undertaken to determine the aeroacoustic properties of swirling jets. The purpose of the study was to verify the analytically predicted far-field noise suppression, while recording sufficient aerodynamic data to gain a better understanding of the suppression mechanism and the thrust loss.

1.2.2.1 Experiment Apparatus, Test Setup and Conditions

The tests were conducted on the single-flow facility of the Jet Engine Noise Outdoor Test Stand (JENOTS) at Evendale. This facility (Figure 96) is capable of producing exhaust gas over a wide range of pressure, temperature, and mass flow for the subscale simulation of turbojet engine exhaust nozzles. Test air is supplied from in-plant reciprocating compressors at slightly higher-than-ambient temperature, and is heated by a two-stage burner system (Figure 97) using JP-4 fuel. The first stage (preburner) is a modified J-47 combustion can, with a J-73 large- and small-slot fuel nozzle, mounted in the air line. The second stage (afterburner), also mounted in the air line, is comprised of an ignitor torch, eight "dual" spraybars and a "V"-gutter flameholder, followed by a water-jacketed flame tunnel. The preburner can be used to obtain gas temperatures as high as 1500° R, while both stages are required for operation at higher temperatures.

An existing 5.71" exit diameter (D_8) converging conical nozzle was used for this series of tests. A converging nozzle was chosen since the effects of swirl were to be studied in subsonic (and sonic) jets prior to any consideration of the more complex phenomena of swirling supersonic jets. The vanes were located in a 6.5" I.D. section mounted in the air line immediately upstream of the nozzle, as illustrated in Figures 98 and 99. Sixteen constant-thickness, constant-chord, circular-arc airfoils with 35° camber angle were placed in an annular region comprising the outer 89% of the available flow area. The vanes were located upstream of the nozzle throat to allow wakes and induced secondary flows to "mix out" in the nozzle. A nozzle with low area ratio (A_{max}/A_{exit}) was chosen in order to minimize the loss of

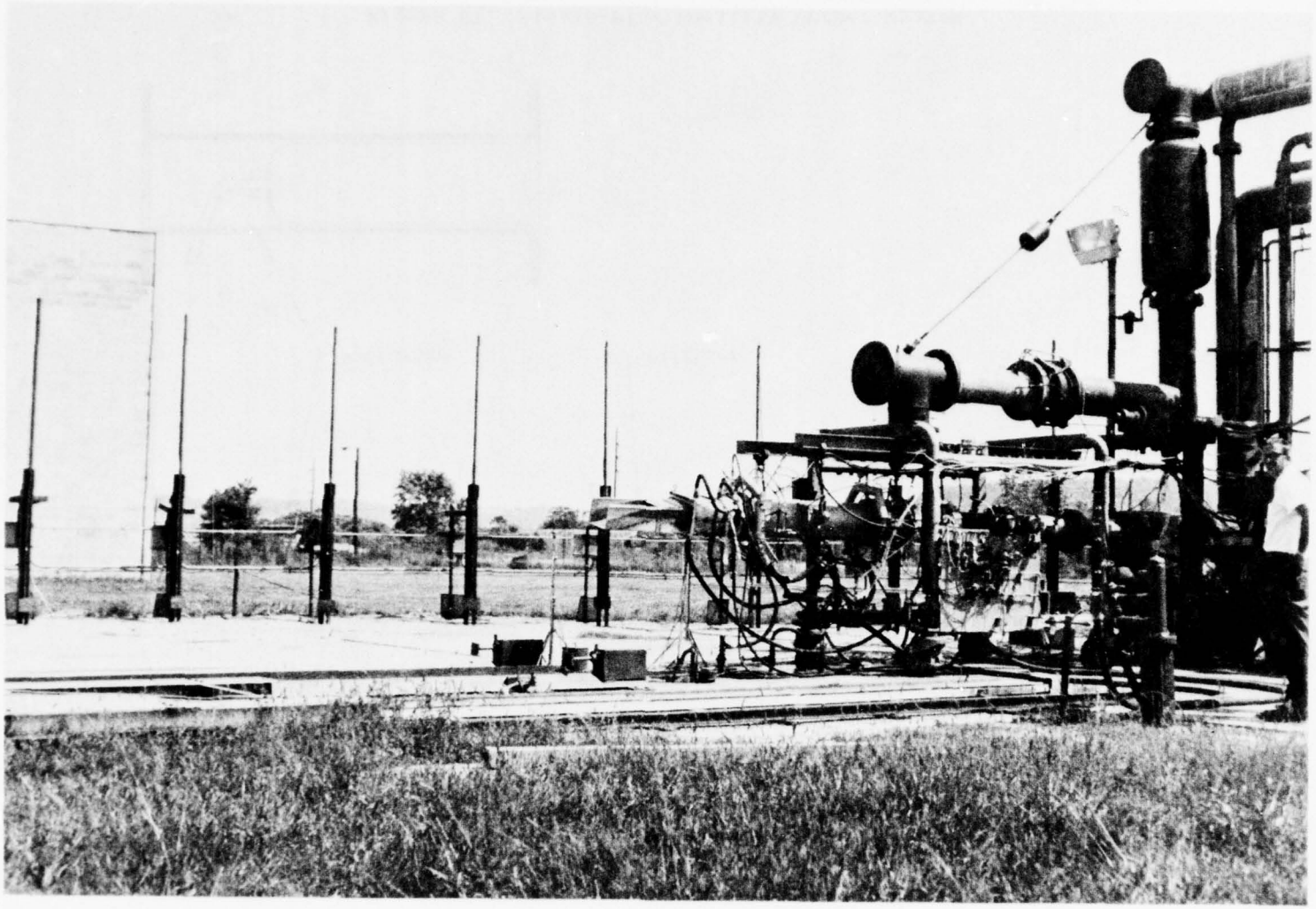


Figure 96. JENOTS Single-Flow Facility.

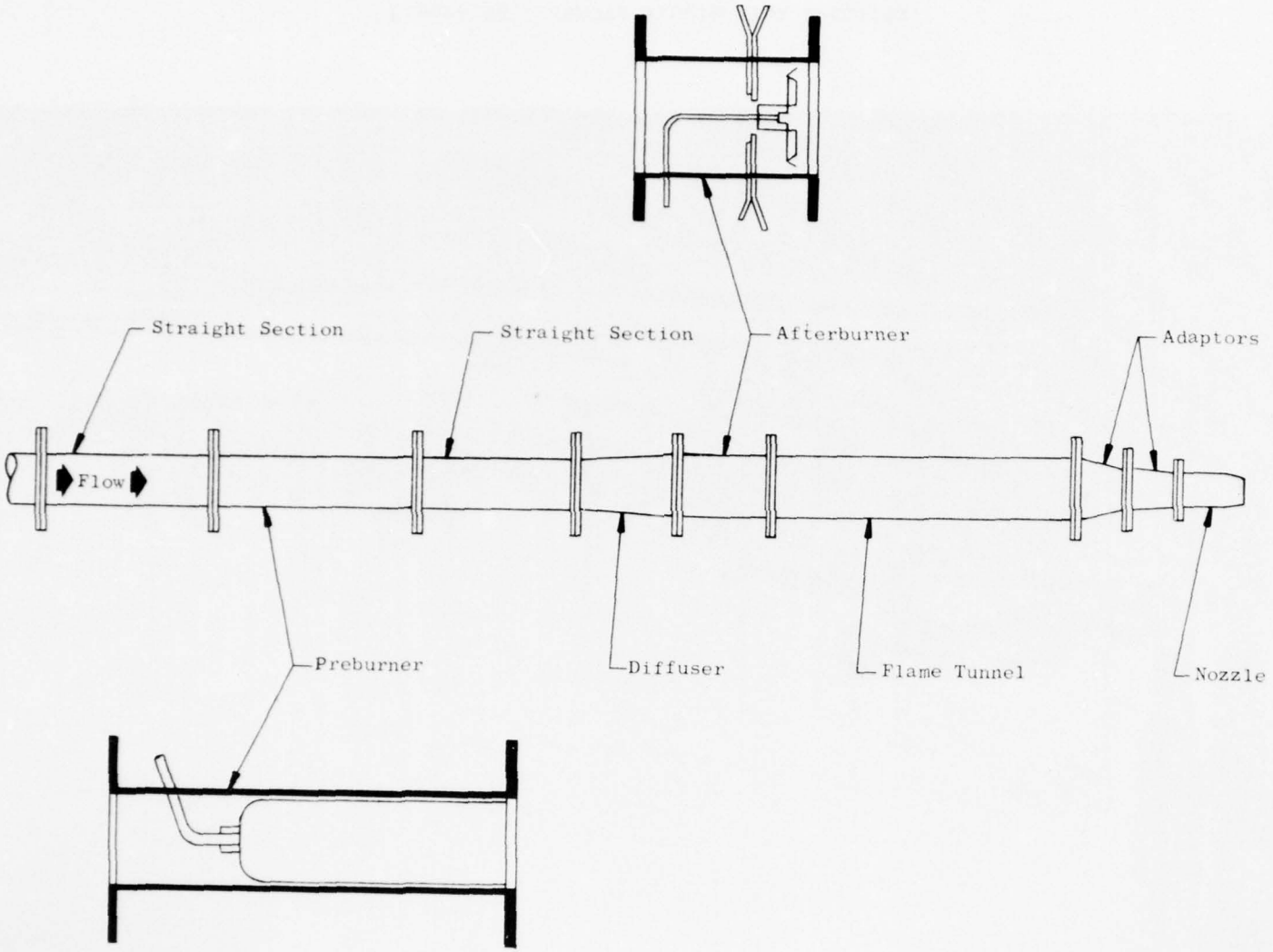


Figure 97. Single-Flow Facility Burner System.

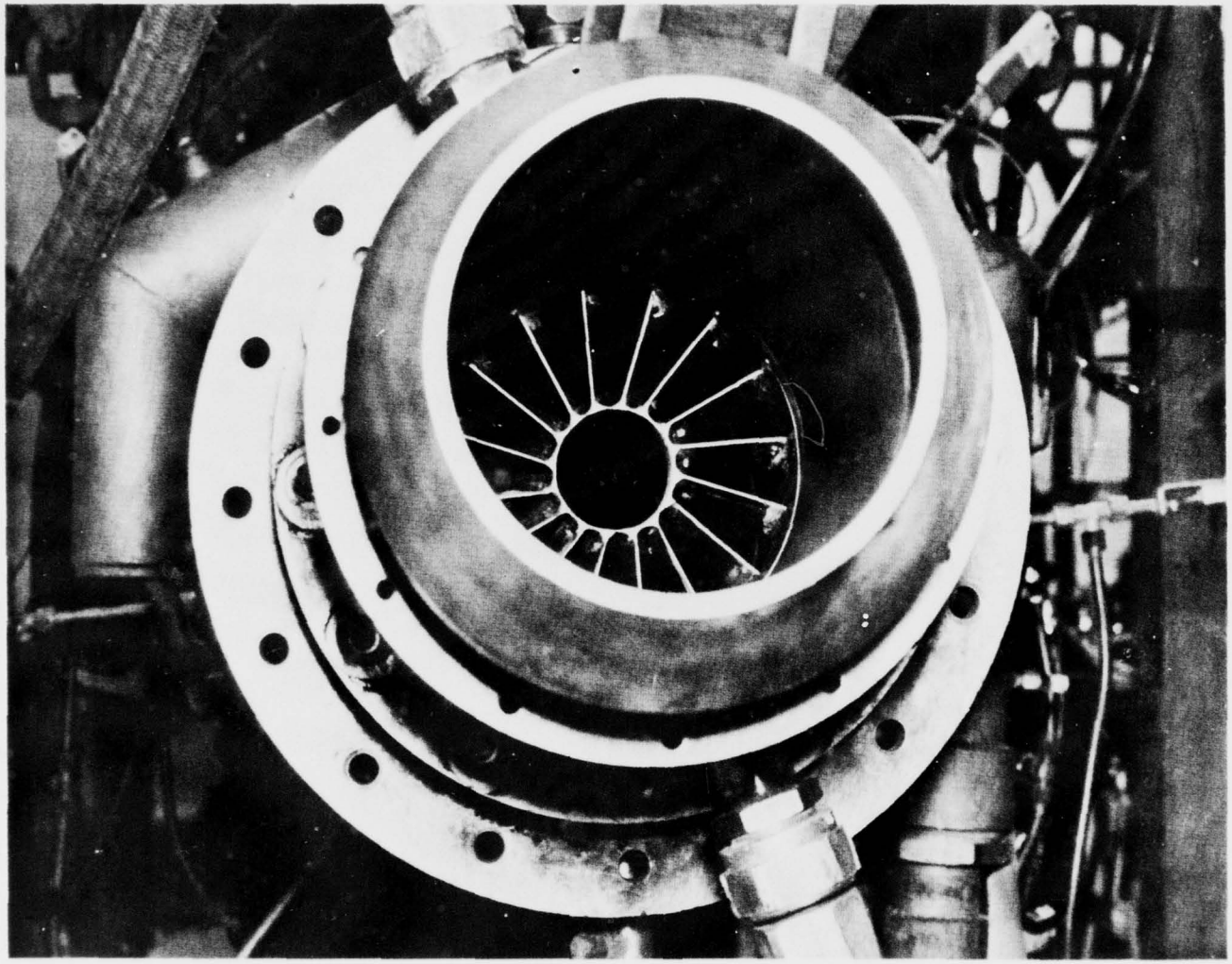


Figure 98. Swirl Test Setup with View of Swirl Vanes.

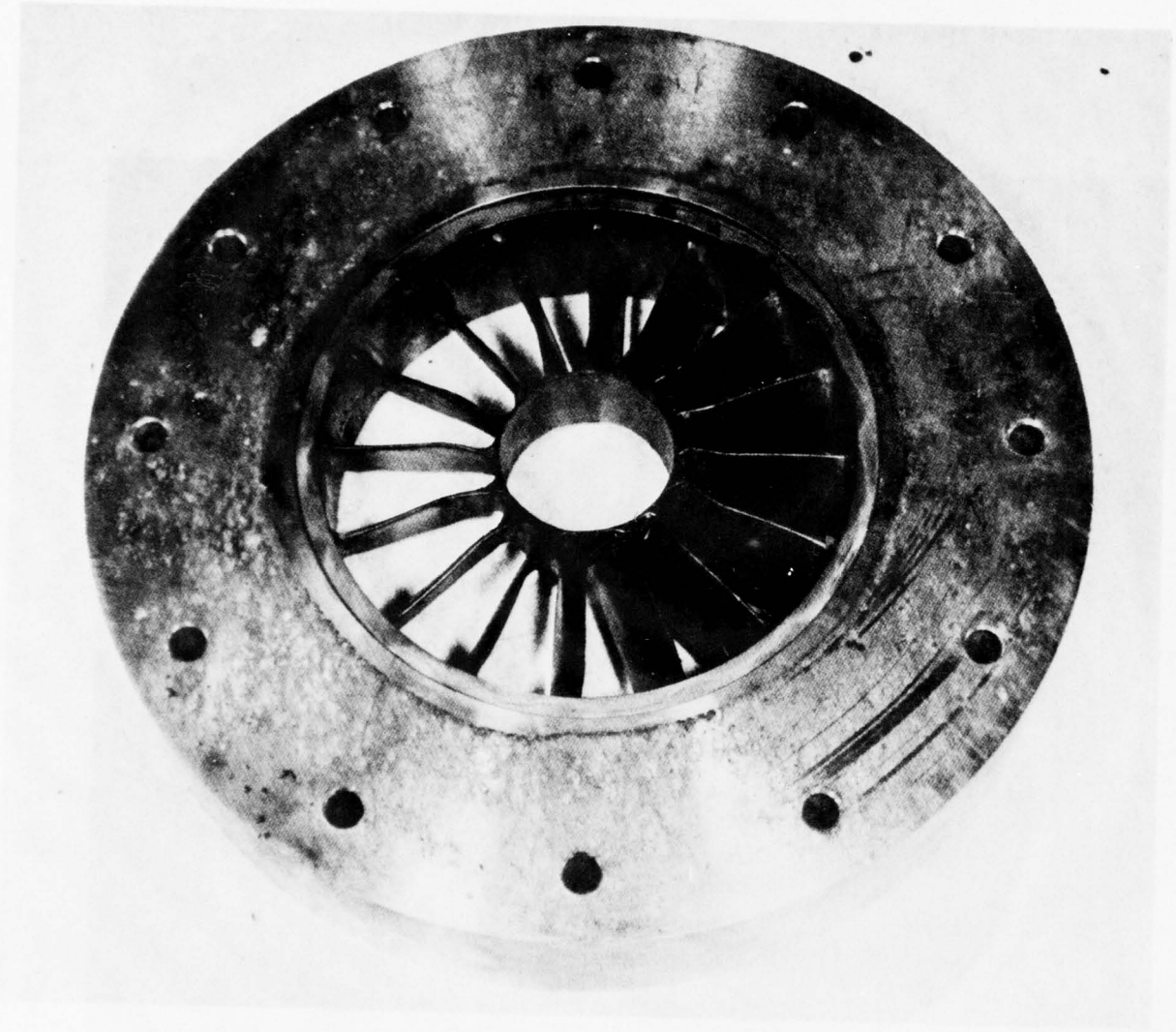


Figure 99. Swirl Vane Section.

swirl strength due to contraction (radius reduction). The overall system was designed to produce an average swirl angle of 20-25° at the nozzle exit plane. Two configurations were tested:

- 5.71" D_8 conical nozzle without swirl vanes (baseline)
- 5.71" D_8 conical nozzle with swirl vanes

These configurations are shown schematically in Figure 100.

Facility instrumentation is provided for the measurement of airflow, fuel flow, preburner and afterburner discharge total temperature, and nozzle upstream plenum static pressure. This last quantity is measured at the downstream end of the flame tunnel (see Figure 100), and is used to calculate nozzle exit total pressure, based on the assumption of one-dimensional isentropic flow. The facility data and barometric pressure were used to set test points.

Far-field acoustic measurements were made with 1/4" Bruel and Kjaer condensor microphones (type 4135) mounted at a height of 15.93' from the ground on a 40' arc. Fourteen microphones were used, at 10° intervals, starting from an angle of 20° to the jet axis (Figure 101). The signals were recorded on a 28-channel Sangamo tape recorder (80 KHz flat response with appropriate corrections). The microphones were calibrated with a piston phone prior to each test. All acoustic data were reduced in 1/3-octave-band form, corrected to standard day conditions of 59° F, 70% relative humidity. In addition, some of the data were reduced in 10-Hz narrowbands.

Measurements of the mean and fluctuating axial velocity were made at several points in the jet plume using General Electric's Laser Velocimeter (LV). The LV (References 37 and 38) is a noncontact optical technique in which the velocities of seed particles are measured as they pass through the fringes of an interference pattern created by two intersecting beams of coherent radiation. The mean and RMS turbulence velocities of the flow (in one coordinate direction) are then determined from a statistical analysis of the distribution of particle velocities over a sufficient period of time. A schematic arrangement of the LV optics package is shown in Figure 102. The LV equipment is a three-part package consisting of an LV head mounted on a remotely actuated platform (Figure 103), the signal processor, and the seeder.

Radial profiles of total pressure and swirl angle at an axial station 1/2" downstream of the nozzle exit were obtained, for the swirl configuration only, with a traversing, self-nulling cobra probe. The probe (Figure 104) has a 3/16" X 1/16" sensing head with three orifices for pressure measurement. It is aligned in the direction of flow by a self-nulling yaw (swirl) angle control which balances the pressures sensed by the two "outer" orifices. The total pressure is then determined using the center orifice. Radial traverses are accomplished by remote actuation of the probe drive mechanism. The installation of the probe assembly at JENOTS is shown in Figure 105.

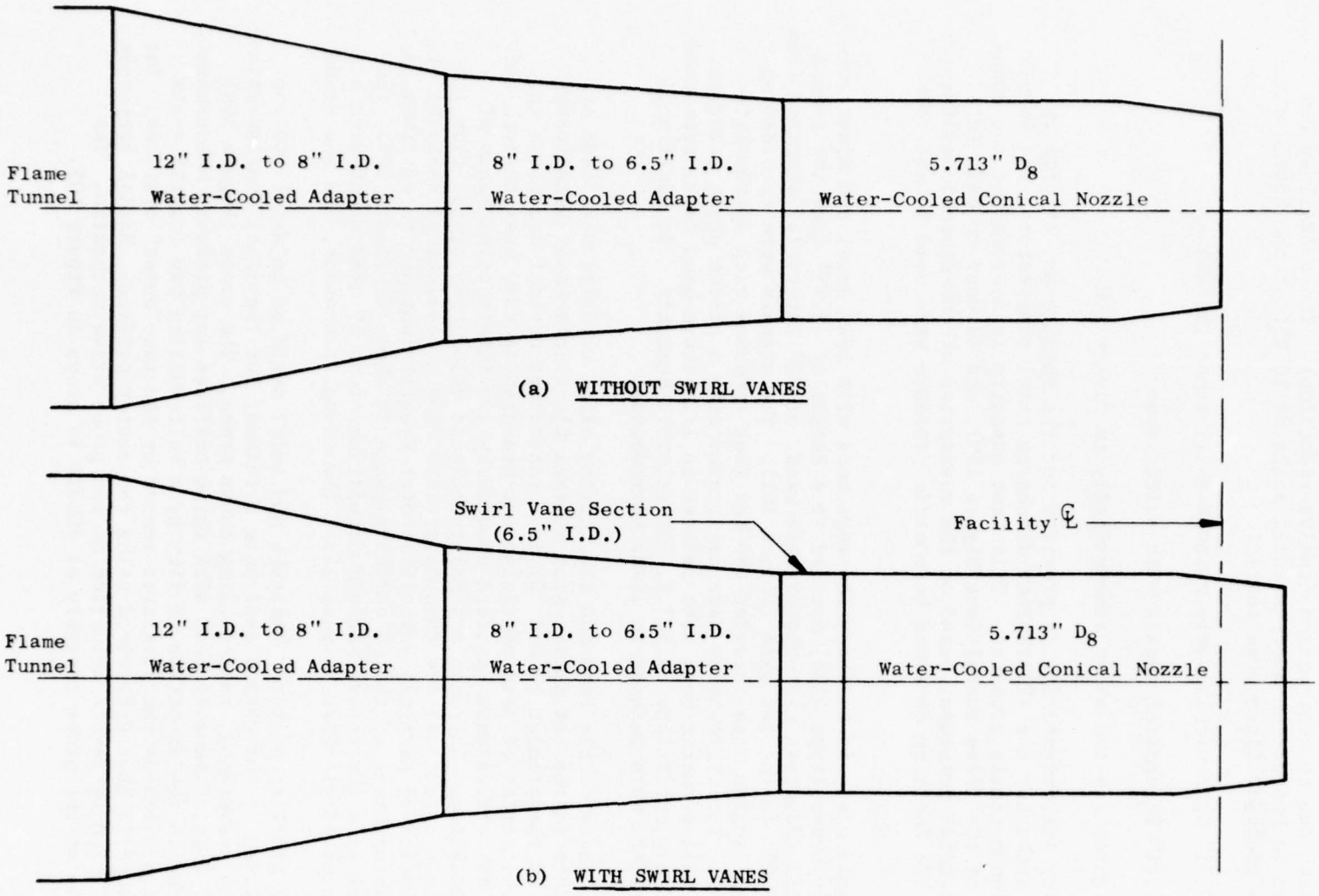


Figure 100. Swirl Test Setup Schematic.

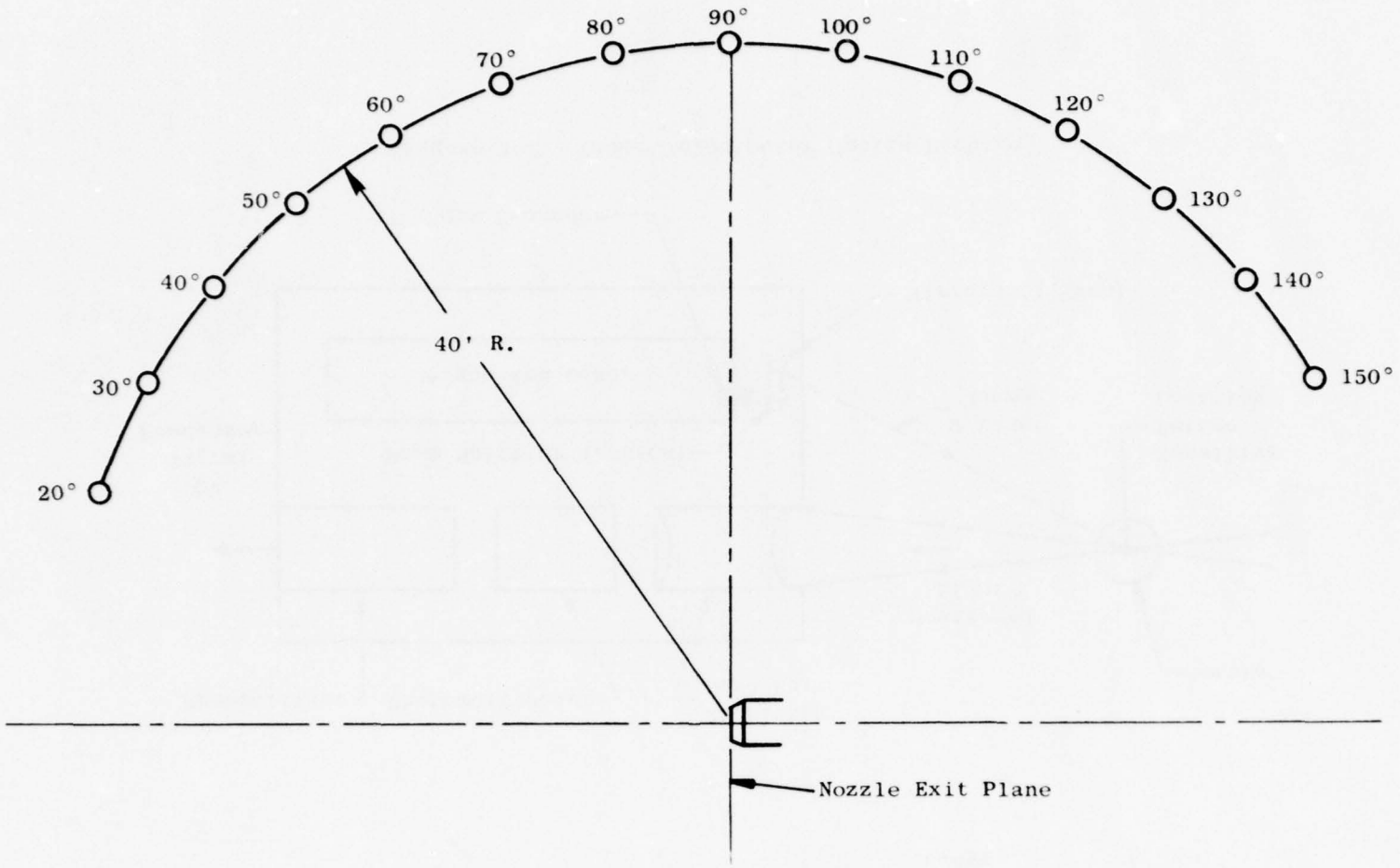


Figure 101. Acoustic Far-Field Measuring Stations.

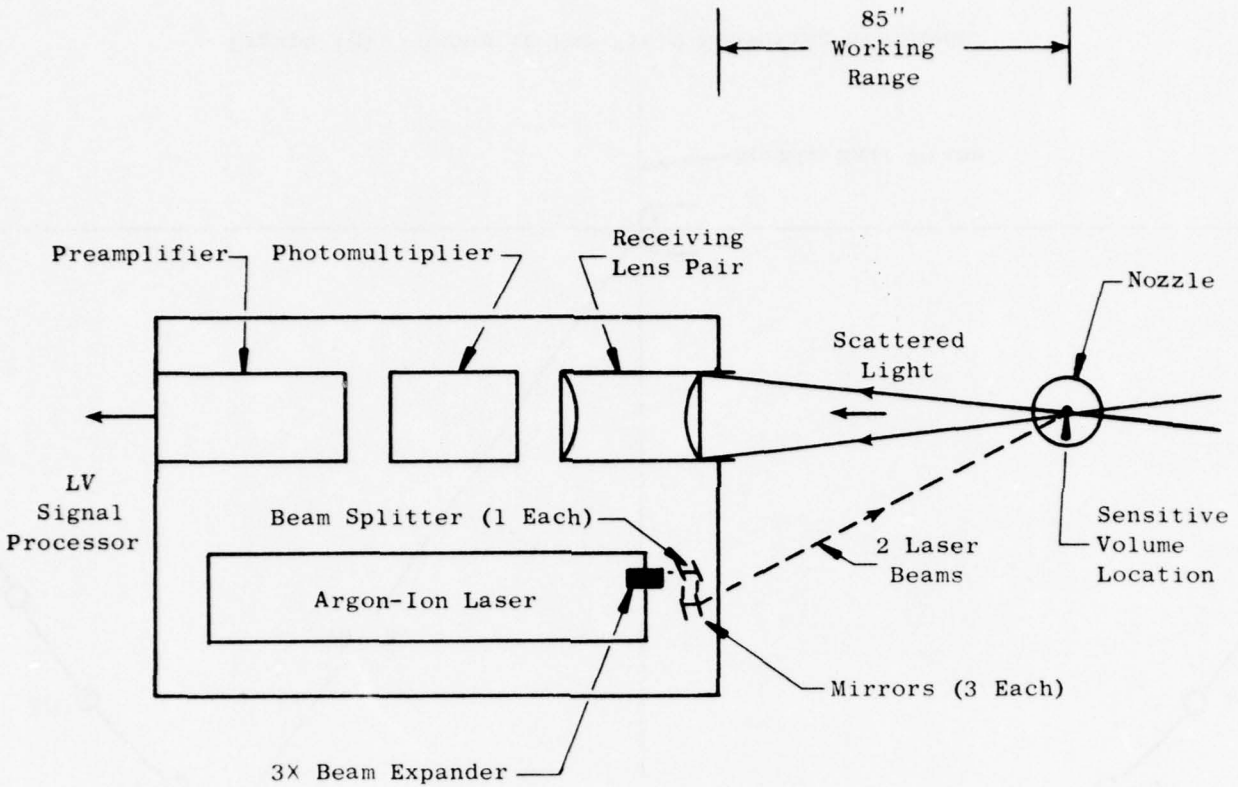


Figure 102. Laser Velocimeter Optics Package.

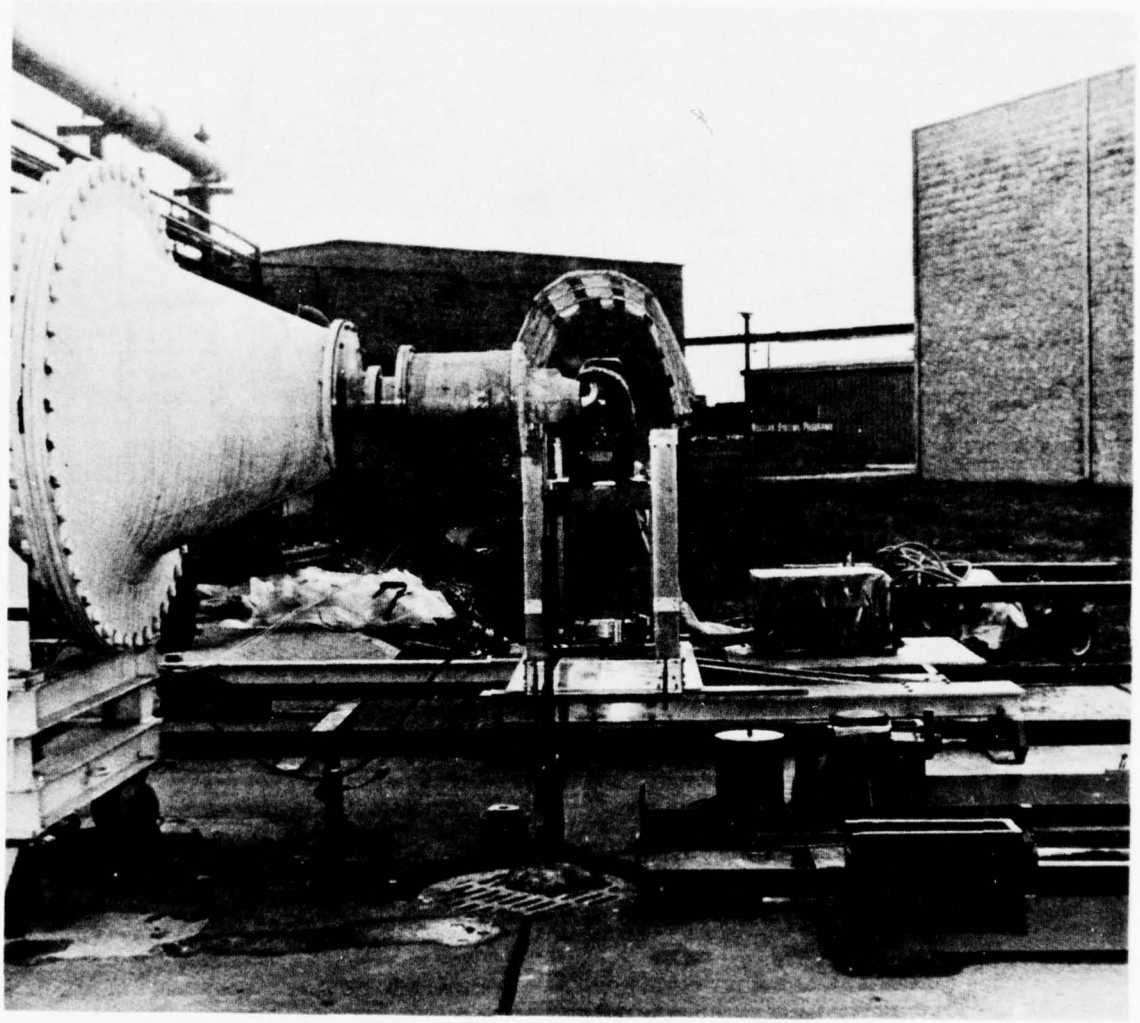


Figure 103. Laser Doppler Velocimeter Setup at JENOTS.

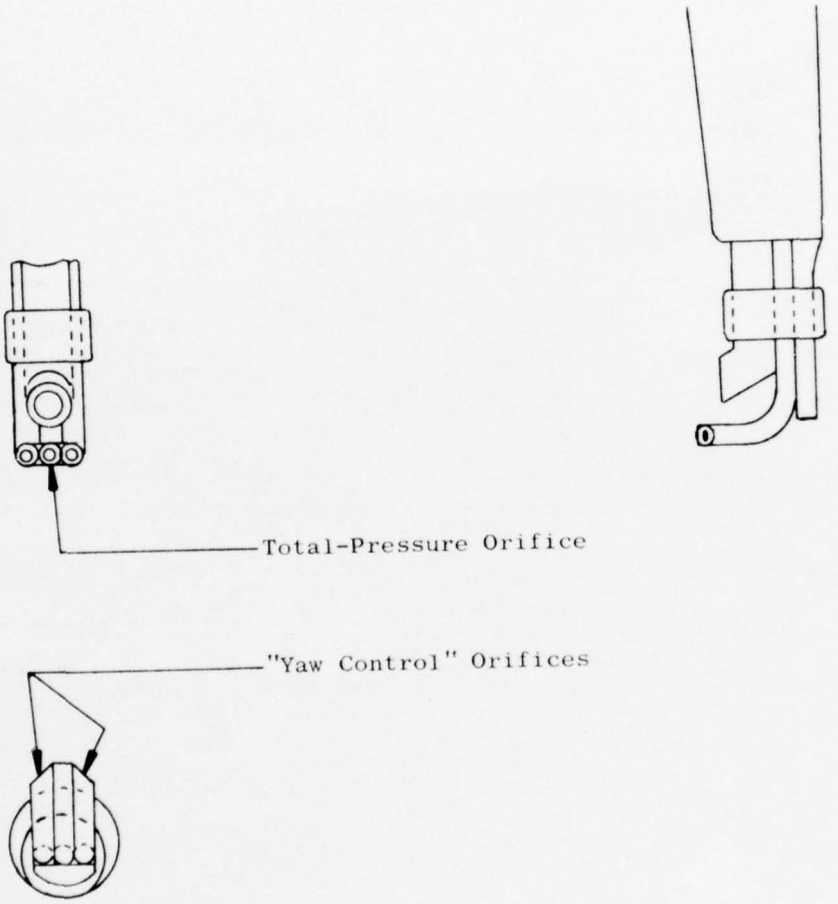


Figure 104. Cobra Probe Sensing Head.

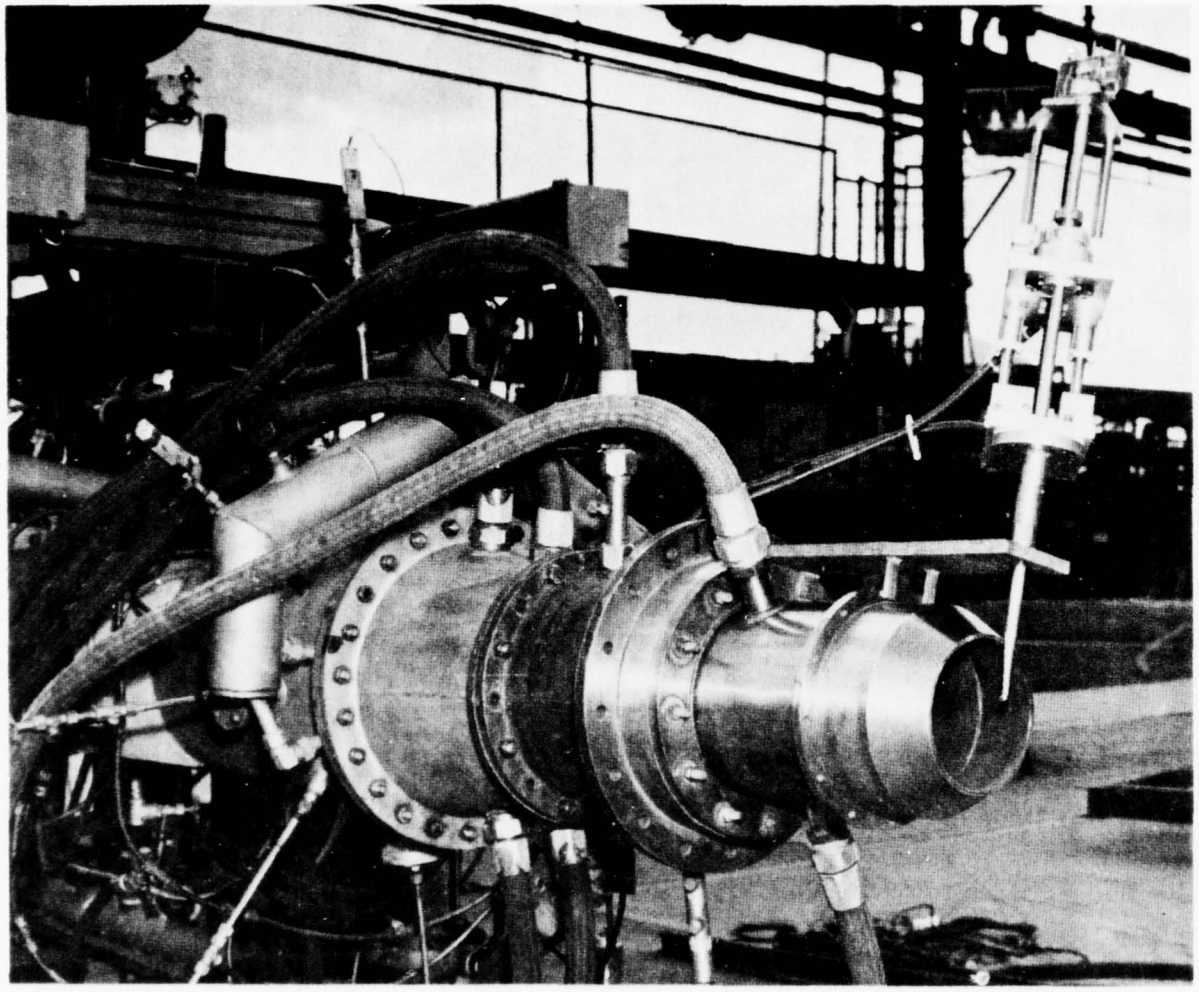


Figure 105. Swirl Test Setup with Cobra Probe.

A test matrix of three points was defined by specifying combinations of nozzle pressure ratio and total temperature. The three points, to be run on both configurations, were:

Test Point	P_t/P	T_t (°R)	M_j
1	1.55	ambient	0.8
2	1.54	1500	0.8
3	1.88	1500	1.0

where M_j is the ideally expanded Mach number for the given conditions. Tolerances of ± 0.5% on indicated pressure ratio and 3.5% on temperature were held throughout the test. The setting of test points was complicated somewhat by the swirl vane total-pressure loss, as will be seen in the following sections.

1.2.2.2 Aerodynamic Results

Cobra Probe Measurements - Measured radial profiles of total pressure and swirl angle at the axial station $x/D_8 = 0.09$ are shown in Figures 106, 107, and 108 for swirl test points 1, 2, and 3, respectively.

The calculated (facility data) nozzle exit total pressure is shown as a dashed line on the P_t profile plots. This calculated pressure is actually the total pressure upstream of the swirl vanes and is equal to the exit plane P_t only when there are no losses (such as those introduced by the vanes) in the system. Note that the total pressure on the centerline, which is not directly affected by the vanes, is approximately equal to the calculated value. The large drop in P_t (around $r/r_8 = 0.3$) is caused by the wake behind the ring (Figure 99) connecting the inner ends of the swirl vanes. These measurements show that a significant (and nonuniform) total-pressure loss is created by the vane assembly. This loss must be taken into consideration in attempts to "match" test points on the two configurations.

A relatively uniform swirl angle distribution was obtained over the outer portion of the flow for all three test points, with values falling into the range of 20-30°. The average level is seen to decrease as jet velocity increases (going from test point 1 to point 2 to point 3) for a fixed configuration. The swirling motion has only partially penetrated the central core of the flow at the exit plane, so that the velocity has no measurable swirl component for $r/r_8 < 0.2$. The oscillations in the swirl angle plots are due to the dynamics of the self-nulling yaw control system rather than actual oscillations in flow angle.

For the cobra probe measurements, test points were set by fixing the "upstream" total pressure (calculated exit plane total pressure) at the defined exit plane value.

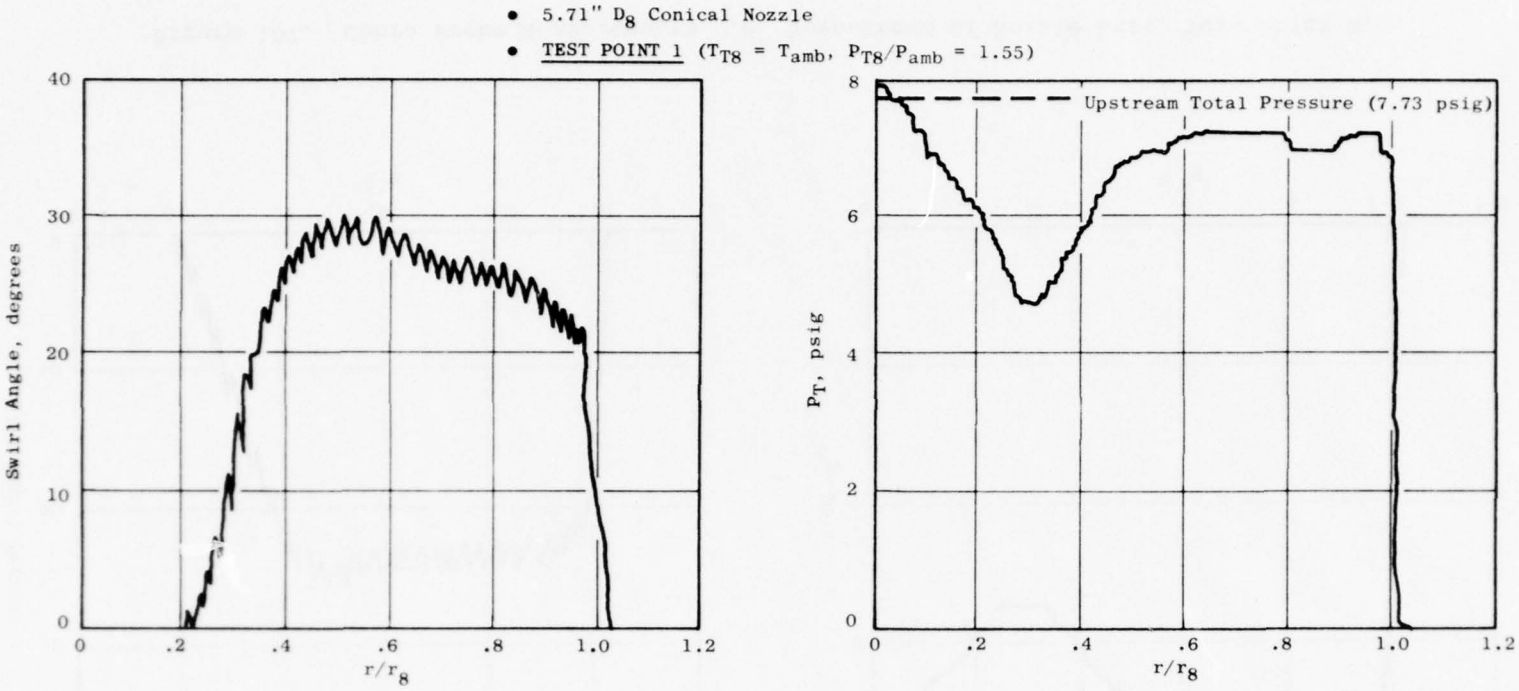


Figure 106. Cobra Probe Measurements 0.5" Downstream of Nozzle Exit, Test Point 1.

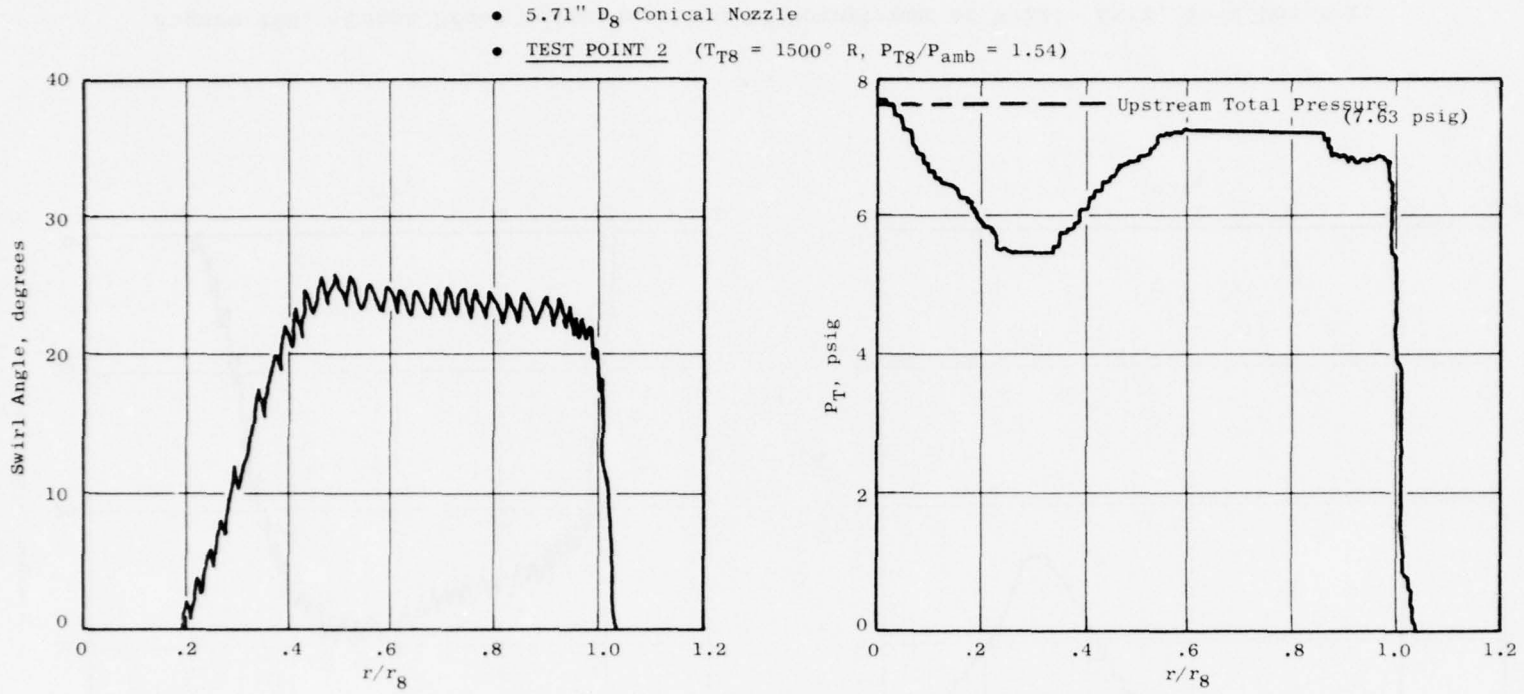


Figure 107. Cobra Probe Measurements 0.5" Downstream of Nozzle Exit, Test Point 2.

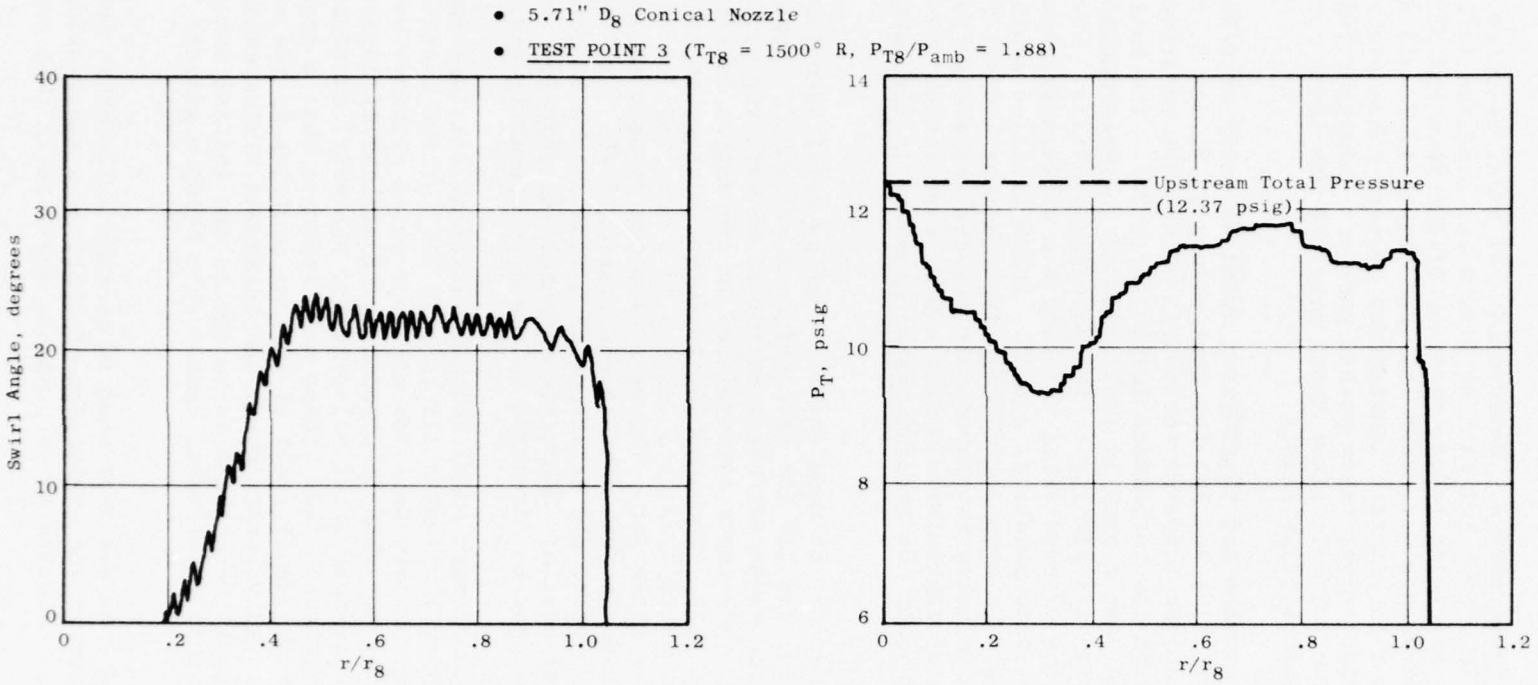


Figure 108. Cobra Probe Measurements 0.5" Downstream of Nozzle Exit, Test Point 3.

Laser Velocimeter Measurements - Measurements of axial velocity were made at several radial locations for each of five axial stations (x/D_8 = 0.09, 2, 4, 6, 8) in order to determine radial profiles of the mean and fluctuating components. These measurements were made for test points 1, 2, and 3 on both configurations. In order to maintain consistency between cobra probe and LDV data for the swirl configuration, tests points were set using the "upstream" total pressure. Thus, actual exit plane total pressure was lower for the swirl points than for the baseline points.

Measured profiles of mean and fluctuating axial velocity at x/D_8 = 0.09 are shown in Figures 109, 110, and 111 for test points 1, 2, and 3, respectively. The profiles for the baseline (no-swirl) points are relatively flat, as would be expected, with low turbulence levels (2 to 3%). The swirling flow turbulence profiles have a peak in the region of the wake behind the center ring, but otherwise are similar to the baseline profiles. However, the swirling flow profiles of mean axial velocity are strikingly nonuniform, particularly for the hot-flow points (2 and 3). These profiles exhibit a peak on the centerline with a substantial negative gradient ($\partial\bar{u}/\partial r$) from there to the edge. The axial velocity is higher than for the comparable nonswirling jet out to a radius of approximately r/r_8 = 0.6, even though the total pressure is lower, because of the reduced static pressure in the center of the swirling jet.

The centerline variations of mean and fluctuating axial velocity are shown in Figures 112, 113, and 114 for test points 1, 2, and 3, respectively. These plots illustrate the essential characteristics of swirling turbulent jets. A higher level of turbulence is developed in the region immediately downstream of the nozzle exit. The enhanced turbulent mixing, in combination with an adverse axial pressure gradient, results in a more rapid rate of velocity decay for the swirling jet. The mean velocity is seen to increase between the exit plane and the next measurement station (x/D_8 = 2) for both configurations. This is due to the existence of a vena contracta downstream of the converging conical nozzle. The maximum centerline velocity, which occured at x/D_8 = 2, was used to normalize all data in these figures.

Radial distributions of mean axial velocity at axial stations downstream of the exit plane are shown in Figures 115 through 117 for the baseline configuration. The mean velocity data for all four axial stations have been collapsed on a single plot for each test point using similarity parameters. The radial distributions of mean axial velocity for the swirl configuration are shown in Figures 118 through 120. These data indicate that a greater distance is required for the development of similar profiles in the swirling jets, despite the more rapid velocity decay and increased mixing exhibited by these flows. This result is thought to be due to the initial nonuniformity of the swirling jets in this experiment, rather than being a general characteristic.

Thrust Calculations - As was mentioned in Section 1.2, thrust loss is an important consideration in the evaluation of swirl as a suppression mechanism for jet noise. Although thrust was not measured in this experiment,

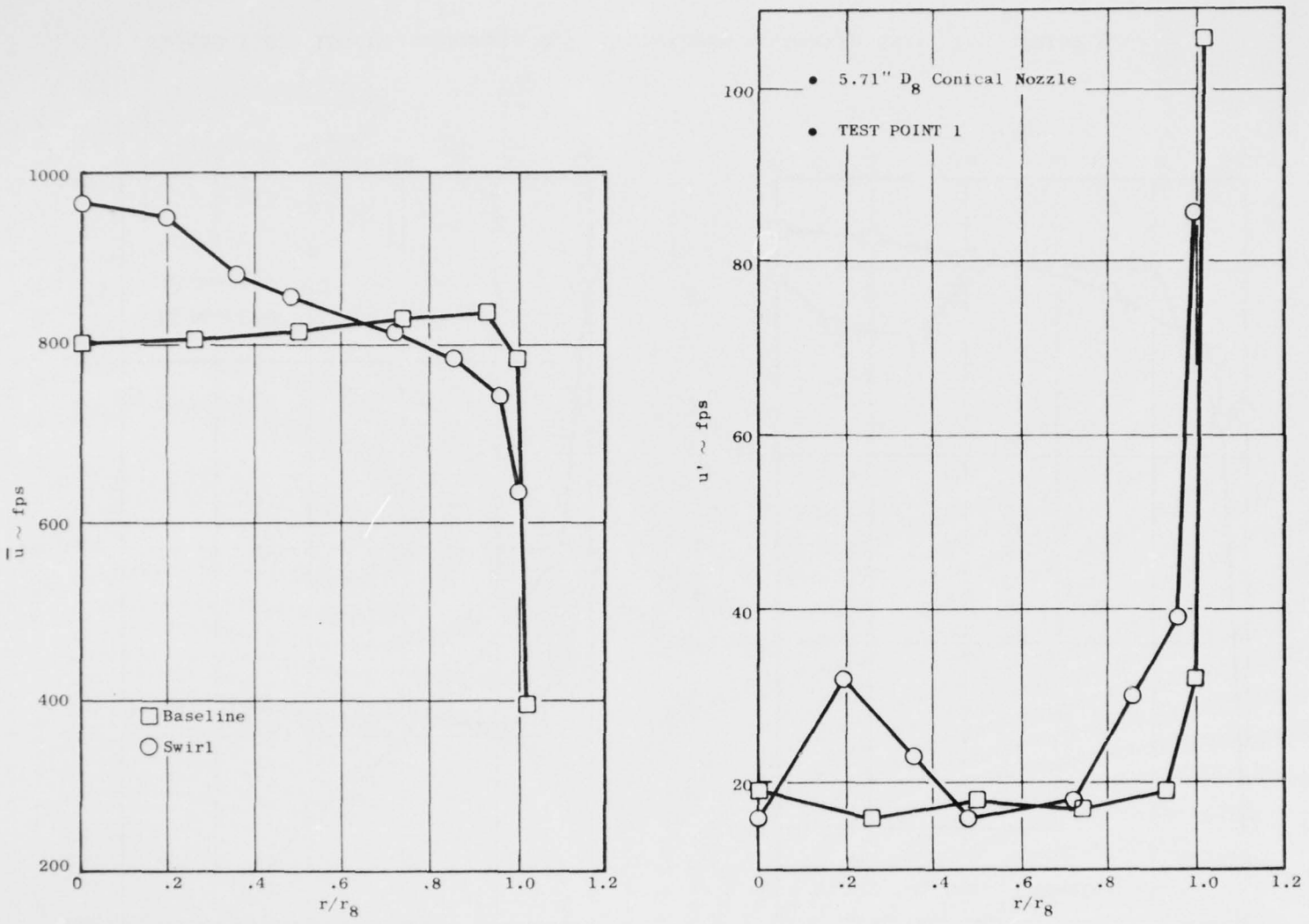


Figure 109. LDV Measurements 0.5" Downstream of Nozzle Exit, Test Point 1.

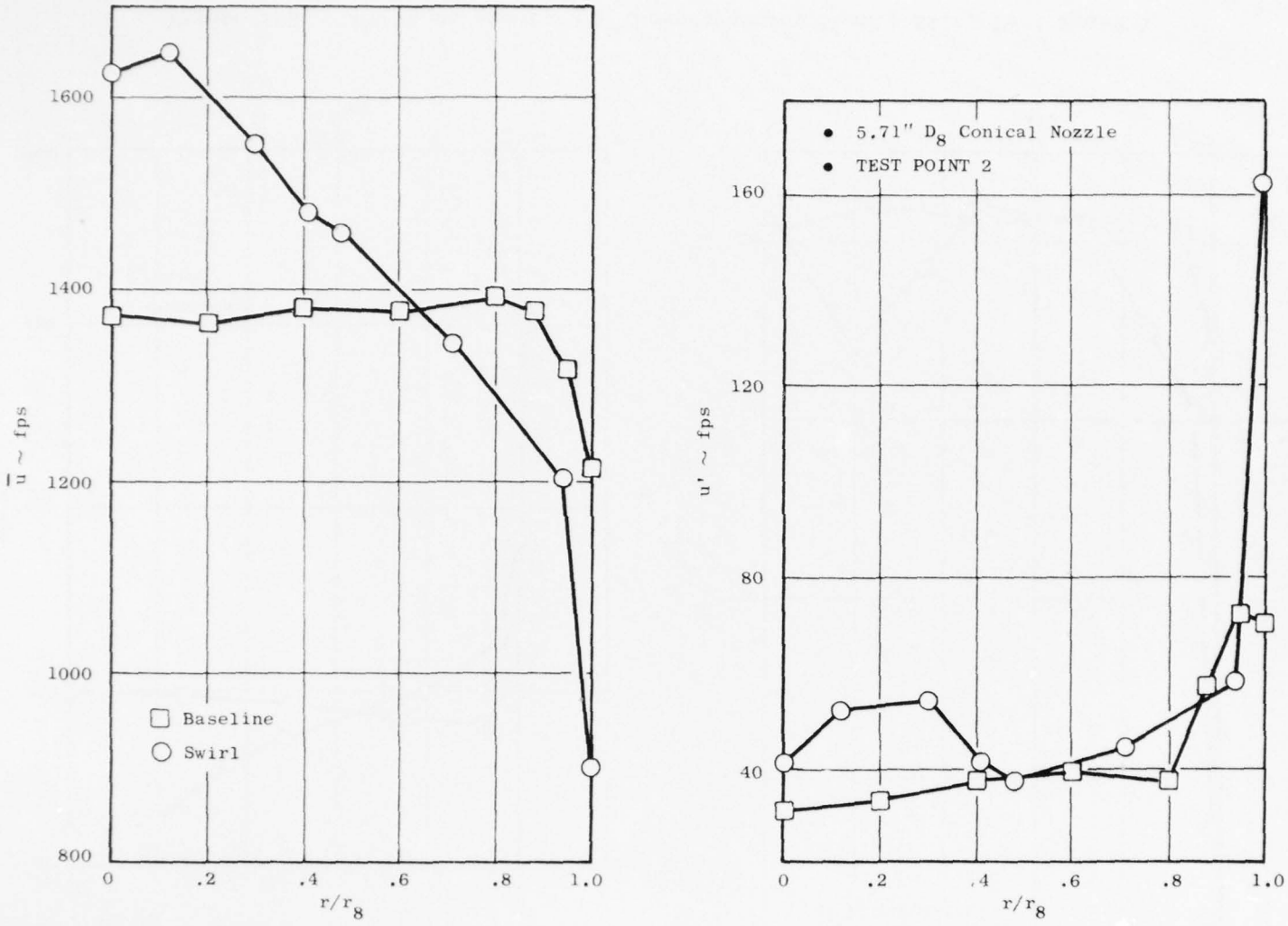


Figure 110. LDV Measurements 0.5" Downstream of Nozzle Exit, Test Point 2.

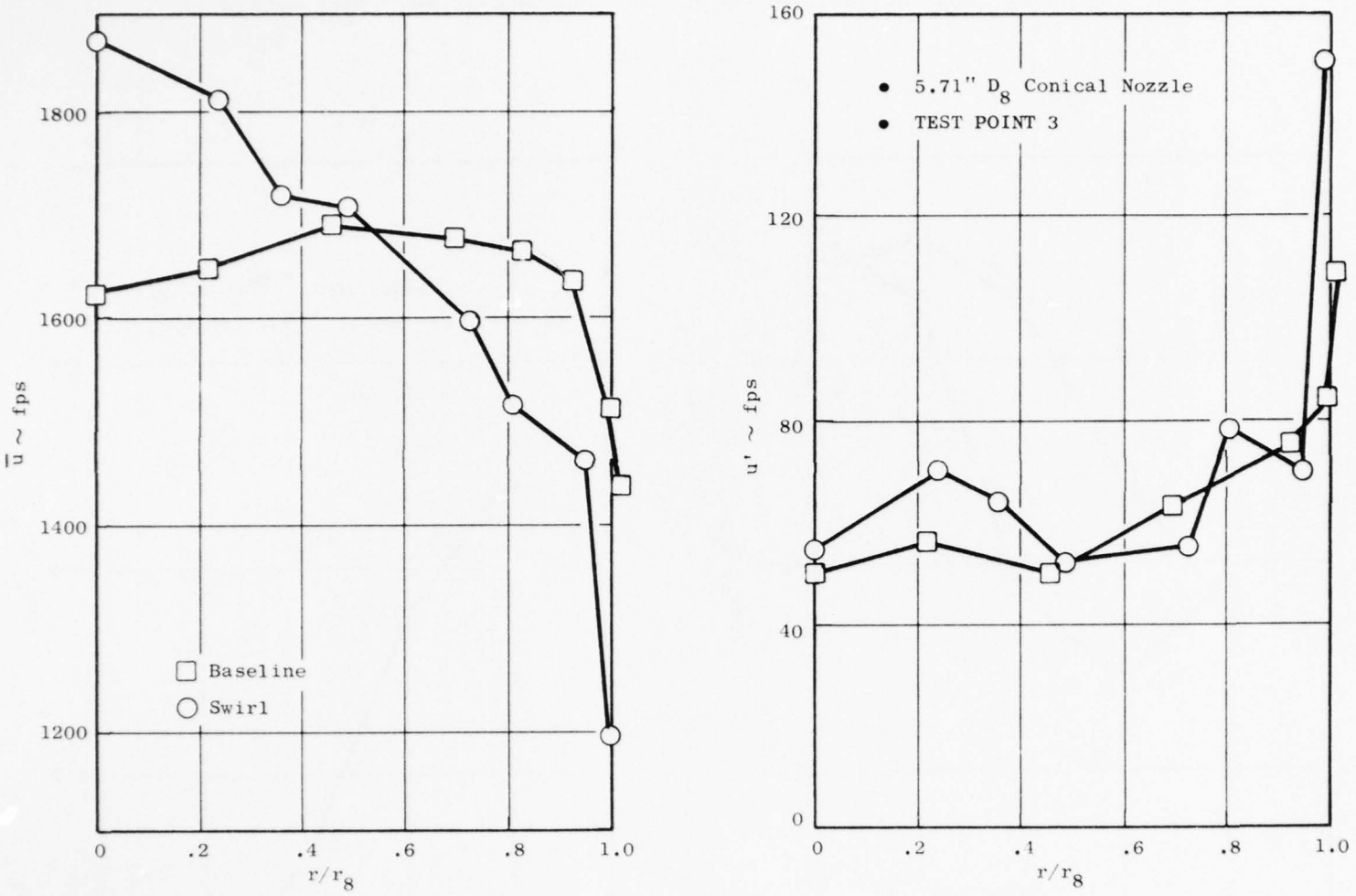


Figure 111. LDV Measurements 0.5" Downstream of Nozzle Exit, Test Point 3.

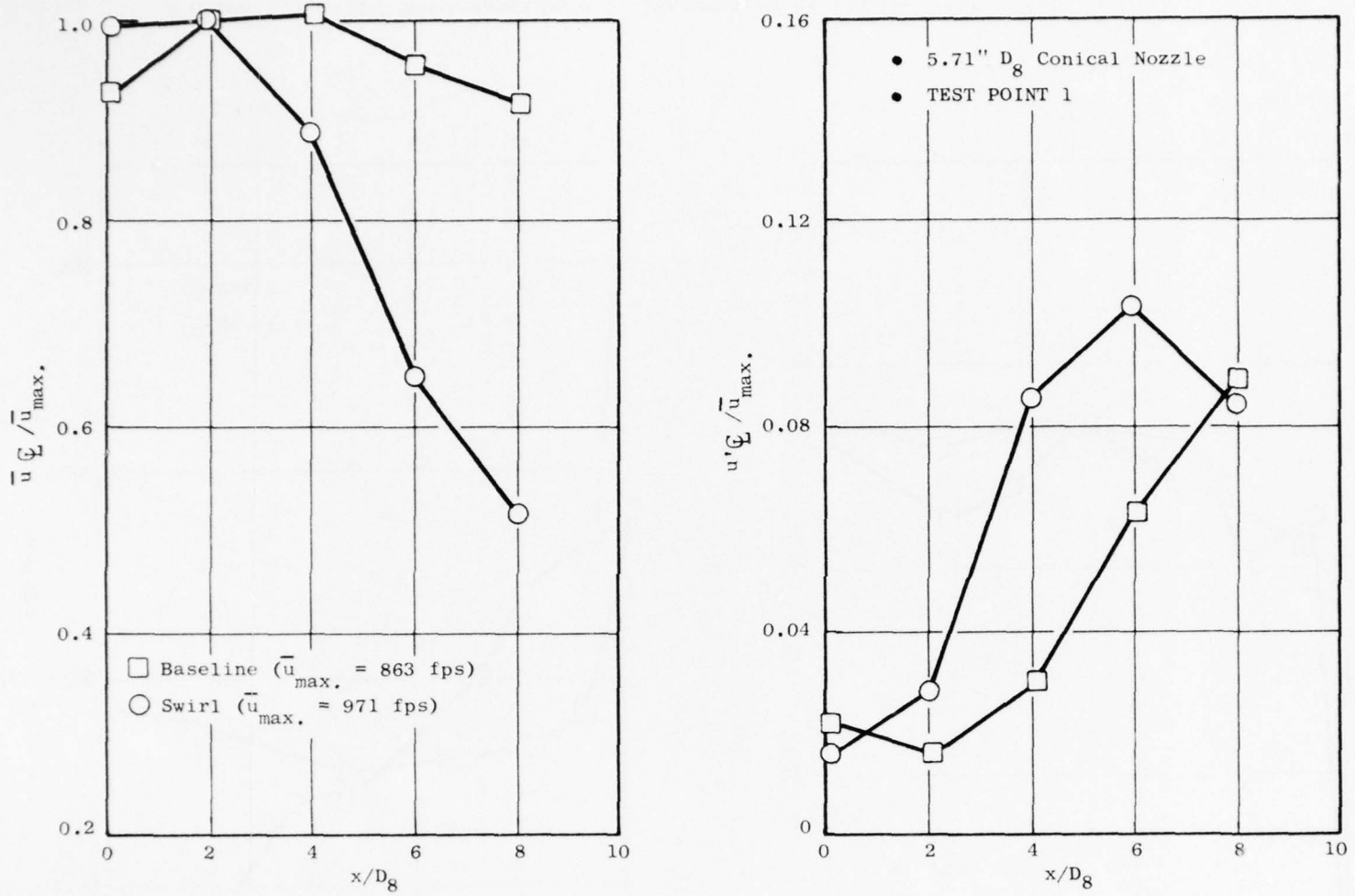


Figure 112. LDV Measurements on the Jet Centerline, Test Point 1.

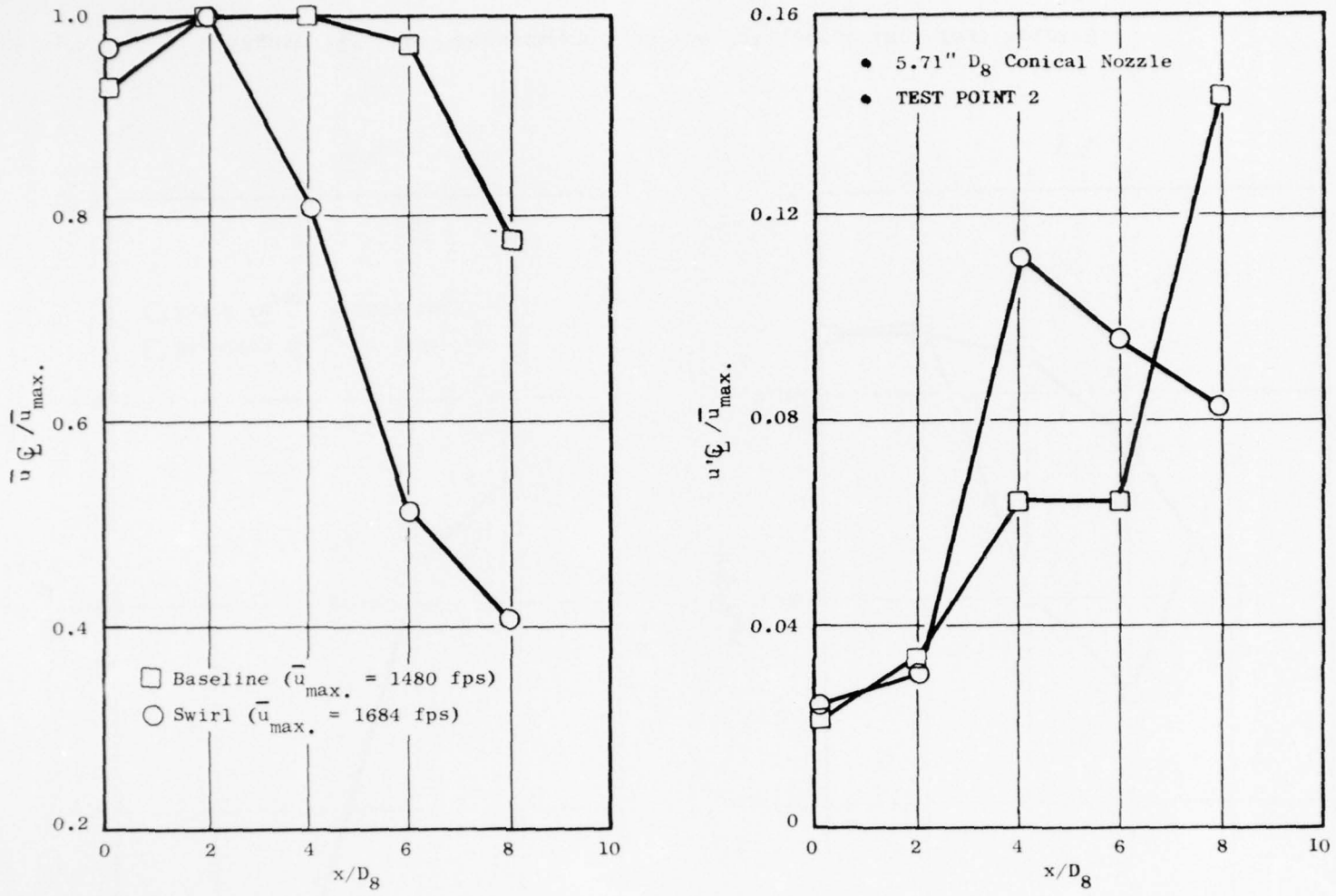


Figure 113. LDV Measurements on the Jet Centerline, Test Point 2.

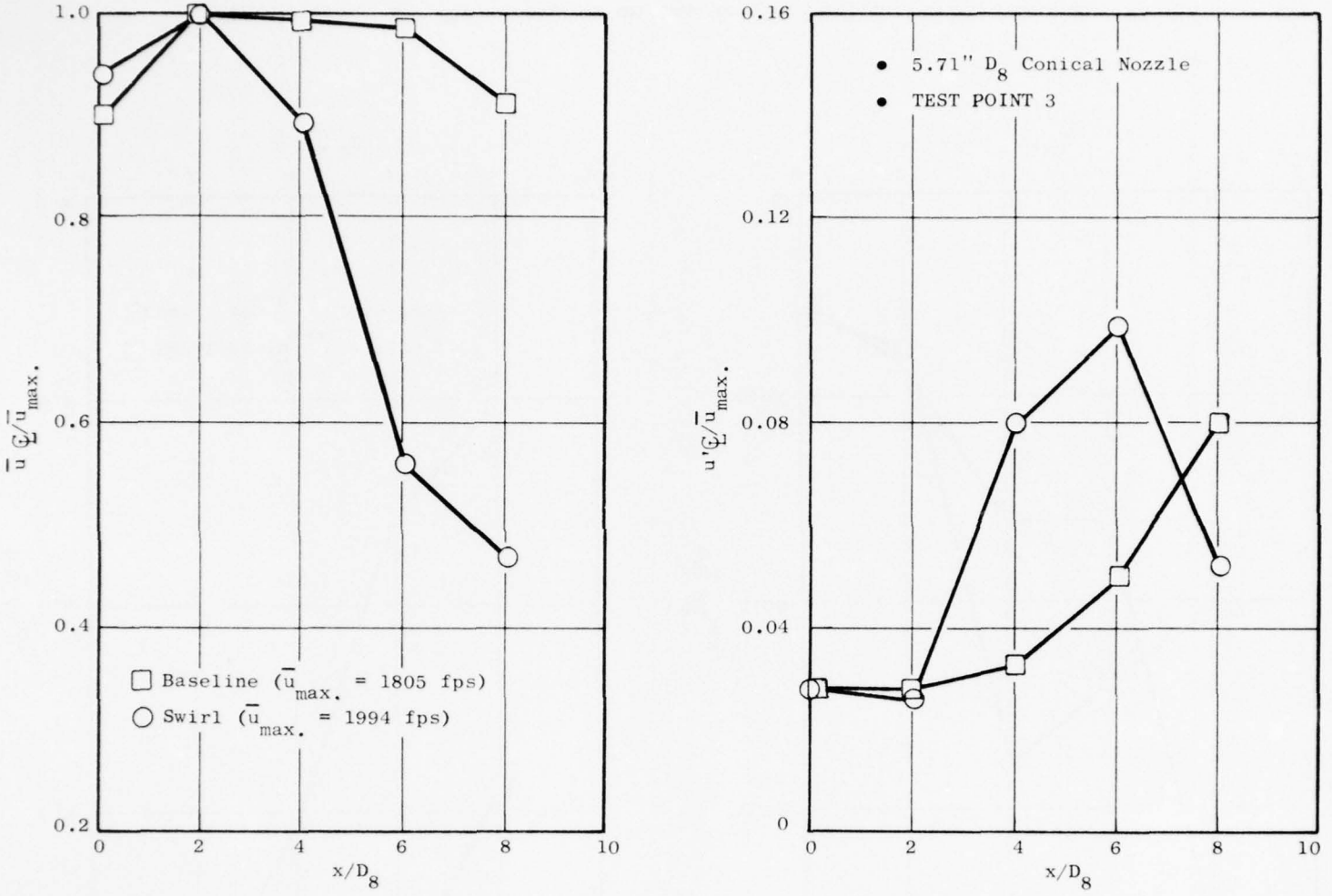


Figure 114. LDV Measurements on the Jet Centerline, Test Point 3.

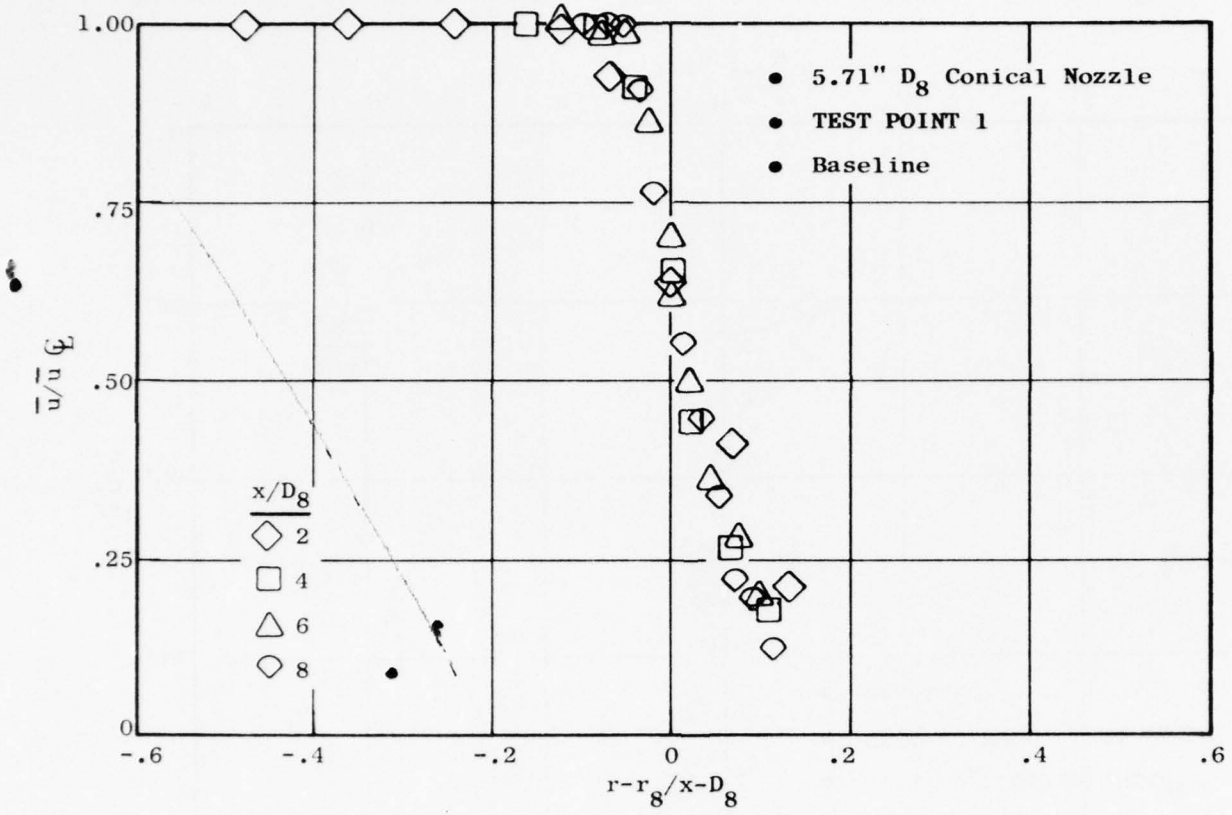


Figure 115. LDV Measurements of Radial Velocity Profiles, Baseline Test Point 1.

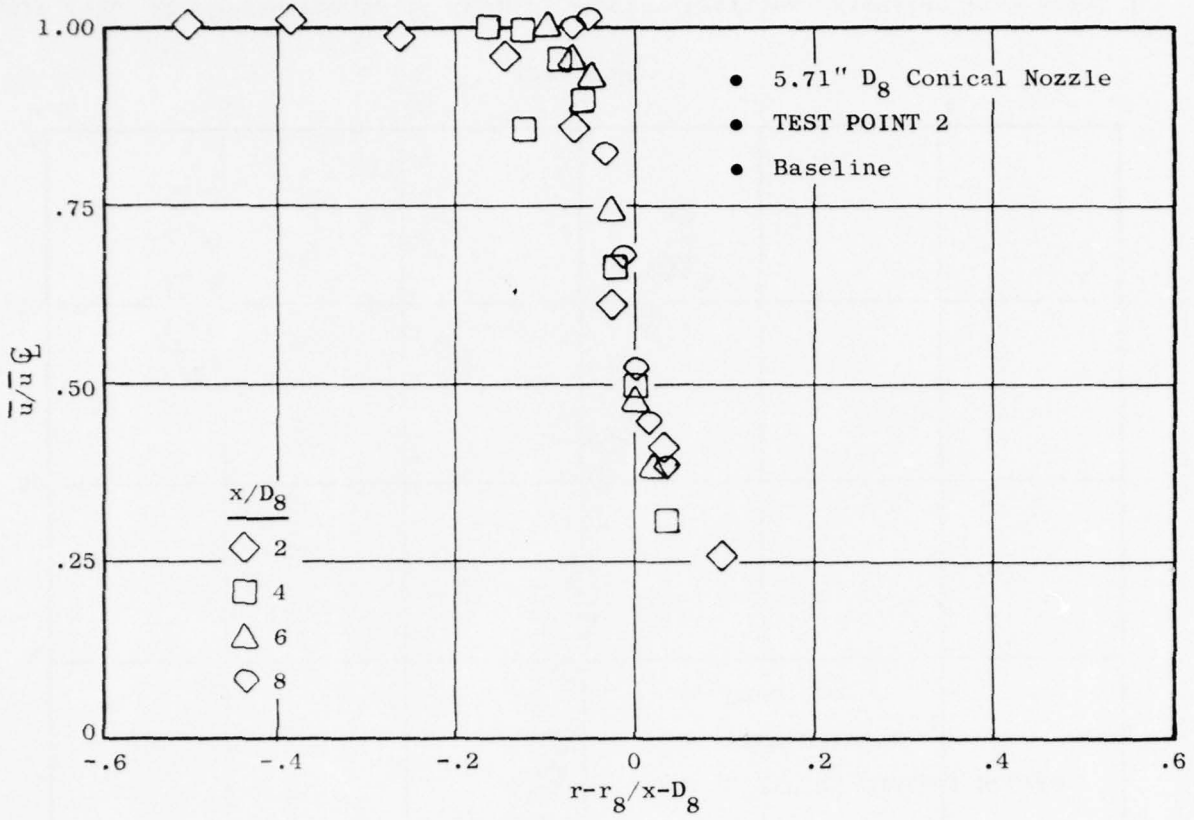


Figure 116. LDV Measurements of Radial Velocity Profiles, Baseline Test Point 2.

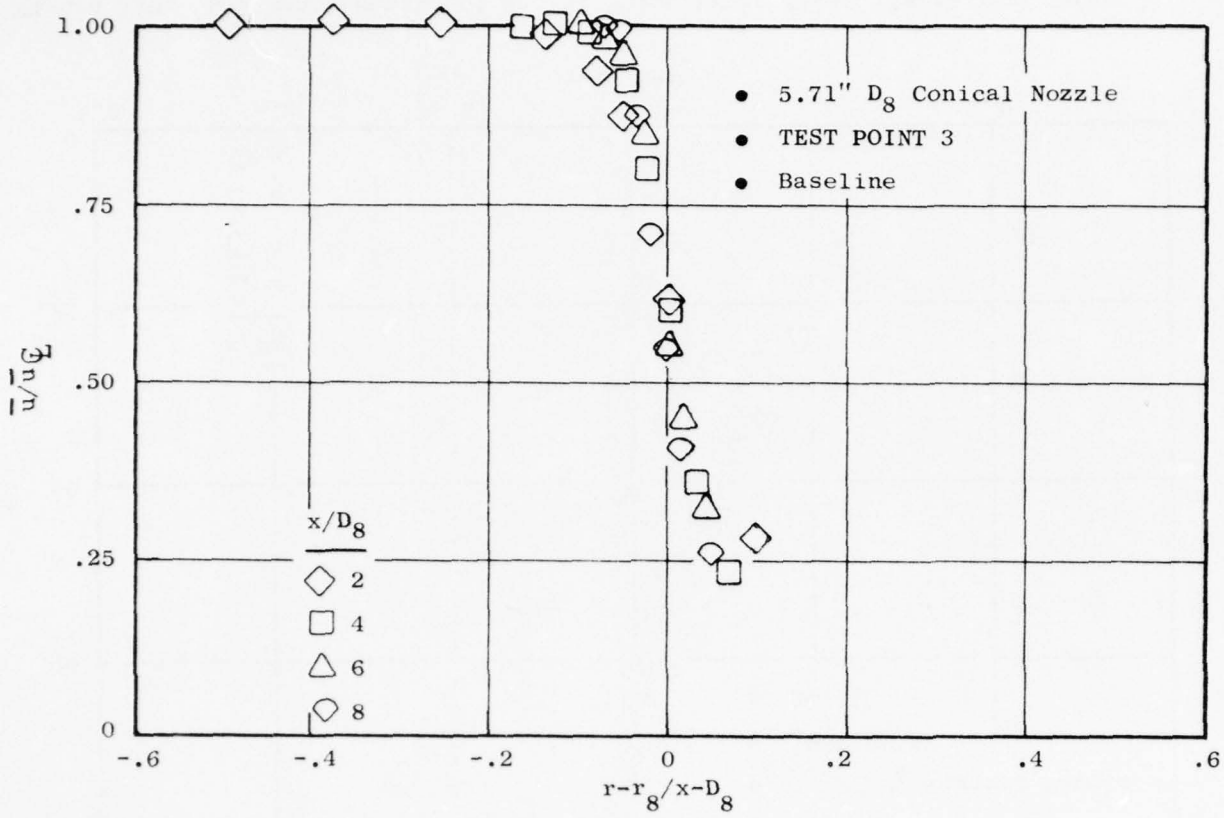


Figure 117. LDV Measurements of Radial Velocity Profiles, Baseline Test Point 3.

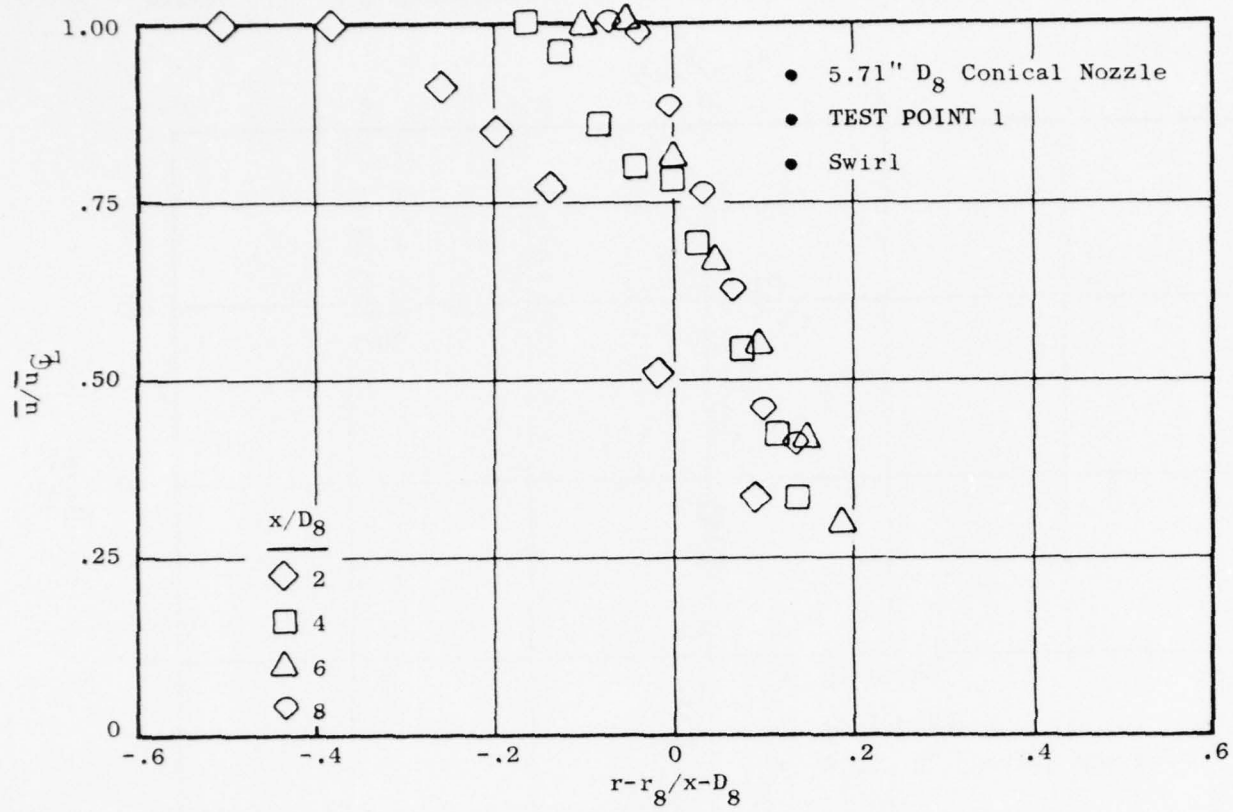


Figure 118. LDV Measurements of Radial Velocity Profiles, Swirl Test Point 1.

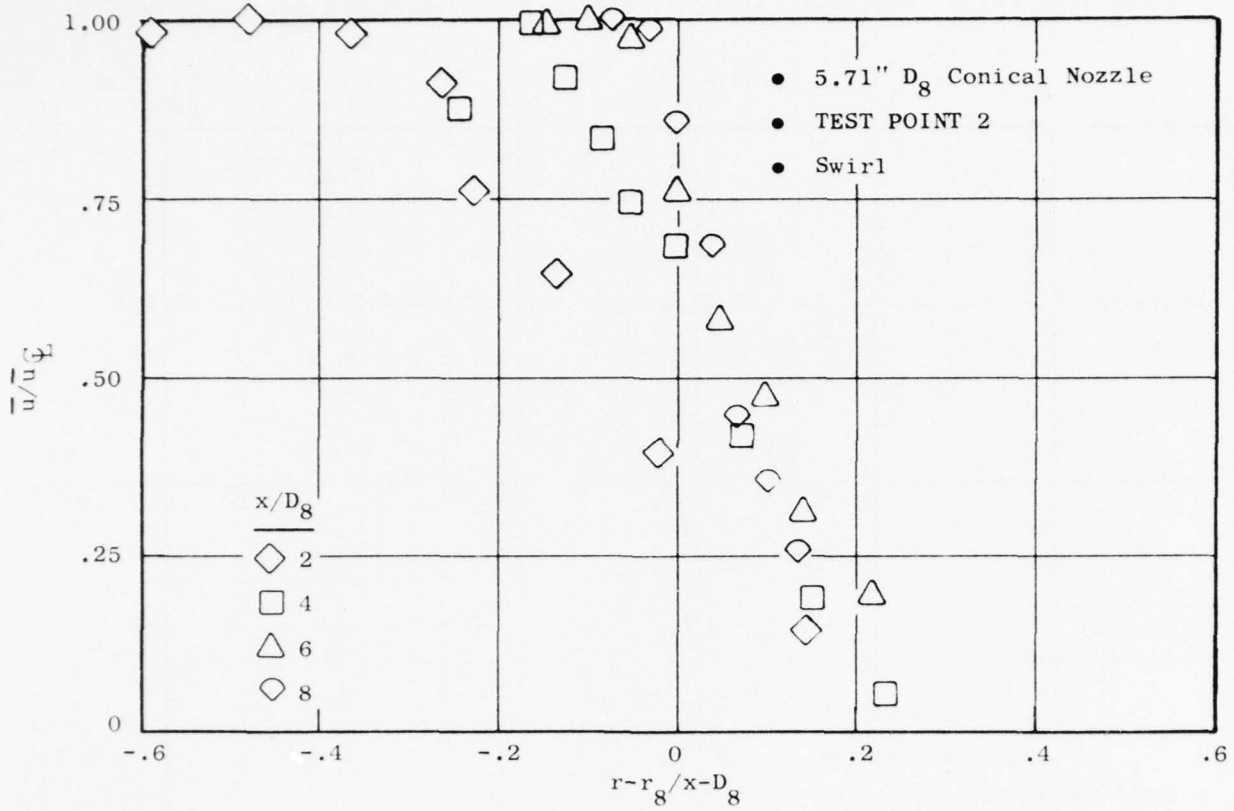


Figure 119. LDV Measurements of Radial Velocity Profiles, Swirl Test Point 2.

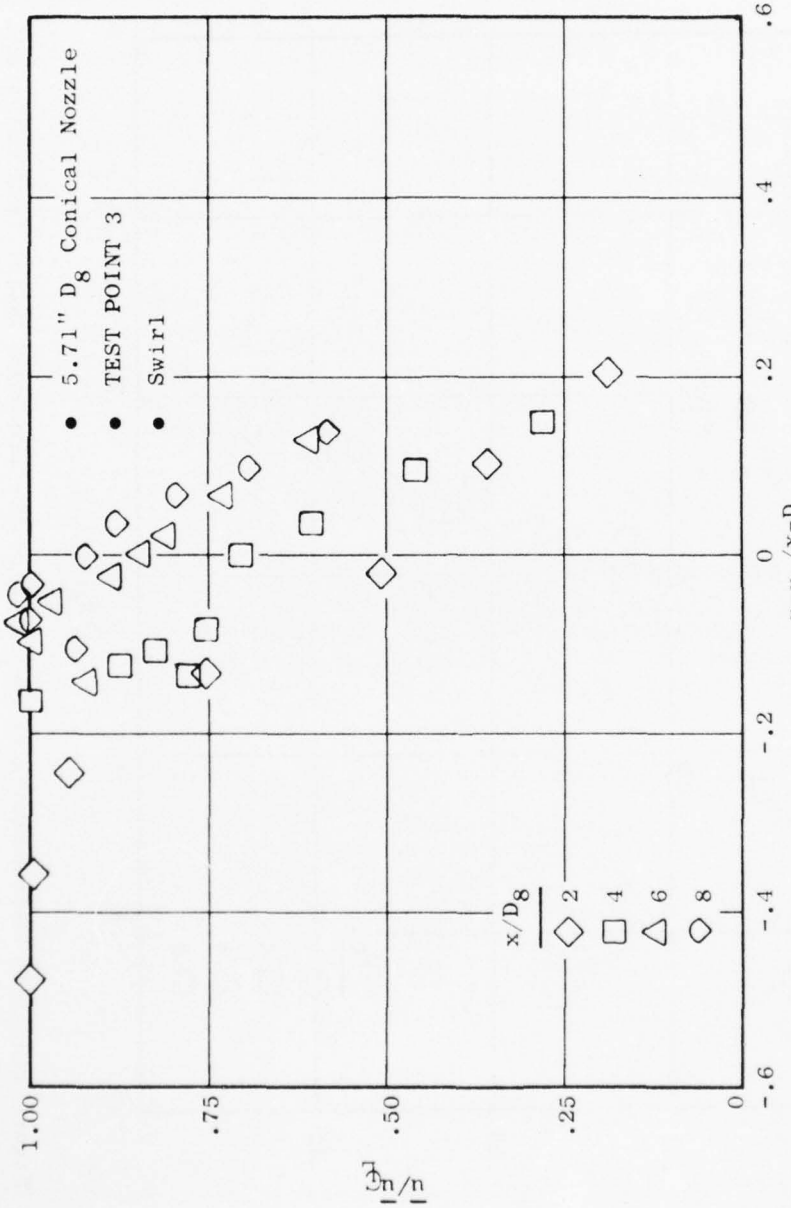


Figure 120. LDV Measurements of Radial Velocity Profiles, Swirl Test Point 3.

the aerodynamic data obtained from cobra probe and LV measurement at the nozzle exit plane ($x/D_8 = 0.09$) can be used to make approximate calculations of gross thrust.

Although measured exit plane profiles of total pressure, swirl angle, and axial velocity are available for all three test points on the swirl configuration, profiles of an additional quantity must be specified in order to uniquely determine fluid properties at the nozzle exit. The most accurate calculations can be made for test point 1, which utilized air at approximately ambient temperature, since a uniform total-temperature profile can be predicted with a high degree of confidence. For this point, the total-pressure and swirl-angle profiles are obtained from Figure 106 and the axial velocity from Figure 109. Figure 121 shows the tangential (swirl) velocity and static-pressure profiles that were calculated using these inputs. Additional properties, such as static temperature and density, can be calculated as required.

Once the profiles of aerodynamic properties have been established, integral properties (such as gross thrust, mass flow, and swirl number) can be determined. The gross thrust of a jet is calculated from equation (163) in terms of mean-density, axial-velocity, and static-pressure profiles. The thrust must be normalized by mass flow:

$$\dot{m} = \int_{A_e} \rho u dA \tag{204}$$

when comparisons are to be made. The gross thrust and mass flow for test point 1 (with swirl) were calculated using Simpson's rule to evaluate the integrals. The results for the swirl case are:

$$F_G = 251.4 \text{ lbf}$$

$$\dot{m} = 11.05 \text{ lbm/sec}$$

$$F_G/\dot{m} = 22.75 \text{ lbf/lbm/sec}$$

The calculated mass flow is within 1.5% of the measured value (11.2 lbm/sec). The identical exit plane total-pressure profile (Figure 106) has been analytically expanded to ambient pressure with no swirl, yielding:

$$F_G = 296.4 \text{ lbf}$$

$$\dot{m} = 11.67 \text{ lbm/sec}$$

$$F_G/\dot{m} = 25.40 \text{ lbf/lbm/sec}$$

This yields a thrust loss of 10.4% that can be attributed directly to swirl. An additional loss would be identified if the total-pressure loss across the swirl vanes were considered.

The swirl number (S) is calculated from equations (183) through (185) in terms of mean-density, axial-velocity, tangential-velocity, and static-

- 5.71" D_8 Conical Nozzle
- TEST POINT 1 ($T_{T8} = T_{amb}$, $P_{T8}/P_{amb} = 1.55$)

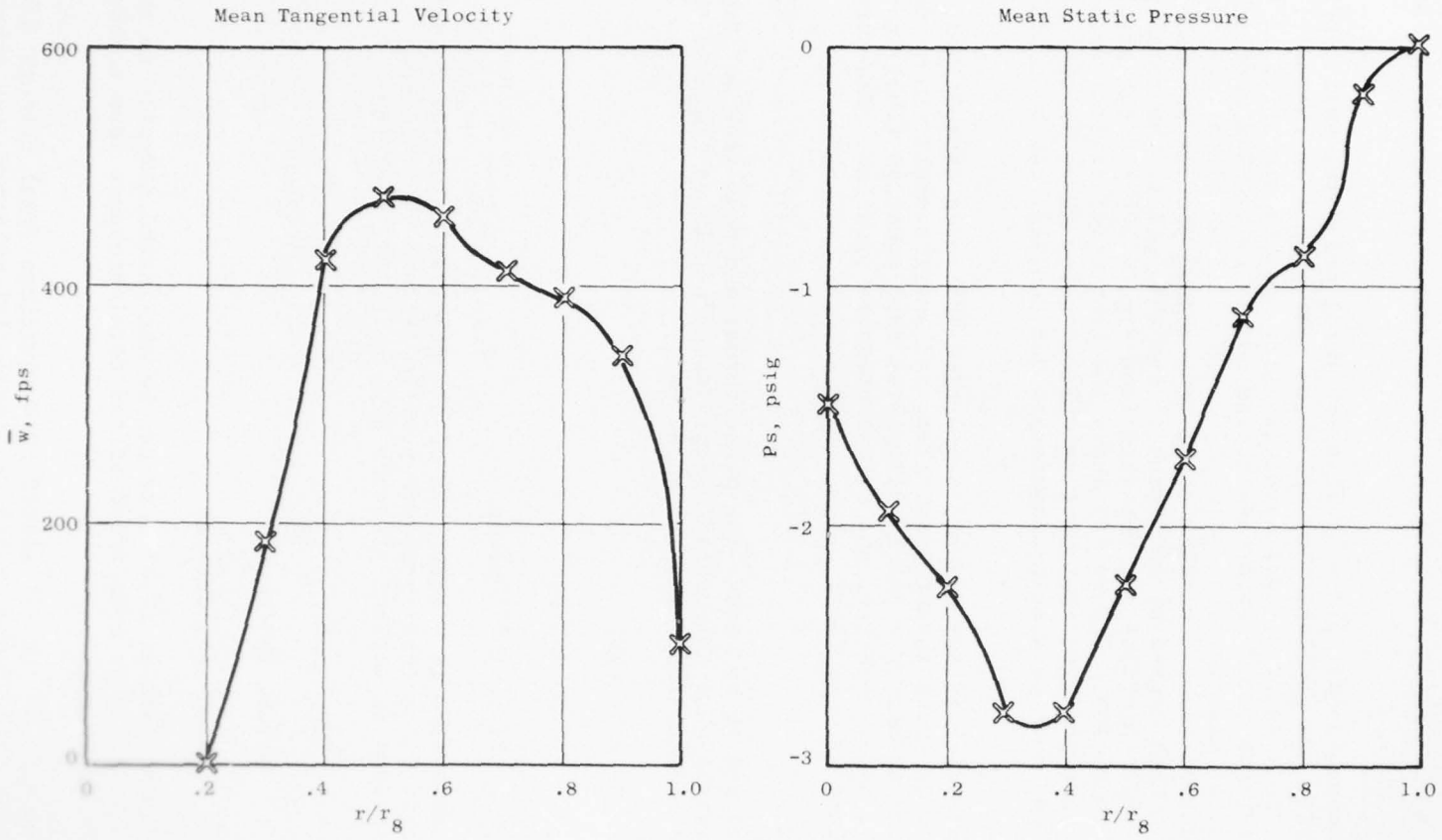
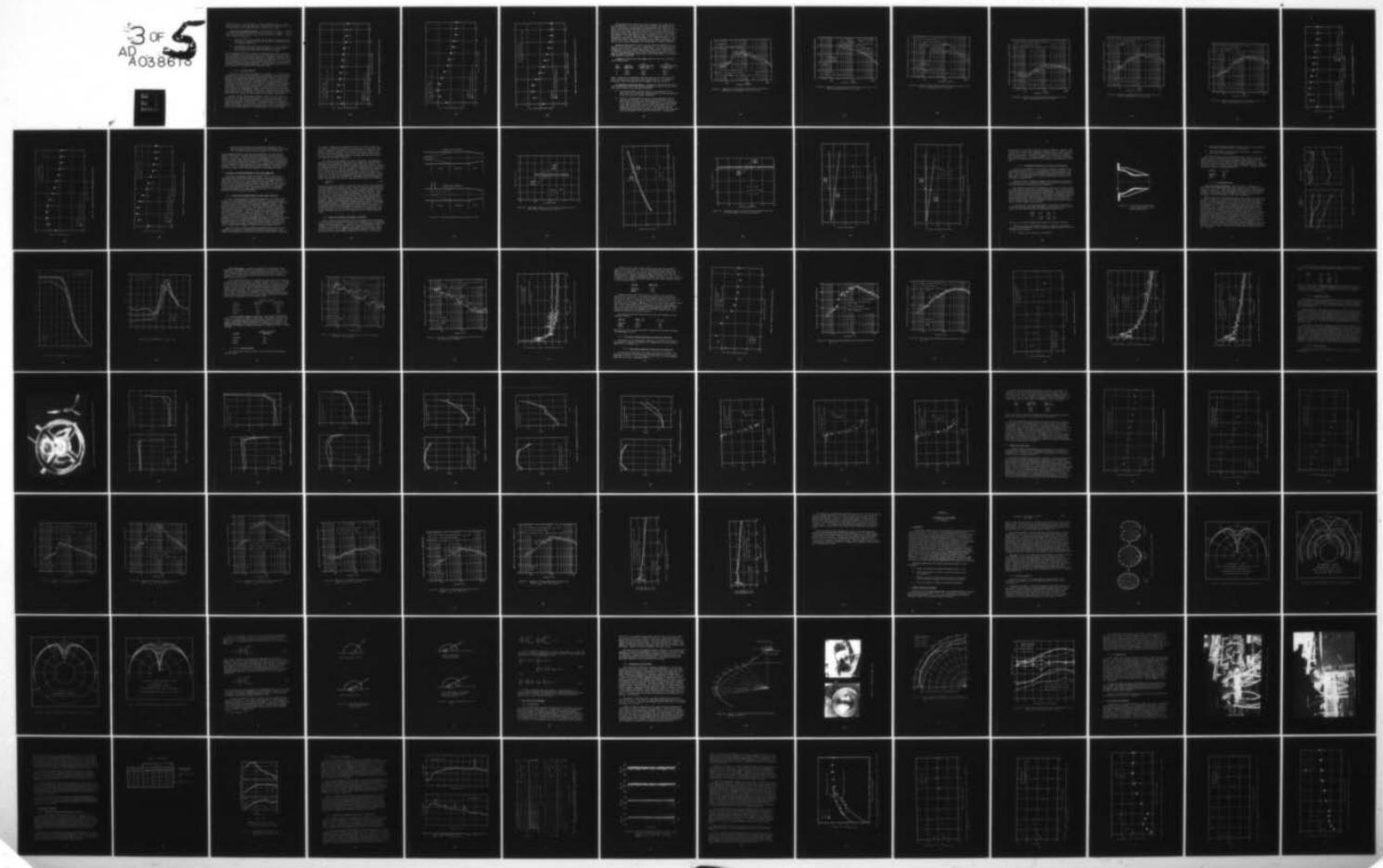
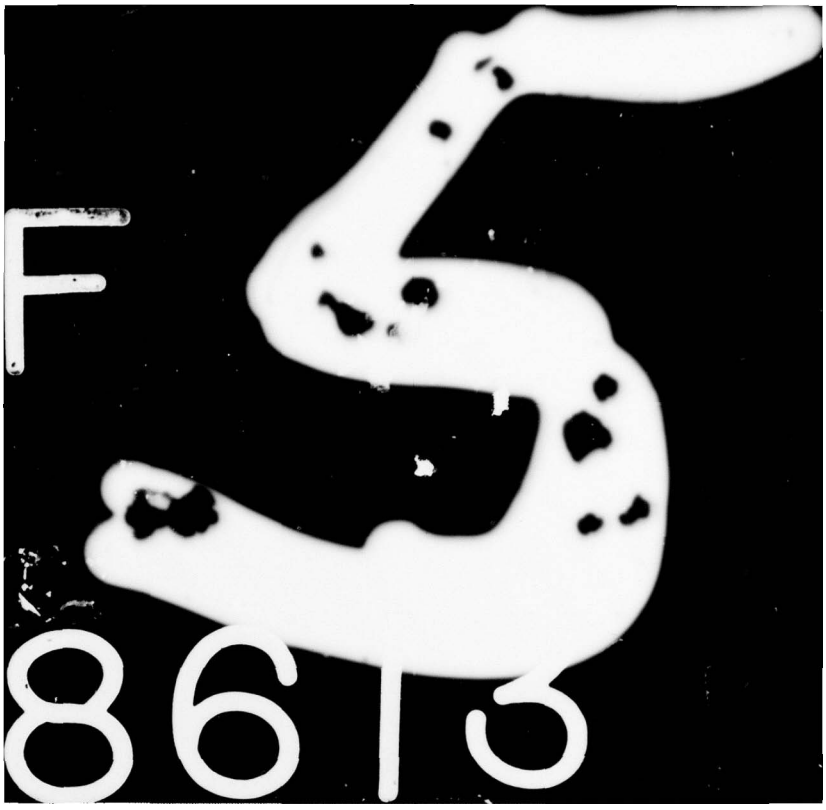


Figure 121. Calculated Profiles 0.5" Downstream of Nozzle Exit.

AD-A038 613 GENERAL ELECTRIC CO CINCINNATI OHIO AIRCRAFT ENGINE GROUP F/G 20/1
SUPERSONIC JET EXHAUST NOISE INVESTIGATION. VOLUME II. TECHNICA--ETC(U)
JUL 76 P R KNOTT, R MANI, C L MERKLE F33615-73-C-2031
UNCLASSIFIED R74AEG452-VOL-2 AFAPL-TR-76-68-VOL-2 NL

3 OF 5
AD A038613




F
8613

pressure profiles. For test point 1, it was calculated to be, S = 0.319. Inspection of the swirl-angle profiles in Figures 107 through 109 shows that the swirl number will be slightly lower for test points 2 and 3.

Verification of Analytical Model - The analytical predictions of Section 1.2.1.2 are for conditions close to those of test point 1. Comparison of the predictions in Figures 92 and 93 with the data presented in Figure 112 leads to the following conclusions:

- Centerline data for the nonswirling jet appear to agree well with predictions, although data were not obtained far enough downstream to completely check this.
- Centerline data for the swirling jet do not agree with predictions. The predicted turbulence levels are higher and the mean axial velocity decay more rapid than indicated by test data.

The discrepancies noted in the case of the swirling jet could be partially due to differences in initial conditions, since the analysis assumes uniform initial profiles of the mean axial velocity and turbulence intensity while the measured profiles were highly nonuniform. An additional explanation for the discrepancies, however, is that the empirical modeling of ℓ, $\sigma_{r\phi}$, σ_e and C_D for swirling flows, having been based on limited data, is not sufficiently "refined" for making general predictions. This would indicate that further work is needed on the swirling-flow aerodynamic model.

1.2.2.3 Acoustic Results

Far-field acoustic data were taken for test points 1, 2, and 3 on both configurations. Since actual exit-plane total pressure cannot be monitored, there is some uncertainty involved in setting test points on the swirl configuration to properly match baseline test points. For this reason, each point was run twice on the swirl configuration, each time using different criteria for setting the point. For one run, the "upstream" total pressure (calculated exit-plane value) was set equal to the baseline total pressure. Recall that, for the baseline configuration, the upstream and exit-plane total pressures are approximately equal. For the second run, the upstream total pressure was set higher by an amount that, based on cobra-probe data, would compensate for the loss due to the vanes, resulting in the same average exit-plane total pressure as was obtained on the baseline configuration.

Measured overall sound pressure levels on the 40' arc are shown in Figures 122, 123, and 124 for test points 1, 2, and 3, respectively. Data for both sets of swirl runs are included, with the OASPL's obtained by "exit-plane matching" consistently 1 to 2 dB higher than those obtained by "upstream matching." For test point 1 (cold flow), there is an increase in OASPL at all angles, while for test points 2 and 3 there is suppression from the jet axis to approximately 50° and enhancement at the larger angles.

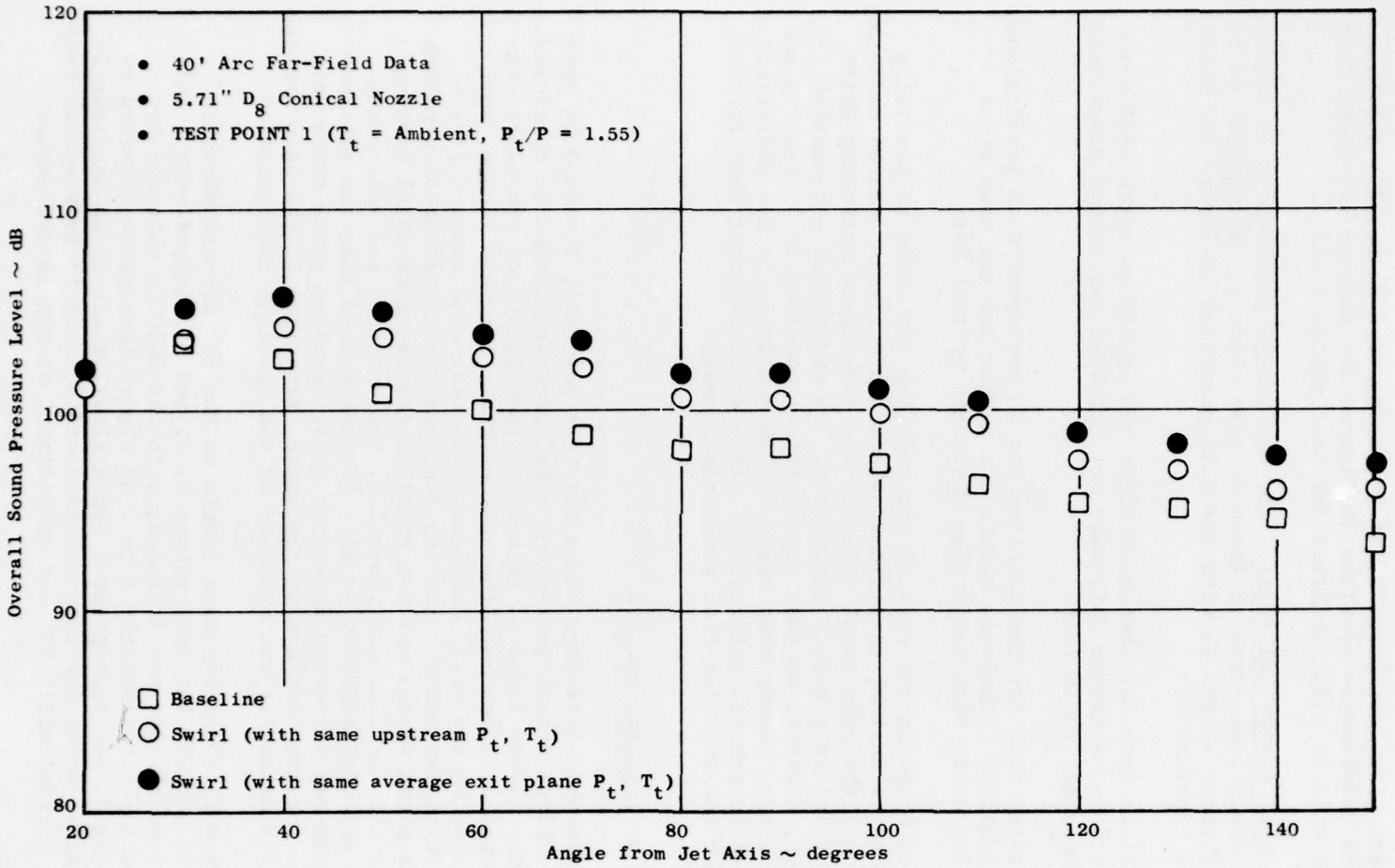


Figure 122. Measured Overall Sound Pressure Levels, Test Point 1.

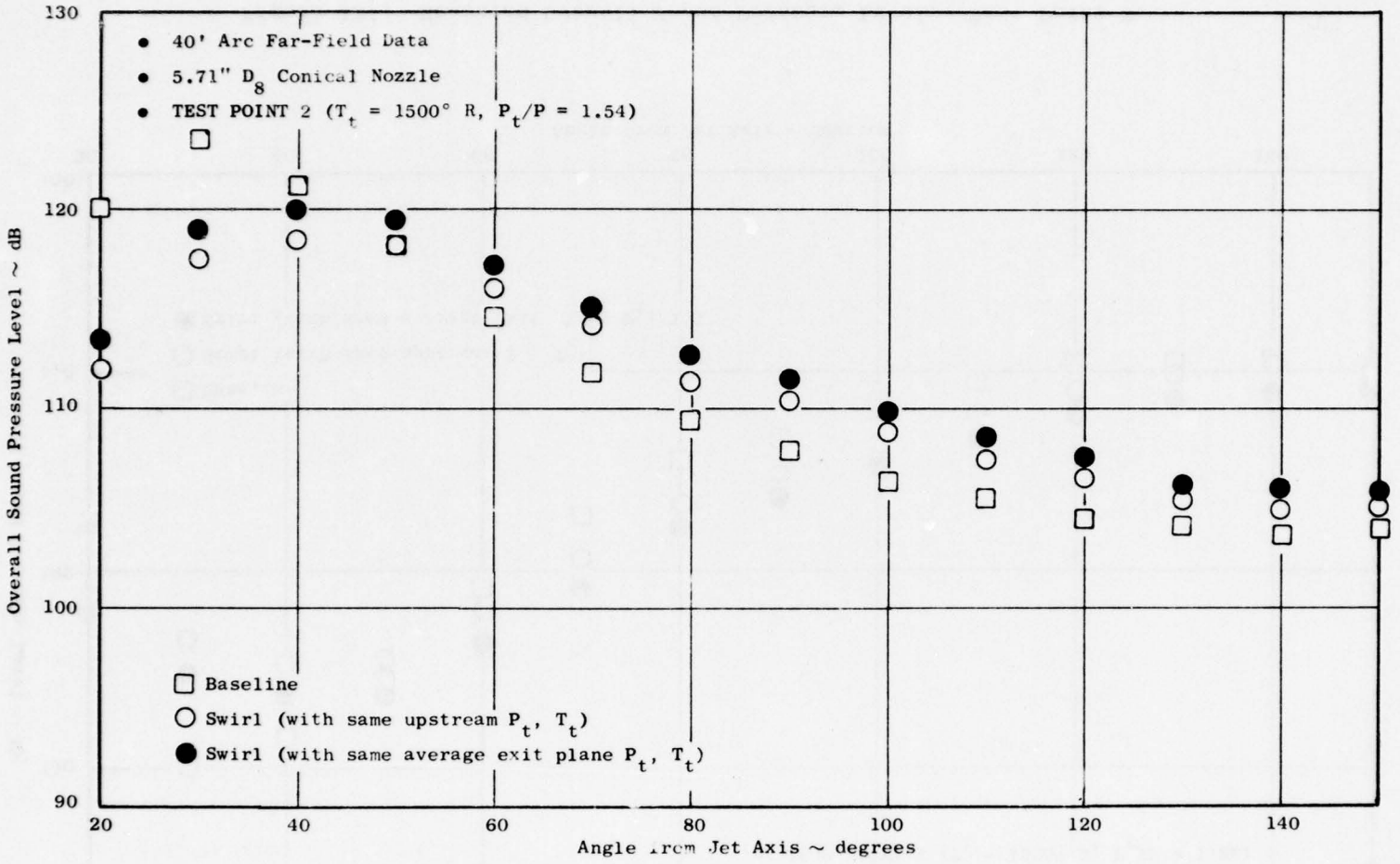


Figure 123. Measured Overall Sound Pressure Levels, Test Point 2.

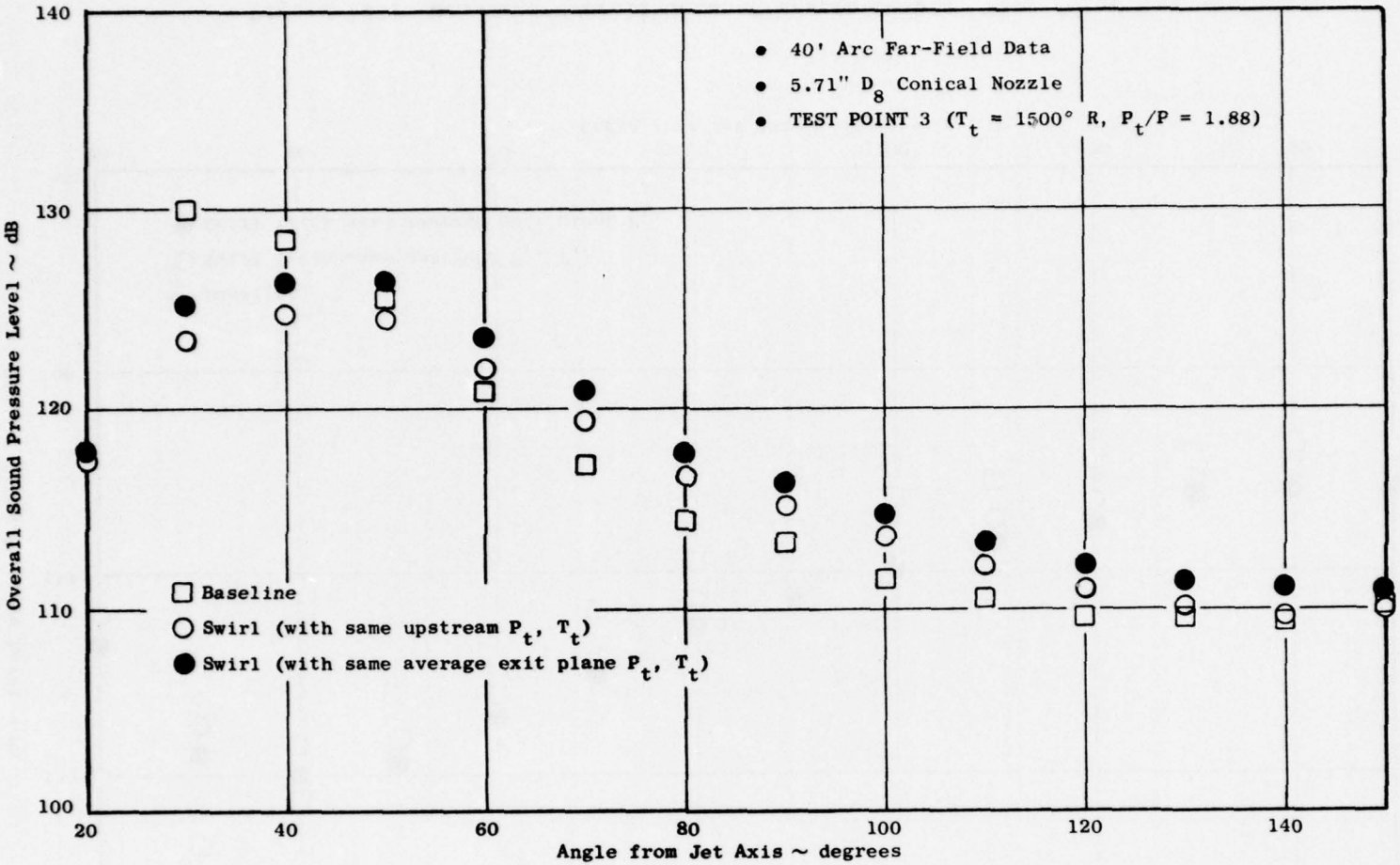


Figure 124. Measured Overall Sound Pressure Levels, Test Point 3.

Sound pressure level spectra are shown in Figures 125 through 127 for the microphone at 30° to the jet axis, and in Figures 128 through 130 for the 90° microphone. Only data for the "upstream matching" conditions are shown, since the spectra are almost identical with a 1- to 2-dB shift for the two sets of swirl runs. For test points 2 and 3, the data indicate that, near the jet axis, suppression due to swirl occurs primarily at frequencies below 2500 Hz, with the highest levels at suppression in the range of 250 and 2500 Hz. At the 90° position, there is some suppression due to swirl at frequencies below 400 Hz, with enhancement at the higher frequencies. The data for test point 1 goes along with this trend, showing some suppression due to swirl at lower frequencies, with enhancement at higher frequencies.

Perceived noise levels on the 40' arc are shown in Figures 131, 132, and 133 for test points 1, 2, and 3, respectively. On this basis, the suppression due to swirl at angles near the jet axis is not as substantial as it appears to be on an overall sound pressure level basis. This is due to the fact that suppression occurs at lower frequencies, generally below the range of greatest annoyance, while there is noise enhancement at the higher, more annoying, frequencies.

A summary of the overall sound power levels for each test is given in the following table:

Test Point	Baseline OAPWL (dB)	Swirl "Upstream Matching" OAPWL (dB)	Swirl "Exit-Plane Matching" OAPWL (dB)
1	143.1	146.1	146.9
2	158.2	156.5	157.5
3	165.5	162.9	164.3

Thus, a reduction in sound power level was obtained, with the addition of swirl, for each of the "hot" jets (test points 2 and 3). An increase in sound power level was obtained for the "ambient" jet (test point 1).

Verification of Analytical Model - Comparison of the analytical predictions in Figures 94 and 95 with the data presented in Figures 122 and 125 for test point 1 leads to the following conclusions:

- The measured OASPL's and SPL spectra for the nonswirling jet agree well with predictions, although there are some discrepancies in the SPL spectra at higher frequencies.

- Data for the swirling jet is only in partial agreement with the analytical predictions. The predictions showed noise reduction due to swirl at all angles. For the ambient jet, noise enhancement at all angles was found. For the heated jets tested, noise reductions were obtained on the order of the predictions, but only at angles near the jet axis (20° - 40°). The predicted spectra indicated noise reductions through the mid band and high frequencies, with an enhancement at the very low frequencies. The measured

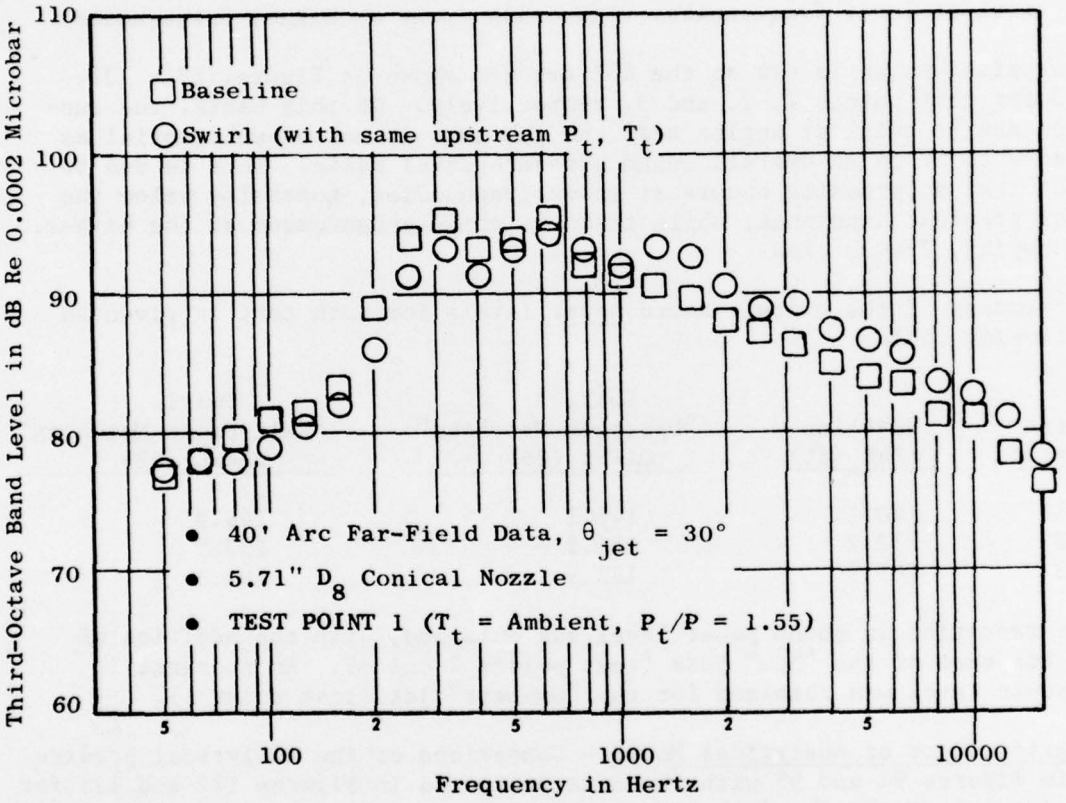


Figure 125. Measured 1/3-Octave-Band Sound Pressure Level Spectra, Test Point 1, Microphone at 30° to Jet Axis.

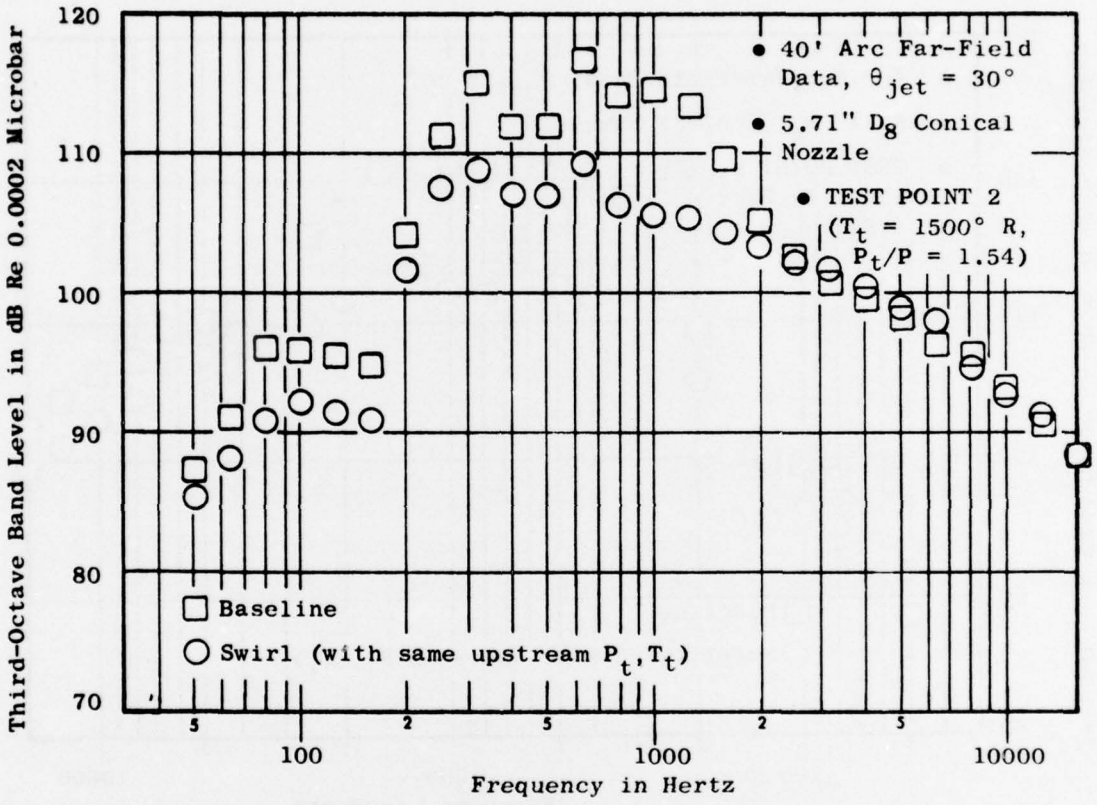


Figure 126. Measured 1/3-Octave-Band Sound Pressure Level Spectra, Test Point 2, Microphone at 30° to Jet Axis.

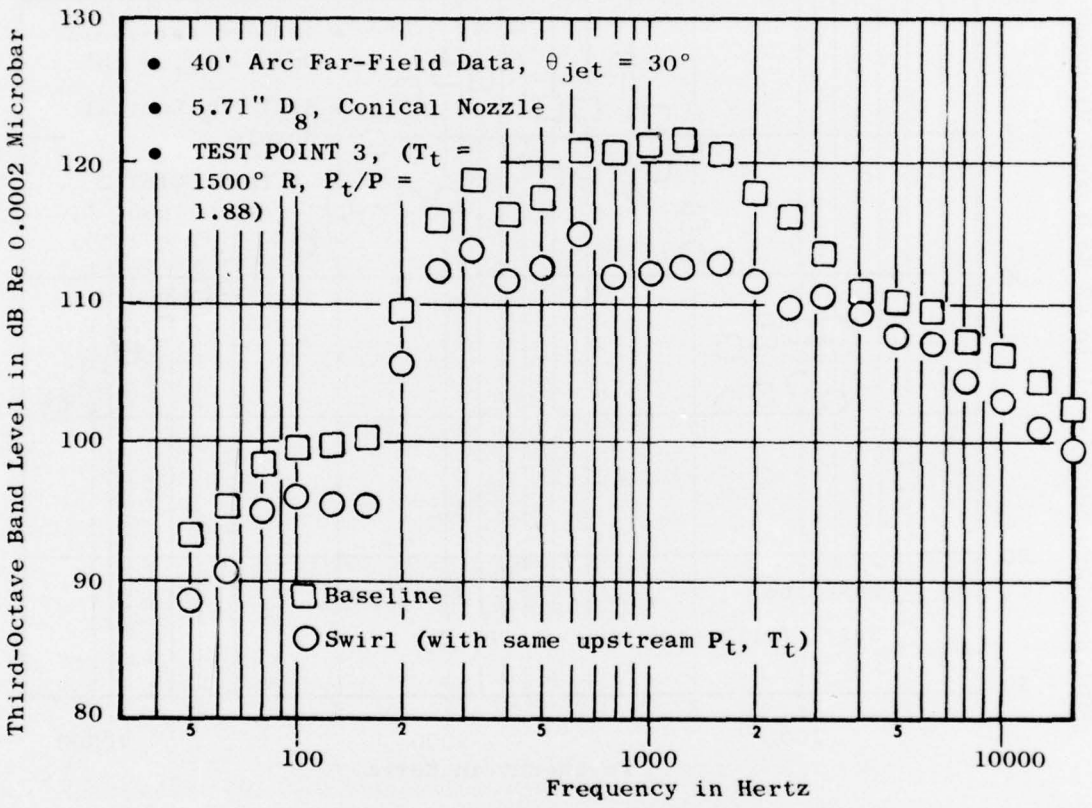


Figure 127. Measured 1/3-Octave-Band Sound Pressure Level Spectra, Test Point 3, Microphone at 30° to Jet Axis.

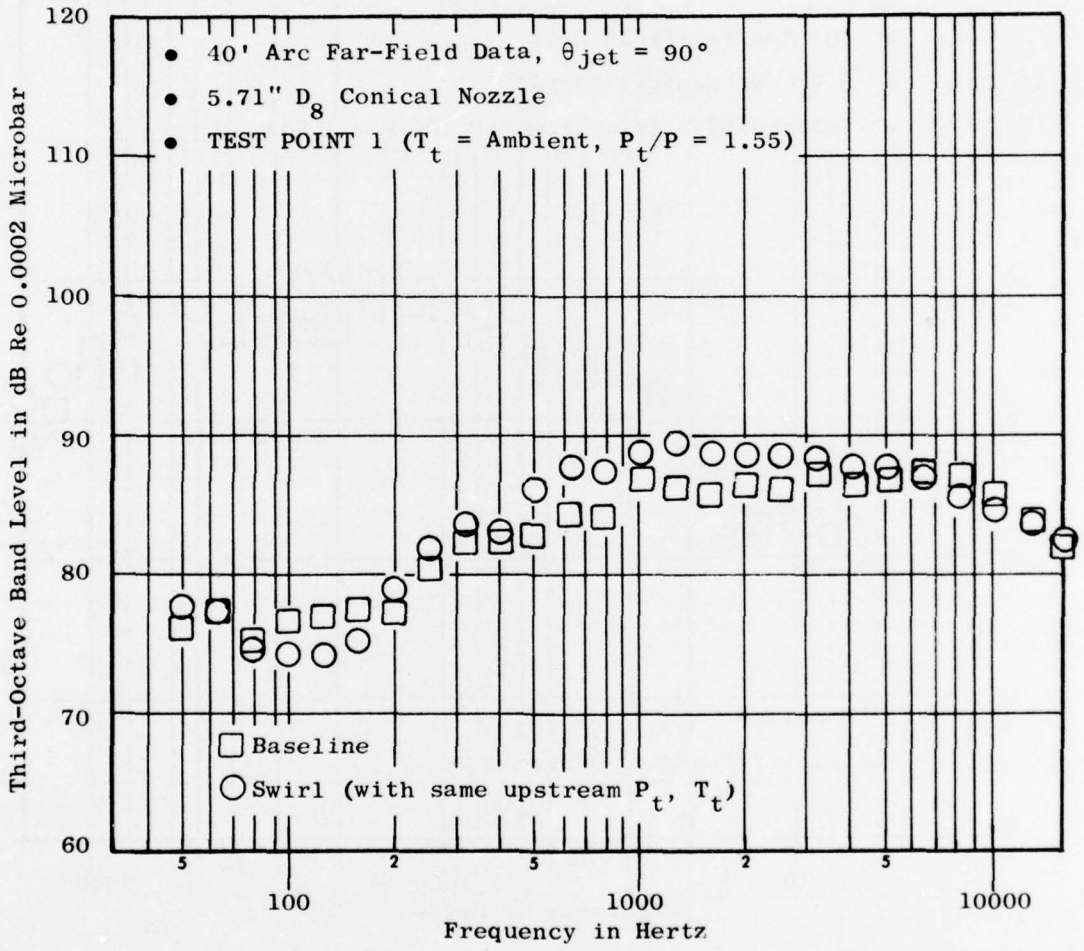


Figure 128. Measured 1/3-Octave-Band Sound Pressure Level, Test Point 1, Microphone at 90° to Jet Axis.

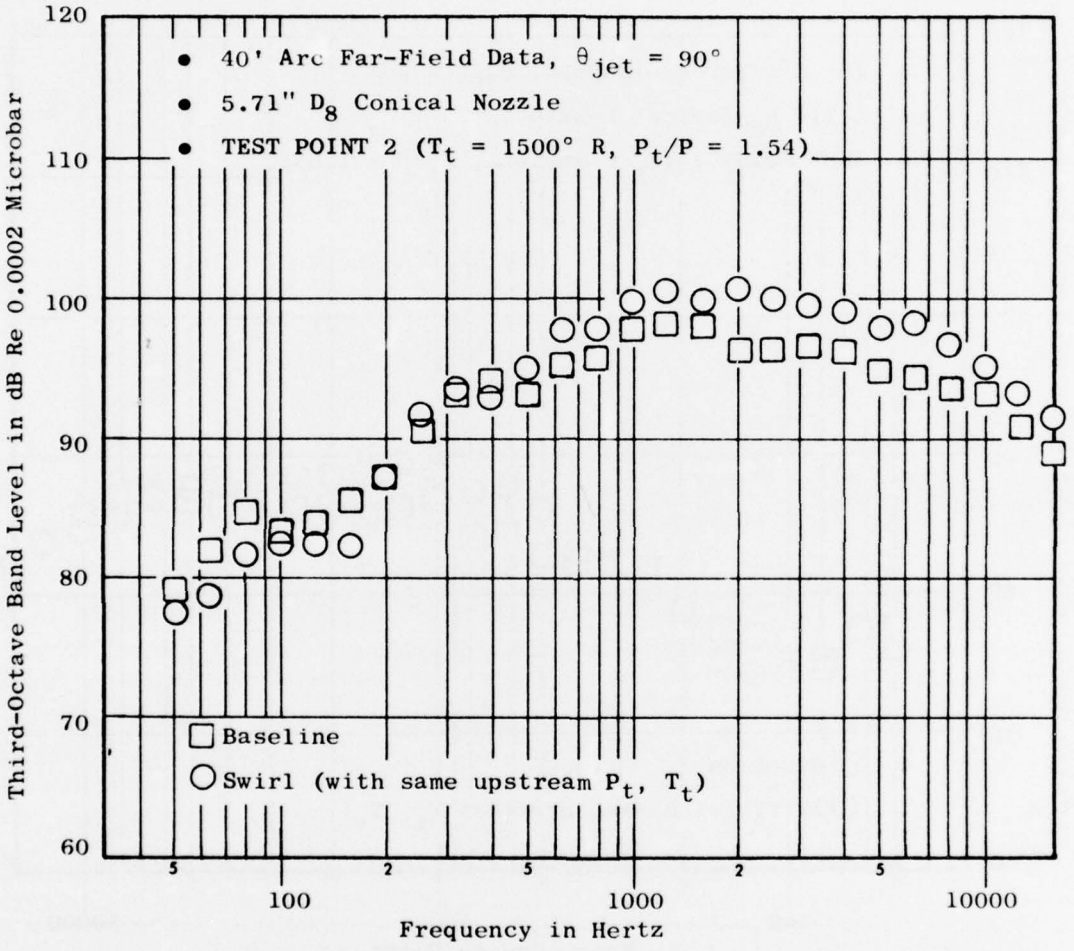


Figure 129. Measured 1/3-Octave-Band Sound Pressure Level, Test Point 2, Microphone at 90° to Jet Axis.

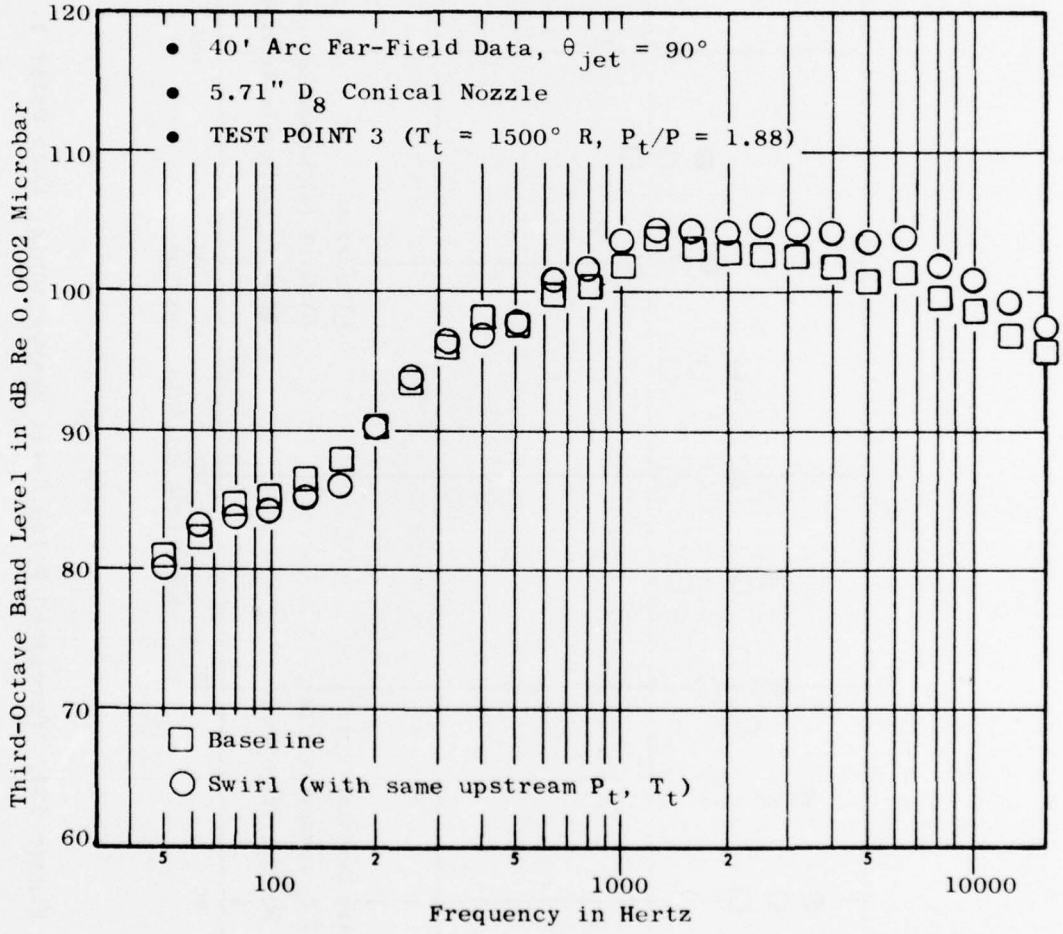


Figure 130. Measured 1/3-Octave-Band Sound Pressure Level, Test Point 3, Microphone at 90° to Jet Axis.

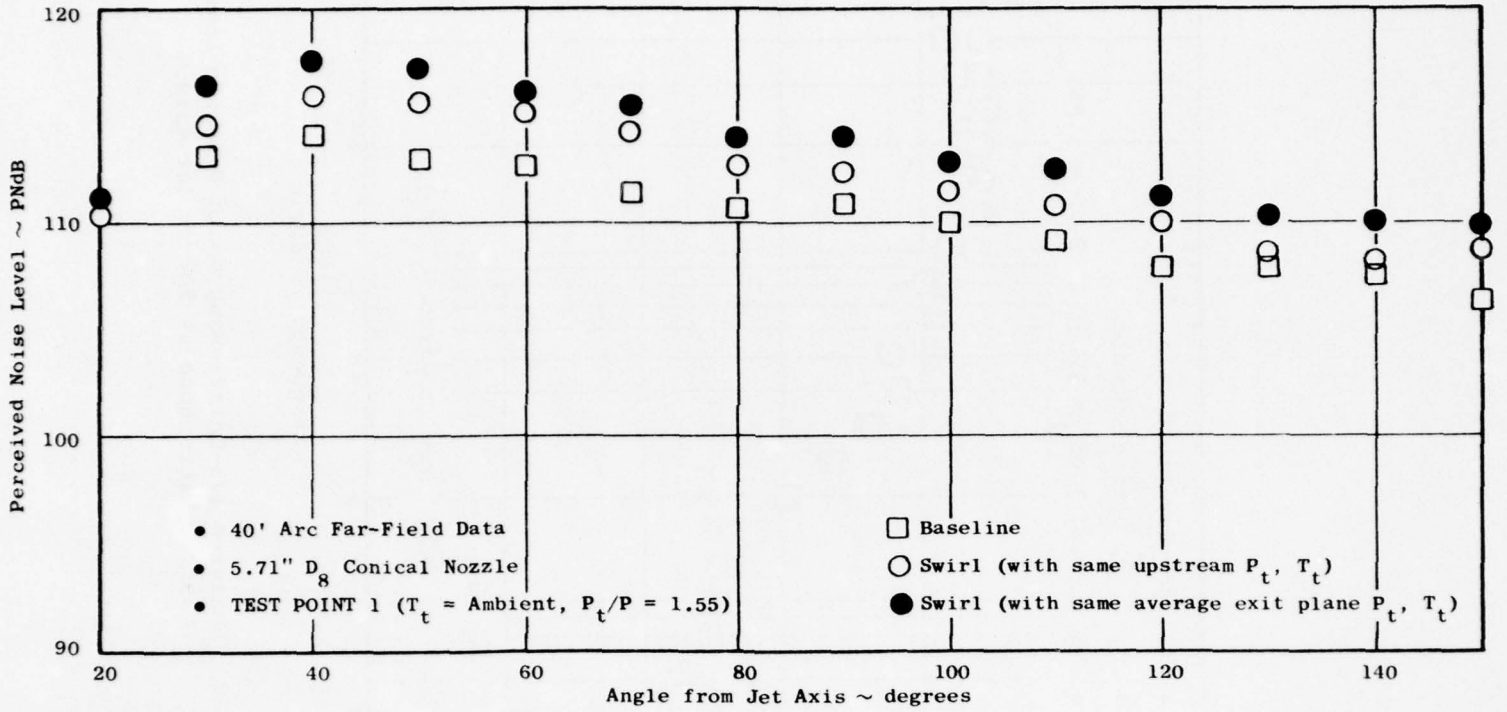


Figure 131. Perceived Noise Level Measurements, Test Point 1.

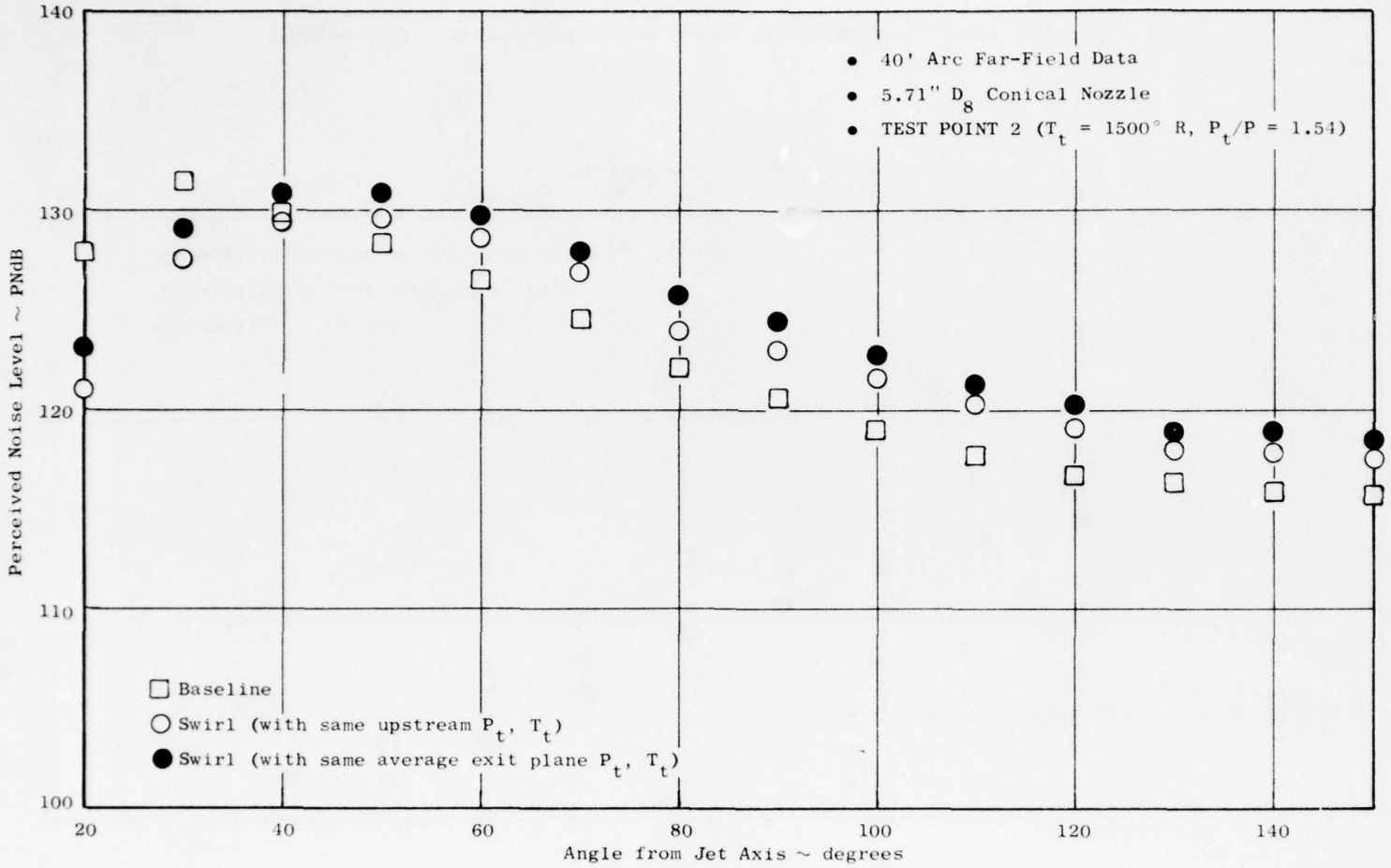


Figure 132. Perceived Noise Level Measurements, Test Point 2.

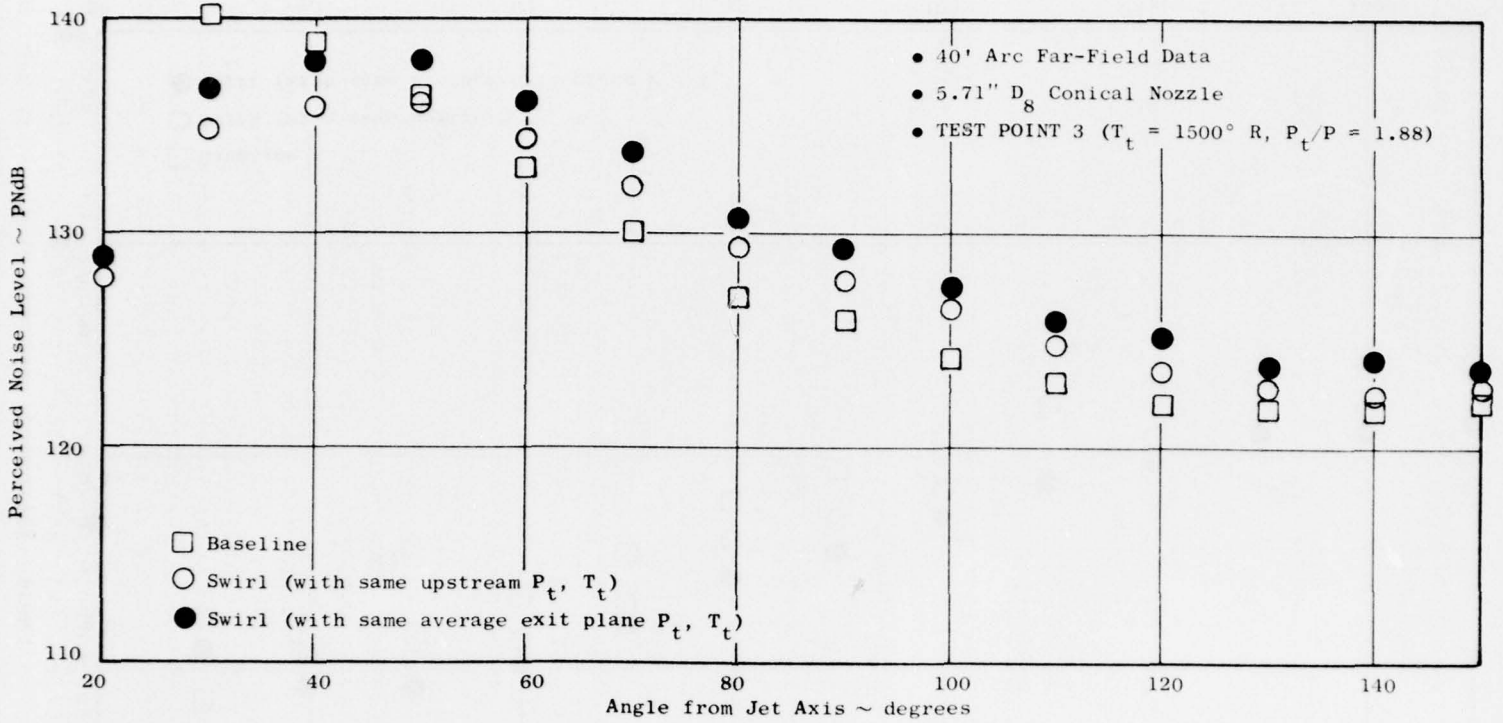


Figure 133. Perceived Noise Level Measurements, Test Point 3.

heated jet spectra showed noise reductions throughout the mid band frequencies, as well as at the very low frequencies (see Figure 128), the latter being in direct contradiction to predictions.

The discrepancies noted in the theory/data comparisons for swirling jets indicate that further refinement of the swirling jet turbulence model is needed. In addition, further refinements are probably necessary in the approximate acoustic model selected for this investigation. It should be noted that the turbulent mixing acoustic model was not modified for the prediction of jet noise in the presence of swirling flow. In particular, the mean swirl velocity component is not considered in the calculations of acoustic source strength. Once the aerodynamic model has been "corrected," the validity of the acoustic model could be further evaluated for swirling-flow fields.

1.3 INFLUENCE OF UPSTREAM TURBULENCE ON JET NOISE GENERATION

Theoretical aeroacoustic prediction models [10,119] indicate that increased levels of upstream (nozzle exit plane) turbulence can result in significant increases in jet noise, particularly at the higher frequencies. These predictions have been corroborated by recent experiments (125) on subsonic jets in which exit-plane turbulence levels were increased from 2-3% to 12-14% using "turbulence generators" in the upstream flow. The purpose of the present experiments was to investigate the effects of increased upstream turbulence due to rough combustion and due to the obstructions typical of a turbojet engine afterburner.

1.3.1 Analytical Aerodynamic Model for Turbulence Production

A control volume analysis of turbulence production in a constant area mixing process was formulated by Ortwerth [126,127] to obtain first-order estimates of the influence of combustor configuration and entrance conditions on the production of turbulence in supersonic combustion ramjets. This analysis considers the problem of two initially uniform streams mixing to uniformity in a constant-area duct. The increase in entropy, occurring in this irreversible process, is assumed to result from the production and dissipation of turbulence. Thus, the maximum total turbulent energy production can be calculated by constraining the flow to have no entropy change (i.e., turbulence is produced but not dissipated). The one-dimensional (integral) equations of motion, including the effects of turbulence, are developed for a control volume surrounding the mixing section. These equations are then solved for the mean and turbulent properties of the flow at the downstream station. At this point, the turbulence energy is assumed to be "frozen," heat is added due to combustion of the fuel-air mixture, and the flow is isentropically expanded to ambient pressure through a nozzle.

Among the several turbulence-generating mechanisms that exist within a combustor or afterburner, this particular analysis is applicable to the turbulence generated by the injection of fuel and by the mixing of stratified

flow regimes created by the combustion process. It should be noted that the analysis considers gaseous fuel (e.g., hydrogen), and that the relationships of compressible gas dynamics are therefore used in formulating the equations of motion. However, in a JP-fueled gas turbine engine or test facility combustor/afterburner, the fuel jet is an atomized liquid spray. This case can be treated approximately by assuming the fuel to be a gas of very high molecular weight (density).

The analysis was programmed for digital computation, and checked out against the results shown in Reference 127 for conditions corresponding to a hydrogen-fueled supersonic combustion ramjet engine flying at $M_\infty = 8.0$. The computer program was then used to perform a parametric study of turbulence generation due to fuel injection for conditions approximating the operation of the JENOTS facility, with the assumption of a high-molecular-weight gas as fuel. The physical configuration for the model is shown in Figure 134. Turbulence intensity at the end of the mixing section was calculated about a nominal set of conditions by independently varying air Mach number, fuel-air ratio, fuel velocity, and fuel swirl for both normal and coaxial injection (Figures 135 through 138). Recall that turbulence intensity is defined as:

$$t = \sqrt{\bar{u}'^2}/\bar{u} \tag{205}$$

in the case of locally isotropic turbulence, where $\bar{u}$ and u' are the mean and turbulent components of axial velocity. These results show that the turbulence generated by the injection of fuel is most strongly influenced by fuel velocity, fuel-air ratio, and injection angle (normal or coaxial). Figure 139 shows the variation in turbulence intensity at the nozzle exit plane as a function of fuel velocity and injection angle. Note that the level of intensities is much lower than at the end of the mixing section (Figure 138), even though the turbulence kinetic energy has not been allowed to dissipate. This is because the mean flow has been accelerated due to heat addition (combustion) and expansion through the nozzle, while the turbulence energy remains "frozen." Comparing the calculated intensities (~0.3%) with the measured JENOTS exit-plane intensities (2~4%) shown in this report, it is apparent that exit-plane turbulence is dominated by other effects, such as pipe turbulence. It is concluded that the effects of variation in the fuel-air mixing process are not very significant to the overall turbulence level.

1.3.2 Combustion Roughness Aeroacoustic Experiment

Rocket exhaust noise experiments [128] have indicated that increases in jet noise can be associated with increases in the intensity of nozzle plenum chamber pressure fluctuations. In these tests, varying degrees of combustion roughness (as indicated by the intensity of pressure fluctuations) were obtained by using different injector types, while the nozzle exit velocity was held constant. The results showed a marked increase in overall sound power level as the plenum chamber roughness was increased. One possible

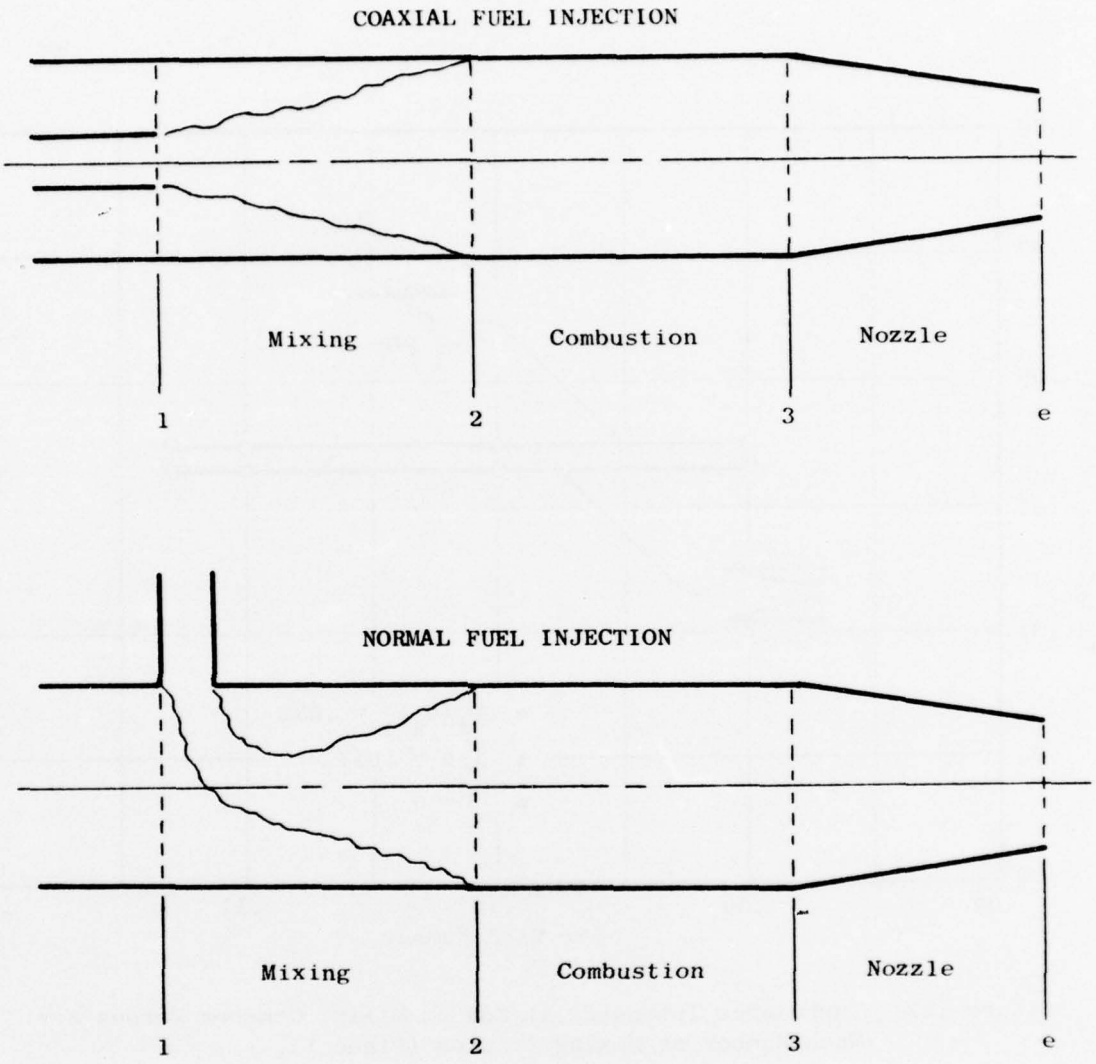


Figure 134. Physical Configuration for Analytical Model.

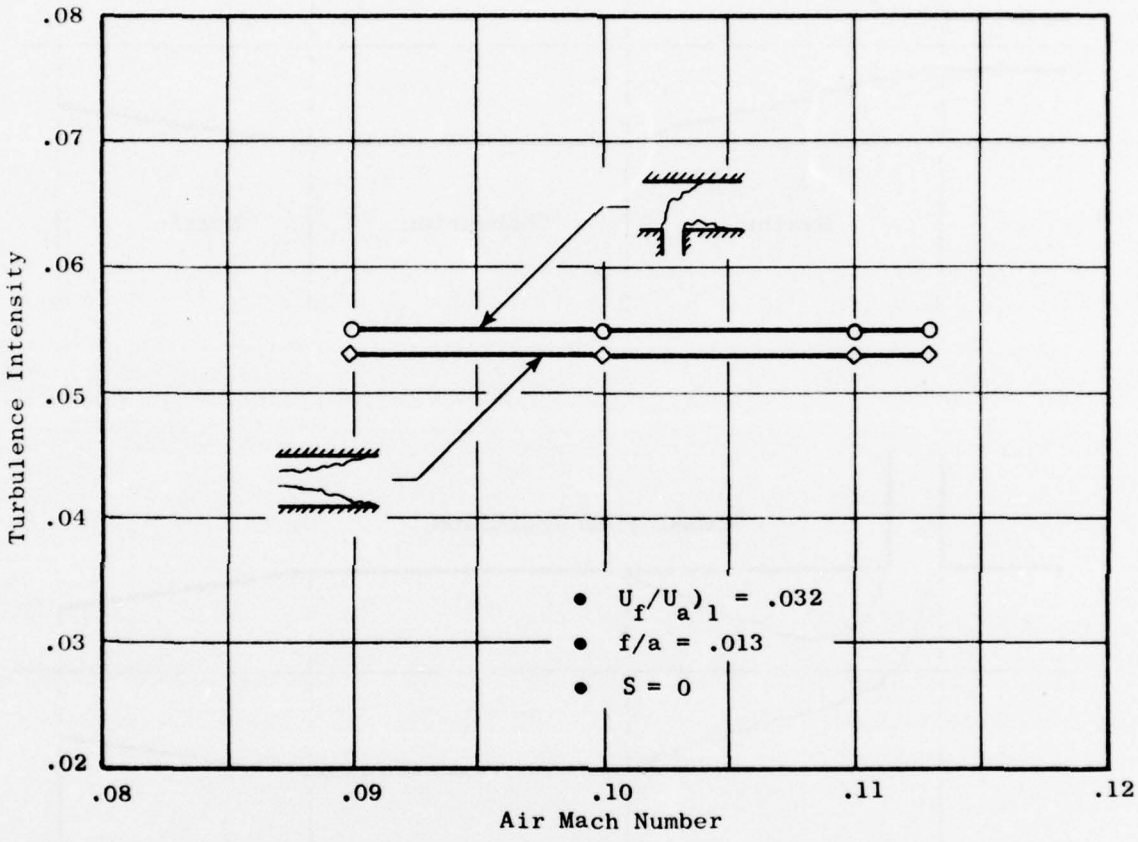


Figure 135. Turbulence Intensity at End of Mixing Chamber Versus Air Mach Number at Mixing Station (Plane 1).

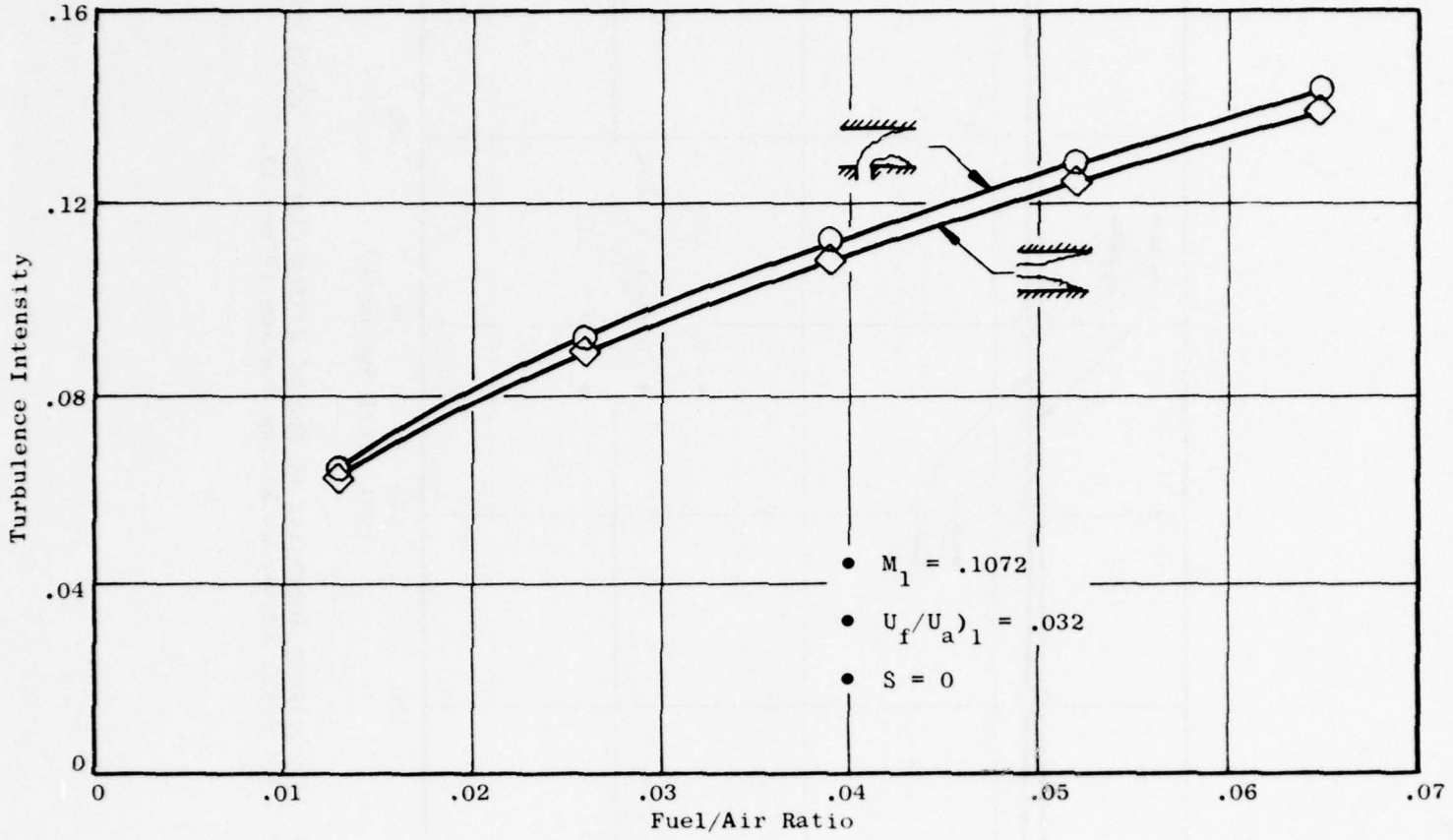


Figure 136. Turbulence Intensity at End of Mixing Chamber Versus Fuel/Air Ratio.

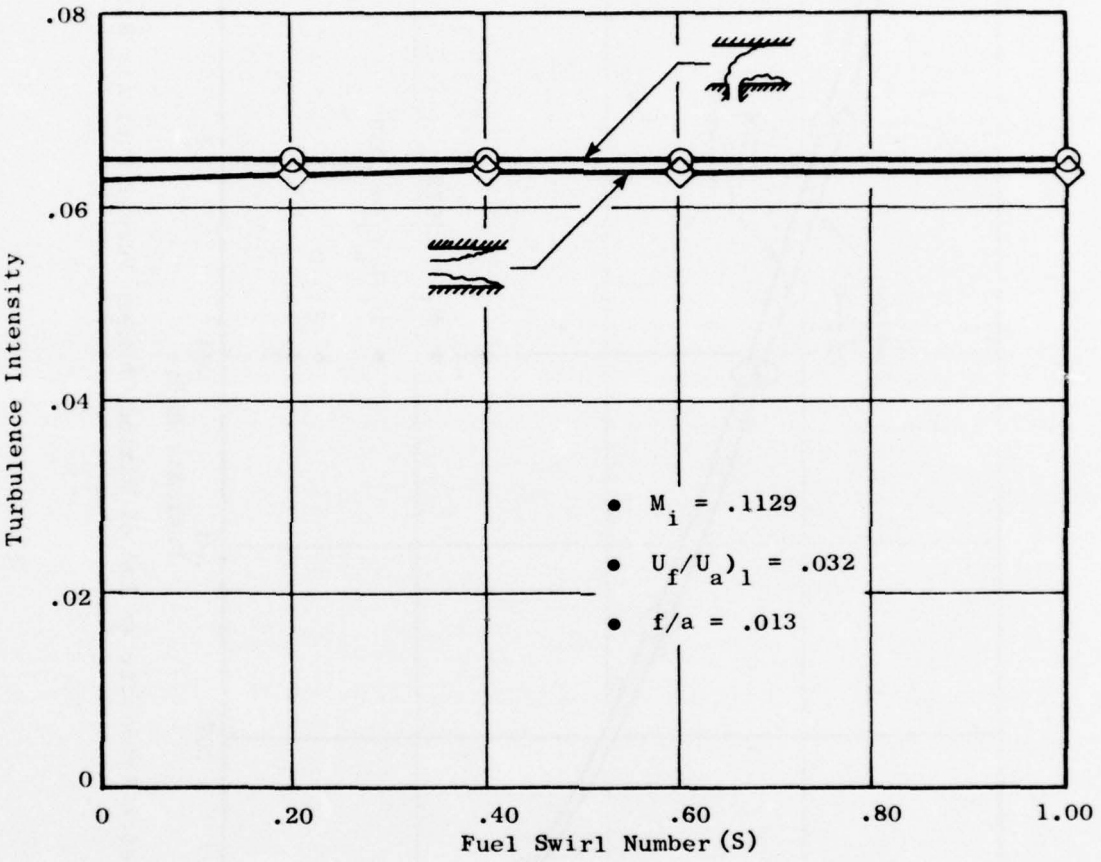


Figure 137. Turbulence Intensity at End of Mixing Chamber Versus Fuel Jet Swirl Number at Mixing Station (Plane 1).

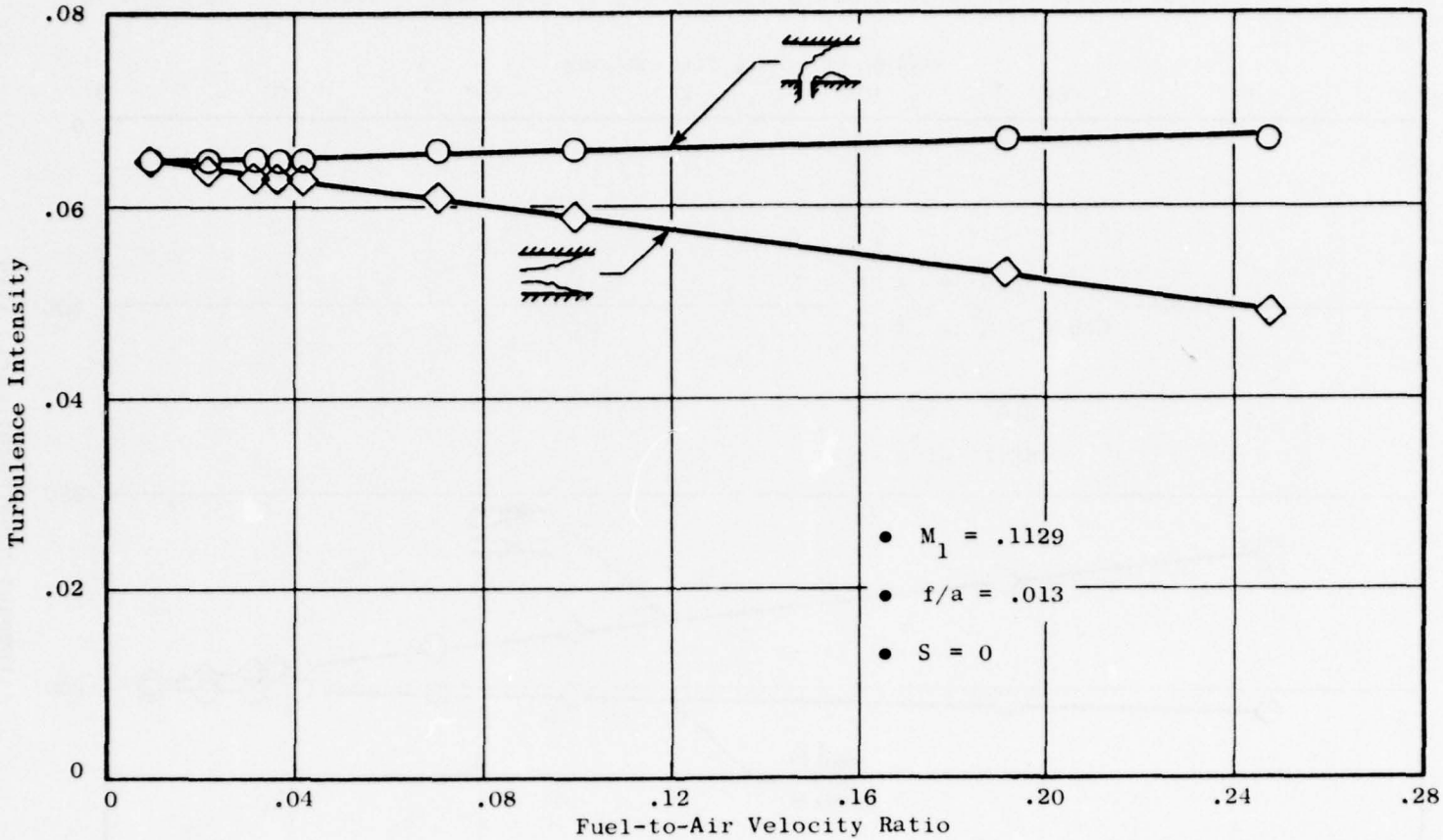


Figure 138. Turbulence Intensity at End of Mixing Chamber Versus Fuel-to-Air Velocity Ratio at Mixing Station (Plane 1).

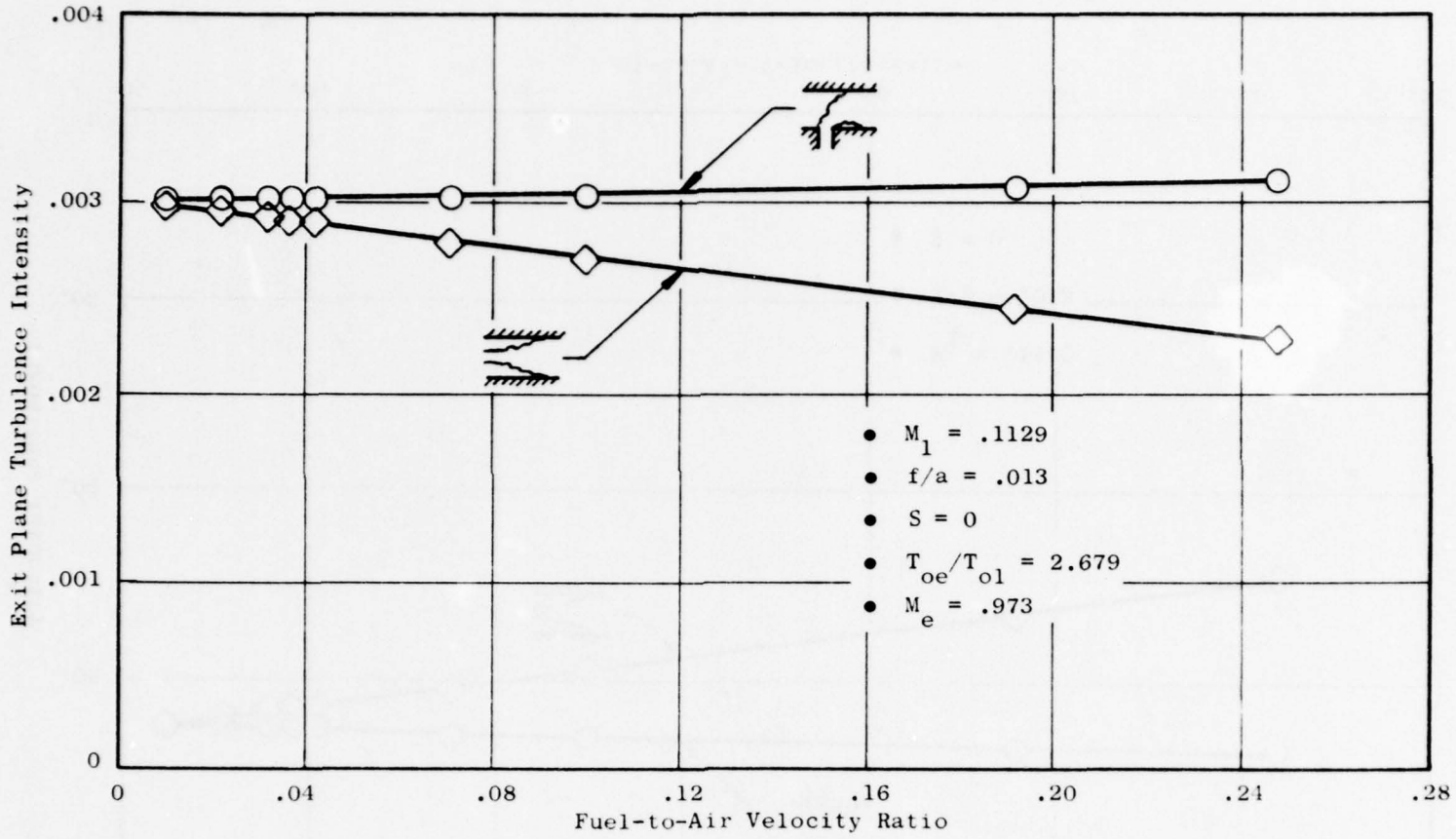


Figure 139. Turbulence Intensity at Nozzle Exit Plane Versus Fuel-to-Air Velocity Ratio at Mixing Station (Plane 1).

explanation for this trend is that the increased combustion roughness leads to an increase in exit-plane turbulence intensity which, in turn, causes an increase in jet noise. The purpose at the present experimental study was to determine the effects of combustion roughness on jet noise at conditions more representative of a jet engine exhaust nozzle. Exit plane turbulence intensity was measured along with burner pressure fluctuations and far-field noise.

1.3.2.1 Experimental Apparatus, Test Setup, and Conditions

The tests were conducted on the single-flow facility of JENOTS, which is described in Section 1.2.2.1. An existing 4.31" throat diameter, (D_8) water-cooled, parallel-flow, converging/diverging nozzle (Figure 140) was used. This nozzle was designed for shock-free operation at an exit-plane Mach number of approximately 1.5, the exact value being a function of gas composition and temperature.

Different levels of combustion roughness were obtained by varying the flow conditions in the two burner sections, while maintaining approximately the same exit-plane total pressure and temperature.

Measurements of mean and fluctuating axial velocities in the jet plume were made using General Electric's Laser Velocimeter (LV). Acoustic measurements were made using the far-field microphone array. Pressure fluctuations in the burners were measured with water-cooled Kulite Semiconducter Products XCEL-31-130-100D pressure transducers. The signals were recorded, along with the far-field acoustic signals, for data reduction in 1/3-octave-band and 10-Hz-narrowband form. Two transducers were mounted at the end of each burner section, (Figure 97), one to measure dynamic static pressure and the other to measure dynamic total pressure.

A test matrix of two points was defined by specifying combinations of nozzle pressure ratio and total temperature. The two points, each of which was run at three different levels of combustion roughness, were:

Test Point	P_t/P	T_t (°R)	M_j
4	3.855	1500	1.55
5	1.05	1650	0.3

where M_j is the ideally expanded Mach number for the given conditions.

Test point 4 was set at different levels of combustion roughness by varying the temperature-rise "split" between the burner sections. The three settings were as follows:

- Preburner only (100% of ΔT in preburner)

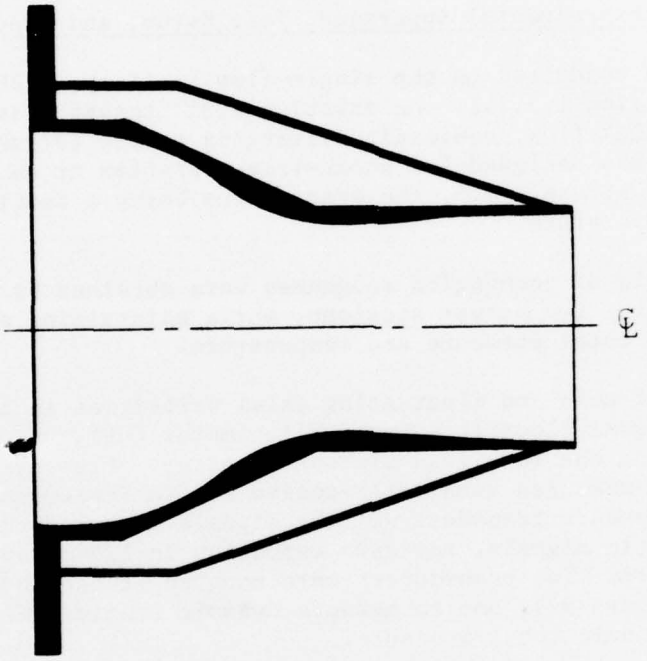


Figure 140. 4.31" Throat Diameter Water-Cooled, Parallel-Flow, Converging/Diverging Nozzle.

- Combined preburner/afterburner operation with very low temperature rise across preburner (22% of ΔT in preburner)

- Combined operation with approximately even split of temperature rise (46% of ΔT in preburner).

Test point 5 was set using the preburner alone. The point was first set to obtain resonant combustion in the preburner, then reset at a slightly higher airflow, just off the edge of resonance ("rough" combustion). The third setting was at an even higher airflow ("smooth" combustion). Since airflow was varied in setting the test point at different levels of roughness, it was not possible to hold exit plane velocity constant. The mean velocities indicated by facility instrumentation were:

Setting	V_j ~ fps
Resonance	522
Rough	545
Smooth	586

1.3.2.2 Aerodynamic Results

Laser Velocimeter Measurements - For test point 4, measurements of axial velocity were made at several radial locations for two axial stations (x/D_8 = 0.12 and 4.0) in order to determine radial profiles of the mean and fluctuating components. These measurements were made for all three burner settings. LV measurements were not made for test point 5, due to time limitations placed on operation at these severe conditions.

Measured profiles of mean and fluctuating axial velocity at x/D_8 = 0.12 are shown in Figure 141 and profiles at x/D_8 = 3.98 are shown in Figures 142 and 143. Of particular interest is the fact that exit-plane turbulence intensity for the "preburner-only" setting is of the order of 2%, while it is approximately 4.5% for the two settings utilizing both preburner and afterburner. Thus, it appears that different upstream turbulence levels can be produced as a function of burner operation. Mean velocity for the "low-preburner-ΔT" setting is seen to be significantly lower (~ 150 fps) than for the other two settings, despite the fact that data from the facility instrumentation indicated that the exit-plane velocities for the three settings were almost identical. This discrepancy, which was also seen in the afterburner flameholder/spraybar experiment, is thought to be caused by distortions in the flame tunnel pressure profiles during extreme off-design operation (e.g., operation of afterburner with very low preburner ΔT or operation of preburner alone with afterburner hardware removed). Recall from Section 1.2.2.1 that the static pressure measured at the downstream end of the flame tunnel is used to calculate exit-plane total pressure and, therefore, velocity.

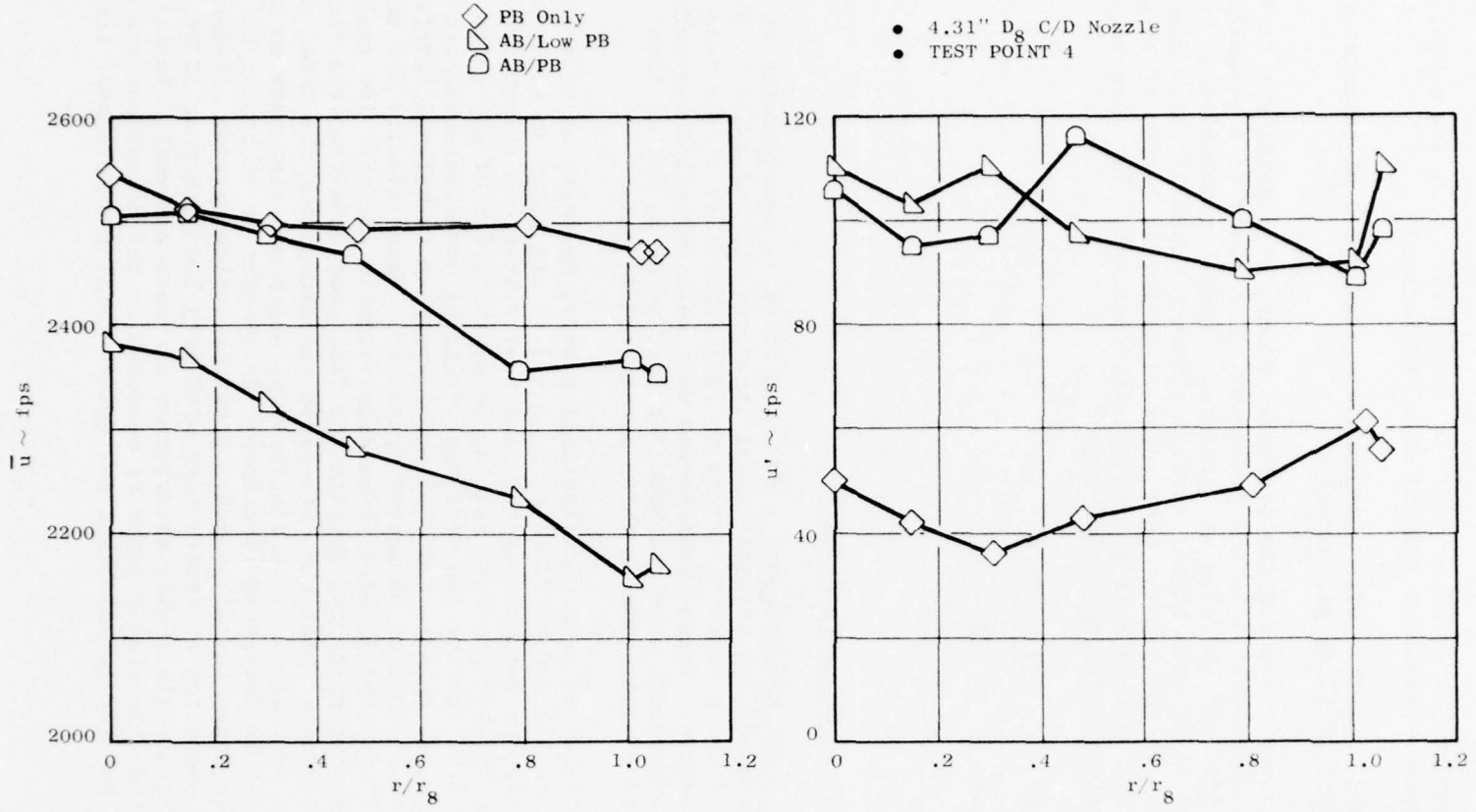


Figure 141. LV Measurements 0.5" Downstream of Nozzle Exit.

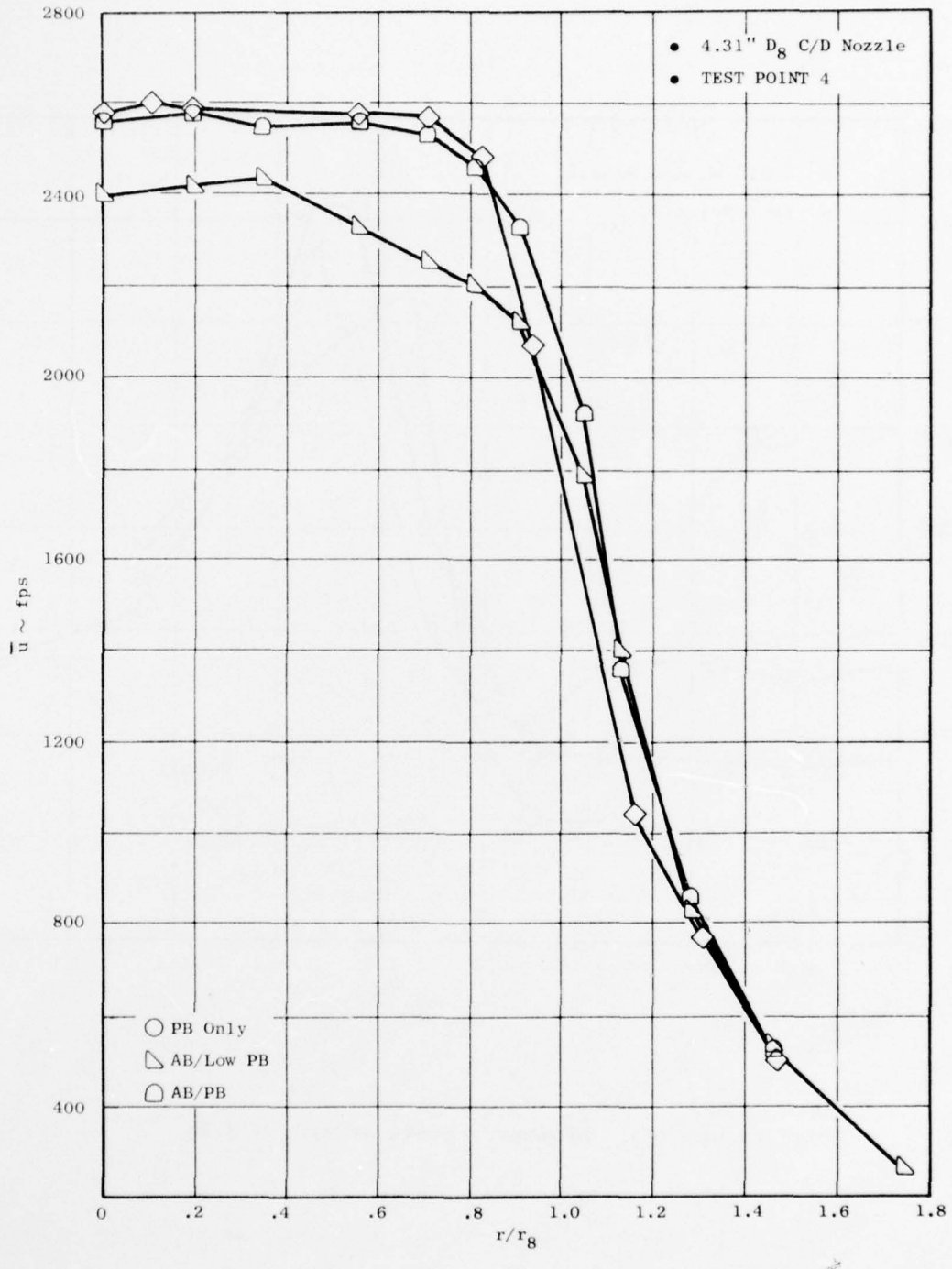


Figure 142. LV Measurements at x/D_8 = 3.98.

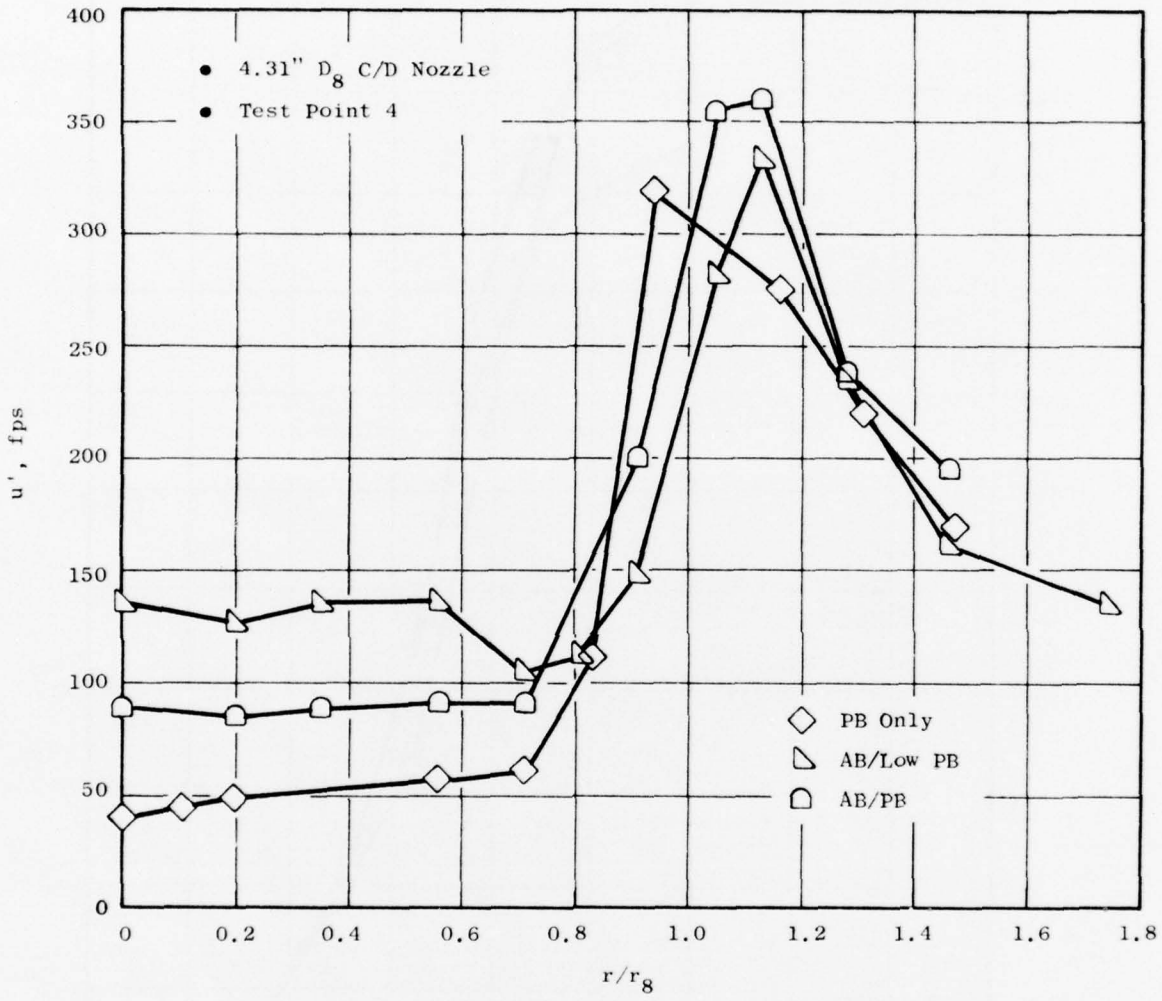


Figure 143. LV Measurements at $x/D_8 = 3.98$.

Kulite Measurements - A number of problems was encountered in the operation of the dynamic pressure instrumentation, with only one of four transducers (preburner static pressure) giving what appeared to be a consistently reliable signal and one (afterburner static pressure) operating sporadically. Acoustic data analysis procedures were used to process the pressure fluctuation data.

A 1/3-octave-band analysis of preburner and afterburner static pressure fluctuation data for test point 4 is shown in Figures 144 and 145. The same trends are seen in the data from each burner section. The spectral data for the two test point settings using both preburner and afterburner are quite similar, and are below the level of pressure fluctuation intensity for the "preburner-only" setting. This is in direct contrast to the exit-plane velocity data which showed the "preburner-only" setting resulting in a lower level of turbulence. The reasons for these seemingly opposite trends are not known at the present time. The rms values of pressure fluctuation intensity are summarized in the following listing:

	$(P_s)_{rms}$ ~ dyne/cm^2	
Setting	Preburner	Afterburner
PB only	2761	2218
AB/low PB	1321	1125
AB/PB	1306	1219

A 10-Hz-narrowband analysis of preburner static pressure fluctuation data for test point 5 is shown in Figure 146. The dominant feature is the "spike" at approximately 100 Hz for the resonant combustion setting. The spread in the data at higher frequencies is thought to be a result of the signal falling below the "noise level" of the electronic equipment. The rms values of pressure fluctuation intensity are summarized in the following listing:

	$(P_s)_{rms}$ ~ dyne/cm^2
Setting	Preburner
Resonance	2793
Rough	1500
Smooth	1466

1.3.2.3 Acoustic Results

Far-field acoustic data were taken for all three burner settings at each test point.

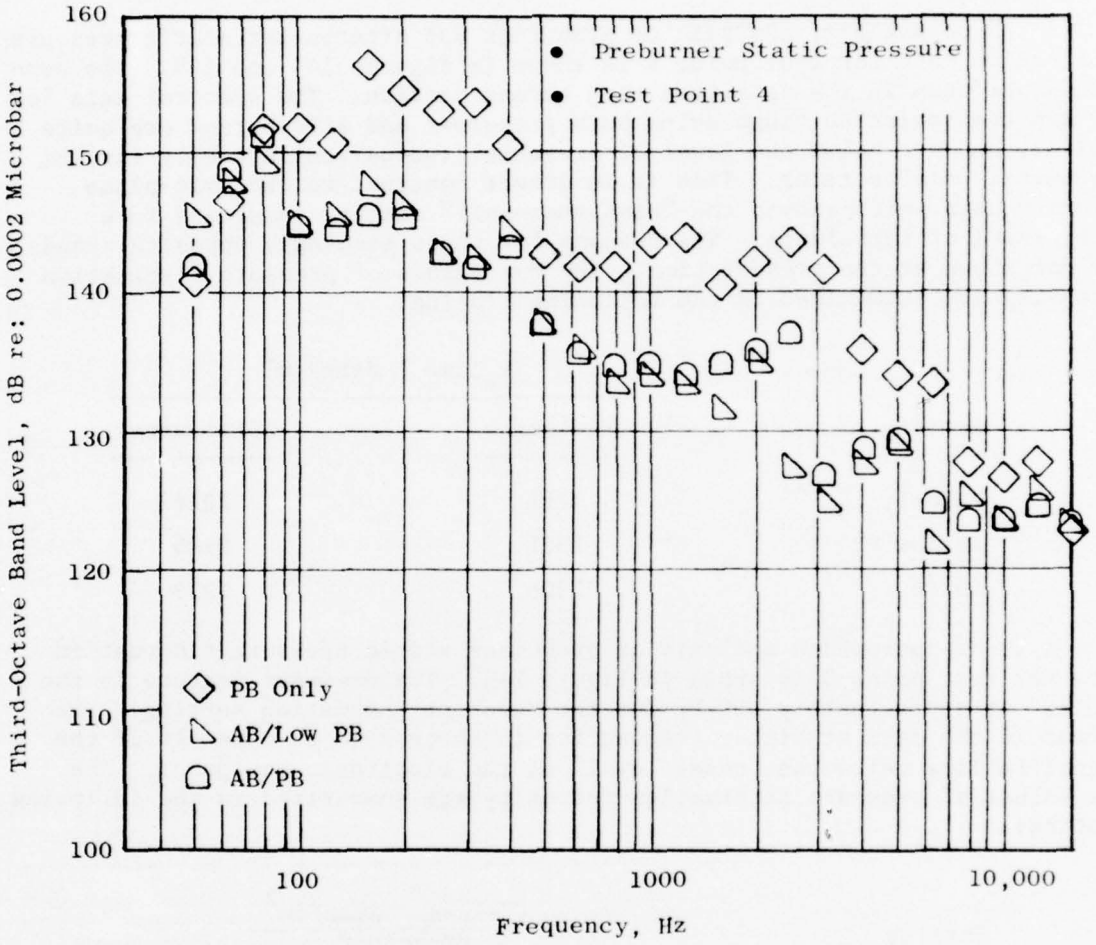


Figure 144. Measured 1/3-Octave-Band Pressure Fluctuation Spectra, Preburner Static Pressure.

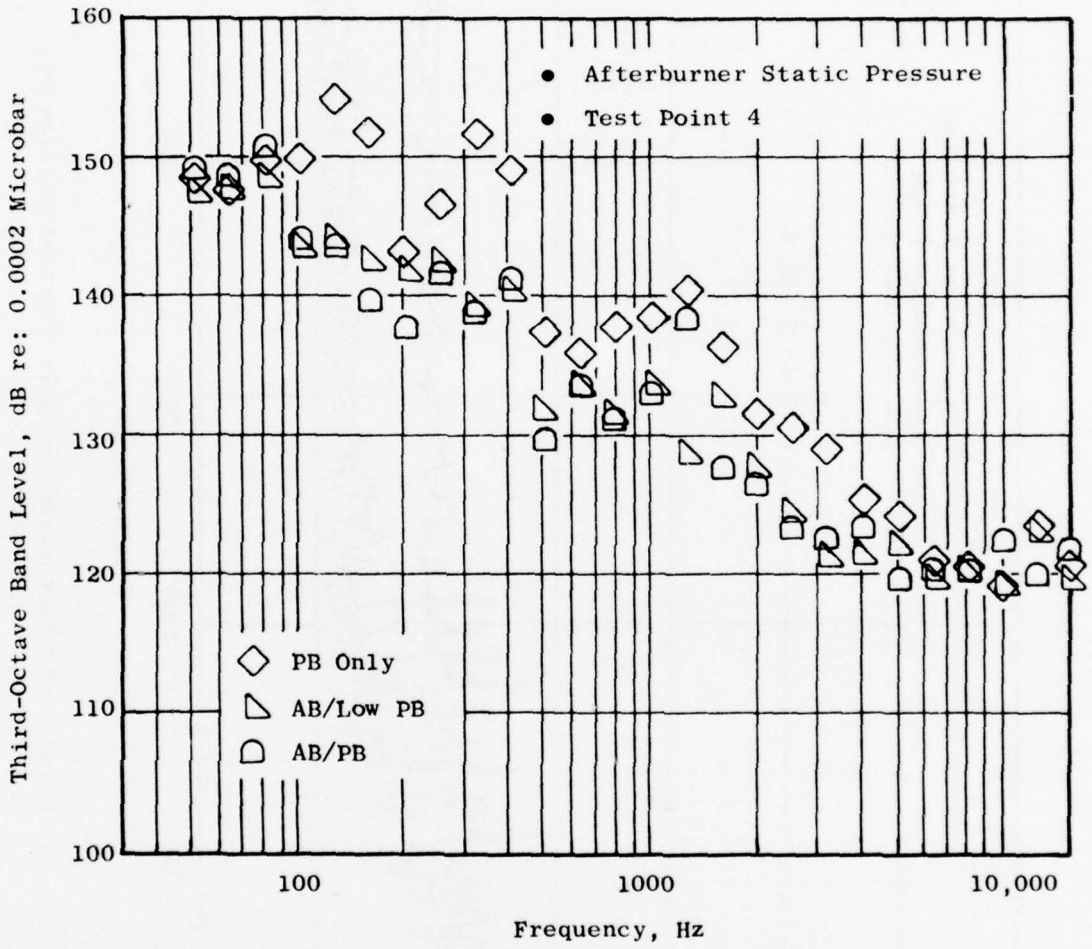


Figure 145. Measured 1/3-Octave-Band Pressure Fluctuation Spectra, Afterburner Static Pressure.

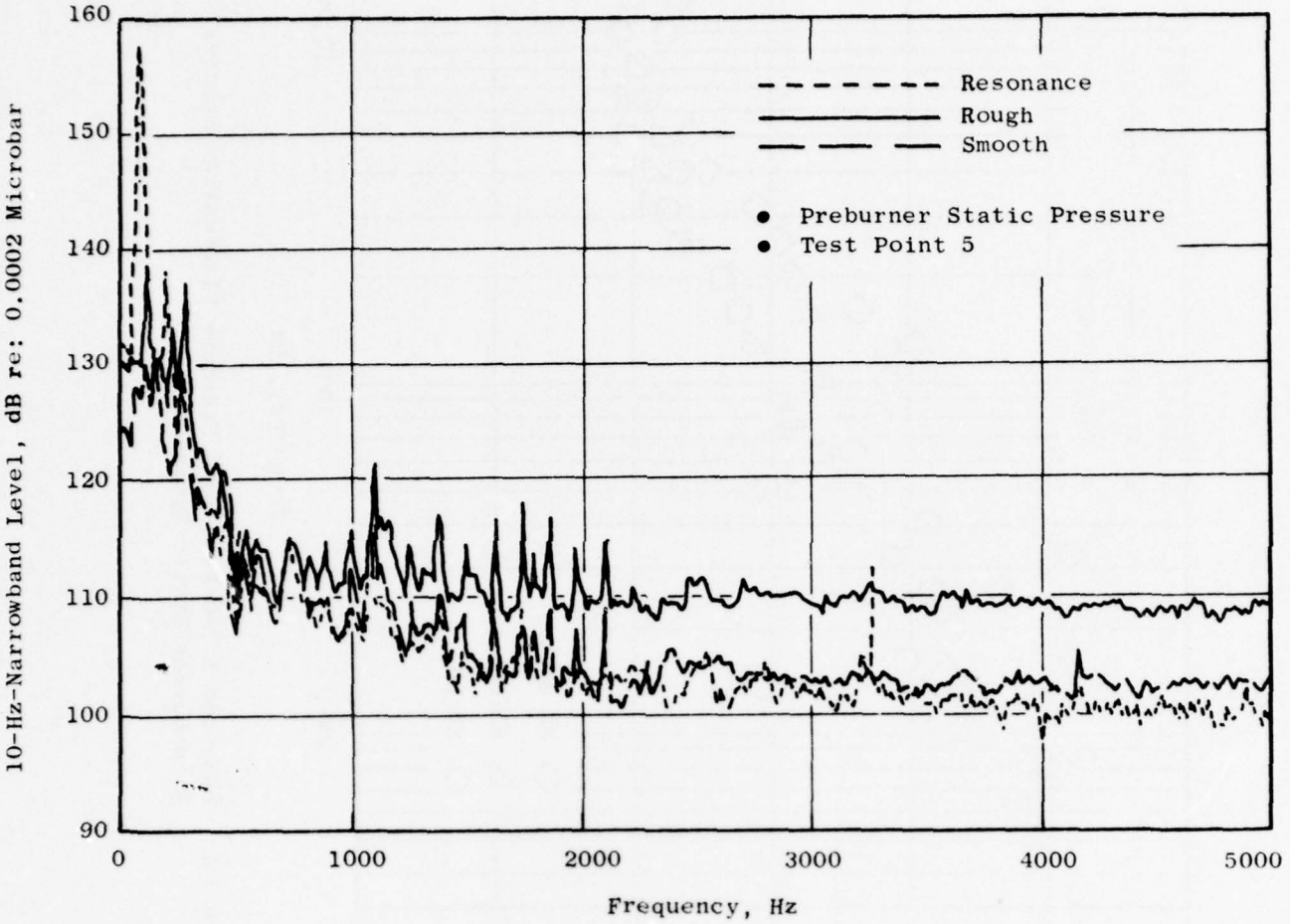


Figure 146. Measured 10-Hz-Narrowband Pressure Fluctuation Spectra.

Measured overall sound pressure levels on the 40' arc are shown in Figure 147 for test point 4. The 1/3-octave-band sound pressure level spectra at 40° and 90° to the jet axis are shown in Figures 148 and 149. The data for the three burner settings are almost identical in all respects, indicating that a change in upstream turbulence intensity from 2 to 4.5% is not sufficient to cause any significant change in jet noise at these conditions. A summary of the overall sound power levels for each burner setting is given in the following listing:

Setting	OAPWL (dB)
PB only	171.3
AB/low PB	171.3
AB/PB	171.0

Measured overall sound pressure levels on the 40' arc are shown in Figure 150 for test point 5. The 10-Hz-narrowband sound pressure level spectra at 30° and 90° to the jet axis are shown in Figures 151 and 152. In this case the effects of upstream disturbances are quite apparent in the far-field noise, although it appears to be a direct rather than indirect effect. Theoretical acoustic models (129) predict that, at low jet Mach numbers ($M_j < 0.45$), the exhaust noise is dominated by upstream, combustion-driven noise sources with jet noise making an insignificant contribution. This concept is supported by the dominance of the 100-Hz resonant tone in the far-field SPL spectra for this test point.

The overall sound power levels for this point are summarized in the following listing:

Setting	OAPWL ~ dB	V_j ~ fps
Resonance	138.6	522
Rough	133.4	545
Smooth	131.6	586

Note that the overall sound power level increases with increasing roughness (and decreasing velocity).

1.3.3 Afterburner Flameholder/Spraybar Aeroacoustic Experiment

The purpose of this experimental study was to determine the effects of the presence of afterburner spraybars and flameholders on the aeroacoustic properties of an exhaust jet.

1.3.3.1 Experimental Apparatus, Test Setup, and Conditions

The tests were conducted on the single-flow facility of JENOTS. The basic test setup and instrumentation were the same as for the swirling jet experiment (Section 1.2.2.1), including the use of the 5.71" exit diameter, water-cooled, conical, converging nozzle.

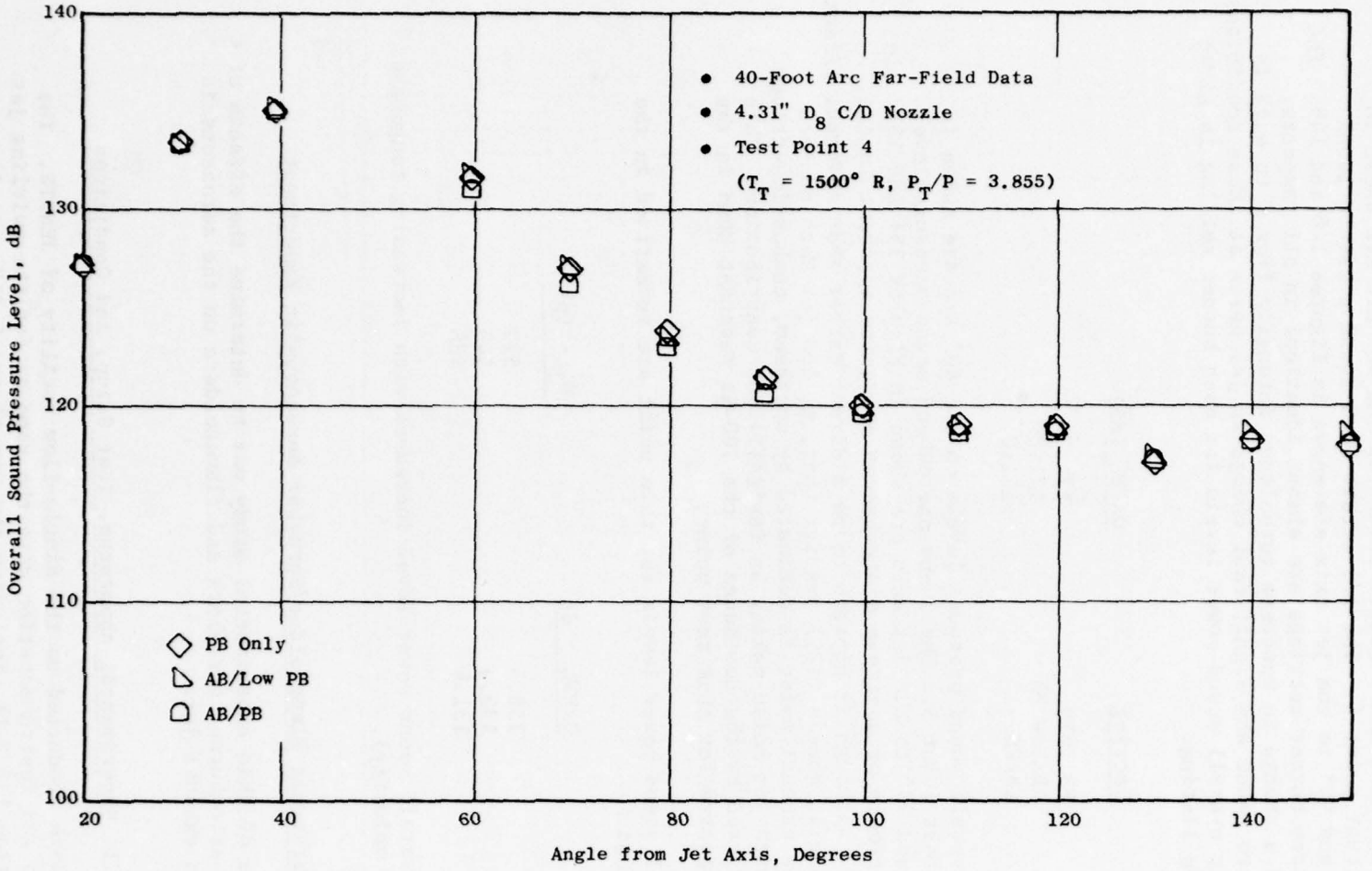


Figure 147. Measured Overall Sound Pressure Levels.

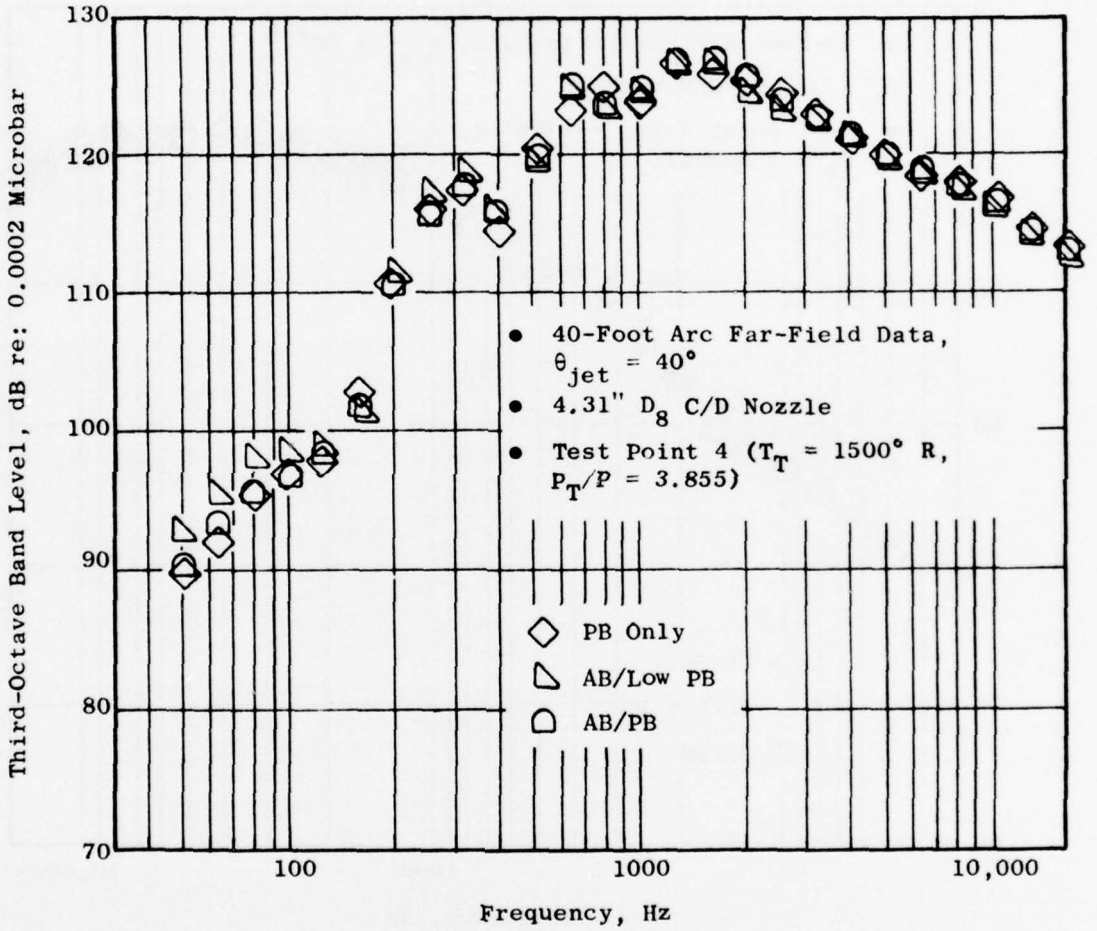


Figure 148. Measured 1/3-Octave-Band Sound Pressure Level Spectra, $\theta_{jet} = 40°$.

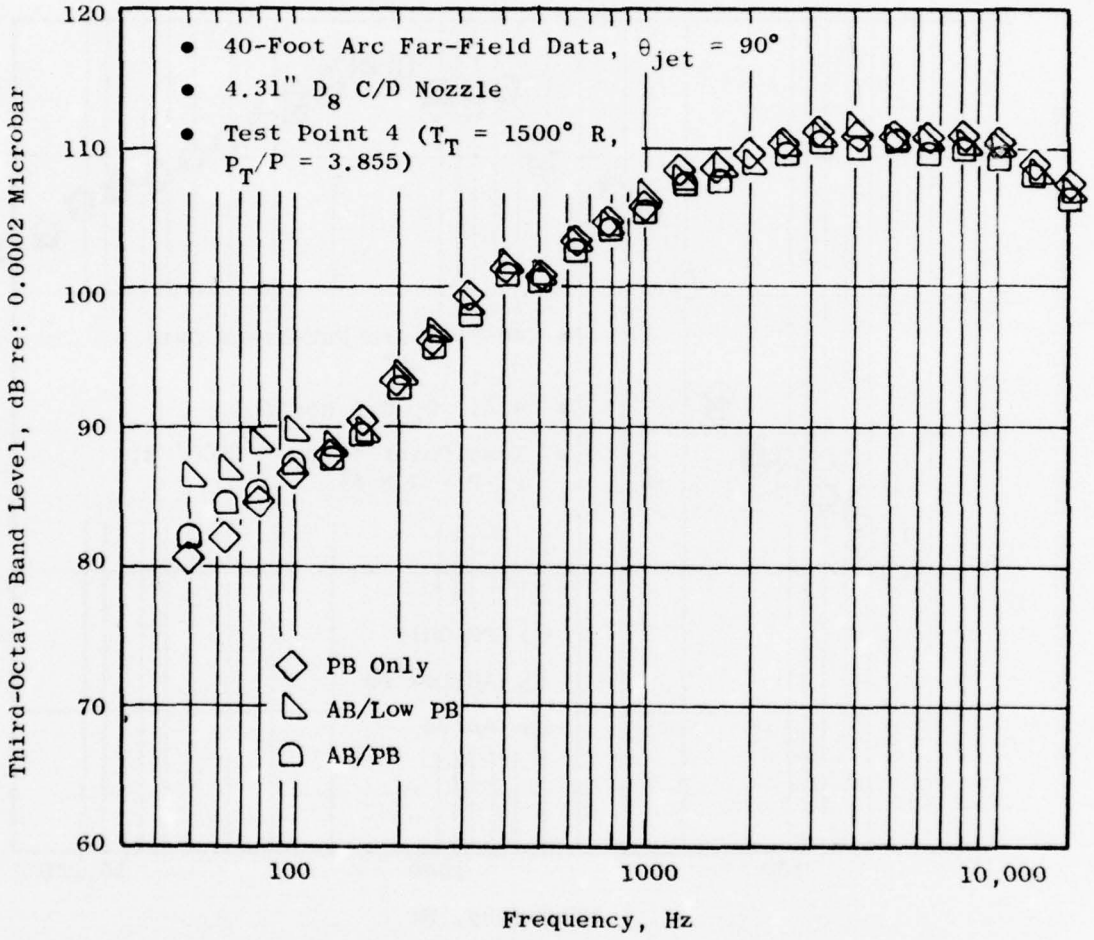


Figure 149. Measured 1/3-Octave-Band Sound Pressure Level Spectra, θ_{jet} = 90°.

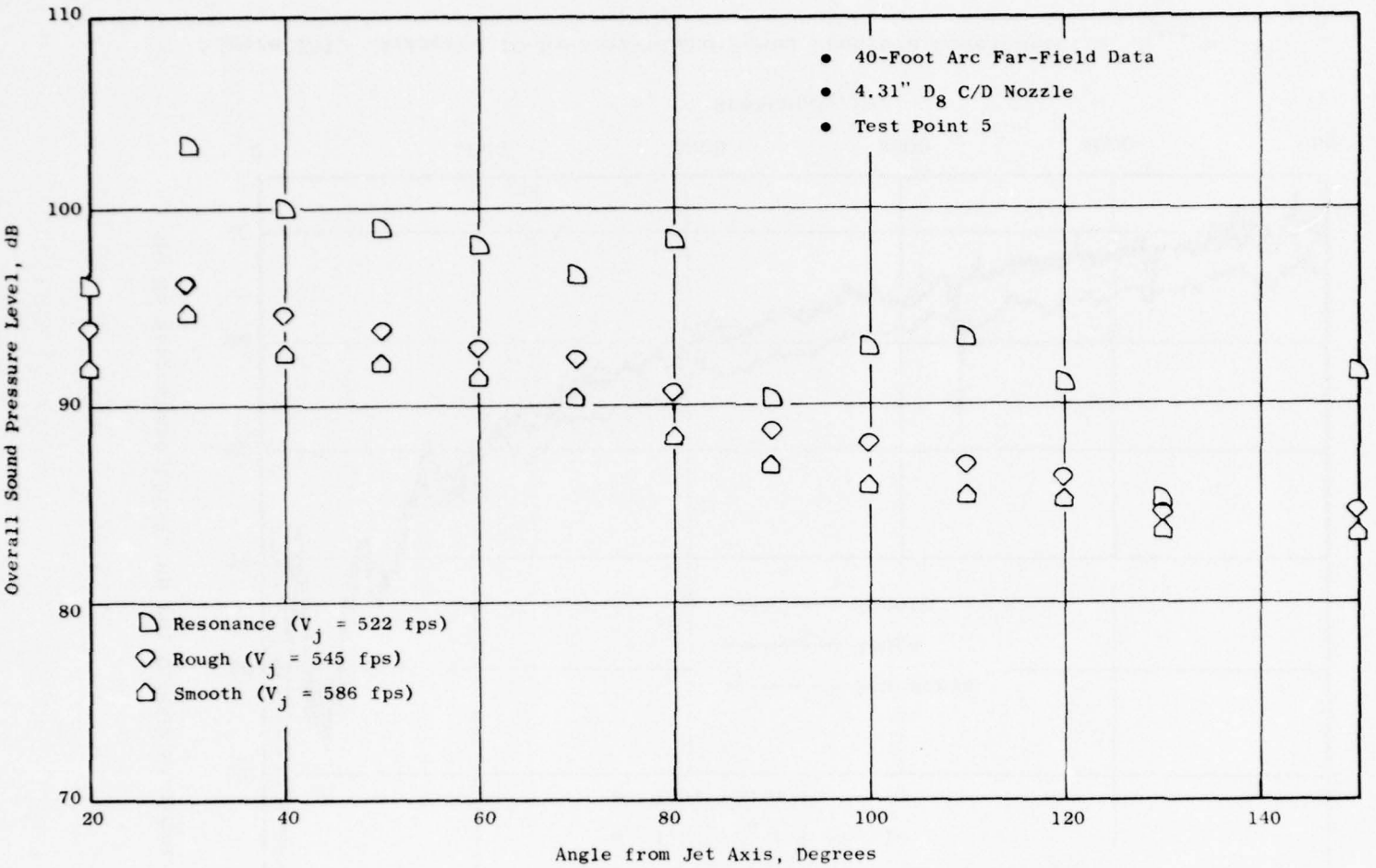


Figure 150. Measured Overall Sound Pressure Levels.

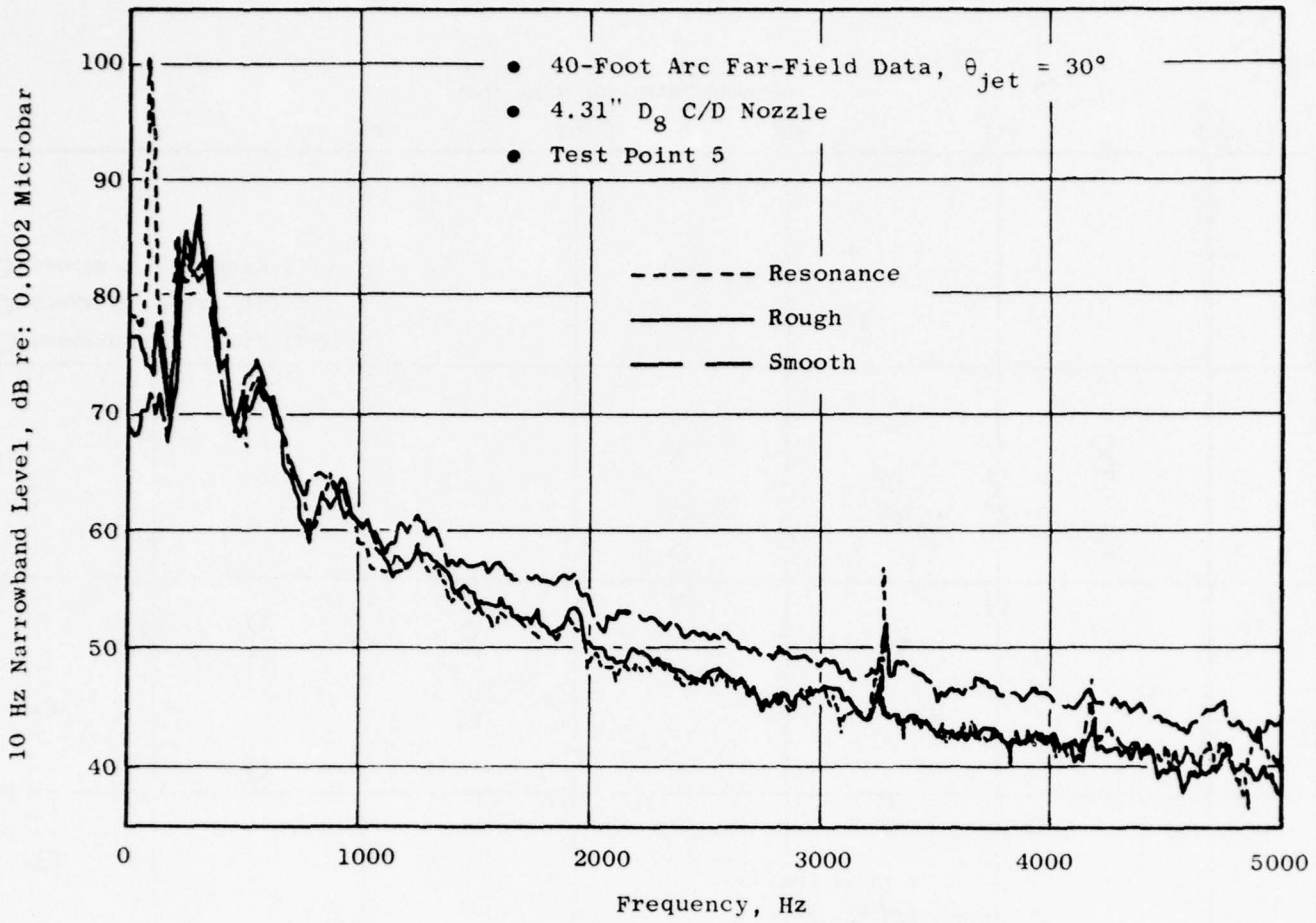


Figure 151. Measured 10-Hz-Narrowband Sound Pressure Level Spectra, θ_{jet} = 30°.

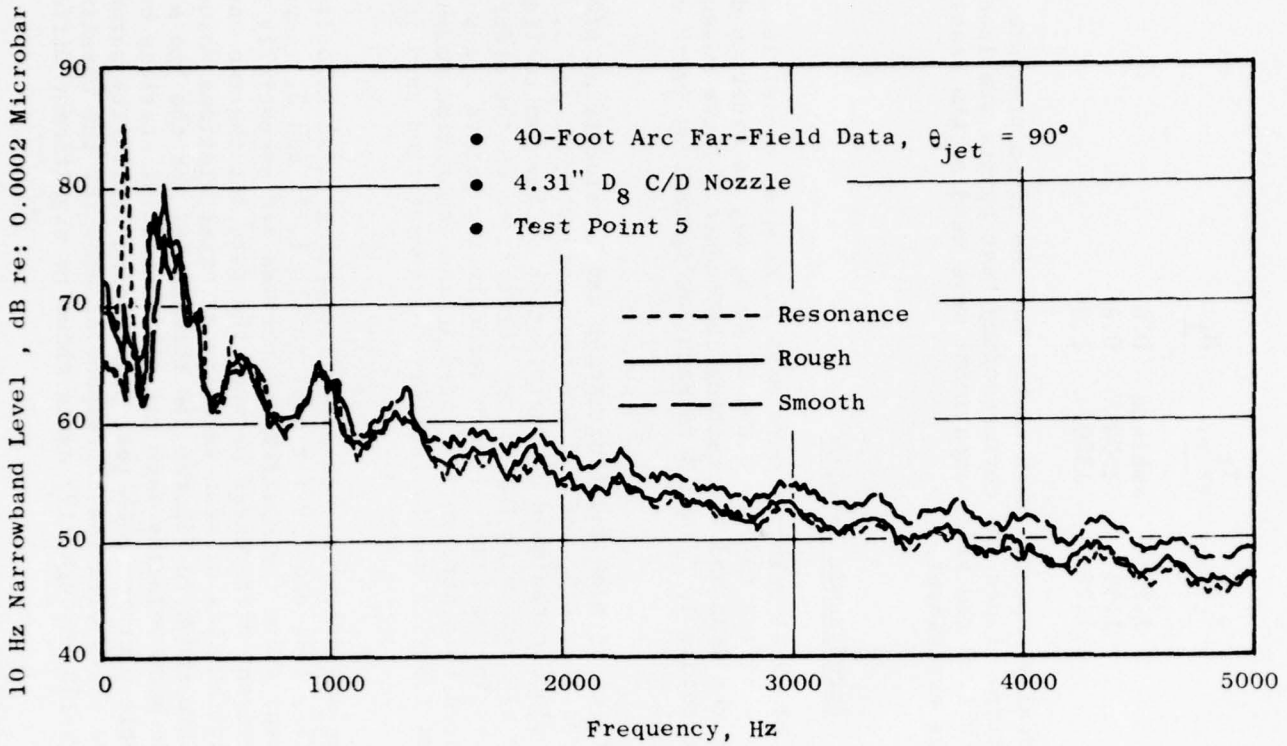


Figure 152. Measured 10-Hz-Narrowband Sound Pressure Level Spectra, $\theta_{jet} = 90°$

The basic test matrix consisted of three points, each run both with and without the afterburner hardware (Figure 153) installed in the JENOTS air line:

Test Point	P_t/P	T_t (°R)	M_j
1	1.55	ambient	0.8
2	1.54	1500	0.8
3	1.88	1500	1.0

where M_j is the ideally expanded Mach number for the given pressure ratio and total temperature. Since the corresponding test points are identical, the "baseline" runs from the swirl experiment were used as the baseline (with A/B) for this experiment.

1.3.3.2 Aerodynamic Results

Measurements of axial velocity were made at several radial locations for each of five axial stations (x/D_8 = 0.09, 2, 4, 6, 8), in order to determine radial profiles of the mean and fluctuating components. These measurements were made for test points 1, 2, and 3 on both configurations (with and without the afterburner).

Measured profiles of mean and fluctuating axial velocity at x/D_8 = 0.09 are shown in Figures 154, 155, and 156 for test points 1, 2, and 3, respectively. The exit-plane turbulence characteristics of the two configurations appear to be quite similar, with turbulence intensities on the order of 2 to 3%. The differences in the level of mean velocity for points 2 and 3 are thought to be related to discrepancies noted in the combustion roughness experiment (Section 1.3.2.2) due to facility instrumentation used in setting the test points.

The centerline variations of mean and fluctuating axial velocity are shown in Figures 157, 158, and 159 for test points 1, 2, and 3, respectively. As would be expected, since the upstream properties are essentially the same, there are no significant differences between the data for the two configurations. Radial distributions of mean velocity at axial stations downstream of the exit plane are shown in Figures 160 through 162 for the "no A/B" configuration. The mean velocity data for all four axial stations have been collapsed on a single plot for each test point using similarity parameters. Comparison of these plots with the corresponding ones for the baseline configuration (Figures 115 through 117) again shows no significant differences.

1.3.3.3 Acoustic Results

Far-field acoustic data were taken for test points 1, 2, and 3 on both configurations.

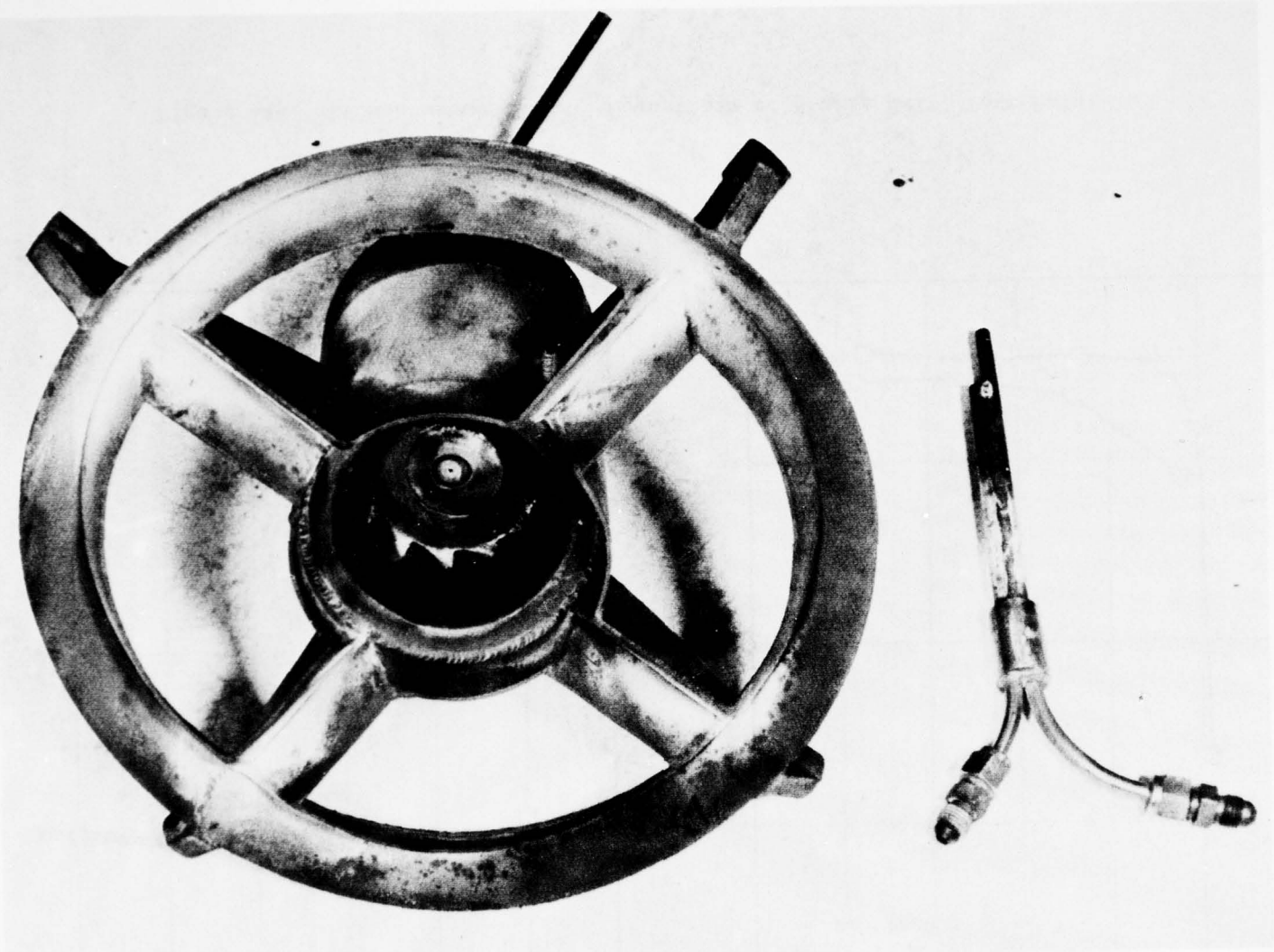


Figure 153. Flameholder and Typical Spraybar from JENOTS Afterburner Section.

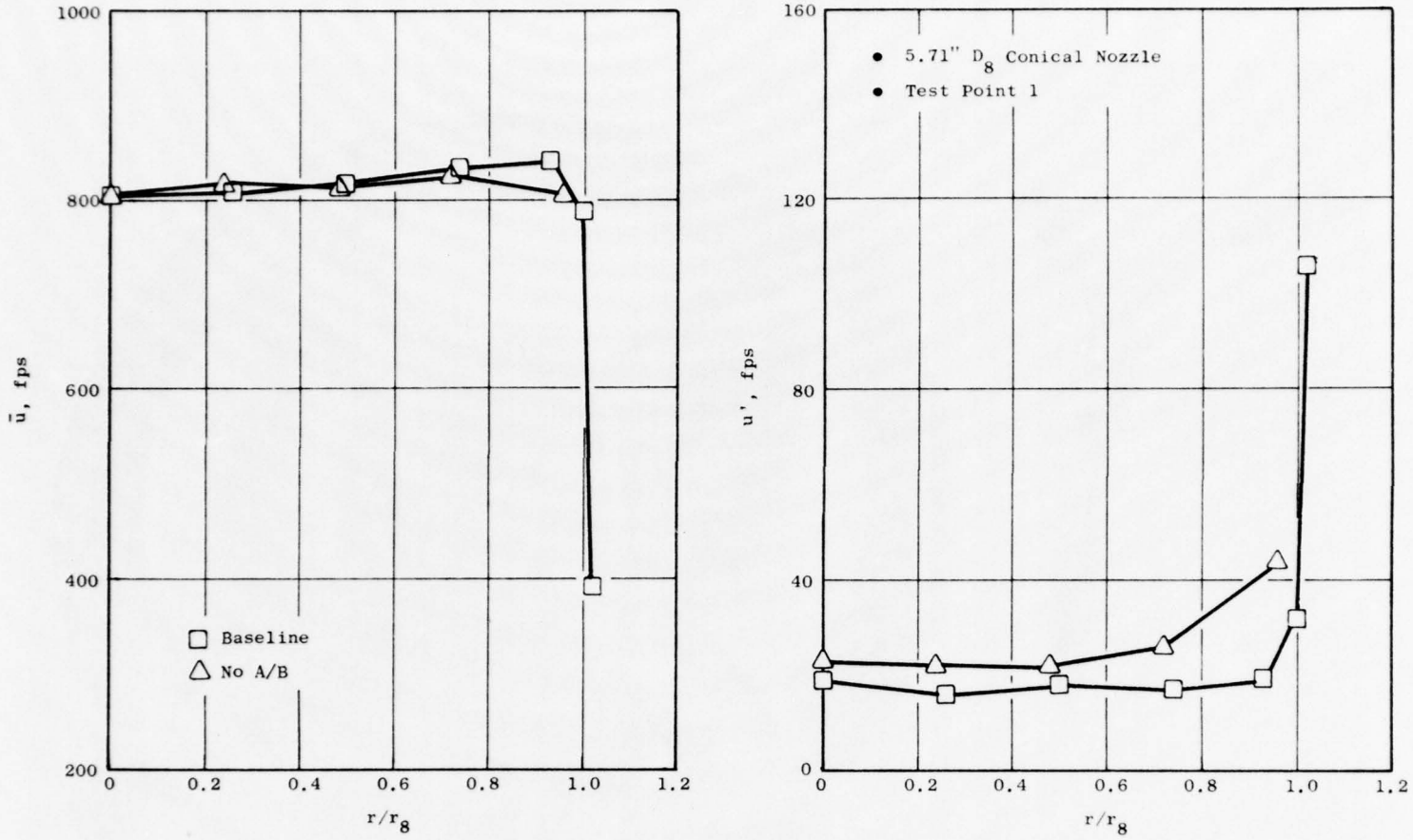


Figure 154. LV Measurements 0.5" Downstream of Nozzle Exit, Test Point 1.

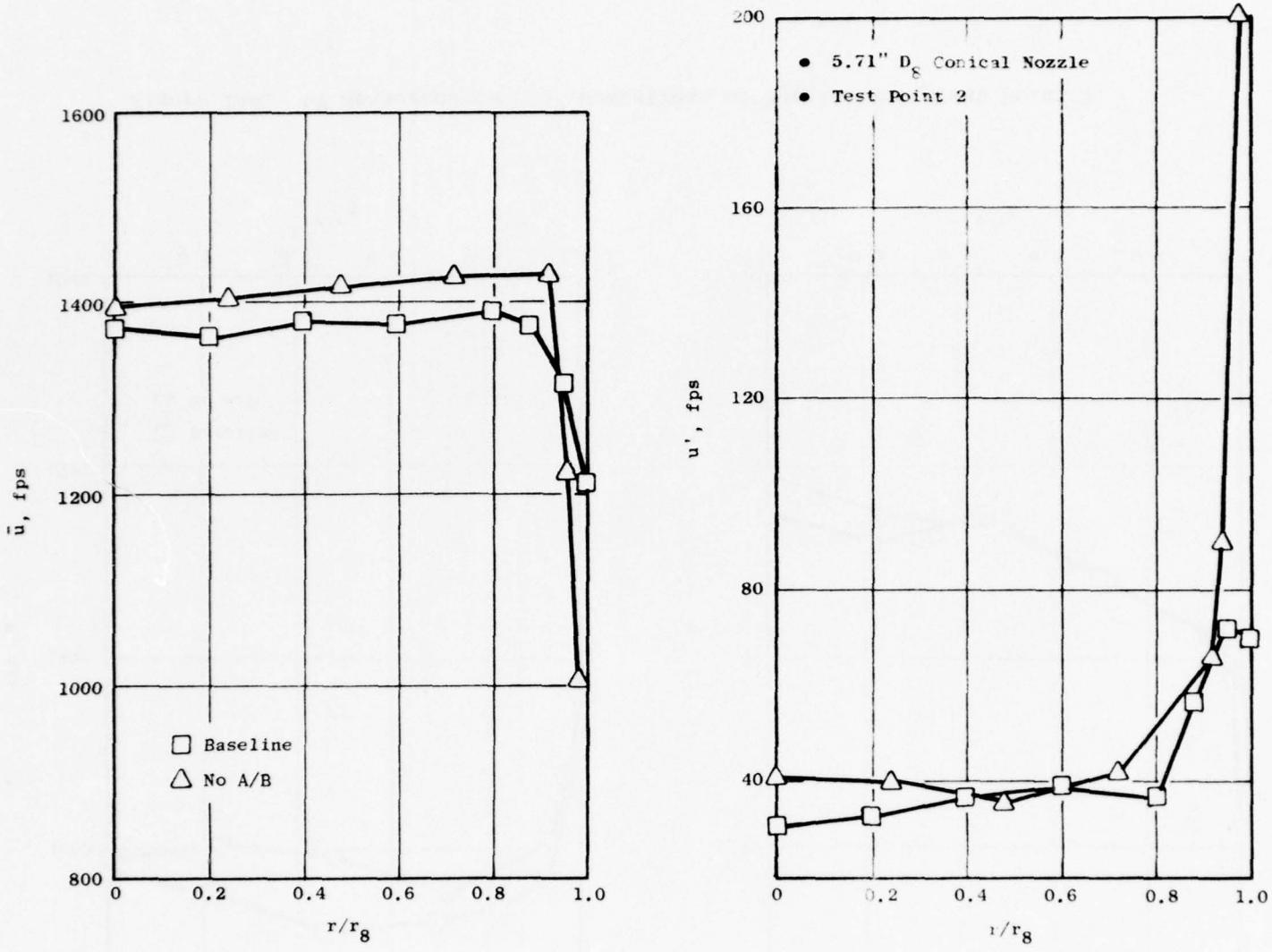


Figure 155. LV Measurements 0.5" Downstream of Nozzle Exit, Test Point 2.

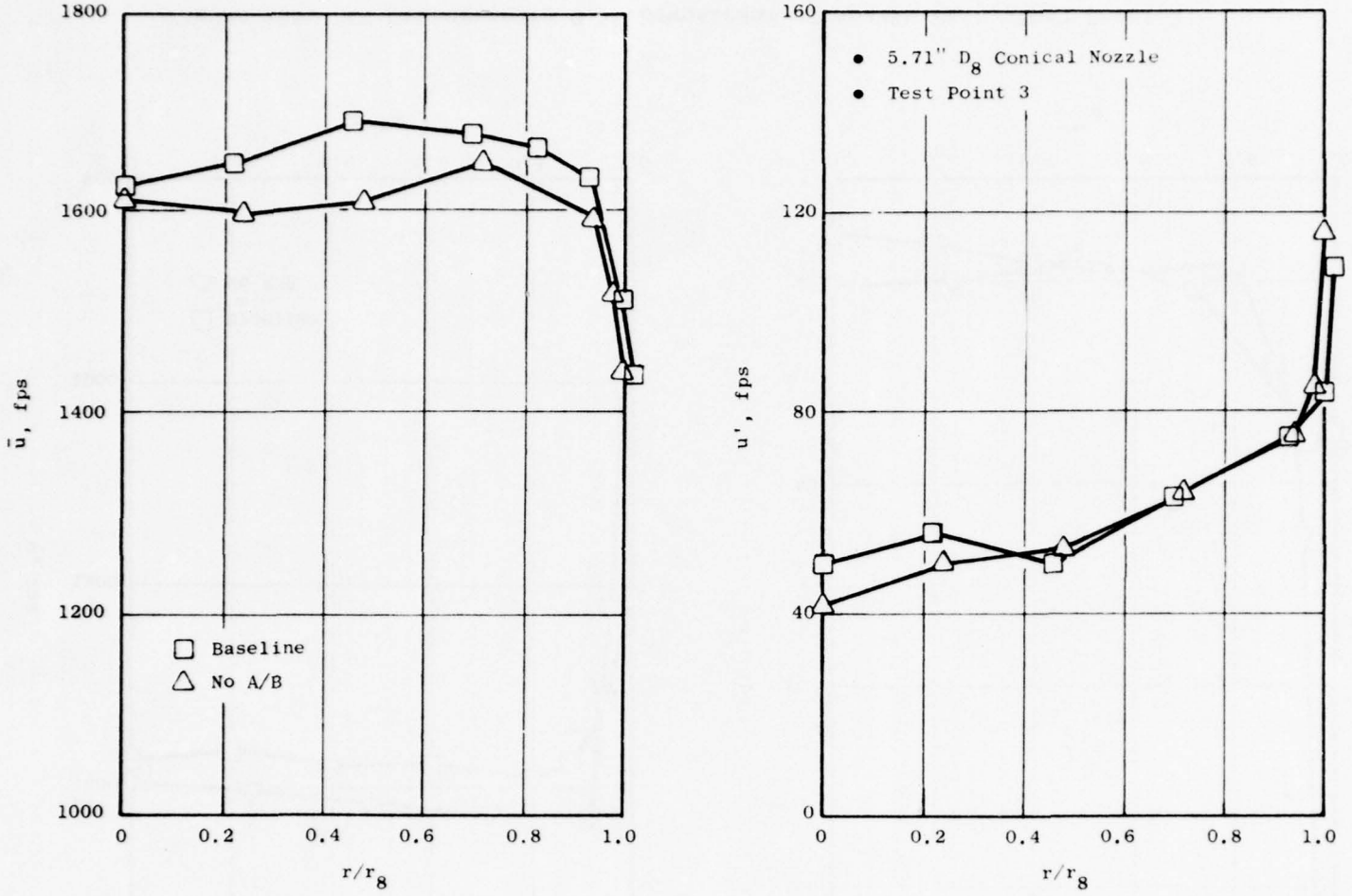


Figure 156. LV Measurements 0.5" Downstream of Nozzle Exit, Test Point 3.

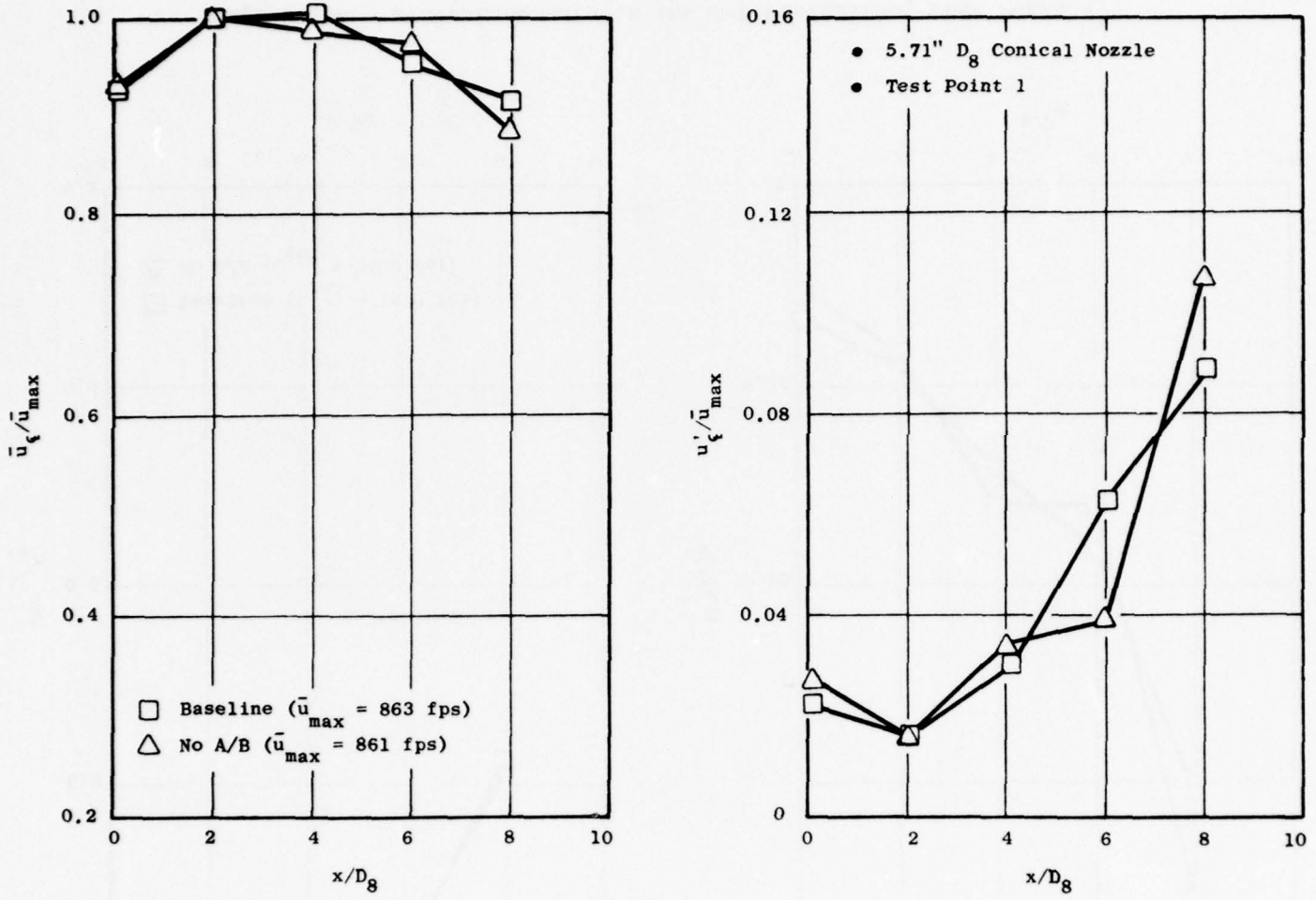


Figure 157. LV Measurements on the Jet Centerline, Test Point 1.

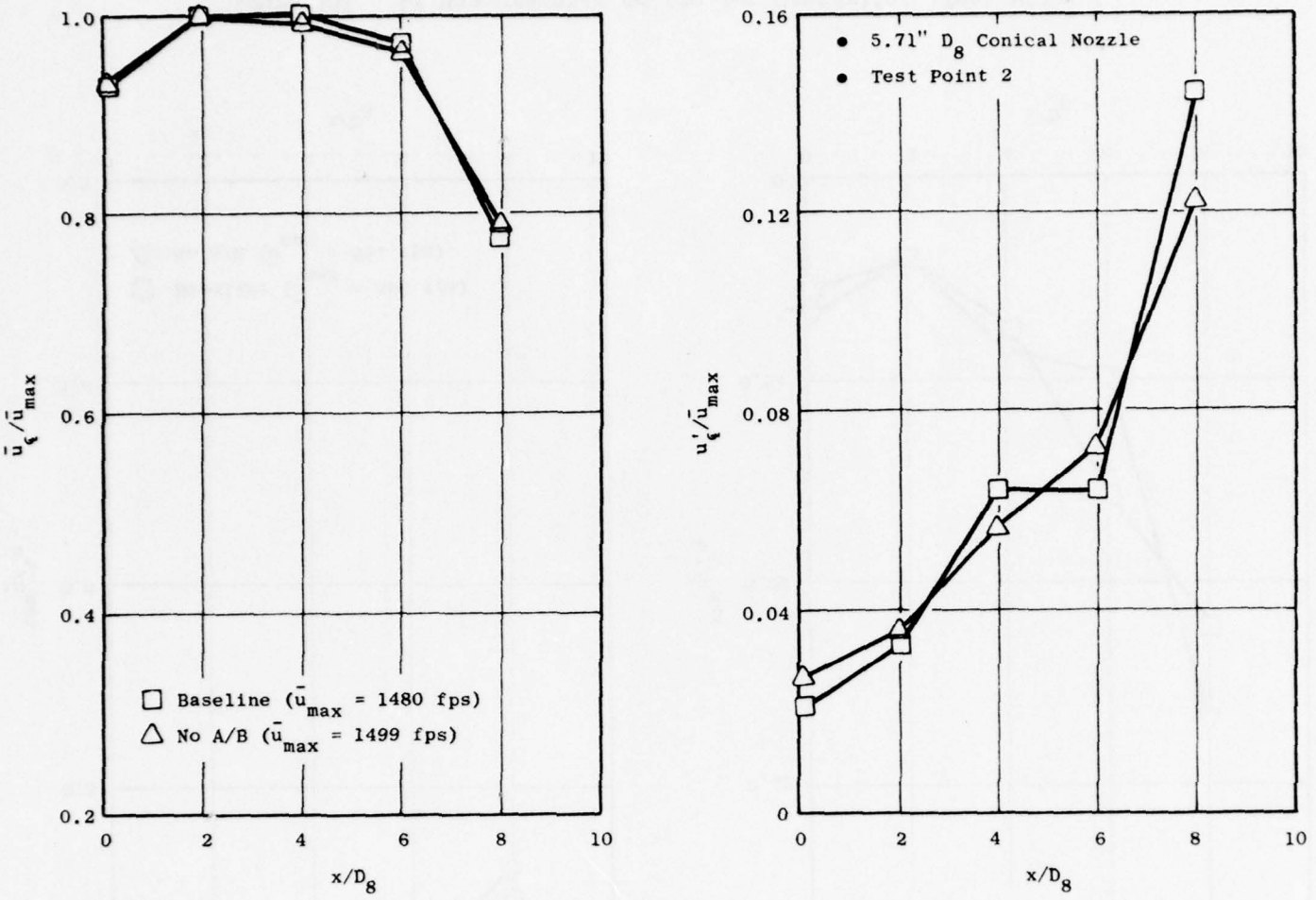


Figure 158. LV Measurements on the Jet Centerline, Test Point 2.

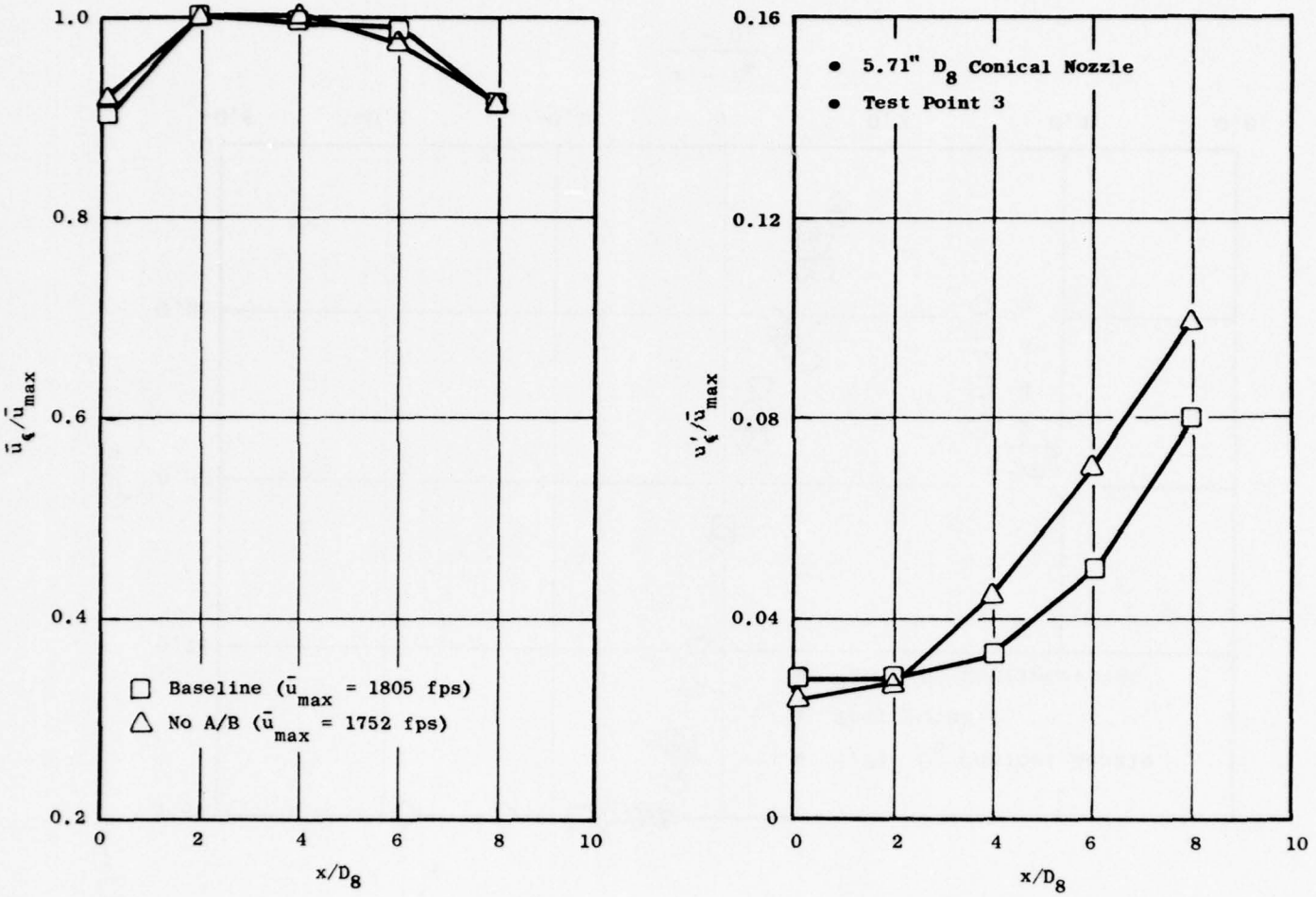


Figure 159. LV Measurements on the Jet Centerline, Test Point 3.

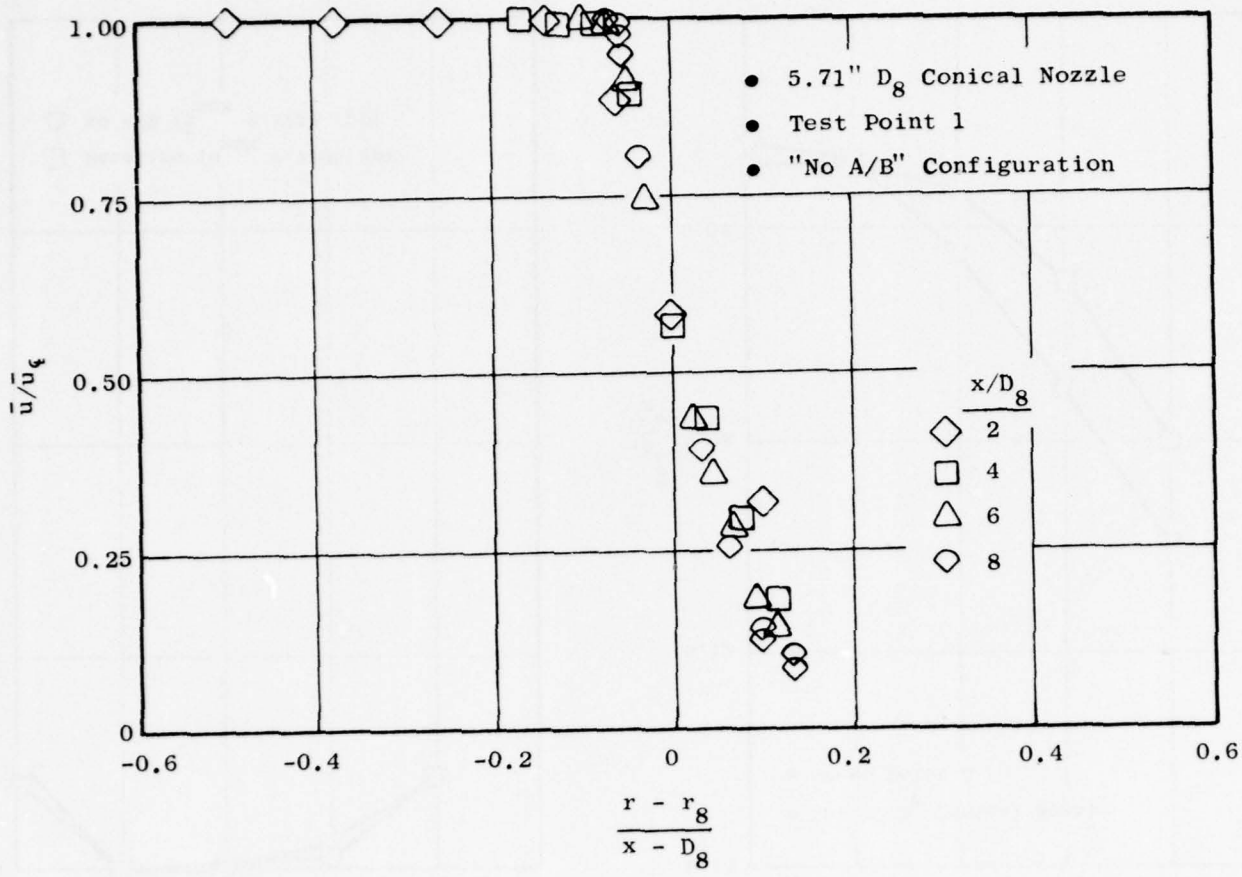


Figure 160. LV Measurements of Radial Velocity Profiles, Test Point 1.

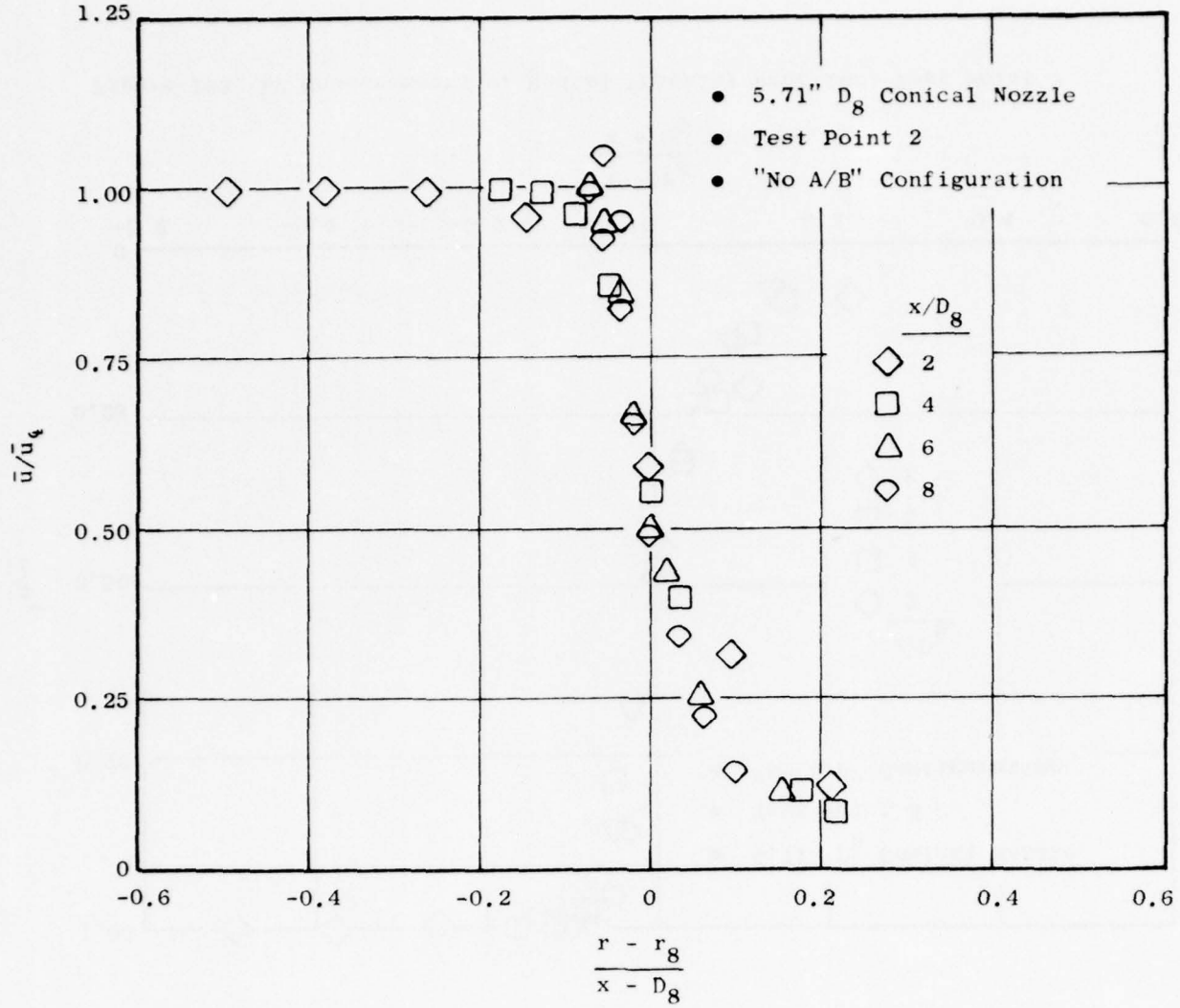


Figure 161. LV Measurements of Radial Velocity Profiles, Test Point 2.

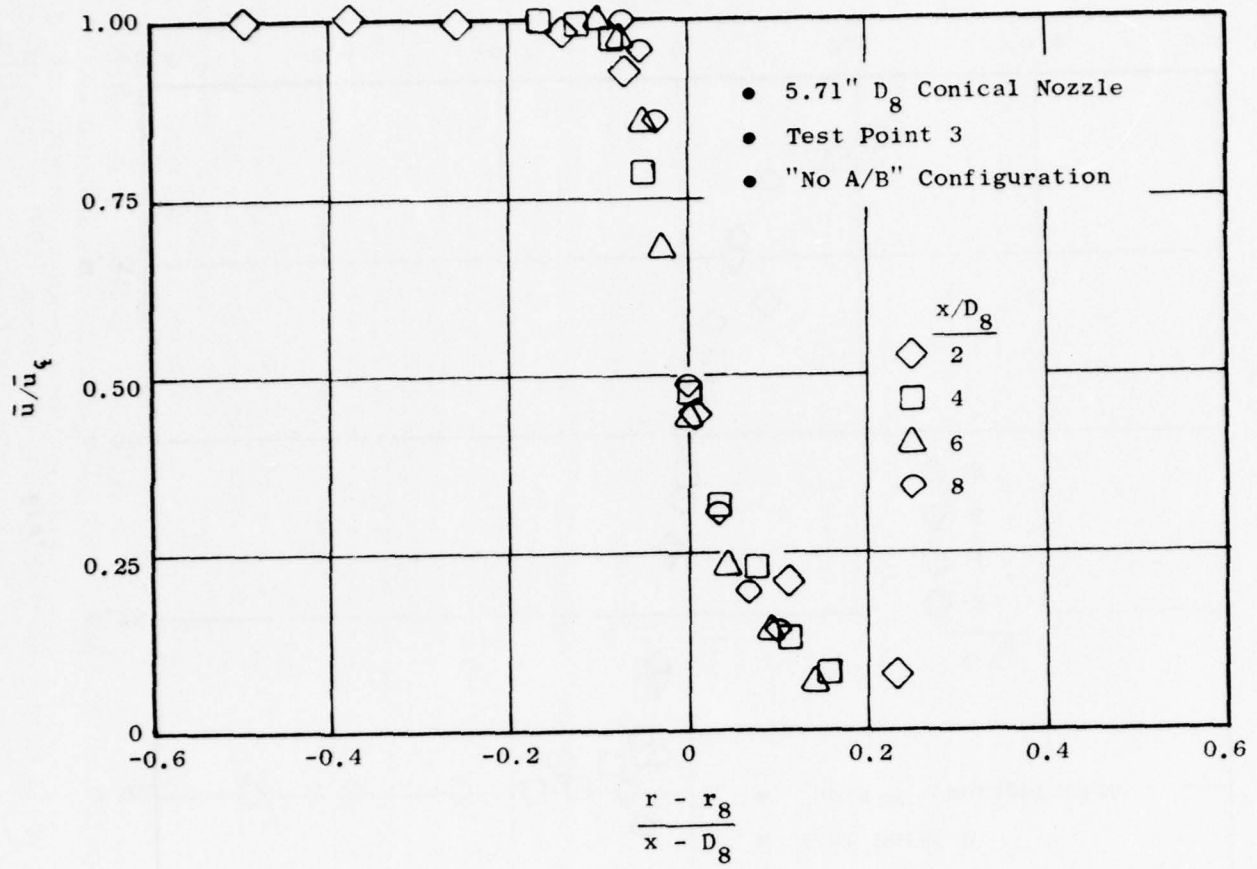


Figure 162. LV Measurements of Radial Velocity Profiles, Test Point 3.

Measured overall sound pressure levels on the 40' arc are shown in Figures 163, 164, and 165 for test points 1, 2, and 3, respectively. For test point 1 (cold flow) there are no significant differences. However, for test points 2 and 3, the removal of the afterburner hardware results in an increase of 1 to 4 dB in OASPL at all angles. This is reflected in the overall sound power levels, which are summarized in the listing below:

Test Point	Baseline OAPWL ~ dB	"No A/B" OAPWL ~ dB
1	143.1	142.1
2	158.2	160.0
3	165.5	167.3

Since there were no significant differences noted in the plume aerodynamic data, such differences in the acoustic data were unexpected.

The 1/3-octave-band sound pressure level spectra are shown in Figures 166 through 168 for the microphone at 30° to the jet axis, and in Figures 169 through 171 for the 90° microphone. The spectral data for the two configurations are similar except in the lower frequency range (particularly 160-250 Hz), where the noise levels for the "no A/B" configuration are significantly higher. The 10-Hz-narrowband SPL spectra for the 90° position are shown in Figures 172 and 173 for test points 2 and 3, respectively. These indicate an increase in broadband noise in the low frequency range with a superimposed pure tone. The increased far-field noise levels are thought to be caused by an increase in combustion-driven instabilities due to the change in burner/duct acoustic characteristics when the afterburner spraybars and flameholder are removed.

1.4 SUMMARY AND CONCLUSIONS

A combined analytical/experimental study was made of the influence of upstream flow disturbances on the aerodynamic and acoustic properties of turbulent jets. In particular, two types of disturbances were studied, upstream swirl and upstream turbulence.

The analytical study of swirling flow utilized a recently developed aerodynamic model of swirling turbulent jets, coupled to an existing acoustic prediction model (which was developed for nonswirling jets). While yielding good agreement with published experimental data for the aerodynamic characteristics of jets with moderate swirl, the coupled model did not accurately predict either the aerodynamic or acoustic results obtained in the experimental study. In particular, the predictions indicate that suppression due to swirl should occur for all mid-band and high frequencies (with enhancement at low frequencies), while data from this and other studies [109] indicate that the suppression occurs primarily at low and mid-band frequencies. Additional analysis and experimentation are required to identify and correct the specific items in the aeroacoustic model which led to the erroneous predictions.

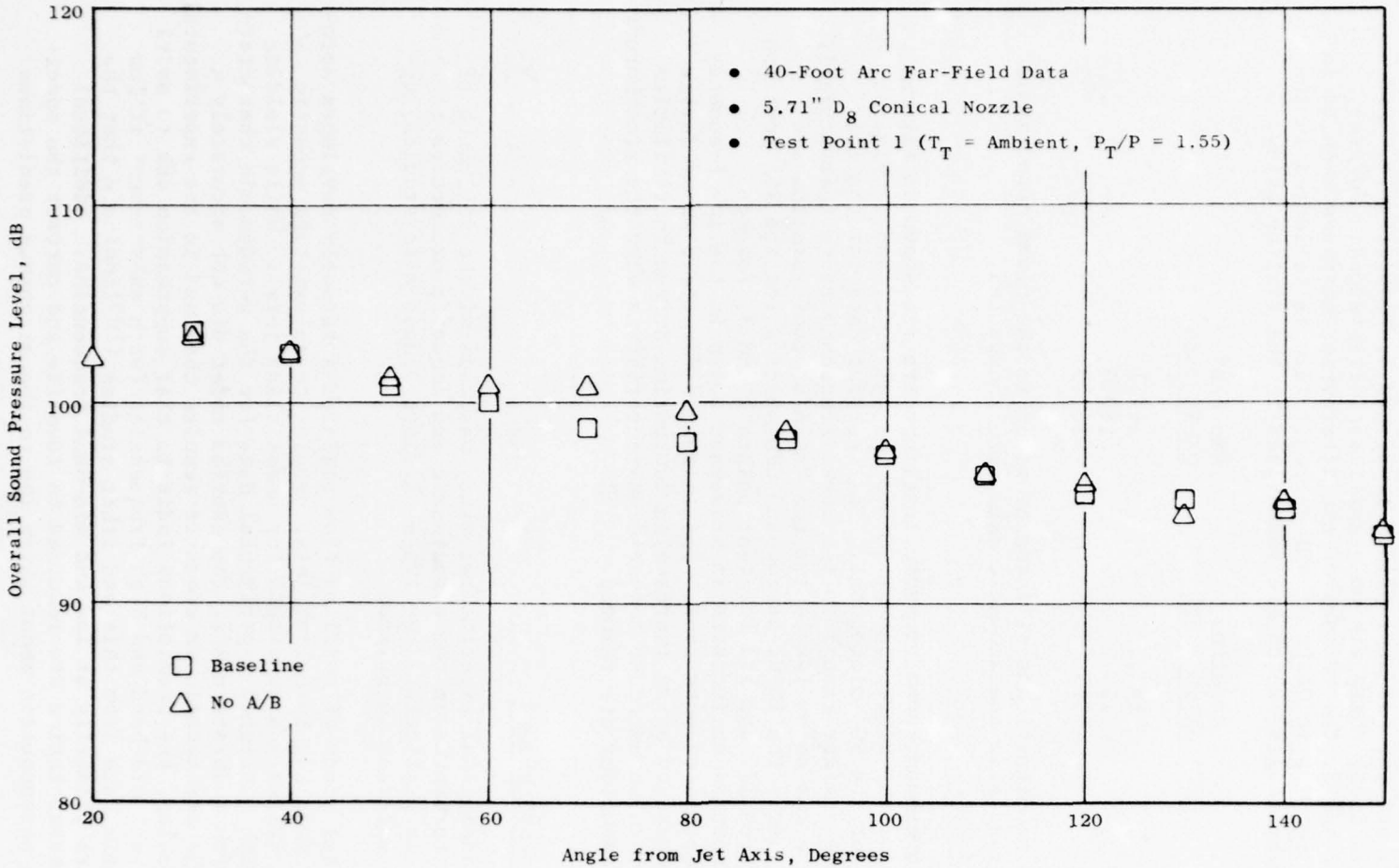


Figure 163. Overall Sound Pressure Levels, Test Point 1.

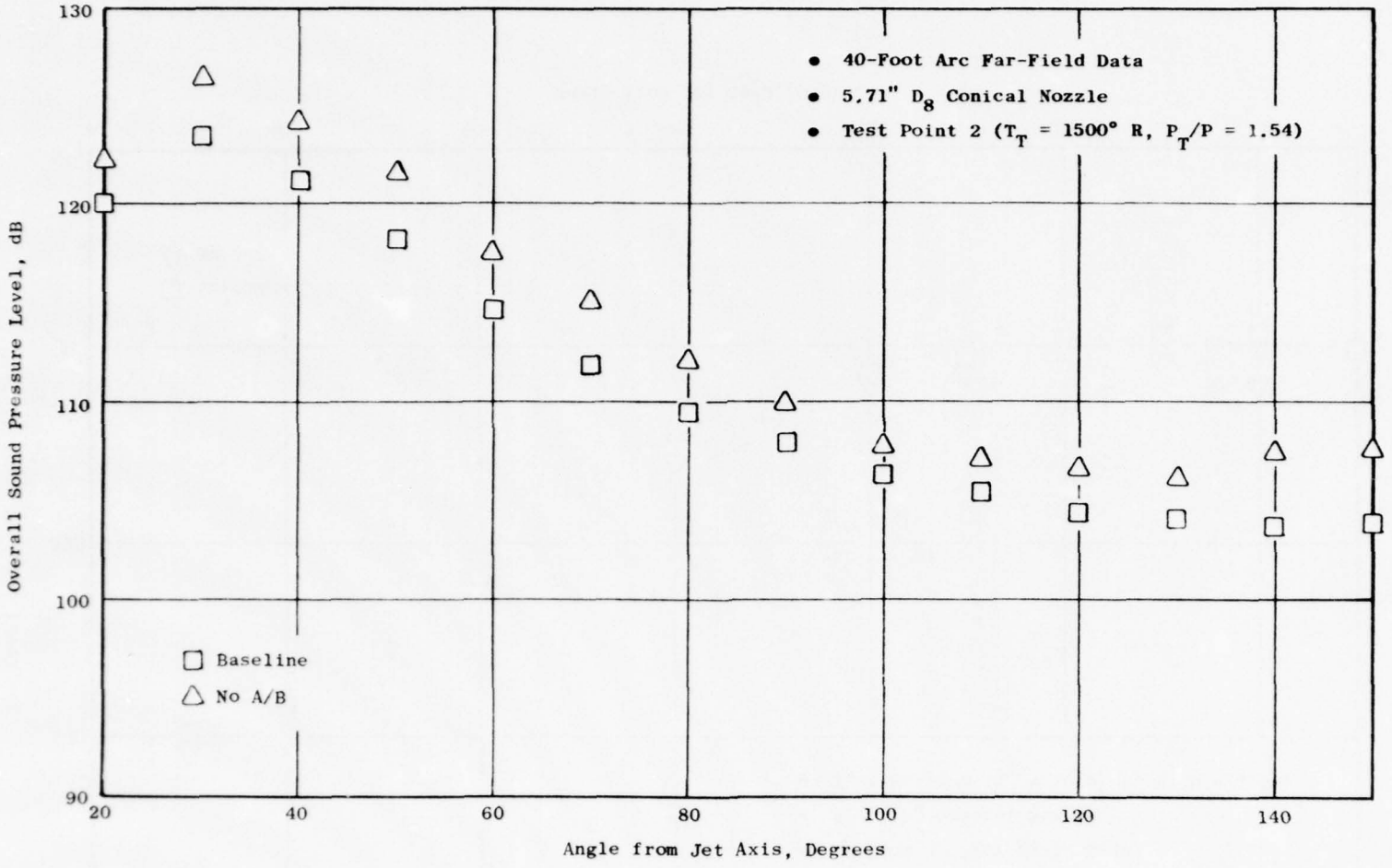


Figure 164. Overall Sound Pressure Levels, Test Point 2.

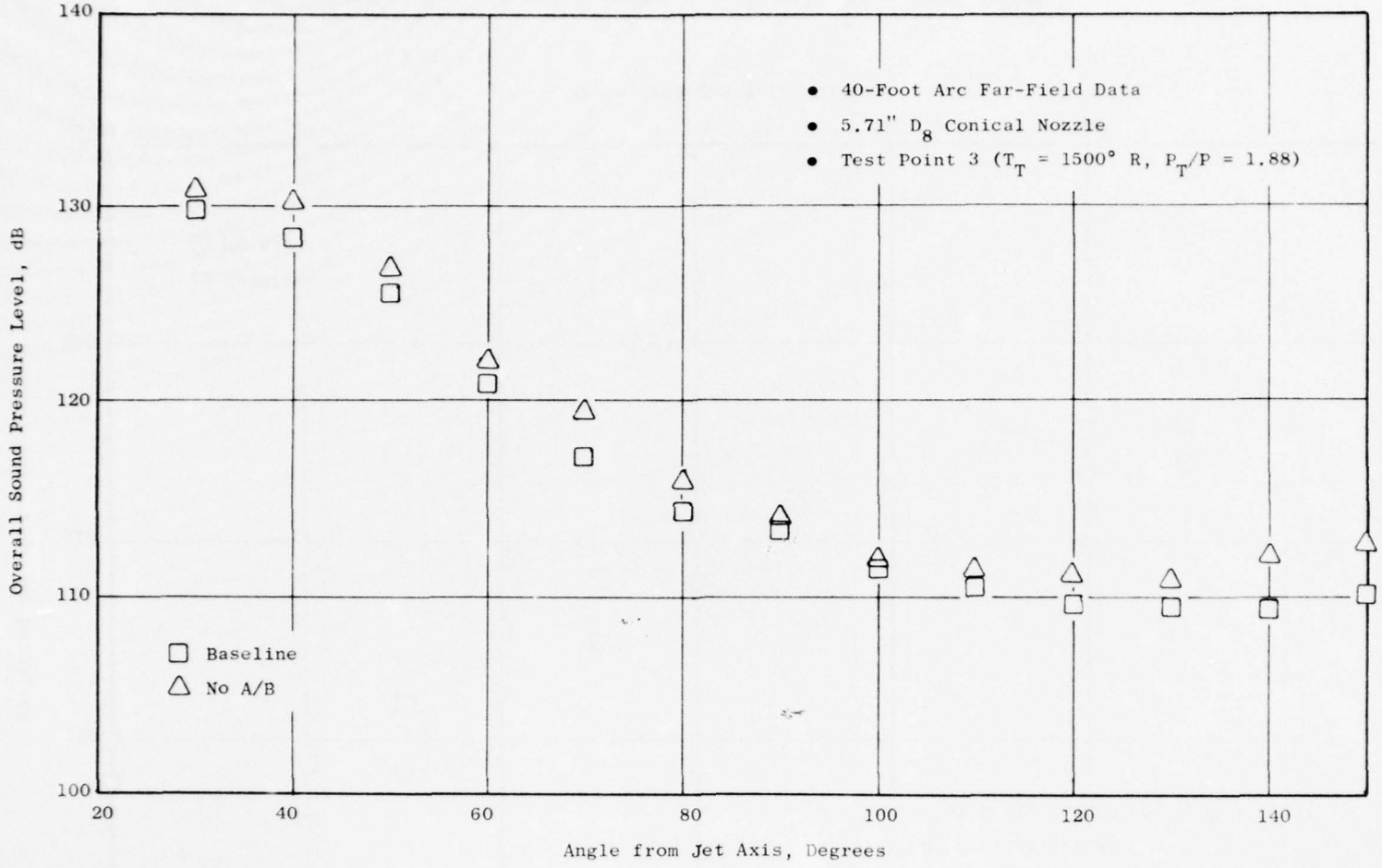


Figure 165. Overall Sound Pressure Levels, Test Point 3.

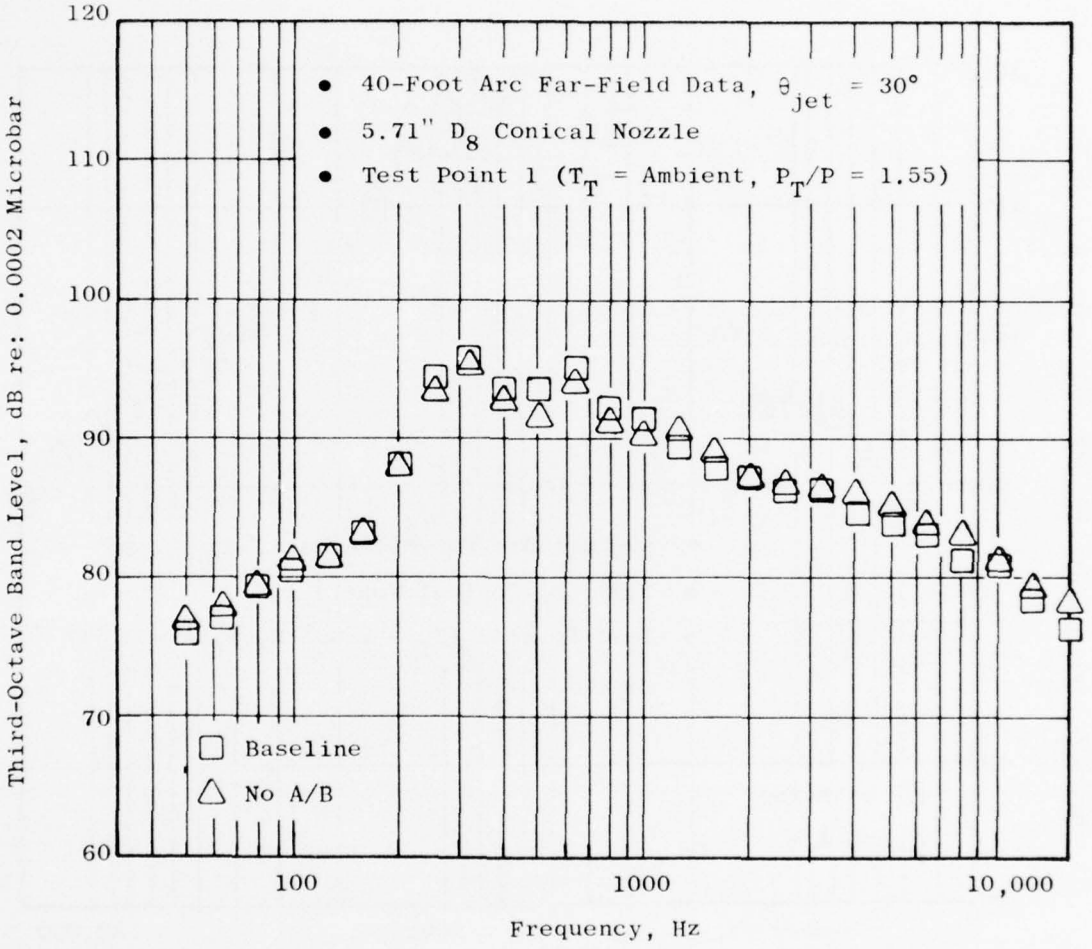


Figure 166. Measured 1/3-Octave-Band Sound Pressure Level Spectra, θ_{jet} = 30°, Test Point 1.

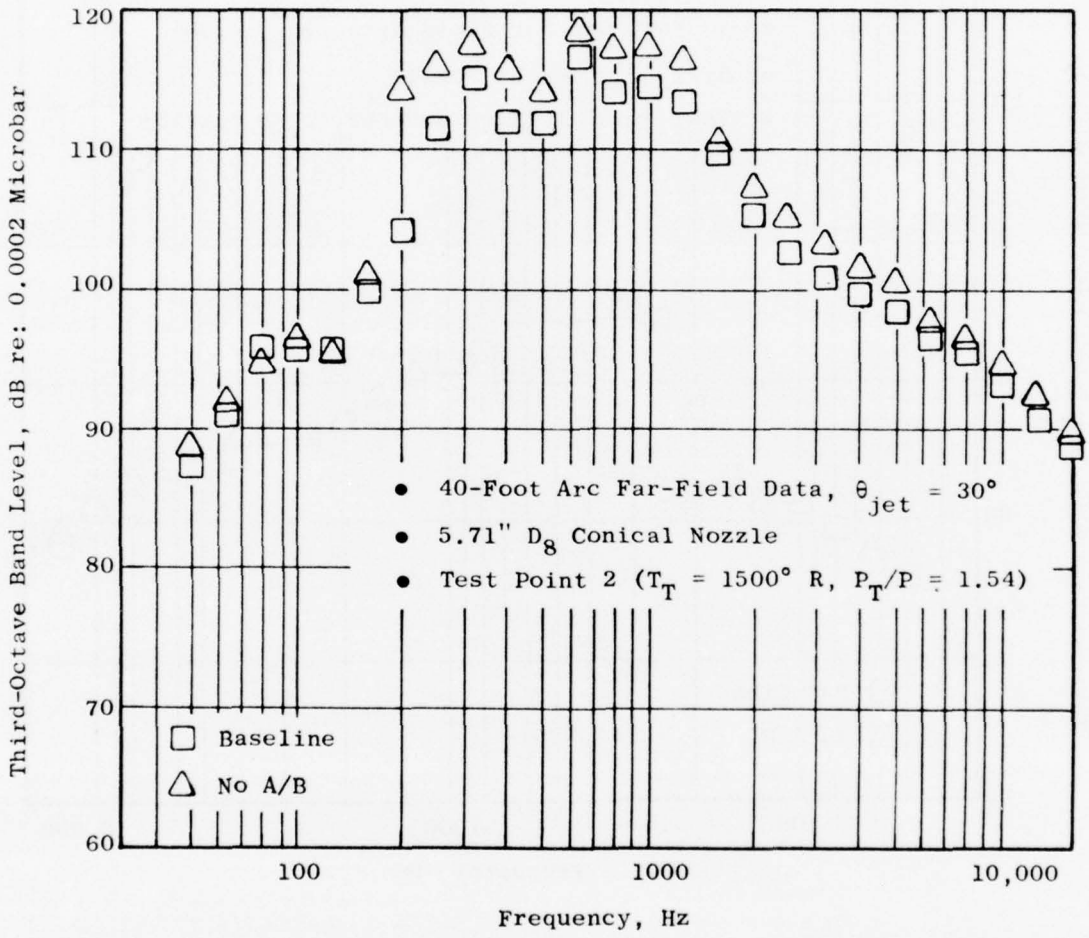


Figure 167. Measured 1/3-Octave-Band Sound Pressure Level Spectra, θ_{jet} = 30°, Test Point 2.

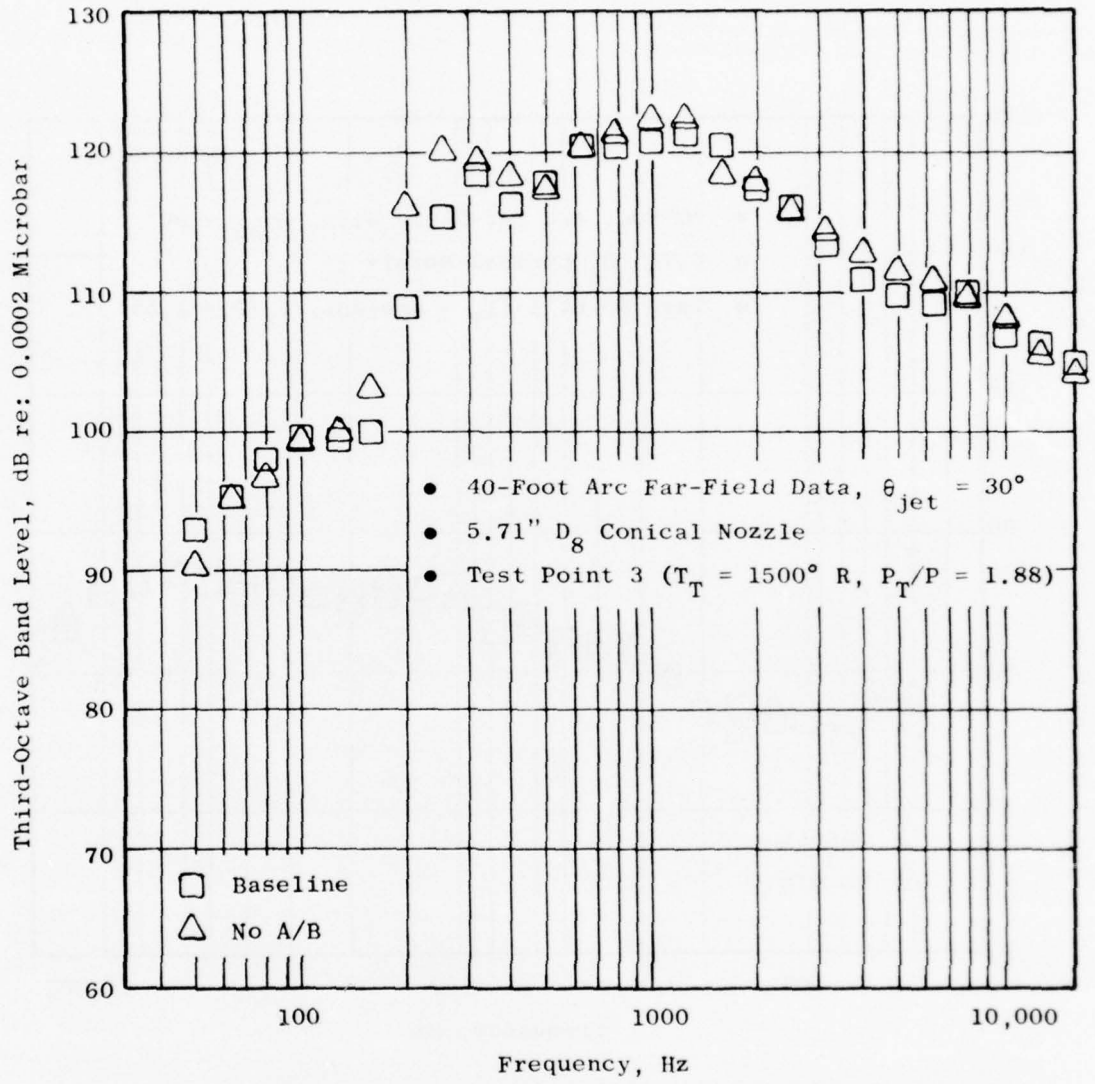


Figure 168. Measured 1/3-Octave-Band Sound Pressure Level Spectra, θ_{jet} = 30°, Test Point 3.

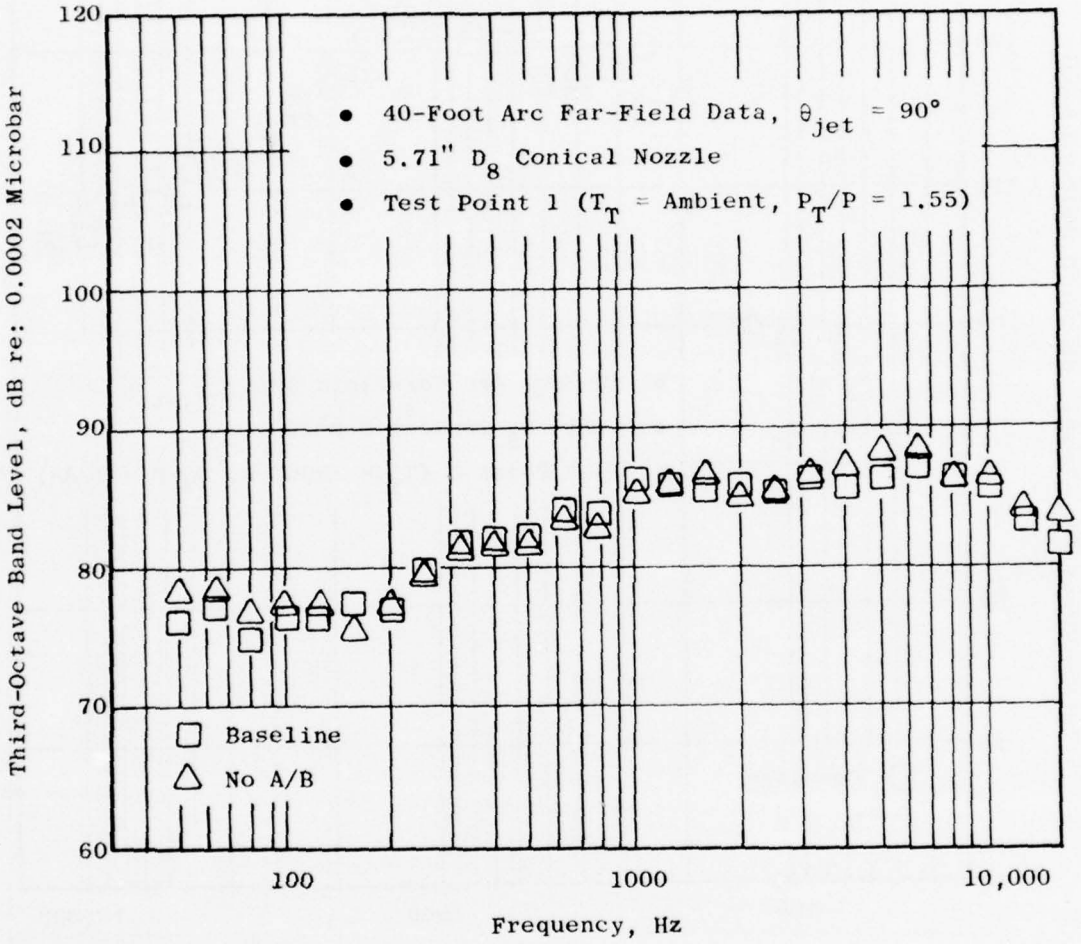


Figure 169. Measured 1/3-Octave-Band Sound Pressure Level Spectra, θ_{jet} = 90°, Test Point 1.

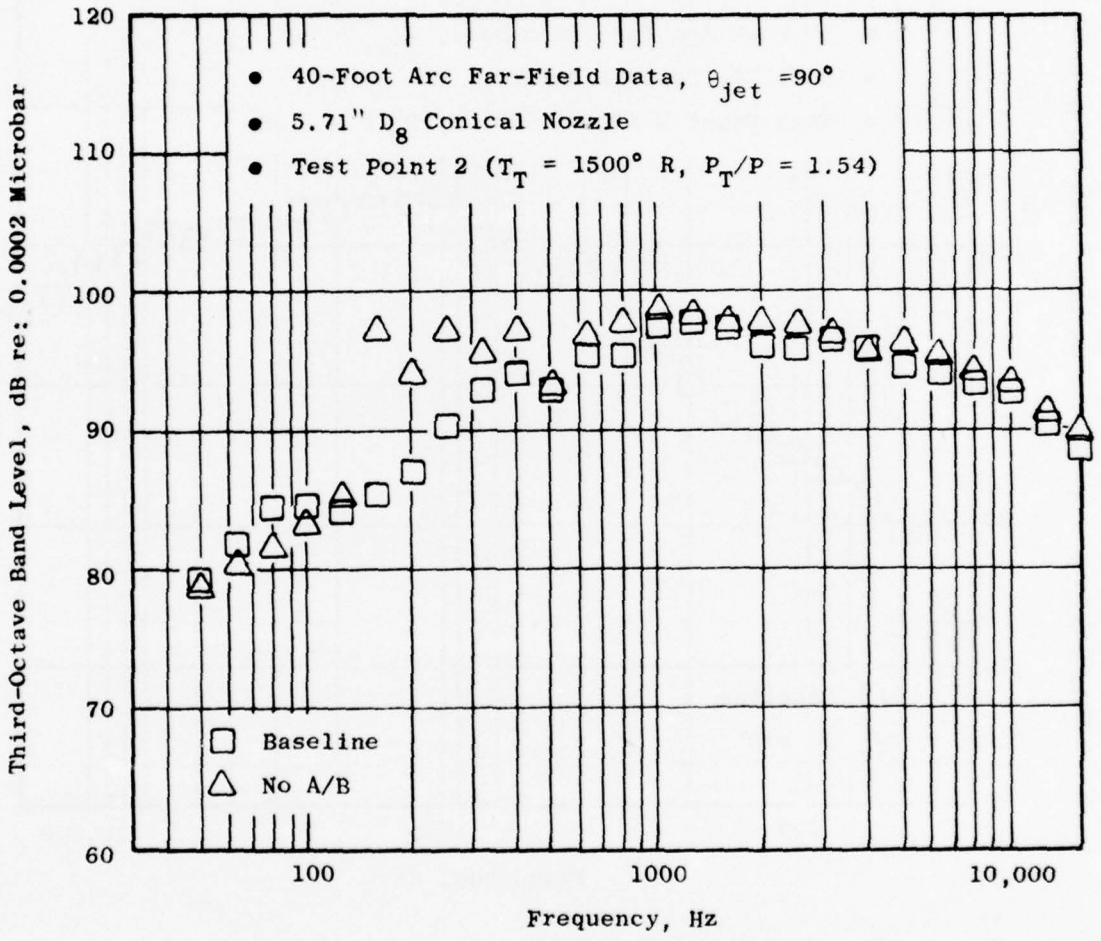


Figure 170. Measured 1/3-Octave-Band Sound Pressure Level Spectra, θ_{jet} = 90°, Test Point 2.

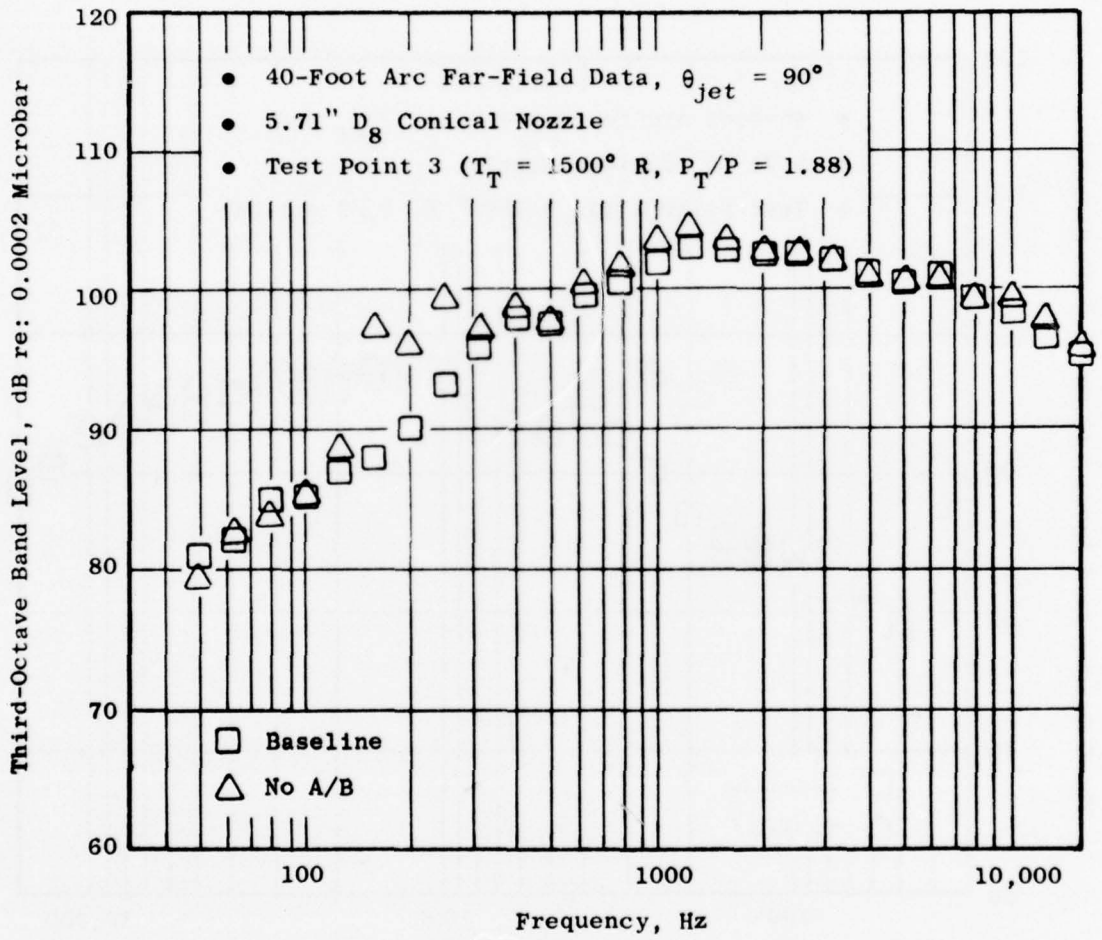


Figure 171. Measured 1/3-Octave-Band Sound Pressure Level Spectra, θ_{jet} = 90°, Test Point 3.

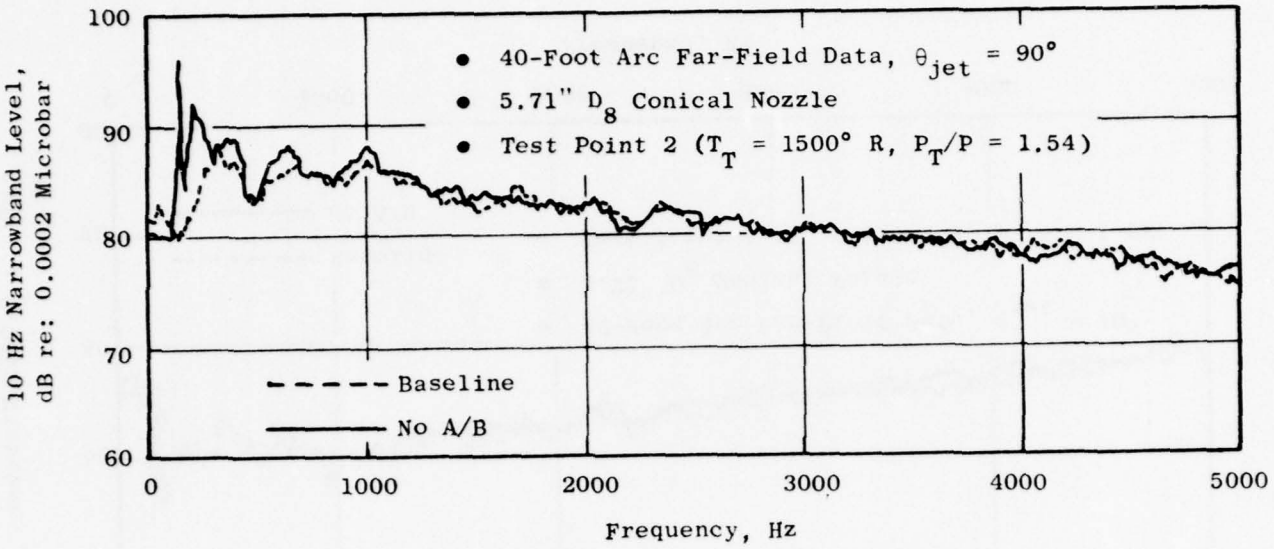


Figure 172. Measured 10-Hz-Narrowband Sound Pressure Level Spectra, Test Point 2.

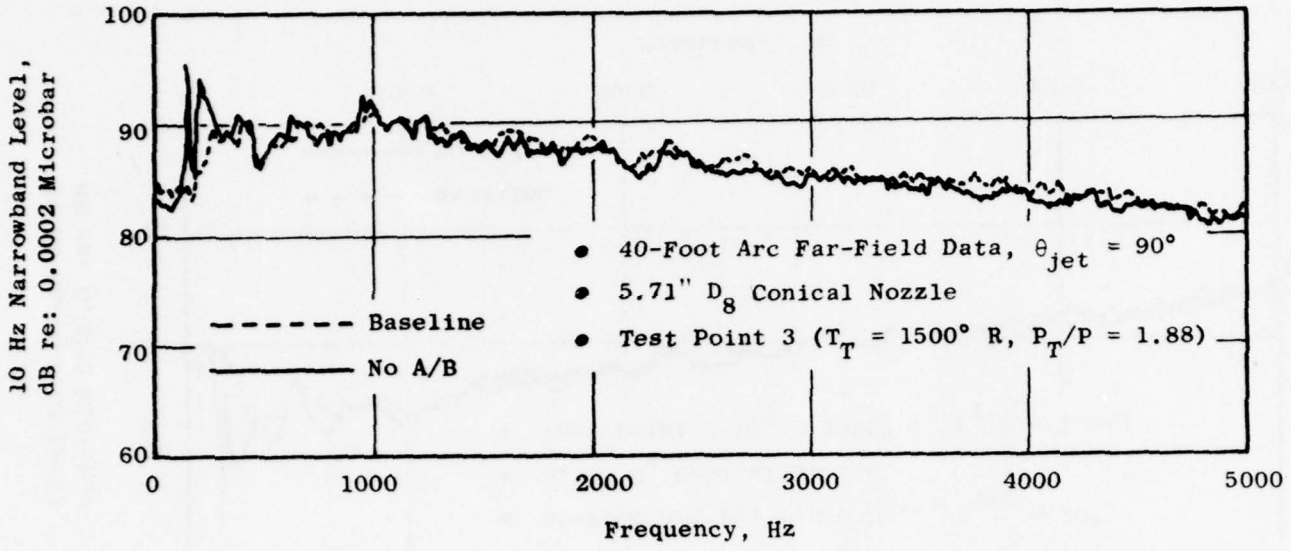


Figure 173. Measured 10-Hz-Narrowband Sound Pressure Level Spectra, Test Point 3.

The swirling jet experiment demonstrated that swirl can be used to suppress low and mid-band frequencies of jet noise at angles close to the jet axis, although accompanying increases in high frequency noise somewhat reduce the overall effectiveness of swirl as a suppression mechanism. One item which must be given maximum attention in any future studies is the thrust loss due to swirl, or, more important, the additional fuel flow required to maintain constant thrust. Data obtained in this experiment suggest that substantial thrust losses, on the order of 10%, result from the introduction of swirl to a jet.

Both the analytical and experimental studies of upstream turbulence failed to provide significant insight into processes in a jet engine capable of producing a wide-enough range of turbulence intensities to have an appreciable effect on jet noise. Increases in low frequency noise were observed when the facility afterburner flameholder/spraybars were removed and for certain of the combustion roughness settings. These increases are attributed to heightened combustion noise which is transmitted through the nozzle, rather than to enhanced jet noise.

SECTION 2.0

JET REFRACTION EXPERIMENTS

K.R. Bilwakesh

2.1 BACKGROUND

A considerable number of jet noise experiments has shown the heart-shaped directivity patterns of jet noise. It has been postulated by several authors (References 11, 24, 34, 130, 131) that this is the result of competing effects of convection amplification and refraction. Experiments conducted by Ribner and his associates (References 13-15) at the University of Toronto have shown that, at low velocities and temperatures, the effects of refraction and convection can be corrected out of measured jet noise patterns to yield a "basic directivity" of the eddy noise generators. This in essence indicated that, starting with the known and reasonably well-established formulations of basic jet noise directivity and effects of convection, one could now introduce the experimentally determined correction factors for refraction effects in order to obtain, empirically, the overall directivity of jet noise. This could then be compared with measurements of overall directivity, and adjustments of empirical formulations could be made. Such a procedure was accomplished with reasonable success by MacGregor, et al, in the temperature range 0-500° F and in the Mach number range 0-0.5. Extension of such an analytical-empirical procedure to jets at realistically high velocities and temperatures thus appears very desirable.

The basic objectives in the current study were chosen to be the following:

- Verify the refraction concepts advanced by Ribner, et al.
- Extend the concepts for realistic heated and high velocity jet conditions.
- Based on the above, obtain empirical inputs for refraction effect applicable to heated jet noise prediction methods.
- Obtain information on tone-flow interaction phenomena.

2.2 RIBNER'S REFRACTION CONCEPTS

The basis for the current work has been the conceptual model of jet noise directivity advanced by Ribner[11, 14, 34]. According to this model, the basic directional pattern (i.e., with convection and refraction effects excluded) produced by the turbulent eddies is given by:

$$\text{Intensity} \sim \underset{\text{self shear}}{A+B\ (\text{Cos}^4\theta + \cos^2\theta)/2} \qquad (206)$$

and is a quasi-ellipsoid with the long axis in the direction of the jet axis (Figure 174a). The convection of the eddy sources by the mean flow causes amplification of the noise pattern in the downstream direction (Figure 174b). The temperature and velocity gradients in the flow cause a pronounced valley along the jet axis in the directivity pattern (Figure 174c).

Extensive experimental work has been done at the University of Toronto (References 11, 13-15, 24, 34, 130, 131) to evaluate quantitatively this refraction effect. The far-field directivity pattern of an injected point source immersed in a subsonic jet flow (Figure 175) was found to be very similar to the far-field directivity pattern of the jet noise analyzed with a narrowband filter (Figure 176). Such a similarity gave credence to the assertion that the observed downstream valley in the filtered jet noise was due to refraction rather than the inherent directivity of the aerodynamic sources. These experiments also showed that the refraction valley (in the case of the tone source immersed in the jet) deepened and widened as the jet velocity was increased (Figure 175) and deepened as the jet temperature was increased (Figure 177) or when the source frequency was increased (Figure 178).

MacGregor, et al, use the same technique to measure the change in the far-field intensity of the point source due to ambient temperature jets at velocities up to M=0.9. This was related to the jet noise intensity by use of conservation of acoustic energy within the hemisphere to obtain quantitative refraction factors as functions of velocity, temperature, and frequency. Applying this refraction correction and the convection amplification term in reverse to the measured overall directivity, they obtained an empirical basic directivity. This experimentally obtained basic directivity showed reasonably good agreement with a theoretically derived basic directivity using equation 206.

2.2.1 Method of Approach

Based on the success of the injected point source method at low velocities and temperatures, the same method was chosen in the current investigation.

The method principally consisted of injecting a pure tone by means of a point source located axially, two-nozzle-diameters downstream of the nozzle exit plane. Acoustic intensity was measured at different angles for each source frequency with the jet on and with the jet off. The difference between the two measurements (expressed in SPL) gave the effect of jet refraction on the tone. The source was then turned off, and the acoustic intensity of the jet alone was measured at the same angles as before.

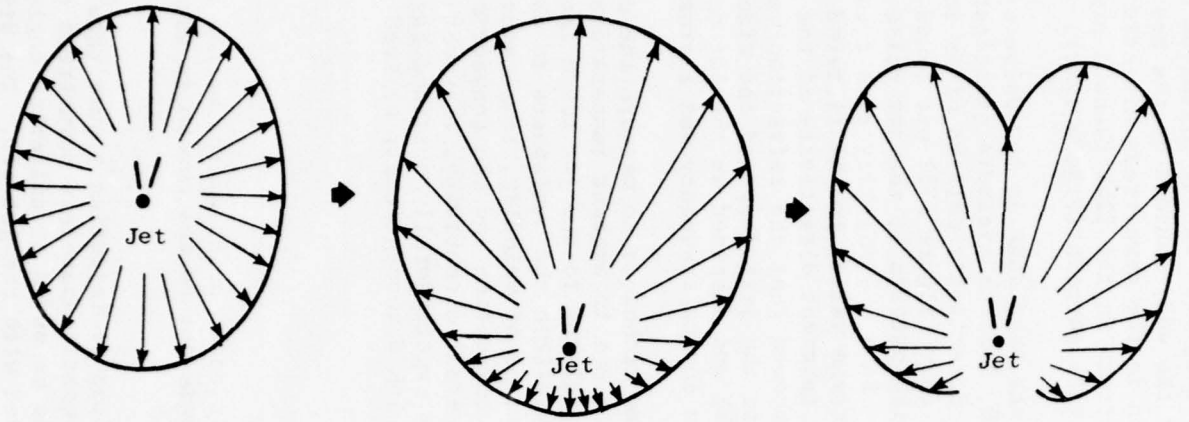


Figure 174. Ribner's Jet Acoustic Refraction Model.

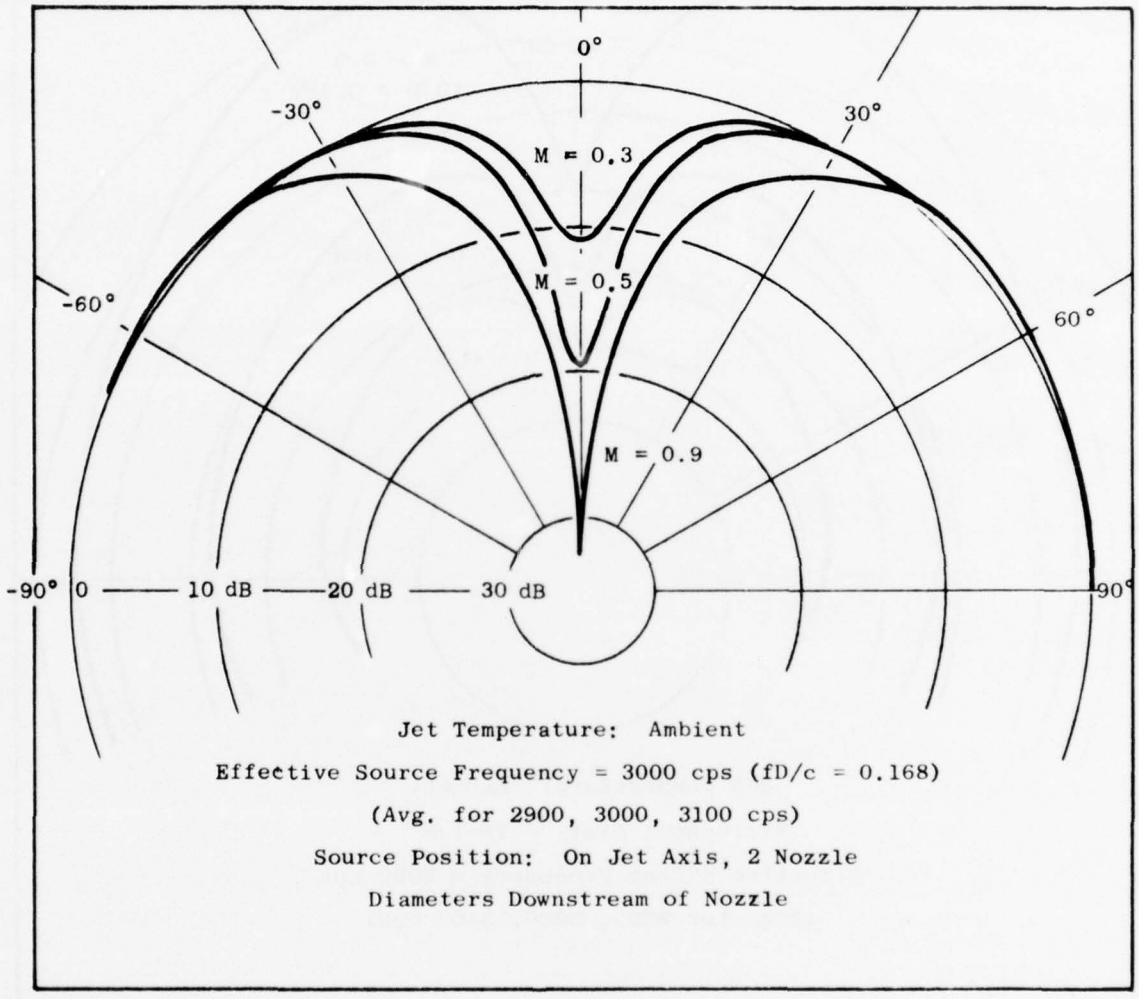


Figure 175. Effect of Jet Velocity on Directivity (Reference 13).

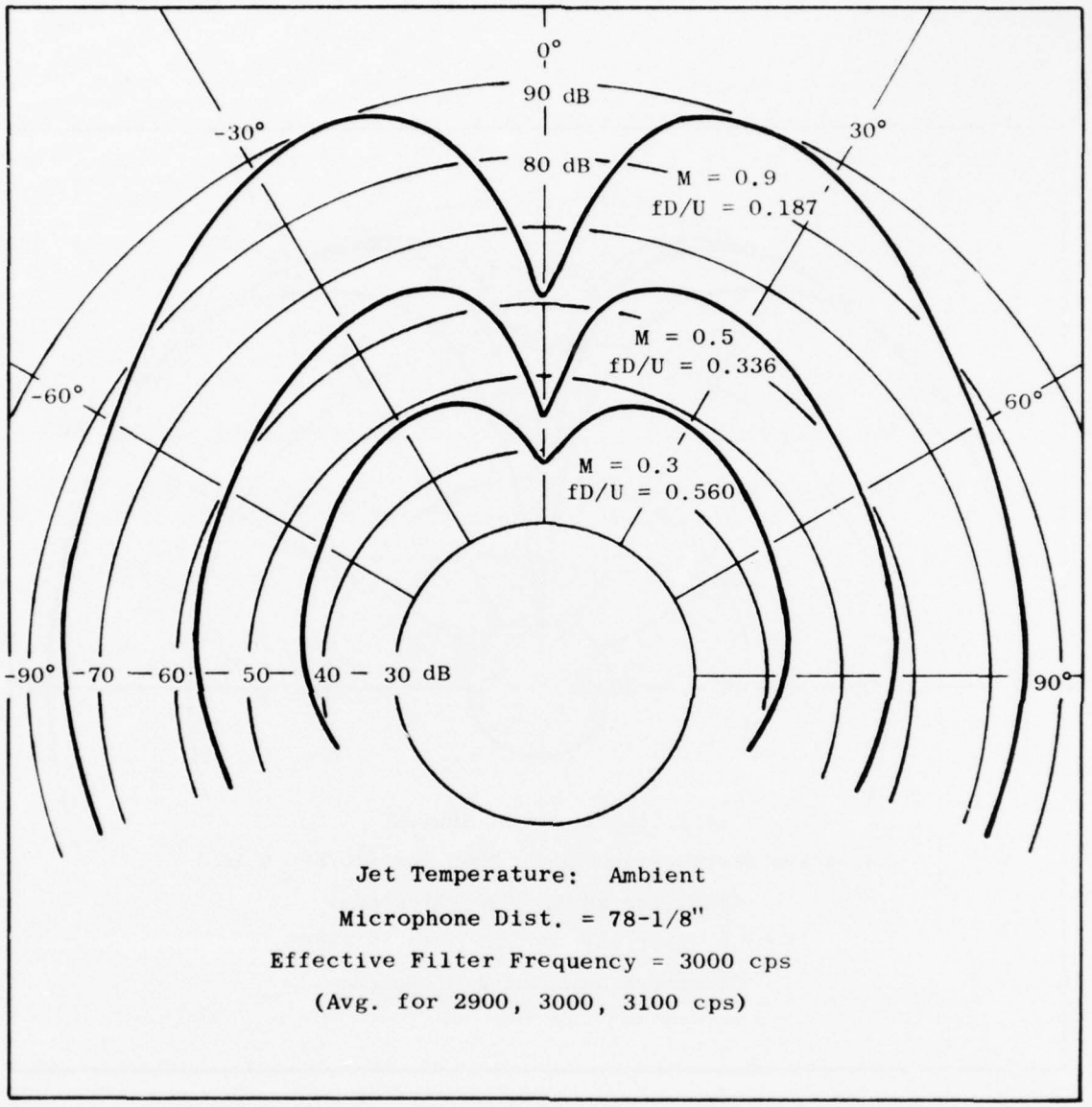


Figure 176. Jet Noise Directivity for Air Jet (Reference 13).

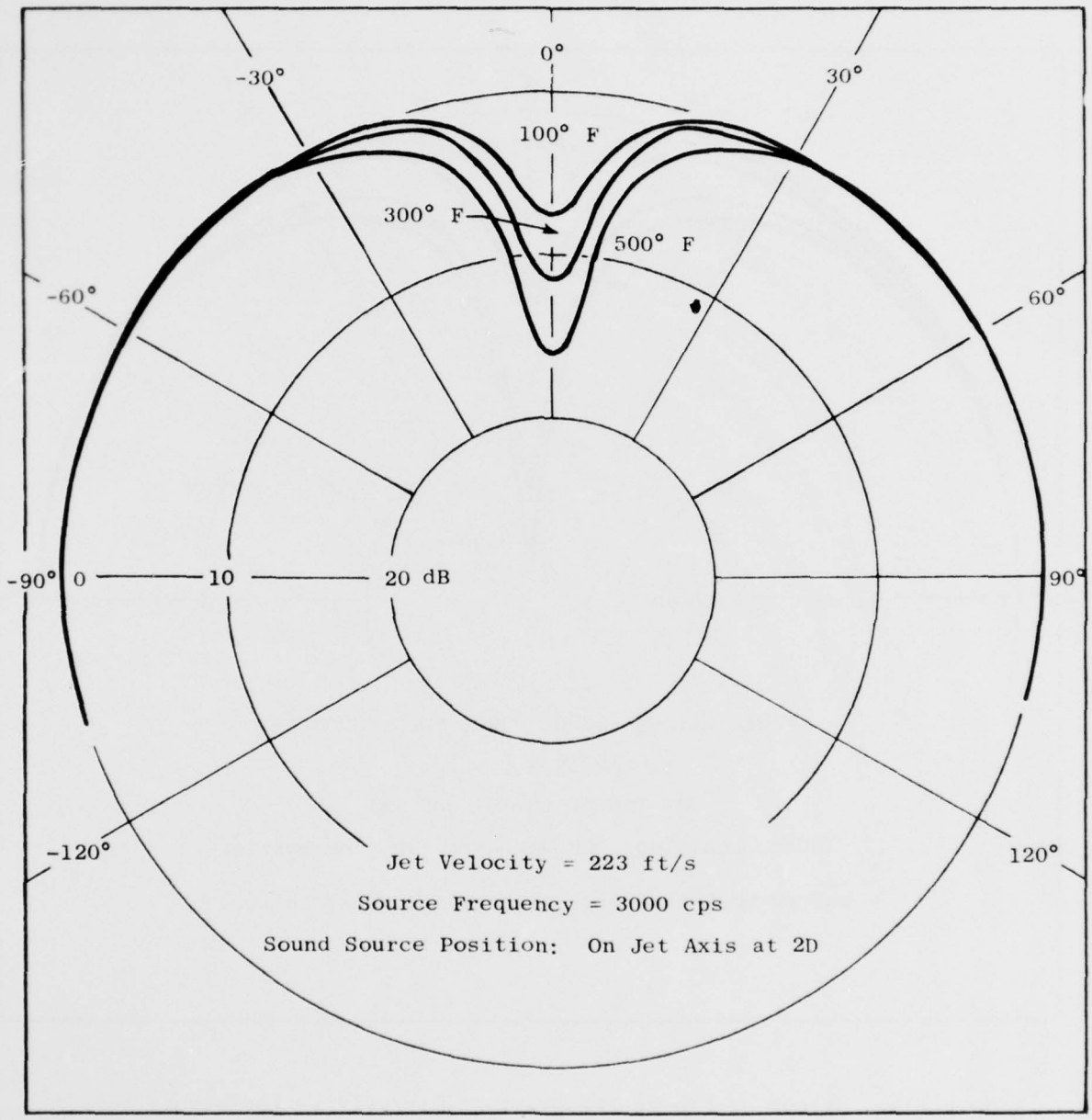


Figure 177. Effect of Jet Temperature on Directivity (Reference 15).

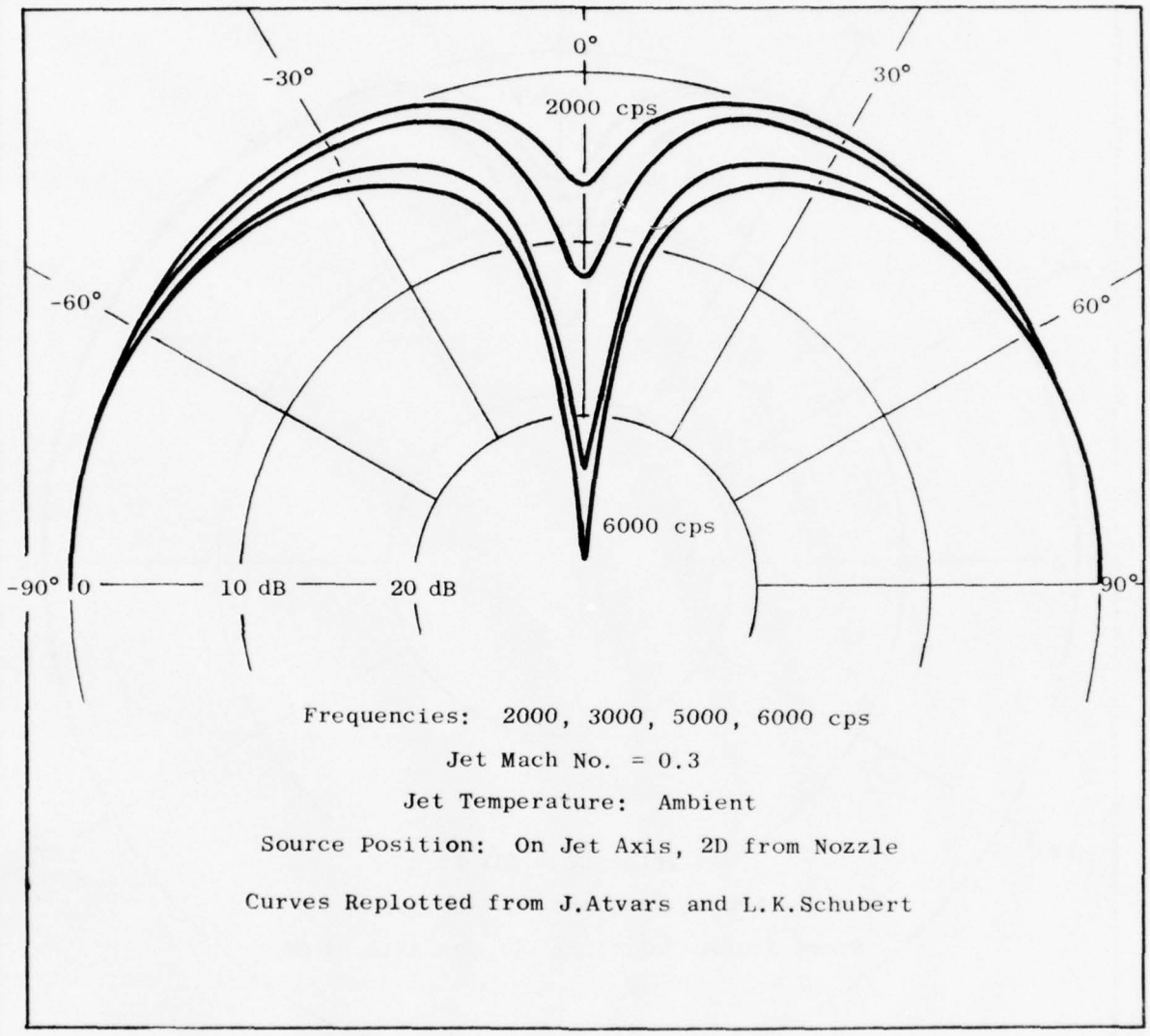


Figure 178. Effect of Source Frequency on Directivity (Reference 13).

By way of illustration, let $I_1(\theta)$ and $I_2(\theta)$ represent the acoustic intensity of the injected point source at a specific far-field polar microphone location (r,θ) with the nozzle exit-plane center as the origin (Figure 179). The refraction effect for the point source $R_p(\theta)$ can then be defined as:

$$R_p(\theta) = \left[\frac{I_2(\theta)}{I_1(\theta)}\right]^{Point}_{f,U,T} \tag{207}$$

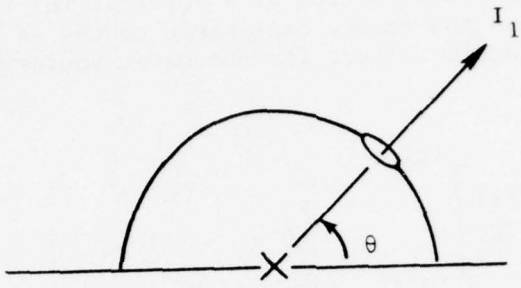
where U and T represent the velocity and temperature of the jet and f represents the injected source frequency. Note that $I_2(\theta)$ and $I_1(\theta)$ are measurable quantities. Now, with the source turned off let $J_2(\theta)$ and $J_1(\theta)$ be the acoustic intensities at the same point (r,θ) of the jet without and with removal of the refraction effect (Figure 180). Obviously, $J_2(\theta)$, exhibiting the overall directivity including refraction effects, is a measurable quantity, while $J_1(\theta)$ is a hypothetical term for jet noise and not physically measurable. The refraction factor for the jet, R_{Jet}) is defined as:

$$R_{Jet} = \left[\frac{J_2(\theta)}{J_1(\theta)}\right]^{Jet}_{f,U,T} \tag{208}$$

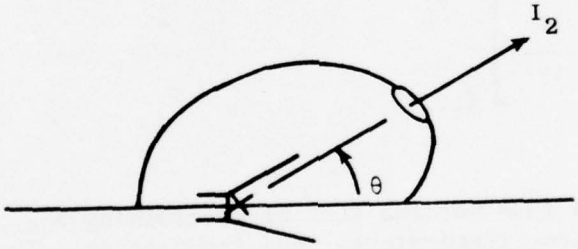
One of the objectives thus becomes that of determining R_{Jet} for a wide range of realistic velocities, temperatures, and frequencies. Then, with $J_1(\theta)$ obtainable from already well-known analytical models, it will be possible to predict the measurable overall directivity $J_2(\theta)$.

It should be noted that the point source, with its ideally spherical directivity pattern, $I_1(\theta)$, cannot truly represent the distributed and moving eddy sources in a jet. Hence, MacGregor, et al, have confirmed this intuitive observation by applying the principle of conservation of energy for the point source and the jet source uses. Following their argument, one can introduce a correction factor $G(\theta)$ which can be used to multiply R_{Point} in order to represent R_{Jet}:

i.e., $R_{Jet} = R_{Point} * G(\theta)$

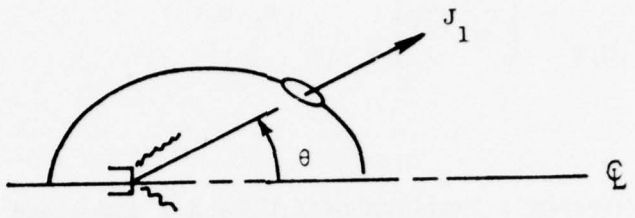


Point Source Alone; Jet Off

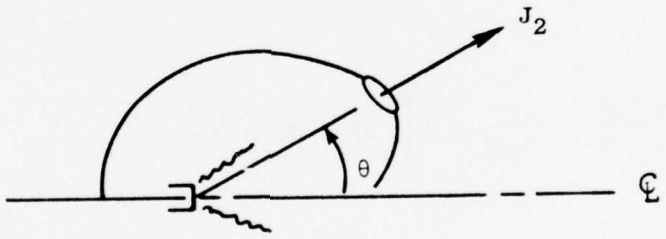


Point Source With Jet On

Figure 179. Refraction Schematic for a Point Source Injected into a Jet Flow.



Basic + Convection
Directivity Pattern



Basic + Convection + Refraction
Directivity ⟶ Jet Overall
Directivity Pattern

Figure 180. Refraction Schematic for a Jet Flow.

$$\text{or} \quad \left[\frac{J_2(\theta)}{J_1(\theta)}\right]_{f,U,T}^{\text{Jet}} = \left[\frac{I_2(\theta)}{I_1(\theta)}\right]_{f,U,T}^{\text{Point}} * G(\theta) \tag{209}$$

$G(\theta)$ is obviously a function of f,U, and T also, and has to be determined empirically. Using the conservation of acoustic energy in a unit sphere, one can then write, following MacGregor, et al:

$$\int_0^{\pi} J_2(\theta) \sin\theta \, d\theta = \int_0^{\pi} J_1(\theta) \sin\theta \, d\theta$$

$$= \int_0^{\pi} J_2(\theta) \frac{I_1(\theta)}{I_2(\theta)} \frac{1}{G(\theta)} \sin\theta \, d\theta \tag{210}$$

Thus,

$$= \int_0^{\pi} J_2(\theta) \left[\frac{I_1(\theta)}{I_2(\theta)} \cdot \frac{1}{G(\theta)} - 1\right] \sin\theta \, d\theta = 0 \tag{210}$$

The whole problem has now been reduced to simply measuring J_2, I_2, and I_1, then determining G from equation (210), and then obtaining R_{Jet} from equation (209). This R_{Jet} can then be used in the existing methods to predict the overall jet noise directivity.

2.3 TEST FACILITY AND APPARATUS

2.3.1 Test Facility

The experiments were conducted in General Electric's JENOTS (Jet Engine Noise Outdoor Test Stand) facility. The facility is capable of operation either as a single- or coannular-flow system, through interchangeable burner and acoustically treated plenum sections. In the single-flow mode, for clean operation from low subsonic through high supersonic jet velocities, the system consists of a preburner and afterburner capable of operating up to 6" diameter nozzles to pressure ratios of 4:1 and temperatures of 3000° F. In the current set of experiments, the facility was used in the single-flow

mode with a 4.31" diameter water-cooled conical nozzle. The basic single jet test rig consists of a primary 10" air pipe, a preburner, and a 12" water-jacketed afterburner section, followed by a flame tunnel ending in a flange for mounting the test nozzle. For these experiments, a water-cooled adapter section was inserted between the flame tunnel and the nozzle. This adapter provided the entry for the output tube from the siren mounted beside the nozzle. Figure 181 shows a schematic of the test setup.

The acoustic arena is exposed to ambient conditions. The ground plane is composed of concrete to approximately a 20-foot radius from the nozzle exit. The remainder of the acoustic arena is composed of gravel from 20 ft to 40 ft in radius with a grassy field beyond and with no structures present that would cause acoustic reflection interference at the microphone positions. The nozzle centerline is 55 inches above the concrete.

2.3.2 Description of Tone Source

The tone source consisted of a constant-cross-section, 0.87"-ID tube attached to the stator of a siren. The siren consisted of a 60-slot rotor wheel (Figure 182) driven by a synchronous electric motor whose rpm could be controlled within extremely close limits (± 1 rpm at the maximum rpm of 6000) by means of an oscillator. The stator output-port diameter was 2.6 inches. The constant-diameter tube was welded directly onto the stator exit in such a way as to provide a maximum area opening; the remainder of the stator port was sealed. This method was determined by prior tests to provide the maximum acoustic output from the siren for the limited output diameter of the source that was required. The source diameter was chosen to provide reasonably spherical directivity up to 4500 Hz without excessive penalty in acoustic output. Tubes of different sizes were tested in JENOTS during the initial stages of development of the source, in order to determine the limits of the possible test matrix. Figure 183 shows polar plots of directivity of the siren with a 0.81" ID tube as output port in the frequency range 500-5000 Hz. The measurements were made with microphones flush-mounted to the ground on a 20-foot arc.

The acoustic output was found to be nearly spherical and uniform at 2000 and 5000 Hz. A sharp drop in output was noticed below 800 Hz as seen in the curve for 500 Hz. No data were obtained beyond 5500 Hz due to the design limitations on the siren.

Figure 184 shows a comparison of the source output with measured jet noise data at a velocity of 1670 ft/sec at 1500° R. While the one-third octave band jet noise appeared to be higher than the siren output, filtering the jet noise with a 1 Hz narrowband filter at the frequencies of interest would obviously enable the siren tone to be very easily picked up above the jet noise. Since the jet noise spectrum starts to drop beyond the frequency corresponding to peak Strouhal number while the siren output appeared to increase somewhat with frequency, extraction of the tone, particularly at high frequencies, promised to be an easily achievable objective.

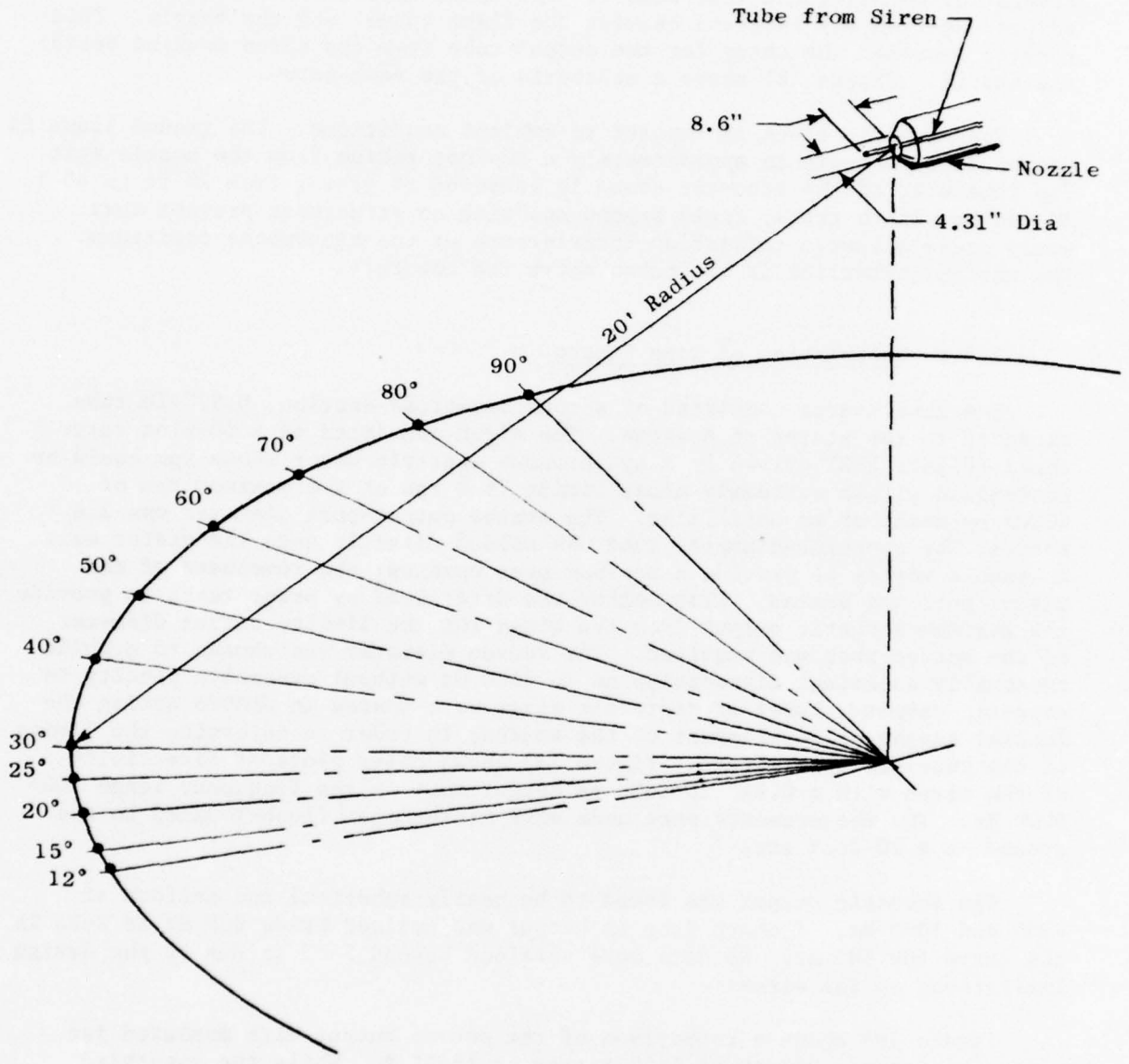


Figure 181. Schematic of Experimental Setup for Acoustic Far-Field Measuring Stations.

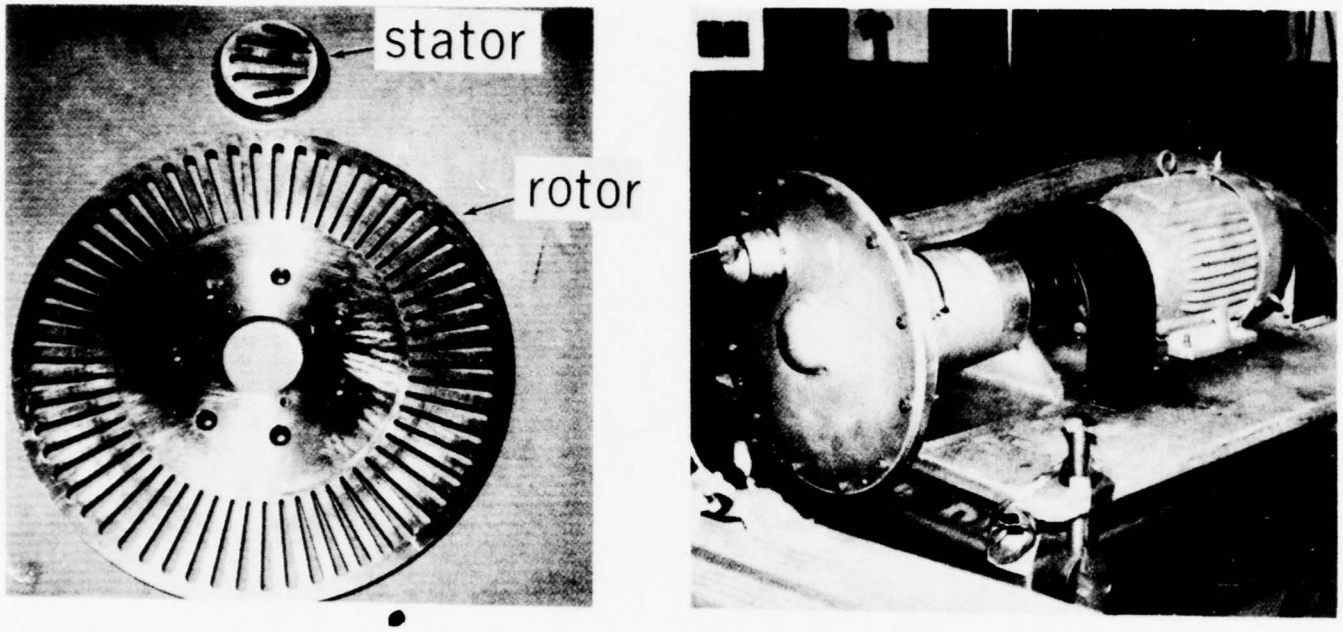


Figure 182. Siren Used for Point Source.

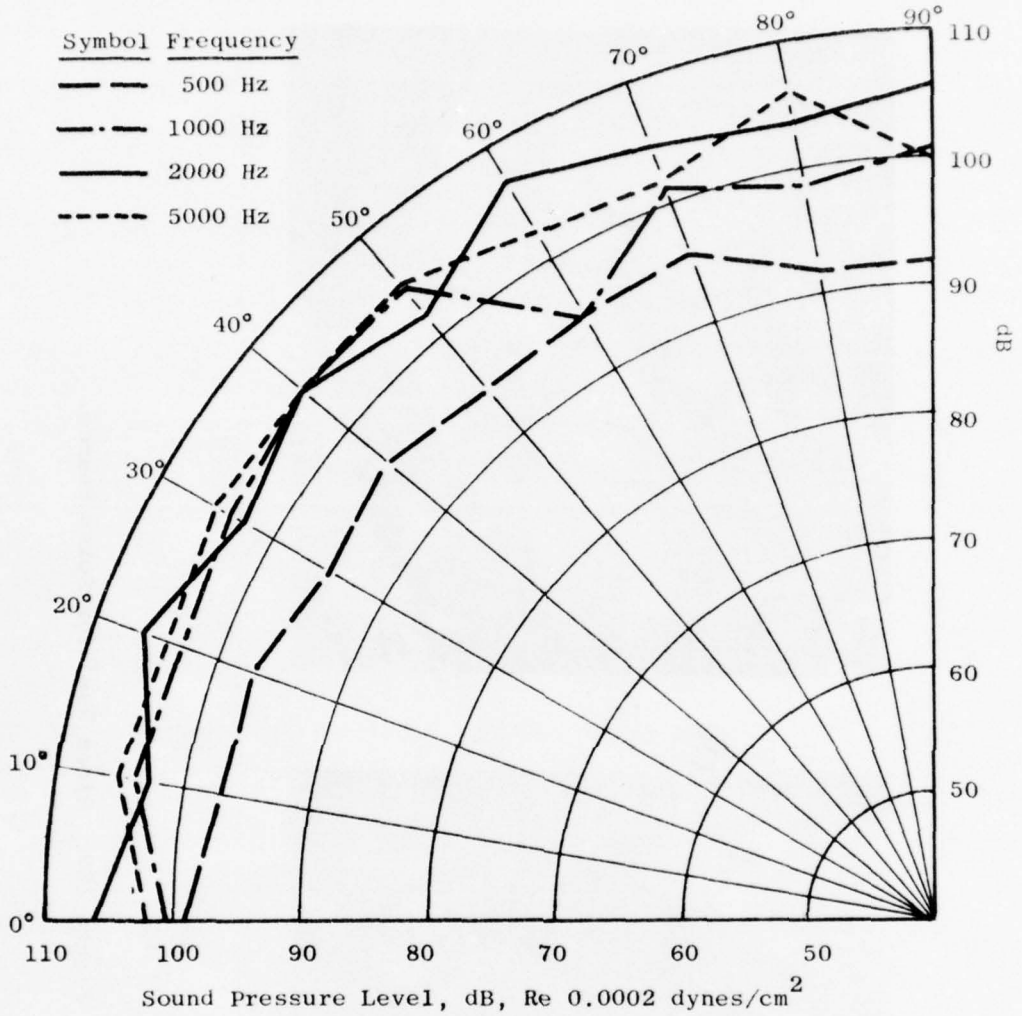


Figure 183. Directivities of Siren Output in the 500-5000 Hz Frequency Range on a 20-foot Arc with a 0.81" ID Output Port.

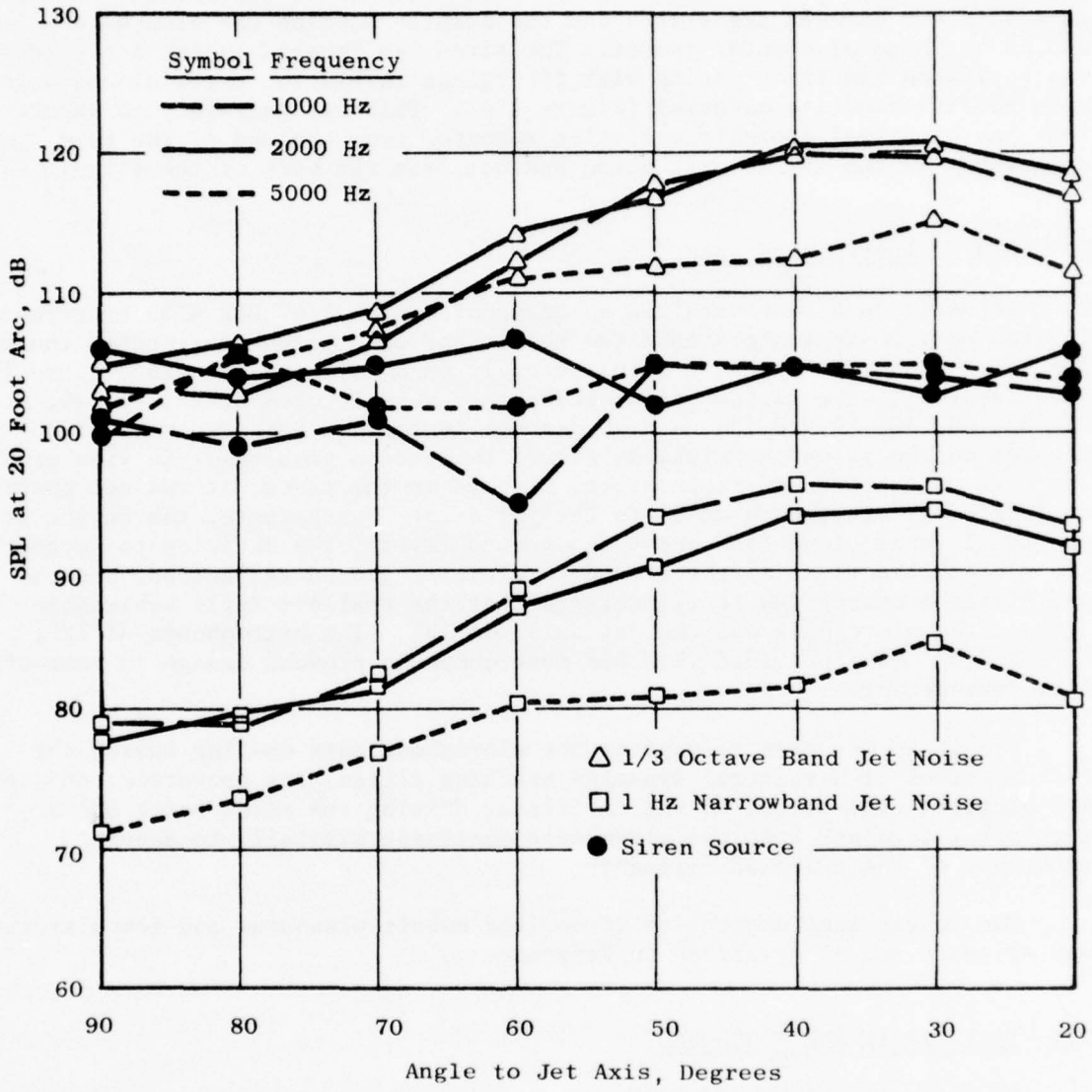


Figure 184. Comparison of Sound Source Output with Measured Jet Noise Data; Jet at 1670 ft/sec and T_T = 1500° R.

The experimental setup with the siren source is shown in Figure 185. The source tube entered the nozzle through a water-cooled adapter section upstream of the nozzle. The outlet plane of the tube was located two nozzle diameters (8.62") downstream of the nozzle exit plane. The portion of the tube that was between the stator and the adapter section was also water-cooled by means of a water jacket. The siren was located inside a one-inch-thick plywood box lined inside with fiberglass insulation material and outside with cousti-composite material (Figure 186). This was necessary to ensure that the principal acoustic radiation emanated from the end of the tube downstream of the nozzle exit plane and not from the body of the siren.

2.3.3 Instrumentation

Acoustic data were obtained by means of eleven 1/4" B&K 4135 microphones located on a 20-foot arc around the nozzle and one microphone located inside the box. Data were recorded simultaneously on a 28-channel Sangamo Sabre IV tape recorder. The 11 far-field microphones were located at 12, 15, 20, 25, 30, 40, 50, 60, 70, 80, and 90 degrees to the jet axis and were flush-mounted on the ground to minimize ground reflection problems. In view of the high velocities and temperatures planned in the tests, it was not possible to locate any microphone at 0° to the jet axis. Furthermore, the height of the nozzle exit plane (55" above the ground level), the decision to locate the microphones flush to the ground to minimize ground reflection, and the arc distance chosen (20 feet) dictated that the smallest angle achievable between the microphone and the jet axis was 12°. The microphones at 12°, 15°, and 20° were provided with B&K nose cones to prevent damage in case of flow impingement.

Provision was made to monitor the microphone data on-line during the test by means of a spectral dynamics tracking filter, log converter, and an X-Y plotter. The output of the oscillator driving the siren motor and a tachometer feedback from the siren were monitored digitally to assure constancy of the selected frequency.

The nozzle instrumentation to monitor nozzle pressures and temperatures was standard and as described in Reference 7.

2.4 TEST MATRIX AND PROCEDURE

Several unusual considerations had to be taken into account in designing a test matrix for this program. The principal objectives were to choose as wide and representative a range of temperatures, velocities, frequencies, and Strouhal numbers as physically feasible within the several experimental limitations. The limitation was obviously the acoustic output of the siren. This was limited by the requirement that the tube diameter be within one quarter wavelength of the highest frequency tone to be generated for the radiative pattern to be spherical. The output tube diameter, in turn, controlled to a very large extent the acoustic output recoverable from the siren.

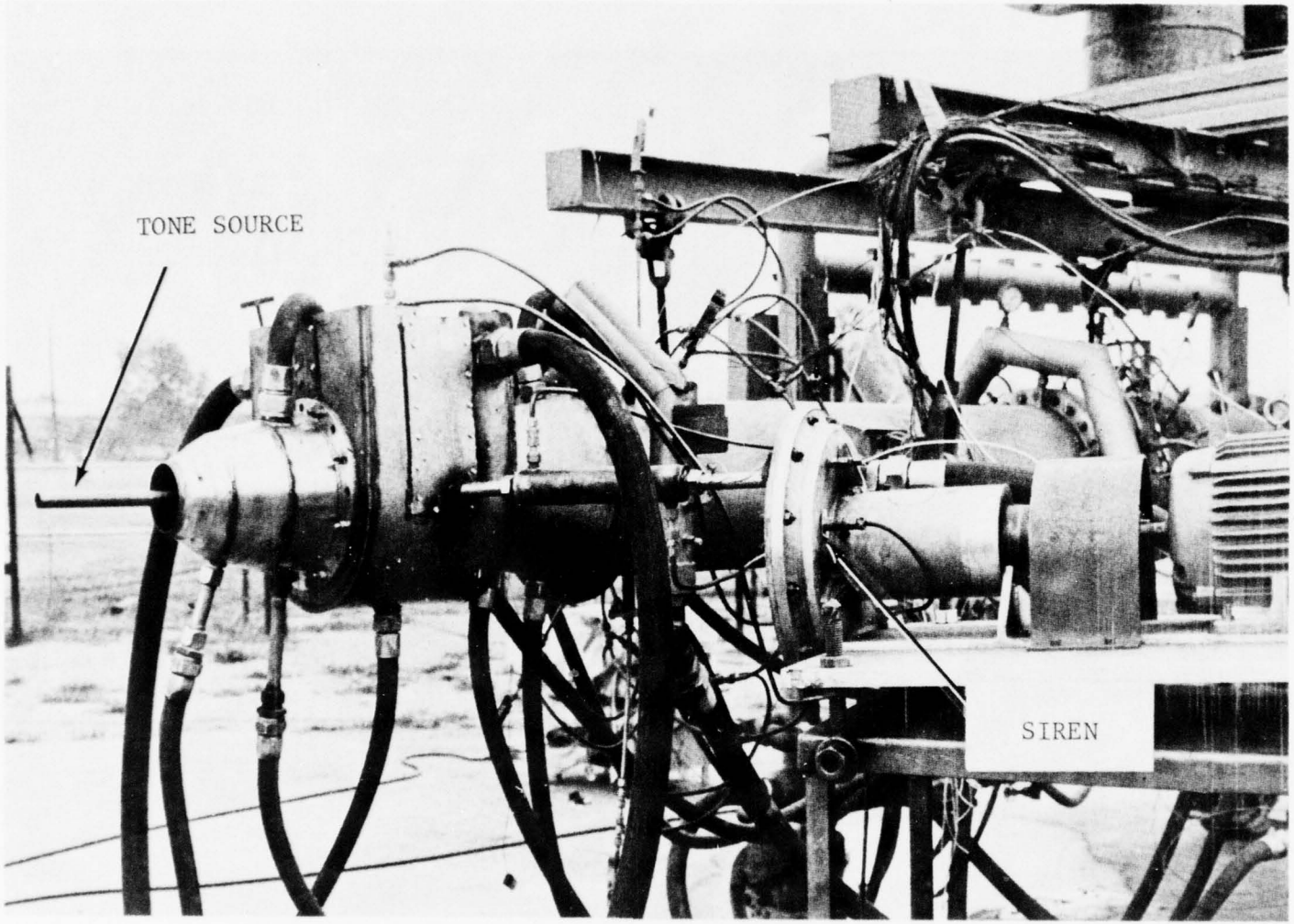


Figure 185. Refraction Experimental Setup with Siren Uncovered.

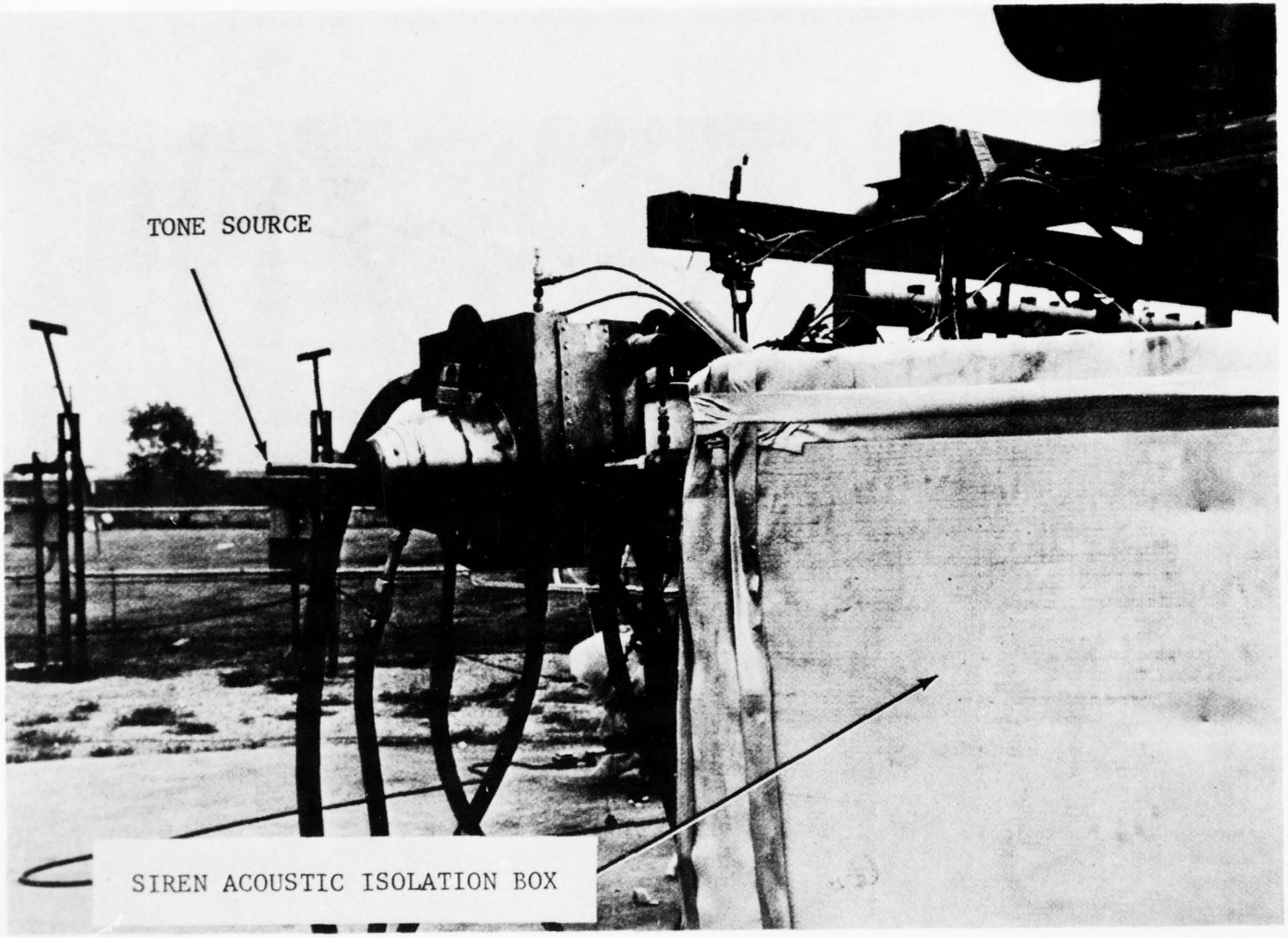


Figure 186. Refraction Experimental Setup with Siren Acoustically Isolated.

With these considerations, the frequency range was limited to 500-5000 Hz. The limitation on jet temperature primarily arose from the material limitation of the source output tube which, as seen from Figure 185, was located in the middle of the jet flow. Cooling of the tube inside the nozzle was considered and rejected due to the complexities involved and the increased blockage and obstruction that the larger tube would provide to the nozzle area. Combinations of pressure ratios and temperatures were chosen to obtain only subsonic jet Mach numbers to avoid complexities from shock waves.

The test matrix chosen, subject to these constraints, is shown in Table 3. The acoustic Mach number, defined by V_j/C_o, was varied between 0.5 and 1.5 with the total temperature variation ranging from ambient to 2000° R. At each one of the test conditions chosen, the tone source frequency was varied over a range of 520-4500 Hz, corresponding to Strouhal numbers (fD/V_j) of 0.11 to 2.9.

The test procedure consisted of first recording the siren output alone at the chosen frequencies. This was followed by letting the nozzle flow at one chosen condition, recording the jet-only noise, setting the siren at the different chosen frequencies (with the jet still on), and recording the microphone data each time. Specific microphones were chosen periodically to record on-line narrowband spectra on an X-Y plotter to check for consistency and validity of the data.

At the conclusion of the above tests, the tone source hardware was removed from the nozzle, and all the flow conditions were repeated with the "clean" nozzle. This was done to determine whether the jet noise characteristics of the clean nozzle were altered by the presence of the additional hardware in the jet stream.

2.5 DISCUSSION OF RESULTS

2.5.1 Influence of Tone Source Hardware on Jet Noise

One of the fundamental questions that needs to be answered in an experiment of this nature is the extent, if any, of contamination of the jet noise characteristics of the nozzle due to the insertion of the source hardware. Insertion of obstructions like struts, tootses, etc., into flows is known to generate tones characterized by a Strouhal number based on a strut dimension and sometimes also broadband noise (References 132-136). Such tones and broad-band noise will make interpretation of the influence of jet flow on the injected tone and of the injected tone on the jet flow difficult.

Figure 187 is a comparison of one-third octave band SPL data for jet noise with and without the tone source hardware in the nozzle, for a typical case of $Uj/C_o = 0.9$ at a jet total temperature of 540° R. It can be seen that the presence of the hardware had no significant effect on the jet noise. Similar results were noted at other test conditions also.

Table 3. Test Matrix.

U_j/C_o	U_j, fps	T_T', ° R			
		Ambient	1000	1500	2000
0.5	545	(✓)	---	---	---
0.7	790	✓	---	---	---
0.9	1012	(✓)	✓	✓	✓
1.3	1450	---	✓	✓	✓
1.5	1675	---	---	✓	✓

- Frequency Range 520 TO 4500 H_z
- $\frac{fD}{C_o}$ = 0.17 To 1.44
- $\frac{fD}{U_j}$ = 0.11 To 2.9

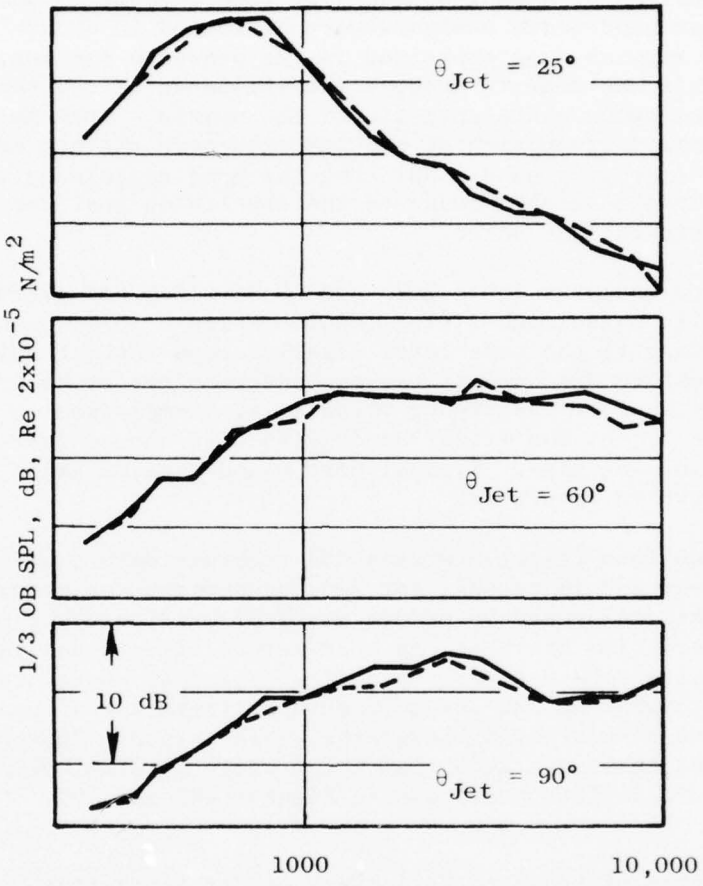


Figure 187. Jet Acoustics with and without the Tone Source Hardware in the Nozzle.

2.5.2 Methods of Data Reduction

During the testing, the output from all 12 microphones, from the oscillator driving the siren motor, and from the tachometer from the motor were simultaneously recorded on a Sangamo Sabre IV tape recorder. Both one-third-octave and narrower band-width analyses were performed in order to achieve different desired results. As explained in the previous section, one-third octave band analysis was done to measure the influence of the tone source hardware on the jet noise characteristic of the nozzle. Such an analysis also proved that the introduction of the injected tone did not amplify the jet noise in any 1/3-octave band other than the band containing the injected tone frequency. This basically leads to the conclusion that the tone did not amplify or alternate the jet noise.

The narrowband analysis (both 2 Hz and 10 Hz wide) was performed using a Federal Scientific ubiquitous filter (UAG). While a 10-Hz bandwidth analysis was adequate to identify the tone level clearly above the jet noise level for most of the test conditions, it was necessary to resort to a 2-Hz band-width analysis for some of the higher velocities. Comparison of the absolute levels of the tone by the two filter bandwidths also showed that the tone was generally less than 2-Hz wide. Typical narrowband data obtained by such procedures are shown in Figure 188.

The F.S. ubiquitous filter averages the recorded data over a period of 12 seconds for 10-Hz and 16 seconds for 2-Hz band-width analyses. Since any random fluctuations caused by sudden gusts of wind, etc., can cause errors in such short-time averages, another method of data analysis was used wherein the data recorded for the entire period of about 120 seconds were processed through 2-Hz and 10-Hz tracking filters and a log converter to obtain a continuous plot of SPL over the whole period. Judgement was used to obtain reasonable averages from these plots by eliminating random fluctuations. Typical plots are shown in Figures 189 and 190.

2.5.3 Influence of Velocity Variations on Jet Refraction

The influence of velocity, temperature, and frequency on the tone level could be studied independently, as can be seen from the test matrix shown in Table 3. The basic effect of the jet flow was to vary the tone level at some or all of the angles; hence, the change in tone level (defined by $\Delta SPL = SPL_{tone + jet} - SPL_{tone\ only}$) was used as the acoustic parameter to compare independently the influences of the various jet flow parameters.

The effect of varying the velocity at a jet total temperature of 540° R is shown in Figure 191 for a tone frequency of 783 Hz. The ΔSPL at all the microphone angles is shown for $M_o = Vj/C_o = 0.5$, 0.7, and 0.9. It can readily be seen that, at all the three velocities, there is an attenuation of the tone level at angles below 60° to the jet axis. Also, the data at $M_o = 0.5$ and 0.7 show a monotonic increase in attenuation as one approaches the jet axis, the magnitude of the attenuation also increasing with increasing velocity. Also shown for comparison on the same figure are data obtained by MacGregor, et al,

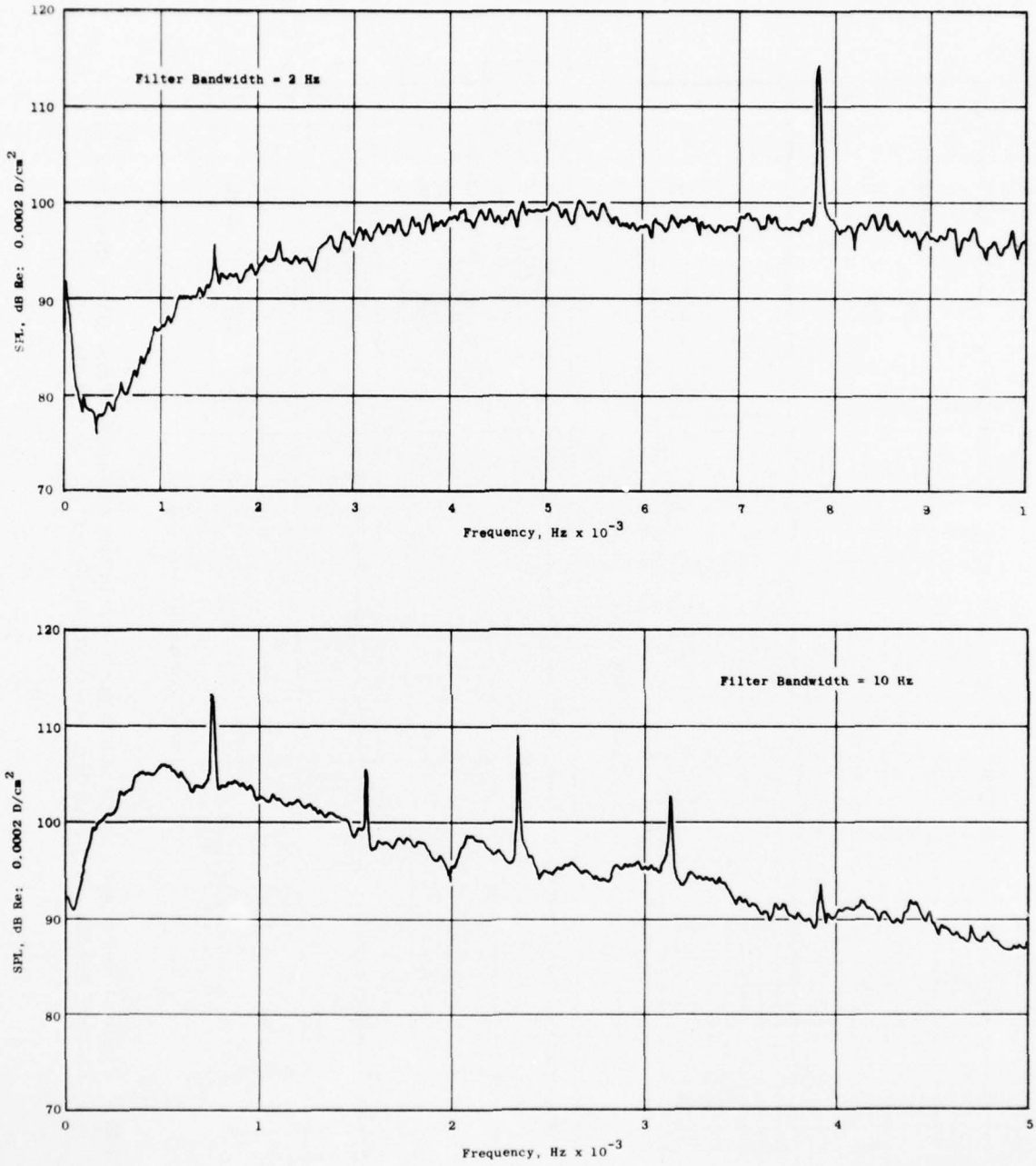


Figure 188. Typical 2-Hz and 10-Hz Bandwidth Data f_{tone} = 783 Hz, M_o = 1.3, $T_{T_{jet}}$ = 1500° R, and θ_{jet} = 20°.

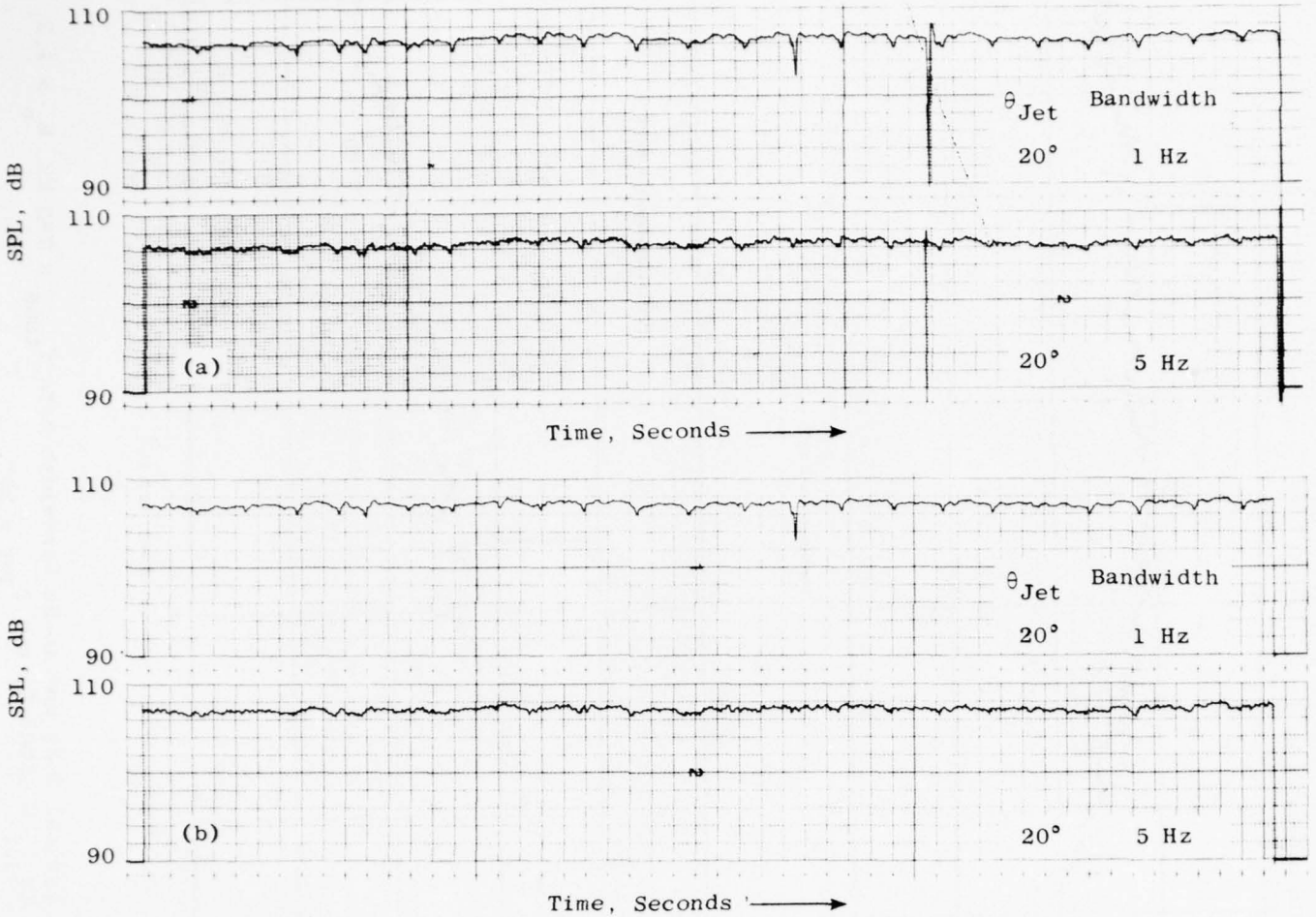


Figure 189. Typical 1-Hz and 5-Hz Bandwidth Analysis of Siren Tone Data Over the Entire Period of Recording (~ 120 secs), f_{tone} = 783 Hz, No Jet.

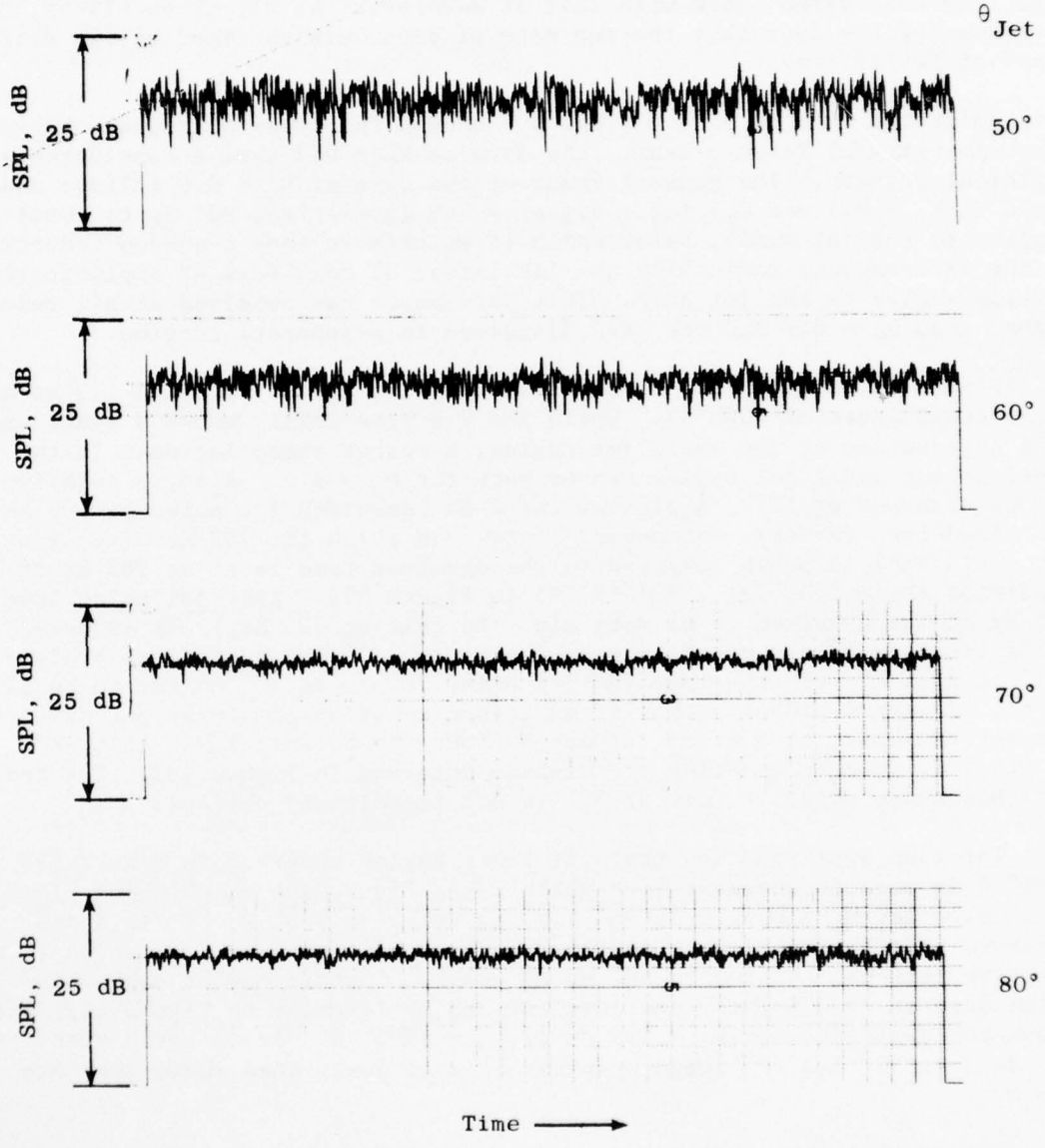


Figure 190. Typical 2-Hz Bandwidth Analysis of (Tone + Jet) Data Over the Entire Period of Recording (~ 120 Seconds), f_{tone} = 783 Hz, M_o = 0.9, $T_{T_{jet}}$ = 2000° R.

at M_o = 0.5 at a jet temperature of 540° R and a frequency of 4500 Hz. The data at this frequency are compared to the data at 783 Hz of the current work on the basis of a constant Strouhal number, $F/D_{Jet}/C_o$). The agreement of the data from the current work with that of MacGregor, et al, is excellent, notwithstanding the fact that the two sets of data were obtained at two different types of facilities.

While the data at M_o = 0.5 and 0.7 showed the types of trends observed by the University of Toronto team, the data at M_o = 0.9 show a considerably different pattern. The general trend of the data at M_o = 0.9 follows the trend at M_o = 0.5 and 0.7 (at a higher - ΔdB level) from 90° up to about 25° (angles to the jet axis), below which it appears to show a sudden reduction in the attenuation, indicating the likelihood of some form of amplification at shallow angles to the jet axis. This phenomenon was observed at all velocities higher than M_o = 0.7 and has been discussed in a separate section.

Figure 192 shows plots of ΔSPL vs. θ_{jet} for V_J/C_o = 0.9 and 1.3 at a jet total temperature of 1000° R. While the 0.9 case still shows a small amount of tone attenuation at the small jet angles, a rather steep increase in the tone level at the small jet angles can be seen for M_o = 1.3. Also, a negative peak can be observed at 50°. A plot of the 2-Hz bandwidth jet noise at 700 Hz (obtained from the same narrowband plots from which the 783-Hz siren tone level was extracted) is shown compared to the absolute tone level at 783 Hz at this condition (M_o = 1.3, $T_{T_{Jet}}$ = 1000° R) in Figure 193. (The jet noise level at 700 Hz can be expected to be very close to that at 783 Hz.) It is noted that, while the tone levels at all the angles except 50° are considerably higher than the jet noise level, the tone and jet noise levels at 50° appear to be almost equal. It seems probable that if an autocorrelation should be performed to extract the exact tone level, it may be found to be even lower than it is plotted, thereby lowering the minimum observed in Figure 193. The reason for this sharp negative peak at 50° is not immediately obvious.

The tone amplification trend at lower angles observed in Figure 192 at 1000° R is seen to increase with velocity in Figure 194 which shows plots of ΔSPL vs. Θ for M_o = 0.9, 1.3, and 1.5, at $T_{T_{jet}}$ = 1500° R. It is again observed that there exists a negative peak at 50° for M_o = 1.3, while this negative peak has shifted to 60° at M_o = 1.5. Comparisons of narrowband jet noise data at 700 Hz with tone level at 783 Hz (similar to Figure 193) are shown in Figure 195 for M_o = 1.5 at $T_{T_{jet}}$ = 1500° R. It is again seen that the data at 50° and 60° could possibly be even lower than where they are shown.

Figure 196 shows ΔSPL vs. θ_{jet} for M_o = 0.9, 1.3, and 1.5 at $T_{T_{jet}}$ = 2000° R where once again, the tone amplification is seen to increase with velocity.

It thus can be prostulated that, while the stationary injected source appears to be subjected only to refractive effects at low velocities (below and up to M_o = 0.7), some form of convective type of amplification becomes evident at velocities corresponding to M_o = 0.9 and above. The slug flow model (Chapter I, Section 1.0) of Mani was adapted in an attempt to describe this phenomenon and is discussed in detail in Section 2.6.

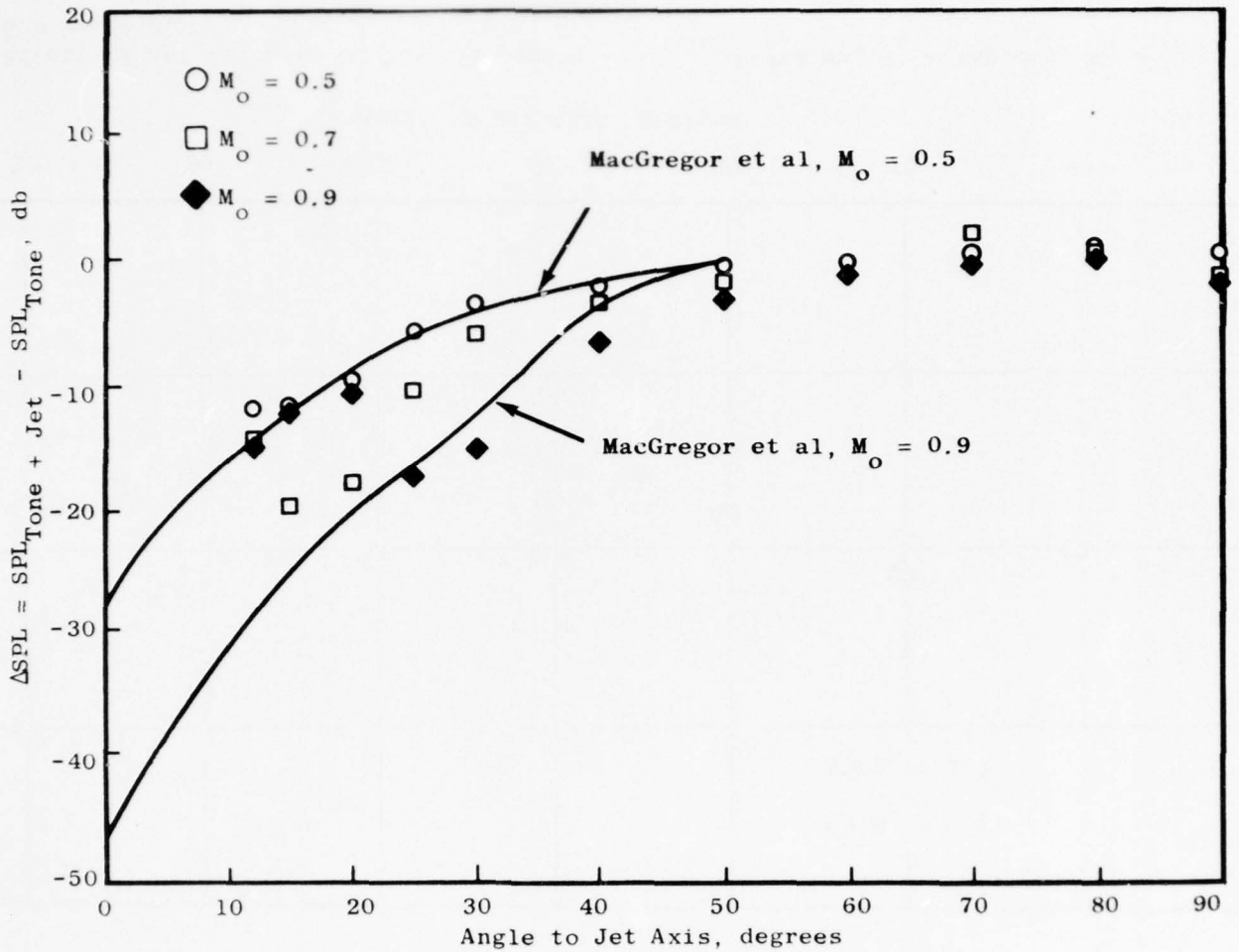


Figure 191. Effect of Jet Velocity on Tone Directivity, f_{tone} = 783 Hz, T_o = Ambient, M_o = 0.5, 0.7, 0.9.

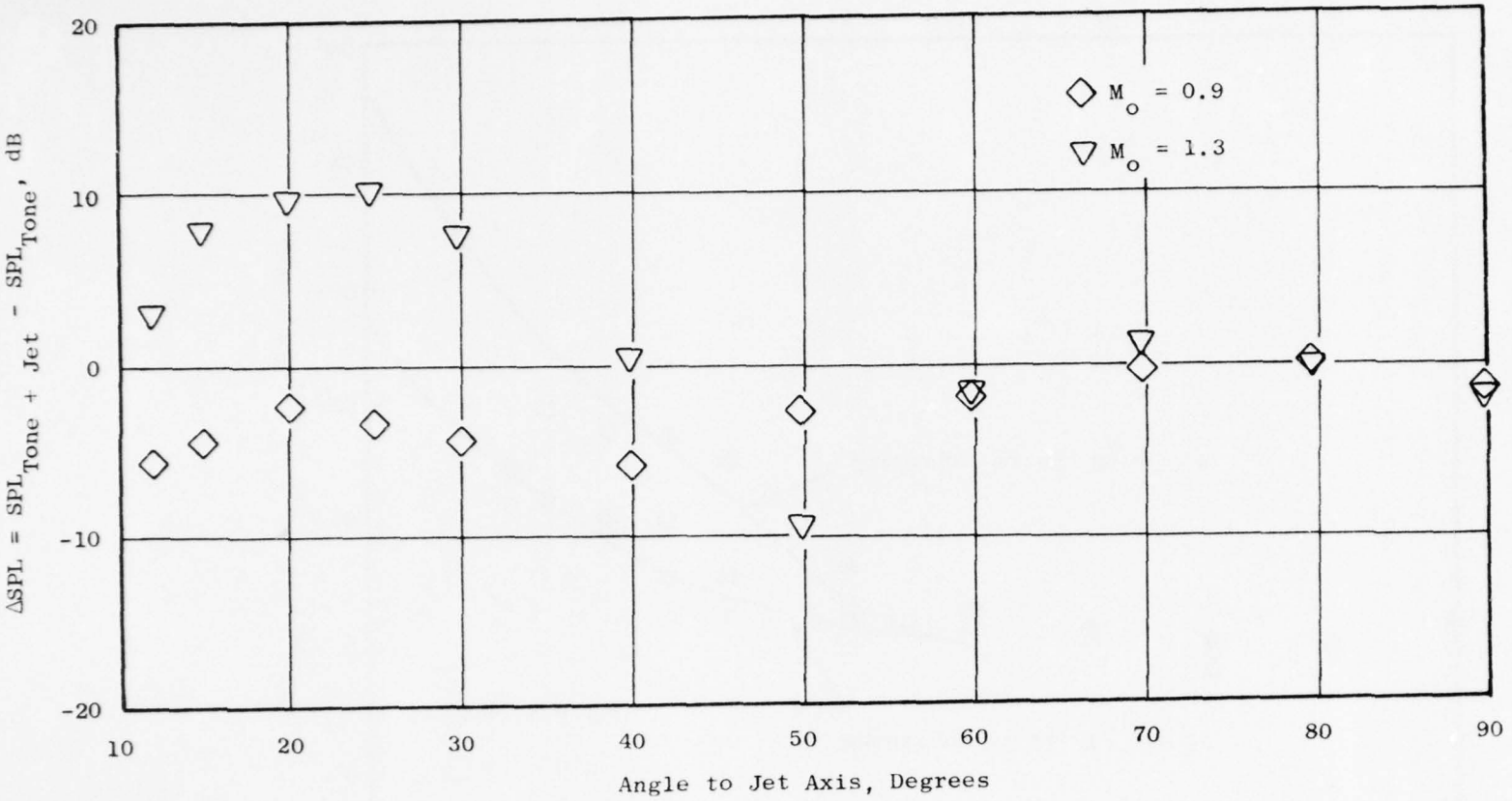


Figure 192. Effect of Jet Velocity on Tone Directivity, f_{tone} = 783 Hz, T_o = Ambient, M_o = 0.9 and 1.3.

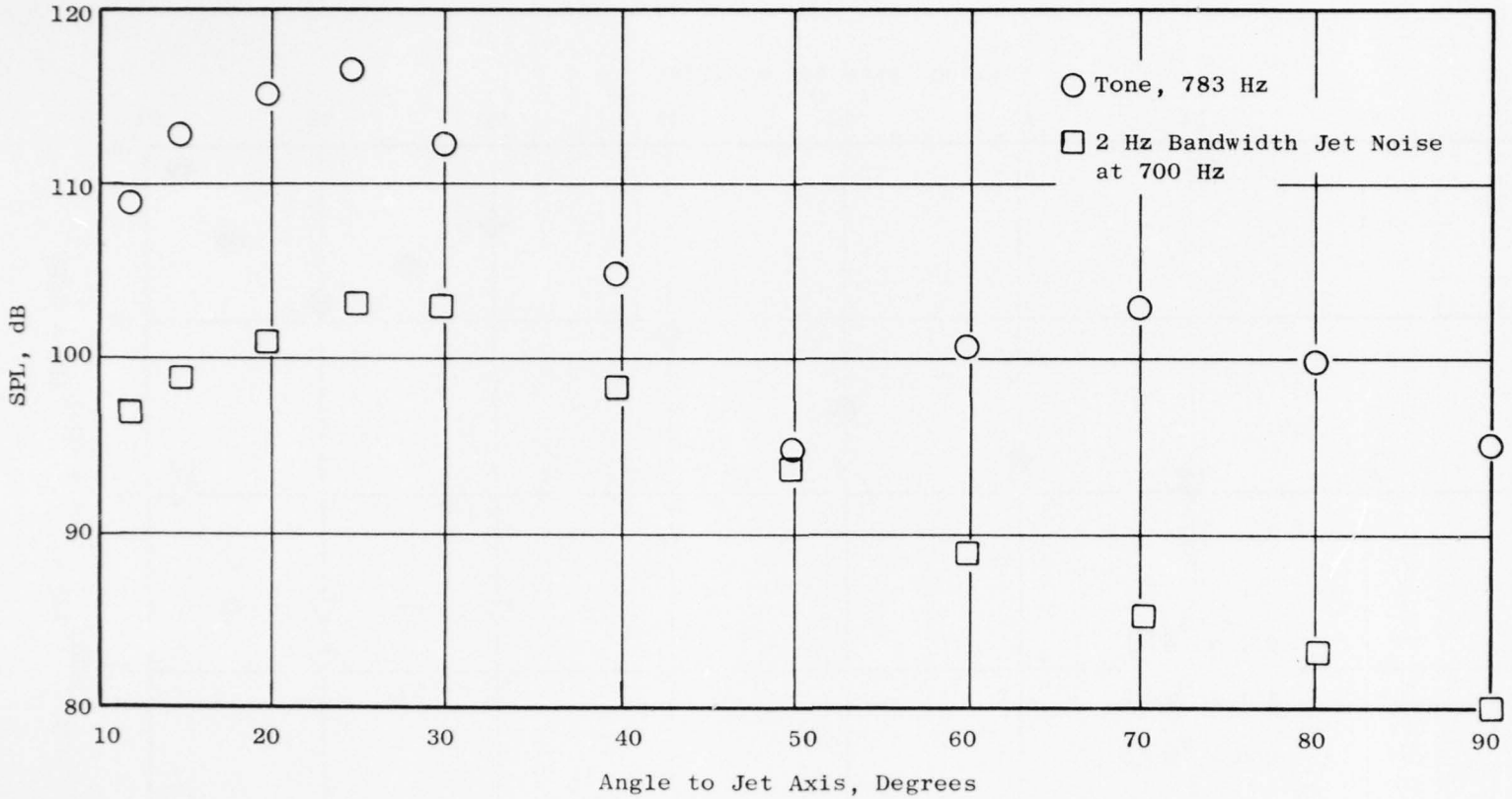


Figure 193. Comparison of 2-Hz Narrowband Jet Noise Directivity with Siren Tone Directivity, $M_o = 1.3$, $T_{T_{jet}} = 1000°$ R.

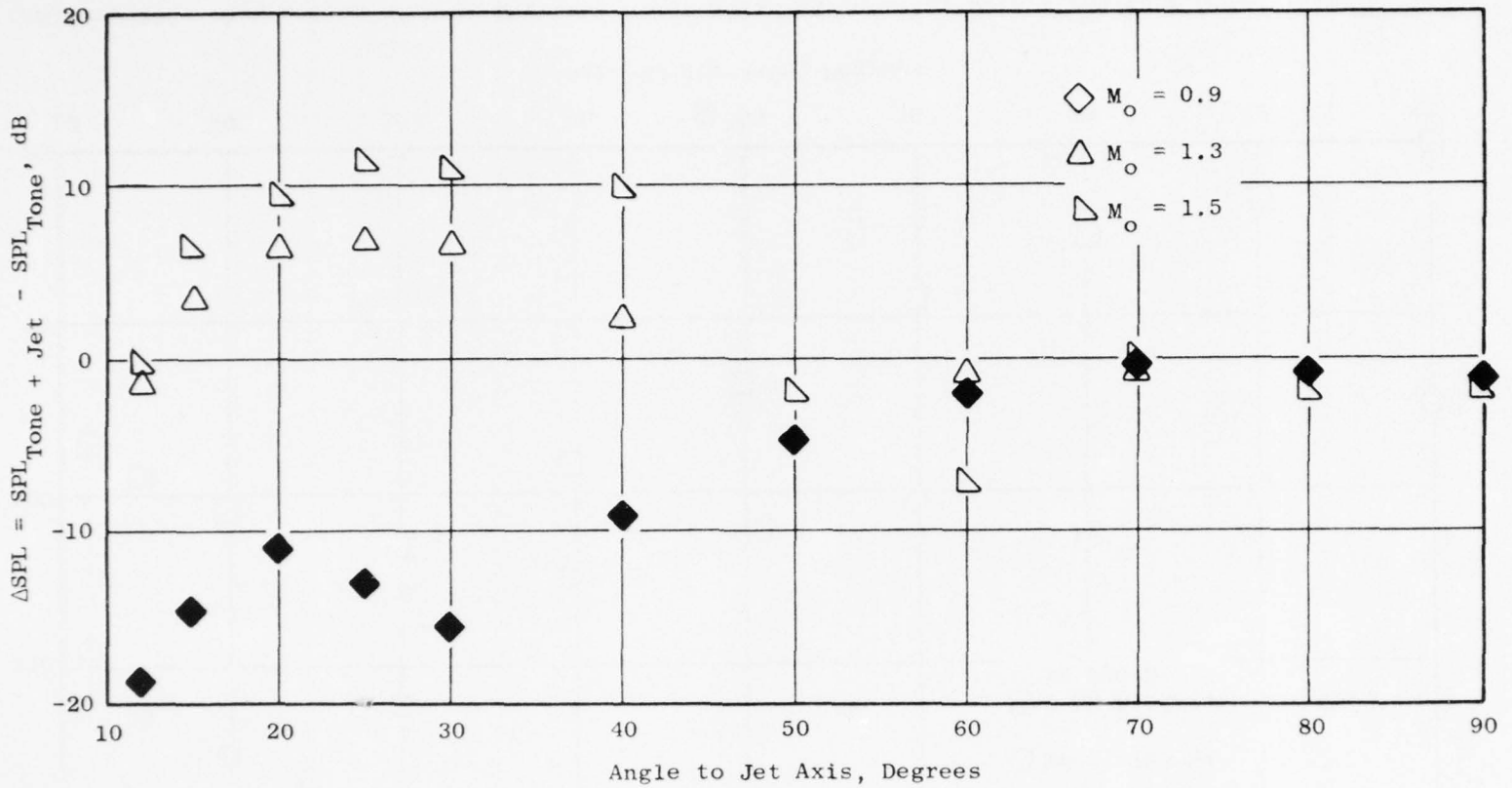


Figure 194. Effect of Jet Velocity on Tone Directivity, M_o = 0.9, 1.3, 1.5, $T_{T_{jet}}$ = 1500° R.

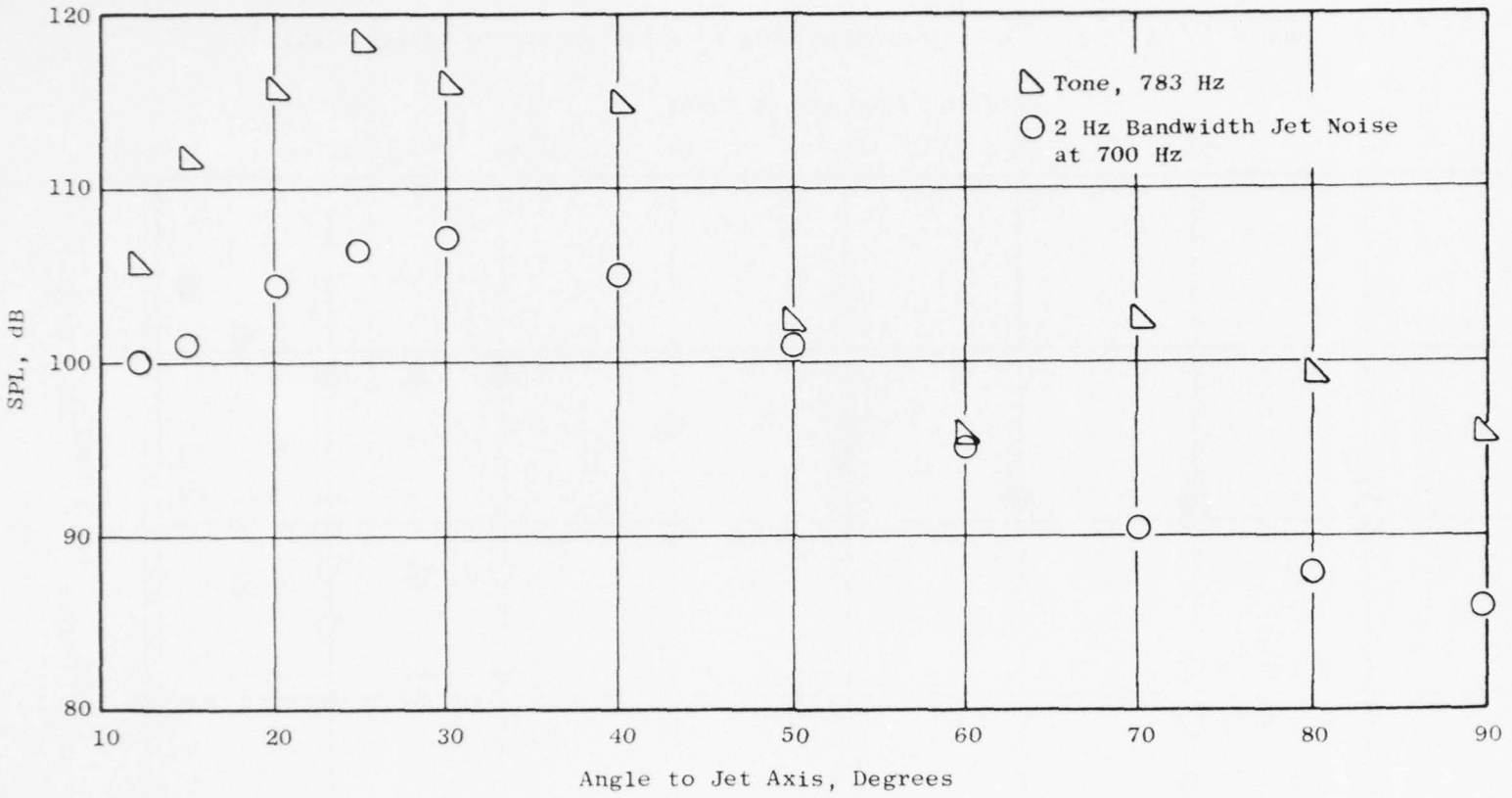


Figure 195. Comparison of 2-Hz Narrowband Jet Noise Directivity with Siren Tone Directivity, M_o = 1.5, $T_{T_{jet}}$ = 1500° R.

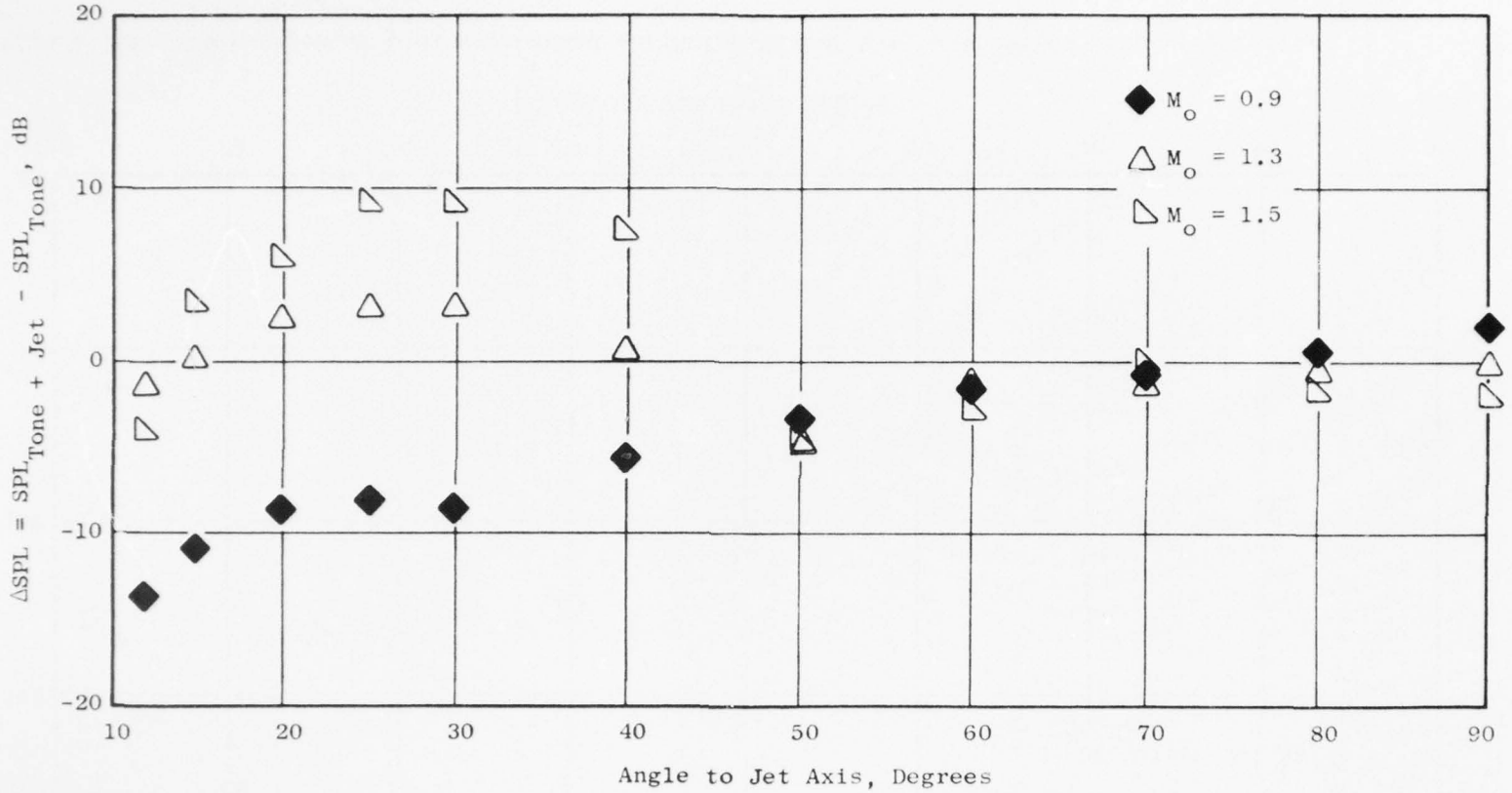
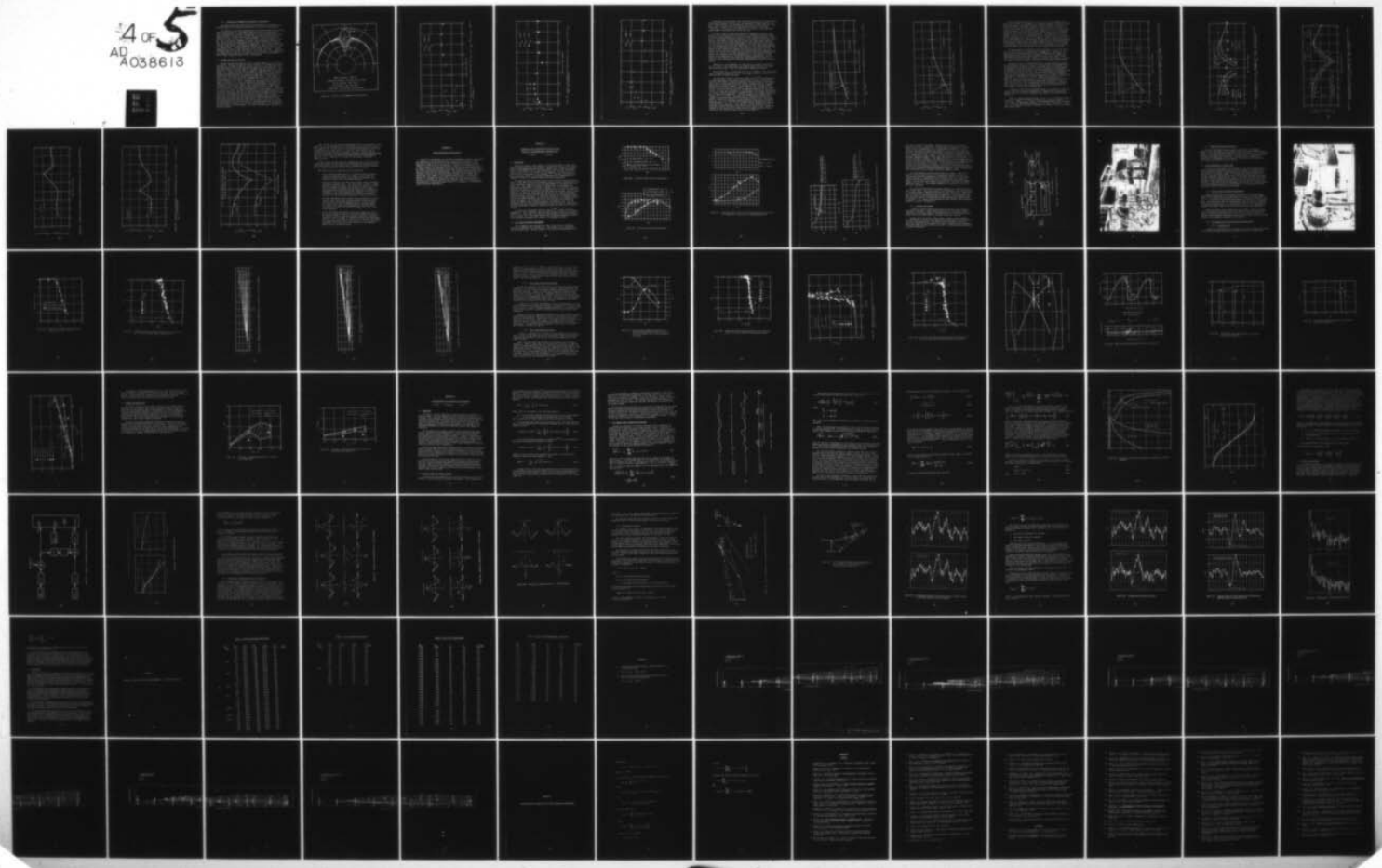
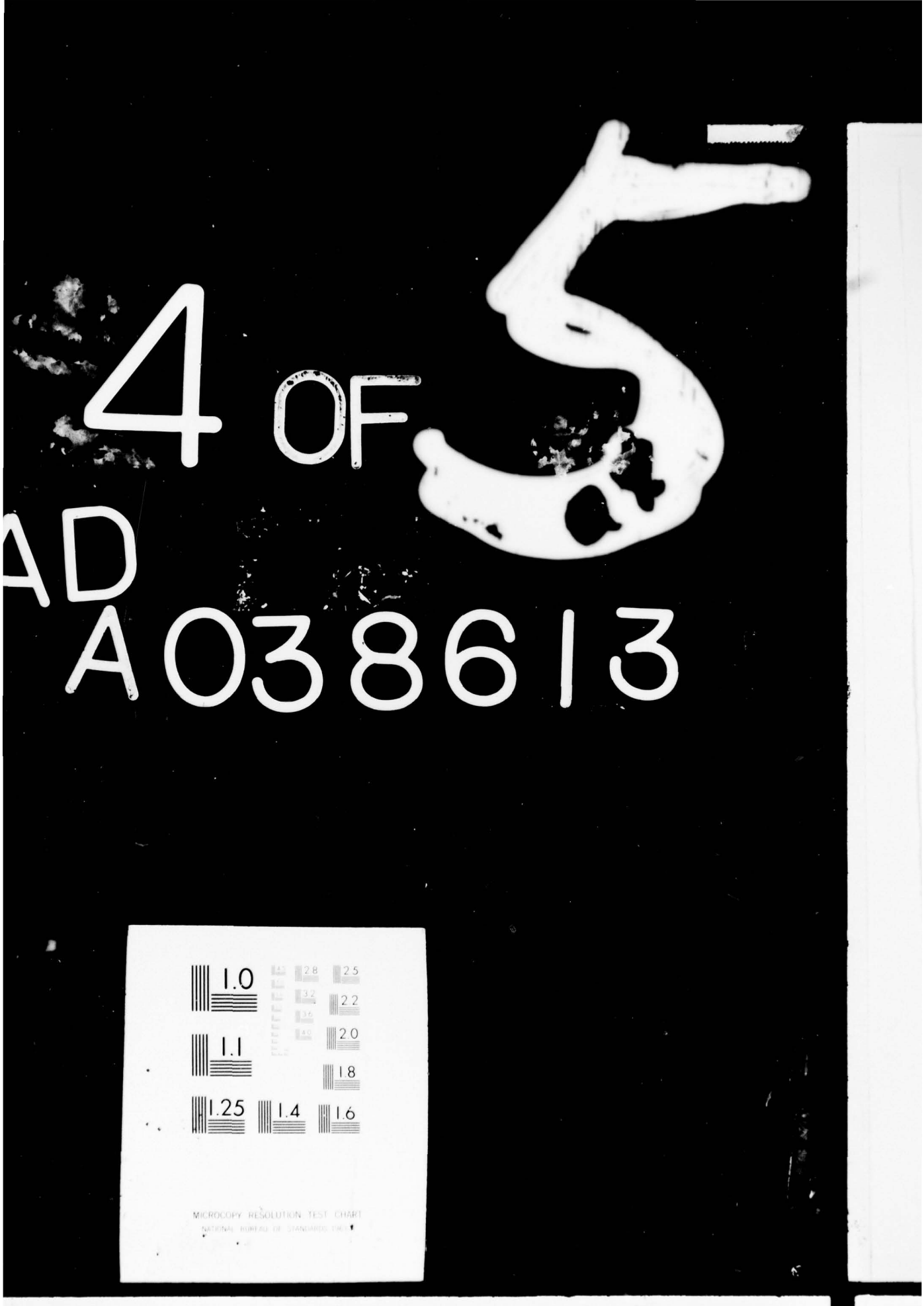


Figure 196. Effect of Jet Velocity on Tone Directivity, M_o = 1.5, $T_{T_{jet}}$ = 2000° R.

AD-A038 613 GENERAL ELECTRIC CO CINCINNATI OHIO AIRCRAFT ENGINE GROUP F/G 20/1
SUPERSONIC JET EXHAUST NOISE INVESTIGATION. VOLUME II. TECHNICA--ETC(U)
JUL 76 P R KNOTT, R MANI, C L MERKLE F33615-73-C-2031
UNCLASSIFIED R74AEG452-VOL-2 AFAPL-TR-76-68-VOL-2 NL

4 OF 5
AD A038613




4 OF 5
AD
A038613
1.0
1.1
1.25
1.4
1.6
2.8
2.5
3.2
2.2
3.6
2.0
4.0
1.8
MICROCOPY RESOLUTION TEST CHART
NATIONAL BUREAU OF STANDARDS 1963-A

2.5.4 Influence of Temperature Variations on Refraction

Classical studies have indicated that the influence of increasing temperature would be to increase the refractive dip at the lower jet angles.

This effect was confirmed experimentally by Grande as shown in Figure 197, taken from Reference 13. The dramatic amplification at shallow angles at -356° F emphasized the influence of temperature on jet noise directivity. In order to examine this at higher temperatures, the data obtained at different temperatures at a constant velocity were compared. Figure 198 shows the ΔSPL vs. θ at $M_o = 0.9$ at $T_{T_{jet}} = 1000°$ and 1500° R at tone frequency of 783 Hz. While the apparent tendency to deviate from the monotonic increase of ΔSPL (as the jet axis is approached) is still seen, it also can be noticed that the refractive dip increases with temperature. This is more readily seen in Figures 199 and 200 where temperature effects are plotted at $M_o = 1.3$ and 1.5, respectively. At both velocities, the difference in ΔSPL at different temperatures is seen to scale according to the 20 log ρ_j/ρ_o law. Comparison of Figures 198, 199, and 200 shows that, to a certain extent, the shallow angle tone amplification trend due to higher velocities and the close attenuation due to higher temperature appear to act concurrently.

2.6 FURTHER ANALYSIS OF THE DATA

We first discuss the question of how a speaker immersed in a jet flow may be modelled. The key question here (since interest is in comparing the SPL's with and without flow) is what the speaker puts out or, more precisely, what near-field quantity remains changed or unchanged with and without flow. One possibility would be to argue that the speaker's immediate ambient is a static region (i.e., there is no flow in the immediate neighborhood of the speaker) and that the speaker physically displaces a small spherical surface in this neighborhood back and forth at a given rate regardless of whether there is flow or not. This would be called a displacement source. Such a model was found reasonable at low velocities by Ingard, et al, in their studies with injected sources on duct walls. Secondly, we can assume that no such static region is produced (i.e., that the immediate neighborhood of the speaker is essentially a uniform flow region), but a given fluctuating volumetric flux is produced by the speaker across a small spherical control surface drawn around the speaker. This model could be called a velocity source. Ingard, et al, found such a model to be more representative of what happens in the cases of higher velocities. Thirdly, we could be assured the same situation as the second case but assume that what is specified to be unchanged with and without flow is the fluctuating mass flux across the spherical control surface. Variations four, five, six, and seven involve similar assumptions about the near-field fluctuating pressures remaining the same with and without flow. Two possibilities are that either they are the same or they vary as (P_j/P_o). Two more possibilities refer to where this fluctuating pressure is specified. One possibility is directly fore and aft, while the other is in the sense of an area average around the speaker. All these variations may be described as pressure sources.

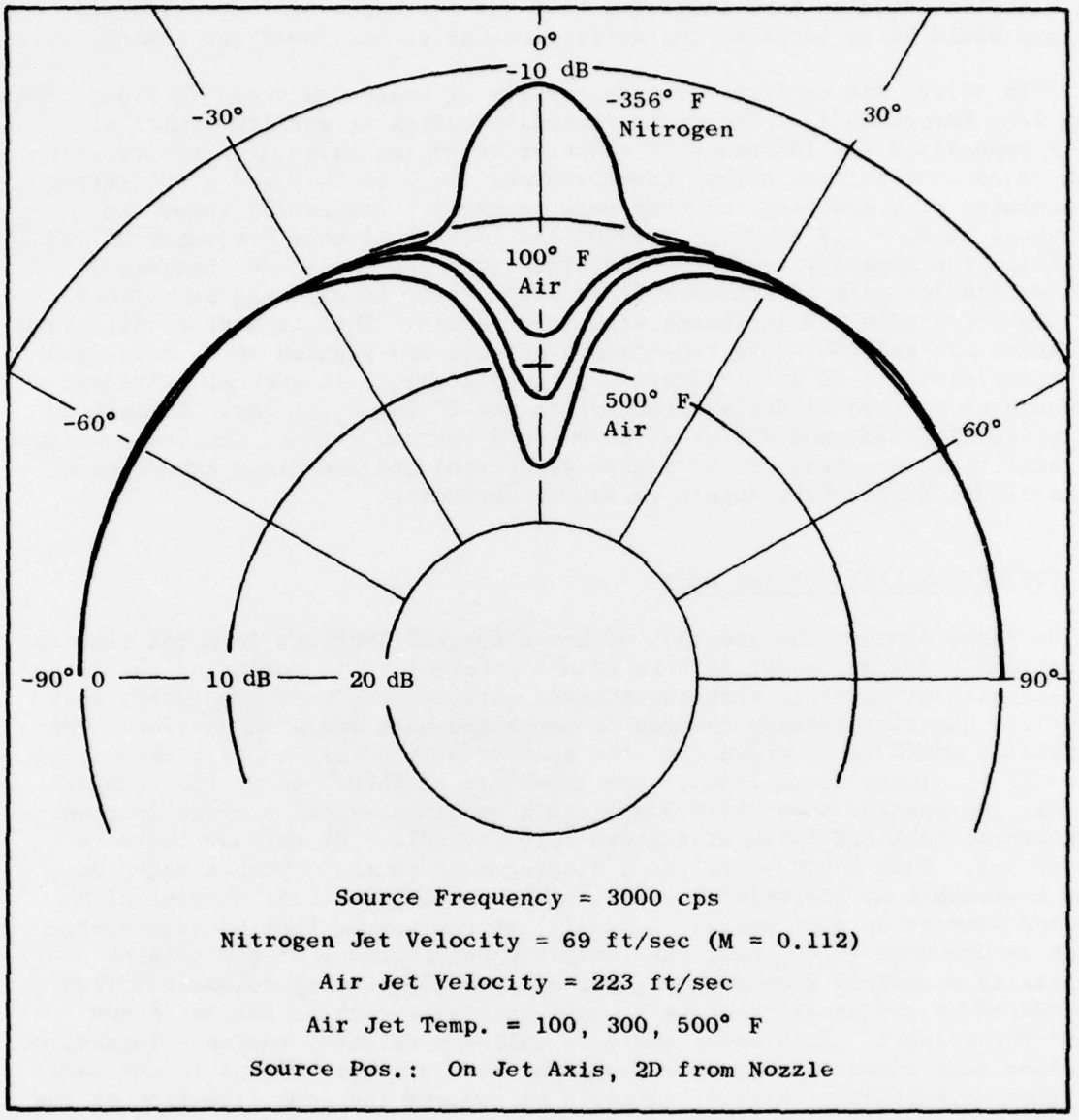


Figure 197. Effect of Jet Temperature on Directivity.

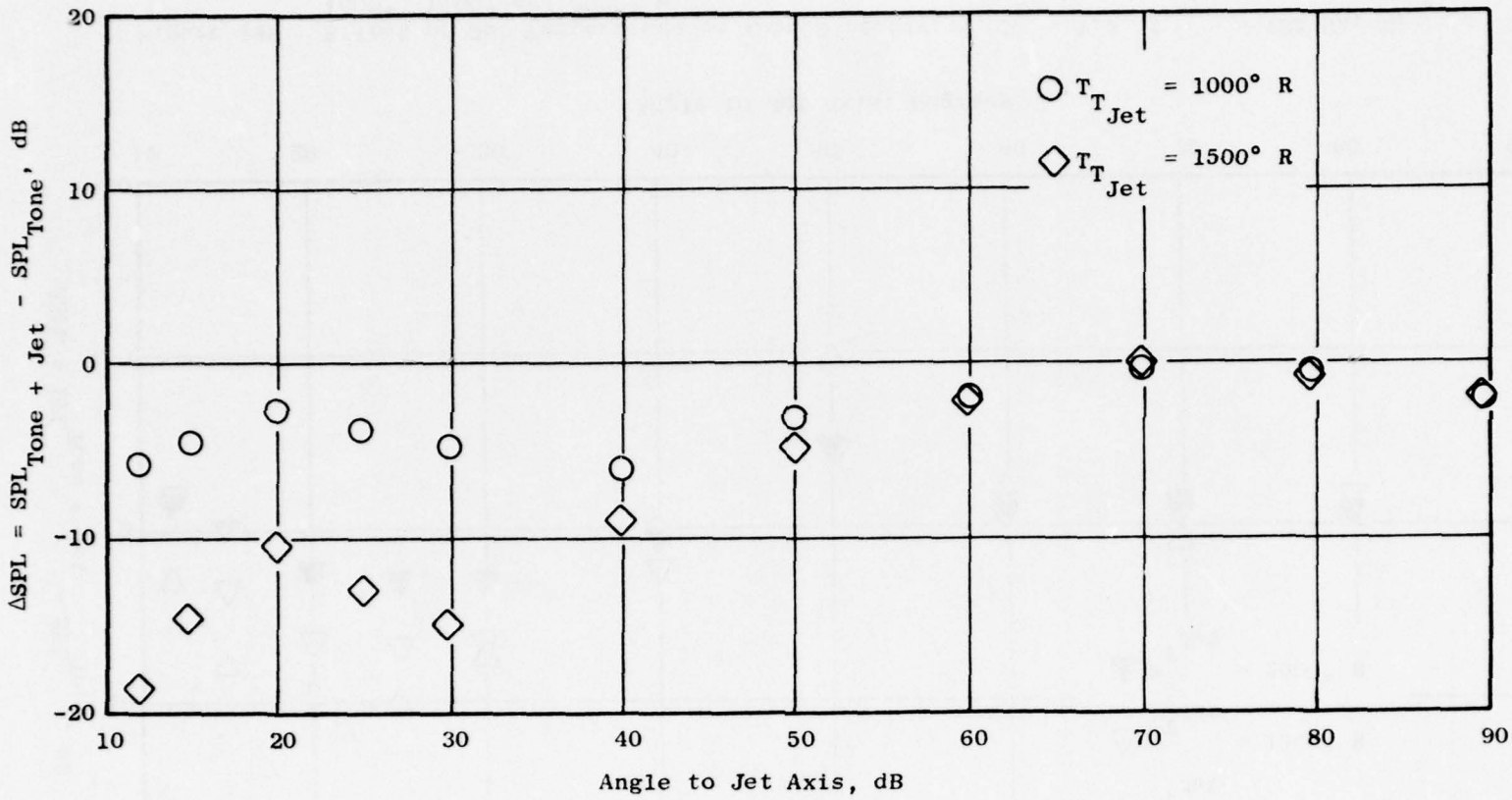


Figure 198. Effect of Jet Temperature on Tone Directivity, $M_o = 0.9$, $f_{tone} = 783$ Hz, $T_{T_{jet}} = 1000°$ R and 1500° R.

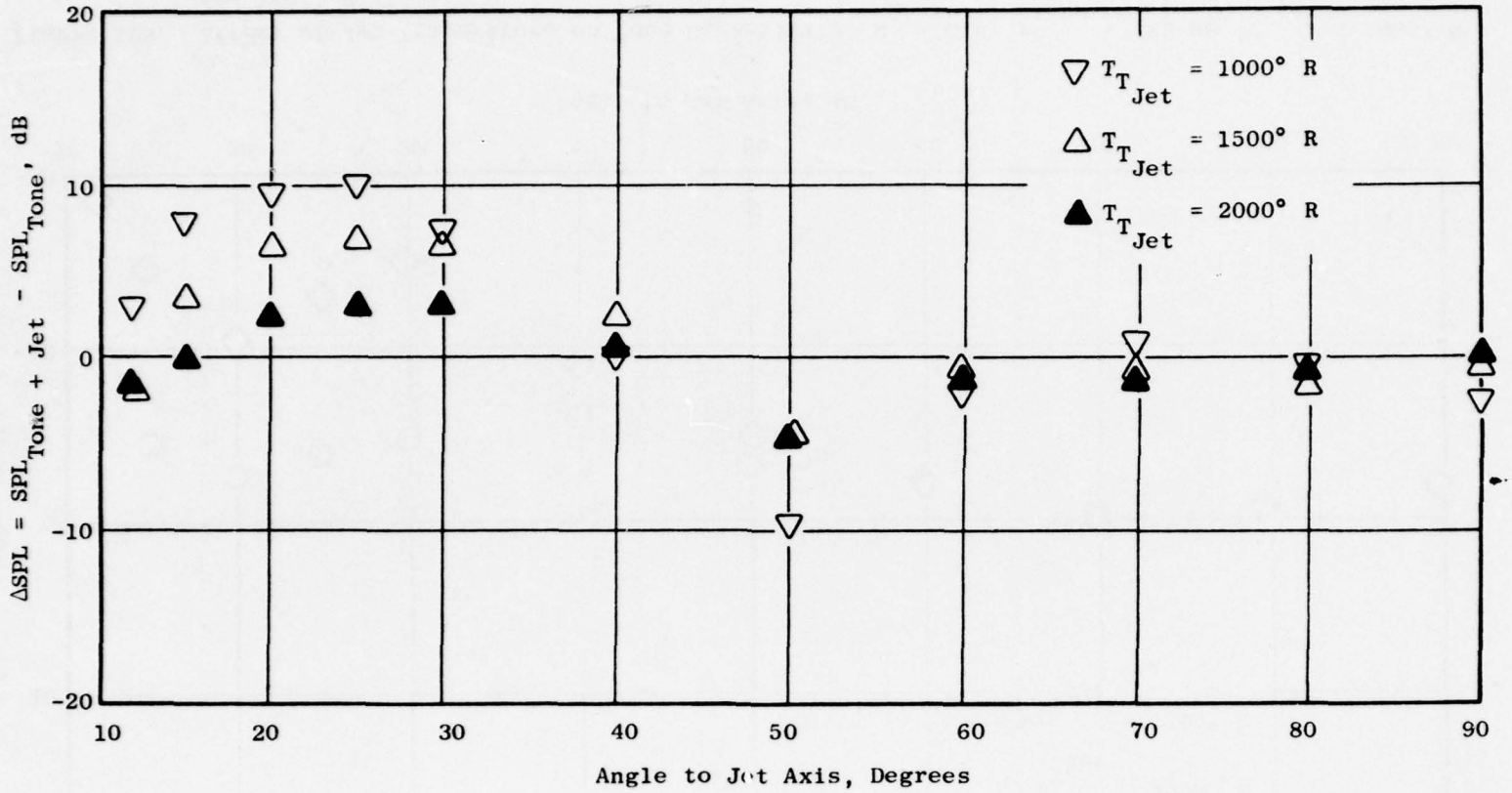


Figure 199. Effect of Jet Temperature on Tone Directivity, M_o = 1.3, f_{tone} = 783 Hz, $T_{T_{jet}}$ = 1000°, 1500° and 2000° R.

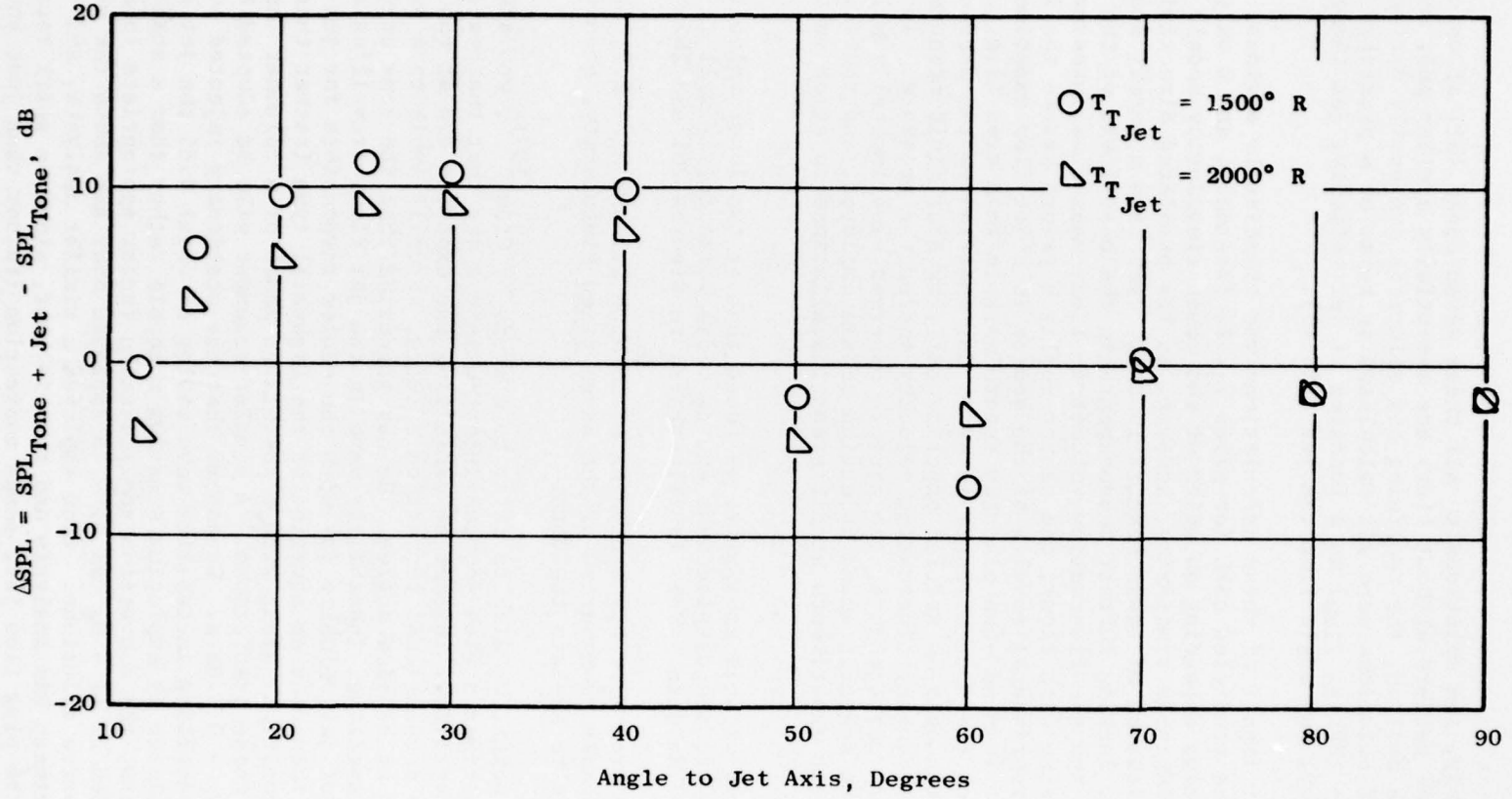


Figure 200. Effect of Jet Temperature on Tone Directivity, M_o = 1.5, f_{tone} = 783 Hz, $T_{T_{jet}}$ = 1500° and 2000° R.

Fortunately, the solutions to all these seven cases (all of which yield an omnidirectional pattern without flow) are essentially similar and, once any one of them is derived, the remaining six solutions are easily derived. These seven types of solutions were all calculated in terms of a predicted Δ [$(SPL)_{flow}$ - $(SPL)_{no\ flow}$] as a function of jet velocity, jet temperature, sound frequency, and angle from the jet axis (θ).

One major impact of these calculations was immediately obvious. The answers for the predicted ΔSPL for given V_j, T_j frequency, and θ vary widely in absolute value depending on which of the seven singularity models is used. There is considerable similarity, however, in the predicted directivity indices. The main implication of these results is that, even from a purely acoustic point of view, lacking further measurements in the near-field of the source (to determine how the fluctuating volumetric flux, mass flux, pressure levels, etc. are changing with flow), one cannot really a priori assess the impact of flow on the experimental results of the source in a jet flow experiment. This should be kept in mind when planning future work in this area (i.e., the question of how the source itself is or is not modified by the presence of the flow). This can only be settled experimentally by near-field measurements of the discrete frequency fluctuating velocity and/or the pressure. In the absence of such measurements, the answers observed experimentally will be a function of the specific sound injection scheme employed, and there is no reason to expect experiments at different installations to agree on the final answers.

Regardless of this ambiguity, we found that at two lower velocities of M_o = 0.5 and 0.7, the displacement source model works fairly well in correlating the 783 Hz data. This is illustrated in Figures 201 and 202.

Starting from M_o = 0.9 and going on to M_o = 1.3 and M_o = 1.5, it was found that no reasonable combination of the seven <u>fixed</u> singularity, acoustic solutions was able to explain the data.

At this point, we wish to refer to a study by Crow[137], who also found in source experiments with sources injected into a jet that the resulting far-field directivity, instead of exhibiting the expected dip at the shallow angles due to conventional refraction effects, actually exhibits a bulge or amplification at shallow angles. He has suggested that the tone actually triggers a travelling, instability wave in the jet flow, travelling at about 0.65 or 0.80 of jet velocity (as with the eddies responsible for jet noise itself). He then used an equation of the Lighthill type (rather than Phillips' or Lilley's equation) along with a postulated model of a columnar instability wave to make noise predictions. A similar argument will be adopted here to explain the M_o = 0.9 data. We assume that the stationary injected tone triggers a travelling instability wave moving at about 0.65 the jet speed, which is simulated by employing a moving monopole rather than a stationary monopole. Thus, the convection amplification factor appropriate to distributed monopoles of $(1 - M_c \cos \theta)^{-3}$ is employed over and above the previous stationary source solutions. Crow employed a similar analysis, and the difference between his analysis and ours is that, since we still retain the presence of the plug flow jet, sound convection (rather than just source convection) and refraction effects are still accounted for.

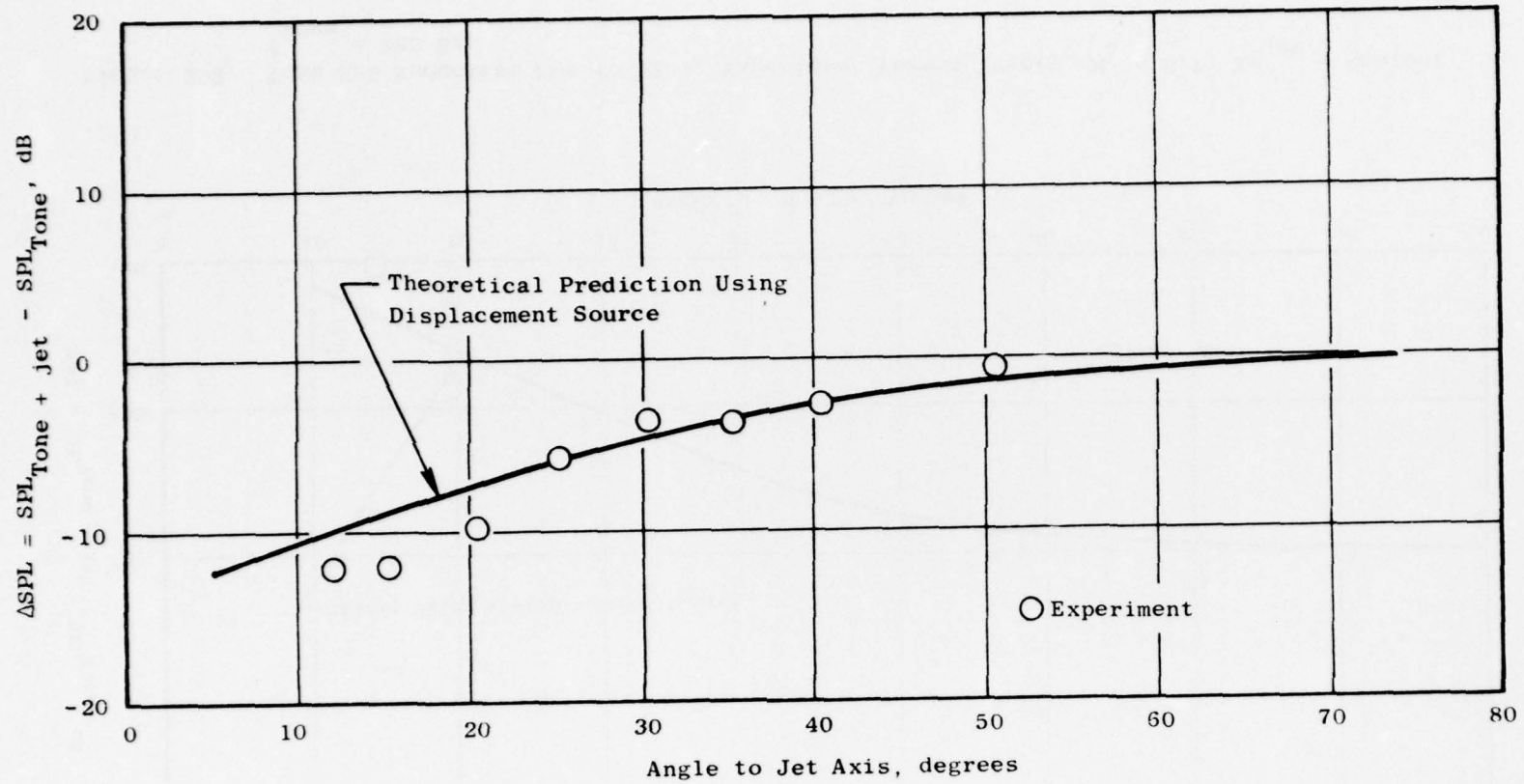


Figure 201. Tone SPL Reduction Due to Flow, Experiment Versus Theory, $M_o = 0.5$, $T_{T_{jet}}$ = Ambient, $f_{tone} = 783$ Hz.

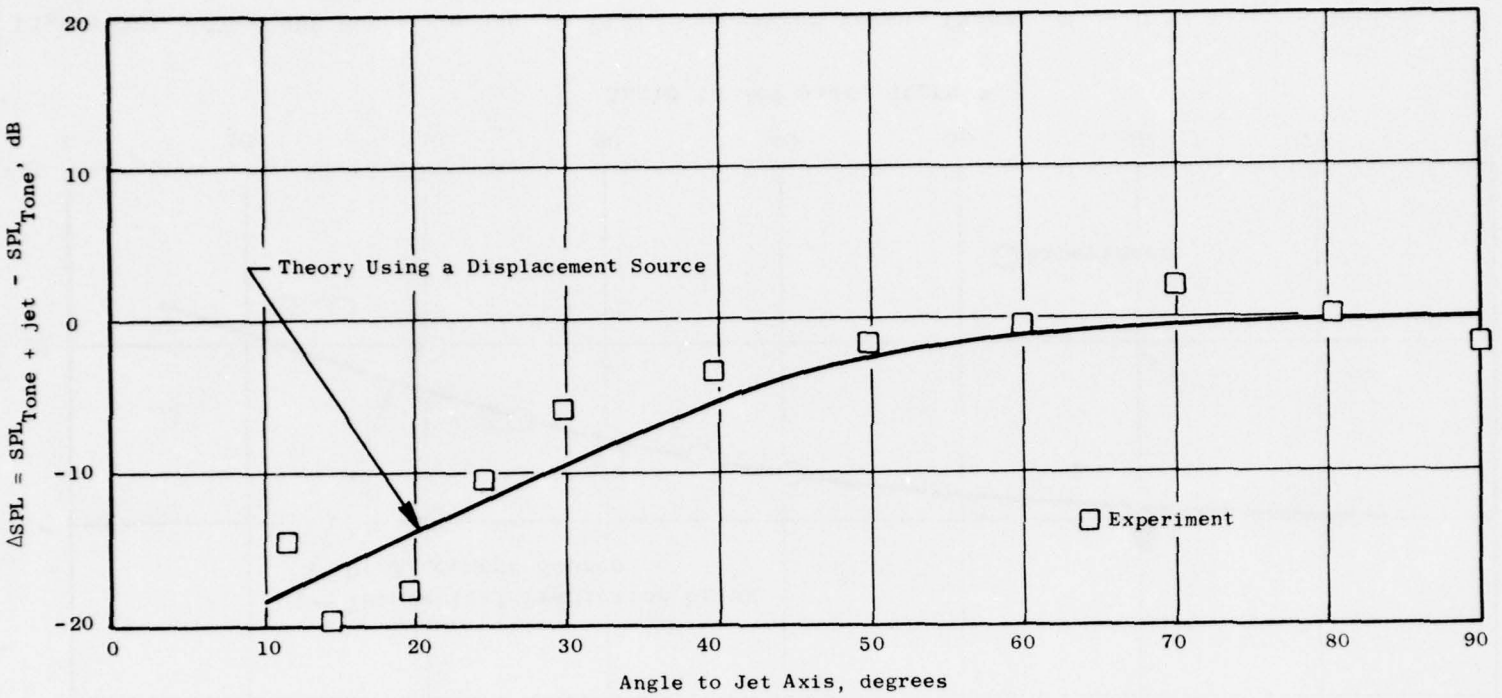


Figure 202. Tone SPL Reduction Due to Flow, Experiment Versus Theory, M_o = 0.7, $T_{T_{jet}}$ = Ambient, f_{tone} = 783 Hz.

Using this additional factor of $(1 - M_c \cos\theta)^{-3}$, which admittedly is a purely ad hoc factor to accommodate the mechanism suggested by Crow, but otherwise still using a displacement source, reasonable success is obtained in correlating the $M_o = 0.9$ data, though the wiggle in the data between $\theta = 12°$ to 25° is not predicted (see Figure 203). Going on to $M_o = 1.3$ (Figure 204), the data between $\theta = 10°$ and 50° and again between 75° to 90° are reasonably predicted. One conspicuous discrepancy is that a second peak is predicted between $\theta = 50°$ to 70° which was not measured. This peak is due to purely acoustic effects [i.e., is present even in the stationary source calculations without including the $(1 - M_c \cos\theta)^{-3}$ factor]. Crow, in fact, does report such a second peak in his data at about 80°, though it is much less pronounced relative to the major peak at the shallow angles than the current prediction would indicate. Since this is a purely acoustic effect due to the presence of the jet flow, Crow's analysis itself, which uses Lighthill's equation and therefore neglects jet flow effects, fails to predict this second peak.

Two other features of Figure 204 are worth noting. Both in the case of $M_o = 1.3$ and of $M_o = 1.5$ in accord with the suggestion of Ingard, et al, a velocity source model works better than a displacement source model. An additional feature is that, once M_o exceeds 1, the theory for stationary displacement or velocity sources predicts a null at $\cos^{-1}(1/M_o)$. For M $M_o = 1.3$, this works out to 40°. There is a tendency for the data to exhibit a minimum at about 50° though a very deep null is certainly not observed.

Going onto the $M_o = 1.5$ data (Figure 205), another observation made by Crow is needed to correlate the data. Crow points out that the speed of the instability waves triggered by the source appears not to rise continuously in proportion to the jet velocity but tends to saturate at a fixed value beyond which it does not increase. For this fixed value, Crow suggests using C_o, but we found that the $M_o = 1.5$ data are best explained by assuming a value of $0.845\ C_o$ which is actually $(0.65) \times (1.3)$. With this assumption, some measure of agreement is certainly achieved with the data at least in the range $10° \leq \theta \leq 50°$ and $80° \leq \theta \leq 90°$. Again, as with the $M_o = 1.3$ data, the second predicted peak at $\theta = 70$ is not observed though we wish to reiterate that Crow's data do show a second peak at about 80°. Again, a null at $\cos^{-1}(1/1.5) \sim 50°$ is predicted. At this location in the experiments, the tone levels were buried in the jet noise as indicated by the encirclement of those points in Figure 205.

In Figures 206 and 207 the predicted change in the quantity $\Delta\ (SPL)_{flow} - (SPL)_{no\ flow}$ due to change of temperature is compared with the measured change. The prediction does reasonably well except in the angular sector 50° to 70°.

Finally in Figure 208 we show that, for $M_o = 1.5$, the predicted change in raising the frequency from 783 Hz to 3000 Hz is to drop the quantity $\Delta\ (SPL)_{flow} - (SPL)_{no\ flow}$ by about 25 dB at shallow angles to about 5 dB at 90°. This is in qualitative agreement with the data of MacGregor, et al[14] (at $M_o = 0.9$ and due to change of frequency by a factor of 1.5), but disagrees with current data.

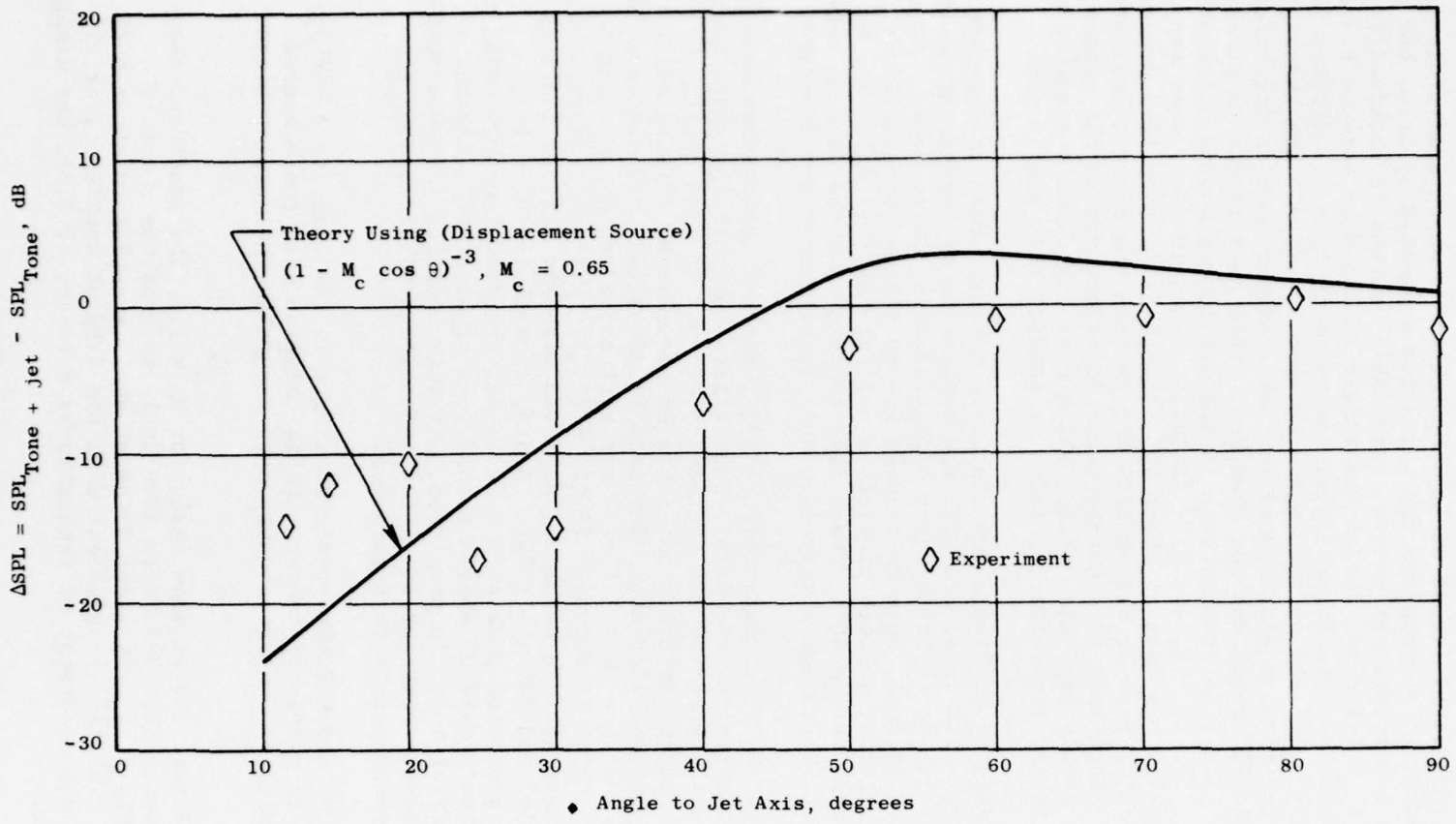


Figure 203. Tone SPL Reduction Due to Flow, Experiment Versus Theory, Including Convection Amplification Factor, $M_o = 0.9$, T_T = Ambient, $f_{tone} = 783$ Hz.

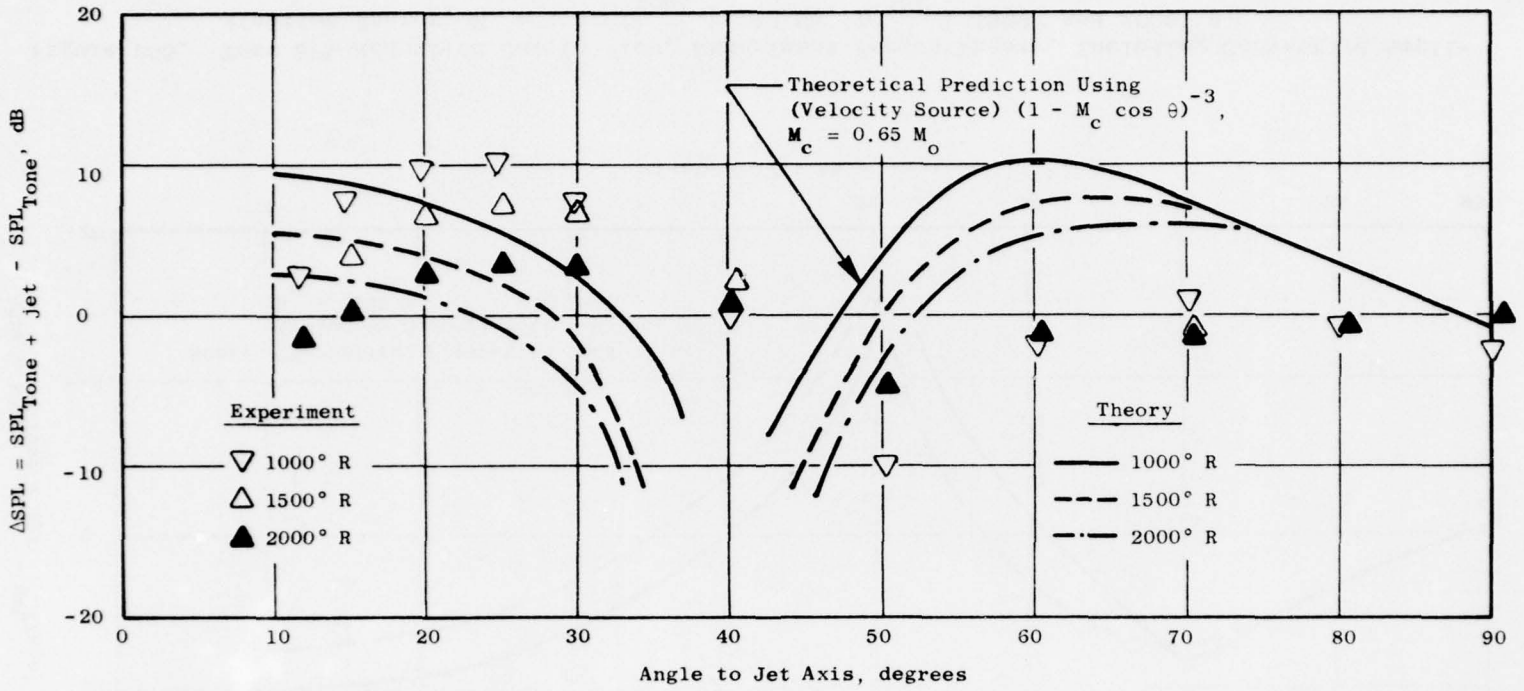


Figure 204. Tone SPL Reduction Due to Flow, Experiment Versus Theory, Including Convection Amplification Factor, M_o = 1.3, f_{tone} = 783 Hz, $T_{T_{jet}}$ = 1000°, 1500°, and 2000° R.

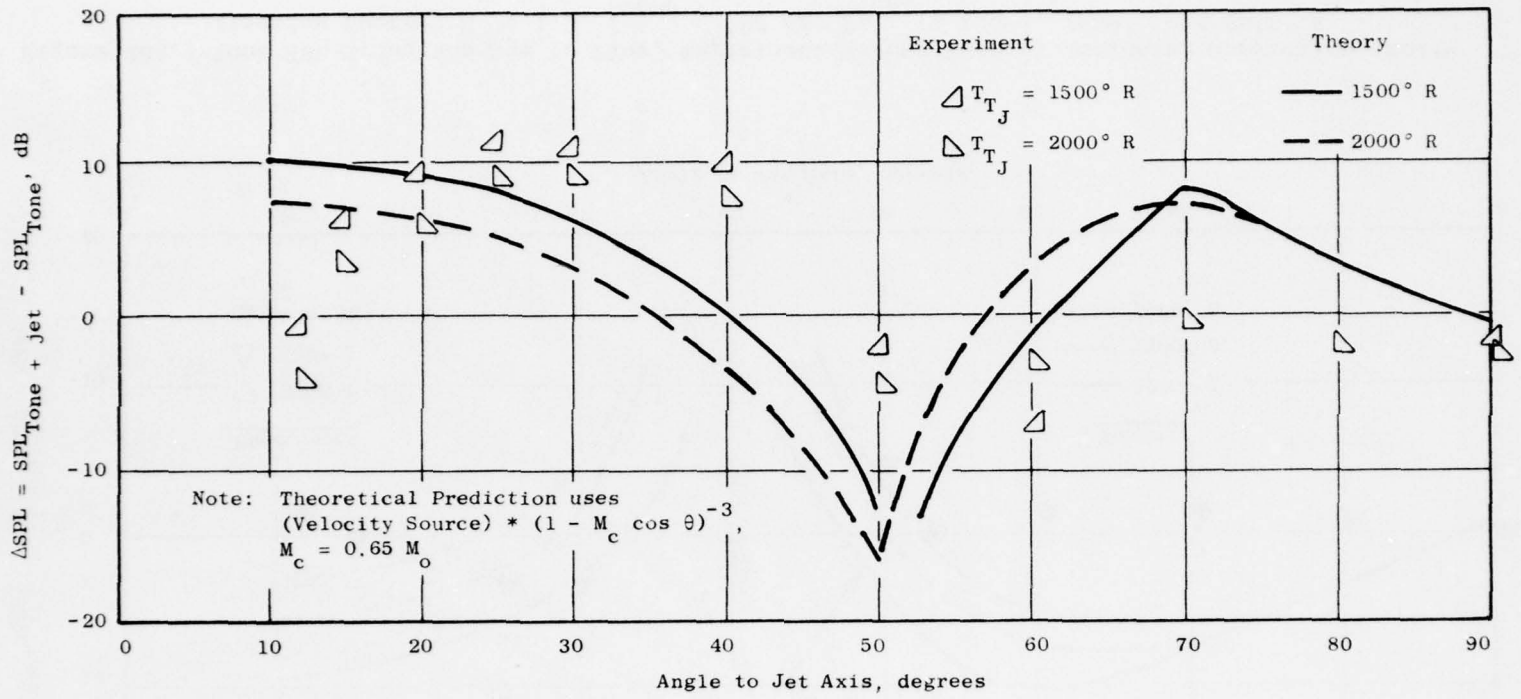


Figure 205. Tone SPL Reduction Due to Flow, Experiment Versus Theory, Including Convective Amplification Factor, $M_o = 1.5$, $f_{tone} = 783$ Hz, $T_{T_{jet}} = 1500°$ and $2000°$ R.

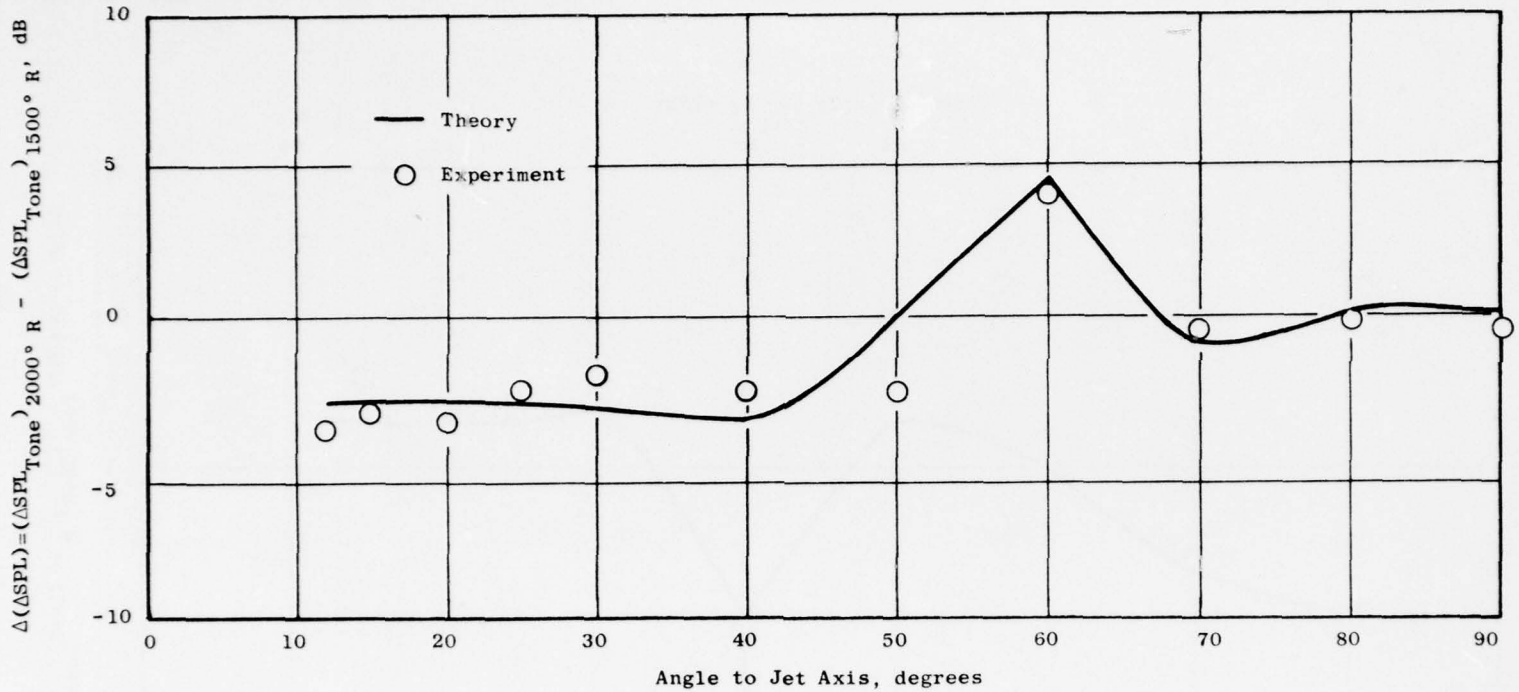


Figure 206. Influence of Jet Temperature on Tone SPL Reduction Due to Flow, Experiment Versus Theory.

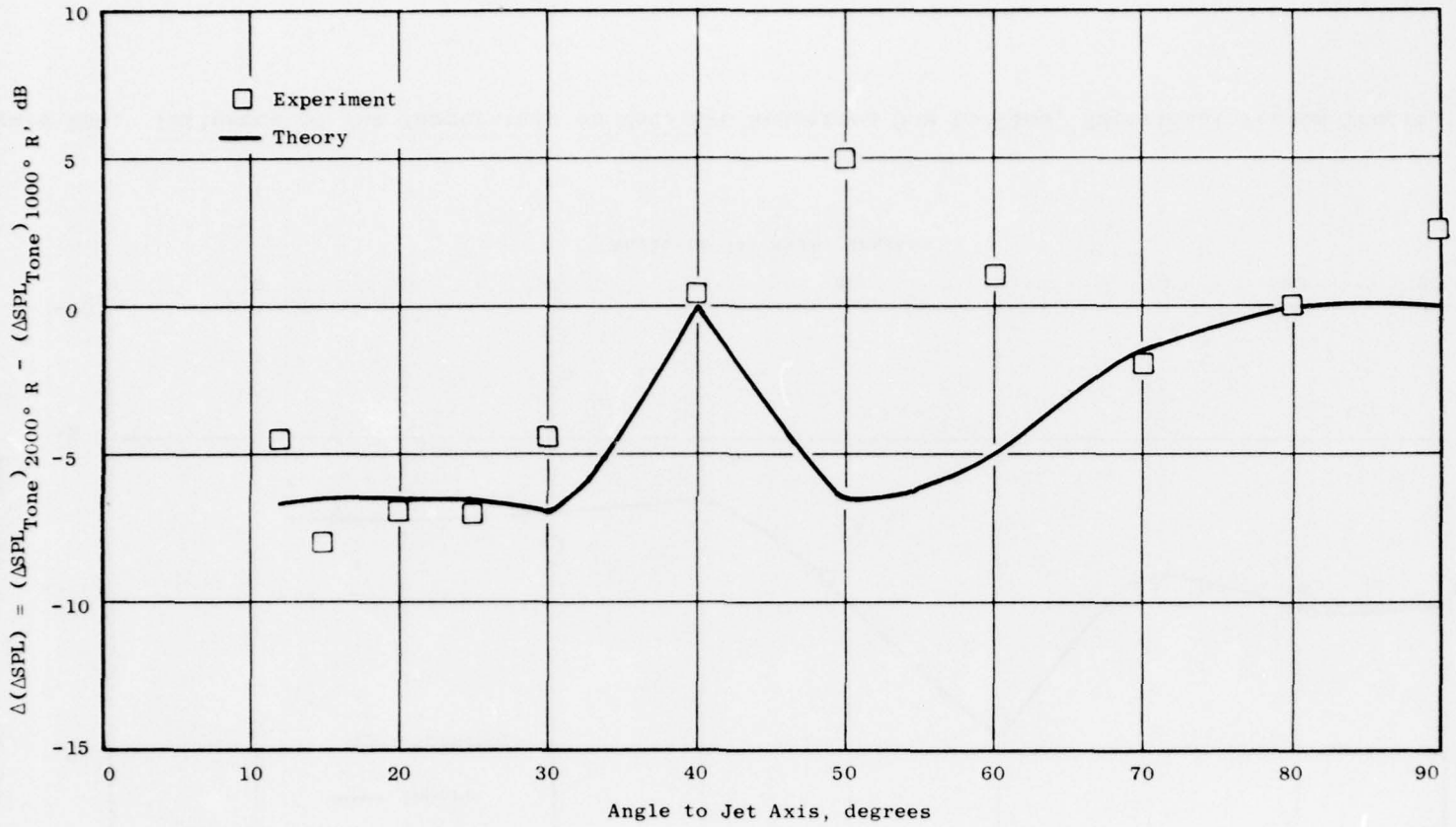


Figure 207. Influence of Tone Frequency on Tone SPL Reduction Due to Flow, M_o = 1.5, T_T = 2000° R, f_{tone} = 783 and 3000 Hz.

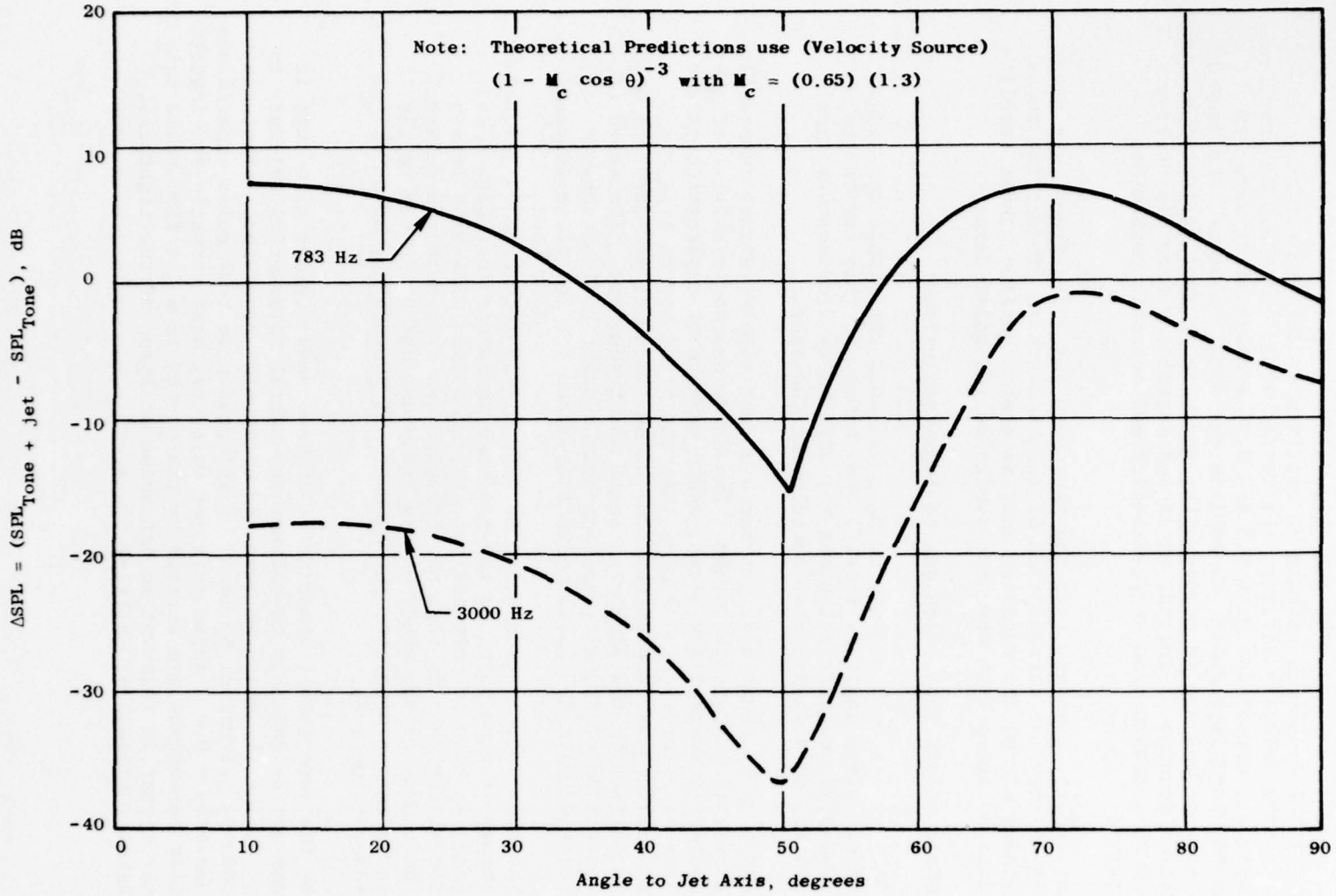


Figure 208. Influence of Tone Frequency on Tone SPL Reduction Due to Flow Theory, $M_o = 1.5$, $T_T = 2000°$ R, $f_{tone} = 783$ and 3000 Hz.

Thus, overall, the velocity and temperature effects are explained to some extent but not the frequency effects as observed in the present test series. With regard to the velocity effects, the reader would certainly be justified in objecting that, except for $M_o = 0.5$ and 0.7, a bewildering array of assumptions has been introduced to explain the data. However, the fact is that these assumptions are in accord with, and were in fact motivated by, what other injection studies of Ingard, et al and especially Crow did observe. Above $M_o = 0.9$, a combination of instability and acoustic mechanisms seems operative.

We must repeat, however, that the broadband jet noise itself was never influenced by either the introduction of the hardware to produce the tones or the switching air of the torques; and, as stated earlier, these baseline jet noise data do agree with the best available jet noise data.

This whole effort thus leads one to four conclusions:

1. Only at low Mach numbers of $M_o \leq 0.7$ does the simple refractive effect alone manifest itself, and, hence, in this regime the classical acoustic solutions for stationary displacement type sources do a good job of correlating the data.

2. Above M_o of about 0.9, jet flows do not simply refract internally generated or rejected noise. The noise source is able to trigger convected instability waves, and a measure of explanation of the data is afforded by assuming that the fixed source triggers a travelling source distribution (whose frequency and strength are determined by the source strength and frequency). The speed of convection of these travelling source distributions appears to coincide with the usual convection speed for jet noise sources.

3. The above observation seems to have little relevance to jet noise though it does point to the profound influence that high speed jets can have on internally generated noise. The main reason for saying this is that no influence was ever detected during the course of the study on the broadband jet noise due to the introduction of either the hardware to produce the tones of the tones themselves.

4. By the same token, observation 2 above does suggest also that it may not be possible to extract any useful information relevant to jet noise (by which we mean the externally generated, turbulence induced jet noise) by means of injected pure tone noise experiments above $M_o = 0.9$. Above this jet velocity, both acoustic and instability mechanisms are excited by the source in a jet flow while only the former is relevant to jet noise analyses of the Lighthill, Ribner, Lilley, or Phillips types.

CHAPTER III

LASER VELOCIMETER INVESTIGATIONS

Chapter III concentrates on a series of experiments aimed at illustrating the usefulness of the General-Electric developed laser velocimeter (LV). Particular attention was directed toward performing measurements in high temperature, high velocity, jet exhausts. Section 1.0 at Chapter III describes a series of LV experiments aimed at defining the plume characteristics of heated subsonic and supersonic shock-free and shocked flow exhaust jets. The results illustrate the mean velocity and turbulent velocity characteristic axial and radial velocity distributions. The results show significant differences in velocity distributions between subsonic and supersonic jets, particularly with regard to the turbulence distributions. Section 2.0 of Chapter III discussed how the LV may be used for noise source location. Section 2.0 discusses the analysis for computing cross correlations of LV-measured, in-jet velocity and far-field acoustic pressure. An experiment is also presented illustrating General Electric's LV capability for performing cross-correlation measurements.

SECTION 1.0

PARAMETRIC LASER VELOCIMETER STUDIES OF HIGH-VELOCITY, HIGH-TEMPERATURE, TURBULENT JETS

P. Knott P. Mossey

1.1 BACKGROUND

During the course of this program, a considerable amount of effort was directed toward developing the capability of measuring velocity in the exhaust plume of high-temperature, high-velocity, exhaust jets. During the initial phase of this program [138], it was demonstrated that the laser velocimeter could indeed be used for performing such measurements. During the initial portion of the second phase of this program [139], the laser velocimeter was used to perform a series of calibration experiments and to demonstrate the capability of the LV to perform turbulent spectrum measurements.

To illustrate some of the past results, Figures 209 and 210 show measurements of axial mean velocity and turbulent velocity decays by General Electric's laser velocimeter compared with hot-film measurements for an ambient Mach 0.5 exhaust jet. Also shown is a series of similar hot-wire measurements by Wooldrige and Wooten [140] for a Mach 0.3 ambient jet. This series of measurements was then extended to define the characteristics of a Mach 1.55 shock-free heated jet. Figure 211 illustrates the axial mean and turbulent velocity decay properties for this jet (see references 139 and 141 for further measurements from this series. Figures 209-211 characterize some key differences between subsonic and supersonic jets. Of particular interest is the extended potential core for the heated supersonic jet and the distributions of turbulence in the nozzle lip region. For the subsonic jet, the turbulence ratio behind the nozzle lip remains rather uniform throughout the potential core. For the supersonic jet, this velocity distribution is much more peaked. These results are very reminiscent of acoustic radiation of power per unit slice of distributions.

To illustrate LV-measured turbulence spectra [142], Figure 212 shows a comparison of laser velocimeter and hot-film turbulence spectra for an ambient Mach 0.5 jet. Also shown is a laser-velocimeter-measured turbulent spectrum for a hot sonic jet. With these results, the following presentation contains more information obtained from a series of LV parametric studies.

1.2 THE LASER VELOCIMETER ARRANGEMENT

The arrangement used was similar to that of the 1971 A.F. Program as reported in AFAPL-TR-72-52, Chapter 125. The details of that report will not be repeated here. Instead, changes or new features and improvements that

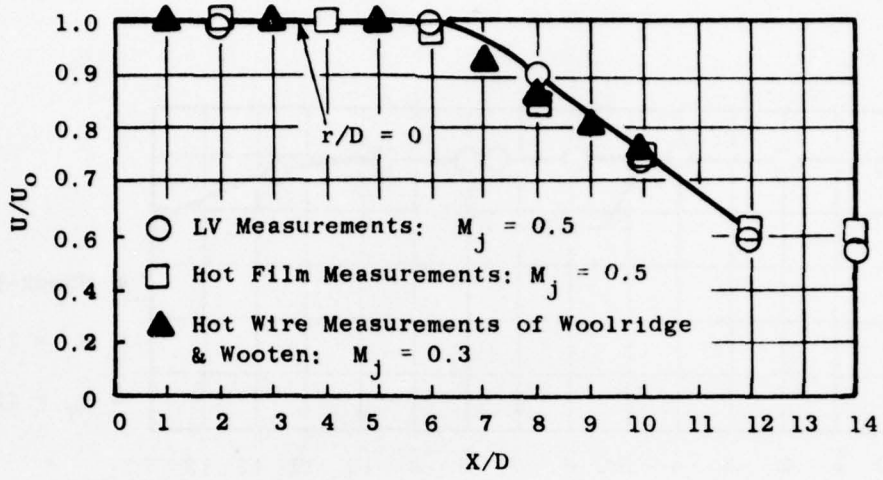


Figure 209. LV Hot-Film Mean Velocity Measurements.

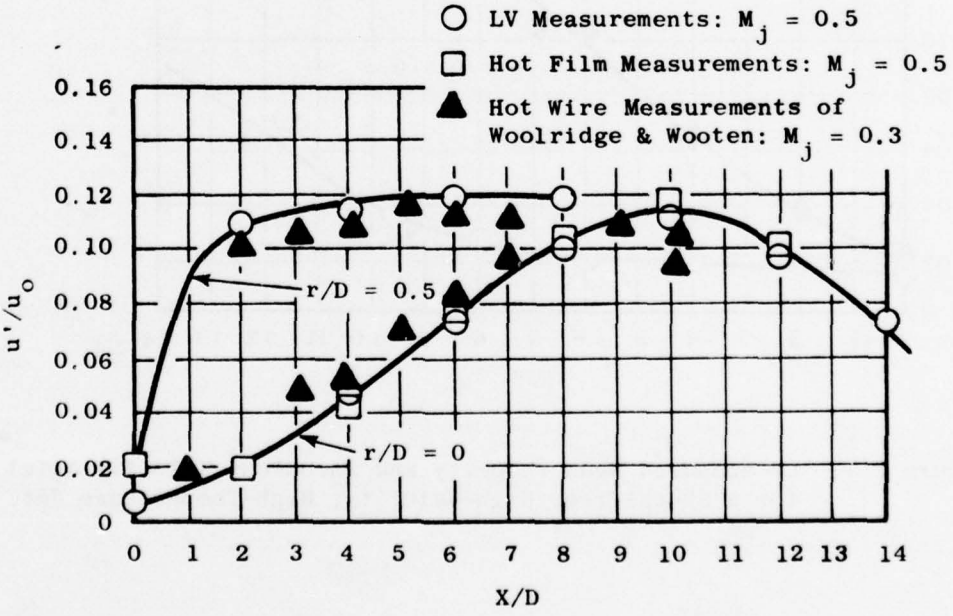


Figure 210. LV Hot-Film Turbulent Measurements.

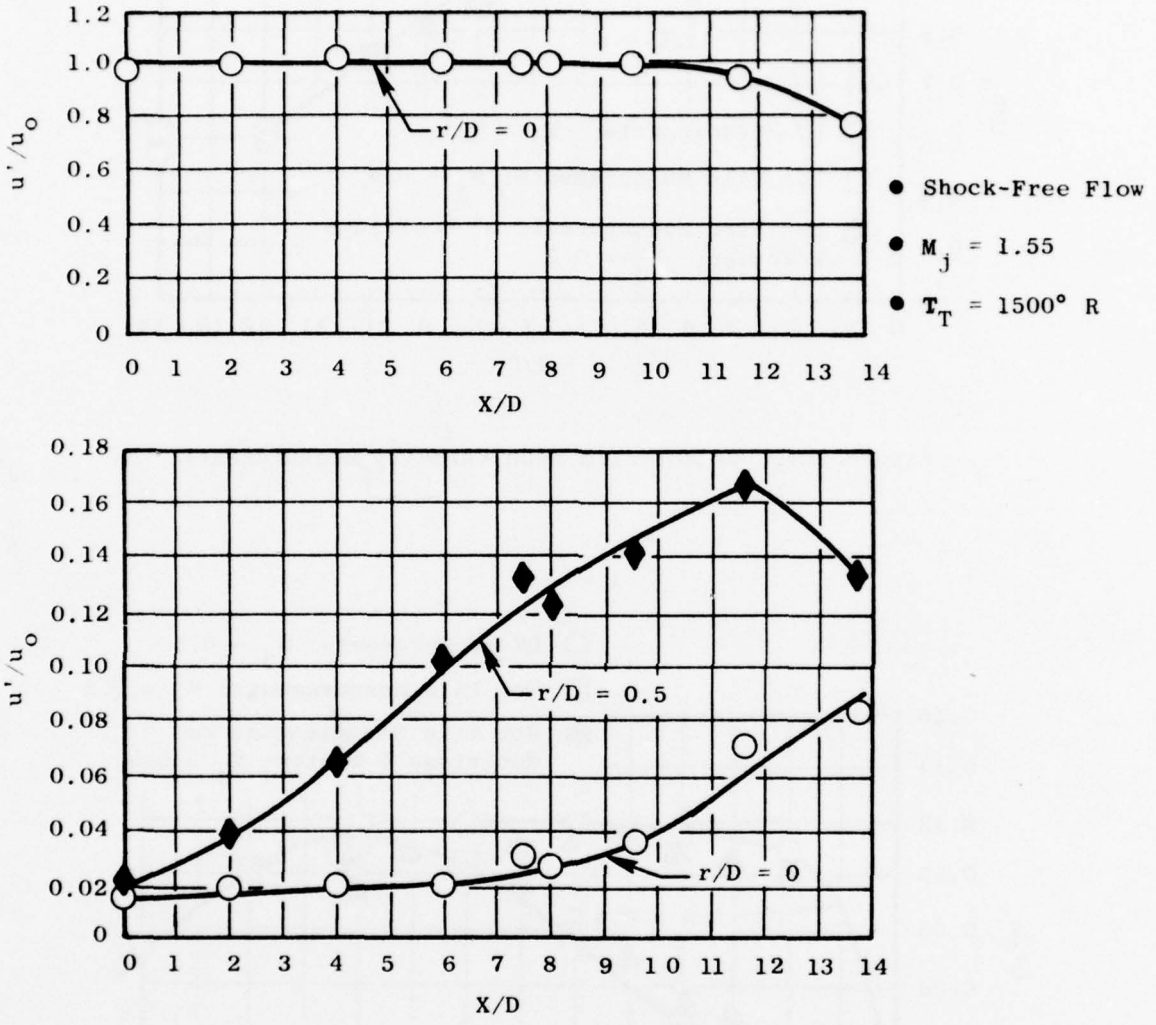
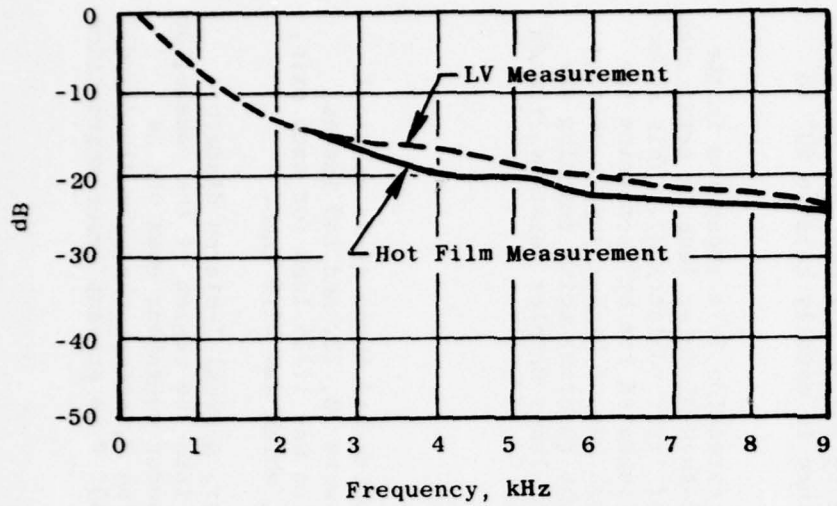
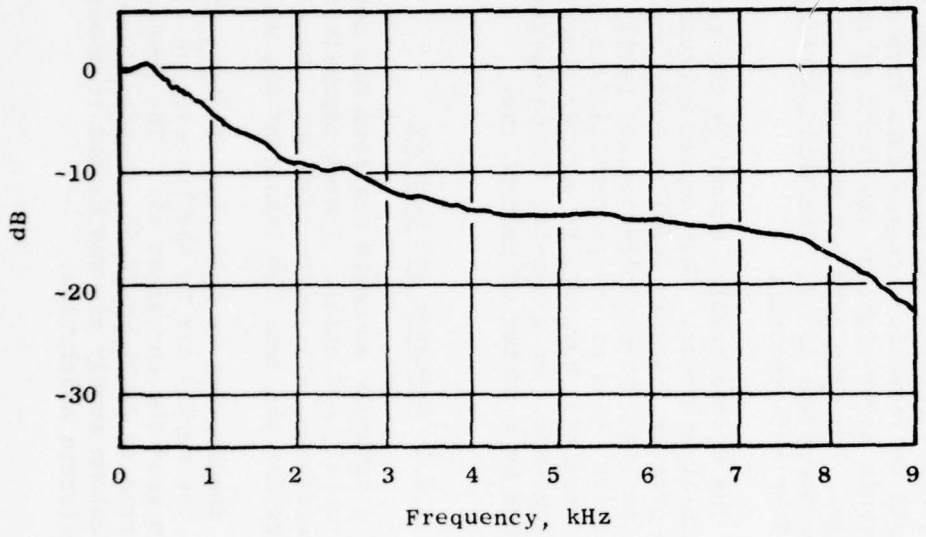


Figure 211. LV-Measured Mean Velocity and Turbulent Velocity Axial Decays for a Shock-Free, High-Velocity, High-Temperature Jet.



Comparison of Laser Velocimeter and Hot Film Turbulence Spectra

$M_j = 0.5$, $X/D = 6$, $r/r_o = 1$



Measured Laser Velocimeter Turbulent Spectrum for a Hot Sonic Jet

$M_j = 1.0$, $T_8 = 1500°$ R, $X/D = 10$, $r/r_o = 0$

Figure 212. LV-Measured Turbulent Spectrum for Ambient and Heated Jets.

have been used will be described. The basic optics system used was the differential Doppler, backscatter, single-package arrangement that has the proven feature of ruggedness for our rather severe environment. A substantial improvement in temperature stability of the optics alignment was made that also allowed greater range without sacrificing spatial resolution of the measurement volume. Figure 213 shows a schematic arrangement of the laser package used on this program. The laser beams are projected from below the lens, forming an angle, α, that keeps the major axis of the control volume ellipsoid to a minimum. The dimensions of the control volume are 0.25 inch for the major axis and 0.020 inch for the minor axis. The range has been extended from 40 inches to 85 inches. At this distance from the jet, a protective enclosure was not necessary. The three steering mirrors and the beam splitter were remounted on adjustable supports, all of the same aluminum alloy, which eliminated temperature-alignment problems. Figure 214 shows the Laser Velocimeter setup at General Electric's JENOTS facility.

The range extension to 85" brought about two problems. The first of these is the increased sensitivity to temperature gradients in the air intervening between the package and the sensitive volume. This has caused a small decrease in accepted data rate in cold weather, when convection gradients occur right at the front of the package,, where the laser beams emerge. The data rate was estimated to drop by 20% to 30% when the outdoor temperature was 25° F. The package temperature is usually held to 60° to 80° F by a thermostat.

The second problem caused by the range extension is a reduction in the return light power. This occurs because a 6-inch-diameter lens is being used at a greater distance (smaller solid angle of light collection). This reduction in light power collected was partly compensated for by increasing the electrical gain of the photomultiplier through use of higher supply voltage. This resulted, however, in greater shot (light quantum) noise reaching the LV processor. As a result, the percentage of laser Doppler bursts validated dropped by a factor of perhaps two.

1.2.1 Actuator and Seeding

A remotely actuated platform was used which had three axes: vertical, horizontal, and axial. Travel capabilities were 32, 32, and 240 inches, respectively, all remote read-out. Resolution was ±1/16 inch for each axis, except for the last 208 inches of the axial, which was ±1/8 inch.

Seeding was by injection of AL_2O_3 powder, nominal 1-micron diameter, into the supply air to the burner, and also into the region of the nozzle, so as to seed the entrained air. The powder feeder equipment used was as reported in AFAPL-TR-72-52, Chapter V, section 3, except that the fluidized bed column supply air was heated to about 250° F to prevent power aggregation by moisture absorption.

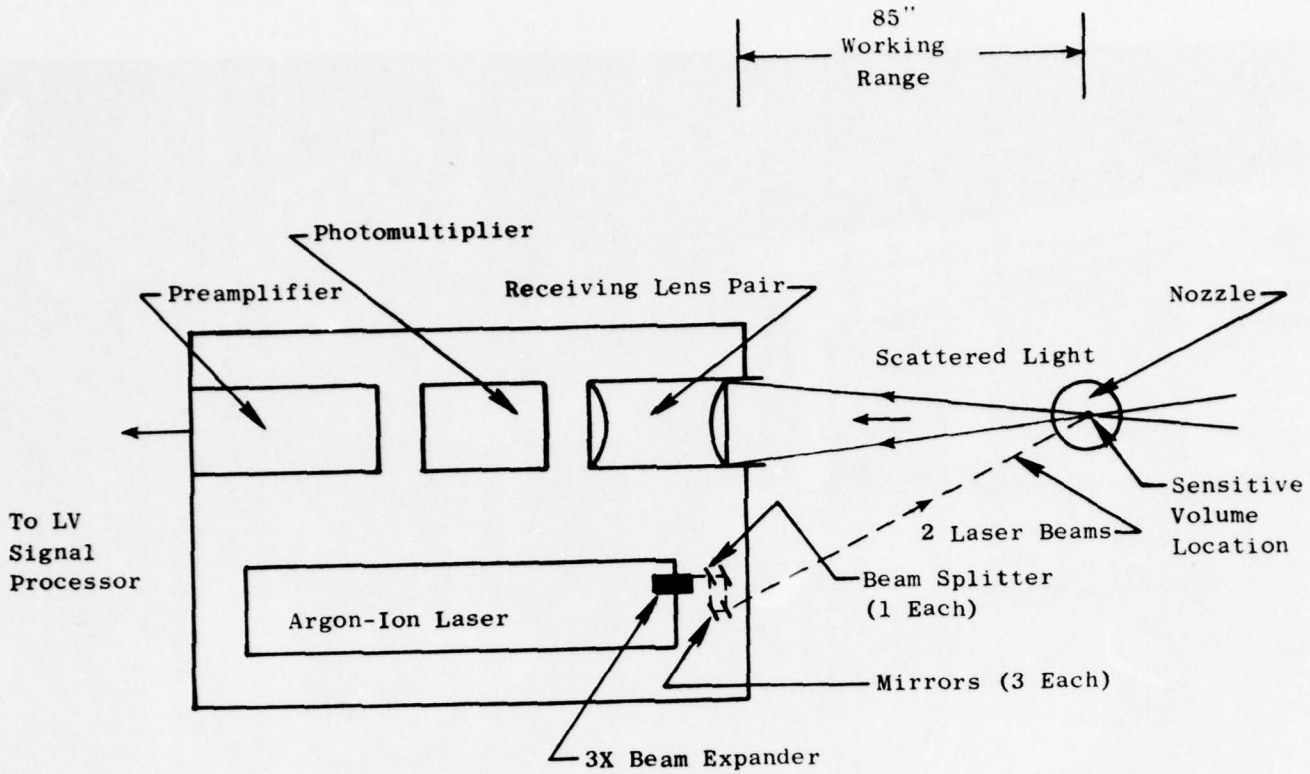


Figure 213. Laser Velocimeter Optics Package.

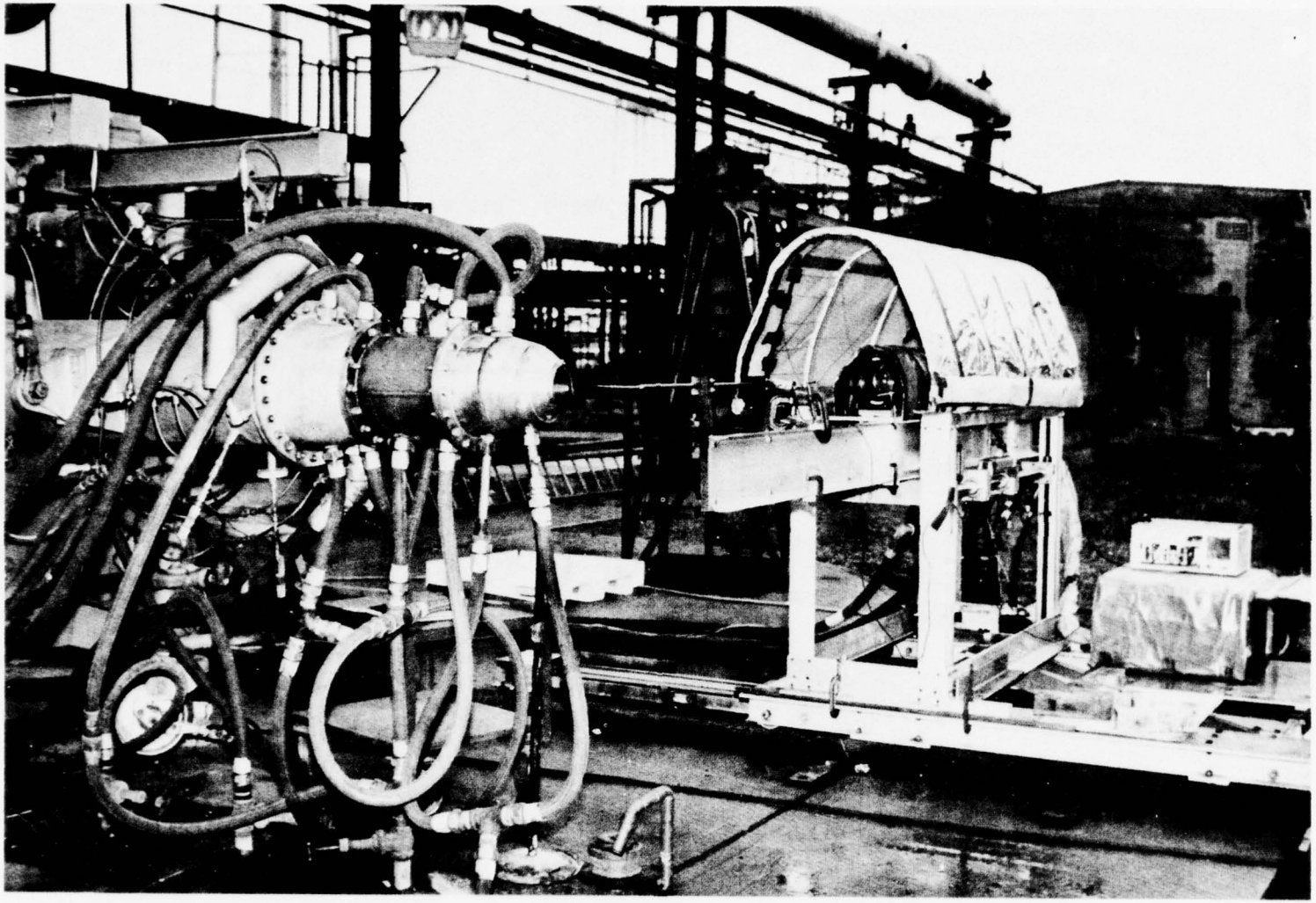


Figure 214. Laser Velocimeter Setup at JENOTS.

1.2.2 Signal Processing and Recording

The laser velocimeter signal processor used was the GE-developed direct-counter (time-domain)-type similar to that reported in AFAPL-TR-72-52 Chapter V, but with some improvements made during 1973 as part of a GE internal program. These improvements resulted in a lowered rate of false validations and improved linearity and resolution. Turbulent velocity probability distributions (histograms) were recorded by a NS633 Pulse Height Analyzer, 256-Channel, and dumped into an X-Y plotter.

1.3 LASER VELOCIMETER JET PLUME SURVEY

As part of the development and evaluation of the laser velocimeter as a useful noncontact aeroacoustic probe, extensive surveys of the mean velocity and turbulent rms velocity characteristics were performed on subsonic and supersonic hot jet exhaust plumes. The nozzles used during testing were a 4.3-inch convergent conical nozzle and a 4.3-inch-throat-diameter convergent-divergent nozzle (see Reference 134, pages 143 and 144, for pictures of these nozzles). For the validation tests mentioned in 1.1 Background, a hot-film anemometer probe (Thermo Systems Model 1210) was used for the subsonic cold jet tests. Figure 215 shows the arrangement used for the hot-film measurements. An extension beam was attached to the automatic LV traversing cart so that accuracy of probe location could be obtained.

1.3.1 Cold Jet Laser Velocimeter Measurements

Figure 210 shows the axial variation distribution of the centerline mean velocity as measured by the laser velocimeter and the hot-film anemometer. Also shown are hot-film measurements of Wooldridge and Wooten[140] at $M_j = 0.3$. The LV/hot-film/hot-wire measurements are seen to be in good agreement. The results show that the mean velocity in the core began to decrease at an axial location of X/D ~ 6. Between X/D = 6 and 15, the flow undergoes a complicated readjustment toward a self-similar region. For completeness, Appendix 3 includes a tabular listing of the actual hot-film measurement.

Figure 216 shows a typical radial velocity profile. Figure 217 illustrates LV-measured normalized radial mean velocity profiles for the ambient Mach 0.5 jet for axial stations of 2, 4, 6, 8, 10, 12, and 14 diameters. Figures 218-220 represent LV-measured contour plots of mean velocity, turbulent velocity, and turbulence intensity for the same jet.

1.3.2 Hot Supersonic Jet Laser Velocimeter Measurements

1.3.2.1 Shock-Free Jet

Figure 211, discussed earlier, illustrates the axial variation distribution of the centerline mean velocity and turbulent velocity for a shock-free

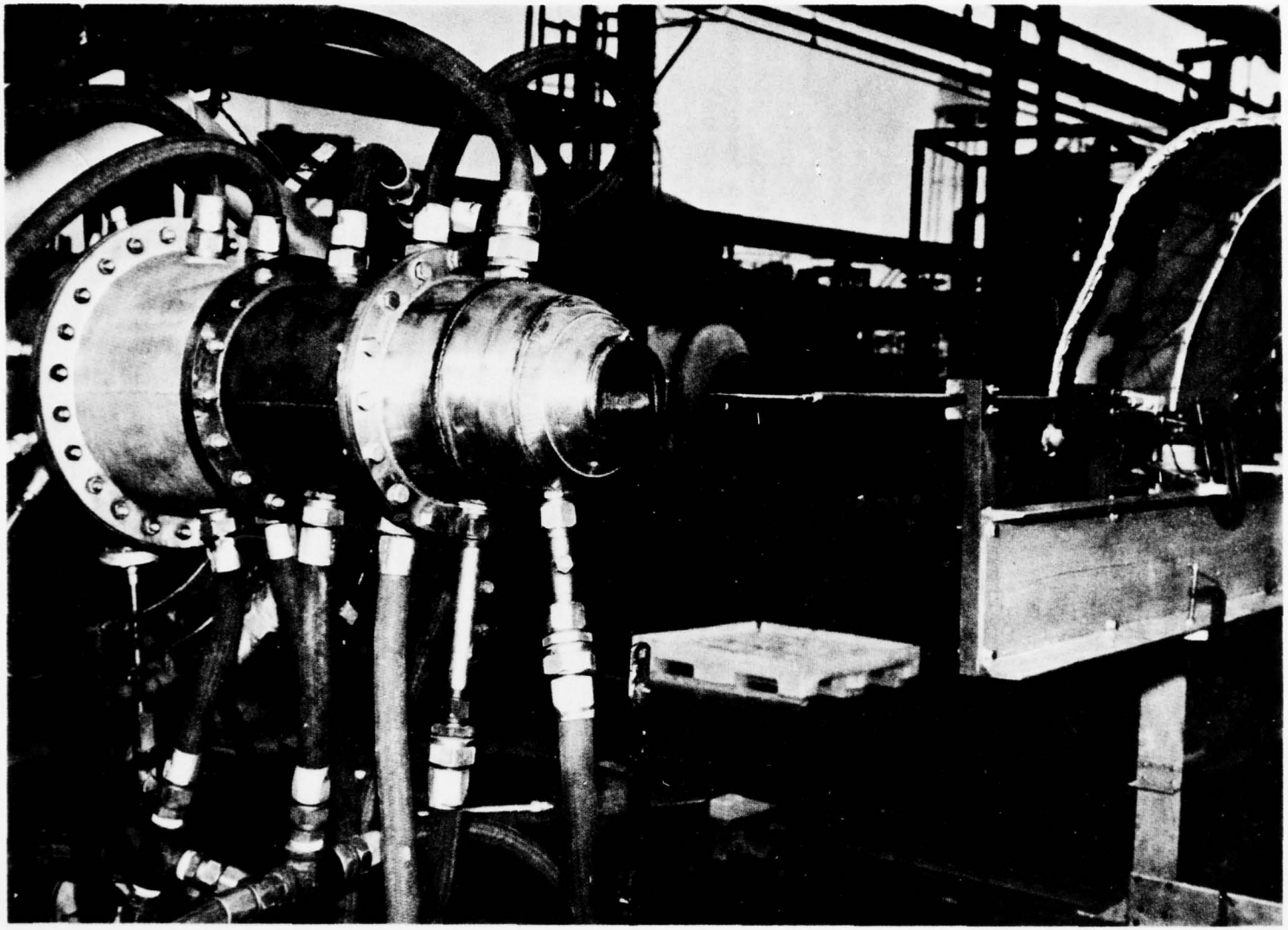


Figure 215. Hot-Film Arrangement on Laser Velocimeter Cart.

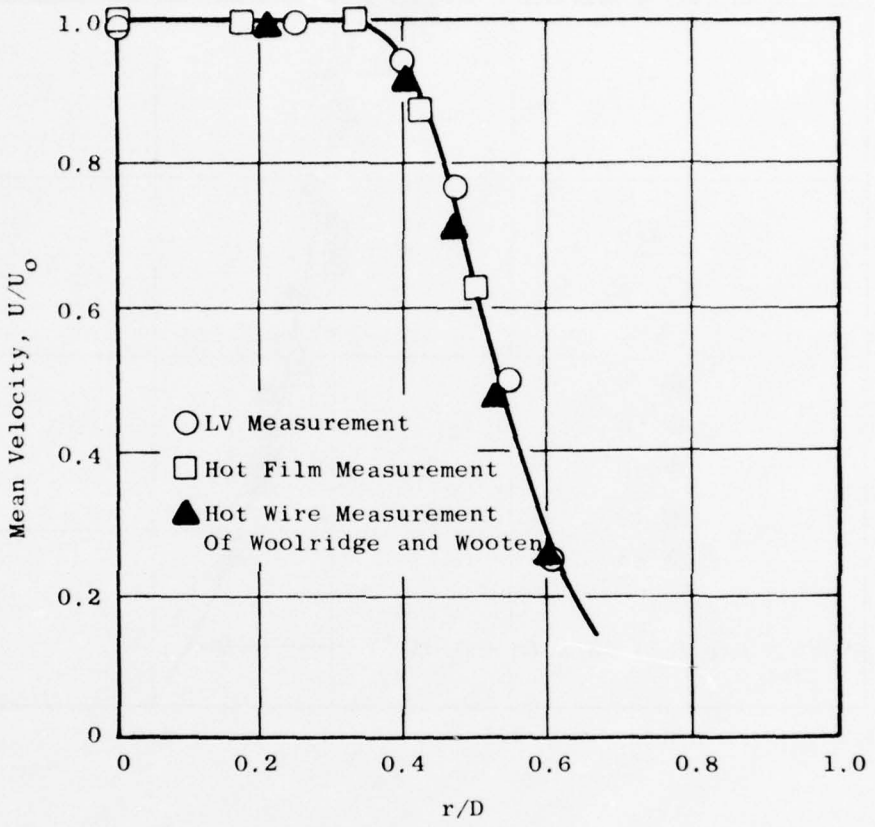


Figure 216. Mean Velocity Profile Comparison of LV with Hot-Film; X/D = 2.0 , M_j = 0.5.

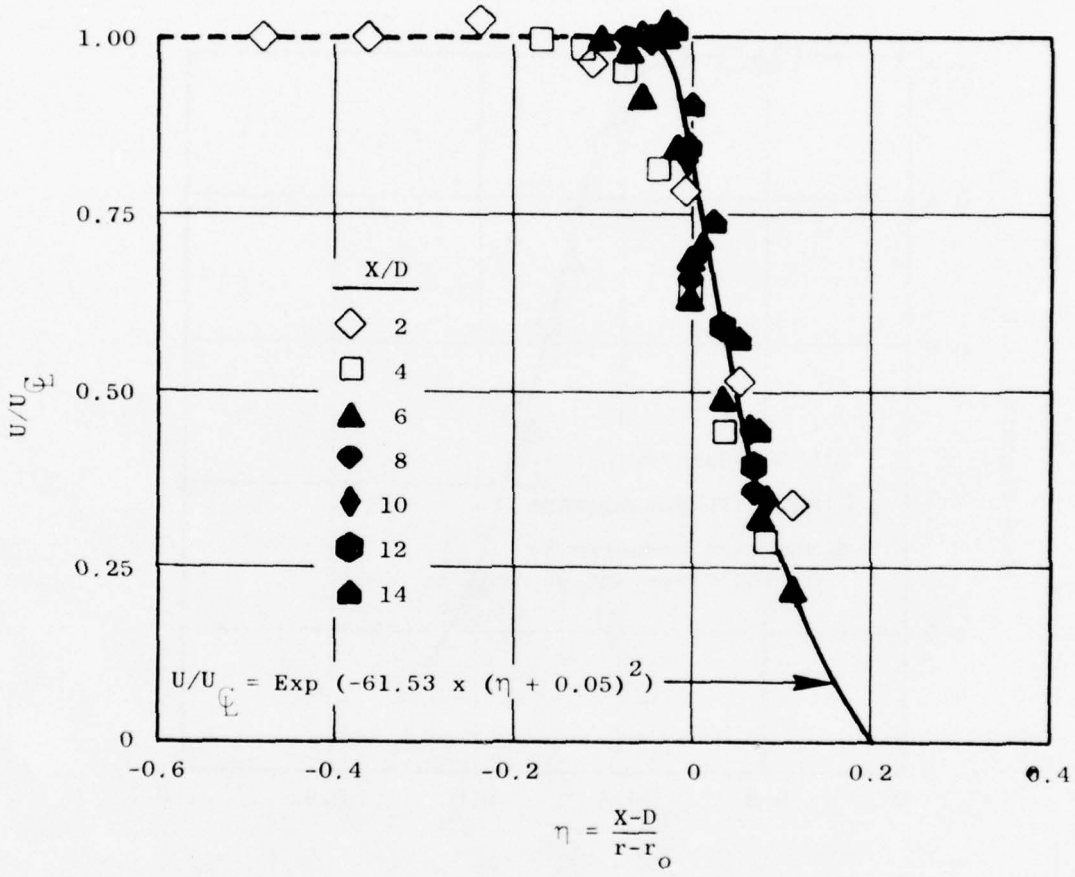


Figure 217. LV-Measured Normalized Radial Mean Velocity Profiles for M_j = 0.5, T_T = Ambient (Conical Nozzle Data).

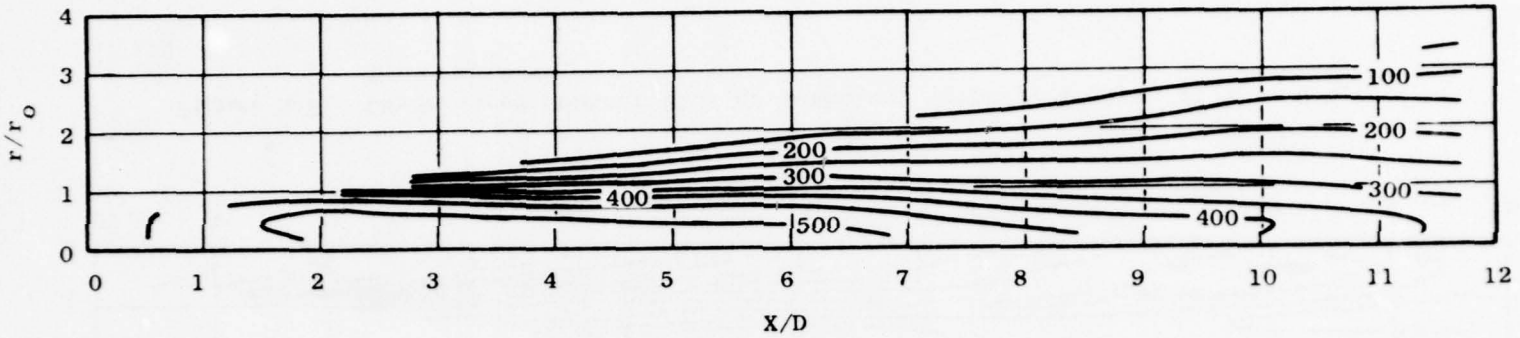


Figure 218. LV-Measured Contour Plot of Mean Velocity in fps at M_j = 0.5, T_T = Ambient.

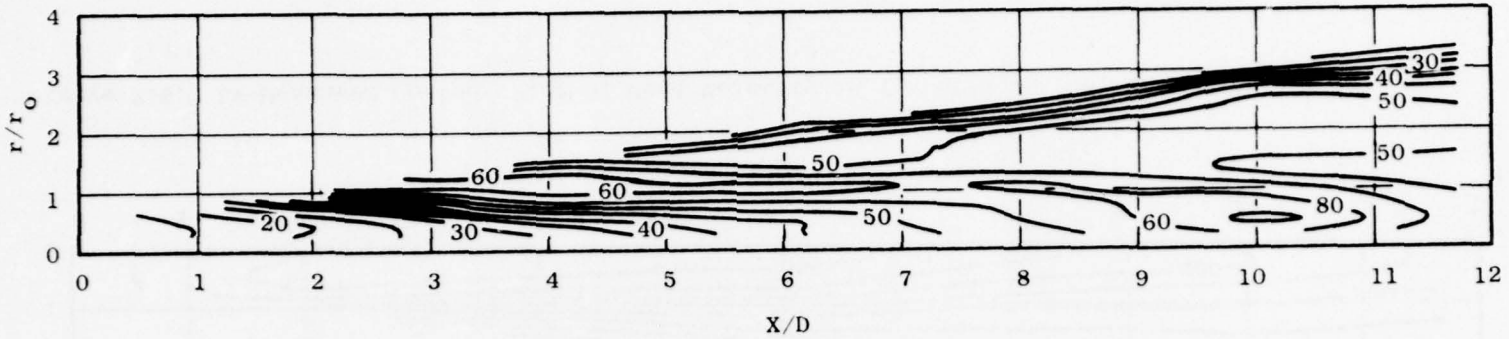


Figure 219. LV-Measured Contour Plot of Turbulent Velocity in fps at M_J = 0.5, T_T = Ambient.

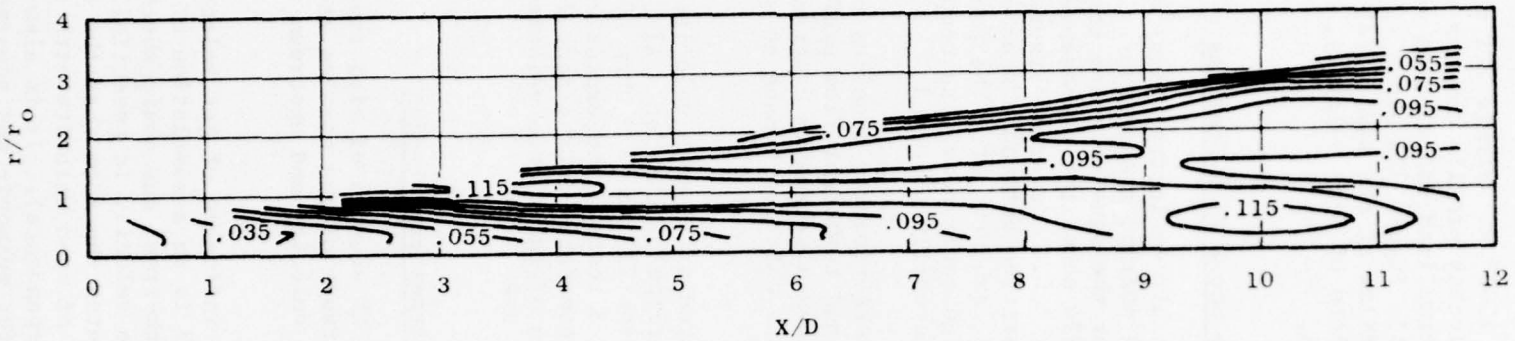


Figure 220. LV-Measured Contour Plot of Turbulent Intensity at M_j = 0.5, T_T = Ambient.

exhaust jet at M_j = 1.55, T_T ~ 1500° R. Figure 221 shows a typical radial mean velocity and turbulent velocity profile for the same shock-free jet. Figure 222 shows LV-measured normalized radial mean velocity profiles at X/D = 2, 4, 6, 8, 10, 12, and 14, while Figure 223 shows LV-measured normalized radial turbulence velocity profiles at the same axial locations. Appendix 4 includes a series of contour plots of mean velocity, and turbulent velocity based on the above measurements.

1.3.2.2 Conic Nozzle Shock Flow Profiles

In order to complement the high-velocity, high-temperature measurements performed on the shock-free C/D nozzle, a series of plume measurements was also taken on a conic nozzle for the same upstream condition as for the C/D shock-free condition. Figure 224 shows the LV-measured normalized radial mean velocity profiles for this jet. Comparing Figure 222 with 224 illustrates the flow property similarities between a shock-free and shocked-flow, high-velocity, high-temperature, exhaust jet. The pressure of the expansions and compression in the off-design conic nozzle as compared with the fully expanded nozzle configuration is easily observed.

In addition to the above measurements, a series of measurements was also made to define better the mean and turbulent flow profiles of the conic nozzle shock structure. Figure 225 shows a schematic diagram of the predicted shock location and the series of points which were made to study the shock flow properties.

Figure 226 shows the measured axial mean velocity and turbulent velocity characteristics along the centerline of the jet. Also shown are the predicted velocity characteristics. Figures 227 and 228 show LV-measured turbulent velocities for the series 2 and 3 tests. The expansion and contraction in the shock-flow region is clearly represented in the mean flow axial velocity distribution. The amplification of turbulence velocity due to the shock is also evident in Figures 227 and 228.

1.3.2.3 Exit Plane Parametric Studies

In order to complement the LV studies of high temperature high velocity jets, a series of exit plane surveys of the nozzles studied was performed to illustrate the influence of jet velocity and upstream temperature on exit plane turbulence.

Figure 229 illustrates the influence of jet velocity on exit-plane turbulence. Shown in Figure 229 is an accumulation of results for ambient-subsonic, heated-supersonic shock-free, and conic shocked-flow nozzles. The results show that the turbulence velocity is essentially proportional to the mean velocity ($u' \sim u$). This refutes the idea that the turbulence velocity is proportional to lower powers of mean velocity with increasing speed (and thus lower acoustic power law dependence). It is also observed that the exit-plane turbulence is lower for subsonic and supersonic shock-free jets than is found for the conic shocked-flow nozzles.

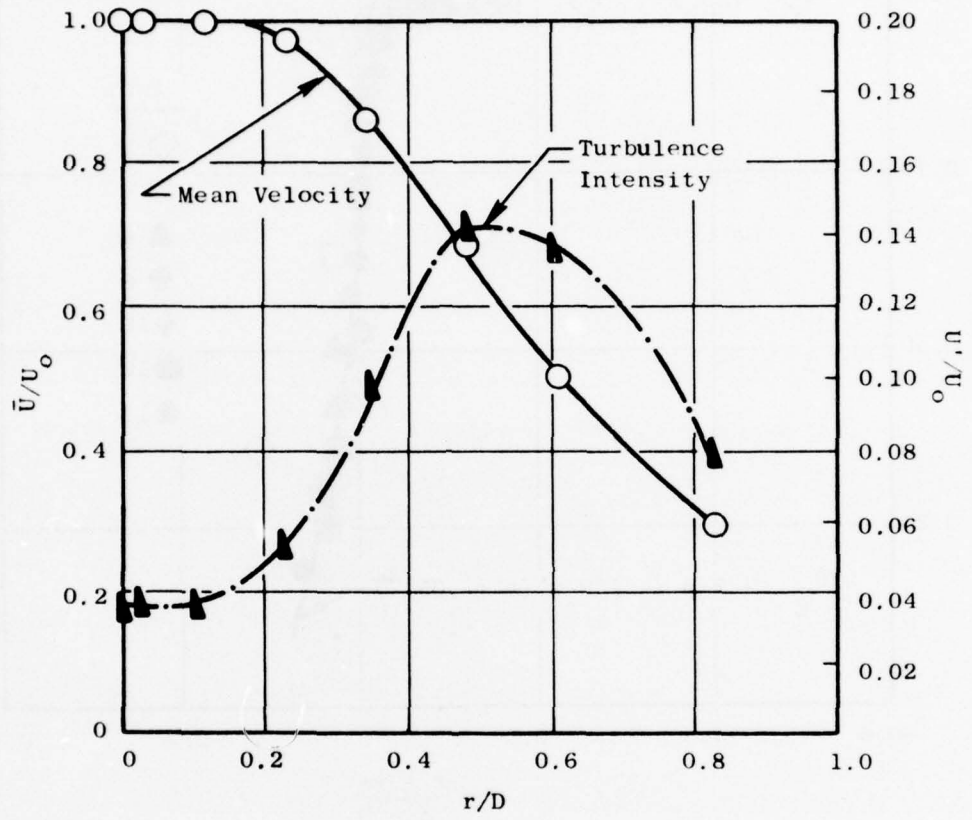


Figure 221. Laser-Velocimeter-Measured Mean Velocity and Turbulent Intensity Radial Profiles; M_j = 1.55, T_T = 1500° R, X/D = 9.6 (C/D Shock-Free Data).

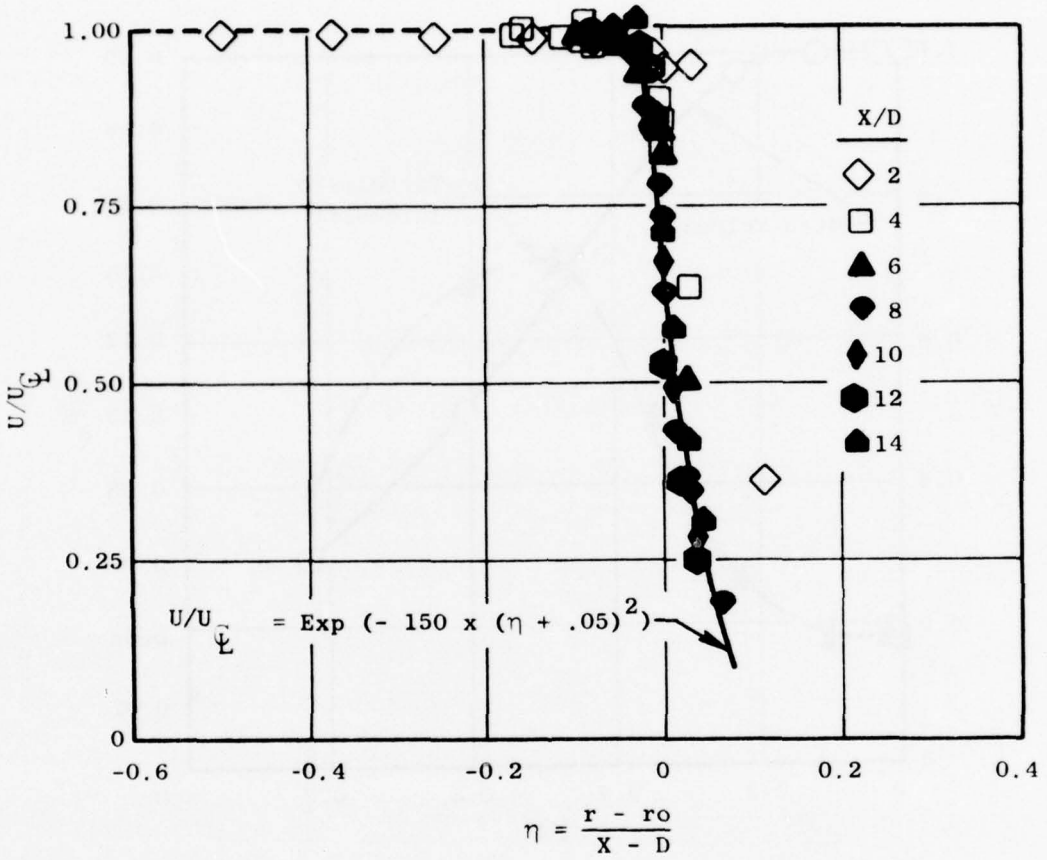


Figure 222. LV-Measured Normalized Radial Mean Velocity Profiles for M_j = 1.55, T_T = 1500° R (C/D Shock-Free Data).

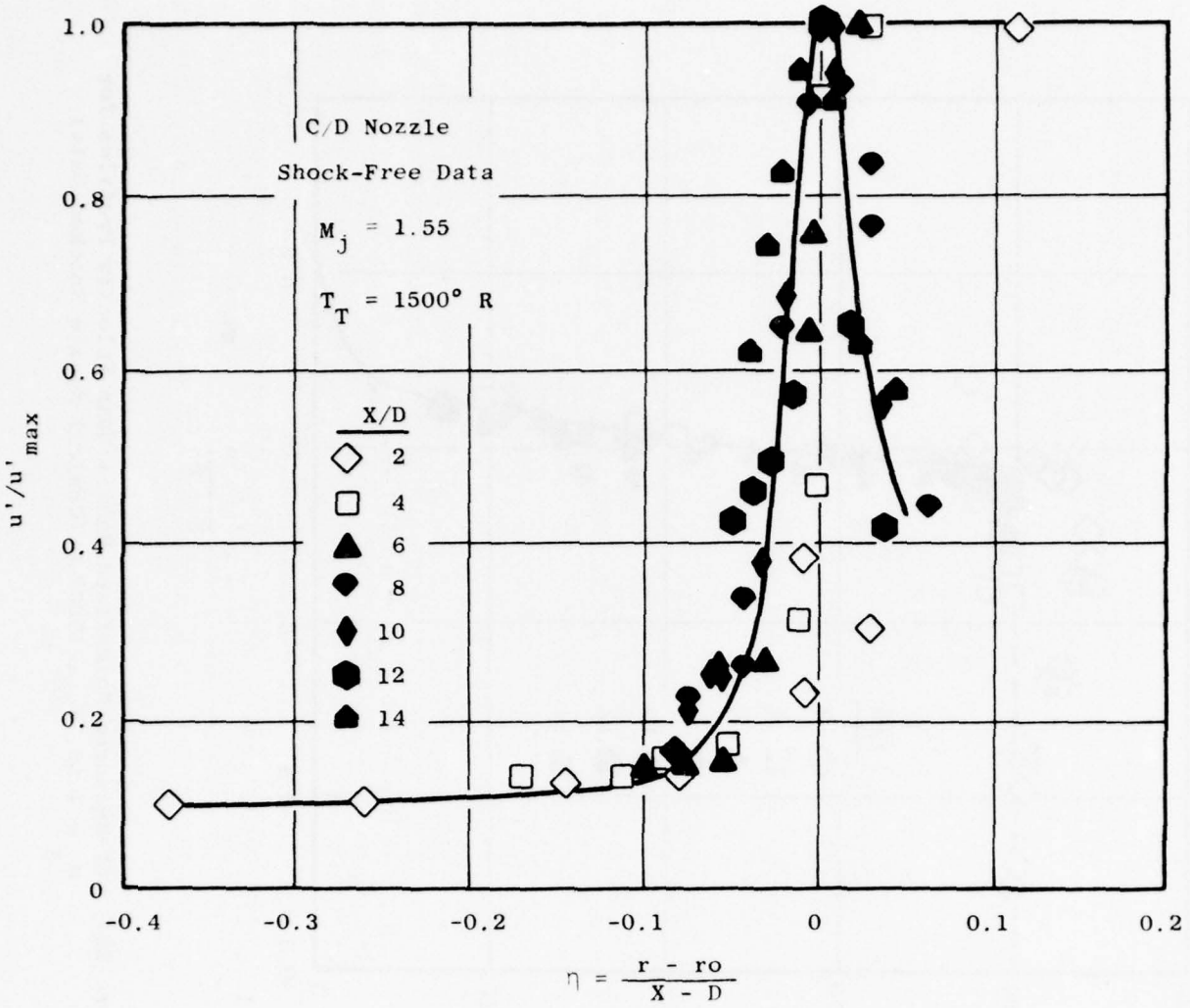


Figure 223. LV-Measured Normalized Radial Turbulence Velocity Profiles for M_j = 1.55, T_T = 1500° R.

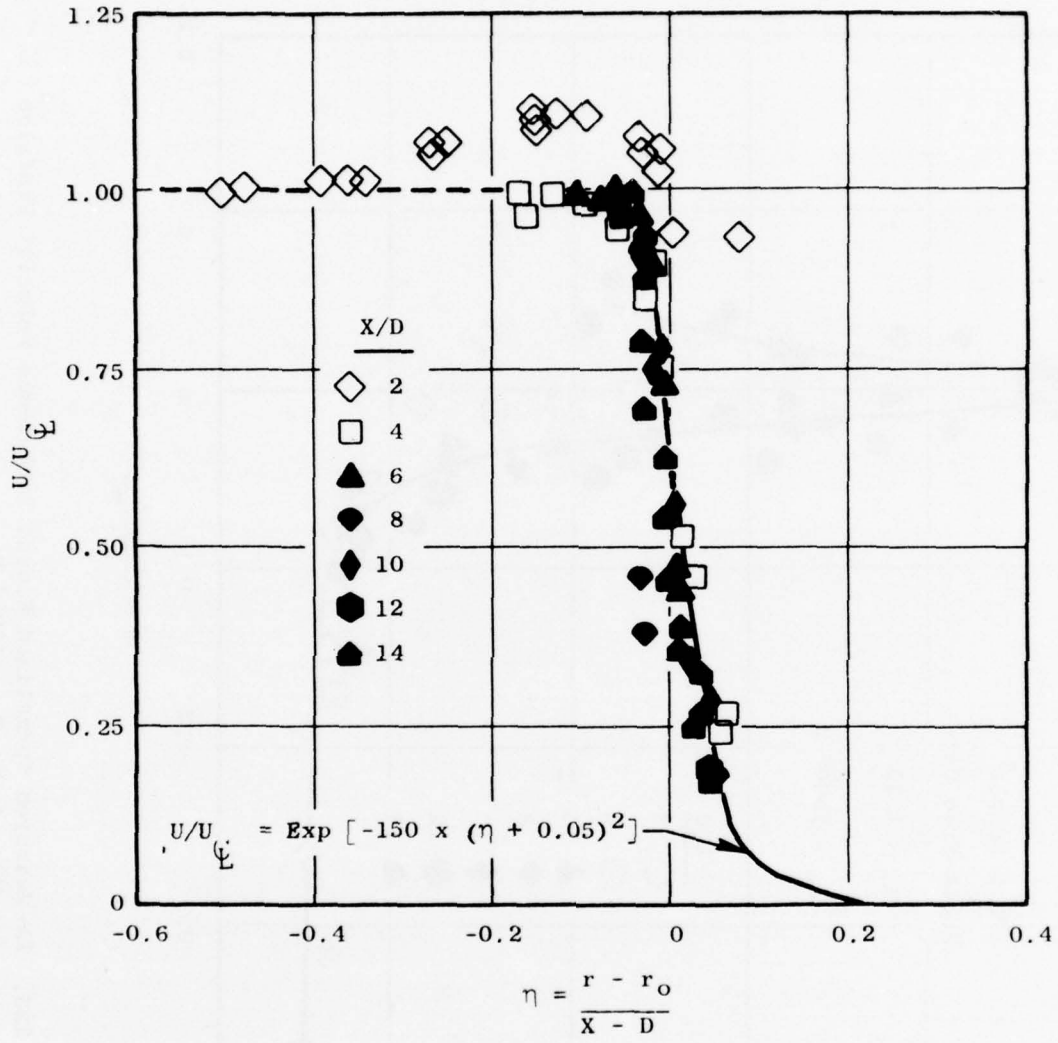


Figure 224. LV-Measured Normalized Radial Mean Velocity Profiles for $M_j = 1.55$, $T_T = 1500°$ R (Conical Nozzle Shocked Data).

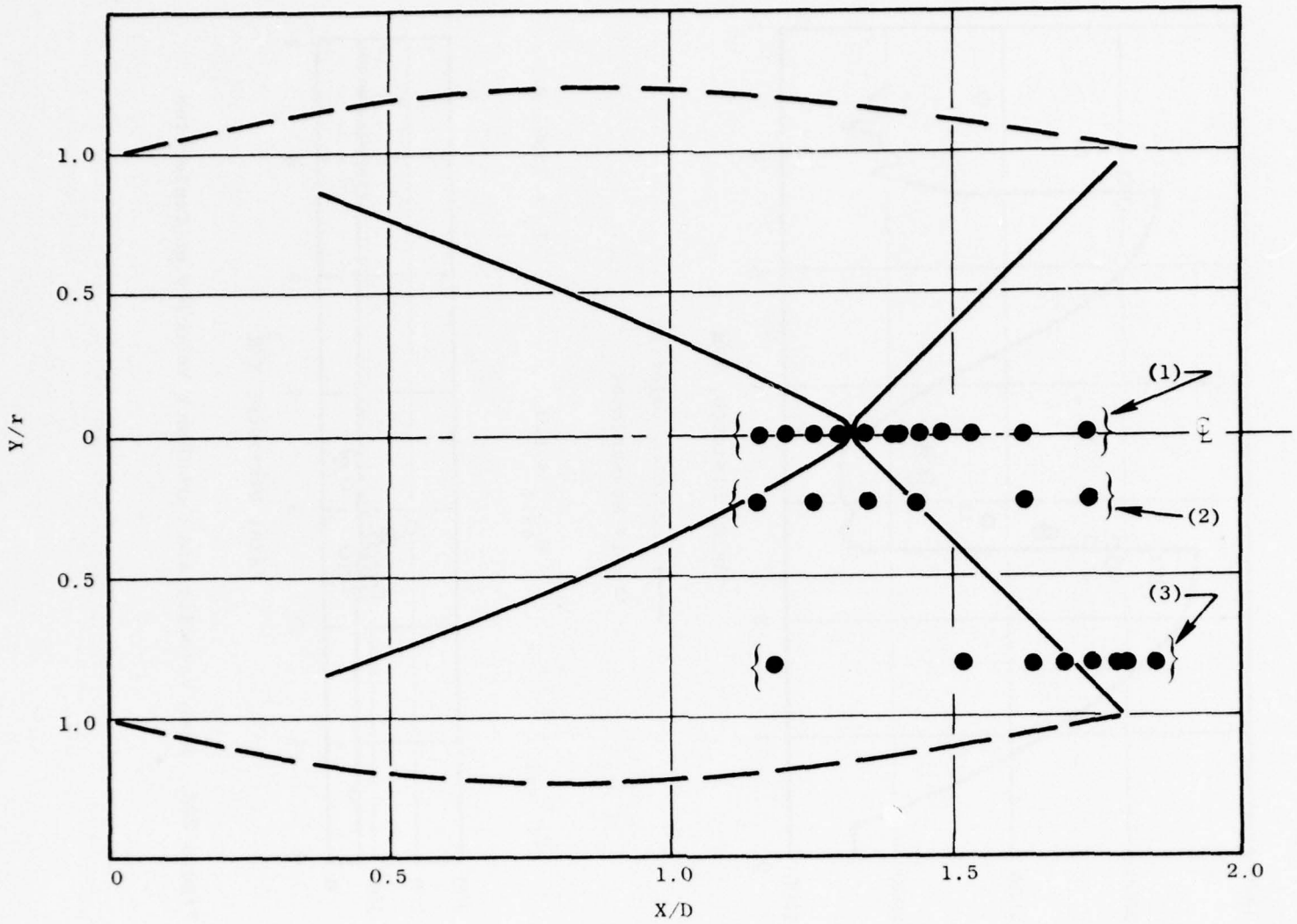


Figure 225. LV Measuring Positions for Shock Turbulence Study.

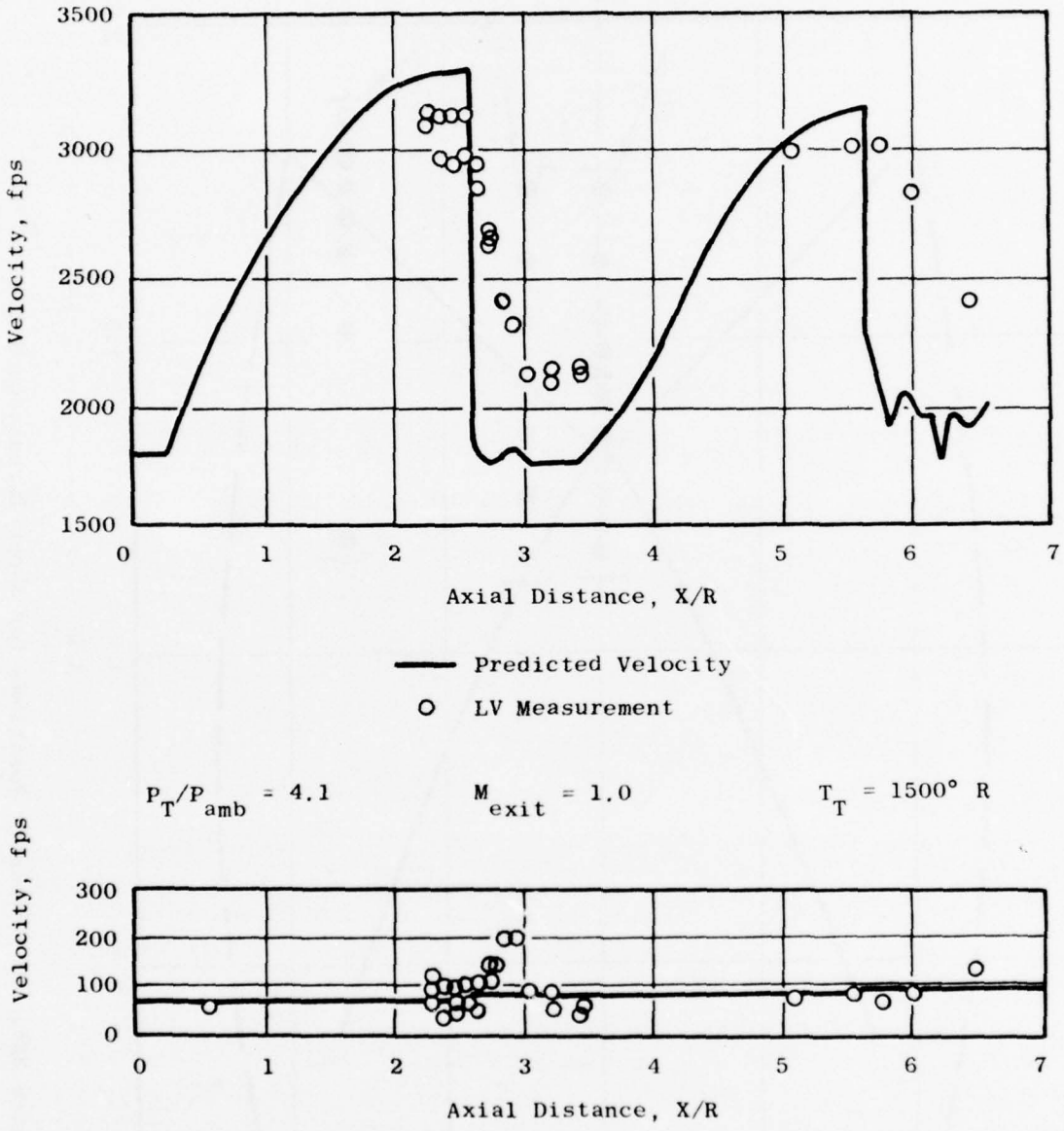


Figure 226. Mean Velocity and Turbulence Velocity on Centerline.

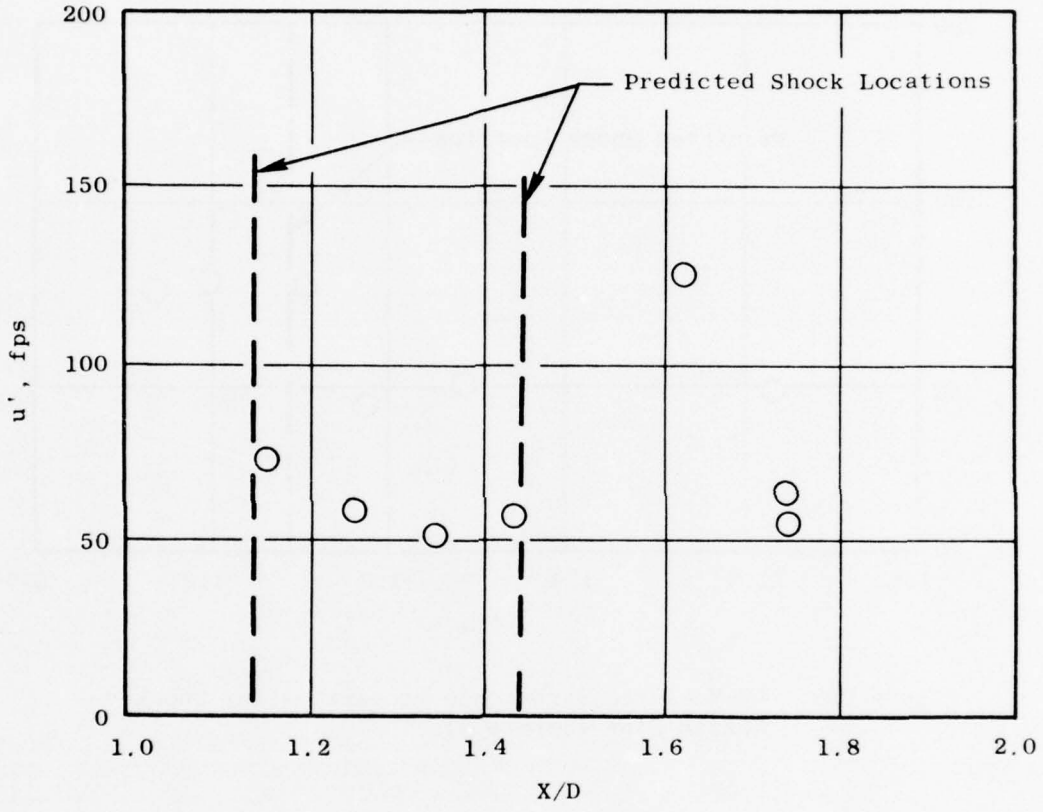


Figure 227. LV-Measured Turbulence Properties for Shocked Nozzle Flow (Series 2).

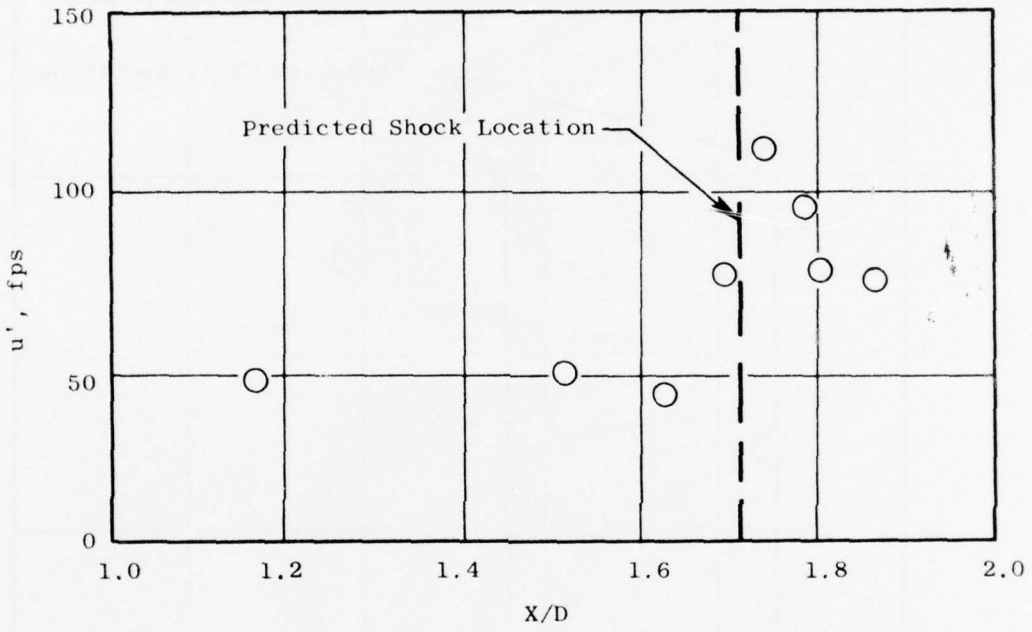


Figure 228. LV-Measured Turbulence Properties for Shocked Nozzle Flow (Series 3).

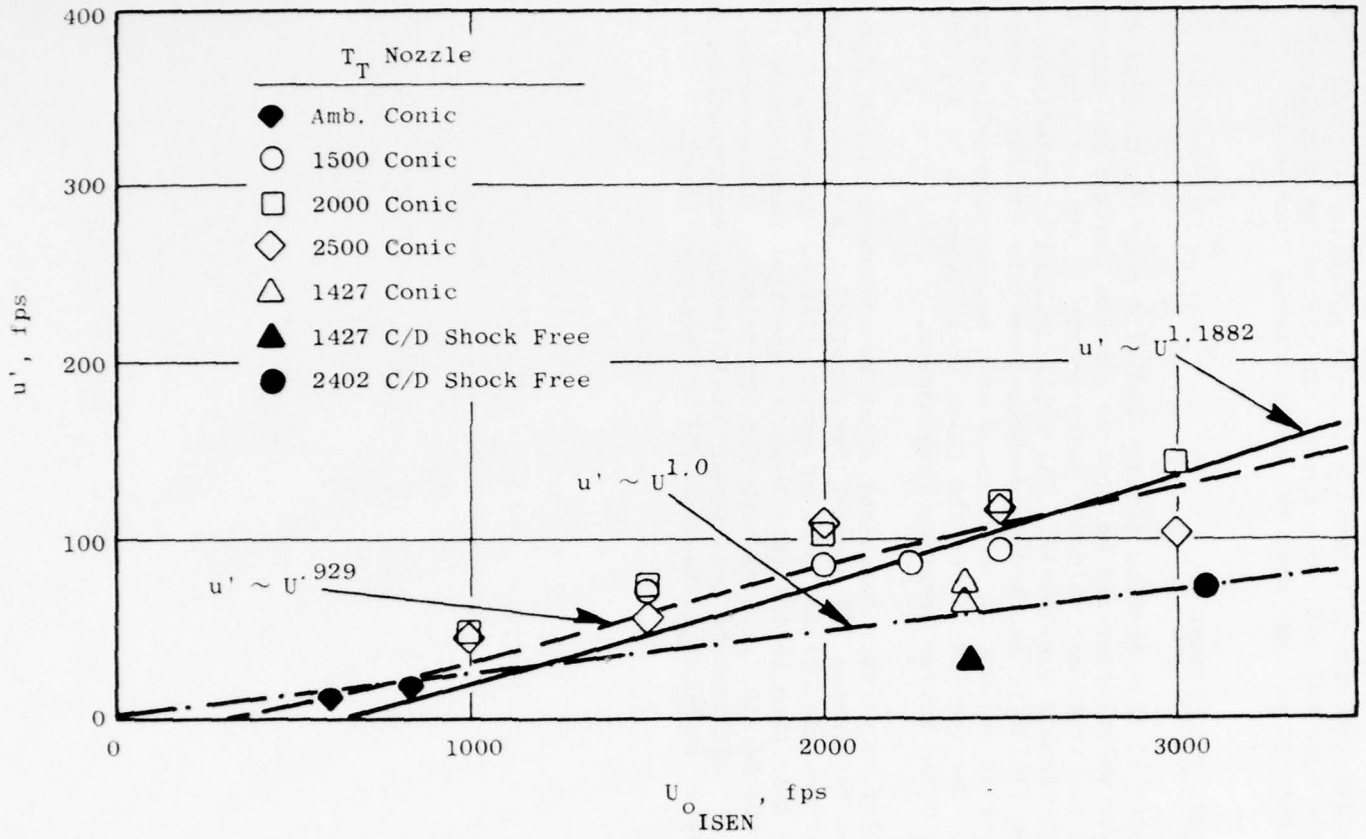


Figure 229. Influence of Jet Velocity on Exit-Plane Turbulence.

The influence of upstream temperature over a range of velocities on exit-plane turbulence is illustrated in Figures 229 and 230. Figure 231 shows that the relative turbulence intensity is only slightly affected by temperature for model scale nozzles; and, once again, the shock-free turbulence level is observed to be less than the conic shocked-flow-level.

1.4 SUMMARY AND CONCLUSIONS

The results of this section clearly indicate that the General-Electric-developed laser velocimeter can be used to perform routine and accurate mean velocity and turbulent velocity measurements in exhaust plumes where they were unobtainable previously. The applicability of this instrument for examining flow fields of shocked- and shock-free jets for the purpose of better aerodynamic definition and aeroacoustic source term definition was demonstrated. The results showed the laser velocimeter to be a prime candidate for noise source location development.

The ability to perform turbulent spectrum measurements has also been mentioned (see References 139 and 142 for details). In this area the General Electric laser was also found to be of great utility. However, it would be misleading at this time to indicate that the spectral measurements are routinely performed (as are done with the rms velocity measurements). Although it is felt that this type of measurement could become more routine, more work and refinement of computer software would be necessary first.

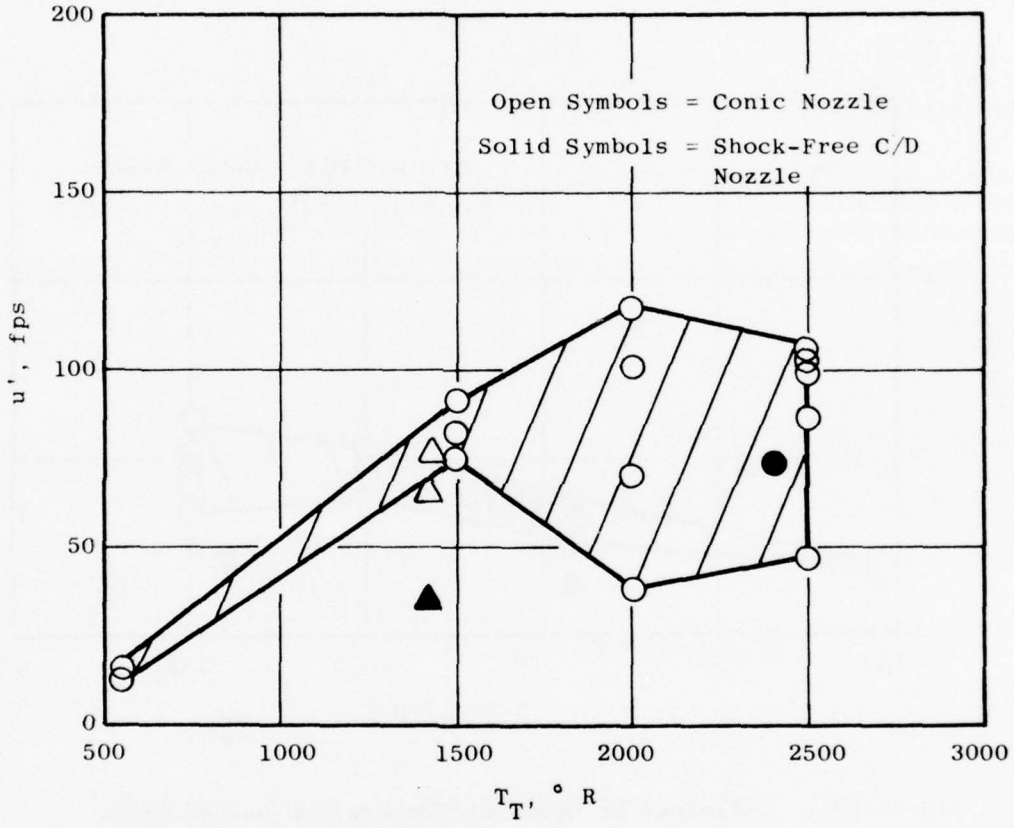


Figure 230. Influence of Upstream Temperature on Jet Exit-Plane Temperature.

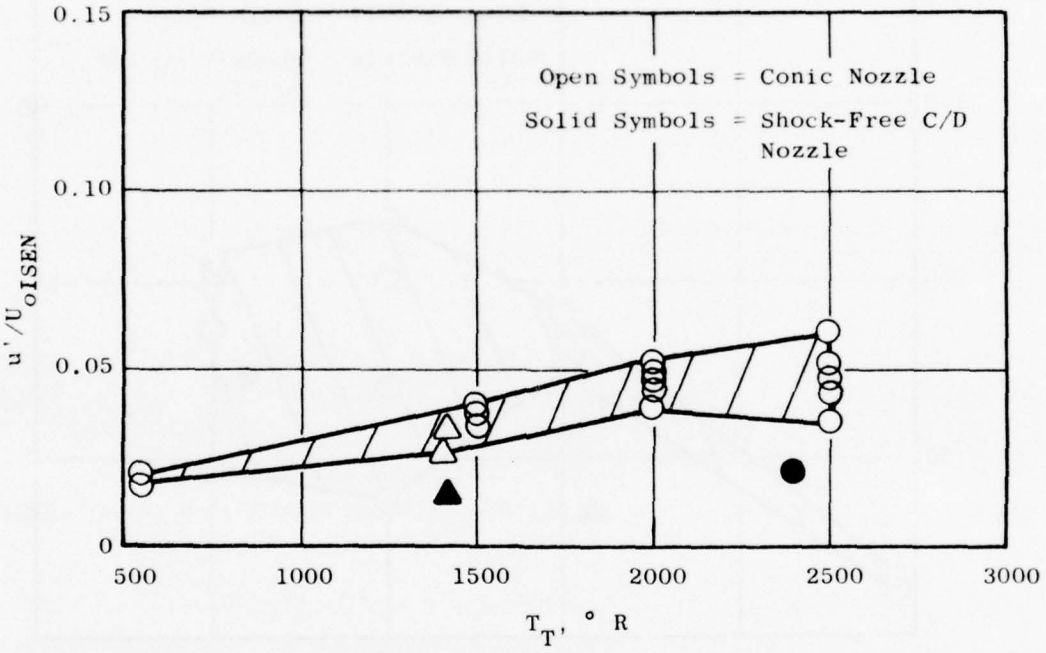


Figure 231. Influence of Upstream Temperature on Jet Exit-Plane Turbulence Intensity.

SECTION 2.0

IN-JET/FAR-FIELD CROSS-CORRELATION EXPERIMENTS

P. Scott F. Ahlgrin P. Knott

2.1 BACKGROUND

The subject of in-jet noise source location has been of interest for a number of years. Particular emphasis has been placed on this area due to the Government's and industries' revived interest in developing understanding and technology associated with noise source definition and reduction for high- and low-velocity exhaust jets. In addition to many theoretical considerations (such as selection of the proper noise source terms), the selection of the proper instrumentation to perform such measurements is of importance if the developed techniques are to be used in more than the most ideal laboratory conditions.

Key developers of the concepts of in-jet cross-correlation/noise source location techniques have been Meecham[143], Lee and Ribner[41], Siddon[144], and many others. The users of causality principles have primarily worked with pressure probes or hot-wire/hot-film probes. A degree of sophistication has been obtained in previous studies; however, the presence of the probe and its influence in the sound field is always a difficult task to assess. Additionally, the probe durability under the extreme conditions expected for industry's applications has also been of much concern (Reference 145 indicates that work along this line is progressing).

The point of view taken in the following study was to develop the techniques advanced by researchers for in-jet to far-field noise source location for the laser velocimeter. Because of the technology development in laser velocimetry, particularly at the General Electric Company, it was decided to extend the capability of our laser velocimeter to perform in-jet to far-field cross correlation and noise source location.

Discussed below is a study aimed at demonstrating the feasibility of the technology for utilizing the laser velocimeter for noise source correlation. The study indicates the additional analytical complications necessary when treating a signal of discrete character as opposed to continuous-type signals. The results show that the laser velocimeter can indeed be used for such measurements, but it must be pointed out that success is highly dependent on the type of signal processor used.

2.2 ACOUSTIC THEORY AND GENERAL APPROACH

Procedures have been developed to use the laser velocimeter to make in-jet pressure to far-field pressure correlation measurements. The technique used

was developed by Lee and Ribner[41] and involves manipulation of the Lighthill equation to obtain the correlation between the far-field pressure contribution due to an element of jet and the total far-field pressure in terms of the in-jet velocity of the jet element and far-field pressure. We repeat the derivation of this result. Starting with the Proudman formulation of the Lighthill equation:

$$dp'(t) = \frac{\rho_o}{4\pi X C_o^2} \frac{\partial^2}{\partial t^2} U_x^2 \, (t-X/C) \, dv \tag{211}$$

where, $dp'(t)$ is an element of the far-field pressure

U_x (t) is the in-jet velocity in the direction of the far-field observer
x is the distance between the observer and the jet element
and, ρ_o and C are the static density of air and the velocity of sound.

We now multiply both sides of this equation by $p(t)$, the far-field pressure, and take expectations of both sides; assuming that all linear operators commute, we have:

$$d\, E\left[p'(t)\, p\, (t+\tau)\right] = \frac{\rho_o}{4\pi X C^2} E\left[\frac{\partial^2}{\partial t^2} U_x^2 \, (t-X/C)\, p\, (t+\tau)\right] dv \tag{212}$$

By the linear operation theorem of probability[146], we may commute the derivative and expectation operators to obtain:

$$d\, E\left[p'(t)\, p\, (t+\tau)\right] = \frac{\rho_o}{4\pi X C^2} \frac{\partial^2}{\partial \tau^2} E\left[U_x^2 \, (t-X/C)\, p\, (t+\tau)\right] dv \tag{213}$$

Finally, if all processes are stationary and ergodic, we may replace the ensemble averages with time averages, so that:

$$d\overline{p'p}(\tau) = -\frac{\rho_o}{4\pi X C^2} \frac{\partial^2}{\partial \tau^2} \overline{U_x^2 p\, (\tau+X/C)}\, dv \tag{214}$$

In other words, we find that the contribution to the far-field pressure autocorrelation function from an element of jet volume is proportional to the second derivative with respect to lag of the cross correlation between the in-jet velocity squared and the far-field pressure evaluation at the retarded time, x/c.

In our experiments, we attempt to determine the quantity of the LHS of equation 214 by computing the quantity of the RHS. Because the laser velocimeter (LV) is to be used to measure the in-jet velocity, a special cross-correlation estimator is developed to cope with the random arrival of velocity information at the LV output. The required computations are realized on a PDP 11/45 mini-computer, which also controls the taking of the data and the intersample timing.

The sections that follow deal with a theoretical development of the random sample correlation estimator and an explanation of the sampling scheme used. The method selected for estimating the second derivative in equation 214 is discussed together with the special window function developed to reduce the variance of the statistic. Results of a simulation performed to test the computer programs and demonstrate the convergence of the estimator are given. The last section describes a series of demonstration experiments.

2.3 THE RANDOM SAMPLE CORRELATION ESTIMATOR

Because the operation of the laser velocimeter (LV) is based on the random arrival of particles at the probe volume, velocity information is available only as point estimates at random times. Thus, a special estimator is required to construct the cross correlation between the square of the LV output and the far-field microphone data. The approach we use is based on interpreting "expectation" as a discrete time average, as we may do for stationary, ergodic processes. We use the random arrival of an LV point to trigger the sampling of an equispaced far-field pressure record, square the velocity value, and form the product with the points in the microphone data record. This gives us one ensemble of lag values. Successive ensembles are then averaged to obtain the required amount of statistic stability. Thus, the equation for the cross-correlation estimator is:

$$\widehat{\overline{U_x^2 p(n_T)}} = \frac{1}{N} \sum_{i=1}^{N} U_x^2 \ (t_i)\ p\ (t_i + nT) \tag{215}$$

where the t_i are n random times at which velocity samples are available at the LV output. If the retarded time, X/C, is longer than the retarded time minus the largest lag value of interest, the arrival of a velocity sample may be used to trigger the pressure record sampling. This is illustrated in Figure 232. It is easy to show that $\widehat{U_x^2 p(nT)}$ is in an unbiased estimate of $E[\widehat{U_x^2 p(nT)}]$, since we have:

$$E\left[\widehat{U_x^2 p(nt)}\right] = \frac{1}{N} \sum_{i=1}^{N} E\left[U_x^2\ (t_i)\ p\ (t_i + nT)\right]$$

$$= E\left[U_x^2 p\ (nT)\right] \tag{216}$$

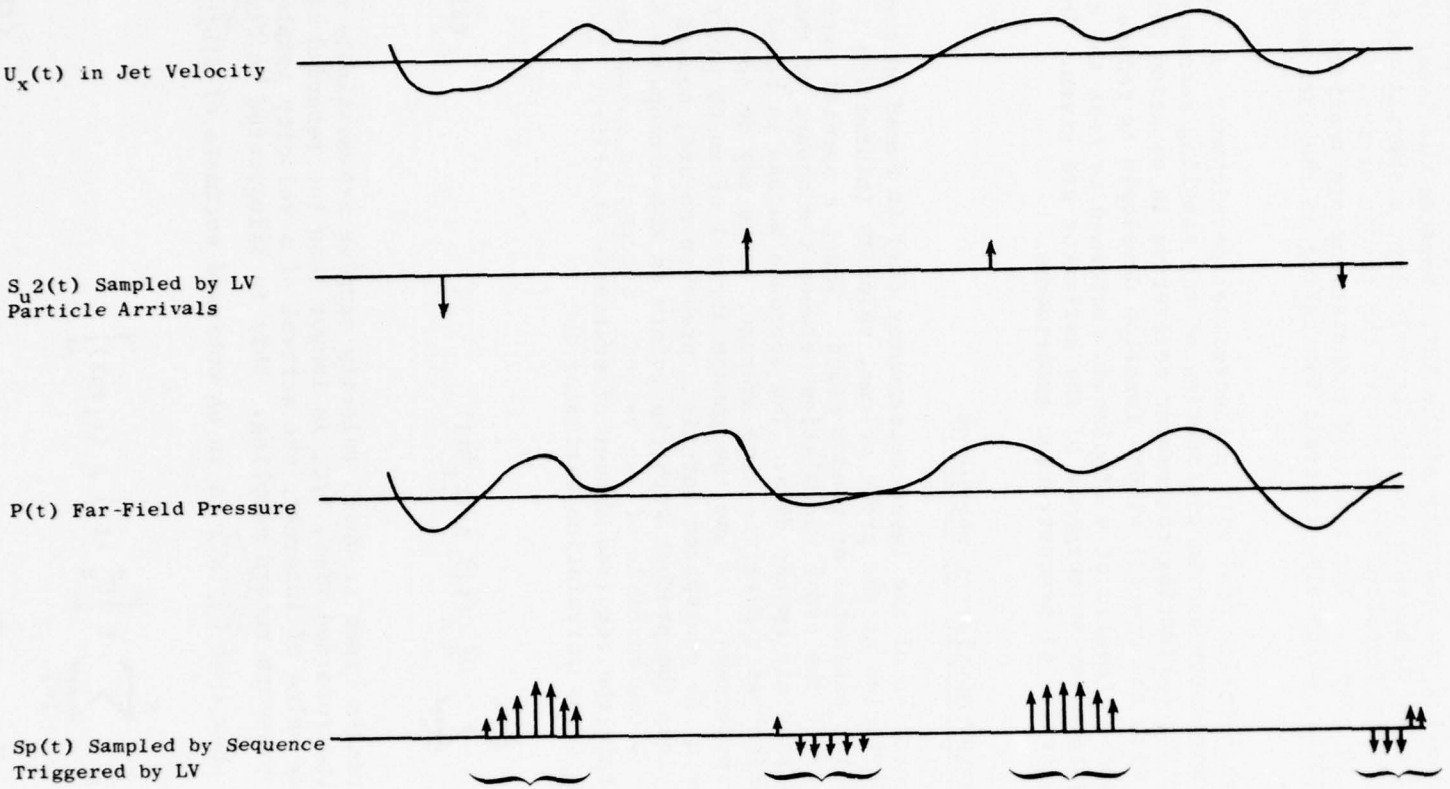


Figure 232. Schematic of Sampling Scheme.

The variance of the estimator may be determined assuming U_x^2 and $p(t)$ are jointly normal random variables and $E[p(t)]=0$. This gives:

$$\text{VAR}\left[\widehat{U_x^2 p}(nT)\right] = \frac{\sigma^2_{U_x^2}\,\sigma^2_p}{N}\left[1 + \rho^2_{U_x^2 p}(nT)\right] \tag{217}$$

where:

$$\sigma^2_{U_x^2} = \text{VAR}\,(U_x^2)$$

$$\sigma_{p^2} = \text{VAR}\,(p^2)$$

and, $\rho_{U_x^2 p}$ is the correlation coefficient as a function of lag value between U_x^2 and p.

Thus, the variance of the estimator is finite and the estimate converges to the true value as $1/\sqrt{N}$. If we assume the N is large enough to invoke the Central Limit Theorem, we may write a confidence statement for $\overline{U_x^2}\ p(nt)$ as:

$$\left|\ \widehat{\overline{U_x^2 p}(nt)} - U_x^2 p(nt)\ \right| \leq Z_{\alpha/z}\sqrt{\frac{1-\rho(nt)_{U_x^2 p}}{N}}\ \sigma_{U_x^2}\sigma_p \tag{218}$$

which is true with a probability of $(1-\alpha)$, where $Z_{\alpha/2}$ is the point on the unit normal distribution corresponding to the cumulative upper tail probability of $\alpha/2$. Thus, we have determined a method of estimating the cross correlation between the in-jet velocity squared and the far-field pressure.

The cross-correlation estimator is realized using a PDP 11/45 computer equipped with an AD converter, remote trigger, and real time clock in the form of a Digital Equipment Corporation LPS (Lap Peripheral System). Arrival of an LV output signals the computer via the remote trigger line to read the LV output using one channel of the A/D converter and to start the real-time clock. The clock times the delay to the first required pressure value and a second A/D channel is used to digitize an equispaced pressure data record. The computer then squares the velocity value and multiplies it by all points in the pressure record to form a lag ensemble. The new lag ensemble is then added to the previous data. The process is repeated until enough ensembles are added to obtain sufficient accuracy in the estimate as computed by equation 218. The result is then divided by the total number of ensembles added to obtain the average lag value as required by equation 216.

Now that we have developed a technique to obtain the cross-correlation function from LV and microphone data, we need a method for estimating its second derivative. We may show that there are several identities for the

second derivative of the cross-correlation function. Some of these are:

$$\frac{\partial^2}{\partial_\tau{}^2}\ \overline{U}^2 p(\tau) = -\frac{\partial}{\partial_\tau}\ \overline{U^2 \frac{\partial p}{\partial_t}}\ (\tau) \tag{219}$$

$$= \overline{U^2 \frac{\partial^2}{\partial_\tau{}^2}\ p(t)}\ (\tau) \tag{220}$$

$$= -\frac{1}{2\pi} \int_{-\infty}^{\infty} (-\omega^2) \left[\int_{-\infty}^{\infty} \overline{\overline{U}^2 p(\tau)}\ e^{-i\omega\tau} d\tau \right] e^{i\omega\tau}\, dw \tag{221}$$

Equations 219 and 220 suggest we may take one or two derivatives of the pressure, before it is sampled, if we are sure these quantities are sufficiently band-limited for our analysis. Equation 221 suggests that we may perform the differentiation in the frequency domain by multiplying the associated cross spectrum by ω^2. A modification of this approach is to operate on the sampled version of the cross correlation with a set of weights which we may derive using Shannon's sampling theorem(147). Under the assumption that the cross spectra satisfies

$$S_{U_x^2 p}\ (\omega) = 0 \text{ for } |\omega| > \frac{\pi}{T} \tag{222}$$

where T is the spacing of the cross-correlation samples, $U_x^2 p(\tau)$ is related to its sampled version by:

$$U_x^2 p(\tau) = \sum_{n=-\infty}^{\infty} U_x^2 p(nT)\ \frac{\text{Sin}\ (\frac{\pi\tau}{T} - n\pi)}{(\frac{\pi\tau}{T} - n\pi)} \tag{223}$$

By directly differentiating both sides, we have:

$$\left.\frac{\partial^2 \widehat{\overline{U_{xp}^2(\tau)}}}{\partial \tau^2}\right|_{\tau=kT} = -\frac{\pi^2}{3T^2}\,\widehat{\overline{U^2p(kT)}} + \sum_{\substack{n=-\infty \\ n\neq k}}^{\infty} -\frac{(-1)^n}{T^2n^2}\,2\,\widehat{\overline{U^2p}\,[(k-n)T]} \qquad (224)$$

This is an unbiased estimate of the second derivative under the band-limited assumption. It also gives a smaller error, when $S_{U_x^2\,p}(\omega)$ is not exactly band-limited, than other derivative estimates based on weights. Take, for example, the "standard" three-point estimate of the second derivative:

$$\frac{\partial^2}{\partial \tau^2}\,\overline{U_{xp}^2(nT)} = \frac{1}{T^2}\left\{U_{xp}^2\left[(n-1)\,T - 2\,\overline{U_{xp}^2(nT)} + U_{xp}^2\quad(n+1)T\right]\right\} \qquad (225)$$

Figure 233 shows the comparison between the "Shannon theorem" estimate: and the "three-point" estimate of the second derivative of the cross-correlation function whose cross spectrum is also shown. From Figure 234 we observe two things. First, the Shannon estimate has an associated bias error about half of the three-point estimate. Second, for the bias error to be reduced to 10%, $T = \pi/\omega_c$ must be about 30 times the three dB point of the cross spectrum. This is because taking the second derivative is equivalent to multiplying the cross spectrum by $(-\omega^2)$. Thus, the "tails" are greatly accentuated. The stability of the second derivative is difficult to measure in terms of parameters available to the experimenter before the data are taken. A rather crude series of approximations suggests that:

$$\left|\frac{\partial^2}{\partial \tau^2}\,\widehat{U_{xp}^2(\tau)}\right|_{\tau=kT} - \left.\frac{\partial^2}{\partial \tau^2}\,U_{xp}^2(\tau)\right|_{\tau=kT} \leq \sqrt{\frac{40}{N}}\;\frac{\sigma_{U_x^2}\sigma_p}{T^2}\,Z_{\alpha/2} \qquad (226)$$

might be true with a probability of $(1-\alpha)$. More work should be done to obtain a better confidence statement for the second derivative estimator.

Finally, to reduce the variance of the estimate, the cross-correlation function is multiplied by a window function before the derivative is estimated. The window function $\omega(nt)$, has properties:

$$\omega(0T) = 1 \qquad (227)$$

$$\omega(nT) = 0 \text{ for } n \geq N \qquad (228)$$

and,
$$\omega(nT) = \omega(-nT) \qquad (229)$$

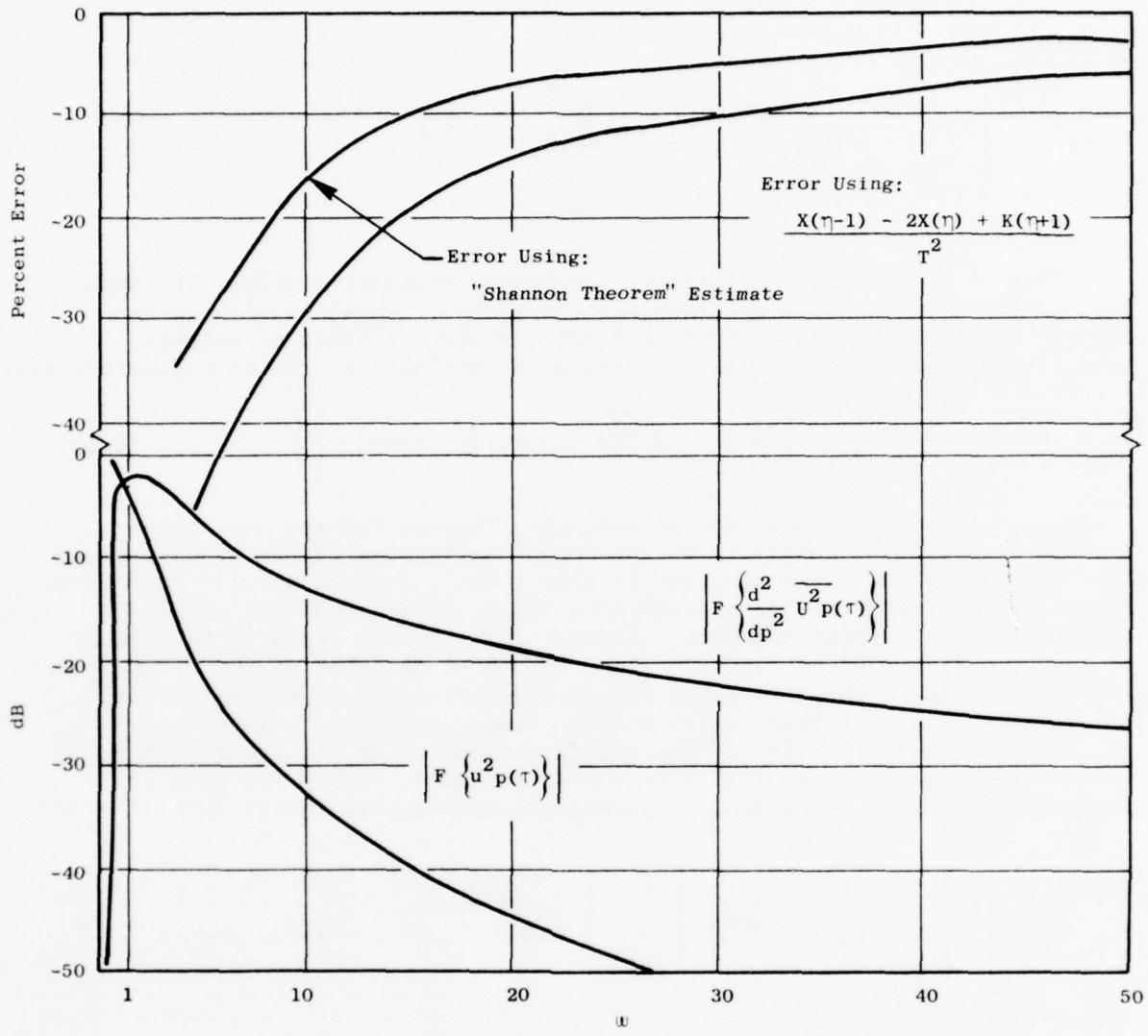


Figure 233. Bias Error in Derivative Estimate as a Function of Cut-Off Frequency.

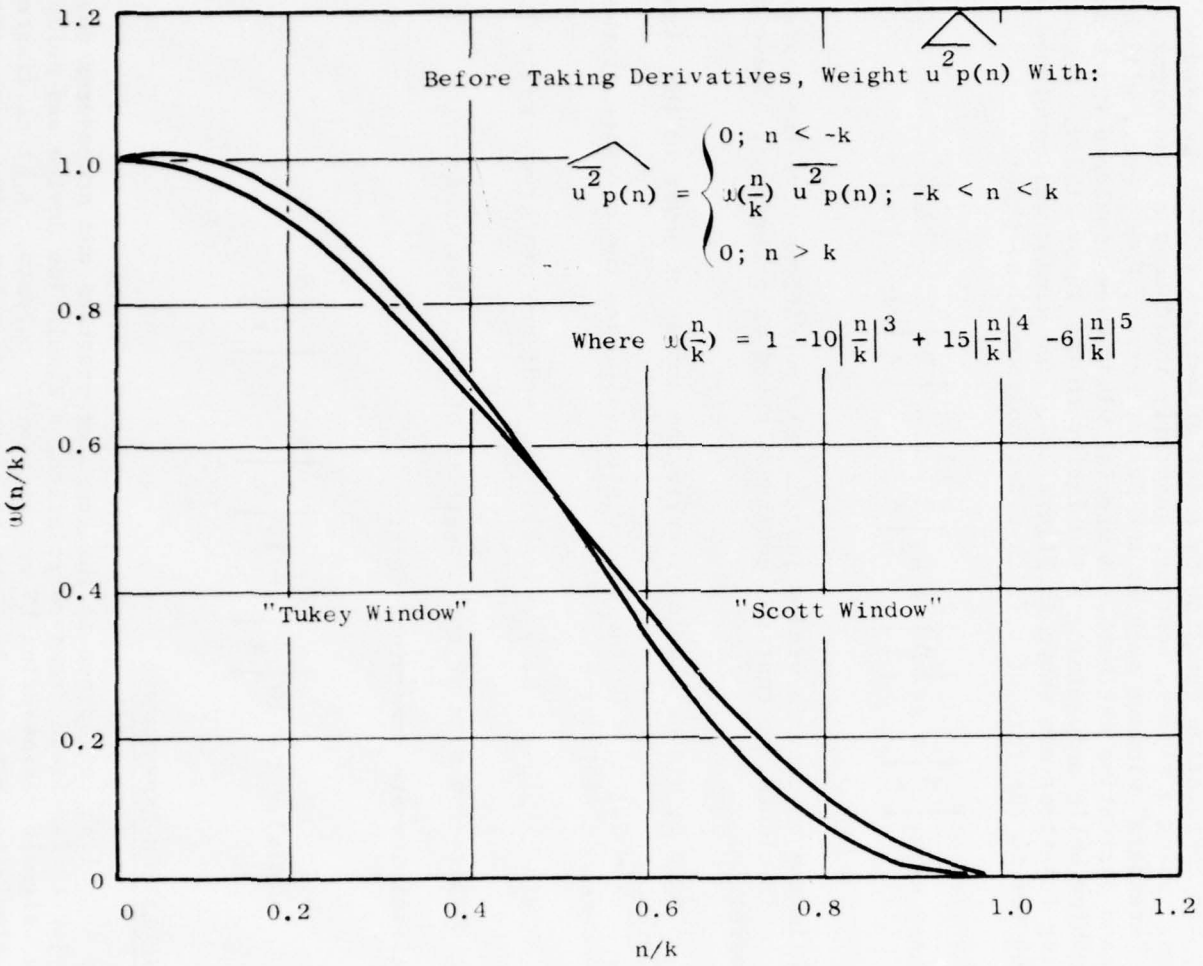


Figure 234. Influence of Window Function to Improve Stability of Second Derivative.

The purpose of the window may be seen through the following reasoning. By equation 217 we note that the variance of each point in the cross correlation has about equal error, independent of value. Thus, the smaller the value of a point in the cross correlation, the higher the fractional error associated with the point. In estimating the second derivative, we would like to give less attention to the high-error points than the low-error points, so we multipy the correlation function by a set of weights called the window function. Using a window, however, generally introduces a bias error. Most of the "standard" windows such as the Tukey, Parzen, Hann, etc., will bias the second derivative estimate. A special window was developed which avoided this problem while maintaining a simularity to the Tukey window. These weighting functions are shown in Figure 234. The window was developed by assuming for it the form of a fifth-order polynomial so that:

$$\omega(n/k) = a_o + a_1 \left|\frac{n}{k}\right| + a_2 \left|\frac{n}{k}\right|^2 + a_3 \left|\frac{n}{k}\right|^3 + a_4 \left|\frac{n}{k}\right|^4 + a_5 \left|\frac{n}{k}\right|^5 \qquad (230)$$

where k is the adjustable window length. Six conditions were then established on the coefficients, so that the constants could be determined. These conditions were:

1. $a_o = 1$, window should preserve the amount of power in the signal.

2. $a_1 = 0a$; $a_2 = 0$; the window shouldn't bias the estimate of the second derivative.

3. $\omega(n/k)\big|_{n = k} = 0$; $\frac{\partial}{\partial n}(n/k)\big|_{n = k} = 0$; and $\omega(n/k)\big|n = k/2 = 0.5$

which preserve some of the properties of the Tukey window.

The coefficients are determined to give

$$\omega(n/k) = 1 - 10\left|\frac{n}{k}\right|^3 + 15\left|\frac{n}{k}\right|^4 - 6\left|\frac{n}{k}\right|^5.$$

2.4 SIMULATION EXPERIMENTS

To establish confidence in the computer programs and procedures developed for in-jet to far-field cross correlation, a simulation device was built to provide signals representing LV and microphone outputs. A block diagram of the simulation hardware is shown in Figure 235. Two White noise generators were used to supply uncorrelated Gaussian noise sources. These sources were then filtered to give them spectra like those expected in the actual experiment to be conducted. These are shown in Figure 236. A constant

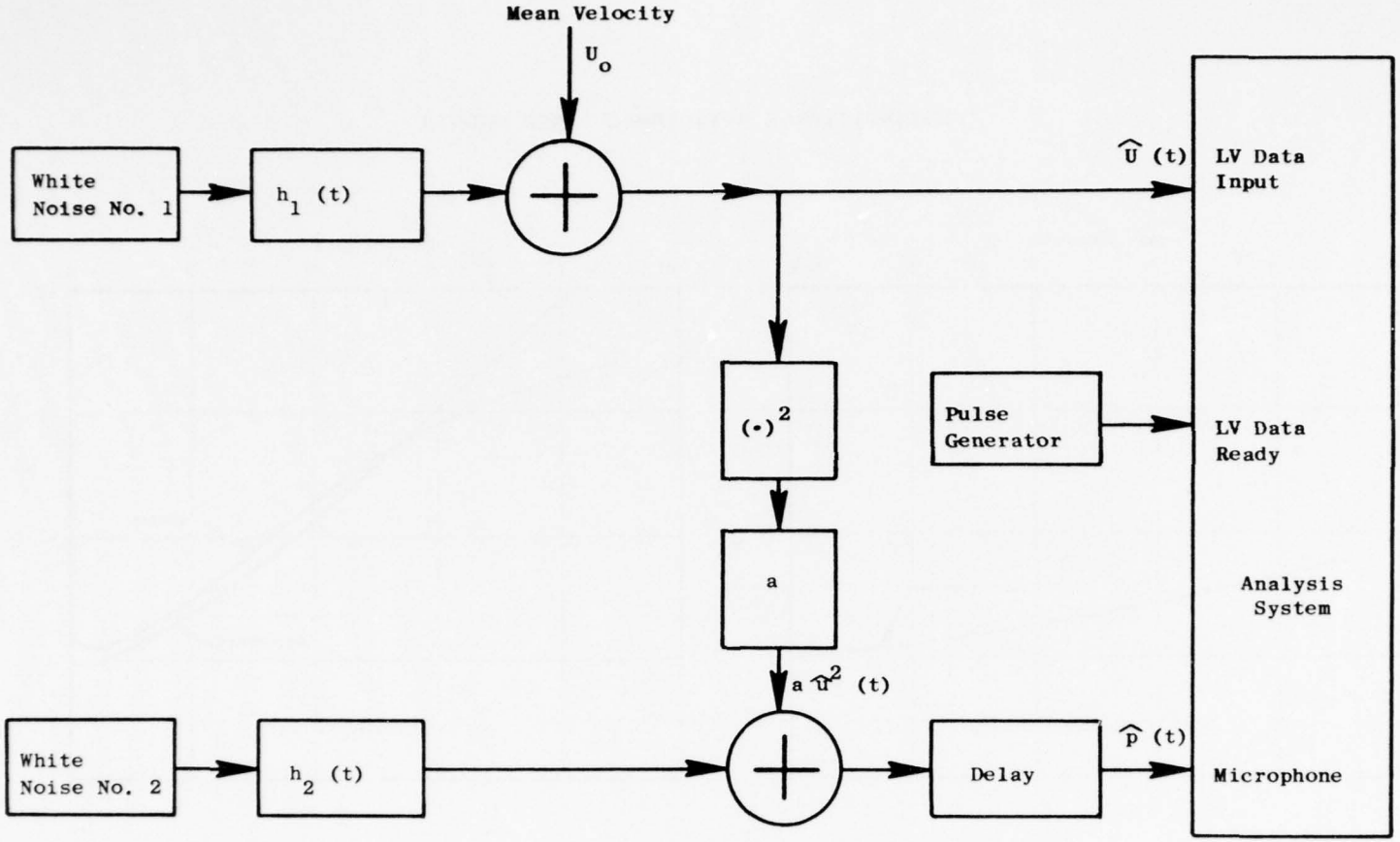


Figure 235. Schematic of System Used to Generate Simulated Data.

Expected Jet and Far Field Conditions: $u/U = 0.2$, $M_j = 0.8$, $X/D = 4$, $R/R = 1$

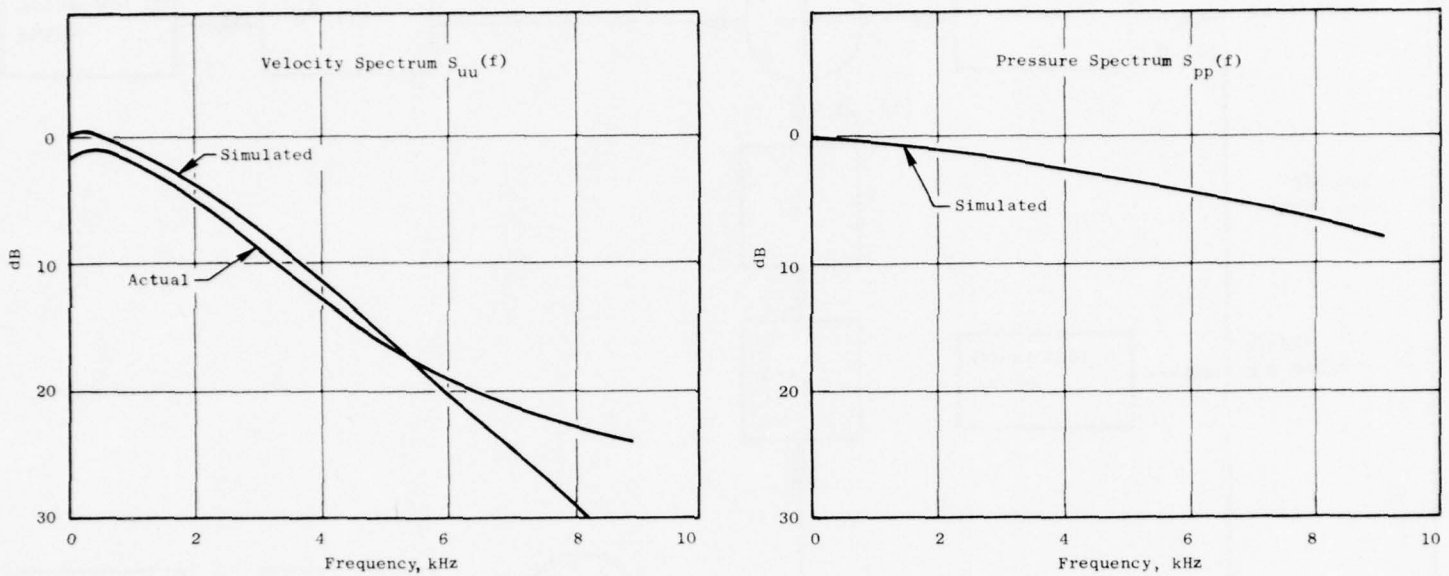


Figure 236. Simulation Specifications.

value was added to the velocity channel to represent the mean velocity and this signal was then sent though an analog squaring circuit and added to the pressure channel. The pressure signal thus was correlated to the velocity squared. The simulator was used to obtain estimates of

$$\overline{U_x^2 p}(\tau) \text{ and } \frac{\partial^2}{\partial \tau^2} \overline{U_x^2 p}(\tau)$$

for cases where the correlation coefficient between U_x^2 and p(t) was 0.1, 0.3 and 1. The number of data ensembles averaged in each case was 20,000, 100,000, and 500,000.

The 500,000 ensemble average represents a definite practical upper limit on data processed, since it represents about 4 hours of test data. The results show that for these conditions, it is easy to resolve when $\rho = 1$ and fairly easy when $\rho = 0.3$. However, when $\rho = 0.1$ difficulty was encountered in obtaining a reliable estimate of the second derivative. This may be seen by examining Figures 237 through 239. The pressure spectrum in the simulation contained frequency components far above those in the velocity squared, and this fact made estimating the second derivative difficult.

2.5 CROSS-CORRELATION EXPERIMENTS WITH GENERAL ELECTRIC'S LASER VELOCIMETER

In order to verify the concepts for in-jet to far-field cross correlation and noise source location using a laser velocimeter, a demonstration experiment was performed at General Electric's JENOTS facility. The aim of the experiment was to assess the capability of General Electric's laser velocimeter of performing cross-correlation-type measurements, and to examine our first cut at setting up a proper random data and error analysis acceptable for the discrete signals of the laser velocimeter instrument. This experiment can and should be thought of as only a first try in the complicated development chain for extending the capability of the laser velocimeter for performing advanced-type measurements in realistic exhaust jets.

2.5.1 Experimental Arrangement and Test Conditions

The experiments were performed at General Electric's outdoor test site (JENOTS). A 4-5/8" diameter conic nozzle was used as the test nozzle. The laser was set up so that the measuring control volume was centered 30° off the centerline jet axis. The measuring volume was located at an axial station of four diameters, and a radial location of one-half diameter (the region of peak turbulence). The far-field microphone (a 4136 B&K) was located 50 diameters away at the 30° jet angle position. Preliminary tests were taken with the microphone in the horizontal plane of the jet. However, the reflected wave was found to influence the shape of the cross-correlation function in the region of the retarded time. In order to move the reflected wave farther away from the retarded time, the microphone was raised slightly. This put the

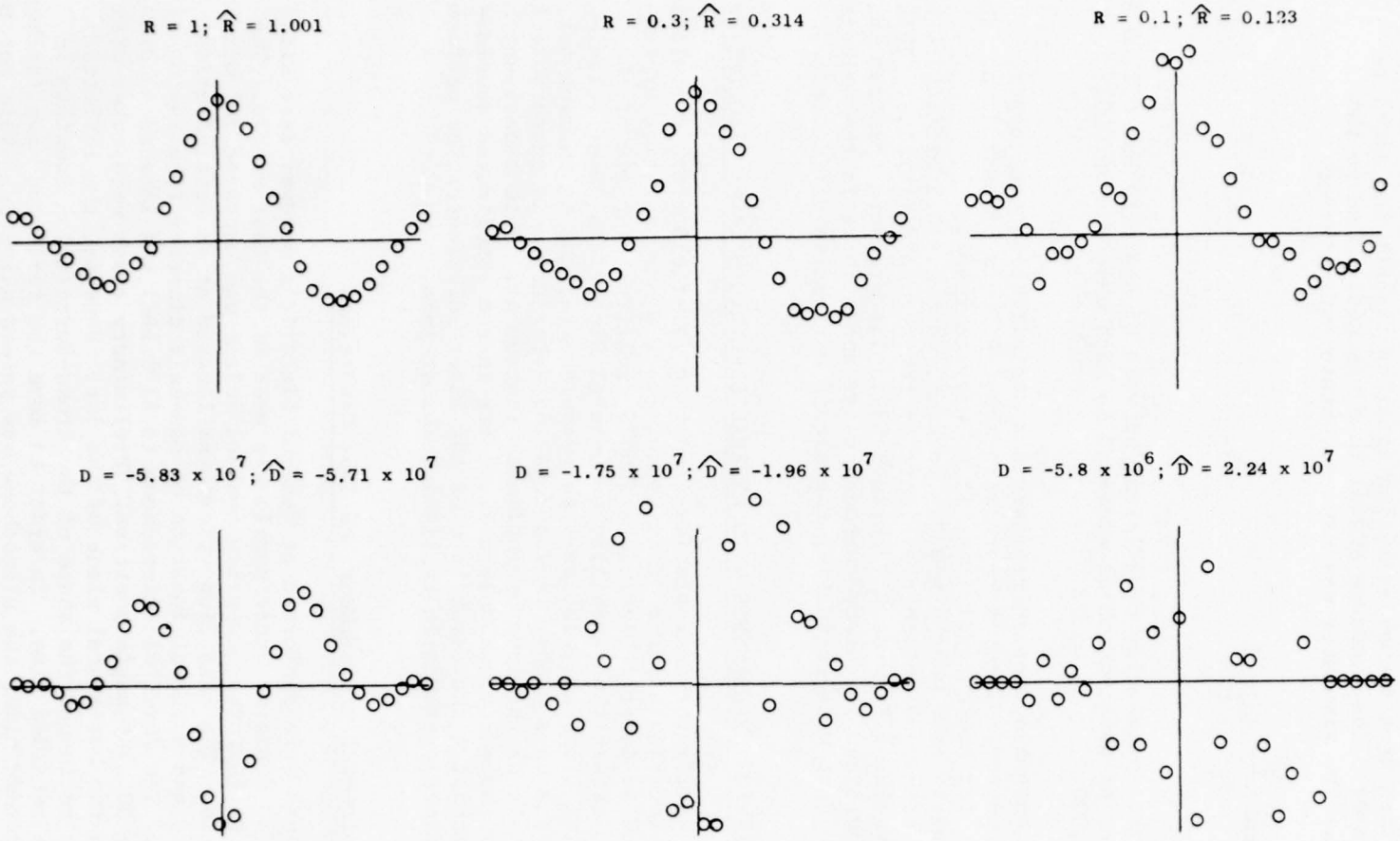


Figure 237. Analysis of Simulated Data, N = 20,000 Samples.

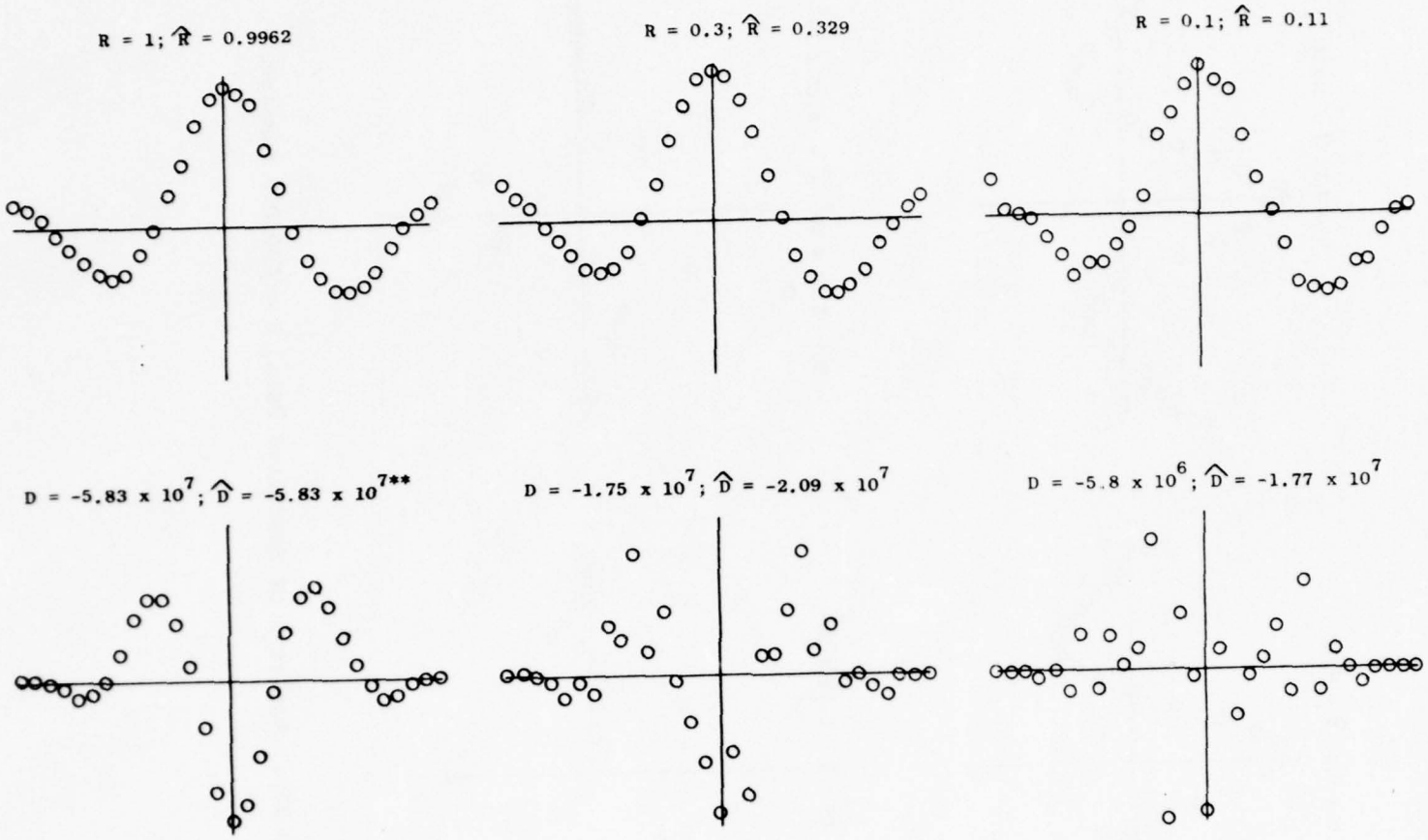


Figure 238. Analysis of Simulated Data, N = 100,000 Samples.

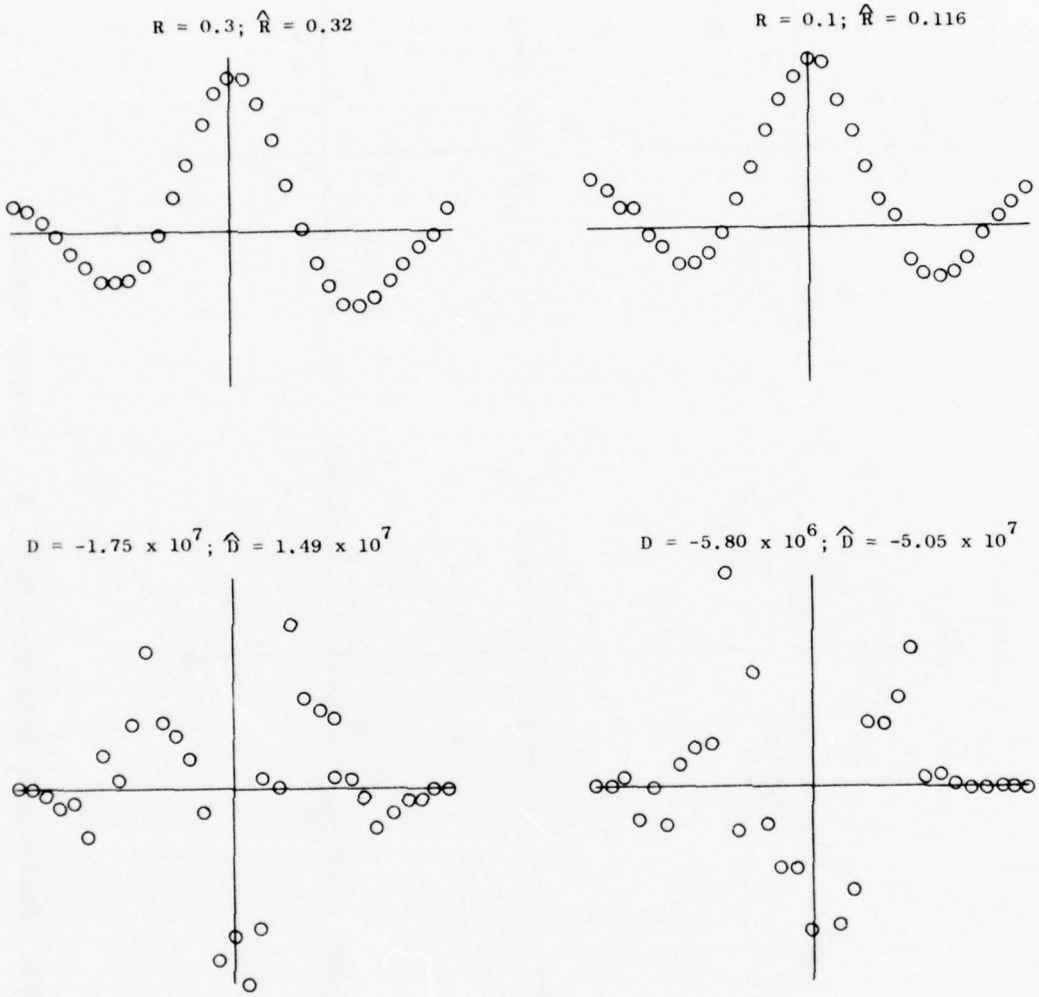


Figure 239. Analysis of Simulated Data, N = 500,000 Samples.

microphone 7° out of the plane of measurement. Figures 240 and 241 illustrate the arrangement used for performing the measurements.

The flow test conditions were a pressure ratio of 1.75 and a total temperature of 700° R. The resulting exhaust velocity was 600 ft/sec.

2.5.2 Discussion of Results

The validity of the results are dependent on the sampling frequency used in the pressure data acquisition. In this case, a sampling interval of 40 μ sec was used. Thus it is assumed that the cross power spectrum (Fourier transform of the cross-correlation function) is zero above 12.5 KHz.

The cross correlation between the time-dependent velocity and the far-field acoustic pressure signal was constructed from six records of 20,000 product pair ensembles which were considered suitable for processing (120,000 average product pairs). Because the experiments were taken outdoors, there existed ambient temperature changes as well as ground reflections. Each 20,000 record sample was corrected for temperature and ground reflections.

The temperature correction involved shifting each record so that the retarded time was at the same record point. The retarded time was calculated from $\tau_r = a_o/R$ for each record. Figure 242 shows the correction applied to a typical record.

The correction of acoustic data for ground reflection is at best approximate because the reflectivity coefficient is unknown and, for the case of ideal reflection, information is lost from the record. If the ground reflection in pressure is modeled as:

$$p'(t) = p(t) + (1-\varepsilon)\, p(t - \Delta R/a_o)$$

where,

$p'(t)$ is the measured acoustic pressure

$p(t)$ is the actual acoustic pressure

ε is the absorption coefficient of the reflected surface

We find that the result of cross correlating $p'(t)$ with $v^2(t)$, the in-jet velocity squared, is:

$$R_{v^2p'}(\tau) = R_{v^2p}(\tau) + (1-\varepsilon)\, R_{v^2p}(\tau-\Delta R/a_o)$$

It may be shown (Appendix 5) that, to recover $R_{v^2p}(\tau)$, we must provide the operation:

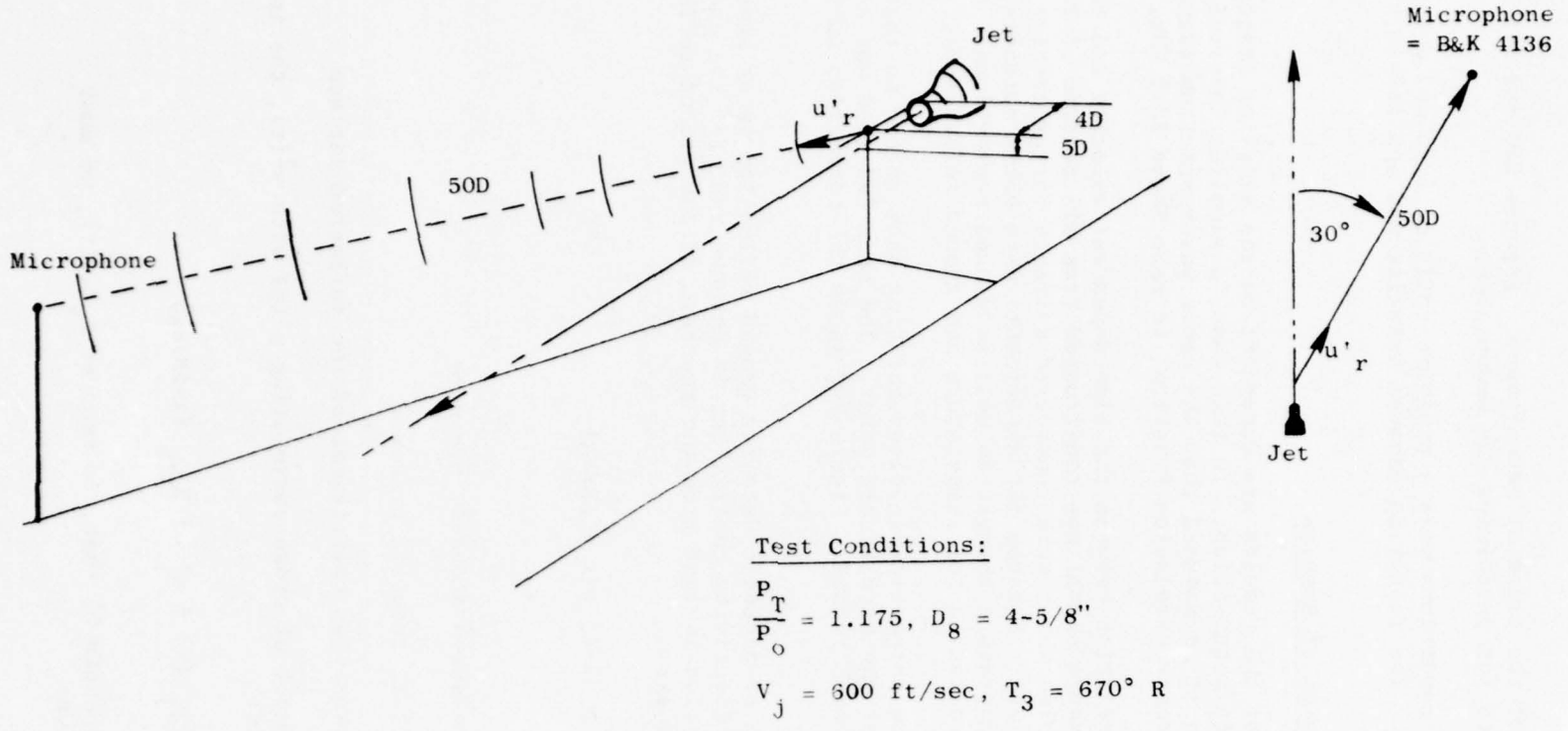


Figure 240. General Arrangement for LV to Far-Field Acoustic Cross-Correlation Experiments.

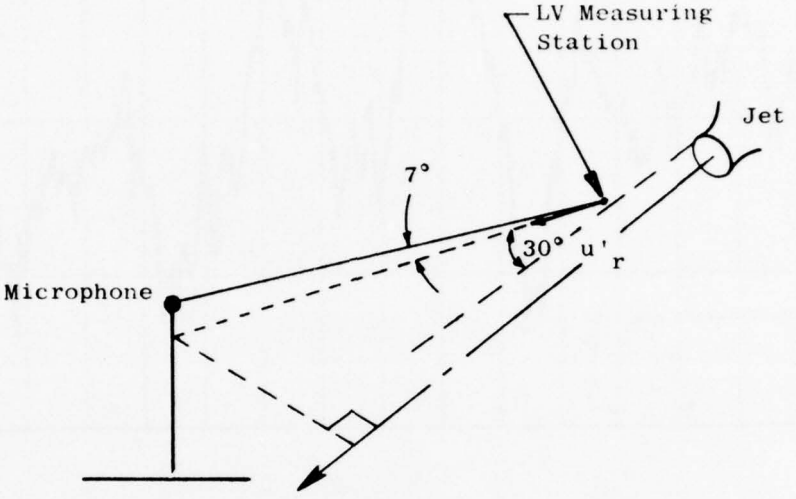


Figure 241. Test Arrangement Showing Microphone Slightly Out of Plane for LV Far-Field Acoustic Cross-Correlation Experiments.

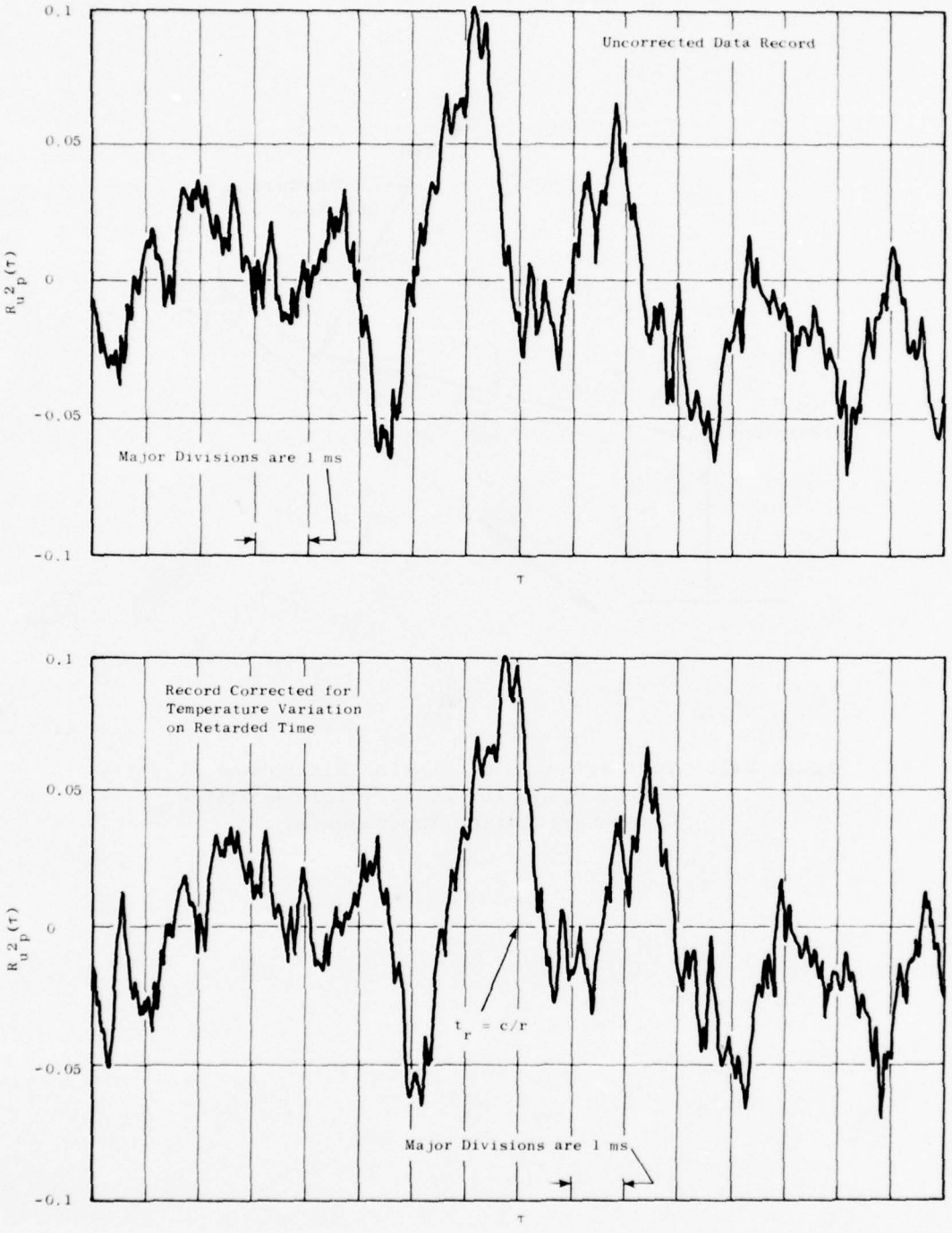


Figure 242. LV-Measured Normalized Cross Correlation of In-Jet Velocity to Far-Field Acoustic (180,000 Samples).

$$R_{v2_p}(\tau) = \sum_{k=0}^{\infty} (1-\varepsilon)^k \, R_{v2_p'}(\tau-\tau_o k)$$

From this we see that the absorption coefficient also determines the effective number of values of $R_{v2_p}'(\tau)$ necessary for the reconstruction and that the uncertainty in $R_{v2_p}(\tau)$ will increase as $\varepsilon \to 0$. Thus the choice of ε depends on:

1. The level of uncertainty in the data
2. The length of $R_{v2_p}'(\tau)$ available
3. The actual value of ε.

Experimentation with the data showed that $\varepsilon = 0.4$ is a "good" choice. Figure 243 shows the application of this filter to a typical 20,000-point cross-correlation record. Notice that the random variation of the record is increased, the peak at the retarded time becomes more symmetric, and the "image" at the ground reflection delay time is suppressed.

The correction procedure was applied to all six of the 20,000 product subensembles to obtain a 120,000 averaged product pair record. This correlation function estimate is shown with and without the ground reflection correction in Figure 244. Note the removal of the image peak and the improved symmetry of the peak at the retarded time. It may also be seen that the ground reflections will have a serious effect on the value of the second derivative evaluated at the retarded time.

The cross spectra were also evaluated. These appear as Figure 245. The bandwidth is approximately 200 Hz.

Examination of the cross-correlation records in Figure 244 indicated that direct estimation of the second derivative was not possible. Particularly, the approach based on Shannon's Theoren, which yielded unusable results due to insufficient data in the estimate. An indirect method was also attempted. The expansion of the cross-correlation function in a power series of the form:

$$R_{v2_p}(\tau) \simeq \sum_{i=0}^{\infty} a_i \, (\tau-\tau_r)^i$$

where a_i is determined by a least squares technique. The second derivative at τ_r is then:

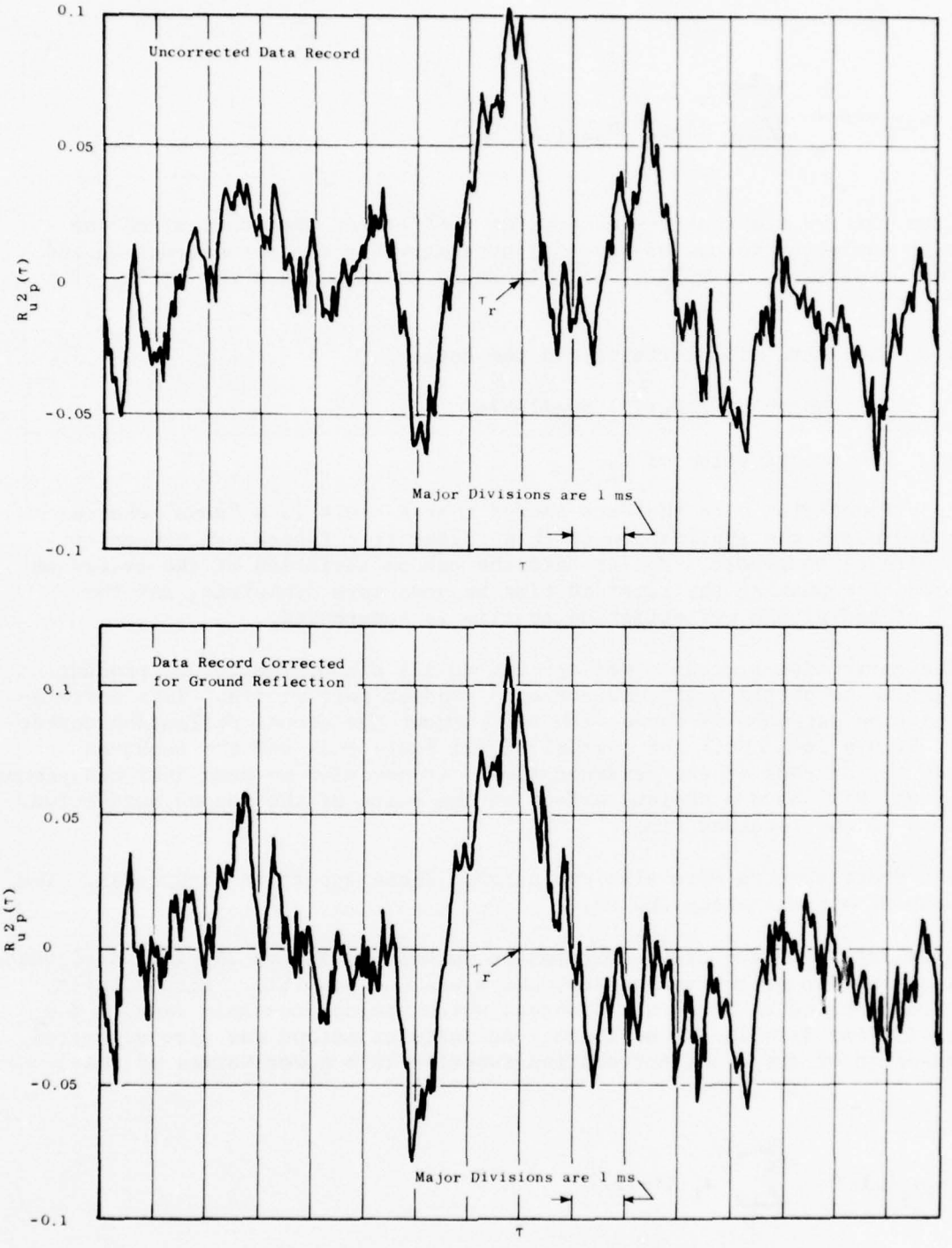


Figure 243. LV-Measured Cross-Power Spectrum.

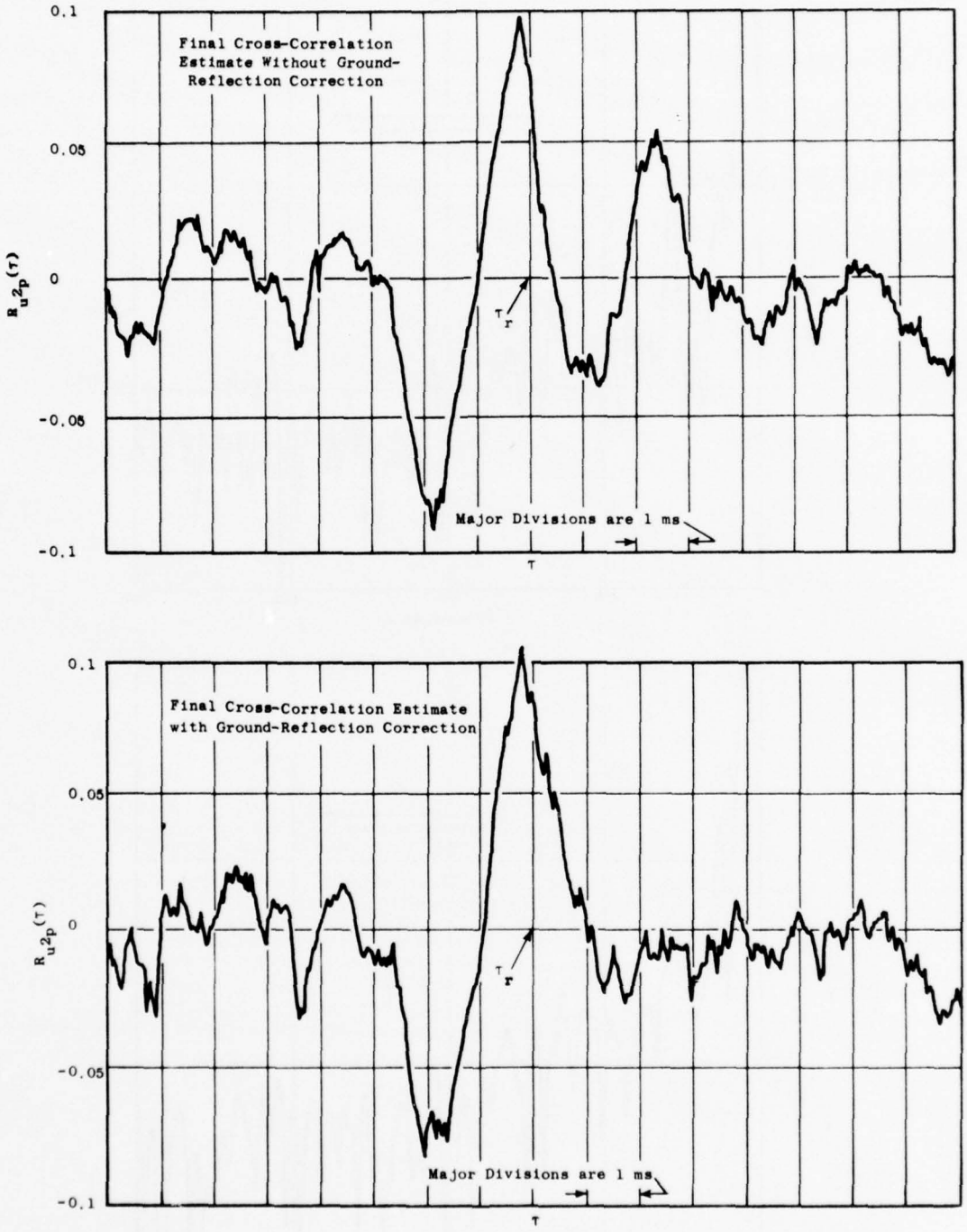


Figure 244. Expected Shape of Cross Correlation and Cross-Power Spectrum without Ground Reflection.

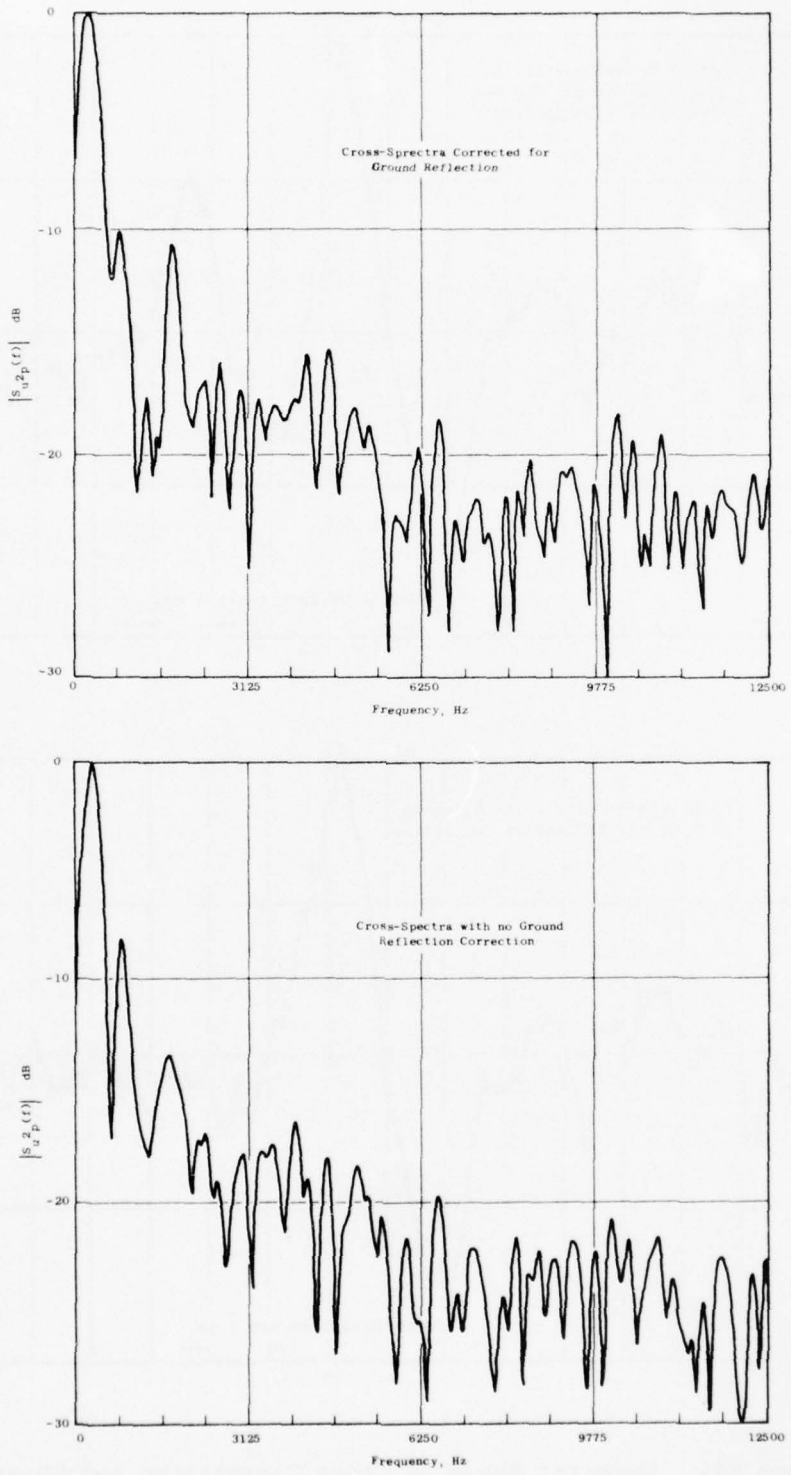


Figure 245. Cross Spectra of Final Correlation Files.

$$\left[\frac{\partial^2}{\partial\tau^2} R_{v^2p}(\tau)\right]_{\tau=\tau_r} = Z\, a_2$$

Unfortunately, a polynomial of reasonable order could not be found which sufficiently approximated $R_{v^2p}(\tau)$.

Two other methods may be suitable, but were not attempted due to insufficient time. The first may be derived from a nonlinear least squares regression analysis based on acoustic theory. The second approach could be a modification of this approach using autoregressive techniques, specifically, a new technique called Linear Predictive Filtering. Both of these techniques should be evaluated in the future. The Shannon procedure, however, would be sufficient and would provide the most accurate estimate of the second derivative if enough product pairs were used in the cross-correlation estimate.

2.6 CONCLUSIONS

The main conclusion to be drawn is that we have good indications that the laser velocimeter can soon be developed for noise source location, and for more than just laboratory environments. The cross correlation measurements discussed here, as well as the LV parametric studies for high-temperature, high-velocity jets, and the turbulent spectrum measurements performed by the General Electric Company using the laser velocimeter lift the classification of this tool into a category of noncontact-type measurement devices of a very advanced and important nature.

The statistical and error analysis approach used for construction of the cross correlation was found adequate for these demonstration experiments. However, to perform these measurements quicker and more routinely (which is highly desireable), better utilization of the validated data should and can be implemented. Current estimates are that the data efficiency can be improved by a factor of 8, and even faster data taking could occur through better seeding techniques.

Better methods of determining the second derivative by using information about the structure of the cross-correlation function based on acoustic theory are probably possible. Particularly, the application of linear predictive filtering techniques may hold the solution to this problem.

The demonstration experiment was a success, but it is evident that ways must be investigated for the handling of the reflected waves. This could be done through a test arrangement designed to move the reflected wave sufficiently away from the prime region of interest (as far as testing full-size out of doors) or by testing model scale in an anechoic environment such as that being constructed at the Aircraft Engine Group of the General Electric Company.

APPENDIX 3

TABULAR LISTING OF HOT-FILM/LV MEASUREMENT ON 4.3-INCH CONIC NOZZLE

Table 4. Hot-Film Turbulence Measurements

X/D	r/r_o	$\bar{U}$, fps	$\bar{U}/V_o$	u´, fps	u'/v_o	V_o
2.00	0.0	575.7	1.011	13.99	.025	569.32
	.35	569.3	1.000	15.14	.027	
	.66	569.3	1.000	28.12	.049	
	.83	492.6	.865	66.10	.116	
	1.00	336.9	.592	82.10	.114	
4.00	0.0	569.3	1.000	21.35	.038	
	.28	552.3	.970	28.77	.051	
	.51	511.8	.899	49.03	.086	
	.76	426.5	.749	78.89	.139	
	1.00	298.5	.524	82.09	.144	
6.00	0.0	541.6	.951	44.79	.079	
	.25	537.3	.944	51.15	.090	
	.49	490.4	.861	69.30	.122	
	.74	409.4	.719	81.02	.142	
	1.00	292.1	.513	83.17	.146	
8.00	0.0	490.4	.861	63.95	.112	
	.5	426.5	.749	66.10	.116	
	1.00	311.3	.547	81.03	.142	
	1.53	181.2	.318	68.24	.120	
10.0	0.0	422.2	.742	69.37	.122	
	.25	414.3	.728	71.34	.125	
	.49	376.6	.661	77.32	.136	
	1.00	277.5	.487	77.31	.136	
	1.52	228.0	.400	69.37	.122	
12.00	0.0	348.9	.613	63.42	.111	
	.25	340.9	.599	67.40	.118	
	.49	299.3	.526	71.36	.125	
12.00	1.00	269.6	.521	65.40	.115	
	1.52	188.31	.331	59.47	.104	
14.00	0.0	346.9	.609	65.42	.115	
	.50	297.3	.522	70.38	.124	
	1.00	277.5	.487	66.41	.117	
	1.51	222.0	.390	60.45	.106	
	2.00	168.5	.296	54.51	.076	

Table 5. LV Turbulence Measurements.

X/D	r/r_o	u´,fps	$\bar{u}$,fps	$u'/U_{1\,SEN}$
1.996	0	37	557	.066
	.347	44	561	.078
	.516	45	552	.080
	.687	58	501	.103
	.852	61	391	.109
	1.011	70	316	.125
	1.190	82	174	.146
	1.345	40	83	.071
4.00	0	56	508	.100
	.344	67	471	.119
	.681	69	392	.123
	1.011	74	321	.132
	1.270	63	236	.112
	1.516	57	172	.102
	1.779	49	97	.087

Table 6. Mj = 0.5 LV Measurements

X/D	r/r_o	u'	$\bar{u}$	u'/U_{ISEN}
4.000	2.032	39	78	.070
4.000	0	52	405	.093
4.000	.347	65	378	.070
4.000	.687	69	340	.123
4.000	1.031	56	246	.100
4.000	1.361	71	209	.127
4.000	1.695	50	118	.089
4.000	2.032	28	76	.050
4.000	2.372	17	70	.030
6.881	.485	65	217	.116
6.881	.492	62	350	.111
6.881	.492	63	347	.112
6.881	.357	54	341	.096
6.881	.222	59	347	.105
6.881	.088	71	333	.127
6.881	.061	67	302	.119
6.881	.179	70	261	.125
6.881	.485	58	212	.103
6.881	.718	47	178	.084
6.881	.960	51	133	.091
6.881	1.210	41	117	.073
6.881	1.466	35	82	.062
6.881	1.729	23	68	.041
9.99	0	42	264	.071
9.99	.344	49	254	.083
9.99	.681	49	223	.083
9.99	1.011	43	197	.073
9.99	1.355	51	177	.087
9.99	1.681	48	149	.081
9.99	2.022	39	142	.066

Table 6. Mj = 0.5 LV Measurements (Concluded)

X/D	r/r_o	u'	$\bar{u}$	u'/U_{ISEN}
9.99	2.353	38	102	.065
9.99	2.692	22	79	.037
9.99	2.726	22	61	.037
12.43	.003	39	211	.066
12.43	.347	42	197	.071
12.43	.681	43	170	.073
12.43	.997	40	166	.068
12.43	1.351	45	148	.076
12.43	1.685	47	119	.080
12.43	2.029	41	99	.070
12.43	2.362	28	87	.048
12.43	2.689	28	80	.048
13.76	.003	36	175	.061
13.76	.347	38	175	.065
13.76	.681	36	169	.061
13.76	1.011	40	159	.068
13.76	1.348	36	158	.061
13.76	1.688	42	134	.071
13.76	2.022	37	109	.063
13.76	2.355	31	85	.053
13.76	2.696	26	72	.044
13.76	3.029	19	73	.032

APPENDIX 4

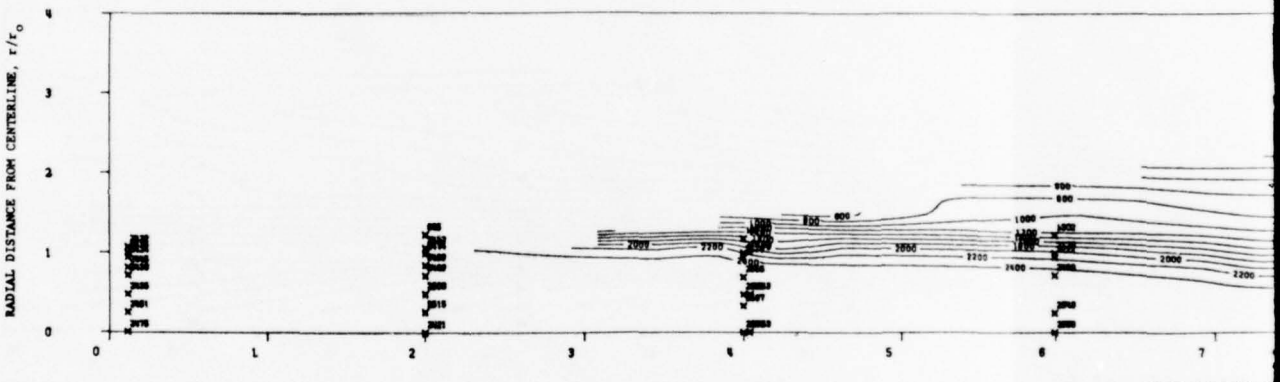
- Contour Plots of Mean Velocity, Turbulent Velocity for C/D Shock-Free Flow

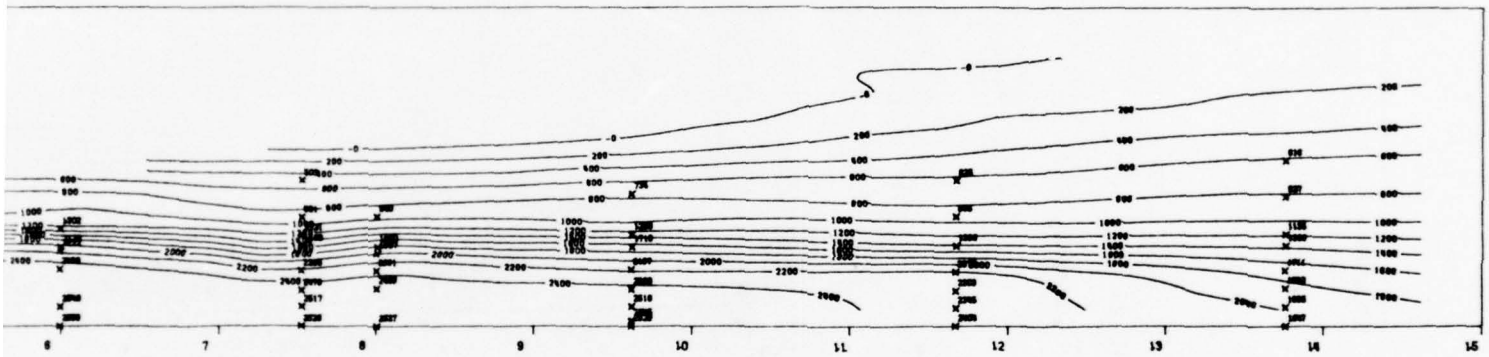
  $Mj = 1.55$, $T_T \simeq 1500°, 2500°$ R

- Contour Plots of Mean Velocity and Turbulent Velocity for a Conic Nozzle (Shocked-Flow)

  $Mj \sim 1.55$, $T_T \sim 1500°$ R

LV MEASURED MEAN VELOCITY CONTOURS (fps)
4.31" THROAT DIAMETER C/D NOZZLE
M_j = 1.55
T_{T_8} = 1427 °R
P_{T_8}/P_o = 3.9

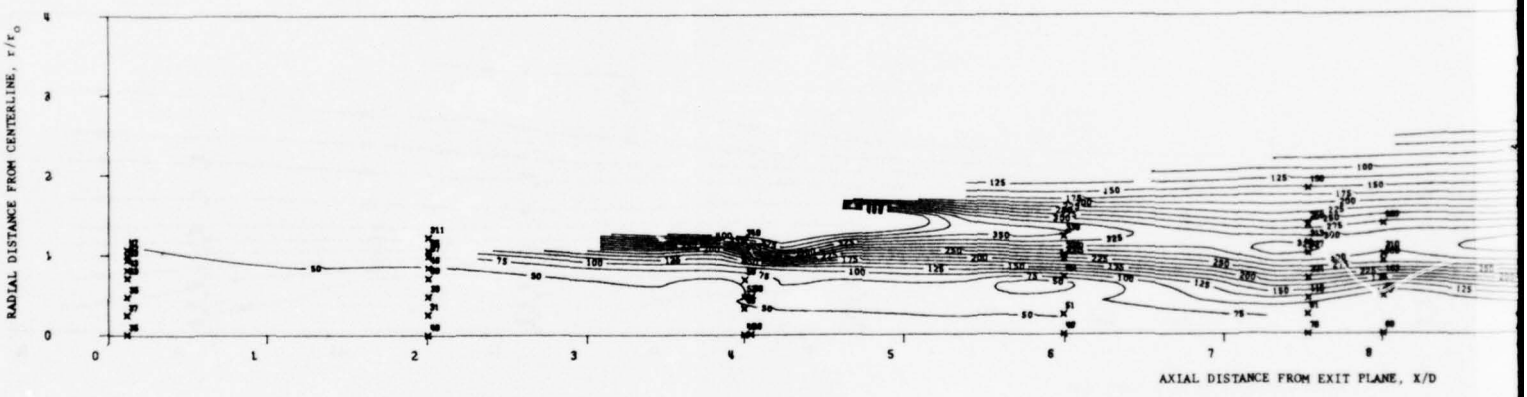


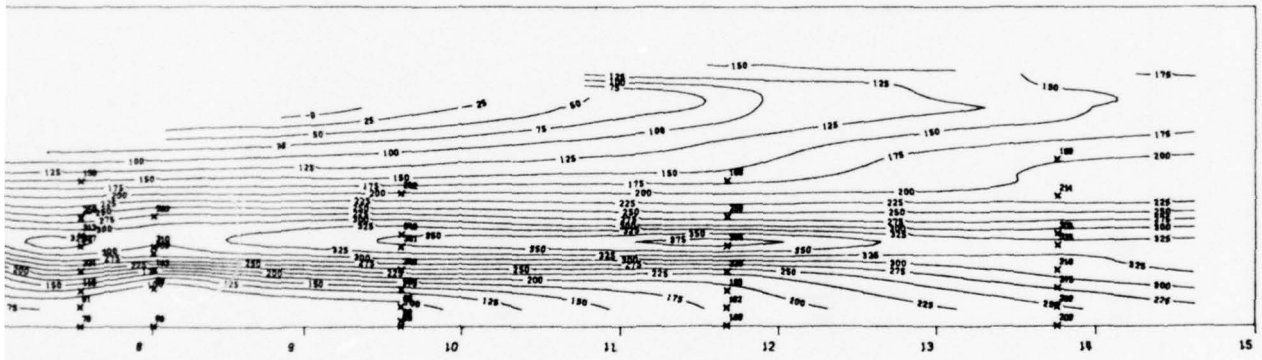


AXIAL DISTANCE FROM EXIT PLANE, X/D

PRECEDING PAGE BLANK-NOT FILMED

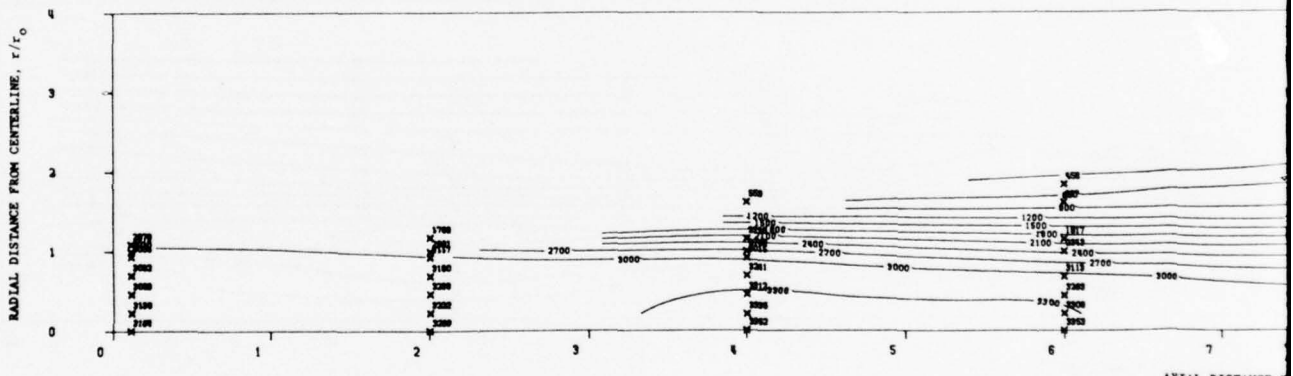
LV MEASURED TURBULENCE VELOCITY CONTOURS (fps)
4.31" THROAT DIAMETER C/D NOZZLE
M_J = 1.55
T_{T_B} = 1427°R
P_{T_B}/P_o = 3.9

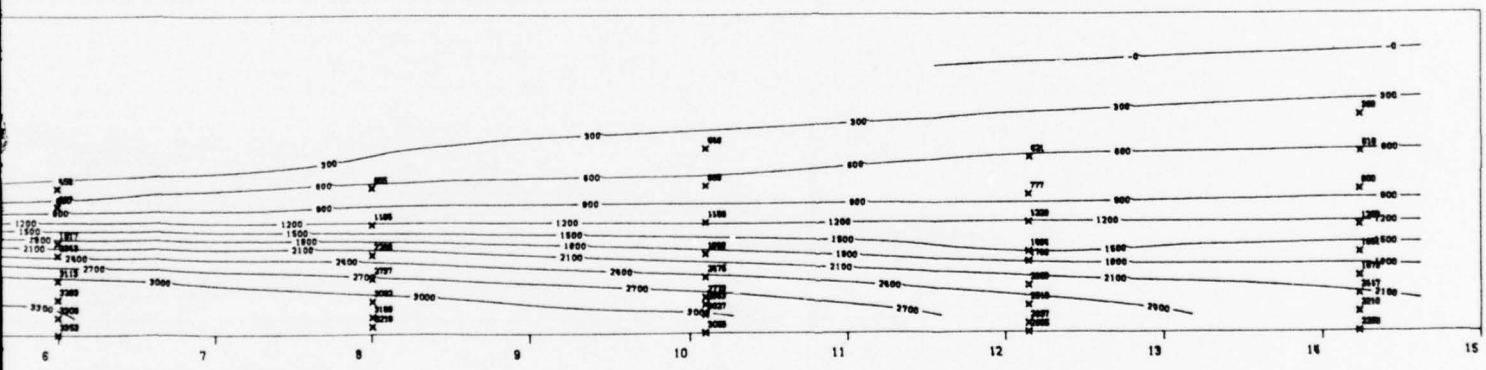




TANCE FROM EXIT PLANE, X/D

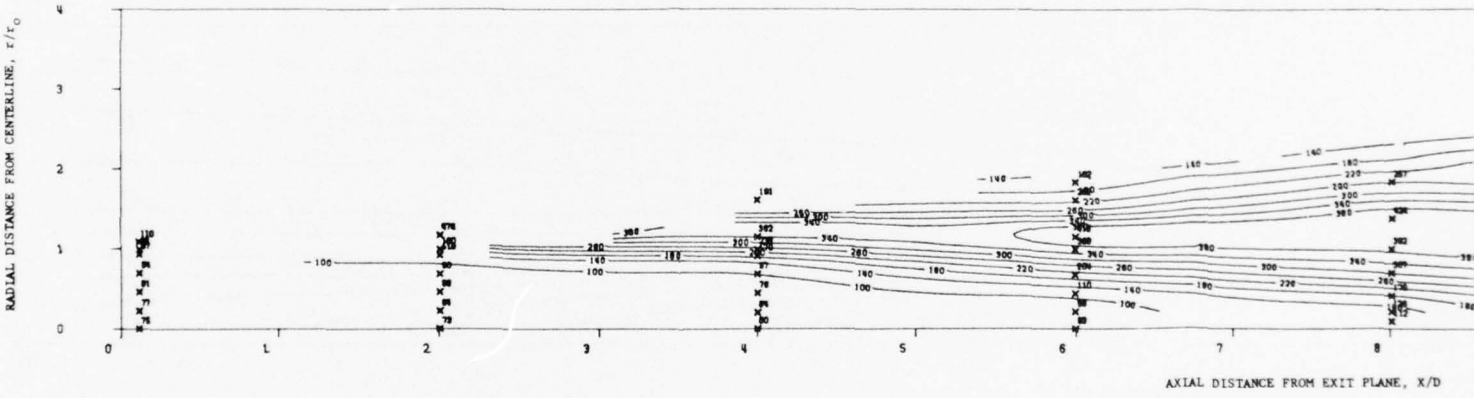
LV MEASURED MEAN VELOCITY CONTOURS (fps)
4.31" THROAT DIAMETER C/D NOZZLE
M_j = 1.56
T_{T_8} = 2402°R
P_{T_8}/P_o = 3.88

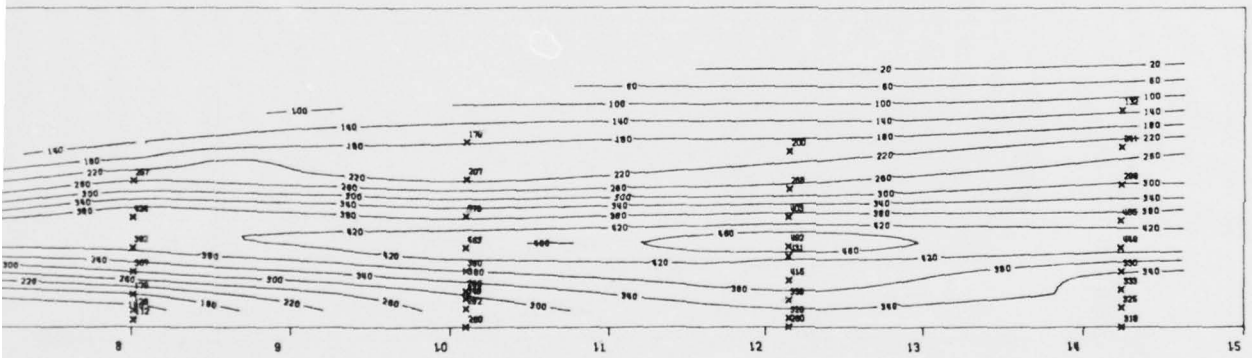




AXIAL DISTANCE FROM EXIT PLANE, X/D

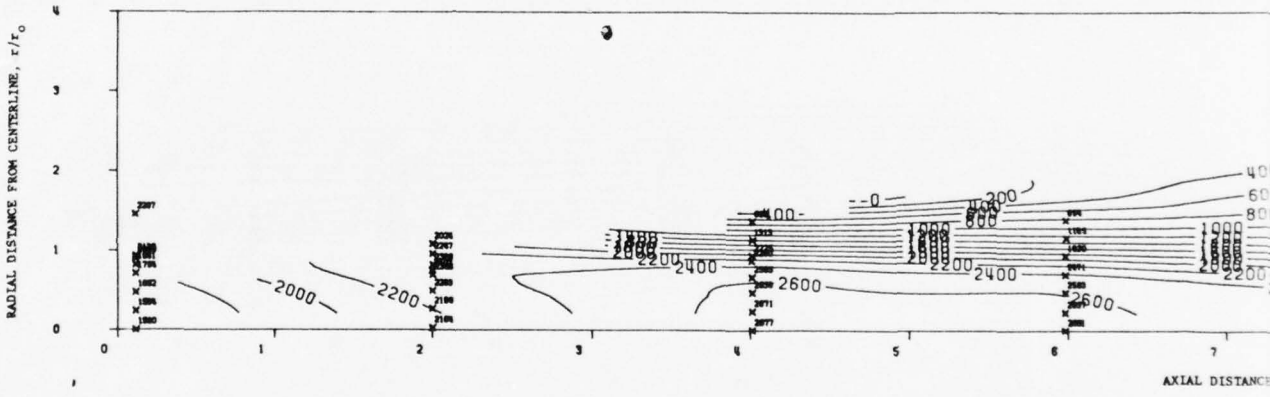
LV MEASURED TURBULENCE VELOCITY CONTOURS (fps)
4.31" THROAT DIAMETER C/D NOZZLE
$M_J = 1.56$
$T_{T_8} = 2402°R$
$P_{T_8}/P_o = 3.88$

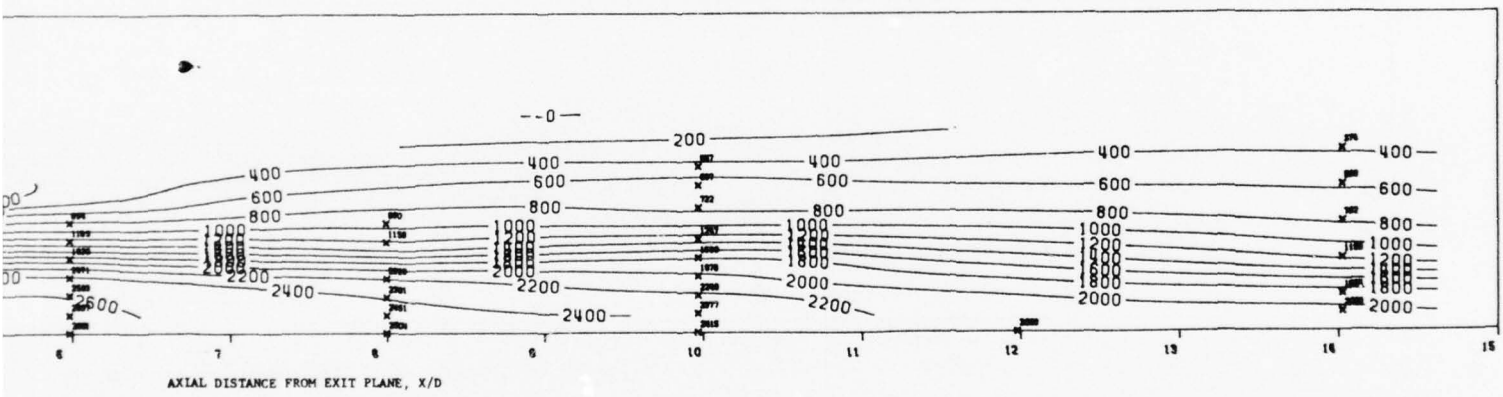




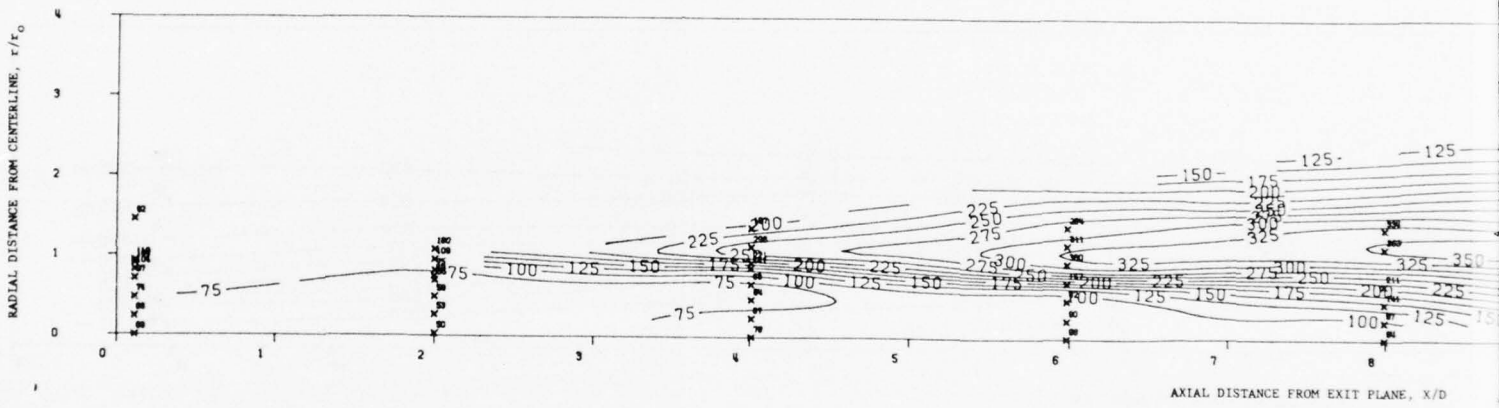
CE FROM EXIT PLANE, X/D

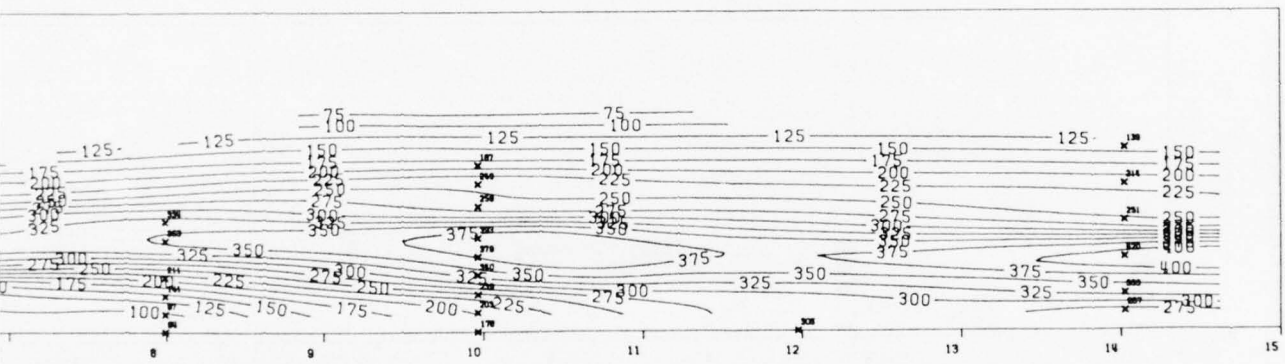
LV MEASURED MEAN VELOCITY CONTOURS
4.31" DIAMETER CONICAL NOZZLE
$M_J = 1.55$
$T_{T_8} = 1427°R$
$P_{T_8}/P_o = 3.9$




0
200
400
600
800
1000
1200
1400
1600
1800
2000
2200
2400
6
7
8
9
10
11
12
13
14
15
AXIAL DISTANCE FROM EXIT PLANE, X/D

LV MEASURED TURBULENCE VELOCITY CONTOURS (fps)
4.31" DIAMETER CONICAL NOZZLE
$M_j = 1.55$
$T_{T_8} = 1427\,^{\circ}R$
$P_{T_8}/P_o = 3.9$




75
100
125
150
175
200
225
250
275
300
325
350
375
400
8
9
10
11
12
13
14
15
DISTANCE FROM EXIT PLANE, X/D

APPENDIX 5

GROUND REFLECTION CORRECTION FOR CROSS-CORRELATION MEASUREMENTS

We have that:

$$R_{v2_\rho 1}(\tau) = R_{v2_\rho}(\tau) + (1 - \varepsilon)\, R_{vp2}(\tau - \tau_o)$$

where, $\tau_o = \Delta R/C$.

If we define $S_{v2_\rho}(\omega)$ as the Fourier Transform of $R_{v2_p 1}(\tau)$,

$$S_{v2_p}(\omega) = \int_{-\infty}^{\infty} R_{v2_\rho}(\tau)\, e^{-j\omega\tau}\, d\tau$$

then,

$$S_{v2_p 1}(\omega) = S_{v2_\rho}(\omega) + (1 - \varepsilon)\, e^{-j\tau_o}\, S_{v2_p}(\omega)$$

or,

$$S_{v2_\rho}(\omega) = \frac{1}{\left[1 + (1 - \varepsilon)\, e^{-j\omega\tau_o}\right]} S_{v2_p I}(\omega).$$

Thus, we may write:

$$R_{v2_\rho}(\tau) = \int_{-\infty}^{\omega} h(u)\, R_{v2_\rho 1}(\tau - u)\, du$$

where,

$$h(u) = F^{-1}\left[\frac{j}{1 + (1 - \varepsilon)\, e^{-j\omega\tau_o}}\right]$$

Since, $o \leq \varepsilon \leq 1$, we have:

$$\left|(1 - \varepsilon)\, e^{-j\omega\tau_o}\right| \leq 1$$

so, that,

$$h(u) = F^{-1}\left[\sum_{k=0}^{\infty} (1-\varepsilon)^k \, e^{-j\omega k\tau_o}\right]$$

Performing the Fourier Transform inversion term by term,

$$h(u) = \sum_{k=0}^{\omega} (1-\varepsilon)^k \, u_o \, (u - k\tau_o)$$

and,

$$R_{v2_p}(\tau) = \sum_{k=0}^{\infty} (1-\varepsilon)^k \, R_{v2_\rho 1}\left(\tau - \frac{k\Delta R}{C}\right)$$

REFERENCES

VOLUME I

1. Benzakein, M.J., and Knott, P.R.; "Supersonic Jet Exhaust Noise," AFAPL-TR-82-52 (August 1972).

2. Knott, P.R., et al.; "Supersonic Jet Exhaust Noise Investigation," AFAPL-TR-74-25 (June 1974).

3. Rotta, J.; "Statistical Theory of Non-Homogeneous Turbulence," Part II, NASA TTF-11 696, June 1968.

4. Glushko, G.S.; "Turbulent Boundary Layer on a Flat Plate in an Incompressible Fluid," NASA TTF-10, 030, 1965.

5. Spalding, D.B., and Patankar, S.V.; Heat and Mass Transfer in Boundary Layers, Morgan-Grampian: London, 1967.

6. Heck, P.H., and Ferguson, D.R.; "Analytical Solution for Free Turbulent Mixing in Compressible Flows," AIAA Paper 71-4, 1971.

7. Heck, P.A., and Merkle, C.L.; Analytical Flow Field Analysis for Compressible Turbulent Jets. Chap. 1 of "Supersonic Jet Exhaust Noise." Benzakein, M.J., Knott, P.R.; AFAPL-TR-72-52 (August 1972).

8. Merkle, C.L.; Theoretical Developments of the Aerodynamics of Supersonic Jets. Chap. 1 of "Supersonic Jet Exhaust Noise." Knott, P.R., et al.; AFAPL-TR-74-25 (June 1974).

9. Merkle, C.L., Keith, J.S., Knott, P.R.; "Prediction of the Flow Field of Turbulent Jets," Proceedings of Heat Transfer and Fluid Mechanics (1974).

10. Knott, P.R., and Benzakein, M.J.; Analytical and Experimental Supersonic Jet Exhaust Noise Research," AIAA 73-188 (1973).

11. Ribner, H.S.; The Generation of Sound by Turbulent Jets. Advances in Applied Mechanics. New York, London: Academic Press. Volume VIII, pp. 103-182 (1964).

12. Ribner, H.S.; Canadian Aeronautical and Space Journal 14, 281-298. Turnbull Lecture. Jets and Noise (1968).

13. Grande, E.; University of Toronto Institute for Aerospace Studies TN 110 (NASA CR-840 (1967)). Refraction of Sound by Jet Flow and Temperature.

14. Mac Gregor, G.R.; Ribner, H.S., Lam, H.; Journal of Sound and Vibration 27 (4), 437-454. "Basic Jet Noise Patterns."

15. Atvars, J., Schubert, L.K., Grande E., and Ribner, H.S.; University of Toronto, Institute for Aerospace Studies. TN 109 (NASA CR-494) Refraction of Sound by Jet Flow or Temperature.

16. Ribner, H.S.; "Reflection, Transmission and Amplification of Sound by a Moving Medium," J.A.S.A. 29, p. 435 (1957).

17. Ribner, H.S.; The Question of Convection and Refraction Coupling in Jet Noise Turbulent Mixing Theories, Chap. 2, Section 3, Supersonic Jet Exhaust Noise Investigation, Knott, P.R., ed., AFAPL-TR-74-25.

18. Lush, P.A.; "Measurements of Supersonic Jet Exhaust Noise and Comparisons with Theory," Journal of Fluid Mechanics, 46, pp. 477-500 (1971).

19. Hoch, R.G., et al., "Studies of the Influence of Density on Jet Noise, presented at the First International Synposium on Air Breathing Engines, Marseille, France, June 19-23, 1972.

20. Mani, R.; "Moving Source Models for Jet Noise," Chap. II, Section 1., Supersonic Jet Exhaust Noise Investigation, Knott, P.R., ed., AFAPL-TR-74-25.

21. Phillips, O.M.; "On the Generation of Sound by Supersonic Turbulent Shear Layers," J. Fluid Mech., 9, pp. 1-28 (1960).

22. Ffowcs -Williams, J.E.; Phil. Trans. Roy. Soc. A., 255, 469.

23. Ribner, H.S.; Energy Flux from an Acoustic Source Contained in a Moving Fluid Element and its Relation to Jet Noise, J.A.S.A., 32 (9), 1159.

24. Ribner, H.S.; Aerodynamic Sound from Fluid Dilitations: A Theory of the Sound from Jets and Other Flows. JTIAS No. 86.

25. Powell, A.; "Concerning the Noise of Turbulent Jets," J.A.S.A., 32, 1609.

26. Csanady, G.T.; "The Effect of Mean Velocity Variations on Jet Noise," Journal of Fluid Mechanics, 26, pp. 183-187 (1960).

27. Davies, P.A.O.L., et al.; "The Characteristics of the Turbulence in the Mixing Region of a Round Jet," J. Fluid Mechanics, 15, 337. (1069).

28. Lilley, G.M.; AFAPL-TR-72-53, Vol. IV (1972).

29. Goldstein, M.E., Howes, W.L.; "New Aspects of Subsonic Aerodynamic Noise Theory," NASA TN-D-7158.

30. Jones, I.S.F.; "Aerodynamic Noise Dependent on Mean Shear," J. Fluid Mechanics, 33, (1), 65.

31. Gottlieb, P.; J.A.S.A., 32 (3), 117.

32. Mollo-Christenson, E., Narasimha, R.J.; "Sound Emission from Jets at High Subsonic Velocities," J. Fluid Mechanics 8, (1), 49.

33. Berman, C.H.; Noise from Turbulent Flows, AIAA 74-2.

34. Ribner, H.S.; "Quadrupole Correlations Governing the Pattern of Jet Noise," J. of Fluid Mechanics, 38, 1969.

35. Ahuja, K.K., and Bushell, K.W.; "An Experimental Study of Subsonic Jet Noise and Comparison with Theory," J. Sound and Vibration, 30 (3), 317.

36. Nagamatsa, H.T., Sheer, R.E.; Advanced Fluid Probe Developments, Chap. VI, Supersonic Jet Exhaust Noise Investigation, Benzakein, M.J., Knott, P.R., eds., AFAPL-TR-72-52 (August 1972).

37. Mossey, P.W., Asher, J.A., Knott, P.R.; Differential Laser Velocimeter Investigation, Chap V, Supersonic Jet Exhuast Noise Investigations, Benzakein, M.J., Knott, P.R., eds., AFAPL-TR-72-52 (August 1972).

38. Knott, P.R., Mossey, P.W.; Laser Velocimeter Measurements in High Speed High Temperature Jet Exhausts, Proceedings of the 1974 Purdue Laser Velocimeter Workshop, March 1974.

39. Scott, P.F.; Theory and Implementation of the Laser Velocimeter Turbulence Spectrum Measurements, Proceedings of the 1974 Purdue Laser Velocimeter Workshop, March 1974.

40. Scott, P., Mossey, P.A., Knott, P.R.; Laser Velocimeter Developments, Supersonic Jet Exhaust Noise Investigation, Knott, P.R., ed., Chap. IV of AFAPL-TR-74-25.

41. Lee, H.K., Ribner, H.S.; "Direct Correlation of Noise and Flow of a Jet," J.A.S.A. 52, 1280-1290 (1972).

42. Siddon, T.E.; "Proceedings of Inter-Noise 1972 Conference, October 4-6, 1972, Washington, D.C., pp. 452-457.

43. Schwartz, I.R., "Jet Noise Suppression by Swirling the Jet Flow," AIAA 73-1003, October 1973.

VOLUME II

44. Lighthill, M.J.; 1952 Proceedings of the Royal Society A211, 564-587. "On Sound Generated Aerodynamically. I. General Theory."

45. Lighthill, M.J.; 1954 Proceedings of the Royal Society A222, 1-32. "On Sound Generated Aerodynamically. II. Turbulence as a Source of Sound."

46. Lighthill, M.J.; 1962 Proceedings of the Royal Society A267, No. 1329. 147-182. The Bakerian Lecture 1961. "Sound Generated Aerodynamically."

47. Ahuja, K.K. and Bushell, K.W.; "An Experimental Study of Subsonic Jet Noise and Comparison with Theory," J. Sound and Vibration, 30 (3), 317.

48. Hoch, R.G., et al.;"Studies of the Influence of Density on Jet Noise," J. Sound and Vibration, 28 (4), 649.

49. Eldred, K.M., et al.;"Suppression of Jet Noise with Emphasis on the Near Field," ASD-TDR-62-578.

50. Tester, B.J., and Burrin, R.H.; "On Sound Radiation from Sources in Parallel Sheared Jet Flows," AIAA Paper 74-57.

51. Berman, C.H.;"Noise from Variation from Turbulent Flows," AIAA 74-2.

52. Ribner, H.S.; "Energy Flux from an Acoustic Source Contained in a Moving Fluid Element and its Relation to Jet Noise," (1960), J.A.S.A., 32 (9), 1159.

53. Ribner, H.S.;"Aerodynamic Sound from Fluid Dilatation. A Theory of the Sound from Jet and Other Flows," (1962), UTIAS Report No. 86.

54. Mani, R.;"The Jet Density Exponent Issued for the Noise of Heated Subsonic Jets," J. Fluid Mechanics, 64 (3), 611.

55. Lee, H.K., and Ribner, H.S.; "Direct Correlation of Noise and Flow of a Jet," J.A.S.A., 52 (5), Part I, 1280.

56. Lighthill, M.J., Introduction to Fourier Analysis and Generalized Functions, Cambridge (1959).

57. Bushell, K.W.; "A Survey of Low Velocity and Coaxial Jet Noise with Application to Prediction," J. Sound and Vibration, 17, 271.

58. Tanna, H.K., et al.; "Effect of Temperature on Supersonic Jet Noise," AIAA 73-991.

59. Hoch, R.G., et al.; J. Sound and Vibration, 28 (b), 649.

60. Hoch, R.G.; (1974), Private Communication.

61. Lighthill, J.M.; 1963 American Institute of Aeronautics and Astronautics Journal. I. 1507-1517. Wright Brothers Lecture. Jet Noise.

62. Schubert, L.K.; 1972 Journal of the Acoustical Society of America 51, 447-463. "Numerical Study of Sound Refraction by a Jet Flow. II. Wave Acoustics."

63. Lilley, G.M., Morris, P.J., and Tester, B.J.; 1973 AIAA Paper No. 73-987. "On the Theory of Jet Noise and its Application."

64. Mani, R.; 1972 Journal of Sound and Vibration 25, 337-347. "A Moving Source Problem Relevant to Jet Noise."

65. Mani, R.; 1974, The Influence of the Flow on Jet Noise. Part I: The Noise of Unheated Jets. Part II. The Noise of Heated Jets. Sec I VIII, pp. 103-182.

66. Pao, S.P., and Lowson, M.V.; 1969 Wyle Laboratories - Research Staff, Report WR 68-21, prepared for NASA. "Spectral Techniques in Jet Noise Theory."

67. Goldstein, M.E., and Rosenbaum, B.M.; 1972 NASA TN D-6939. "Emission of Sound from Axisymmetric Turbulence Convected by a Mean Flow with Application to Jet Noise."

68. Morris, P.J.; 1972 Institute for Aerospace Studies, University of Toronto (unpublished). "Hot Wire-Microphone Cross-Correlation Based on Ribner's Source Terms, to Indicate Separately the Shear-Noise and Self-Noise Contributions to Jet Noise."

69. Seiner, J.M., and Reethof, G.; 1974 AIAA Paper No. 74-4. "On the Distribution of Source Coherency in Subsonic Jets."

70. Mollo-Christensen, E., Kolpin, M.A., Martucelli, J.R.; (1963) Mass. Inst. of Tech., Aeroelastic and Struct. Res. Lab., ASRL-TR-1007. "Experiments on Jet Flows and Jet Noise Farfield Spectra and Directivity Patterns."

71 Ahuja, K.K.; 1972 M. Phil. Thesis, University of London. "An Experimental Study of Subsonic Jet Noise with Particular Reference to the Effect of Upstream Disturbances."

72. Chu, W.T.; (1974) Dept. of Aerospace Engineering, University of Southern California. (Unpublished narrow band measurements of jet noise, carried out in U.S.C. anechoic jet facility.)

73. Proudman, I.; 1952 Proceedings of the Royal Society A214, 119-132. "The Generation of Noise by Isotropic Turbulence."

74. McCartney, J.R.; (1974) J. Sound and Vibration. "Ratio of Peak Frequencies of Jet Self and Shear Noise Spectra."

75. Powell, Alan.; 1960 Program, 59th Meeting of the Acoustical Society of America, Providence, Rhode Island, June 9-11, Paper 05 (Abstract). "Fundamental Notions Concerning Convection of Aerodynamic Noise Generators."

76. Ribner, H.S.; 1960 Journal of the Acoustical Society of America 32, 1159-1160. "Energy Flux from an Acoustic Source Contained in a Moving Fluid Element and its Relation to Jet Noise."

77. Benzakein, M.J., Chen, C.Y., and Knott, P.R.; 1971 AIAA Paper No. 71-583. "A Computational Technique for Jet Aerodynamic Noise."

78. Knott, P.R., Chen, C.Y.; 1972 Ch. II. Analytical Acoustic Model Developments for Supersonic Farfield Jet Noise in Supersonic Jet Exhaust Noise, Benzakein, M.J., and Knott, P.R., Ed., General Electric Co., Aircraft Engine Group, sponsored by Air Force Aero Propulsion Lab. Report, AFAPL-TR-72-52, pp. 118-179.

79. Chen, C.Y., 1973 Ph. D. Thesis, Dept. of Mechanical Engineering, Univ. of Cincinnati. "Investigation of Far Field and Near Field Jet Noise."

80. Tam, C.K.W.; 1972, "On the Noise of a Nearly Ideally Expanded Stability in Edgetone Generation," AIAA J., Vol. 12, p. 1457.

81. Betchov, R., and Criminale, W.O., Jr.; 1967, Stability of Parallel Flows, Academic Press, New York.

82. Crow, S.C., and Champagne, F.H.; 1971, "Orderly Structure in Jet Turbulence," JFM, Vol. 48, p. 547.

83. Berman, C.H., Ffowcs-Williams, J.E.; "Instability of a Two Dimensional Compressible Jet," JFM, 42 (1), p. 151.

84. Hussain, A.K.M.F., and Reynolds, W.C.; 1970, "The Mechanics of an Organized Wave in Turbulent Shear Flow," JFM, Vol. 41, p. 241.

85. Reynolds, W.C., and Hussain, A.K.M.F., 1972, "The Mechanics of an Organized Wave in Turbulent Shear Flow. Part 3. Theoretical Models and Comparisons with Experiment," JFM, Vol. 54, p. 263.

86. Liu, J.T.C.; 1974, "Developing Large-Scale Wavelike Eddies and the Near Jet Noise Field," JFM, Vol. 62, p. 437.

87. Ko, D.R.S., Kubota, T., and Lees, L.; 1970, "Finite Disturbance Effect in the Stability of a Laminar Incompressible Wake behind a Flat Plate," JFM, Vol. 40, p. 315.

88. Ko, D.R.S., 1971, "Integral Theory for the Instability of Laminar Compressible Wakes behind Slender Bodies," AIAA J., Vol. 9, p. 1777.

89. Lin, C.C., 1955, Theory of Hydrodynamic Stability, Cambridge University Press.

90. Morris, P.J.; 1974, "A Model for the Orderly Structure of Turbulence as a Source of Noise," AIAA Paper 74-1.

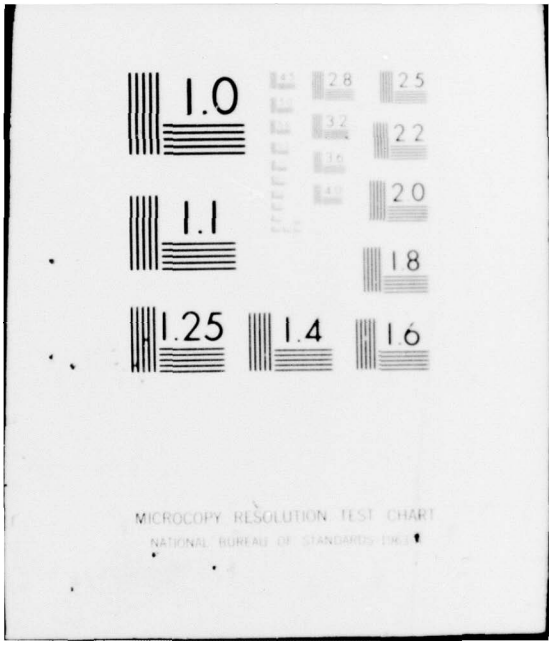
91. Liu, J.T.C.; 1971, "On Eddy-Mach Wave Radiation Source Mechanism in the Jet Noise Problem," AIAA Paper 71-150.

AD-A038 613 GENERAL ELECTRIC CO CINCINNATI OHIO AIRCRAFT ENGINE GROUP F/G 20/1
SUPERSONIC JET EXHAUST NOISE INVESTIGATION. VOLUME II. TECHNICA--ETC(U)
JUL 76 P R KNOTT, R MANI, C L MERKLE F33615-73-C-2031
UNCLASSIFIED R74AEG452-VOL-2 AFAPL-TR-76-68-VOL-2 NL

5 OF 5
AD
A038613



END
DATE
FILMED
5-77


1.0
1.1
1.25
1.4
1.6
2.8
2.5
3.2
2.2
3.6
2.0
4.0
1.8
MICROCOPY RESOLUTION TEST CHART
NATIONAL BUREAU OF STANDARDS 1963-A

92. Woolley, J.P., and Karamcheti, K.; "Role of Jet Stability in Edgetone Generation," AIAA Journal, Vol. 12, No. 11, 1974, pp. 1457-1458.

93. Bishop, K.A., Ffowcs-Williams, J.F., and Smith, W.; 1971, "On the Noise of the Unsuppressed High-Speed Jet," JFM, Vol. 50, p. 21.

94. Michalke, A., "The Production of Sound by Amplified Disturbances in Free Shear Layers," Royal Aircraft Establishment LT-1517, 1970.

95. Chan, Y.Y.; 1974, "Spatial Waves in Turbulent Jets," Phys. of Fl., Vol. 17, No. 1, p. 46.

96. McLaughlin, D.K., and McColgan, C.J.; 1974, "Hot-Wire Measurements in a Supersonic Jet at Low Reynolds Numbers," AIAA J., Vol. 12, p. 1279.

97. Fuchs, H.V.; 1972, "Space Correlations of the Fluctuating Pressure in Subsonic Turbulent Jets," J. Sound and Vibration, Vol. 23, p. 77.

98. Scharton, T.D., and White, P.H.; 1972, "Simple Pressure Source Model of Jet Noise," J. Acoust, Soc. Am., Vol. 52, No. 1.

99. No, N.W.M., and Davies, P.O.A.L.; 1971, "The Near Field within the Potential Cone of Subsonic Cold Jets," JFM, Vol. 50, p. 49.

100. Lilley, G.M., Morris, P.J., and Tester, B.J.; 1973, "On the Theory of Jet Noise and its Applications," AIAA Paper 73-987.

101. Rose, W.G.; "A Swirling Round Turbulent Jet," Journal of Applied Mechanics, Vol. 29, December 1962, pp. 616-625.

102. Chigier, N.A., and Beér, J.M.; "Velocity and Static Pressure Distributions in Swirling Air Jets Issuing from Annular and Divergent Nozzles," Journal of Basic Engineering, Vol. 86, December 1964, pp. 788-798.

103. Kerr, N.M., and Fraser, D.; "Swirl, Part I: Effect on Axisymmetrical Turbulent Jets," Journal of the Institute of Fuel, Vol. 38, December 1965, pp. 519-526.

104. Chigier, N.A., and Chervinsky, A.; "Experimental Investigation of Swirling Vortex Motion in Jets," Journal of Applied Mechanics, Vol. 34, June 1967, pp. 443-451.

105. Pratte, B.D., and Keffer, J.F.; "The Swirling Turbulent Jet," Journal of Basic Engineering, Vol. 94, December 1972, pp. 739-748.

106. Chigier, N.A., and Chervinsky, A.; "Aerodynamic Study of Turbulent Burning Free Jets with Swirl," Eleventh International Symposium on Combustion. The Combustion Institute, Pittsburgh, Pa., 1967, pp. 489-499.

107. Chervinsky, A.; "Turbulent Swirling Jet Diffusion Flames," AIAA Journal, Vol. 7, October 1969, pp. 1877-1883.

108. Schwartz, I.R.; "Effects of Rotating Flows on Combusion and Jet Noise," AIAA Paper 72-645, June 1972 (or, see "A Preliminary Investigation of Combustion with Rotating Flow in an Annular Combustion Chamber," NACA RM L51E25a, 1951).

109. Schwartz, I.R.; "Jet Noise Suppression by Swirling the Jet Flow," AIAA Paper 73-1003, October 1973.

110. Norton, D.J., Farquhar, B.W., and Hoffman, J.D.; "An Analytical and Experimental Investigation of Swirling Flow in Nozzles," AIAA Journal, Vol. 7, October 1969, pp. 1992-2000.

111. Baker, V.D., Johnson, R.A., Brasket, R.G., and Lamb, O.P.; "Experimental Results with Lift Engine Exhaust Nozzles," AIAA Paper 65-574, June 1965.

112. Boussinesq, J.; "Théorie de l'écoulement Tourbillant," Mém prés Acad Sci, Vol. 23, 1877, p. 46.

113. Prandtl, L.; "Bericht Über Untersuchungen zur ausgebildeten Turbulenz," ZAMM, Vol. 5, 1925, pp. 136-139.

114. Prandtl, L.; "Über ein neues Fromelysystem der ausgebildeten Turbulenz," Nachr. Akad. Wiss. Gottingen, 1945, pp. 6-19.

115. Kolmogorov, A.N.; "Equations of the Turbulent Motion of an Incompressible Turbulent Fluid," Izv. Akad. Nauk. SSSR, Ser. Phys. VI, 1942, pp. 56-58.

116. Launder, B.E., and Spalding, D.B.; Mathematical Models of Turbulence, Academic Press, 1972.

117. Birch, S.G., Rudy, D.H., and Bushnell, D.M., (Eds.), "Free Turbulent Shear Flows, Volume I - Conference Proceedings," NASA SP-321, 1973.

118. Spalding, D.B., et al.; "Turbulent Mixing in Combustion Chambers," Northern Research and Engineering Corporation, Report No. 1118-1, October 1966.

119. Benzakein, M.J., Chen, C.Y., and Knott, P.R.; "A Computational Technique for Jet Aerodynamic Noise," AIAA Paper 71-583, June 1971.

120. Rubel, A.; "Swirling Jet Turbulent Mixing and Combustion Computations," NASA CR-2231, March 1973.

121. Koosinlin, M.L., Launder, B.E., and Sharma, B.I.; "Prediction of Momentum Heat and Mass Transfer in Swirling Turbulent Boundary Layers," AIAA Paper 74-703 (also ASME Paper 74-HT-23), July 1974.

122. Lilley, D.G.; "Prediction of Inert Turbulent Swirl Flows," AIAA Journal, Vol. 11, July 1973, pp. 955-960.

123. Koosinlin, M.L., and Lockwood, F.C.; "The Prediction of Axisymmetric Turbulent Swirling Boundary Layers," AIAA Journal, Vol. 12, April 1974, pp. 547-554.

124. Lilley, D.G., and Chigier, N.A.; "Nonisotropic Turbulent Shear Stress Distribution in Swirling Flows from Mean Value Distributions," International Journal of Heat and Mass Transfer, Vol. 14, 1971, pp. 573-585.

125. Kazin, S.B., and Matta, R.K., (Eds); "Core Engine Noise Control Program, Volume II - Identification of Noise Generation and Suppression Methods," Federal Aviation Administration FAA-RD-74-125, II, December 1974.

126. Ortwerth, P.J.; "Mechanism of Mixing of Two Nonreacting Gases," Air Force Aero Propulsion Laboratory AFAPL-TR-71-18, October 1971.

127. Ortwerth, P.J.; "Mechanism of Mixing of Two Nonreacting Gases," AIAA Paper 71-725, June 1971.

128. Kushida, R., and Rupe, J.; "Effect on Supersonic Jet Noise of Nozzle Plenum Pressure Fluctuations," AIAA Journal, Vol. 10, July 1972, pp. 946-948.

129. Platt, E.G., and Summerfield, M.; "Jet Engine Exhaust Noise Due to Rough Combustion and Nonsteady Aerodynamic Sources," Journal of the Acoustical Society of America, Vol. 56, August 1974, pp. 516-522.

130. Schubert, L.K.; "Numerical Study of Sound Refraction by a Jet Flow, I. Ray Acoustics," Journal of the Acoustic Society of America, 51, 1972, pp. 439-446.

131. Schubert, L.K.; "Numerical Study of Sound Refraction by a Jet Flow, II. Wave Acoustics," Journal of Acoustic Society of America, 51, 1972, pp. 447-463.

132. Bilwakesh, K.R., Kazin, S.B., Matta, R.K., et al.; "Core Engine Nnise Control Program, Vol. II - Identification of Noise Generation and Suppression Mechanisms," General Electric Company, DOT/FAA Report No. FAA-RD-74-125, III.

133. Hayden, Richard E.; "Noise from Interaction of Flow with Rigid Surfaces: A Review of Current Status of Prediction Techniques," Bolt, Beranek and Newman Report No. 2276.

134. Sharland, I.J.; "Sources of Noise in Axial Flow Fans," Journal Sound Vibration, 1 (3), 1964, pp. 302-322.

135. Gordon, Colin G.; (a) "Spoiler-Generated Flow Noise. I. The Experiment," Journal Acoustic Society, America, 43 (5), May 1968.

136. Paterson, R.W., Vogt, P.G., Fink, M.R., and Munch, C.L.; "Vortex Noise of Isolated Airfoils," Paper 72-656, AIAA 5th Fluid and Plasma Dynamics Conference, Boston, 1972.

137. Crow, S.C.; "Acoustic Grain of a Turbulent Jet," American Physical Society, T.G. 25th Annual Meeting of the Division of Fluid Dynamics, November 20-22, 1972.

138. Benzakein, M.S., Knott, P.R., "Supersonic Jet Noise," AFAPL-TR-72-52 (August 1972).

139. Knott, P.R., et al.; "Supersonic Jet Exhaust Noise Investigation," AFAPL-TR-74-25 (June 1974).

140. Wooldridge, C.E., Wooyen, D.C., Amaro, A.S., "The Structure of Jet Turbulence Producing Jet Noise," Stanford Research Institute Annual Report, June 1971.

141. Knott, P.R., Mossey, P.W.; "Laser Velocimeter Measurements in High Speed High Temperature Jet Exhausts,"Proceedings of the 1974 Purdue Laser Velocimetry Workshop, March 1974.

142. Scott, P.F.; "Theory and Implementation of Laser Velocimeter Turbulence Spectrum Measurements,"Proceedings of the 1974 Purdue Laser Velocimeter Workshop, March 1974.

143. Meecham, W.C.; "On the Sample - Source Theory of Sound from Statistical Turbulence," Journal of Statistical Physics, Vol. 8, No. 2, 1973.

144. Siddon, T.E.; "Fluctuating Pressure Probe/Design and Calibration," Bolt, Beranek and Newman Report, July 1971.

145. Hurdle, P.M., Meecham, W.C.; "Investigation of the Aerodynamic Noise Generating Region of a Jet Engine by Means of the Simple Source/Fluid Dilatation Model," JASA, March 1974.

146. Papooulis, A.; Probability, Randoni Variables and Stochastic Processes, McGraw-Hill, 1965.

147. Papoulis, A.; Fourier Transform and its Application, McGraw-Hill, 1962.

VOLUME III

148. Townsend, A.A.; The Structure of Turbulent Shear Flow, Cambridge Press, 1956.

149. Hinze, J.O.; Turbulence, McGraw-Hill Book Company, 1959.

150. Corrisin, S.; "Local Isotropy in Turbulent Shear Flow," NACA RM58B11, May 1958.

151. Bradshaw, P., Feriss, D.H., and Atwell, N.P.; "Calculation of Boundary Layer Development Using the Turbulent Energy Equation," Journal of Fluid Mechanics, Vol. 28, Pt. 3, 1967, p. 593.

152. Mellor, G.L., and Herring, H.J.; "Two Methods of Calculating Turbulent Boundary Layer Behavior Based on Numerical Solutions of the Equations of Motion," Proceedings - Conference on Computation of Turbulent Boundary Layer Prediction, Stanford University, 1968.

153. Harsha, P.T.; "Free Turbulent Mixing: A Critical Evaluation of Theory and Experiment," in AGARD-CP-93, January 1972.

154. Kelly, J.T.; "Multiple Underexpanded Plume Computational Technique Including Turbulent Mixing and Non-Equilibrium Chemistry," AIAA Paper 73-695, 1973.

155. Edelman, R.B., and Weilerstein, G.; "A Solution of the Inviscid-Viscous Equations with Applications to Bounded and Unbounded Multi-Component Reacting Flows," AIAA Paper 69-83, 1969.

156. Chen, C.Y.; "Estimation of Jet Noise," General Electric Co., R72AEG341, December 1972.

APPENDIX 1

157. Bradshaw, P., and Ferriss, D.H.; "Calculation of Boundary-Layer Development Using the Turbulent Energy Equation. II - Compressible Flow on Adiabatic Walls," NPL Aero Report 1217, 1966.

158. Mellor, G.L., and Herring, H.J.; "A Method of Calculating Compressible Turbulence Boundary Layers," NASA CR-1144, September 1968.

159. Ollerhead, J.B.; "On the Prediction of Nearfield Noise of Supersonic Jets," NASA CR-857, August 1967.

160. Spalding, D.B., and Patankar, S.V.; Heat and Mass Transfer in Boundary Layers, Morgan-Grampian, London, 1967.

161. Laurence, J.C.; "Intensity, Scale and Spectra of Turbulence in Mixing Region of a Free Subsonic Jet," NACA Report 1292, 1956.

APPENDIX 2

162. Averenkova, G.I., Ashratov, E.A., and Volkonskaia, T.G.; "Investigation of the Parameters of Axisymmetric Underexpanded Ideal Gas Jets," Vychislitelnye Metody: Programmirovanie, No. 15, Moscow Univ. Press, pp. 92-101, 1970.

163. MacCormack, R.W., and Paullay, A.J.; "Computational Efficiency Achieved by Time Splitting of Finite Difference Operators," AIAA Paper 72-154, 1972.

164. Richtmyer, R.D., and Morton, K.W.; Difference Methods for Initial Value Problems, 2d. ed., Interscience, New York, 1967.

165. Moretti, G.; "The Importance of Boundary Conditions in the Numerical Treatment of Hyperbolic Equations," PIBAL Rept. 68-34, Polytechnic Institute of Brooklyn, Nov. 1968.

166. Abbett, M.J.; "Boundary Condition Calculation Procedures for Inviscid Supersonic Flow Fields," Proceedings, AIAA Computational Fluid Dynamics Conference, AIAA, New York, 1973.

167. Presley, L.L., and Kutler, P.; "Comparison of a Discrete-Shock, Finite-Difference Technique and the Method of Characteristics for Calculating Internal Supersonic Flows," Proceedings, AIAA Computational Fluid Dynamics Conference, AIAA, New York, 1973.

168. Love, E.S., Grigsby, C.E., Lee, L.P., Woodling, M.J.; "Experimental and Theoretical Studies of Axisymmetric Free Jets," NASA TR-R-6, 1959.

169. Oswatitsch, K., Gas Dynamics, Academic Press, New York, 1956.

170. Abbett, M., "The Mach Disc in Underexpanded Exhaust Plumes," AIAA Paper 70-231, 1970.

171. Fox, J.H.; "On the Structure of Jet Plumes," AIAA Journal, Vol. 12, p. 105, January, 1974.

172. Ribner, H.S.; "Connection of a Pattern of Vorticity Through a Shock Wave," NACA TN 1164, 1954.

173. Ribner, H.S.; "Shock Turbulence Interaction and the Generation of Noise," NACA TN 1233, 1955.

174. Ribner, H.S.; "Acoustic Energy Flux from a Shock-Turbulence Interaction," Journal of Fluid Mechanics, Vol. 35, p. 299, 1969.

APPENDIX 3

175. Ribner, H., et al.; "Refraction of Sound by Jet Flow or Jet Temperature," UTIAS TN 109; NACA CR 494 (1966).

176. Schubert, L.K.; "Computer Study of Refraction of Sound by Jet Flow and Jet Temperature," UTIAS Rept. 144.

177. Mani, R.; "A Moving Source Problem Relevant to Jet Noise," GE Class I Report (May 1972).

163. MacCormack, R.W., and Paullay, A.J.; "Computational Efficiency Achieved by Time Splitting of Finite Difference Operators," AIAA Paper 72-154, 1972.

164. Richtmyer, R.D., and Morton, K.W.; Difference Methods for Initial Value Problems, 2d. ed., Interscience, New York, 1967.

165. Moretti, G.; "The Importance of Boundary Conditions in the Numerical Treatment of Hyperbolic Equations," PIBAL Rept. 68-34, Polytechnic Institute of Brooklyn, Nov. 1968.

166. Abbett, M.J.; "Boundary Condition Calculation Procedures for Inviscid Supersonic Flow Fields," Proceedings, AIAA Computational Fluid Dynamics Conference, AIAA, New York, 1973.

167. Presley, L.L., and Kutler, P.; "Comparison of a Discrete-Shock, Finite-Difference Technique and the Method of Characteristics for Calculating Internal Supersonic Flows," Proceedings, AIAA Computational Fluid Dynamics Conference, AIAA, New York, 1973.

168. Love, E.S., Grigsby, C.E., Lee, L.P., Woodling, M.J.; "Experimental and Theoretical Studies of Axisymmetric Free Jets," NASA TR-R-6, 1959.

169. Oswatitsch, K., Gas Dynamics, Academic Press, New York, 1956.

170. Abbett, M., "The Mach Disc in Underexpanded Exhaust Plumes," AIAA Paper 70-231, 1970.

171. Fox, J.H.; "On the Structure of Jet Plumes," AIAA Journal, Vol. 12, p. 105, January, 1974.

172. Ribner, H.S.; "Connection of a Pattern of Vorticity Through a Shock Wave," NACA TN 1164, 1954.

173. Ribner, H.S.; "Shock Turbulence Interaction and the Generation of Noise," NACA TN 1233, 1955.

174. Ribner, H.S.; "Acoustic Energy Flux from a Shock-Turbulence Interaction," Journal of Fluid Mechanics, Vol. 35, p. 299, 1969.

APPENDIX 3

175. Ribner, H., et al.; "Refraction of Sound by Jet Flow or Jet Temperature," UTIAS TN 109; NACA CR 494 (1966).

176. Schubert, L.K.; "Computer Study of Refraction of Sound by Jet Flow and Jet Temperature," UTIAS Rept. 144.

177. Mani, R.; "A Moving Source Problem Relevant to Jet Noise," GE Class I Report (May 1972).

178. Paterson, A.R.; NATO AGARD Rept. 460 (1963).

179. Crow, S.C.; Lawrence Radiation Lab., UCRL 70189 (1966).

180. Obermeier, F.; 1967 Acustica, 18, 4, 38 (1967).

181. Pao, S.P.; "Development of a Generalized Theory of Jet Noise," AIAA J. Vol. 10, No. 5, pp. 596 (May 1972).

182. Liepmann, H.W.; "On the Acoustic Radiation from Boundary Layers and Jets," Guggenheim Aeronautical Laboratory, CIT, August 1952.

183. Laufer, M.T., Ffowcs-Williams, J.E., and Childress, S.; AGARDograph, 90 (1964).

184. Landau, L.; "Stability of Tangential Discontinuities in a Compressible Fluid," C.R. Acad. Sci., U.S.S.R. 44, pp. 139-141 (1944).

185. Sedelnikov, T. Kh.; "The Frequency Spectrum of a Supersonic Jet," NASA TT F-538, pp. 71 (1969).

186. Tam, C.K.W.; 1973, "Supersonic Jet Noise Generated by Large-Scale Disturbances," AIAA Paper 73-882.

187. Lilley, G.M.; "On the Noise from Air Jets," ARC 20, 376 (1958).

188. Maestrello, L., McDaid, E.; "Acoustic Characteristics of a High Subsonic Jet," AIAA 9, No. 6, 1058-1066 (1971).

189. Pao, S.P.; "Aerodynamic Noise Emission from Turbulent Shear Layer," JFM (1973).

190. Howes, Walton, L., Callaghen, Edmund E., Coles, Williard D., and Mull, Harold R.; "Near Noise Field of a Jet-Engine Exhaust," NACA Rept. 1338, 1957 (Supersedes NACA TN's 3763 and 3764).

191. Wolfe, M.O.W.; "Near Field Jet Noise," Report 113, NATO AGARD, April-May 1957.

192. Hermes, P.H., and Smith, D.L.; "Measurement and Analyses of the J57-P21 Noise Field," AFFDL-TDR-66-147, 1967.

193. Morgan, L.C., Sutherland, and K.J. Young; "The Use of Acoustic Scale Models for Investigating Nearfield Noise of Jet and Rocket Engines," WADD-TR-61-178, April, 1961.

194. Franken, Peter, A., and Kerwin, E.M., Jr.; "Methods of Flight Vehicle Noise Predictions," WADC-TR-58-343, November, 1958.

195. Plumblee, H.E., Ballentine, J.R., and Passinas, B.; "Near Field Noise Analyses of Aircraft Propulsion Systems with Emphasis on Prediction Techniques for Jets," WADC-TR-58-343, August, 1967.

196. Franz, G.J.; "The Near-Sound Field of Turbulence," David Taylor Model Basin, Rept. 986, AD 630684, October, 1959.

197. Chen, C.Y.; "Analytical Models for Nearfield Jet Noise Calculations," General Electric Co., AEG TM 72-349 (1972).

☆ U. S. GOVERNMENT PRINTING OFFICE: 1977 — 757-001/217